Can the Gluon Polarization in the Nucleon be Extracted from HERMES Data on Single High-p_T Hadrons?

Dissertation

Zur Erlangung des Doktorgrades
des Fachbereichs Physik
der Universität Hamburg

vorgelegt von

Patricia Liebing
aus Leipzig

Hamburg, Juni 2004

Gutachter der Dissertation:	Prof. Dr. R.-D. Heuer Prof. Dr. A. Schäfer Prof. Dr. T. Sjöstrand
Gutachterin/Gutachter der Disputation:	Prof. Dr. R.-D. Heuer Prof. Dr. B. Naroska
Datum der Disputation:	23. Juli 2004
Vorsitzender des Prüfungsausschusses:	Prof. Dr. F. W. Büßer
Vorsitzender des Promotionsausschusses:	Prof. Dr. R. Wiesendanger
Dekan des Fachbereichs:	Prof. Dr. G. Huber

Abstract

Data on double spin asymmetries of single high transverse momentum (p_T) hadrons taken with the HERMES experiment at DESY were analyzed to extract the polarized gluon density in the nucleon using additional information from a Monte Carlo model. The main focus of this work was to adapt this Monte Carlo model, PYTHIA 6, to the HERMES energy range. The gluon polarization was extracted from quasireal photoproduction data with $p_T \geq 1.35$ GeV to be

$$\frac{\Delta G}{G}\Big|^{Photo}_{\langle x_G\rangle=0.15} = 0.10 \pm 0.04(\text{stat.}) \pm 0.01(\text{exp. syst.})^{+0.07}_{-0.14}(\text{model syst.}).$$

and from semi-inclusive data with $p_T \geq 1$ GeV to be

$$\frac{\Delta G}{G}\Big|^{semi}_{\langle x_G\rangle=0.16} = -0.09 \pm 0.10(\text{stat.}) \pm 0.01(\text{exp. syst.})^{+0.02}_{-0.16}(\text{model syst.}). \quad (1)$$

The large statistics of the quasireal photoproduction data facilitated the study of the p_T dependence of the gluon polarization. Inconsistencies in the results obtained from independent data samples on positive and negative hadrons and on negative hadrons from proton and deuteron targets were observed. The possible reasons, most likely lying in an incomplete description of the data by the Monte Carlo were discussed.

Kurzfassung

Doppelspin-Asymmetrien von inklusiven Hadronen mit hohem Transversalimpuls (p_T), gemessen mit dem HERMES Experiment am DESY, wurden analysiert und gemeinsam mit Informationen eines Monte Carlo Modells genutzt, um die polarisierte Gluonendichte des Nukleons zu extrahieren. Der Hauptanteil der Arbeit bestand in der Adaption des Monte Carlo Modells, PYTHIA 6, an den energetischen Bereich von HERMES. Die Gluon-Polarisation von Daten in quasi-reeller Photoproduktion mit $p_T \geq 1.35$ GeV ist

$$\frac{\Delta G}{G}\Big|^{Photo}_{\langle x_G\rangle=0.15} = 0.10 \pm 0.04(\text{stat.}) \pm 0.01(\text{exp. syst.})^{+0.07}_{-0.14}(\text{model syst.}),$$

und die von semi-inklusiven Daten mit $p_T > 1$ GeV ist

$$\frac{\Delta G}{G}\Big|^{semi}_{\langle x_G\rangle=0.16} = -0.09 \pm 0.10(\text{stat.}) \pm 0.01(\text{exp. syst.})^{+0.02}_{-0.16}(\text{Modell syst.}). \quad (2)$$

Mit der hohen Statistik der Photoproduktionsdaten konnte die p_T Abhängigkeit der Gluonenpolarisation untersucht werden. Es wurden Inkonsistenzen festgestellt zwischen den Ergebnissen für unabhängige Datensätze von positiven und negativen Hadronen, und für negative Hadronen von Proton- und Deuterontargets. Die möglichen Ursachen, die wahrscheinlich in einer unvollständigen Beschreibung der HERMES Daten durch das Monte Carlo liegen, wurden diskutiert.

Contents

Introduction **i**

1 The HERMES Experiment at HERA **1**
1.1 The Beam Polarization and its Measurement 1
1.2 The Internal Gas Target 3
1.3 The Spectrometer 6
1.3.1 The Spectrometer Magnet 6
1.3.2 The Tracking Devices 6
1.3.3 The Particle Identification (PID) Devices 8
1.3.3.1 The PID algorithm 12
1.3.4 Luminosity Measurement and Trigger 13

2 Theoretical Issues and Motivation **15**
2.1 Kinematics and Cross Section in Deep Inelastic Scattering 15
2.1.1 Cross Sections and Asymmetries in Lepton-Nucleon Scattering 16
2.1.2 Virtual Photon Cross Sections and Asymmetries 19
2.2 Structure Functions in the Simple Quark-Parton Model 20
2.3 The Quark-Parton Model in QCD 22
2.3.1 Scaling Violations of Structure Functions 22
2.3.2 Factorization of Structure Functions in QCD 26
2.3.3 Extraction of Parton Distributions 27
2.3.4 Renormalization and Factorization Schemes 29
2.3.5 Applicability of Perturbative QCD 30
2.4 Semi-inclusive DIS and Fragmentation Functions 30
2.5 Photoproduction and Photon Physics 33
2.5.1 The Photon Structure in Perturbative QCD 34
2.5.2 Soft Photoproduction and Vector Meson Dominance 37
2.6 DIS Sum Rules and the Spin Crisis 41
2.7 Direct Measurements of the Gluon Polarization 46
2.7.1 Heavy Flavor Production 46
2.7.2 Prompt Photon Production 48
2.7.3 High-p_T Jet Production 50
2.7.4 High-p_T Hadron Pair Production 51
2.7.5 Inclusive High-p_T Hadron production 55

3 Data Analysis **58**
3.1 HERMES Data Structure and Data Quality . . . 58
3.1.1 Data Quality for Unpolarized Data . . . 59
3.1.2 Data Quality for Double Spin Asymmetries . . . 59
3.1.3 Time Dependence of Yields . . . 60
3.2 Double Spin Asymmetries of High-p_T Hadrons . . . 63
3.2.1 Kinematic Regions and Cuts . . . 63
3.2.2 Extraction of Double Spin Asymmetries . . . 64
3.2.3 Results for the Raw Asymmetries . . . 65
3.2.4 Possible Sources of Background: Charge Symmetric Events . . . 67
3.2.5 Possible Sources of Background: Lepton/Hadron Separation . . . 69
3.2.6 Possible Sources of Background: Pion/Kaon Separation . . . 72
3.3 Systematic Studies on the Measured Asymmetries . . . 74
3.3.1 Time dependence of Asymmetries . . . 74
3.3.2 Beam Helicity . . . 75
3.3.3 Normalization Uncertainties . . . 76
3.3.4 Detector Alignment . . . 77
3.3.5 Systematic Uncertainties . . . 82
3.4 Observed Cross Sections . . . 85
3.4.1 Semi-inclusive Cross Sections . . . 85
3.4.2 Exclusive ρ^0 Production . . . 88
3.4.3 Photoproduction Cross Sections . . . 90

4 Adaption of PYTHIA 6.2 to the HERMES Data **92**
4.1 The PYTHIA 6.2 Generator . . . 92
4.1.1 Monte Carlo Methods . . . 92
4.1.2 The Hermes Monte Carlo Implementation . . . 93
4.1.3 The Physics of PYTHIA 6.2 . . . 95
4.1.4 Strategy to Adjust PYTHIA Parameters to HERMES Data . . . 98
4.1.5 The Virtual Photon Flux Factor . . . 100
4.2 Implementation of QED Radiative Corrections to PYTHIA . . . 100
4.2.1 Physical Issues of QED radiative corrections . . . 101
4.2.2 A Structure Function for PYTHIA . . . 102
4.2.3 PYTHIA Results with Radiative Corrections . . . 103
4.3 The Vector Meson Dominance Model in PYTHIA . . . 107
4.3.1 Exclusive Vector Meson Cross Sections . . . 107
4.3.2 Comparisons of Exclusive ρ^0 Cross Sections . . . 110
4.3.3 Exclusive ω and ϕ Cross Sections . . . 111
4.3.4 Non-resonant Exclusive π Production . . . 112
4.4 Contribution of Diffractive Events to the Semi-inclusive Data . . . 114
4.4.1 Extraction Method . . . 114
4.4.2 Fractions of Exclusive ρ^0/ϕ Events in the Semi-inclusive Data . . . 116

4.4.3 Exclusive and Diffractive VMD Fractions from PYTHIA . . . 120
4.5 The Semi-inclusive Cross Section in PYTHIA . . . 121
4.5.1 Tuning of Fragmentation Parameters . . . 121
4.5.2 Cross Section Parameters . . . 124
4.5.3 Results of the Parameter Study . . . 125
4.6 The Quasireal Photoproduction Cross Section in PYTHIA . . . 127
4.6.1 The Pion Pair Production Cross Section . . . 128
4.6.2 Inclusive Hadron Cross Sections . . . 131

5 Extraction of the Gluon Polarization 134
5.1 General Considerations . . . 134
5.1.1 Formalism . . . 134
5.1.2 Cut Studies . . . 136
5.2 Results for the 'Photoproduction' Region . . . 138
5.2.1 Results From the Standard Monte Carlo . . . 139
5.2.2 Kaon Results . . . 142
5.2.3 Systematic Studies . . . 142
5.3 Results in the 'Transition' Region . . . 148
5.3.1 Results From the Standard Monte Carlo . . . 148
5.3.2 Systematic Studies . . . 150
5.4 Interpretation of the Results . . . 155
5.4.1 The Internal Consistency of the Data . . . 155
5.4.2 Kinematic Correlations and the Low-p_T Processes . . . 162
5.5 Final Results and Systematic Errors . . . 164
5.5.1 p_T and x_G Dependence of $\frac{\Delta G}{G}$ in the 'Photoproduction' Region . . . 165
5.5.2 Integrated Values for $\frac{\Delta G}{G}$ . . . 171

Conclusions 172

A Trigger Efficiencies 176
A.1 Trigger Logic . . . 176
A.2 Time Dependence of Trigger Efficiencies . . . 177
A.3 Trigger Efficiencies for Cross Sections . . . 178

B QED Radiative Corrections in PYTHIA 186
B.1 Radiative Corrections in gmc_DISNG . . . 186
B.2 Merging PYTHIA with RADGEN . . . 188
B.3 Normalization of PYTHIA Events . . . 190

C Monte Carlo Asymmetries 194
C.1 Event Wise Asymmetry Calculation for PYTHIA . . . 194
C.2 The Statistical Error of $\Delta G/G$ . . . 201

D Tables 202

D.1 Standard PYTHIA Parameter Settings 202
D.2 Measured Asymmetries 204
D.2.1 Photoproduction Region 204
D.2.2 'Transition' Region 209
D.2.3 'SIDIS' Region 214
D.3 Final Results on $\frac{\Delta G}{G}(p_T)$ in the 'Photoproduction' Region. 219
D.3.1 Integrated Results 219
D.3.2 Positive Hadrons from Proton in the 'Photoproduction' Region 220
D.3.3 Negative Hadrons from Proton in the 'Photoproduction' Region 221
D.3.4 Positive Hadrons from Deuteron in the 'Photoproduction' Region 222
D.3.5 Negative Hadrons from Deuteron in the 'Photoproduction' Region 223
D.3.6 Charged Hadrons from Proton and Deuteron in the 'Photoproduction' Region 224

Bibliography **225**

Introduction

This thesis investigates to what extent the data taken by the HERMES experiment on hadrons with high transverse momentum[1] above 1 GeV can reveal information about the polarization of the gluons in the nucleon.

In the HERMES experiment the polarized deep inelastic scattering process is used as a tool to study the spin structure of the nucleon, in particular the helicity distributions of the nucleon constituents. In the first chapter of this thesis, the experiment will be introduced. The HERMES experiment was designed for precision measurements of the polarized structure function g_1 and its decomposition into the various quark flavors. The latter can be achieved through the observation of coincident hadrons. For the detection of both the scattered lepton and the hadrons produced in the scattering process not only a large geometrical acceptance is required, but also an excellent performance of the particle identification system. In order to gain information about the helicity structure of the nucleon it is necessary to have both the lepton beam and the target longitudinally polarized. HERMES uses the polarized electron or positron beam of HERA together with a fixed, gaseous atomic hydrogen or deuterium target with a very high polarization of about 80%.

The second part of the thesis deals with the theoretical basis for the study presented here. Although the fundamental interactions among the nucleon constituents are understood in the framework of Quantum Chromodynamics it is still impossible to calculate the structure of the nucleon from first principles. The reason is the nature of the strong force holding the nucleon compounds together such that it is impossible to observe them as free, individual particles. The unknown nucleon structure is usually parametrized in terms of so called structure functions describing the momentum and helicity distributions of its constituents. These structure functions can be measured in deep inelastic scattering (DIS). It will be shown how DIS can be used to probe the structure of the nucleon.

The deep inelastic regime is characterized by large momentum and energy transfer to the nucleon through the exchange of a virtual vector boson (γ, Z, $W^{\pm}$, depending on the flavor of the incident leptons and the available energy). At the energies accessible by fixed target experiments like HERMES and with charged incident leptons the exchange of a single virtual photon dominates. This photon couples to the electric charge of the nucleon constituents. It has long been revealed by DIS experiments at SLAC that these charged constituents are free, pointlike elementary particles. In the late 60s these so called 'partons' were identified by Bjorken and Feynman with the earlier postulated quarks. It has also been established that these quarks are spin $\frac{1}{2}$ particles. If in addition to the scattered lepton also the final state hadrons are detected, information about the flavor of the struck quarks can be obtained. From the unpolarized structure functions measured in unpolarized DIS, where the spins of beam and target particles are not considered, the momentum distribution of the quarks can be retrieved. It has been found out that only about 50% of the nucleon momentum is being carried by the quarks. The remaining nucleon momentum can be assigned to the gluons, the mediators of the strong interactions between the quarks. The gluons, whose existence has been proven experimentally in 1979 by the experiments at the PETRA e^+e^- storage ring, are spin 1 particles.

[1] High transverse momentum in the context of the HERMES experiment always refers to values between approximately 1 and 2 GeV, due to the restricted energy range of the (fixed target) experiment.

For scattering on truly free, pointlike particles the measured structure functions would scale, i.e., be independent of Q^2, the momentum transfer to the nucleon by the virtual photon. The observation of scaling violations in the unpolarized structure functions can again be attributed to the interactions of quarks with gluons. From precision measurements of the scaling violation of the unpolarized structure function over five orders of magnitude in both x (the momentum fraction of the nucleon carried by the quark in the interaction) and Q^2 the gluon density has been inferred. Information about the gluon distribution can also be retrieved by the isolation of processes involving a gluon in the initial state. The signature of such a process would be the additional production of jets of hadrons at high energies with a large transverse momentum (p_T) or the production of charmed hadrons. Such processes have not only been studied in DIS, but also in proton-proton and proton-antiproton collisions.

Experiments in polarized deep inelastic scattering have been performed since the 80s, where it was soon revealed that only about 30% of the spin of the nucleon is carried by quarks. This result is known as the 'nucleon spin crisis', and it indeed came as a surprise as it was expected from measurements of magnetic moments of nucleons and hyperons that the nucleon spin should be completely contained among its valence quarks. Since then a number of new experiments have been performed, confirming the early results of the EMC experiment with much higher precision. Not only the spin of the gluons can contribute to the spin of the nucleon but also the orbital angular momenta of quarks and gluons. It is thus an important step to determine the gluon polarization $\Delta G/G(x)$. Also here, the scaling violation of the polarized structure function g_1 can reveal information about the helicity distribution of the gluons. Presently, all polarized DIS experiments are fixed targets experiments, such that in the restricted kinematic range accessible by them the shape of the gluon helicity density can hardly be constrained. Analogously to the unpolarized case, processes initiated by gluons can be tagged to increase the sensitivity to the gluon helicity. In DIS the most promising processes are the production of open charm or of jets of hadrons with high transverse momentum. The energy of HERMES is just above the threshold for the production of a charm quark pair, resulting in a too low rate of open charm events. The HERMES energy is also too small to observe collimated jets of hadrons going into the direction of the quarks produced in the hard scattering process. As an alternative to jets, the observation of pairs of hadrons or of single hadrons with high transverse momentum could serve the purpose as well. In this case it is particularly important to understand the processes in which hadrons are produced from the outgoing quarks. For the study presented here, single charged hadrons with transverse momenta above 1 GeV are investigated towards their sensitivity to the PGF process and therefore to the gluon helicity.

Chapter three of the thesis describes the extraction of the data on high p_T hadrons from the HERMES data taken on polarized hydrogen and deuterium targets. Experimentally, asymmetries are measured by evaluating differences of cross sections for two different beam and target spin configurations (parallel and antiparallel) relative to the unpolarized cross section. These asymmetries are measured as a function of the transverse momentum of the detected hadrons. Detailed systematic checks are performed in order to ensure a good quality and stability of the data. Possible sources of background are investigated. The asymmetries are measured in three distinct kinematic regions defined by the acceptance of the HERMES spectrometer for the scattered lepton and its kinematics. In the first region the scattered lepton escapes detection meaning for the bulk of the data that they are produced at very low Q^2, in quasi-real photoproduction. The event kinematics cannot be reconstructed in this region due to the missing lepton. In the other two kinematic regions, the scattered lepton is detected. While the detection of the lepton is a sufficient requirement in the second region, further cuts on the event kinematics define the third region. All regions have advantages and disadvantages, but as it is not clear beforehand which region is the most sensitive one to the gluon polarization, all three are considered.

The selection of hadrons with high p_T does not uniquely isolate the PGF process. In general, a mixture of other processes, which have to be regarded as background, contributes to the cross section as well. The fraction of these processes and their asymmetries can only be inferred from a

Monte Carlo model. The fourth chapter in this thesis is therefore devoted to the Monte Carlo model that will be used for the extraction of the gluon polarization, PYTHIA 6.2. This Monte Carlo and its default parameter settings have originally been tuned to data from high energy colliders. As the center of mass energy of HERMES is much smaller, it is likely that some of these parameters have to be changed in order to achieve a good description of the HERMES data. These changes will be presented, together with comparisons to measured cross sections and other observables. Special emphasis is laid not only on the description of inclusive cross sections, but also on cross sections for elastically produced ρ^0 mesons. Their production is described in the Vector Meson Dominance (VMD) model in which photons fluctuate into a vector meson or a quark-antiquark pair before the interaction with the nucleon. The contribution from these processes becomes especially important in quasireal photoproduction. Therefore it needs to be ensured that the model incorporated in PYTHIA is in agreement with the HERMES data.

In the last part, chapter five, the final results will be presented, extracted on the basis of the tuned PYTHIA Monte Carlo. In the HERMES kinematic region there are still considerable theoretical uncertainties in the description of the subprocess mixture, the underlying kinematics, the contribution of the different quark species to the background asymmetry and even the hadronization processes. At the relatively small scale at which the gluon distribution is probed also large higher order corrections to the perturbative cross sections can be expected that cannot be modeled with the Monte Carlo. In order to estimate the possible size of the theoretical uncertainties, a number of studies were performed. The results have to be interpreted in view of inconsistencies in the values for the gluon polarization extracted from independent data sets on positively and negatively charged hadrons, proton and deuteron targets. These inconsistencies can well be due to an inadequate description of the fragmentation processes at HERMES energies, or a wrong model for soft processes. These issues will be discussed thoroughly. It will be shown, however, that once the inconsistencies can be reduced, the HERMES data provide a first significant estimate of the gluon polarization, and even allow to infer information about its x dependence via the p_T dependence of the results and the kinematic correlations between p_T and x.

Chapter 1

The HERMES Experiment at HERA

HERMES is located in the east hall of the HERA storage ring at DESY in Hamburg. HERA consists of two rings, one of which contains 27.5 GeV positrons or electrons and the other one stores counter rotating protons at 900 GeV. HERMES shares the ring with three other experiments. Figure 1.1 shows a sketch of the ring setup as it was until 2000. H1 and ZEUS are experiments using the two colliding beams, whereas HERA-B has the proton beam interacting with a fixed target. The

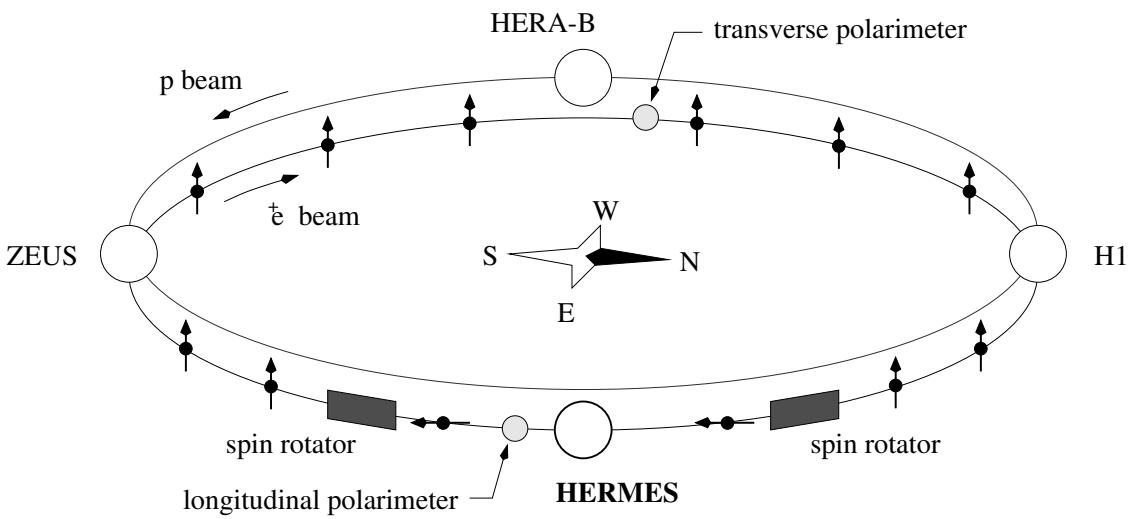

Figure 1.1: Sketch of the HERA positron storage ring (in the setup for the years 1995 to 2000) with the four experiments. The spin rotators around HERMES turn the positron spin from transverse to longitudinal and back. Also shown are the polarimeters where the transverse and longitudinal polarization is measured in the ring.

positron (electron) beam and a fixed gaseous target internal to the beam line are used by HERMES. This experiment has been designed for precision measurements of asymmetries in polarized deep inelastic scattering. Therefore high beam and target polarizations are required.

1.1 The Beam Polarization and its Measurement

In the following, if not particularly mentioned, the term 'positrons' refers to both e^+ and e^-. Conventions for the HERA coordinate system are: The z direction is defined by the proton beam momentum, the $+x$ axis points away from the center of the ring and the $+y$ axis points upward. Synchrotron radiation in a storage ring exhibits a small asymmetry in the spin-flip amplitude such that a positron would slightly prefer spin-flips turning its spin *parallel* to the direction of the

guiding magnetic field (i.e., the y direction) over those turning it into the opposite direction. For electrons the antiparallel direction is the preferred one. This so called Sokolov-Ternov (ST) effect [Sok64] is exploited at HERA to achieve high polarization of the positron beam. Over time positron (e^+) states with spin orientation parallel to the magnetic field direction become more populated than those with antiparallel spin orientation. In an ideal synchrotron without vertically deflecting magnetic fields (a 'flat' machine) the beam polarization develops in time like

$$P_{ST}(t) = P_{ST}\left(1 - e^{-\frac{t}{\tau_{ST}}}\right) \tag{1.1}$$

with the universal maximum polarization

$$P_{ST} = \frac{8}{5\sqrt{3}} = 92.38\%, \tag{1.2}$$

and the rise time constant

$$\tau_{ST} = \frac{8}{5\sqrt{3}} \frac{m_e^2 c^2 \rho^3}{e^2 \hbar \gamma^5} = 37 \text{ min}, \tag{1.3}$$

that depends on machine parameters like the effective radius ρ and the Lorentz boost factor $\gamma = E/m_e$. For HERA, $\rho = 707$ m and $\gamma \simeq 53.9 \cdot 10^3$ for a positron energy of $E = 27.56$ GeV [Bar94]. In a real machine the magnetic field is not always exactly vertical. Small misalignments of magnets or the positrons running slightly off the design orbit makes them experience non-vertical field components. Synchrotron radiation itself causes kinks in the positron orbit. All these effects induce depolarization. The strength of this depolarization can be summarized into a depolarizing time constant τ_{dep}, such that the asymptotic polarization becomes:

$$P_{max} = P_{ST}\frac{\tau_{dep}}{\tau_{dep} + \tau_{ST}} \quad \text{and } \tau = \tau_{ST}\frac{\tau_{dep}}{\tau_{dep} + \tau_{ST}}. \tag{1.4}$$

The maximum achievable polarization becomes smaller and the rise time shorter, while Eq. (1.1) stays valid when exchanging $P_{ST} \to P_{max}$ and $\tau_{ST} \to \tau$. Efforts taken at HERA to empirically optimize the positron orbit [Bar94] helped to achieve polarization values of 50 to 60% during the data taking periods 1995 to 1997.
The *longitudinal* polarization necessary for HERMES can be obtained by rotating the spin vectors of the positrons from the transverse into a direction along the positron orbit. This is done with a spin rotator, a device consisting of six interleaved horizontal and vertical dipole magnets generating a pattern of vertical and horizontal orbit deflections. After having traversed a spin rotator a positron will not have its beam trajectory changed, but the orbit kicks will cause a series of rotations of the spin vector such that it is finally turned by 90°. Between 1995 and 2000 two rotators were installed, one before the HERMES interaction point (IP) turning the spin into the axis of the beam momentum and one after the HERMES IP turning the spin back to the transverse direction. From 2001 on such sets of spin rotators have also been placed enclosing the H1 and ZEUS experiments.

The uncertainty in the beam polarization constitutes an important part of the systematic uncertainty for precision measurements of polarized cross sections, asymmetries etc. Therefore it is essential to provide precise and frequent measurements of the beam polarization. At HERA, two polarimeters are in operation. Both polarimeters make use of a cross section asymmetry in the Compton scattering of circularly polarized photons off polarized positrons. The Transverse Polarimeter (TPOL) was installed in the HERA west hall in 1992 and measures the transverse polarization. A detailed description can be found in Refs. [Bar93, Tip99]. Circularly polarized light from a continuous argon ion laser (514 nm) is directed against the positron beam at a shallow angle, with its helicity being switched with a frequency of 83.8 Hz. The backscattered photons are detected with a tungsten-scintillator sandwich calorimeter consisting of two identical halves separated along the beam plane. If the positron polarization is in the y direction (i.e. perpendicular to the orbit plane), the Compton scattered photons are distributed asymmetrically along the y direction. The

asymmetry is proportional to the sine of the azimuthal photon scattering angle around the beam axis and to the positron polarization into the y-direction [Bec00]. By measuring the asymmetry in the energy deposition of backscattered photons between the top and bottom halves of the calorimeter the mean average vertical position $\langle y \rangle$ can be inferred. From the difference

$$\Delta y = \frac{\langle y \rangle_R - \langle y \rangle_L}{2} \sim P_y \Pi_y \tag{1.5}$$

of the means $\langle y \rangle$ measured with right (R) and left (L) circularly polarized light the transverse positron polarization P_y can be derived. The analyzing power Π_y is derived from the spin-dependent cross section and equals the shift of means if the both the light and the positrons were completely polarized. Within one minute the positron polarization can be determined with an absolute statistical error of about 0.01. The absolute calibration is performed with (dedicated) measurements of the rise time τ using the relation

$$\frac{\tau}{\tau_{ST}} = \frac{P_{max}}{P_{ST}}. \tag{1.6}$$

The uncertainty of the rise time calibrations dominates the systematic uncertainty of the TPOL of 3.4% for 1996/1997.

The Longitudinal Polarimeter (LPOL) measures the longitudinal polarization behind the HERMES IP in the East Right straight section of the HERA positron ring. It was installed in 1995/1996. The setup is similar to that of the TPOL, it consists of a pulsed Nd:YAG laser ($\lambda = 532$ nm) generating circularly polarized light with alternating helicity at each pulse. The light crosses the beam 53 m downstream of the HERMES target at an angle of about 9 mrad. Several thousand photons are backscattered when the laser pulse crosses a positron bunch. Their energy sum is measured by a radiation hard calorimeter consisting of an array of four $NABi(WO)_2$ crystals of 20 cm length. For longitudinal positron polarization the Compton cross section is independent of the azimuthal scattering angle, but switching the laser helicity will modify the energy spectrum. The asymmetry of the energy weighted sums of backscattered photons ζ determines the longitudinal positron polarization P_z:

$$A = \frac{\zeta_L - \zeta_R}{\zeta_L + \zeta_R} \sim P_z \Pi_z. \tag{1.7}$$

Again, Π_z is the analyzing power, i.e., the Compton cross section asymmetry for the case of fully polarized laser light and positrons, folded with the response function $r(E_\gamma)$ (efficiency) of the calorimeter. The largest systematic uncertainty comes from the knowledge of the response function which had been determined correctly only after 1998. For the years 1999 and 2000 the fractional systematic uncertainty of the LPOL was 1.6%. From 1996 to 1998 the systematic error was larger, $\delta P_z / P_z \simeq 4\%$, mainly arising from the fact that it the absolute calibration was performed with rise time measurements. A detailed description of the setup and performance of the LPOL can be found in Ref. [Bec02].

1.2 The Internal Gas Target

HERMES uses a gas target internal to the positron beam line. Basically it has three components: an atomic beam source (ABS) producing polarized hydrogen or deuterium atoms, a storage cell around the central axis of the positron beam and diagnostic devices to measure the polarization (Breit-Rabi-Polarimeter, BRP) and atomic fraction of the gas (Target Gas Analyzer, TGA). Figure 1.2 shows the setup with these main components. The ABS [Nas03] is a device making use of the Stern-Gerlach effect [Ger21] to generate atomic polarization of hydrogen or deuterium. First, the molecular gas is dissociated by means of a radio frequency dissociator (from 2000 on a microwave dissociator was used instead) causing a discharge inside a glass tube. The atomic gas then enters a sextupole magnet system with a radial field dependence. Due to the Stern-Gerlach effect atoms traversing a magnetic field with a gradient perpendicular to their motion experience different forces

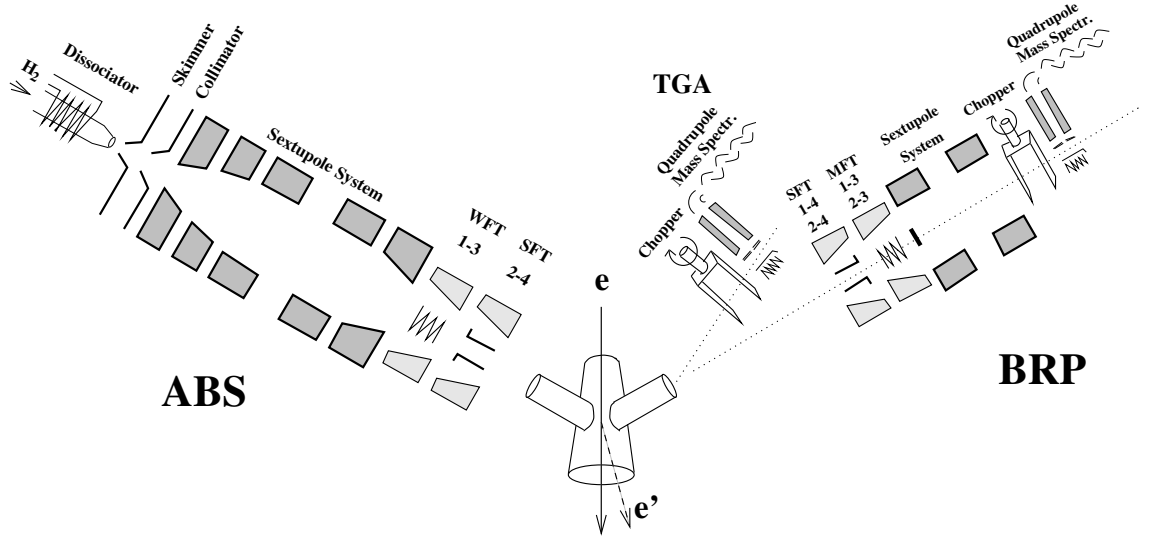

Figure 1.2: Representation of the Atomic Beam Source (ABS), Breit-Rabi-Polarimeter (BRP) and Target Gas Analyzer (TGA) with the storage cell in the center.

according to their magnetic moments. Those atoms having a positive magnetic moment are focused toward the axis of the magnet, those with a negative magnetic moment are defocused toward the pole tips. Thus the sextupole magnets select only those atoms having electrons with spin projection $m_s = +\frac{1}{2}$. In order to obtain *nuclear* polarization, transitions between hyperfine states are induced. The relative energies of the four (six) hyperfine states of hydrogen (deuterium) are displayed in figure 1.3 as a function of the ratio of the external magnetic field B to the critical field B_c. In this

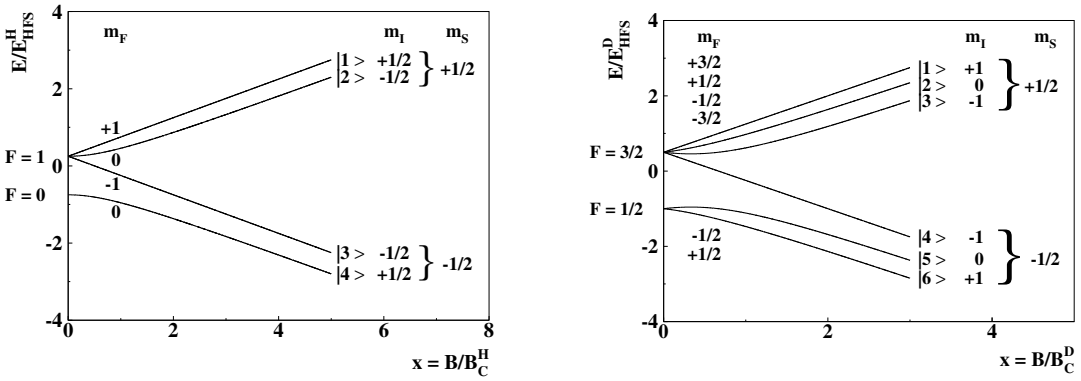

Figure 1.3: Splitting of the energy levels of hyperfine states of hydrogen (left) and deuterium (right) as a function of the magnetic holding field B relative to the critical field B_c. The energy is given relative to the hyperfine splitting at $B = 0$.

figure m_I is the spin projection number of the nucleon ($\pm\frac{1}{2}$ for proton, $\pm 1, 0$ for deuteron), m_s that of the electron ($\pm\frac{1}{2}$) and $m_F = m_s + m_I$ is the total spin projection. F is the spin of the combined system. For instance for hydrogen, the states $|1\rangle$ and $|2\rangle$ are selected by the sextupole, and then state $|1\rangle$ is transformed to $|3\rangle$ to obtain positive proton polarization, or state $|2\rangle$ is transformed to $|4\rangle$ for negative proton polarization. For deuterium, combining two states out of the original three ($|1\rangle|2\rangle|3\rangle$) and transforming either one of these results in negative polarization (states $|3\rangle$ and $|4\rangle$), positive polarization (states $|1\rangle$ and $|6\rangle$) or 'tensor' polarization (states $|2\rangle$ and $|5\rangle$ or $|3\rangle$ and $|6\rangle$). The combination of injected states can be changed within a fraction of a second. The nucleon polarization is being flipped randomly on the time scale of a minute, fast enough to reduce systematic influences on asymmetry measurements to a minimum and slow enough to avoid

synchronization problems in the data acquisition.
After the selection of the hyperfine states the gas is fed into the storage cell [Bau03a], whose purpose is the increase of the areal target density by about two orders of magnitude compared to a free jet target. The areal target density obtained is about 10^{14} atoms/cm^2. The storage cell is an open ended elliptical tube (40 cm long, 29 mm wide and 9.8 mm high) made of thin (75 μm) ultra pure aluminum. It is being cryogenically cooled in order to reduce the thermal velocities of the gas atoms inside. A feed tube through which the polarized gas atoms are injected into the cell is installed perpendicular to the beam axis in the center of the cell. After a number of wall collisions the atoms diffuse into the ultra high vacuum of the positron beam line where they are being pumped away by a high speed differential pumping system. During the diffusion process the atoms cross the positron beam many times. The cell is coated with a radiation hard hydrophobic silicon based polymer called Drifilm in order to reduce depolarization and recombination of atoms due to wall collisions. As the Drifilm ages and gets damaged after a few weeks of HERMES running, a monolayer of solid H_2O/D_2O forms on the interior of the cell. This layer was found to compensate for the loss of Drifilm. For the data taking of 2000, the storage cell was replaced by a smaller one (21 mm wide instead of 29 mm) which resulted in an additional increase of areal target density by a factor 1.6. A uniform magnetic holding field of 335 mT along the beam axis generated by a superconducting magnet providing the spin quantization axis and effectively decoupling the electron and nucleon magnetic moments. It is also possible to feed unpolarized gas into the storage cell. In contrast to the polarized gas, whose density is limited by the performance of the ABS, the density of the unpolarized gas is restricted to less than a maximum contribution to the reduction of the beam life time. An exception is the so called 'end of fill' running when unpolarized gas is filled into the storage cell close to the end of a positron fill. Then the target density is basically only limited by the detector rates, and densities about two orders of magnitude larger than that with the ABS can be achieved.

To measure the atomic polarization a small fraction of the target gas is extracted through a sampling tube and analyzed by a Breit-Rabi-Polarimeter (BRP) [Bau02]. A system of RF hyperfine transitions and sextupole magnets allows to separate the different hyperfine states. Atoms with a selected state enter a quadrupole mass spectrometer (QMS) and are finally counted by a channel electron multiplier. The polarization can be calculated by measuring the relative occupation numbers of the four (six) hyperfine states. As the BRP can only measure the atomic polarization, the fraction of atoms and molecules in the gas has to be measured as well. This is what the Target Gas Analyzer (TGA) is being used for [Bau03b]. It is mounted in front of the entrance to the BRP at an angle of 7° to the sampling tube. Essentially, it is a quadrupole mass spectrometer with a channel electron multiplier to measure the fluxes of atoms Φ_a and of molecules Φ_m. The degree of dissociation of the sample beam is then

$$\alpha_{TGA} = \frac{\Phi_a}{\Phi_a + \Phi_m}, \tag{1.8}$$

which can be related to the degree of dissociation in the storage cell by a sampling correction factor C_α. The uncertainty in this factor is part of the total systematic uncertainty of the polarization measurements. The effective polarization P_T of the target can be computed from the measured atomic polarization P_{BRP}, the sampling correction for the BRP C_P and from the TGA measurements:

$$P_T = C_P \cdot P_{BRP} \cdot \alpha_0 \cdot [C_\alpha \alpha_{TGA} + \beta(1 - C_\alpha \alpha_{TGA})]\,, \tag{1.9}$$

where α_0 is the injected atomic fraction and β is the relative polarization of the molecules with respect to the atoms. The effective polarization in 1997 (hydrogen target) was 0.850 with a systematic error of ± 0.033. For the deuterium target used in 2000 it was 0.851 ± 0.029 and 0.840 ± 0.026, where the two values refer to target spins parallel and antiparallel to the beam momentum, respectively [Reg03].

1.3 The Spectrometer

The HERMES detector is an open forward magnetic spectrometer consisting of two identical halves above and beneath the HERA beam pipes. It has three main components: the spectrometer magnet, the tracking system consisting of three sets of tracking chambers in front, inside and behind the spectrometer magnet and a particle identification (PID) system. The location of the various detectors is shown in figure 1.4. A detailed description of the detector components can be found in Ref. [Ack98]. The axes for the HERMES coordinate system are defined such that the z

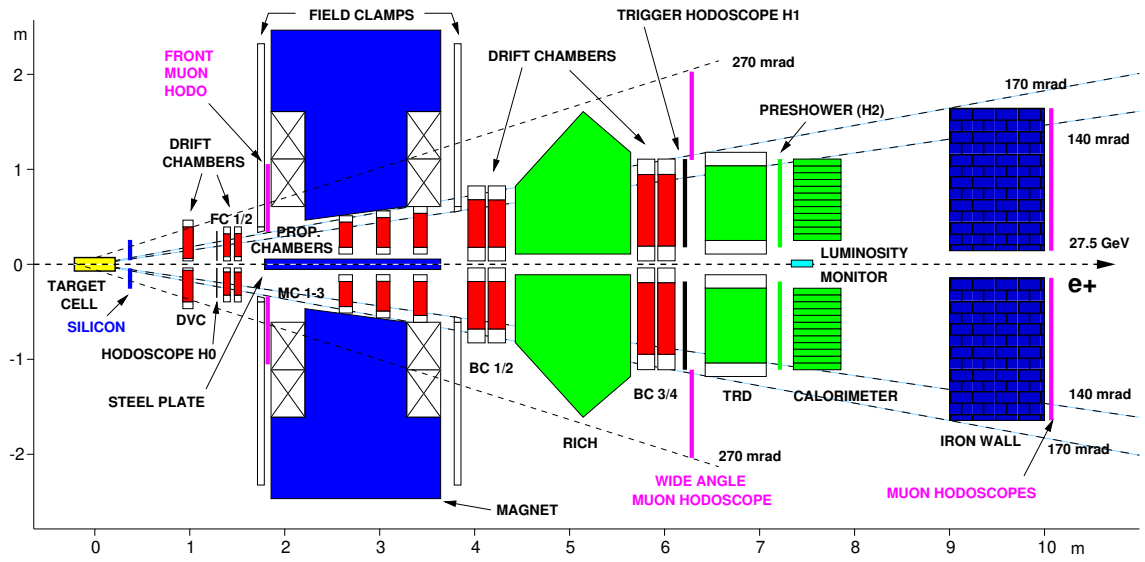

Figure 1.4: A two dimensional, vertical cut of the HERMES spectrometer. Until 1997 a threshold Cherenkov detector was in place of the Ring Imaging Cherenkov (RICH), the silicon detector was not installed until 2001.

direction is along the positron momentum, x points towards the center of the HERA ring and y points upward.

1.3.1 The Spectrometer Magnet

During data taking the spectrometer magnet is operated at a deflecting power of $\int B\,dl = 1.3$ Tm. The magnetic dipole field is oriented in the vertical direction, deflecting charged particles horizontally. The aperture of the magnet limits the geometrical acceptance of the spectrometer to ± 140 mrad in the vertical and ± 170 mrad in the horizontal direction. To maintain good acceptance for low momentum particles the acceptance of the detector in the horizontal plane is increased by ± 100 mrad starting from the center of the magnet. The lower limit on the vertical acceptance of ± 40 mrad is given by a septum plate in the horizontal plane that shields both HERA beams from the field of the spectrometer magnet.

1.3.2 The Tracking Devices

Except for the silicon detector right next to the target, all tracking devices are wire chambers, each consisting of several planes. The planes come with three different wire orientations, vertical and tilted by $\pm 30^\circ$ with respect to the vertical axis. The two most important chambers are the front chambers (FC) [Bra01] at about 1.6 m from the target center, just in front of the magnet, and the back chambers (BC) [Ber98] that are combined into two groups in front of and behind the RICH detector. Each of their modules consists of six wire planes, where one set of planes has the wire positions staggered by half the drift cell size with respect to the other to help resolve left-right

ambiguities.
The two modules of the front chambers have drift cells of 7 mm width and 8 mm depth. They are filled with a mixture of 90% Ar, 5% CO_2 and 5% CF_4. The choice of this particular mixture results from three requirements: non-flammability, fast electron drift velocities, small aging effects (assured by the CF_4 component). The resolution per plane is 225 μm, the single plane efficiency ranges from 97% to 99% depending on the position in the cell.
The BCs have a drift cell size of 15×16 mm and the same gas mixture as the FCs. The resolutions are 210 μm for BC1/2 and 250 μm for BC3/4. For positrons, the BC plane efficiency was found to be well above 99%, while it is somewhat smaller for hadrons (about 97%) because of their reduced ionization density.
The three magnet chambers (MC) [And01] are located in the gap of the magnet. Initially they were intended to help resolve multiple tracks in case of high track occupancies. This turned out not to be necessary because of the low backgrounds. Still, they are helpful in determining the momentum of low energy particles (for instance from Λ decays) that do not reach the back part of the detector due to the large deflection in the magnet. The MCs are proportional wire chambers (MWPC) able to operate in a strong magnetic field. Each chamber has three planes with a cell width of 2 mm, providing a resolution of 700 μm. A digital single bit-per-wire readout was chosen to accommodate the readout electronics for a large number of channels (5504) within a very restricted space volume.
Another set of drift vertex chambers (DVC) was installed 1.1 m downstream of the target between the 1996 and 1997 data taking periods. They consist of six planes of conventional drift chambers with a design similar to that of the FCs, albeit smaller, and the same gas mixture as the FCs. The acceptance is somewhat larger though, extending vertically from ± 35 to ± 270 mrad and horizontally to ± 200 mrad. The planes have a wire spacing of 6 mm and a resolution of 220 μm per plane.
The silicon detector (Lambda-Wheels) [Beu01] has been installed in 2002. Two sets of disk-shaped silicon detectors are mounted 45 and 50 cm downstream of the target cell. The disks have a diameter of 33.6 cm and a hole of 9 cm leaving space for the beam pipe and wake field suppressors around it. This detector increases the acceptance for longer living particles such as Λ, Λ_c, K_s that decay outside the target region.

Track Reconstruction

The combined information of many tracking detectors is needed to uniquely reconstruct tracks. At HERMES, a tree-search algorithm is applied for fast and efficient track finding. The principle of this method is to look at the whole hit pattern of the detectors in several iterative steps, doubling the resolution at each step. For a given resolution, the algorithm checks if the hit pattern contains a subpattern consistent with an allowed track, by comparing with all sets of allowed patterns stored in a database. If it is, the procedure is repeated at increased resolution, otherwise the pattern is rejected. The HERMES reconstruction program (HRC) [Wan96] needs about 11 iterations to find a track. This is done independently for the hits in the front and back part of the detector, resulting in a set of front and back partial tracks. In a next step, all combinations of front and back partial tracks are tested if they match spatially in the $x - y$ plane within a defined tolerance. Matching combinations are refitted to form a full track. The track momentum is determined by comparing the position of the track in front and its slopes in front and behind the magnet with numbers in a look-up table. This look-up table contains the momentum of a given track as a function of the relevant track parameters. Using interpolation methods, the contribution of HRC to the precision of track momentum determination is less than $\Delta p/p = 0.5\%$ The overall resolutions are somewhat lower due to multiple scattering and bremsstrahlung in the spectrometer material.
In many of the data productions the information of the DVCs was not used. Instead, a slightly different method was developed to reconstruct tracks using only the FC and BC hits. The matching of the front and back partial tracks is first done with somewhat larger tolerances. Then, by fixing the matching point to that of the higher quality back track in the middle of the magnet, the front track parameters are recalculated. In an iterative procedure thus the momentum resolution can be considerably improved. This method is called force bridging, i.e., the front track is forced to match

the back track in the center of the magnet.
In 1998 the threshold Cherenkov detector in between BC1/2 and BC3/4 was replaced by a Ring Imaging Cherenkov detector (RICH). The RICH material has a considerably larger radiation length than that of the Cherenkov, resulting in an increase of the total radiation length of the spectrometer by a factor 20. As a consequence, the resolution of data taken with the RICH decreased by up to a factor of two with respect to data taken with the Cherenkov counter. Figure 1.5 shows the momentum and angular resolutions obtained for data with the RICH detector. The figure is taken from [Air03].

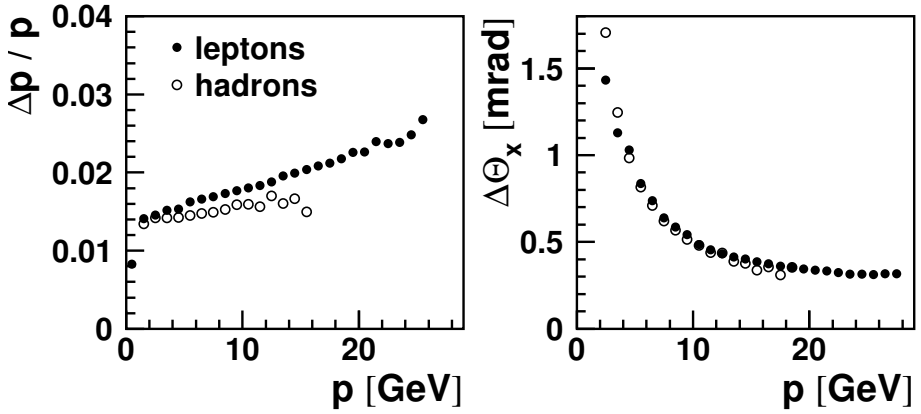

Figure 1.5: The relative momentum (left) resolutions and the angular resolutions (right, displayed is the horizontal scattering angle θ_x) for positrons and hadrons as a function of momentum.

1.3.3 The Particle Identification (PID) Devices

The HERMES PID system consists of four different particle identification (PID) detectors, a lead glass calorimeter, a preshower detector, a transition radiation detector (TRD) and a threshold Cherenkov detector that was replaced by a ring imaging Cherenkov detector (RICH) in 1998. A probabilistic algorithm utilizing the response of these detectors provides a very clean separation of the scattered positron from hadrons. The Cherenkov detector has been used to separate pions from other hadrons as well as for lepton/hadron separation at low momenta. The main task of the RICH detector is the positive identification of pions, kaons and protons, but it will be shown below that it can help to identify positrons as well.

The electromagnetic calorimeter consisting of 420 lead glass blocks in each detector half is located at the downstream end of the spectrometer. The length of the lead glass blocks of 50 cm corresponds to 18 radiation lengths. Each block is viewed from the rear by a photo multiplier tube (PMT) measuring the amount of Cherenkov light produced by secondary leptons generated in an electromagnetic shower. The gain of the PMTs is monitored continuously by a dye laser sending light pulses through glass fibers to every PMT as well as to a reference photo diode. A comparison of the PMT signals to that of the reference diode measures the relative gain of the PMTs. The energy resolution of the calorimeter can be parametrized as $\sigma(E)/E[\%] = (5.1\pm1.1)/\sqrt{E[GeV]}+(1.5\pm0.5)$, the spatial resolution of the impact point is $\sigma \approx 0.7$ cm. Besides for PID the calorimeter is used for detection and energy determination of photons and it is part of the first level trigger. For particle identification the ratio E/p of the deposited energy to the momentum of the particle is considered. In contrast to positrons producing electromagnetic showers containing almost all their energy, hadrons only deposit a fraction of their energy due to ionization losses and nuclear interactions. The top left panel of figure 1.6 shows the probability distributions for hadrons and positrons to deposit a fraction E/p of their energy in the calorimeter. The positrons have a distinct peak at $E/p \simeq 1$, while the hadron distribution is much wider and mostly at lower values. If positrons

with high momentum radiate bremsstrahlung photons in the detector material in front or inside the magnet, the photons will travel along the positron path and may hit the same calorimeter cluster as the positron. Thus the detected energy in the calorimeter can be larger than the positron momentum determined by the magnet *after* the photon emission – this explains the large tail at $E/p > 1$.

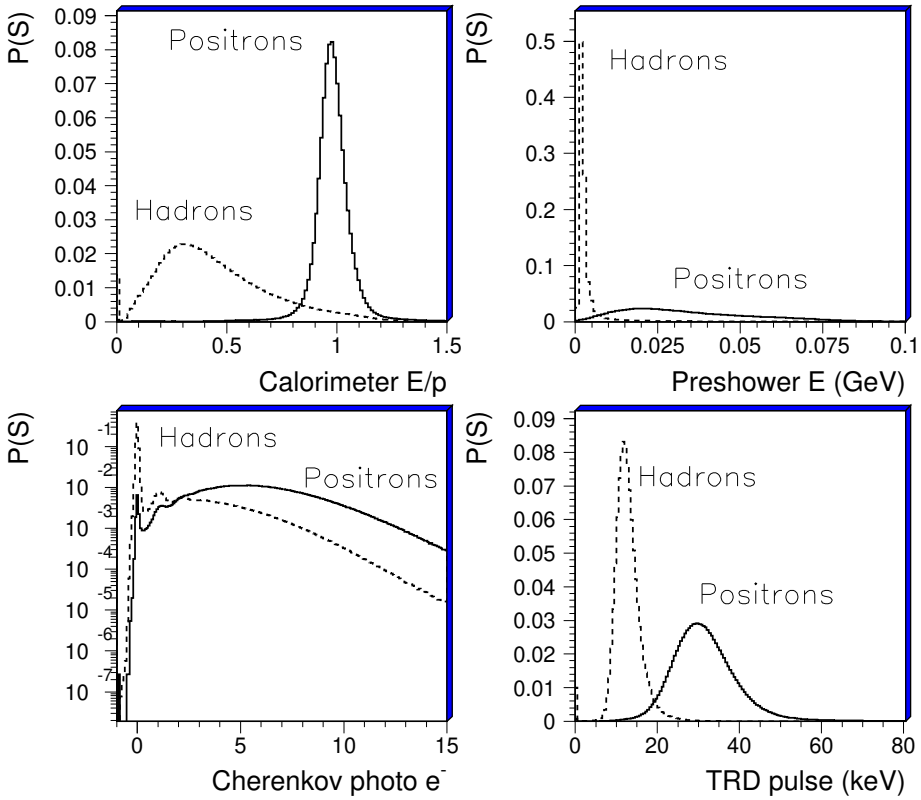

Figure 1.6: The probability distributions for the four PID detectors installed until the end of 1997. The dashed lines show the response of hadrons, the solid line that of positrons.

Right in front of the calorimeter a preshower detector consisting of a wall of 42 vertically oriented plastic scintillator paddles behind an 11 mm thick lead plate (corresponding to 2 radiation lengths) is installed. Adjacent paddles are staggered with some overlap for maximum efficiency. Each paddle is read out individually by a PMT. Positrons may initiate electromagnetic showers in the lead plate and deposit energy with a mean of 20-40 MeV in the scintillators whereas hadrons only produce a minimum ionizing signal of 2 MeV. The probability distributions for the preshower signal are shown in the top right of figure 1.6.
The transition radiation detector (TRD) in front of the preshower detector plays an essential role in the PID system. Transition radiation (TR) is created when a charged particle crosses the boundary between two media with different dielectric constants ϵ. For the boundary between vacuum (or air) and a medium with a plasma frequency ω_p, the energy radiated by a particle with charge ze is $E \sim \alpha z \gamma \omega_p$, where α if the fine structure constant and $\gamma = \frac{E}{m}$ the Lorentz boost factor. Half the energy is radiated by photons in the energy range $0.1 < \hbar\omega/\gamma\hbar\omega_p < 1$, such that a particle with a Lorentz factor 1000 (corresponding to a positron with 0.5 GeV) will radiate mainly X-ray photons between 2 and 20 GeV. The HERMES TRD consists of six modules in each detector half. The modules themselves are MWPCs filled with a Xe/CH_4 gas mixture for good sensitivity to X-ray photons. Transition radiation is created in the radiators of each module which are about 6.35 mm thick and formed from layers of loosely packed polyethylene/polypropylene fibers. The layering provides many boundaries (about 270) for the positron to traverse, such increasing the intensity of radiated photons. The angular distribution of the photons goes as $1/\gamma$, so that with the position information

from the MWPCs the photons can be associated with a track. A significant amount of TR can only be detected from particles with a Lorentz factor of $\gamma > 500$. At HERMES energies only positrons are above this threshold. Other particles can only deposit energy due to ionization losses. The combination of the six modules allows to identify positrons at around 5 GeV with a pion rejection factor (the number of pions divided by the number of pions misidentified as positrons) of ≈ 300 at a positron identification efficiency of 90%. The lower right panel of figure 1.6 shows the distributions of hadrons and positrons in terms of the deposited energy in the TRD, integrated over all momenta.

Until the end of 1997 a threshold Cherenkov counter was used to provide positron identification below the threshold momentum for pions, i.e., at momenta $p < 4$ GeV. Each of the counters in top and bottom consisted of a gas radiator, a system of 20 spherical mirrors and 20 matching photo multiplier tubes mounted on the outside of the aluminum enclosure containing the mirrors and the gas. The threshold velocity of a charged particle to radiate Cherenkov light in a medium with refractive index n is given by:

$$v \geq \frac{c}{n} \quad \text{corresponding to} \quad p_{th} = \beta_{th}\gamma_{th}m_0 = m_0\sqrt{\frac{1}{n^2-1}}. \tag{1.10}$$

Here p_{th} is the threshold momentum for a particle with mass m_0 ($\beta = p/E$). The radiator gas was a mixture of 70% N_2 and 30% C_4F_{10}, resulting in a p_{th} of 20.9 MeV for $e^{\pm}$, 3.8 GeV for pions and 13.9 GeV for kaons. For tracks classified as a hadron by the other PID detectors, the Cherenkov detector could be used to identify pions in a momentum range from 3.9 to 13.9 GeV. The number of photons radiated by a particle with momentum p is proportional to $1 - 1/(\beta^2 n^2)$, i.e., it is increasing with momentum from the threshold on and has a maximum for $\beta = 1$. Positrons at all momenta normally caused signals with 5 to 6 photoelectrons, while pions below 4 GeV left no signal in the PMTs and above the threshold the mean number of photoelectrons was roughly 3. The corresponding distributions for all momenta and for all hadrons as well as positrons can be seen in the lower left panel of figure 1.6.

The Cherenkov counter was replaced by a Ring Imaging Cherenkov detector in the shutdown break in the spring of 1998. It uses the same support structure as the Cherenkov counter. Two radiators with rather significantly different refractive indices are used, enabling the identification of pions, kaons and protons over a momentum range from $1 < p < 15$ GeV. The first radiator is a wall of of 10.5×10.5 cm^2 aerogel tiles with an entire thickness of 5.5 cm, installed right behind the entrance window. They are stacked in 5 layers with 5 horizontal rows and 17 vertical columns. Aerogel is a silica gel foam, i.e. containing air, the refractive index is 1.0304. The second radiator is a heavy gas, C_4F_10 with a refractive index of 1.0014, filling the volume of the detector. Cherenkov photons are reflected from a spherical mirror array onto a photon detector in the focal plane above the gas radiator. The photon detector is an array of 1934 photo multipliers with a diameter of 18.6 mm, arranged in a hexagonal closed packed matrix. Each of the PMTs is surrounded by an aluminized plastic foil funnel to maximize light collection. Figure 1.7 shows a schematic vertical cut through the top rich detector. A detailed description of the HERMES RICH detector can be found in [Ako02].

For hadron identification, the threshold behavior in the two radiators as well as the information about photon angles are used. Cherenkov photons are emitted in a cone around the particle trajectory, with an opening angle

$$\cos\theta_c = \frac{1}{\beta n}. \tag{1.11}$$

Figure 1.8 shows an example for an event with a positron and a pion in the bottom half and a kaon in the top half of the detector. The image of the 'ring' of Cherenkov photons around the path of the particles is distorted to an ellipsoid when projected onto the PMT matrix. The photon angles are measured with respect to the 'virtual track hit point', the point where the track would intersect

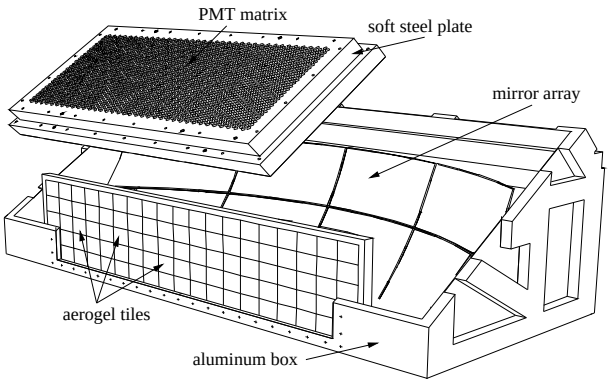

Figure 1.7: A vertical cut through the top RICH detector.

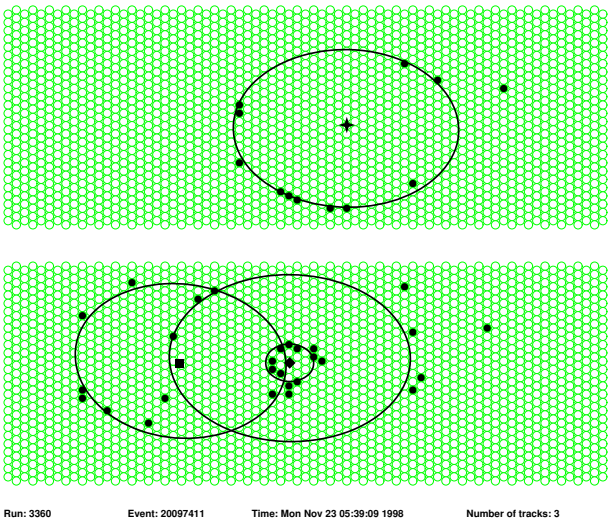

Figure 1.8: RICH event display where the hit PMTs are shown as black points for an event with a 5 GeV kaon in the upper half and a 1.5 GeV pion (left) with a 14.6 GeV positron (right) in the lower half of the detector. See text for more details.

the PMT matrix if it were reflected by the mirror. The virtual track hit points are indicated by the markers in the middle of the rings in figure 1.8. The solid curve shown there is a spline fit to a few simulated photon hits.

Since the RICH was optimized to provide hadron separation, an important piece of information on lepton/hadron discrimination at momenta below 4 GeV was missing that was filled before by the threshold Cherenkov counter. The calorimeter and the TRD, providing the bulk of information above 4 GeV, are not optimized for momenta below that. Low energy hadrons can leave a high fraction of their energy in the calorimeter due to an enhanced probability of nuclear interactions. In the TRD, the TR created by low momentum positrons has to compete with the ionization losses of hadrons of the same order. In fact the RICH information can be used similar to that of the threshold Cherenkov detector for lepton/hadron separation at low momenta. A positron with $p > 0.5$ GeV emits photons in the aerogel and in the gas, at angles close to the maximum ($\beta \to 1$) of $\theta_A \simeq 250$ mrad for the aerogel and $\theta_G \simeq 50$ mrad for the gas respectively. The threshold for pions to radiate Cherenkov light is $p > 0.6$ GeV in the aerogel and $p > 3.8$ GeV in the gas. The average angle of photons emitted by pions in the aerogel is still smaller and the number of photons is less than for electrons. A discriminating signal for the RICH can such be the number of hit PMTs in a window defined by a ring with a radius corresponding to the expected Cherenkov angle for a positron and a width of $\pm 2\sigma_\theta$ around that radius. The resolution $\sigma_\theta \simeq 8$ mrad is mostly dominated by the size of a pixel, i.e. the diameter of the photo multiplier tubes. Since below $p = 3.8$ GeV pions do not radiate Cherenkov photons in the gas, the signal in a window around the expected positron gas angle should be quite unambiguous. Figure 1.9 shows the probability distributions for hadrons and positrons to fire a number of PMTs in the above defined window around the expected positron angles. While the aerogel does not have a large discriminating power, except at very low momenta $p < 1$ GeV, with the signal from the gas hadrons can be clearly separated from positrons by the distinctive peak at zero PMTs.

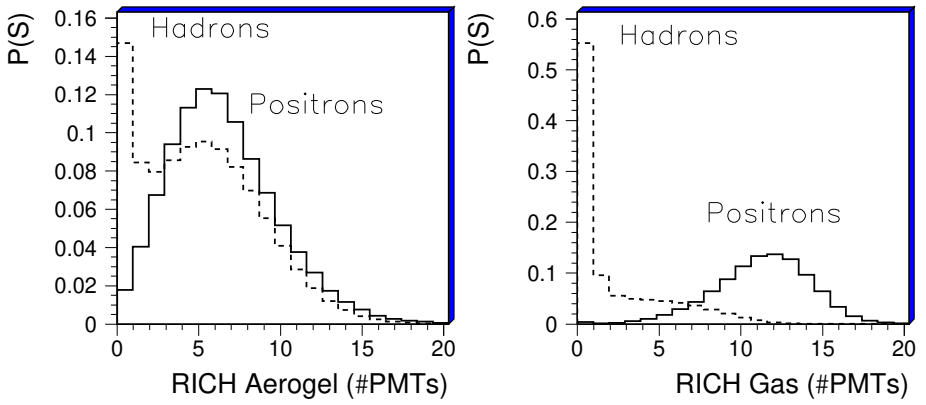

Figure 1.9: The probability distributions for the RICH aerogel radiator (left) and the gas radiator (right). The dashed lines show the response of hadrons, the solid line that of positrons. All particles have momenta $p < 4$ GeV.

1.3.3.1 The PID algorithm

The final goal of the PID analysis is the identification of positrons and/or hadrons with a high efficiency and as little as possible contamination. An algorithm was developed [Wen03] to assign to each particle a likelihood ratio obtained from the combined information of all PID detectors. For each detector i a logarithmic likelihood ratio PID_i can be defined:

$$PID_i = \lg \frac{P(S|e,p)}{P(S|h,p)}, \tag{1.12}$$

where $P(S|e(h),p)$ is the probability that a positron (hadron) with a momentum p causes a specific signal S in the detector. These probabilities are called parent distributions. In figure 1.6 some parent distributions integrated over all momenta are shown. Various combinations of the PID_i values are commonly used:

$$\begin{aligned} PID2 &= PID_{calo} + PID_{preshower} \\ PID3 &= PID_{calo} + PID_{preshower} + PID_{Chere\,(RICH)} \\ PID5 &= PID_{TRD} = \sum_{i=1}^{6} PID_{TRD,i} \end{aligned} \tag{1.13}$$

where the six TRD modules and the aerogel and gas radiators of the RICH are treated as independent detectors. The (conditional) probability $P(e(h)|S,p,\theta)$ that a particle with momentum p and polar angle θ having produced a signal S in a PID detector is a positron (hadron) is according to Bayes' Theorem:

$$P(e(h)|S,p,\theta) = \frac{P(S|e(h),p)P(e(h)|p,\theta)}{P(S|e,p)P(e|p,\theta) + P(S|h,p)P(h|p,\theta)}, \tag{1.14}$$

i.e., it is proportional to the product of the parent distributions and the probability that a particle with (p,θ) actually is a positron (hadron). The latter is called the particle flux $\phi_{e,(h)}$. The complete information about the type of a particle is thus stored in a quantity

$$PID = \lg \frac{P(S|e,p)P(e|p,\theta)}{P(S|h,p)P(h|p,\theta)} = PID3 + PID5 - \lg \Phi, \quad \Phi = \frac{\phi_h}{\phi_e}. \tag{1.15}$$

The fluxes and parent distributions are determined from data in an iterative procedure [Wen03, Wen99].

The separation of pions, kaons and protons by the RICH is done by comparing the measured average Cherenkov angle $\langle\theta\rangle^h_{A,G}$ of photons assumed to be emitted by a particle with the theoretically expected angles $\theta^{th,h}_{A,G}$. For each track, the theoretical emission angles are computed with each hadron type hypothesis $h = \pi,\ K,\ p$, assuming that the photon was emitted in the aerogel (A) or in the gas (G). The Cherenkov angles are determined from the hits on the PMT matrix associated to a particle track using an inverse ray tracing algorithm [Ako02]. The average Cherenkov angle $\langle\theta\rangle^h_{A,G}$ is determined for each radiator and each hypothesis by including only hits lying within $\pm 2\sigma_\theta$ around the theoretically expected angle. The likelihood for a hadron type hypothesis is then (assuming a Gaussian distribution of Cherenkov angles around the expectation):

$$\mathcal{L}^h_{A,G} = \exp\left[-\frac{\left(\theta^{th,h}_{A,G} - \langle\theta\rangle^h_{A,G}\right)^2}{2\sigma^2_{\langle\theta\rangle^h_{A,G}}}\right]. \tag{1.16}$$

The particle hypothesis with the largest likelihood $\mathcal{L}^{h(max)} = (\mathcal{L}^h_A \mathcal{L}^h_G)^{max}$ is assigned to the track, with a confidence defined in the quality parameter rQp

$$rQp = \lg \frac{\mathcal{L}^{h(max)}}{\mathcal{L}^{h(2)}}, \tag{1.17}$$

where $h(2)$ is the hypothesis with the second largest likelihood. A hadron can be considered as identified when $rQp > 0$. For a detailed analysis, especially of kaons and protons, a procedure is applied taking into account efficiencies and contaminations associated with this algorithm. This procedure will be explained in section 3.2.6.

1.3.4 Luminosity Measurement and Trigger

The HERMES luminosity monitor consists of two small calorimeters, located on both sides of the beam pipe in the horizontal plane, about 7.2 m downstream of the target. The luminosity monitor is particularly sensitive to Bhabha scattering ($e^+e^- \to e^+e^-$) and annihilation processes ($e^+e^- \to \gamma\gamma$) between beam positrons and the shell electrons of the target atoms. For an electron beam, as in 1998, the measurable process would be Møller scattering ($e^-e^- \to e^-e^-$). Events from these processes can be separated from background by requiring coincident high energy clusters in each calorimeter. The calorimeters consist of 3×4 arrays of radiation resistant $NaBi(WO_4)_2$ crystals, each of which is read out by an individual photo multiplier. The very well known cross section for the scattering and annihilation processes is integrated and folded with the detector acceptance and efficiency. From this and the coincidence rate the luminosity can be determined with an accuracy of $\Delta L/L \simeq 6\%$. For asymmetry measurements only the relative luminosity from data with two different spin configurations is relevant, here the uncertainty is much smaller, $\Delta R/R \simeq 0.9 - 1.5\%$. In [Ben01] a detailed description of the luminosity monitor and the contribution of systematic uncertainties to the luminosity measurement is given.

The HERMES trigger system selects events interesting for physics analysis. Additional triggers are used for detector monitoring and calibration. The first level trigger decision is made within about 400 ns after the event occurred, using some combinations of signals from the scintillator hodoscopes (H0 directly upstream of the FCs, H1 directly in front of BC3/4, and H2 is the preshower detector), some of the wire chambers and the calorimeter. The main trigger selects candidates for the scattered positron in deep inelastic scattering by requiring coincident signals in the three hodoscopes in one detector half and a minimum energy deposited in two adjacent calorimeter columns in the same half. From the middle of the 1996 running period on, for running with a polarized target the trigger energy threshold of the calorimeter has been set to 1.4 GeV. Before that period, it was at 3.5 GeV. The high threshold suppresses events with only hadrons (i.e. photoproduction events where the small angle of the scattered positron prevents it from detection),

because their energy deposition in the calorimeter is usually smaller. For running with unpolarized gas at higher densities, the threshold is usually set to 3.5 GeV to reduce trigger rates. In order to extend the range of possible measurements, photoproduction triggers where introduced, selecting events with two or more hadrons. These triggers usually require coincident signals in the top *and* bottom half of the spectrometer in all three hodoscopes as well as the BCs or MCs.
Not all of the generated triggers can be accepted by the HERMES data acquisition system (DAQ). During the time needed for readout, newly generated triggers cannot be accepted, leading to a 'dead time' of the trigger system. The dead time is defined as the ratio of rejected trigger requests to the total number of generated triggers. The DAQ system digitizes the analog and timing information for an accepted trigger in the ADC and TDC modules located in Fastbus crates. The information from the Fastbus modules is then sent to a Linux PC farm and stored on hard disks. During the breaks in between HERA fills the data on these disks are copied to tapes for permanent storage. The HERMES DAQ is capable of reading out the detector information at rates up to 500 Hz with dead times below 10%.

Chapter 2

Theoretical Issues and Motivation

2.1 Kinematics and Cross Section in Deep Inelastic Scattering

In deep inelastic scattering (DIS), leptons are used as a probe of the nucleon structure. As opposed to elastic or inelastic scattering, in DIS the lepton energy is large enough to destroy the nucleon, leaving a continuous spectrum of hadrons in the final state. Figure 2.1 shows a sketch of the deep inelastic scattering process. The incident lepton ($E^{\pm}$, $\mu^{\pm}$, ν, $\bar{\nu}$) with momentum $\vec{k}$ and energy E

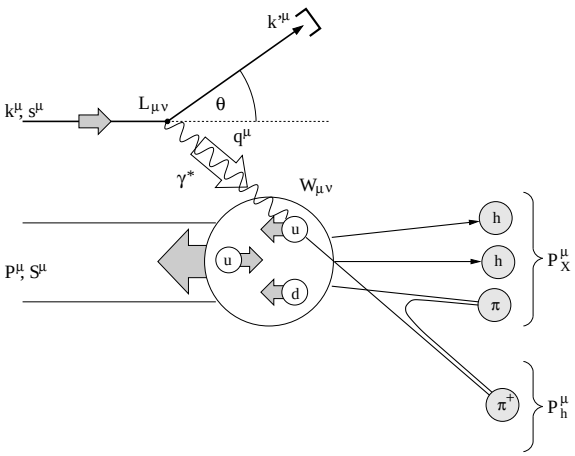

Figure 2.1: Sketch of the deep inelastic scattering process as seen in the laboratory system. The big arrows indicate the spins of the particles. Deep inelastic scattering is here pictured as the scattering off the nucleons constituents, the distribution of which is described by the quantity $W_{\mu\nu}$. A detailed explanation of its meaning will be given in in sections 2.1.1 and 2.2.

transfers a momentum $\vec{q}$ and energy ν to the nucleon. The interaction takes place via the exchange of a virtual boson with mass $q^2 \equiv -Q^2$. The type of the exchange boson depends on the lepton type and the energy involved in the experiments. For (anti-) neutrino beams, a charged vector boson $W^{\pm}$ is the mediator of the interaction. With charged leptons, the exchange of a Z^0 boson may become important at very high Q^2, for instance at collider experiments like at HERA. At smaller energies, photons are the dominant exchange bosons. In the following, only photons will be considered, as those are the only relevant exchange bosons in the case of the HERMES experiment, the contribution from Z^0 bosons is completely negligible. The virtual photon (denoted by γ^*) is absorbed by a nucleon with mass M and momentum $\vec{P}$. Eventually the nucleon breaks up into its constituents that hadronize into a number of hadrons with total invariant mass $W^2 = (q+p)^2$. Since the baryon number is conserved, the final state mass must be at least that of the nucleon, $W \geq M$. In inclusive DIS, only the outgoing lepton with momentum $\vec{k'}$ is detected, thus integrating over all possible final state hadrons. In semi-inclusive DIS, hadrons are detected in coincidence with the outgoing lepton. Measuring their momenta $\vec{p}_h$ and possibly their energy helps to gain more information on the particles and the type of process involved in the scattering. The following variables are commonly used to describe DIS:

$(E, \vec{k})$	four momentum of the incoming lepton
$(E', \vec{k'})$	four momentum of the outgoing lepton
$(M, \vec{P})$	four momentum of the target nucleon
s^μ, S^μ	four spin vectors of the incoming lepton and target nucleon
$\nu = E - E'$	energy transfer to the virtual photon
$q = k - k'$	four momentum transfer to the virtual photon
$Q^2 = -q^2 \overset{\text{lab}}{\simeq} 4EE' \sin^2 \frac{\theta^2}{2}$	virtuality of the photon, θ = lepton scattering angle in the lab frame
$y = \frac{p \cdot q}{p \cdot k} \overset{\text{lab}}{=} \frac{\nu}{E}$	fractional energy transfer to the nucleon
$x = \frac{-q^2}{2p \cdot q} \overset{\text{lab}}{=} \frac{Q^2}{2M\nu}$	Bjorken scaling variable
$W^2 = (p+q)^2 \overset{\text{lab}}{=} M_p^2 + 2M_p\nu - Q^2$	invariant mass of the virtual photon-nucleon subsystem
$z = \frac{p \cdot p_h}{p \cdot q} \overset{\text{lab}}{=} \frac{E_h}{\nu}$	fraction of the virtual photon energy carried by a hadron h
$p_\parallel = \frac{\vec{p}_h \cdot \vec{q}}{\lvert\vec{q}\rvert}$	longitudinal momentum of a hadron h in the $\gamma^* - N$ center of mass system
$p_T = \frac{\lvert\vec{p}_h \times \vec{q}\rvert}{\lvert\vec{q}\rvert}$	transverse momentum of a hadron h in the $\gamma^* - N$ center of mass system
$x_F = \frac{2p_\parallel}{W}$	Feynman scaling variable, scaled longitudinal momentum of a hadron h in the $\gamma^* - N$ center of mass system
P_X, M_x	total four momentum and invariant mass of the *undetected* hadronic final state

The *inclusive* cross section depends on two independent variables. In the laboratory system (where the target nucleon is at rest), one usually uses (E', θ), with $0 < \theta < \pi$. Alternatively one can use two invariants like (x, Q^2) or (x, y). The requirement that $W^2 > M^2$ leads to $0 \leq x \leq 1$, or $Q^2 \leq 2M\nu$, with $0 < \nu < E$. To express the semi-inclusive cross section, three more variables are necessary to characterize the final state hadrons, for instance their fractional energy z relative to the virtual photon energy, their transverse momentum p_T relative to the photon direction and their azimuthal angle ϕ, measured against the plane of scattering. For many measurements, the azimuthal angle is integrated over, also for this analysis.

2.1.1 Cross Sections and Asymmetries in Lepton-Nucleon Scattering

The material for this subsection can be found for instance in Refs. [Jaf96], [Man92] or [Tho01]. The differential cross section for the inclusive process in figure 2.1 is:

$$d\sigma = \sum_X \int \frac{d^3k'}{(2\pi)^3 2E'} (2\pi)^4 \delta^4(k + p - k' + p_X) \frac{|\mathcal{M}|^2}{(2E)(2M)}, \tag{2.1}$$

where the scattering amplitude $\mathcal{M}$ is given by:

$$i\mathcal{M} = (-ie)^2 \left(\frac{-ig_{\mu\nu}}{q^2} \right) \langle k' | j_l^\mu(0) | k, s \rangle \langle X | j_h^\nu(0) | P, S \rangle. \tag{2.2}$$

Here, $j^\mu_{l(h)}$ represents the electromagnetic leptonic (hadronic) current. Note that the spin of the outgoing lepton is not measured, thus the amplitude contains a sum over the final state spins. With the squared amplitude

$$\mathcal{M}\mathcal{M}^* \sim \langle P, \lambda | j_h^\mu(0) | X \rangle \langle X | j_h^\nu(0) | P, \lambda \rangle \langle k, s | j_{\mu l}(0) | k' \rangle \langle k' | j_{\nu l}(0) | k, s \rangle \tag{2.3}$$

conventionally a leptonic tensor $L_{\mu\nu}$ and a hadronic tensor $W^{\mu\nu}$ are defined by ($\alpha = e^2/(4\pi)$):

$$\left|\frac{\mathcal{M}}{4\pi}\right|^2 = \frac{\alpha^2}{Q^4} L_{\mu\nu} W^{\mu\nu}. \tag{2.4}$$

The leptonic tensor then becomes:

$$\begin{aligned} L^{\mu\nu} &= \sum_{\text{final spins}} \langle k,s|j_l^\mu(0)|k'\rangle\langle k'|j_l^\nu(0)|k,s\rangle \\ &= \sum_{\text{final spins}} \bar{u}(k,s)\gamma^\mu u(k')\bar{u}(k')\gamma^\nu u(k,s) \\ &= 2\left(k^\mu k'^\nu + k^\nu k'^\mu - g^{\mu\nu}(k\cdot k' - m_l^2) - i\epsilon^{\mu\nu\alpha\beta}q_\alpha s_\beta\right). \end{aligned} \tag{2.5}$$

The polarization vector of the lepton is defined as

$$2s^\mu = \bar{u}(k,s)\gamma^\mu\gamma_5 u(k,s), \tag{2.6}$$

which for a longitudinally polarized lepton in the extreme relativistic limit gives $s = hk$, with $h = \pm 1$ the lepton helicity. The antisymmetric Levi-Civita tensor by convention has $\epsilon_{0123} = +1$.

Including the sum over all hadronic final states X satisfying $q + p - p_X = 0$, the hadronic tensor can be written as:

$$\begin{aligned} W^{\mu\nu} = \frac{1}{4\pi}\sum_X \Big\{ &(2\pi)^4\delta^4(q+p-p_X)\langle P,S|j_h^\nu(0)|X\rangle\langle X|j_h^\mu(0)|P,S\rangle \\ &-(2\pi)^4\delta^4(q+p_X-p)\langle P,S|j_h^\nu(0)|X\rangle\langle X|j_h^\mu(0)|P,S\rangle\Big\}. \end{aligned} \tag{2.7}$$

The second term in the sum is always zero for the physically allowed region where $p_X^0 > p^0$, because $M_X^2 > M^2$. Since also $q^0 > 0$, the term $q^0 + p_X^0 - p^0$ is always bigger than zero, and the delta function can never be satisfied. Using

$$\langle P,S|j_h^\nu(x)|X\rangle = \langle P,S|j_h^\nu(0)|X\rangle e^{i(p-p_X)\cdot x} \quad \text{(translational invariance)}, \tag{2.8}$$

$$(2\pi)^4\delta^4(K) = \int d^4x e^{ix\cdot K} \quad \text{and} \tag{2.9}$$

$$\sum_X |X\rangle\langle X| = \mathbf{1} \tag{2.10}$$

one gets:

$$W^{\mu\nu} = \frac{1}{4\pi}\int d^4x e^{iq\cdot x}\langle P,S|\left[j_h^\nu(x), j_h^\nu(0)\right]|P,S\rangle. \tag{2.11}$$

The spin vector of the nucleon is defined analogously to that of the lepton, in the target rest frame it is $S = (0,\vec{S}) = (0,0,0,\pm M)$ for a spin 1/2 target polarized along the z direction. The reason to express $W^{\mu\nu}$ in terms of the commutator is its analytic structure when continued to *outside* the physical region, a method used to calculate forward amplitudes.

$W^{\mu\nu}$ describes the absorption of the virtual photon by the nucleon, therefore it must contain all the information concerning the structure of the nucleon. This tensor is unknown, and in fact the subject under study in DIS. The most general form of the tensor depends on P, q and S. Fundamental symmetry considerations and conservation laws, which are

- Lorentz invariance,
- invariance of electromagnetic interactions under parity transformations, charge conjugation and time reversal (separately) and the
- conservation of the electromagnetic current $\partial_\mu W^{\mu\nu} = -iq_\mu W^{\mu\nu} = 0$,

reduce the tensor to a form where it can be parametrized by four independent structure functions F_1, F_2, g_1 and g_2,

$$\begin{aligned} W_{\mu\nu} &= \left(-g_{\mu\nu} + \frac{q_\mu q_\nu}{q^2}\right) F_1 + \left(P_\mu - \frac{p\cdot q}{q^2} q_\mu\right)\left(P_\nu - \frac{p\cdot q}{q^2} q_\nu\right)\frac{F_2}{p\cdot q} \\ &+ i\epsilon_{\mu\nu\lambda\sigma}\frac{q^\lambda S^\sigma}{p\cdot q} g_1 + i\epsilon_{\mu\nu\lambda\sigma}\frac{q^\lambda}{(p\cdot q)^2}\left(p\cdot q S^\sigma - S\cdot q p^\sigma\right) g_2. \end{aligned} \tag{2.12}$$

The dimensionless structure functions depend on two Lorentz invariant observables, x and Q^2. When contracted with the leptonic tensor, only those terms survive that are either both symmetric or both antisymmetric under interchange of indices $\nu \leftrightarrow \mu$. Thus the cross section can be separated into an unpolarized (spin independent) part:

$$\frac{d^2\sigma}{dxdy} = \frac{4\pi\alpha^2}{Q^2}\frac{1}{y}\left\{ y^2\left(1 - \frac{2m_e^2}{Q^2}\right) F_1(x,Q^2) + \left(1 - y - \frac{Q^2}{4E^2}\right)\frac{F_2(x,Q^2)}{x}\right\}, \tag{2.13}$$

and a part where both beam and target are polarized:

$$\begin{aligned} &\frac{d^3\left(\sigma(\alpha) - \sigma(\pi-\alpha)\right)}{dxdyd\phi} = \\ &= \frac{e^4}{4\pi^2 Q^2}\Bigg\{ \cos\alpha\left(1 - \frac{y}{2} - \frac{Q^2}{4E^2} - \frac{m_e^2 y^2}{Q^2}\right) g_1(x,Q^2) - \frac{y}{2}\gamma^2 g_2(x,Q^2) \\ &- \sin\alpha\cos\phi\sqrt{\gamma^2\left(1 - \frac{y}{2} - \frac{Q^2}{4E^2}\right)}\left(\frac{y}{2}\left(1 + \frac{m_e^2 y^2}{Q^2}\right) g_1(x,Q^2) + g_2(x,Q^2)\right)\Bigg\}. \end{aligned} \tag{2.14}$$

The difference here is between cross sections with opposite target polarizations with respect to that of the beam. The angle α is the angle between the polarization vector of the target and the beam direction whereas ϕ is the azimuthal angle between the scattering plane defined by $\vec{k}$ and $\vec{k'}$ and and the polarization plane spanned by the beam axis and the target polarization vector (see figure 2.2). The factor γ^2 is equal to Q^2/ν^2.

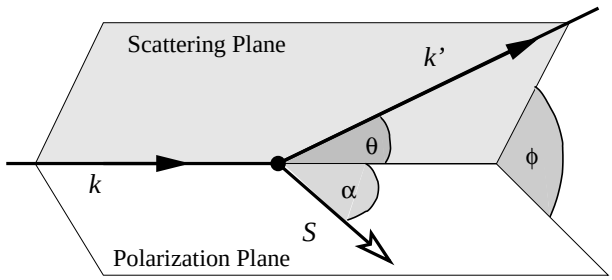

Figure 2.2: Definition of the scattering plane and the polarization plane in polarized lepton-nucleon scattering on a fixed target.

For the unpolarized cross section, only F_1 and F_2 are relevant, whereas g_1 and g_2 only contribute to the cross section if both the beam and the target are polarized. For a longitudinally polarized target ($\alpha = 0$), the cross section difference of Eq. 2.14 becomes:

$$\frac{d^2\Delta\sigma_\parallel}{dxdy} = \frac{8\pi\alpha^2}{Q^2}\left\{\left(1 - \frac{y}{2} - \frac{Q^2}{4E^2} - \frac{m_e^2 y^2}{Q^2}\right) g_1(x,Q^2) - \frac{y}{2}\gamma^2 g_2(x,Q^2)\right\}. \tag{2.15}$$

In this case, the contribution from g_2 is suppressed by a factor Q^2/ν^2 that is usually small for experiments like HERMES. At polarized experiments, what is typically measured to extract g_1 is the asymmetry

$$\frac{\Delta\sigma}{\sigma} \equiv A_\parallel = \frac{\sigma^{\rightleftarrows} - \sigma^{\rightrightarrows}}{\sigma^{\rightleftarrows} + \sigma^{\rightrightarrows}}. \tag{2.16}$$

This has the advantage that systematic uncertainties from efficiencies etc. cancel to a large extent in the ratio of cross sections.

2.1.2 Virtual Photon Cross Sections and Asymmetries

It is possible to write the cross sections and asymmetries of the previous subsection in terms of cross sections for the absorption of virtual photons. This subsection follows the discussions given in Refs. [Hal84] and [Rob90]. In this approach, the virtual photon cross sections can eventually be related to real photon cross sections $\sigma^{\gamma N}$ as $Q^2 \to 0$ which can be written as:

$$\sigma(\gamma N \to X) = \frac{4\pi^2\alpha}{\nu}\epsilon_\lambda^{\mu^*}\epsilon_\lambda^\nu W_{\mu\nu}, \tag{2.17}$$

with the photon polarization vector ϵ_λ and the photon helicity $\lambda = \pm 1$. For virtual photons, also the helicity 0 has to be taken into account. The cross sections of Eq. (2.13) and (2.14) can then be written in terms of the absorption cross section for transverse and longitudinal photons. This is done by factorizing the lepton-nucleon cross section into the probabilities $\Gamma_{L(T)}$ for the emission of a longitudinal (transverse) virtual photon by the initial lepton and the absorption of the virtual photon by the nucleon, with the cross section represented by $\sigma_{L(T)}$. The lepton-nucleon cross section is then the sum:

$$\frac{d^2\sigma^{eN}}{dQ^2 d\nu} = \Gamma_T(Q^2,\nu)\sigma_T(Q^2,\nu) + \Gamma_L(Q^2,\nu)\sigma_L(Q^2,\nu) = \Gamma_T\sigma_T(1+\epsilon R), \tag{2.18}$$

where $R = \sigma_L/\sigma_T$ and $\epsilon = \Gamma_L/\Gamma_T$. The definition of the 'equivalent photon flux' Γ is somewhat arbitrary, so that the fluxes and the virtual photon cross sections by themselves are not observables, only the product of the two. The concept of the Equivalent Photon Approximation is described in detail in [Bud75]. Using the so called Hand-convention [Han63], the flux can be written as:

$$\Gamma_T = \frac{\alpha(1-x)}{2\pi Q^2\nu}\left[y^2\left(1-\frac{2m_e^2}{Q^2}\right) + 2\frac{1}{1+\gamma^2}\left(1-y-\frac{Q^2}{4E^2}\right)\right] \tag{2.19}$$

$$\epsilon = \left[1+\frac{1}{2}\left(1-\frac{2m_e^2}{Q^2}\right)\frac{y^2+\frac{Q^2}{E^2}}{1-y-\frac{Q^2}{4E^2}}\right]^{-1}. \tag{2.20}$$

The absorption cross sections for transverse photons polarized parallel or antiparallel to the target spin orientation ($\sigma_{3/2}$ and $\sigma_{1/2}$) and that for longitudinal photons (σ_L) become:

$$\sigma_{3/2} = \frac{4\pi^2\alpha}{Q^2(1-x)}2x\left[F_1(x,Q^2) - g_1(x,Q^2) + \gamma^2 g_2(x,Q^2)\right] \tag{2.21}$$

$$\sigma_{1/2} = \frac{4\pi^2\alpha}{Q^2(1-x)}2x\left[F_1(x,Q^2) + g_1(x,Q^2) - \gamma^2 g_2(x,Q^2)\right] \tag{2.22}$$

$$\sigma_L = = \frac{4\pi^2\alpha}{Q^2(1-x)}2x\left[\frac{1+\gamma^2}{2x}F_2(x,Q^2) - F_1(x,Q^2)\right]. \tag{2.23}$$

This results in the unpolarized *transverse* cross section

$$\sigma_T = \frac{1}{2}(\sigma_{1/2}+\sigma_{3/2}) = \frac{4\pi^2\alpha}{Q^2(1-x)}2x\left[F_1(x,Q^2)\right] \tag{2.24}$$

and the cross section ratio

$$R = \frac{\sigma_L}{\sigma_T} = \frac{1+\gamma^2}{2x}\frac{F_2}{F_1} - 1. \tag{2.25}$$

In this sense, F_1, F_2 and R are the three quantities describing the unpolarized cross section, two of which are independent. The virtual-photon absorption asymmetry

$$A_1 = \frac{\sigma_{1/2}-\sigma_{3/2}}{\sigma_{1/2}+\sigma_{3/2}} = \frac{g_1 - \gamma^2 g_2}{F_1} \tag{2.26}$$

can be related to the lepton-nucleon asymmetry by

$$A_{\parallel} = D(y,Q^2)(A_1 + \eta A_2), \quad \text{with} \tag{2.27}$$

$$D = \frac{y\left[\left(1+\frac{\gamma^2 y}{2}\right)(2-y) - \frac{2y^2 m_e^2}{Q^2}\right]}{y^2\left(1-\frac{2y^2m_e^2}{Q^2}\right)(1+\gamma^2) + 2(1+R)\left(1-y-\frac{Q^2}{4E^2}\right)} \quad \text{and} \tag{2.28}$$

$$\eta = \frac{\left(1-y-\frac{Q^2}{4E^2}-\frac{y^2m_e^2}{Q^2}\right)}{\left(1+\frac{\gamma^2 y}{2}\right)\left(1-\frac{y}{2}\right)-\frac{y^2m_e^2}{Q^2}}. \tag{2.29}$$

D is the effective polarization of the photon, called the depolarization factor. It depends on the kinematics at the lepton vertex only. The absorption asymmetry for a *transversely* polarized target A_2 appears in the expression for $A_{\parallel}$ because the spin of the virtual photon is quantized along the direction of the photon momentum, whereas the target spin is aligned along the z direction in the lab frame. In the photon-nucleon system then, the photon is sensitive to a transverse spin component of the nucleon. Just like in Eq. 2.15, g_2 is suppressed by factor of γ^2 and in fact it has been measured to be small [Ant03], such that it can be neglected in the case of longitudinally polarized beams and target. A_2 is given by

$$A_2 = \frac{\gamma(g_1+g_2)}{F_1}, \tag{2.30}$$

such that

$$A_{\parallel} \simeq D(y,Q^2)(1+\eta\gamma)\frac{g_1}{F_1}. \tag{2.31}$$

From measurements of unpolarized cross sections, F_2 can be derived as well as the cross section ratio R. From a parametrization of both and using Eq. 2.25, g_1 can thus be extracted from a measurement of $A_{\parallel}$.

2.2 Structure Functions in the Simple Quark-Parton Model

The early SLAC measurements of the unpolarized structure function $F_2(x,Q^2)$ [Blo70] showed that above $W > 2$ GeV, and between $x = 0.1$ and $x = 1$, F_2 was *approximately* independent of Q^2. This is the so called 'scaling behavior', the invariance of the structure functions to a scaling of the external momenta $p_i \to \xi p_i$, and it has been in fact conjectured by Bjorken [Bjo69] and Feynman [Fey69]. It is based on the assumption that at high enough energy, where the target mass can be neglected, the lepton would not scatter on bound nucleon constituents, but on free, pointlike spin 1/2 particles, the 'partons'. The lepton-nucleon cross section can then be evaluated as the incoherent sum of the contributions from all partons in the nucleon. The Quark Parton Model (QPM) emerged as a joint picture of this parton model with the nonrelativistic Quark Model where the nucleon *at low energy* is pictured as a bound state of three constituents, the quarks. At that time, from hadron spectroscopy, four different quarks species (the 'flavors' f) were known that were characterized by their fractional charges $e_f = 2/3$ (for up (u) and charm (c) quarks) and $e_f = -1/3$ (for down (d) and strange (s) quarks) of the lepton charge e. Later on, two other flavors were discovered, the top (t) quark with 2/3 and the bottom (b) quark with -1/3 of the lepton charge. It was also known that quarks have spin 1/2 and an additional quantum number, the 'color' charge, that could take three possible values. As the Quark Model was extraordinarily successful in describing hadron spectra as well as the anomalous magnetic moments of a number of nucleons, the parton model was merged with the Quark Model with the assertion that the partons were (free) quarks and antiquarks.

By the uncertainty principle $\Delta x \Delta p \simeq 1$, and for the size of the nucleon of $\Delta x = \mathcal{O}(fm)$ the intrinsic transverse momentum of partons is about 0.4 GeV and such negligible in the high-energy limit. The kinematic region for which the scaling prediction should hold is the Bjorken scaling

limit where $Q^2 \to \infty$, $\nu \to \infty$ such that $x = Q^2/2M\nu$ is fixed. The scattering amplitude for lepton scattering on a parton with a fraction ξ of the nucleon momentum can be obtained by exchanging the hadronic tensor $W_{\mu\nu}$ in Eq. 2.12 by a 'partonic' tensor $\hat{W}_{\mu\nu}$. This partonic tensor can be obtained from the leptonic tensor, Eq. 2.5 by replacing $k \to \xi p$, $k' \to p'$, $s \to s_p$ and $q \to -q$, and multiplying by the square of the fractional quark charge e_f^2. In addition, for the inclusive cross section, the tensor has to be integrated over the final particle phase space, where $p' = \xi p + q$.

$$\hat{W}_{\mu\nu} = \frac{1}{4\pi} e_f^2 \int \frac{d^3p'}{(2\pi)^3 2E_{p'}} \frac{1}{\xi} (2\pi)^4 \delta^4(\xi p + q - p') \times 2\left(\xi p_\mu p'_\nu + \xi p_\nu p'_\mu - g_{\mu\nu}\xi p \cdot p' + i\epsilon_{\mu\nu\alpha\beta} q^\alpha s_p^\beta\right), \tag{2.32}$$

with the factor $1/\xi$ accounting for proper normalization of the parton states. The spin of the massless parton can be written in terms of its helicity as $s_{p\beta} = h\xi p_\beta$. Since the nucleon is considered to be massless at high energy, also $S = HP$, with the nucleon helicity H. With the condition that the outgoing massless parton be on shell $(\xi p + q - p')^2 = 0$ one obtains:

$$\int \frac{d^3p'}{(2\pi)^3 2E_{p'}} = \int \frac{d^4p'}{(2\pi)^4} (2\pi)\delta\left((\xi p + q - p')^2\right) = \int \frac{d^4p'}{(2\pi)^4} \frac{(2\pi)}{2p \cdot q} \delta\left(\xi + \frac{q^2}{2p \cdot q}\right), \tag{2.33}$$

and the partonic tensor becomes:

$$\hat{W}_{\mu\nu} = \frac{e_f^2}{2\xi p \cdot q}\left(2\xi^2 p_\mu p'_\nu - g_{\mu\nu}\xi p \cdot q + ih\xi\epsilon_{\mu\nu\alpha\beta} q^\alpha p^\beta\right)\delta(\xi - x). \tag{2.34}$$

If $q_f^{hH}(\xi)d\xi$ ($\bar{q}_f^{hH}(\xi)d\xi$) define the probability to find a quark (antiquark) of flavor f with momentum fraction between ξ and $\xi + d\xi$ and helicity equal to that of the nucleon ($hH = +1$) or opposite to it ($hH = -1$), the hadronic tensor can be written as:

$$W_{\mu\nu}(x) = \sum_{f,\pm} e_f^2 \int d\xi \hat{W}_{\mu\nu}\left(q_f^\pm(\xi)\right)\delta(\xi - x) \tag{2.35}$$

This derivation can be found in Ref. [Man92]. The structure functions in the simple QPM can be obtained by comparing this expression to Eq. 2.12:

$$F_1(x) = \sum_f \frac{e_f^2}{2}\left(q_f^+(x) + q_f^-(x) + \bar{q}_f^+(x) + \bar{q}_f^-(x)\right) \tag{2.36}$$

$$F_2(x) = \sum_f e_f^2 x\left(q_f^+(x) + q_f^-(x) + \bar{q}_f^+(x) + \bar{q}_f^-(x)\right) \tag{2.37}$$

$$g_1(x) = \sum_f \frac{e_f^2}{2}\left(q_f^+(x) - q_f^-(x) + \bar{q}_f^+(x) - \bar{q}_f^-(x)\right) \tag{2.38}$$

$$g_2(x) = 0. \tag{2.39}$$

Note some features of this simple Quark-Parton model:

- The structure functions depend only on x, not on Q^2. This scaling behavior is the result of the assumption of scattering on free, massless, pointlike particles. Pointlike particles have no form factor that would show up in a strong Q^2 dependence as in elastic lepton-nucleon scattering for example. Because partons and nucleon are treated as massless, no mass scale can be involved. If the center of mass energy becomes small, such that $W^2 = \mathcal{O}(M^2)$, target mass corrections have to be applied.

- The relation between F_1 and F_2 in the simple QPM is:

$$F_2 = 2xF_1 \tag{2.40}$$

This is the Callan-Cross relation [Cal69] for spin 1/2 Dirac-particles. If the spin of the quarks were 0 for instance, the relation were instead: $2xF_1/F_2 = 0$ (see for instance Ref. [Gri87]). Comparing to Eq. 2.25, the factor $1/(1+R)$ is missing in this relation. This is due to the fact that for the process $\gamma^* q \rightarrow q$ helicity conservation for massless particles implies that $\sigma_L = 0$. The absorption of a photon with helicity 0 could only take place if the helicity of the quark were flipped, which is not allowed in this case. This is also the reason why $g_2 = 0$ in the simple QPM, as it is related to spin components transverse to the quark momentum. It can only be different from 0 when transverse degrees of freedom are involved that have been neglected in this model. For a detailed study on g_2, see for instance Ref. [Jaf96].

- As can be seen from Eqs. 2.36 and 2.38, F_1 can be interpreted as the charge weighted, helicity averaged sum of the quark densities $q(x) = q^+(x) + q^-(x)$ (and the corresponding antiquark densities $\bar{q}(x)$), and g_1 as the sum of the charge weighted helicity differences of quark distributions $\Delta q(x) = q^+(x) - q^-(x)$ and the antiquark distributions $\Delta\bar{q}(x)$. The ratios $\Delta q(x)/q(x)$ are the quark polarizations in the nucleon. Figure 2.3 shows how the virtual photon absorption is sensitive to quark helicities in the simple QPM. Again, helicity conservation implies that longitudinal photons do not contribute, and that virtual photon and target spins have to be antiparallel (i.e. their helicities parallel) to each other. The (transverse) virtual photon flips the spin projection of the quark by one unit, thus retaining the quark helicity. This can be intuitively pictured in a frame where the initial and final quarks move into opposite directions. From figure 2.3 it can be seen that this implies $\sigma_{1/2} \sim q^+(x)$ and $\sigma_{3/2} \sim q^-(x)$.

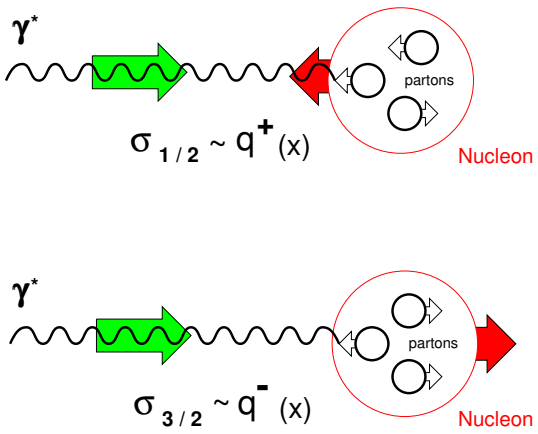

Figure 2.3: The simple QPM explanation of the sensitivity of polarized DIS to the polarized quark distributions. The arrows denote the spins of the particles.

2.3 The Quark-Parton Model in QCD

2.3.1 Scaling Violations of Structure Functions

Deviations from the scaling behavior of the unpolarized structure functions were discovered as soon as more data became available over a wider range in x. Already at SLAC it was seen that F_2 falls at high x when Q^2 goes to higher values [Rio74]. Up to now data were collected from a variety of fixed target and collider experiments that cover five orders of magnitude in Q^2 and x. A collection of data from the more recent experiments is shown in figure 2.4. The logarithmic dependence on Q^2 is now clearly evident. Data on the polarized structure function g_1 taken by fixed target experiments at SLAC, CERN and DESY are less abundant and cover a much smaller range in Q^2, but also there a small Q^2 dependence can be seen (see figure 2.5).

The scaling violations of the structure functions can be understood in the framework of Quantum Chromodynamics (QCD), the theory of strong interactions. An introduction to QCD can be found in [Hal84], the discussion in this section is mainly based on Refs. [Ste95] and [Rob90].

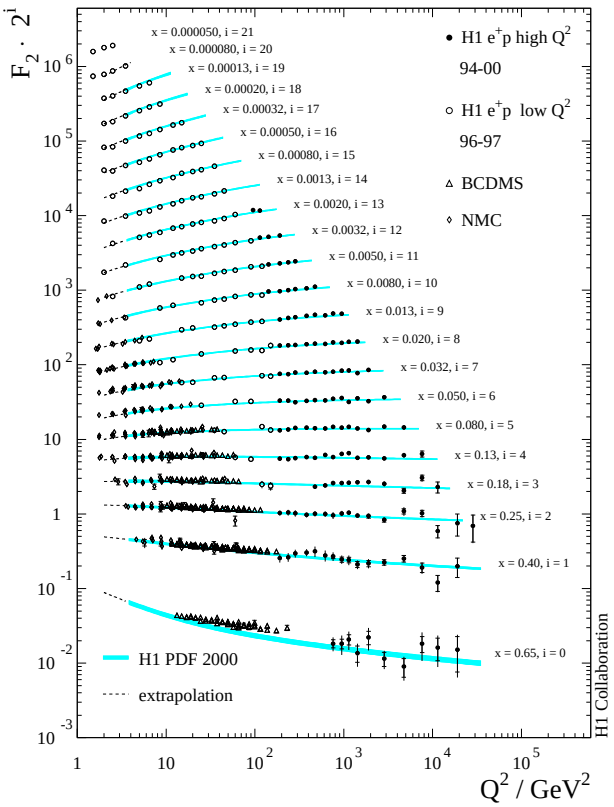

Figure 2.4: Data on F_2 from H1, NMC and BCDMS experiments as a function of Q^2. For each x-bin, F_2 was multiplied by a factor 2^i. The plot is taken from Ref. [Adl03]

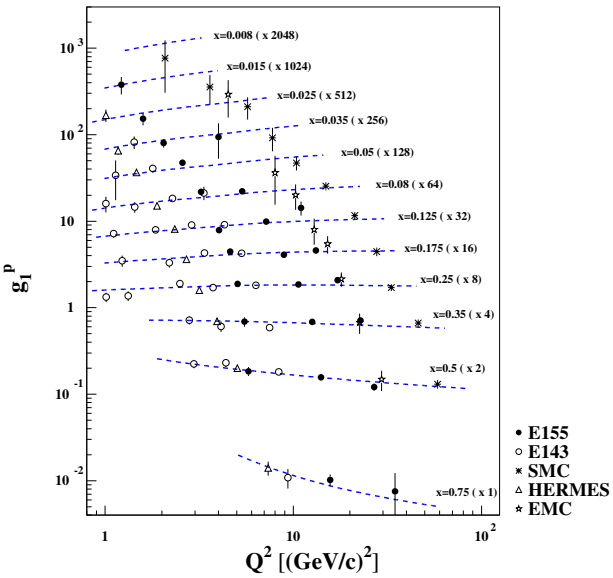

Figure 2.5: Data on g_1 for a proton target from SLAC, SMC and HERMES experiments. For each x-bin, F_2 was multiplied by a factor 2^i. The plot is taken from Ref. [DeN02]

In QCD, the quark color charges couple to spin 1 bosons, the gluons, which introduce interactions between the quarks. The theory is invariant under local transformations of the color charge, a symmetry that is represented by the $SU(3)_c$ symmetry group. Gluons themselves are bicolored, i.e., they carry a color and a (different) anticolor, such that they can couple to each other. This fact is expressed by the non-Abelian character of QCD. The coupling constant of QCD, $\alpha_s = g^2/4\pi$, depends on the renormalization scale μ. Renormalization accounts for virtual fluctuations happening at time scales Δt smaller than $1/\mu$ where quark and gluon loops in the calculation of amplitudes would lead to *ultraviolet divergences*. The bare color charge (the charge 'seen' at a time scale $1/M$ with $M \simeq 10^{15}$ GeV, the scale of 'grand unification') is at a time scale $\Delta t > 1/\mu$ 'dressed' by a cloud of gluon- and quark-antiquark pairs, such that quarks and gluons 'see' an effective color charge whose dependence on μ is described by the renormalization group equations. Any physical quantity, such as cross sections etc., may only depend on a set of measurable external momenta p, but not on the arbitrary renormalization scale μ,

$$\mu \frac{d}{d\mu}\sigma(p,\mu) = 0, \quad \text{with } \sigma(p,\mu) = \sum_{n=1}^{A} a_n(p,\mu) g^{2n}. \tag{2.41}$$

Here, the cross section is expressed as a power series in the coupling g that can in principle be carried out to some fixed order A. Eq. 2.41 leads to

$$\mu \frac{dg(\mu)}{d\mu} = \beta(g(\mu)), \quad \text{with } \beta(g) = -g\left(\frac{\alpha_s}{4\pi}\beta_1 + \left(\frac{\alpha_s}{4\pi}\right)^2 \beta_2 + \dots\right). \tag{2.42}$$

The *beta function* can be calculated from the requirement of Eq. 2.41 using the coefficients a_n of the expansion of the cross section. The $\mathcal{O}(\alpha_s)$ result is (with μ_0 being an arbitrary constant from

the solution of the differential equation 2.42):

$$\alpha_s(\mu) = \frac{\alpha_s(\mu_0)}{1 + \left(\frac{\beta_1}{4\pi}\right) \log\left(\frac{\mu^2}{\mu_0^2}\right) \alpha_s(\mu_0)} \tag{2.43}$$

$$= \frac{4\pi}{\beta_1 \log\left(\frac{\mu^2}{\Lambda^2}\right)} \quad \text{with } \Lambda = \Lambda_{QCD} = \mu_0 \exp\left(\frac{-2\pi}{\beta_1 \alpha_s(\mu_0)}\right) \tag{2.44}$$

Λ_{QCD} is a free parameter that sets the scale for the running coupling $\alpha_s(\mu)$, such that it is in fact independent of the starting scale μ_0. The leading coefficient is

$$\beta_1 = 11 - \frac{2n_f}{3}, \tag{2.45}$$

where n_f is the number of flavors involved in the problem and usually all flavors with a mass smaller than μ are taken into account. In any case, β is positive as the result of the self coupling of gluons. Eq. 2.44 implies that α_s decreases logarithmically as μ increases. This 'asymptotic freedom' eventually justifies the simple Quark Parton Model, since at high scales $\mu^2 = Q^2 \to \infty$ the strong coupling constant becomes so small that interactions between quarks become negligible.

The fact that in QCD quarks and gluons do interact with each other makes the leading order process $\gamma^* q \to q$ (diagram (a) of figure 2.6) receive corrections of the order $\mathcal{O}(\alpha_s)$ of the strong coupling constant α_s (diagrams (b) and (c) of figure 2.6). The resulting Q^2 dependence can

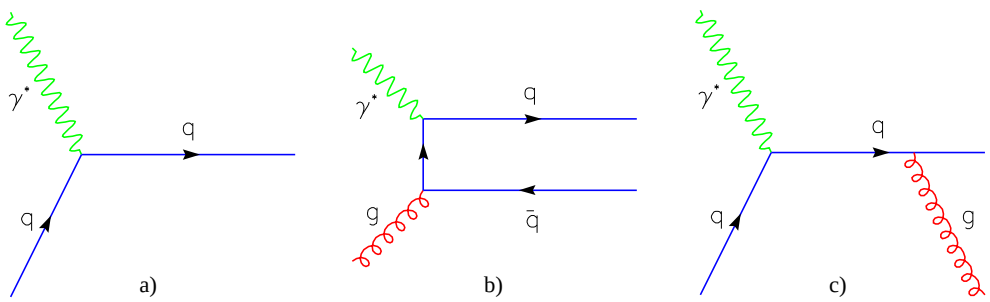

Figure 2.6: Feynman diagrams for the leading order DIS process (a) and the two $\mathcal{O}(\alpha_s)$ QCD processes Photon-Gluon Fusion (b) and QCD Compton scattering (c).

be explained by figure 2.7. The wavelength of a virtual photon determines the spatial resolution $\Delta x \sim \lambda$ with which the nucleon structure is probed. In general the resolution increases as Q^2 increases, since by the uncertainty principle a large momentum transfer is correlated with small distances, such that $\Delta x \sim 1/\sqrt{Q^2}$. A parton density at some $Q^2 > Q_0^2$ is different from the one measured at Q_0^2 because now it can be resolved that the parton measured by $q(x, Q_0^2)$ actually consists of a cloud of partons (quark, antiquarks and gluons) sharing the momentum fraction x. With increasing Q^2 the number of partons measured thus increases at small x and decreases at high x. This is the behavior that can be seen from figure 2.4. The structure functions defined in Eqs. 2.36 to 2.38 as combinations of quark distributions become Q^2-dependent for the same reason. The probability that a parton i in the final state with momentum fraction x in fact originates from a parton j in the initial state with momentum fraction y is proportional to the 'splitting function' P_{ij}. This function can be perturbatively expanded in a series in α_s,

$$P = \frac{\alpha_s(\mu^2)}{2\pi} P^{(1)} + \left(\frac{\alpha_s(\mu^2)}{2\pi}\right)^2 P^{(2)} + \ldots. \tag{2.46}$$

The Feynman diagrams contributing to the Q^2 evolution of parton distributions to leading order are shown in figure 2.8. The Q^2 evolution of the parton distributions f_j, where j stands for all

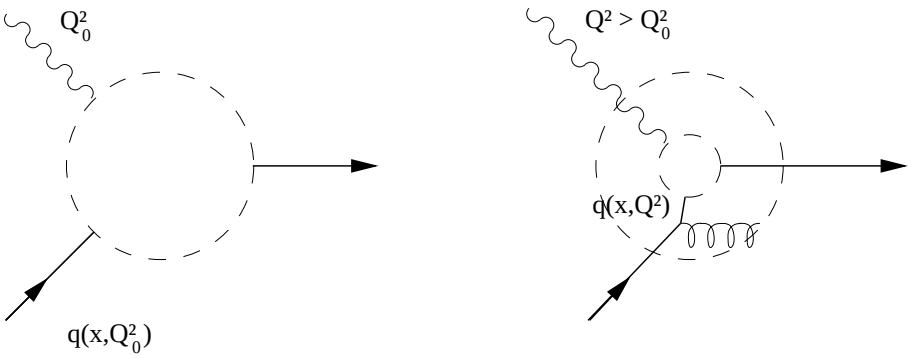

Figure 2.7: Schematic picture explaining the Q^2 (resolution) dependence of the parton distributions.

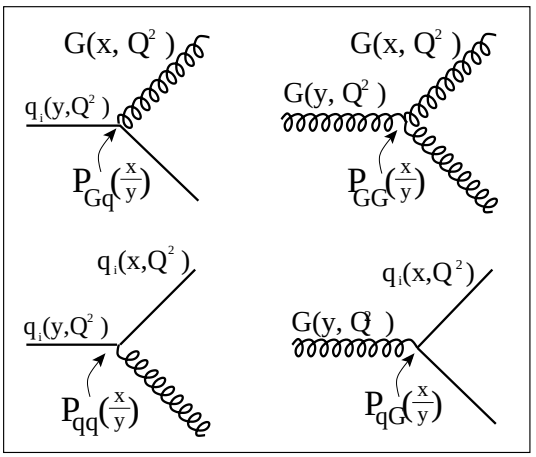

Figure 2.8: $\mathcal{O}(\alpha_s)$ contributions to the splitting functions P_{ij}.

quark- and antiquark flavors f, $\bar{f}$ as well as the gluon G, is described by the DGLAP (Dokshitzer-Gribov-Lipatov-Altarelli-Parisi) evolution equations [Alt77, Gri72, Dok77].

$$\mu^2 \frac{d}{d\mu^2} f_i(x, \mu_f, \mu^2) = \sum_{j=f,\bar{f},G} \int_x^1 \frac{d\xi}{\xi} P_{ij}\left(\frac{x}{\xi}, \alpha_s(\mu^2)\right) f_j(\xi, \mu_f, \mu^2). \tag{2.47}$$

The parton distribution functions (PDF) depend on the *factorization scale* μ_f and on the *renormalization scale* μ. The diagrams of figure 2.8 exhibit collinear and soft singularities in the gluon splittings and gluon emissions/absorptions. This is why the parton distributions themselves are nonperturbative objects, only their evolution can be calculated perturbatively. Those perturbative calculations involve loops with ultraviolet divergences, and the upper cut μ_f is introduced in order to keep the results finite. The factorization scale therefore constitutes something like an *ultraviolet cutoff* in the calculation of loops in the splitting functions. There are 'residual' terms of the form $\ln \frac{\mu_f^2}{\Lambda^2}$ from this cutoff that have to eventually be canceled by the terms $\ln \frac{\mu^2}{\mu_f^2}$ in the hard cross section with which the PDFs have to be convoluted to obtain meaningful cross sections and structure functions.

Conventionally, one writes the DGLAP equations 2.47 in terms of flavor singlet, nonsinglet and gluon distributions. The singlet distribution $(\Delta)\Sigma$ is the sum over all quark- and antiquark distributions. In the following, Δ always stands for the corresponding polarized quantity. Nonsinglet distributions $(\Delta)q^{NS}$ are defined such that gluons do not mix in their evolution (i.e. only P_{qq} con-

tribute in Eq. 2.47). The valence quark distribution in a nucleon for instance is such a nonsinglet distribution:

$$(\Delta)q_v = (\Delta)u - (\Delta)\bar{u} + (\Delta)d - (\Delta)\bar{d} \tag{2.48}$$

Gluons can only affect quark distributions by the creation of a quark/antiquark pair whose contribution cancels in relations like Eq. 2.48 where differences of quark- and antiquark distributions appear. For the singlet and nonsinglet distributions one defines the corresponding splitting functions $(\Delta)P_{qq}^S$ and $(\Delta)P_{qq}^{NS}$. The solution of the DGLAP equations is then ($t = \ln(\mu/\mu_0)$):

$$\begin{pmatrix} (\Delta)\Sigma(x,\mu^2) \\ (\Delta)G(x,\mu^2) \end{pmatrix} = \begin{pmatrix} (\Delta)\Sigma(x,\mu_0^2) \\ (\Delta)G(x,\mu_0^2) \end{pmatrix} + t \begin{pmatrix} (\Delta)P_{qq}^S & 2n_f(\Delta)P_{qG} \\ (\Delta)P_{Gq} & (\Delta)P_{GG} \end{pmatrix} \otimes \begin{pmatrix} (\Delta)\Sigma(x,\mu_0^2) \\ (\Delta)G(x,\mu_0^2) \end{pmatrix}, \tag{2.49}$$

$$(\Delta)q_{NS}(x,\mu^2) = (\Delta)q_{NS}(x,\mu_0^2) + t\left[(\Delta)P_{qq}^{NS} \otimes (\Delta)q^{NS}\right], \tag{2.50}$$

where the convolution $\otimes$ is defined by

$$a \otimes b(x,\mu^2) = \int_x^1 \frac{d\xi}{\xi} a\left(\frac{x}{\xi},\mu^2\right) b(\xi,\mu^2) \tag{2.51}$$

and $\Delta P_{ij} = P_{i^+j^+} - P_{i^+j^-}$ are the polarized splitting functions.

2.3.2 Factorization of Structure Functions in QCD

The factorization theorem of QCD states that the cross section for DIS can be separated into a long distance part corresponding to time scales $\Delta t > 1/\mu_f$ and a short distance part at smaller time scales. The factorization scale defines the separation between the short- and long distance processes. The long distance, nonperturbative part is absorbed into the parton distributions, the short distance part can be calculated perturbatively in the form of hard scattering amplitudes, with $\mu > \mu_f$. Here, μ_f serves as an *infrared cutoff* to avoid soft (infrared) singularities. In QCD, the structure functions can be expressed as:

$$F_1(x,Q^2) = \frac{1}{2}\sum_{i=f,\bar{f},G}\int_0^1 \frac{d\xi}{\xi} C_{1,i}\left(\frac{x}{\xi},\frac{Q^2}{\mu^2},\frac{\mu_f^2}{\mu^2},\alpha_s(\mu^2)\right) f_i(\xi,\mu_f,\alpha_s(\mu^2)) \tag{2.52}$$

$$F_2(x,Q^2) = \sum_{i=f,\bar{f},G}\int_0^1 d\xi\, C_{2,i}\left(\frac{x}{\xi},\frac{Q^2}{\mu^2},\frac{\mu_f^2}{\mu^2},\alpha_s(\mu^2)\right) f_i(\xi,\mu_f,\alpha_s(\mu^2)), \tag{2.53}$$

$$g_1(x,Q^2) = \frac{1}{2}\sum_{i=f,\bar{f},G}\int_0^1 \frac{d\xi}{\xi} \Delta C_{1,i}\left(\frac{x}{\xi},\frac{Q^2}{\mu^2},\frac{\mu_f^2}{\mu^2},\alpha_s(\mu^2)\right) \Delta f_i(\xi,\mu_f,\alpha_s(\mu^2)). \tag{2.54}$$

The coefficients for the hard scattering part of the structure functions $(\Delta)C_{j,i}$ depend on the structure function, on the parton type i and on the renormalization and factorization scales, but not on the type of hadron involved in the scattering. They are 'infrared safe', meaning that all soft and collinear divergences are absorbed into the parton distributions. Parton distributions on the other hand depend on the type of hadron, but not on the specific process. They are 'universal', that is, the same in ep, pp and $\bar{p}p$ scattering. In DIS one usually sets $\mu = \mu_f = Q$. That way no large ratios appear in the arguments of the coefficient functions in Eqs. 2.52 to 2.54 and the perturbative series for the $(\Delta)C_{j,i}$ should be well under control. Except for the dependence on the running coupling constant, they are independent of Q^2 as well. As observables like the structure functions should not depend on the scale choice, this just means that in this case almost all their Q^2 dependence is shuffled into the parton distributions. Note that the parton distributions in turn do not depend on Q^2, *unless one explicitly sets* $\mu^2(\mu_f^2) = Q^2$. The coefficient functions for DIS and the splitting functions have been calculated up to $\mathcal{O}(\alpha_s^2)$ for both the unpolarized (see, for instance [Ste95] and references therein) and the polarized case [Zij94, Mer96, Vog96]. The factorization

theorem expressed in Eqs. 2.52 to 2.54 is a generalization of the simple parton model, in the sense that to lowest order (α_s^0) the coefficient functions become (cf. Eq. 2.35)

$$(\Delta)C_{a,f}^{(0)}(\frac{x}{\xi}) = e_f^2\delta\left(1-\frac{x}{\xi}\right), \qquad (\Delta)C_{a,G}^{(0)}\left(\frac{x}{\xi}\right) = 0, \tag{2.55}$$

for $a = 1, 2$ in the unpolarized and $a = 1$ in the polarized case. The parton distributions are independent of Q^2 to this order. The inclusion of higher order coefficients and splitting functions augments the simple QPM to the so called 'QCD-improved Parton Model'. For the $\mathcal{O}(\alpha_s^n)$ corrections to the structure functions, a convolution of coefficient functions up to $\mathcal{O}(\alpha_s^n)$ with parton distributions evolved with splitting functions to the same order would be needed. With the choice $\mu = \mu_f = Q$, the terms with $t = \ln\frac{Q^2}{\mu_0^2}$ dominate the Q^2 behavior of the structure functions, such that in the *leading logarithmic order* (LO), only terms are convoluted with $C^{(0)}$ and $P^{(1)}$. With Eqs. 2.49 to 2.50 one gets with the factorization theorem:

$$F_1(x,Q^2) = \frac{1}{2}\sum_f e_f^2\left(q(x,Q^2)+\bar{q}((x,Q^2)\right), \quad F_2(x,Q^2) = \frac{F_1(x,Q^2)}{2x}, \tag{2.56}$$

$$g_1(x,Q^2) = \frac{1}{2}\sum_f e_f^2\left(\Delta q(x,Q^2)+\Delta\bar{q}(x,Q^2)\right). \tag{2.57}$$

being different from the simple QPM only by the Q^2 dependence of the parton distributions. To this order, gluons contribute only indirectly via the evolution of parton distributions.

2.3.3 Extraction of Parton Distributions

Eqs. 2.56 and 2.57 imply that if once the structure functions were measured at some scale Q_0^2, they can be predicted at another Q^2 by means of the Altarelli-Parisi evolution equations 2.49 to 2.50. This fact is used in QCD fits to the measured structure functions, where a parametrization for the parton distribution functions $(\Delta)f_i(x)$ at some input scale Q_0^2 is evolved and compared to experimental data on $F_2(x)$ ($g_1(x)$) taken at Q^2. From the evolution of the structure functions the gluon distributions can be fitted. A next to leading order (NLO) analysis of DIS data involves coefficient functions to $\mathcal{O}(\alpha_s)$ and splitting functions to $\mathcal{O}(\alpha_s^2)$, and one expects a direct contribution from gluons to F_1 and g_1 as well as to $R = \sigma_L/\sigma_T \neq 0$. Consequently, at NLO also the strong coupling constant has to be calculated to $\mathcal{O}(\alpha_s^2)$:

$$\alpha_s(\mu^2) \simeq \frac{4\pi}{\beta_1 \ln\frac{\mu^2}{\Lambda^2}}\left[1-\frac{\beta_2}{\beta_1}\frac{\ln\left(\ln\frac{\mu^2}{\Lambda^2}\right)}{\ln\frac{\mu^2}{\Lambda^2}}\right], \qquad \beta_2 = 102-\frac{38n_f}{3}. \tag{2.58}$$

One of the more recent results of NLO fits to unpolarized PDFs comes from a global analysis by the CTEQ collaboration [Pum02] (CTEQ6 PDF sets). In a global analysis, a variety of data from processes sensitive to different parton distributions are taken into account in addition to the inclusive ep DIS data, for instance inclusive jet cross sections in $p\bar{p}$ collisions, DIS with (anti-) neutrinos and potentially also semi-inclusive DIS. In figure 2.9 an example of the CTEQ6 gluon distributions is shown. Statistical errors of the PDFs arising from the experimental uncertainties are also evaluated for the CTEQ6 parton distributions. For comparison, the results of other NLO fits are shown to provide an idea about the systematic uncertainties involved in the fits. From figure 2.9 it can be seen that at relatively small Q^2, the gluon distribution has large errors that can even cover negative values at small x. The uncertainty decreases rapidly with increasing Q^2. Compared to the gluon distribution, the quark distributions can be determined with much better precision. To obtain separate information about quarks and antiquarks it is necessary to include data from neutrino experiments, though.

NLO fits to polarized data have been performed in the last years by, e.g. Refs. [Glü01, Blü02, Geh96]. The results from Ref. [Blü02] are shown in figure 2.10 at $Q^2 = 4$ GeV^2, with the

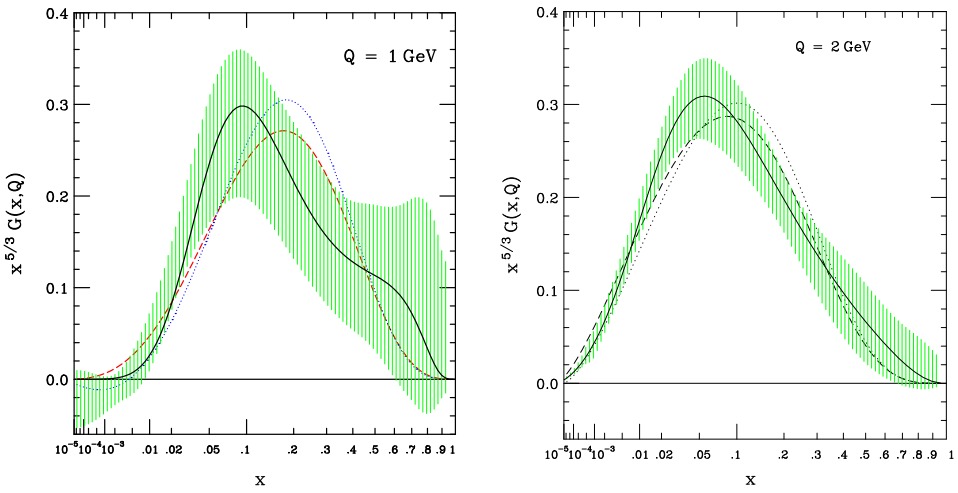

Figure 2.9: The CTEQ6 (solid curve) unpolarized NLO gluon distribution $G(x)$ at $Q^2 = 1$ GeV^2 (left) and $Q^2 = 4$ GeV^2 (right), scaled with $x^{5/3}$. The dashed curve is from CTEQ5 [Lai00], the dotted curve from MRST2001 [Mar02]. The plots are taken from Ref. [Pum02]. The shaded areas indicate the experimental uncertainties.

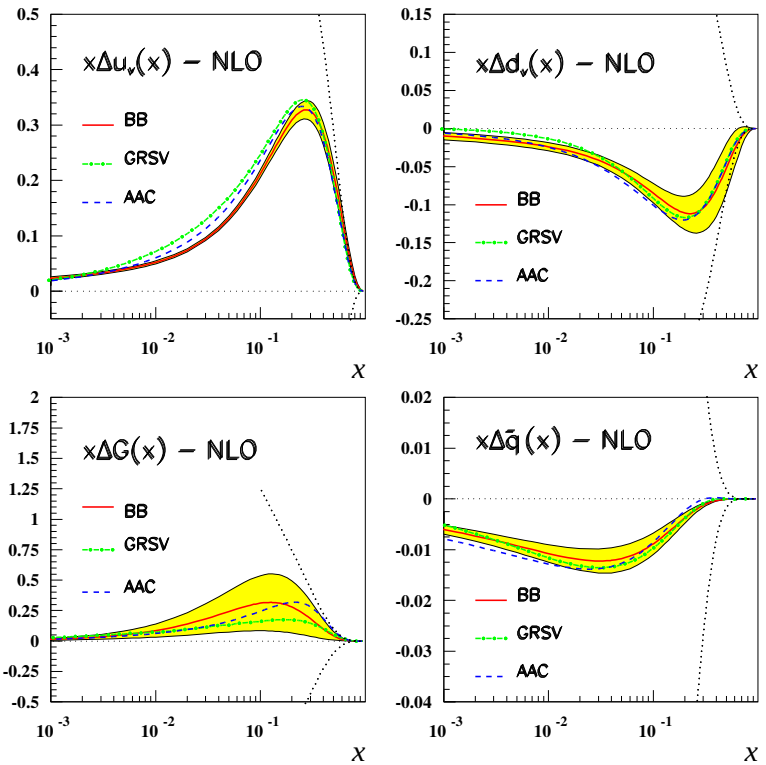

Figure 2.10: Results of NLO fits to g_1 data at the input scale $Q_0^2 = 4$ GeV^2 from Refs. [Blü02] (BB, solid lines with error band), [Glü01] (GRSV, dash-dotted line) and [Got00] (AAC, dashed line). Top left: $\Delta u_v(x) = \Delta u(x) - \Delta\bar{u}(x)$, top right: $\Delta d_v(x) = \Delta d(x) - \Delta\bar{d}(x)$, bottom left: $\Delta G(x)$, bottom right:$\Delta\bar{q}(x) = \Delta\bar{u}(x) = \Delta\bar{d}(x) = \Delta\bar{s}(x) = \Delta s(x)$. The dotted lines indicate the positivity limit $\left|\frac{\Delta f}{f}\right| \leq 1$.

shaded bands indicating the correlated uncertainties from the experiments. The recent fits to the polarized data imply the following:

- The helicity distribution of valence u quarks is large and positive, meaning that the spin carried by them is mostly parallel to the nucleon spin.

- The helicity distribution of valence d quarks is negative and only half the size of $|\Delta u_v|$. The net helicity of d quarks is opposite to the nucleon helicity.

- With inclusive data on g_1 alone it is not possible yet to separately extract helicity densities for individual sea quark flavors. Usually $SU(3)_f$ symmetry assumptions like $\Delta\bar{u} = \Delta\bar{d} = \Delta\bar{s} = \Delta s$ or a similar constraint on the polarizations $\Delta\bar{q}/\bar{q}$ are imposed. The result shown in figure 2.10 used the former assumption. In any case, the sea quark helicity density turns out to be very small and negative, with a much larger relative error than the valence distributions.

- The least determined distribution is the gluon density ΔG. This is due to the fact that the data available are all from fixed target experiments covering a relatively small region in Q^2 from about 0.1 to 100 GeV^2 (cf. figure 2.5), where only the region with $Q^2 > 1$ GeV^2 is included in the fits. With this small lever arm it is hard to determine ΔG solely from the evolution of $g_1(x, Q^2)$. Note that the result shown for ΔG in figure 2.10 is at $Q^2 = 4$ GeV^2. The uncertainty at smaller Q^2 is significantly larger, such that there even the *sign* of the gluon polarization can be considered undetermined.

2.3.4 Renormalization and Factorization Schemes

Any calculation in quantum field theories involving loops leads to ultraviolet divergences that are renormalized in order to obtain finite cross sections. At NLO, this renormalization is not unambiguous anymore, and different *renormalization schemes* are in use. The coupling constant as well as the coefficient and splitting functions in QCD are then also dependent on the scheme conventions, but they can be transformed from one to another scheme with a unique transformation. Observables, however, must not depend on the renormalization scheme, such that the calculation of α_s, C_i and P_{ij} should be done consistently in one scheme where it is ensured that all infinite terms, arbitrary scales etc. cancel in the convolution. Strictly spoken observables become completely scheme independent only if they are calculated to all orders of perturbation theory. If the series is cut off at some order α_s^n, the resulting scheme dependence if of the order α_s^{n+1}. The same holds for the dependence of NLO (and higher order) results on the *factorization scheme*. A factorization scheme is the prescription of defining at the same time the hard scattering functions and the parton distributions. A commonly used renormalization and factorization scheme is the modified minimal subtraction ($\overline{\text{MS}}$) scheme [Bar78] where parton distributions are defined in terms of hadronic matrix elements. For quark fields ψ without transverse degrees of freedom (indicated by $\mathbf{0}_T$) for instance

$$f_{i/h}(x, \mu^2) = \int_{-\infty}^{+\infty} \frac{dy^-}{4\pi} e^{-ixp^+y^-} \langle h, p|\bar{\psi}(y^-, 0^+, \mathbf{0_T})\gamma^+\psi(0^-, 0^+, \mathbf{0_T})|h, p\rangle, \tag{2.59}$$

where the $p^\pm$ are light cone coordinates $p^\pm = p_0 \pm p_z$, and the gauge $A^+ = 0$ for the gluon vector field A was used. Eq. 2.59 becomes gauge invariant, when path ordered integrals of the gluon field are included (see, for instance [Ste95], chapter II.D) in this definition. Gluon and polarized parton densities are defined in the same manner, where for the polarized case the Dirac γ matrix is replaced by $\gamma^+ \to \gamma^+\gamma^5$. The hard scattering matrix elements (ΔC_i) are then defined by the requirement that the structure functions (Eqs. 2.52 to 2.54) should be independent of the fixing of the parton distributions. Moreover, the scheme dependence also includes the definitions of singlet ($(\Delta)\Sigma$) and gluon ($(\Delta)G$) distributions, since the gluon distribution in one scheme can become a sea quark distribution in another factorization scheme.

The method of dimensional regularization used to solve logarithmically divergent (loop) integrals, involves integrals in $n = 4 - \epsilon$ dimensions, with ϵ a small positive number. It is not possible to uniquely define γ^5 in these n dimensions, in contrary to the Lorentz γ^μ. Therefore, in the polarized case there exists a whole family of $\overline{\text{MS}}$ renormalization schemes differing by their

treatment of γ^5. The result of this is that one has the choice to either have gauge invariance of the operators defining parton distributions, or chiral invariance, but not both of them at the same time. The $\overline{\rm MS}$ scheme conventionally used, e.g., in Refs. [Mer96, Vog96] has the feature that the nonsinglet densities are conserved quantities, which is what makes them Q^2 independent. The first moment of $\Delta\Sigma$ (its integral over x between 0 and 1, see section 2.6) however, is not conserved, thus breaking chiral symmetry. This makes it an ill-defined quantity when extrapolating results from the DIS experiments to predictions from the constituent quark model at low energies. The so called AB scheme [Bal96, Alt98] was introduced to avoid such difficulties. In terms of the $\overline{\rm MS}$ definition of parton distributions, the AB densities become

$$\Delta\Sigma(x,Q^2)_{AB} = \Delta\Sigma(x,Q^2)_{\overline{MS}} + n_f\frac{\alpha_s(Q^2)}{2\pi}\int_x^1\frac{dy}{y}\Delta G(y,Q^2)_{\overline{MS}}, \tag{2.60}$$

$$\Delta G(y,Q^2)_{AB} = \Delta G(y,Q^2)_{\overline{MS}}. \tag{2.61}$$

In this scheme now $\Delta\Sigma$ is independent of Q^2 at all orders. The influence of different schemes together with the special role of gluons in the interpretation of polarized DIS data will be covered in section 2.6.

2.3.5 Applicability of Perturbative QCD

The QCD-improved Parton Model adequately describes data in a wide range of energy and processes. Its validity has been established not only in DIS, but also for instance in Drell-Yan (the production of a lepton pair in hadronic collisions) and e^+e- annihilation (jet production etc.) processes, provided that the perturbative expansion and the factorization theorem are applicable. Perturbation theory holds when the scale Q^2 involved is large, $\sqrt{Q^2} \gg \Lambda_{QCD} \sim 200$ MeV, such that $\alpha_s(Q^2)$ is small. The absence of interactions between the partons involved in the hard scattering and those in the (initial or final) hadron state is a prerequisite of the factorization theorem. This ensures that the hard scattering part of the cross sections does not depend on the type of hadrons involved. Note that in the derivation of the cross section in the QPM, those interactions between partons have explicitly been neglected. More generally, the structure functions can be expanded in inverse powers of Q^2 (for instance for F_2):

$$F_2 = \sum_{n=0}^{\infty} C_n(x,Q^2)\left(\frac{M^2}{Q^2}\right)^n. \tag{2.62}$$

This expansion follows from the Operator Product Expansion (OPE) of the electromagnetic currents (see, for instance Ref. [Rob90]). The functions C_n depend logarithmically on Q^2. The QPM cross section only includes the terms with $n = 0$. These terms are referred to as 'leading twist', in contrast to the 'higher twist' terms with $n > 0$. Higher twist terms introduce a hadronic mass scale that is absent in the factorization theorem. They describe the interaction of the struck parton with the partons in the target remnant and thus reflect confinement effects.

At the energies of the fixed target experiments, neither is Q^2/Λ^2_{QCD} always large nor is (M^2/Q^2) always small, such that care has to be taken if perturbative QCD (pQCD) can be applied and to what degree data can be compared with QCD predictions, or if higher twist or target mass corrections have to be considered. In polarized DIS, the pQCD description of asymmetry data turned out to work reasonably well down to $Q^2 \simeq 1$ GeV^2 [Glü01] where higher twist effects might have potentially been important. The reason for this surprisingly good description of the data might be a partial cancellation of nonperturbative effects in the ratio of polarized to unpolarized cross sections.

2.4 Semi-inclusive DIS and Fragmentation Functions

So far, only inclusive deep inelastic scattering has been considered. In pQCD, this corresponds to the integration over all possible final state partons b in the process $\gamma^* a \to bX$. The detection

of the final state particles occurs at time scales much larger than that of the hard interaction, when the partons were produced. Due to color confinement at the small energy scales involved in long distance processes, the final state partons 'hadronize' nonperturbatively to color neutral hadrons. In semi-inclusive DIS (SIDIS), hadrons coincident with the scattered lepton are observed. The unpolarized (polarized) cross section for a hadron h with momentum fraction z of the parton momentum can be factorized in pQCD:

$$\frac{d^3(\Delta)\sigma^h}{dxdQ^2dz} = \sum_{a,b=q,\bar{q},g} (\Delta)f_a(x,Q^2)(\Delta)\hat{\sigma}_{ab}(x,\alpha_s(Q^2))D_{b/h}(z,Q^2). \tag{2.63}$$

The renormalization scale and the factorization scales for the parton distributions and the fragmentation function $D(z,\mu^2)$ have been set here to $\mu^2 = Q^2$, and the two other hadron degrees of freedom ($\mathbf{p_T}$) have been integrated over. The hard scattering cross section, $(\Delta)\hat{\sigma}_{ab}(x,\alpha_s(Q^2)) = \hat{\sigma}(ea \to e'bX)$ can be perturbatively calculated and is the same as for inclusive DIS. At LO, gluons do not contribute and $q_a = q_b$, such that with $s = E_{CM}^2$ the cross section becomes (neglecting the lepton mass and terms Q^2/ν^2):

$$\frac{d^3(\Delta)\sigma^h}{dxdydz} = \frac{4\pi\alpha^2 s}{Q^4}\left(\frac{y^2}{2}+1-y\right)\sum_{a=q,\bar{q}} xe_a^2(\Delta)f_a(x,Q^2)D_{a/h}(z,Q^2) \tag{2.64}$$

$$= \frac{\sum_{a=q,\bar{q}} xe_a^2(\Delta)f_a(x,Q^2)D_{a/h}(z,Q^2)}{\sum_{a=q,\bar{q}} xe_a^2 f_a(x,Q^2)}\frac{d^2\sigma}{dxdy}. \tag{2.65}$$

The fragmentation function $D_{a/h}(z)$ can be interpreted as the probability density of a parton a to fragment into a hadron h carrying a momentum fraction z of the parton. Then, the total energy carried by the hadrons produced from a parton has to be equal to the parton energy

$$\sum_h \int_0^1 dz\, zD_{a/h}(z,Q^2) = 1. \tag{2.66}$$

The normalization is such that the integral of the fragmentation function from a threshold z_{min}, depending on the hadron and the process, is the average hadron multiplicity $\langle n_h\rangle$ of hadron of type h originating from the parent parton a:

$$\sum_a \int_{z_{min}}^1 dz D_{a/h}(z,Q^2) = \langle n_{h/a}\rangle. \tag{2.67}$$

The fragmentation functions $D_{a/h}$ are usually parametrized to behave like $1/z$ at small z. If for large parton momenta p, $z_{min} \to 0$, the multiplicities rise logarithmically with the parton momentum (and therefore with W^2). From semi-inclusive multiplicities

$$\langle(\Delta)n_h\rangle \equiv \frac{\frac{d^2(\Delta)\sigma^h}{dxdy}}{\frac{d^2\sigma}{dxdy}} = \frac{\sum_{a=q,\bar{q}}\left\{e_i^2(\Delta)f_a(x,Q^2)\int_{z_{min}}^1 D_{a/h}(z,Q^2)\right\}}{\sum_{a=q,\bar{q}} e_i^2 f_a(x,Q^2)} \tag{2.68}$$

one can thus retrieve information about the fragmentation functions if the parton distributions are known or, alternatively, one can determine the individual parton distributions if the fragmentation functions are known. Both of these possibilities are exploited at HERMES using Monte Carlo methods [Air03, Asch03].

Fragmentation functions can be measured in *single hadron inclusive* e^+e^- annihilation (SIA) where all events with a hadron of momentum p in the process $e^+e^- \to h(p)X$ are taken into account.

This process can be regarded as the 'crossed' version of inclusive DIS on the antihadron $\bar{h}$: If the hadron is transferred from final to initial state and identified with the $\bar{h}$ and the electron from initial to final state, where it is identified as a positron, one obtains the process $e^+\bar{h} \to e^{+'}X$. The quantity $Q^2 = (p_{e^+} + p_{e^-})^2$ is equal to the center of mass energy squared in e^+e^- annihilation. After integrating over the hadron angles, the cross section for SIA is in the simple QPM:

$$\frac{d\sigma^h}{dz} = 3\sum_q e_i^2 \hat{\sigma}(e^+e^- \to q\bar{q}) D_{q/h}(z) = \frac{4\pi\alpha^2}{Q^2} \sum_q e_q^2 D_{q/h}(z). \tag{2.69}$$

The fragmentation functions in SIA play in this sense a similar role as the parton distributions in inclusive DIS. Since they are universal, i.e., independent of the process, they can also be used to describe fragmentation in semi-inclusive DIS. In QCD, the hard scattering cross section receives corrections of the order $\mathcal{O}(\alpha_s)$ and the fragmentation function evolves according to the DGLAP equations:

$$\mu^2 \frac{d}{d\mu^2} D_{i/h}(z, \mu^2) = \sum_j \int_z^1 \frac{d\xi}{\xi} P_{ij}(\xi, \alpha_s(\mu^2)) D_{j/h}\left(\frac{z}{\xi}, \mu^2\right). \tag{2.70}$$

The radiation of gluons described by the splitting functions and the resulting population of the small z region account for the $1/z$ behavior of the fragmentation functions and the logarithmic rise of the multiplicities with $Q^2 = E_{CM}^2$. As in the case of the PDFs, the nonperturbative nature of fragmentation functions does not allow a calculation from first principles. Still, a variety of models exist to describe hadron formation. Two of these which are also implemented into Monte Carlo models will be introduced here:

- **Independent Fragmentation**
  This model was invented in 1978 by Field and Feynman [Fie78]. It describes the incoherent (independent) fragmentation of the individual partons created during the hadronization process. A quark q_0 originating from the hard process picks up a quark-antiquark pair $q_1\bar{q}_1$ from the vacuum, and combines with the antiquark to form a meson with the quark content $q_0\bar{q}_1$ and energy fraction z, leaving the quark q_1 with energy fraction $(1-z)$ behind. This in turn picks up a next quark-antiquark pair $q_2\bar{q}_2$ to form another hadron and so on. This cascade proceeds until the energy of a quark q_i falls below a certain cutoff. This quark is then left without a partner and neglected. The function $f(z)$ describing the probability that a hadron with energy fraction z is created is parametrized as

  $$f(z) = 1 - a + 3a(1 - z^2), \quad \text{with } a \simeq 0.77. \tag{2.71}$$

  A few model parameters regulate the production of different flavors (using isospin symmetry) and the width of the transverse momentum distribution of the $q\bar{q}$ pairs. Strangeness production and some generation of transverse momentum have been included into the model. The hadronization is explicitly carried out in the hadronic center of mass system, such that the longitudinal momenta of the outgoing hadrons are not Lorentz invariant. Also, because the last quark in the chain is disregarded, color and flavor quantum numbers are not conserved. Gluons cannot be easily included into the independent fragmentation model. Despite these conceptual weaknesses, the model describes many features of hadronization remarkably well.

- **The LUND String Fragmentation Model**
  The string fragmentation (SF) model [And83] shares some of the independent fragmentation models concept and parameters, but conserves all quantum numbers and is invariant under Lorentz transformations. It incorporates the concept of QCD color confinement by the parametrization of a color flux tube (string) with about 1 fm diameter between two colored objects (e.g. a $q\bar{q}$ pair or a quark and a diquark, the nucleon remnant after the struck quark has been removed from it). This color field is described by a linearly rising potential $V = \kappa r$ for the two objects separated at a distance r. The string constant κ is about 1 GeV/fm. If the energy contained in the string is large enough, it can break and a new $q\bar{q}$ pair is formed,

such that now two strings exist. The process is repeated until some lower energy threshold is reached. A schematic picture of the string forming and breaking process is shown in figure 2.11. The splitting of the string at the point where the $q\bar{q}$ pair is produced with a mass m also generates some transverse momentum p_T, with a probability

$$P \sim \exp\left(-\frac{\pi m^2}{\kappa}\right) \exp\left(-\frac{\pi p_T^2}{\kappa}\right) = \exp\left(-\frac{\pi m_T^2}{\kappa}\right), \tag{2.72}$$

with $m_T^2 = m^2 + p_T^2$ the transverse mass of the $q\bar{q}$ pair. This distribution regulates the relative occurrence of flavors by their masses, $u : d : s : c = 1 : 1 : 0.3 : 10^{-11}$. The p_T is assumed to be distributed as a Gaussian with width $\sigma \simeq 0.4$ GeV. The probability distribution for the longitudinal energy sharing between hadrons is given by the LUND symmetric fragmentation function

$$f(z) \sim z^{-1}(1-z)^a \exp\left(-\frac{bm_T^2}{z}\right). \tag{2.73}$$

The parameters $a = 0.3$ and $b = 0.58\text{GeV}^2$ have been derived from high energy e^+e^- data. The model contains additional mechanisms and parameters for baryon production, and naturally incorporates gluons that can be pictured by a kink in the string. The SF model has been implemented into the JETSET package [Sjö94].

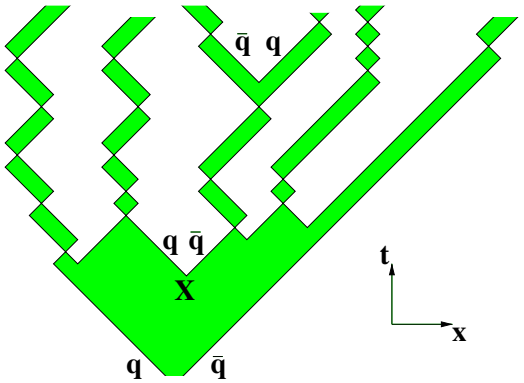

Figure 2.11: Schematic view of the string breaking in the LUND SF model. The initial $q\bar{q}$ pair moves apart in time (upward pointing) with a color field in between, indicated by the shaded area. At the point X the first string break occurs.

2.5 Photoproduction and Photon Physics

The discussion above was restricted to the deep inelastic scattering limit where both Q^2 and ν were assumed to be asymptotically large. In practice, the range of data to be described with perturbative QCD in the parton model extends to values down to Q^2 of the order of a few GeV^2. At smaller Q^2 the description might become more complicated due to higher twist effects and, at lower energies, target mass corrections (cf. section 2.3.5). In order to be safe from complications of this kind, cuts on $Q^2 > 4$ GeV^2 or even $Q^2 > 10$ GeV^2 are imposed where possible. As mentioned in section 2.3.5 it was observed that for polarized data a cut on $Q^2 > 1$ GeV^2 often seems to suffice. In any case this means a significant reduction of the available statistics for most of the experiments, even at collider energies because of the overall Q^{-4} dependence of the DIS cross section. On the other hand, real photons as they can be produced from electron bremsstrahlung or Compton backscattering can be used to probe the nucleon, offering a new possibility to study the nucleon structure and to test the predictions of QCD.

A matter of particular interest are the properties of the photon itself. Data from fixed target experiments with real photons at c.m. energies ≤ 20 GeV could be interpreted in terms of the photon behaving more like a hadron than a pointlike particle (see, for instance Ref. [Bau78] and the references therein). Due to quantum-mechanical fluctuations into virtual $q\bar{q}$ pairs the photon

can act like a source of partons having a rich structure that can be investigated in, e.g., high energy ep or e^+e^- collisions. The 'resolved' structure of the photon also has implications on physics with a quasireal photon beam – the virtual photons emitted by leptons at very low Q^2.

The low Q^2 region of DIS should join smoothly with the real photoproduction limit at $Q^2 = 0$. The relation between the total photoproduction cross section $\sigma^{\gamma p \to X}$ and the structure function F_2 at fixed photon energy ν is (cf. section 2.1.2):

$$\sigma^{\gamma p \to X} = \lim_{Q^2 \to 0} 4\pi^2 \alpha \frac{F_2}{Q^2}. \tag{2.74}$$

Conservation of the electromagnetic current furthermore implies that F_2 should vanish in this limit in order to retain a finite cross section. In general, the photon can be considered as consisting of three parts:

- The 'bare', direct part that interacts with partons in the nucleon coupling to their electromagnetic charge. For real photons, the process $\gamma q \to q$ is kinematically forbidden. It was discussed above that in DIS, Q^2 is always associated with the (spatial) resolution at which the nucleon is probed. At $Q^2 \to 0$, the wavelength of the virtual photon increases to above the size of the nucleon such that it does not make sense anymore to use the DIS picture of virtual photon absorption by partons. The next to leading order processes like PGF and QCDC are possible though, thus enabling the study of parton distributions in the nucleon, particularly the gluon distribution in the PGF channel. In this kinematic regime, another 'resolution' scale is introduced, for instance the transverse momentum p_T of the scattered partons, such that there is no contradiction to the above said.

- The hadronic part where small scale, nonperturbative fluctuations of the photon into a $q\bar{q}$ pair are long-lived enough to create a cloud of gluons around the quarks, such that the $q\bar{q}$ state develops into a hadronic state before the interaction with the nucleon. The hadronic state has the same quantum numbers as the photon, with a consequence that it can be pictured as a superposition of the low mass vector meson states ρ^0, ω and ϕ (sometimes also the J/ψ is included).

- An 'anomalous' part where the fluctuation $\gamma \to q\bar{q}$ happens at sufficiently large scales such that the subsequent evolution of the $q\bar{q}$ state is governed by the DGLAP evolution equations.

2.5.1 The Photon Structure in Perturbative QCD

Measurements of jet cross sections and event shapes can be sensitive to the photon structure in ep as well as e^+e^- collisions. At very high energies, partons produced in a short distance reaction fragment in such a way that all hadrons appear in the final state in about the same direction as the original outgoing parton. Experimentally, *jets* of hadrons are observed in a cone around the original direction of the partons, with the sum of their energies resembling the parton momentum. Each jet can be in principle associated with a parton. Realistically, one needs to define a set of cuts to be imposed on the final state hadrons to decide whether they belong into one or another jet. Such a well defined *jet algorithm* defines the number of jets in an event, and it is possible to perturbatively calculate cross sections for a given number n of jets from that of the processes

$$e^+e^- \to q(p_1) + \bar{q}(p_2) \cdots + \ldots \text{parton}_n(p_n) \tag{2.75}$$

$$ep \to e' + \text{remnant}(p_r) + \text{parton}_1(p_1) + \text{parton}_2(p_2) \cdots + \text{parton}_n(p_n) \tag{2.76}$$

$$pp \to \text{remnant}_1(p_{r1}) + \text{remnant}_2(p_{r2}) + \text{parton}_1(p_1) + \cdots + \text{parton}_n(p_n) \tag{2.77}$$

In fact, the observation of three-jet events in e^+e^- collisions proved the existence of the gluon through the process $e^+e^- \to q\bar{q}g$ where each of the final state partons fragments into a distinct jet [Bra80]. In unpolarized DIS, the measured (multi-) jet production cross sections are used to

determine the gluon density and the strong coupling constant (see, eg, [Adl01]). From the jet transverse momentum (or the transverse energy $E_T = \sum_{hadrons} E_i \sin(\theta_i)$) and its rapidity

$$\eta = \frac{1}{2} \ln \frac{E - p_z}{E + p_z} \simeq - \ln \tan \left(\frac{\theta}{2} \right) \tag{2.78}$$

the parton momentum fraction can be inferred for a leading order process, and *approximately* inferred for higher order processes. The rightmost expression in Eq. 2.78 is strictly valid only in the case of massless jets, and is otherwise referred to as pseudo-rapidity. The angle θ is the jet angle with respect to the beam axis. With the photon parton distribution functions $f_{i/\gamma}(x_\gamma)$ defining the probability density to find a parton i with a fraction x_γ in the photon, the inclusive jet cross section can be written in the lab frame as [1]

$$\frac{d^2\sigma}{dE_T d\eta} = \sum_{a,b} \int_{x_{a,\,min}}^{1} dx_a x_a f_{a/\gamma}(x_a, \mu^2) x_b f_{b/B}(x_b, \mu^2) \frac{4 E_\gamma E_T}{2 x_a E_\gamma - E_T e^\eta} \frac{d\hat{\sigma}^{ab \to \mathrm{jet}+X}}{dt} \tag{2.79}$$

for an incoming photon with energy E_γ and another incoming particle B with energy E_B which can be either another photon or a nucleon. In the inclusive case, the parton momenta cannot be fully reconstructed which is why the integral is performed over the momentum of parton a with

$$x_{a,\,min} = \frac{E_B E_T e^\eta}{2 E_\gamma E_B - E_\gamma E_T e^{-\eta}} \qquad x_b = \frac{x_a E_\gamma E_T e^{-\eta}}{2 x_a E_\gamma E_B - E_B E_T e^\eta}. \tag{2.80}$$

The contribution from the direct (unresolved) photon is included here for $a = \gamma$ with $f_{\gamma/\gamma} = \delta(1 - x_\gamma)$. For the dijet cross section both parton momenta can be reconstructed from the jet rapidities $\eta_{1,2}$ and the transverse momentum (the transverse momenta of the two jets should balance each other):

$$\frac{d^3\sigma}{dE_T^2 d\eta_1 d\eta_2} = \sum_{a,b} x_a f_{a/\gamma}(x_a, \mu^2) x_b f_{b/B}(x_b, \mu^2) \frac{d\hat{\sigma}^{ab \to \mathrm{jet}_1 + \mathrm{jet}_2 + X}}{dt} \tag{2.81}$$

with

$$x_{a,b} = \sum_{hadrons} \frac{E_{T,i} e^{\pm \eta_i}}{2 E_{\gamma,B}}. \tag{2.82}$$

Thus the dijet cross section can be particularly sensitive to the parton densities of the photon. Just as for the proton, the photon PDFs cannot be calculated from first principles alone. The reason is the the occurrence of collinear singularities in the splittings $\gamma \to q\bar{q}$ that prevent perturbation theory to be applicable. The evolution of the parton distributions of the photon is described by

$$\begin{aligned} \frac{d}{d\mu^2} f_{q/\gamma}(x, \mu^2) &= \int_x^1 \frac{d\xi}{\xi} P_{qq}\left(\frac{x}{\xi}, \alpha_s\right) f_{q/\gamma}(\xi, \mu^2) + P_{qG}\left(\frac{x}{\xi}, \alpha_s\right) f_{G/\gamma}(\xi, \mu^2) \\ &\quad + P_{q\gamma}\left(\frac{x}{\xi}\right) f_{\gamma/\gamma}(\xi, \mu^2) \end{aligned} \tag{2.83}$$

$$\frac{d}{d\mu^2} f_{G/\gamma}(x, \mu^2) = \int_x^1 \frac{d\xi}{\xi} P_{Gq}\left(\frac{x}{\xi}, \alpha_s\right) \sum_{q,\bar{q}} f_{q/\gamma}(\xi, \mu^2) + P_{GG}\left(\frac{x}{\xi}, \alpha_s\right) f_{G/\gamma}(\xi, \mu^2). \tag{2.84}$$

The splitting functions P_{ij}, $i, j = q, G$ are the same as for the proton PDFs. The main difference between the photonic and regular hadronic parton distributions is the 'anomalous' term in Eq. 2.83 proportional to $P_{q/\gamma}$ accounting for the $\gamma \to q\bar{q}$ splitting. $P_{q/\gamma}$ can be obtained from $P_{q/G}$ by dropping a color factor, exchanging $\alpha_s \to \alpha_{em}$ and summing over the final state colors. The other terms are referred to as the (hard) 'hadronic' part of the photon. The partonic cross sections are the same as for subprocesses occurring in hadronic physics, i.e., $qq \to qq$, $qg \to qg$, $gg \to gg$, $gg \to q\bar{q}$, $q\bar{q} \to gg$ and related ones involving antiquarks.

[1] Most of the material and equations in this section is taken from Ref. [Kla02]

As for the proton PDFs, photon PDFs can be obtained from fits to data from e.g. PETRA, LEP and other e^+e^- collider experiments measuring the photon structure function $F_2^\gamma(x, Q^2)$. Usually an input distribution similar to $f_{i/\gamma}(x, \mu_0^2) = Nx^\alpha(1-x)^\beta$ is used in the fits. Since the e^+e^- data are dominantly sensitive only to the u quark distribution (note that, unlike for the proton, the antiquark distributions in the photon are equal to the quark distributions), one has to further rely on models like that of Vector Meson Dominance (VMD, see below). For a recent review on photon parton distributions see Ref. [Kla02].

Diagrams contributing to the leading order jet production cross section in ep collisions are shown in figure 2.12. The distinctive feature of resolved, hadronic photon events is the occurrence

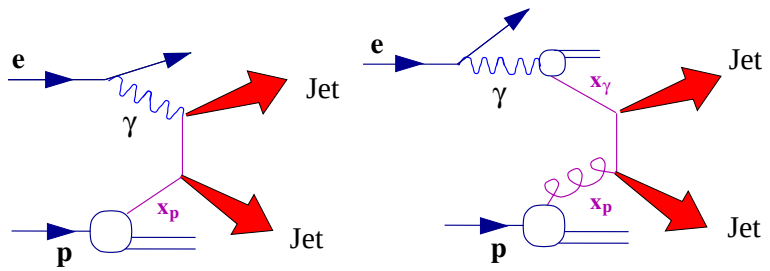

Figure 2.12: Some leading order diagrams for inclusive jet production in direct (a) and resolved (b) photon interactions.

of an additional 'beam remnant' from the spectator partons of the photon, traveling approximately into the same direction as the photon 'beam'. At NLO the definition of the resolved and direct contributions becomes ambiguous because of the different possibilities to factorize collinear singularities into the parton densities.

At the HERA experiments H1 and ZEUS photoproduction events can be selected by tagging or antitagging the scattered electron. The maximum Q^2 of these events is then given by the detector acceptance. The photon energy spectrum is determined from the Weizsäcker-Williams approximation (WWA, see also section 2.1.2)[2]

$$f_{\gamma/e}(y) = \frac{\alpha}{2\pi}\left[\frac{1+(1-y)^2}{y}\ln\frac{Q^2_{max}}{Q^2_{min}} + 2m_e^2 y\left(\frac{1}{Q^2_{max}} - \frac{1}{Q^2_{min}}\right)\right], \tag{2.85}$$

where the minimum possible Q^2 for a given energy fraction y is

$$Q^2_{min} = \frac{m_e^2 y^2}{1-y}, \tag{2.86}$$

The energy fraction y can be either determined from the scattered positron energy or from the energies and longitudinal momenta of the final state hadrons

$$y = \frac{1}{2E}\sum_i (E_i - p_{z_i}). \tag{2.87}$$

A result for the dijet cross section by H1 [Adl00] is shown in figure 2.13. Here, also the contributions of the various photon components extracted from Monte Carlo are shown as a function of x_γ, the parton momentum fraction of the photon. At large x_γ the largest contributions come from the direct photon component and from quarks whereas the small x_γ region is dominated by gluons. A compilation of recent data on jet production and comparisons to LO and NLO calculations is given in Ref. [Kla02].

[2]The expression for the equivalent photon flux in section 2.1.2 was obtained from comparing the ep cross section to the definition of the γp cross section and is thus exact. The WWA is a leading log approximation valid only for small Q^2 and high energy where the target mass is negligible.

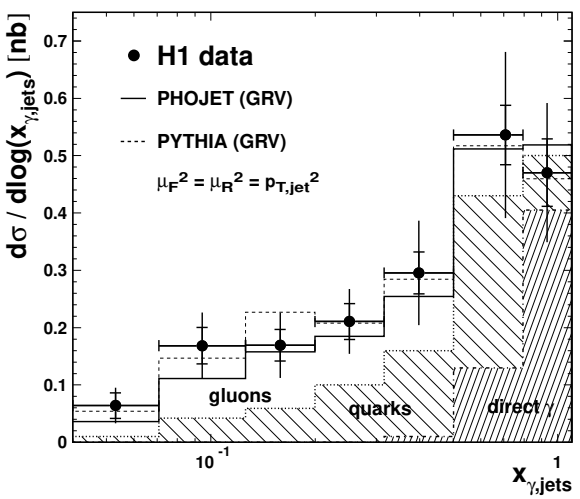

Figure 2.13: The dijet cross section measured by H1 [Adl00] for jets with $E_T > 6$ GeV, $-0.5 < \eta < 2.5$, $0.5 < y < 0.7$ and $Q^2 < 0.01$ GeV^2 as a function of x_γ reconstructed from the two jets. The dashed histogram gives a comparison to PYTHIA 5.7 [Sjö94], the solid histogram to the PHOJET Monte Carlo [Eng96]. Also shown are the contributions from the direct photon component and from the different photon parton distributions. The factorization and renormalization scales were set to the jet p_T.

2.5.2 Soft Photoproduction and Vector Meson Dominance

The perturbative decomposition of the photon into a hadronic, anomalous and direct piece describes the interactions of partons inside the photon with those inside the proton in the framework of the QCD parton model. A good description of the data by perturbative QCD can only be achieved for sufficiently high p_T. At smaller p_T the non-perturbative effects become large, even at high energies. The reason is the *soft* interaction of the hadronic photon component with the proton that up to now can only be phenomenologically described in terms of models for hadron-hadron interactions. The most prominent model that successfully describes photoproduction data over a wide range in energy is the Vector Meson Dominance (VMD) model that interprets the virtual fluctuations of the photon into quarks at small, nonperturbative scales as fluctuations into vector mesons carrying the same quantum numbers $J^{PC} = 1^{--}$ as the photon [Sak60]. The process then factorizes into the photon coupling to the vector meson and the interaction of the vector meson with the nucleon. The hadronic part of the interaction can be described in terms of Regge theory [Reg59]. This theory provides analytical solutions for high energy scattering amplitudes in non-relativistic potentials in terms of a *complex* angular momentum variable. Many of those potentials have singularities only in the complex angular momentum plane. At large s, these so called 'Regge poles' seem to correspond to the exchange of known particles with mass $M^2 = t$ between the scattering particles at (squared) momentum transfer t. The exchanged particles lie on linear trajectories $\alpha(t) = \alpha(0) + \alpha' t$. The most important Regge poles are those corresponding to the exchange of vector mesons (ρ^0, ω, f_2, a etc.) lying on the trajectory with $\alpha(0) = \alpha_R = 0.44$ and $\alpha' = 0.93$ GeV^{-2} ('Reggeons'), and one with an intercept of $\alpha(0) = \alpha_P = \simeq 1.08$ and slope $\alpha' = 0.25$ GeV^{-2}. The latter corresponds to exchange of a particle with vacuum quantum numbers that has never been observed as a final state particle, the 'soft Pomeron'. This particle is needed for the description of the cross sections of a wide variety of hadronic processes. The cross section for a hadronic process $AB \to X$ has the form

$$\frac{d\sigma}{dt} \propto |\beta(t)|^2 \left(\frac{s}{s_0}\right)^{2\alpha(t)-2}, \tag{2.88}$$

where $\beta(t)$ represents that part of the scattering amplitude independent of the center of mass energy s. The optical theorem relates the elastic cross section for the process $AB \to AB$ in the forward limit at $t = 0$ to the total cross section:

$$\left.\frac{d\sigma}{dt}\right|_{t=0} = \frac{1}{16\pi}(1+\eta^2)\sigma_{tot}^2, \tag{2.89}$$

leading to

$$\sigma_{tot} \propto s^{\alpha(t=0)-1}. \tag{2.90}$$

The ratio of real to imaginary parts of the scattering amplitude η is generally assumed to be negligible (in fact it is rapidly decreasing with energy, see for instance [Hag02]). If one would only include the vector meson trajectory with $\alpha_R \simeq 0.5$, the cross section would fall like $\sigma_{tot} \sim s^{-1/2}$. A fall of cross sections in hadron-proton scattering is observed only at small energies $\sqrt{s} < 10$ GeV, above that the cross sections rise with a (small) power corresponding to the intercept of the soft pomeron. Total hadron-hadron cross sections can thus be described by the sum of two terms, one falling and one rising with s:

$$\sigma_{tot} = Y_{AB} s^{-\eta} + X_{AB} s^{\epsilon}, \tag{2.91}$$

The parameters X and Y depend on the type of hadrons participating in the scattering while the constants η and ϵ are universal. Equation 2.91 can as well be applied to the total photon-hadron cross section. The total cross sections for various hadronic processes are displayed in figure 2.14 The

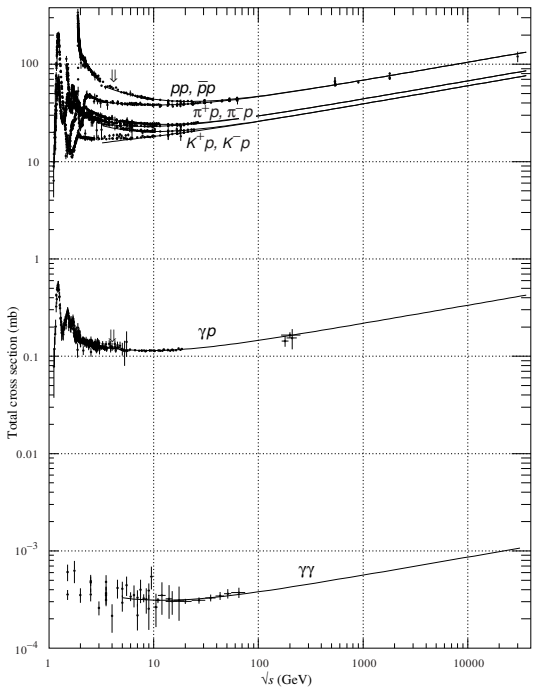

Figure 2.14: Summary plot of hadron-proton, photon-proton and photon-photon total collision cross sections. The plot is taken from the Particle Data Group [Cas98]

data of figure 2.14 were fitted in a global fit by Donnachie and Landshoff [Don92], giving $\eta = 0.4525$ and $\epsilon = 0.0808$. Recent data from HERA for the γp and cross sections at $\sqrt{s} > 100$ GeV suggested the contribution of an additional Regge pole with intercept $\alpha(0) \simeq 1.4$, the 'hard Pomeron' that was included in more recent fits by Donnachie and Landshoff yielding a better description of high energy data [Don98].

Hadronic cross sections can be decomposed into kinematically distinct processes as depicted in figure 2.15:

- Elastic scattering, i.e., the process $AB \to AB$ where the initial hadrons leave the interaction unchanged. At small momentum transfers $t = (p_A - p'_A)^2 = (p_B - p'_B)^2$ the cross section for elastic scattering falls exponentially like ($t < 0$)

$$\frac{d\sigma_{el}}{dt} \sim e^{-b|t|}, \quad \text{with } b = b_0 + 2\alpha' \ln(\alpha' s). \tag{2.92}$$

- Single diffractive scattering, i.e., the processes $AB \to AX$ and $AB \to XB$ where either of the hadrons is transferred into an excited state and eventually splits up and fragments. As in the elastic case the cross section falls exponentially in t, usually with a smaller slope. Also, the cross section behaves as $1/M_X^2$, where M_X is the mass of the excited hadron.

- Double diffractive scattering $AB \to XX$ where both of the hadrons split up. Also, here the cross section exhibits an exponential slope and a behavior like $1/(M_{X_1}^2 M_{X_2}^2)$.

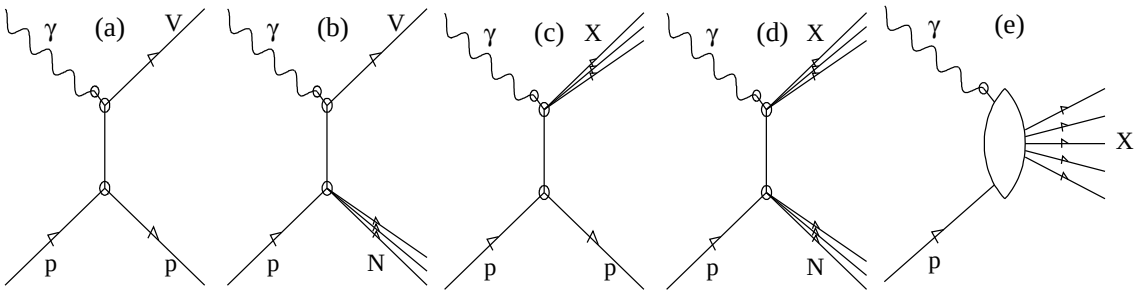

Figure 2.15: Classification of VMD processes: (a) elastic, (b) proton single diffractive, (c) VM single diffractive, (d) double diffractive, (e) non-diffractive.

In all three cases above the momentum transfer is considered to be small enough for the final state hadrons or fragments to travel approximately into the same direction as the initial hadrons. The term 'diffraction' here comes from an analogy to optical diffraction where light rays are deflected at small angles on an opaque obstacle of size b comparable to the wave length and give a characteristic intensity pattern behind that obstacle. At high energies where the Pomeron picture dominates, diffractive events can usually be recognized by large rapidity gaps between the final state jets or hadrons. This large rapidity gap is a feature of the exchange of a color neutral (quasi-) particle in the interaction, because if no color is exchanged, also no string (color flux) needs to be attached between the scattered particles such that they can develop independently from each other.

- There exists another class of processes, the non-diffractive (inelastic) events, basically covering all (hadronic) processes that cannot be described by diffractive or elastic scattering. This includes the soft, 'minimum bias' events (usually described by exchange of soft gluons) as well as hard, high-p_T scattering of the partons in the initial state hadrons that can be described in the Quark Parton Model. No perturbative description exists for low-p_T, minimum bias events. In non-diffractive events color is exchanged between the partons, and the final state particles are distributed rather randomly in rapidity with the consequence that they cannot be associated with either of the initial hadrons.

In the Vector Meson Dominance model, the cross section for, e.g., $\gamma p \to X$ is assumed to be dominated by contributions from the hadronic component of the photon. The cross section factorizes into a probability for the photon to fluctuate into a vector meson and the cross section for that respective vector meson to interact with the proton:

$$\sigma^{\gamma p}_{VMD}(s) = \sum_{V=\rho^0,\omega,\phi,J/\psi} \frac{4\pi\alpha}{f_V^2} \sigma^{Vp}_{tot}(s). \tag{2.93}$$

The cross sections $\sigma^{Vp}_{tot}(s)$ are not directly known. Within the additive quark model [Lev65, Lip66] one can use the measured pion and kaon cross sections instead:

$$\sigma^{\rho^0 p}_{tot} \approx \sigma^{\omega^0 p}_{tot} \approx \frac{1}{2}\left(\sigma^{\pi^+ p}_{tot} + \sigma^{\pi^- p}_{tot}\right) \tag{2.94}$$

$$\sigma^{\phi p}_{tot} \approx \sigma^{K^+ p}_{tot} + \sigma^{K^- p}_{tot} - \sigma^{\pi^- p}_{tot} \tag{2.95}$$

The couplings $\frac{f_V}{4\pi}$ can be inferred either from photoproduction data using the optical theorem:

$$\left.\frac{d\sigma^{\gamma p \to Vp}}{dt}\right|_{t=0} = \frac{4\pi\alpha}{f_V^2}\frac{1}{16\pi}\left(\sigma^{Vp}_{tot}(s)\right)^2 \tag{2.96}$$

or from the process $e^+e^- \to \gamma^* \to V \to$ hadrons, where the partial width of the resonance (equivalent to that of the decay $V \to e^+e^-$) is given by:

$$\Gamma(V \to e^+e^-) = \frac{\alpha^2}{3}\left(\frac{f_V^2}{4\pi}\right)^{-1} m_V, \tag{2.97}$$

with m_V the vector meson mass. The combination of the coupling strengths with the cross sections obtained from the fits by [Don92] yield a total hadronic contribution to the real photon cross section of about 80% to 90%, with the higher value at lower energies. This leaves about 10 to 20% for the direct and anomalous components of the photon. In figure 2.16 a summary of the total γp and the elastic cross sections for the light vector mesons and J/ψ is given.

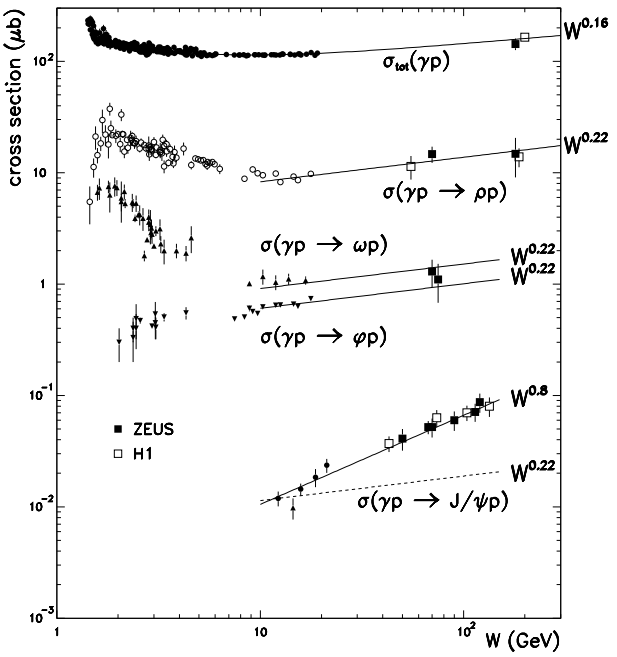

Figure 2.16: The energy dependence of the total photon-proton absorption cross section and the ρ^0, ω, ϕ and $J\psi$ exclusive photoproduction cross sections. The data at lower energy are from fixed target experiments, the high energy data from H1 and ZEUS. See Ref. [Cri97] for details.

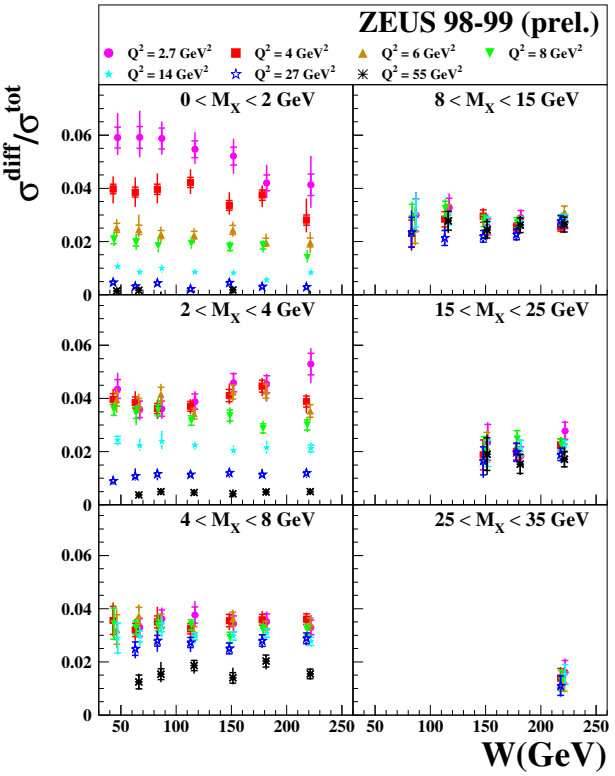

Figure 2.17: The ratios $\frac{d\sigma^{\gamma^* p}_{diff}}{dM_X}/\sigma^{\gamma^* p}_{tot}$ measured in inclusive diffraction at the ZEUS experiment, as a function of W. The different panels correspond to different M_X regions, the different symbols to different Q^2 regions.

There are extensions to the VMD model which for instance include off-diagonal couplings between the different vector meson states or a continuous mass spectrum of vector mesons V' [Sak72]. This is the so called Generalized Vector Meson Dominance (GVMD) Model. An alternative model of (elastic) VMD using perturbative QCD was developed by Ryskin [Rys92] to describe elastic J/ψ production. In this model the photon splits into a $q\bar{q}$ and interacts with the Pomeron described as a gluon ladder. In the leading log approximation, the scattering amplitude is proportional to the gluon density $xG(x)$ in the proton. For pQCD to work, a hard scale is required which could be either the vector meson mass (in case of the J/ψ) or a more general combination $\bar{q}^2 = \frac{1}{4}(m_V^2 + Q^2 + p_T^2)$. For photoproduction of the light vector mesons the Ryskin model can thus not be expected to give meaningful results.

The relation of the VMD real photon cross section to that of the virtual photon is given by a dipole factor

$$\sigma_{VMD}^{\gamma^* p}(s, Q^2) = \left(\frac{m_V^2}{m_V^2 + Q^2}\right)^2 \sigma_{VMD}^{\gamma p}(s). \tag{2.98}$$

At large Q^2 the dipole factor suppresses the hadronic contribution such that the direct contribution from DIS dominates. The cross section is then well described by the absorption of the virtual photon by partons and the QPM is retrieved. In figure 2.17 the fraction of diffractive events in the total cross section measured at ZEUS [Lim03] is given as a function of W^2, Q^2 and M_X. For $M_X < 8$ GeV, the diffractive contribution to the cross section decreases with Q^2. The contribution at $Q^2 = 2.7$ GeV from all $M_X < 35$ GeV is about 20% whereas it is a factor of two smaller at $Q^2 = 27$ GeV.

The fact that the diffractive contribution to the total $\gamma^* p$ cross section decreases very slowly, even at high energies, may constitute a problem for the interpretation of data at the lower Q^2 attainable in fixed target experiments in terms of the QCD parton model only. Several models of structure functions exist that might explain discrepancies between the parton model description and data, for instance in the difference between the proton and neutron structure functions $F_2^p - F_2^n$. Such discrepancies are often attributed to higher twist effects[3] at small Q^2, however, it is possible to explain them at least partially with a contribution of VMD processes to the structure function [Szc00a]. In such a model, the structure function F_2 is decomposed into a non-partonic (VMD) part and a partonic part corresponding to the parton model predictions:

$$F_2(x, Q^2) = F_2^{VMD}(x, Q^2) + F_2^{partons}(x, Q^2) \tag{2.99}$$

with

$$F_2^{VMD}(x, Q^2) = \frac{Q^2}{\pi} \sum_V \frac{4\pi}{f_V^2} \left(\frac{m_V^2}{m_V^2 + Q^2}\right) \sigma_{tot}^{Vp,n}(s) \cdot \Omega_V(x, Q^2) \tag{2.100}$$

$$F_2^{partons}(x, Q^2) = \frac{Q^2}{Q^2 + Q_0^2} F_2^{asymptotic}(x, Q^2). \tag{2.101}$$

Here, $F_2^{asymptotic}(x, Q^2)$ is the standard partonic structure function and $\Omega_V(x, Q^2)$ is an additional (exponential or Gaussian) form factor. Fits to data with this model yield a VMD contribution of as much as 50% at $x < 0.1$ and small $Q^2 \simeq 0.6$ GeV^2, and still about 10% at $Q^2 \simeq 3.5$ GeV^2 [Szc00b]. Similar considerations suggest non-partonic contributions to g_1 [Bad99], although nothing is presently known about the polarized vector meson cross sections $\Delta\sigma_{tot}^{Vp}$. A review of models and kinematic constraints of the structure function F_2 in the limit of low x and Q^2 can be found in Ref. [Bad96].

For the interpretation of data in terms of the QCD parton model the non-partonic parts of the (measured) structure functions have to be considered as background. The size of this background could in principle be inferred from a suitable Monte Carlo simulation. A model implemented in PYTHIA 6.1 [Sjö01] is especially designed to obtain a smooth description of non-partonic and partonic effects in the transition from soft to high energy interactions [Schu93], and as well for the transition from real to virtual photon processes [Fri00]. In this thesis, this model will be used to estimate the non-partonic contribution to HERMES data in quasireal photoproduction and DIS.

2.6 DIS Sum Rules and the Spin Crisis

In DIS, invariant structure functions relate the measured cross sections to parton densities in the nucleon on grounds of the Quark Parton Model. In order to describe the quantum numbers of the

[3] Note that higher twist contributions are usually of the form $(1/Q^2)^n$, $n \geq 1$, such that an expansion in twist would diverge as $Q^2 \to 0$.

nucleon ground state at low energy, integrals of measured parton densities at high energy in DIS thus have to fulfill certain consistency conditions called sum rules. Sum rules can be rigorously established in the framework of the Operator Product Expansion (OPE) where the integrals over parton densities are expressed as expectation values of *local* operators between nucleon states. For a detailed disquisition on the subject of OPE, see for instance Refs. [Tho01] or [Jaf96, Man92]. The QCD operators in the OPE are combinations of gauge invariant quark and gluon operators. In order to relate their matrix elements to measurable quantities, however, often they have to be given in a specified gauge. Those matrix elements can then be associated with moments of structure functions, parton distributions or combinations of parton distributions [4]. As an example, the momentum sum rule

$$\int_0^1 dx\, x(\Sigma(x,Q^2) + g(x,Q^2)) = 1 \tag{2.102}$$

can be derived from the expectation value of the + component of the energy-momentum tensor in light-cone coordinates in the $A^+ = 0$ gauge. In this gauge, quarks fields have only longitudinal degrees of freedom while the gluon fields A^μ have only transverse polarization – this corresponds to the parton model concept of parton distributions. This gauge is therefore inherent in the description of DIS in terms of the parton model [Jaf96]. Since $xq(x)$ ($xg(x)$) in the parton model is the fractional energy carried by quarks (gluons) in an interval dx, the momentum sum rule states that the momenta of all quarks and gluons in the nucleon have to add up to the nucleon momentum. However, it is not possible to fix the normalization of the gluon operator, because the evolution equations for the moments of the singlet quark and gluon distributions stay invariant under certain scaling transformations. By *convention* one chooses a normalization such that the momentum sum rule holds to all orders at all Q^2. This is intuitively conceived as momentum conservation. With this convention, the asymptotic values ($Q^2 \to \infty$) of the fraction of momentum carried by quarks and gluons are $3n_f/(16 + 3n_f)$ and $16/(16 + 3n_f)$, respectively, which for $n_f = 4$ flavors gives $\frac{3}{7}$ and $\frac{4}{7}$. There are several other sum rules for unpolarized DIS data relating to different aspects of the nucleon structure and are more or less fundamental, see, for instance Ref. [Tho01].

For polarized DIS, the analog to the momentum sum rule would be an angular momentum sum rule. However, here the situation is not as simple, for various reasons. In addition to the general ambiguities in separating quark singlet and gluon contributions (see section 2.3), in relativistic quantum mechanics, spin and orbital angular momentum are not conserved separately. A general sum rule for the nucleon angular momentum would have to contain both spin and orbital angular momentum of the partons. With the suggestion by Ji [Ji97a], the nucleon spin can be decomposed as follows

$$J = \frac{1}{2} = J_q + J_g = \frac{1}{2}\Delta\Sigma + L_q + J_g. \tag{2.103}$$

Strictly spoken, this is not a sum rule, because even though $\Delta\Sigma$ is the integral over the polarized singlet parton distribution, the gluon total angular momentum J_g and the quark orbital angular momentum are not the integrals over the gluon and quark angular momentum densities. Thus equation 2.103 is more of an operator *relation* of gauge invariant operators defining the *total* quark and gluon angular momentum that cannot be measured in DIS. Note also, that the gluon angular momentum cannot be further decomposed into spin and orbital angular momentum, because the corresponding operators are not separately gauge invariant. Ji proposed the measurement of J_q via Deeply-virtual Compton Scattering (DVCS) where an exclusive real photon is detected in the final state [Ji97b]. From the Q^2 evolution of the DVCS cross section, also J_g can (in principle) be inferred. The asymptotic partition of the nucleon spin between quarks and gluons approaches the same ratio as for the decomposition of the nucleon momentum, $16 : 3n_f$. A classical sum rule for the angular momentum (more accurate, its projection onto the axis of the virtual photon direction in the infinite momentum frame) was proposed by Jaffe and Bashinsky [Bas98]:

$$J_z = \frac{1}{2} = \frac{1}{2}\Delta\Sigma + \Delta G + L_q + L_g. \tag{2.104}$$

[4] The nth moment of a function $f(x,Q^2)$ is defined as $F^n(Q^2) = \int_0^1 dx\, x^{n-1} f(x,Q^2)$

Each of the terms on the right can be written as an integral over parton distributions and is separately gauge-invariant:

$$J_z = \frac{1}{2} = \int_0^1 dx \, \frac{1}{2}\Delta\Sigma(x,Q^2) + \Delta G(x,Q^2) + L_q(x,Q^2) + L_g(x,Q^2). \tag{2.105}$$

Here $\Delta\Sigma(x,Q^2)$ and $\Delta G(x,Q^2)$ can be identified with the polarized structure functions to be measured in DIS if the corresponding operators are given in the $A^+ = 0$ gauge. On the other hand, there exists up to now no practical way of measuring the distributions of quark and gluon orbital angular momentum. To summarize, from the theory point of view there exists an angular momentum sum rule analogous to the momentum sum rule, Eq. 2.104, but it can only be partly related to measurements. This makes it rather unsuitable for testing the parton model predictions with experiment.

There are other sum rules, however, that can be related to measurements of polarized structure functions. The most fundamental one is the Bjorken sum rule [Bjo66] derived in 1966 from SU(6)⊗SU(6) current algebra, assuming only $SU(2)_f$ isospin invariance. In the OPE, the matrix elements related to the total helicities of quarks are defined by

$$S^\mu(\Delta q + \Delta\bar{q}) = \langle P,S|\bar{q}\gamma^\mu\gamma_5 q|P,S\rangle. \tag{2.106}$$

Using current algebra, one defines more generally flavor singlet, triplet and octet matrix elements A_i by the current operators $j_i^{5\mu} = \bar{\psi}\gamma^\mu\gamma_5\lambda_i\psi$, with the quark field $\psi = (u,d,s)^T$ and the Gell-Mann matrices λ_i, $i = 1,\ldots,8$. The flavor triplet and octet matrix elements are then respectively:

$$A_3 = \tfrac{1}{S^\mu} \langle P,S|\bar{\psi}\gamma^\mu\gamma_5\lambda_3\psi|P,S\rangle = \Delta u + \Delta\bar{u} - \Delta d - \Delta\bar{d}, \tag{2.107}$$

$$A_8 = \tfrac{1}{S^\mu} \sqrt{3}\langle P,S|\bar{\psi}\gamma^\mu\gamma_5\lambda_8\psi|P,S\rangle = \Delta u + \Delta\bar{u} + \Delta d + \Delta\bar{d} - 2(\Delta s + \Delta\bar{s}), \tag{2.108}$$

$$\tag{2.109}$$

and the singlet matrix element is

$$A_0 = \frac{1}{S^\mu}\langle P,S|\bar{\psi}\gamma^\mu\gamma_5\bar{\psi}|P,S\rangle = \sum_{q=u,d,s} \Delta q + \Delta\bar{q} = \Delta\Sigma. \tag{2.110}$$

In the simple QPM, the first moment of g_1 can be written for the proton:

$$\Gamma_1^p = \int_0^1 dx g_1^p(x) = \frac{1}{2}\left(\frac{4}{9}(\Delta u + \Delta\bar{u}) + \frac{1}{9}(\Delta d + \Delta\bar{d} + \Delta s + \Delta\bar{s})\right) \tag{2.111}$$

$$= \frac{1}{2}\left(\frac{1}{6}A_3 + \frac{1}{18}A_8 + \frac{2}{9}A_0\right). \tag{2.112}$$

The neutron moment can be obtained, using isospin symmetry, by interchanging $u \leftrightarrow d$

$$\Gamma_1^n = \int_0^1 dx g_1^n(x) = \frac{1}{2}\left(-\frac{1}{6}A_3 + \frac{1}{18}A_8 + \frac{2}{9}A_0\right). \tag{2.113}$$

On the other hand, the combination $A_3 = (\Delta u + \Delta\bar{u}) - (\Delta d + \Delta\bar{d})$ can be related to neutron β decay through an isospin rotation:

$${}_p\langle P,S|\bar{u}\gamma^\mu\gamma_5 u - \bar{d}\gamma^\mu\gamma_5 d|P,S\rangle_p = {}_p\langle P,S|\bar{u}\gamma^\mu\gamma_5 d|P,S\rangle_n = S^\mu\left|\frac{g_A}{g_V}\right|, \tag{2.114}$$

where g_A and g_V are the axial and vector couplings whose ratio known to high precision: $\frac{g_A}{g_V} = 1.2573 \pm 0.0028$. The subscript $p(n)$ denotes the proton (neutron) state. Thus the Bjorken sum rule states that the difference between proton and neutron moments of g_1 is

$$\Gamma_1^p - \Gamma_1^n = \frac{1}{6}A_3 = \frac{1}{6}\left|\frac{g_A}{g_V}\right|. \tag{2.115}$$

In QCD, the Bjorken sum rule receives moderate corrections that are known to α_s^3 (note that A_3 is just the polarized nonsinglet, valence quark distribution). The theoretical prediction of the Bjorken sum rule is in good agreement with the data, however, since it is difficult to measure a 'pure' neutron structure function, the data are much less precise than the theory.

Ellis and Jaffe made predictions for the moment of the proton structure function alone [Ell74]. Using $SU(3)_f$ symmetry the axial vector couplings from hyperon β decay can be related to other combinations of quark spins, similar to Eq. 2.114,

$$\langle H_j\, P,S|j_i^{5\mu}|P,S\, H_k\rangle = S^\mu(-if_{ijk}F + d_{ijk}D). \tag{2.116}$$

The hyperons H_i, $i = 1,\ldots,8$ are members of the $SU(3)_f$ spin 1/2 baryon octet, and the $f_{ijk}(d_{ijk})$ are the totally antisymmetric and symmetric group constants of $SU(3)_f$. The constants F and D are known experimentally [Mon94]:

$$F = 0.459 \pm 0.008 \qquad D = 0.798 \pm 0.008. \tag{2.117}$$

Assuming full $SU(3)_f$ symmetry one gets [Seh74]:

$$A_3 = F + D = \left|\frac{g_A}{g_V}\right| = 1.2573 \pm 0.0028, \tag{2.118}$$

$$A_8 = 3F - D = 0.579 \pm 0.025 \tag{2.119}$$

resulting in the proton (neutron) moment of g_1

$$\Gamma_1^{p,n} = \pm\frac{1}{12}(F+D) + \frac{5}{36}(3F-D) + \frac{1}{3}(\Delta s + \Delta\bar{s}). \tag{2.120}$$

With the assumption $\Delta s = \Delta\bar{s} = 0$ the prediction from the Ellis-Jaffe sum rule is:

$$\Gamma_1^p \simeq 0.185. \tag{2.121}$$

Even when taking into account the quite large uncertainties in the extrapolation to the unmeasured low-x region, the experimental data lie significantly below this value. This fact is usually referred to as the 'spin crisis' or, better, 'spin puzzle', as the apparent contradiction of data and theory implies that the singlet contribution A_0 to Γ_1^p is significantly smaller than expected. If the nucleon spin was made up completely of the quark spins, one would have $A_0 = \Delta\Sigma = \mathcal{O}(1)$ ($\Delta\Sigma = 1$ only when the quarks are nonrelativistic, with relativistic quarks $\Delta\Sigma \simeq 0.75$). In fact, the data on Γ_1^p suggest that $\Delta\Sigma \ll 1$. Since the Ellis-Jaffe sum rule is not fundamental, there are several possibilities to explain the small value of $\Delta\Sigma$ (see Ref. [Lam98] for a detailed discussion):

a) The assumption $\Delta s = \Delta\bar{s} = 0$ is not valid. Instead, there could be a sizeable negative contribution from strange quarks $\Delta s = \Delta\bar{s} \simeq -0.05$ to -0.1.

b) The assumption of $SU(3)_f$ used to derive Eqs. 2.118 and 2.119 is not valid. This is quite probable, because $SU(3)_f$ relies on $m_u = m_d = m_s$, which is not a very good approximation for the strange quark at least. However, one can picture a fully $SU(3)_f$ broken scenario where the hyperon decay matrix elements are related only to *valence* quark distributions Δu_v, Δd_v. Then Γ_1^p would be ($\Delta\bar{u} \simeq \Delta\bar{d} \equiv \Delta\bar{q}$)

$$\Gamma_1^{p,n} = \pm\frac{1}{12}(F+D) + \frac{5}{36}(3F-D) + \frac{1}{18}(\Delta s + \Delta\bar{s} + 10\Delta\bar{q}). \tag{2.122}$$

In this scenario, even for the extreme case of symmetry breaking with $\Delta s = \Delta\bar{s} = 0$, a negative *light polarized sea* with $\Delta\bar{q} < 0$ can account for the reduced $\Delta\Sigma$.

c) It has been suggested that a large negative contribution from $\alpha_s\Delta G$ contributes to $\Delta\Sigma$, even though there is no direct gluon contribution at leading order. The reason is the so called axial

anomaly, the fact that the singlet axial current is *not conserved*. The divergence of the axial current is

$$\partial_\mu j_0^{5\mu} = n_f \frac{\alpha_s}{2\pi} Tr(F_{\mu\nu}\epsilon^{\mu\nu\alpha\beta}F_{\alpha\beta}), \tag{2.123}$$

where F is the gluon field strength. The axial anomaly introduces a (pointlike) interaction between quarks and gluons, and the singlet matrix element receives an additional contribution from gluons:

$$A_0 = \Delta\Sigma - n_f \frac{\alpha_s}{2\pi}\Delta G. \tag{2.124}$$

In this case a small value of A_0 does not necessarily imply that the quark contribution to the nucleon spin is small. It has been shown [Adl69] that the anomaly equation 2.123 is exact in QCD, i.e., it does not receive higher order corrections. Furthermore, the Altarelli-Parisi evolution equations for the first moment of $\Delta G(x, Q^2)$ imply that

$$\frac{d}{dt}\left[\alpha_s \Delta G(Q^2)\right] = 0 + O(\alpha_s^2). \tag{2.125}$$

This means that the term $\alpha_s\Delta G(Q^2)$ entering the first moment of g_1 through the axial anomaly, behaves like an object of $\mathcal{O}(1)$, and that its contribution can be potentially large even at $Q^2 \to \infty$ where the small strong coupling should indicate the validity of the simple parton model.

Next to leading order corrections were calculated in the $\overline{\rm MS}$ scheme for the first moment of g_1 to be

$$\Gamma_1^p(NLO) = \frac{1}{2}\left(\frac{1}{6}A_3 + \frac{1}{18}A_8 + \frac{1}{9}A_0\right)\left(1 - \frac{\alpha_s(Q^2)}{\pi}\right). \tag{2.126}$$

Results from NLO fits in the $\overline{\rm MS}$ scheme yield at the input scale $\mu^2_{NLO} = 0.34$ GeV^2 small negative values for the light sea polarization ($\Delta\bar{q} = -0.0778$ in the valence scenario) and for the strange sea polarization ($\Delta\bar{q} = \Delta\bar{s} = \Delta s = -0.066$ in the standard scenario), and the quark singlet moment amounts to $\Delta\Sigma_{\overline{\rm MS}} = 0.183\,(0.268)$ for the standard (valence) scenario [Glü01]. Note that in this scheme at NLO the gluon does not contribute to Γ_1^p because the first moment of the gluon coefficient function $\Delta C_g^{(1)}$ vanishes. As a consequence, the quark singlet moment $\Delta\Sigma_{\overline{\rm MS}}$ is Q^2 dependent. In the AB scheme, the first moment of g_1 would be in NLO:

$$\Gamma_1^p(NLO) = \frac{1}{2}\left(\frac{1}{6}A_3 + \frac{1}{18}A_8 + \frac{1}{9}\Delta\Sigma_{AB}\right)\left(1 - \frac{\alpha_s(Q^2)}{\pi}\right) - \frac{1}{9}n_f\frac{\alpha_s}{2\pi}\Delta G(Q^2) \tag{2.127}$$

$$= \frac{1}{2}\left(\frac{1}{6}A_3 + \frac{1}{18}A_8 + \frac{1}{9}A_0^{AB}(Q^2)\right)\left(1 - \frac{\alpha_s(Q^2)}{\pi}\right) + O(\alpha_s^2), \tag{2.128}$$

with $n_f = 3$. The singlet contribution to g_1 in the AB scheme is then given by

$$A_0^{AB}(Q^2) = \Delta\Sigma_{AB} - n_f\frac{\alpha_s}{2\pi}\Delta G(Q^2), \tag{2.129}$$

where now $\Delta\Sigma_{AB}$ does not depend on Q^2, and the gluon does contribute to Γ_1^p. If the gluon polarization were large and positive, this would account for the smallness of the singlet matrix element A_0. The quark contribution $\Delta\Sigma_{AB}$ to the nucleon spin in the sense of the angular momentum sum rule Eq. 2.104 on the other hand could be potentially large in the AB scheme, and close to the quark model result. The difference between the two schemes in interpreting the small singlet matrix element is that the large gluon polarization in the AB scheme is absorbed into a large (light or strange) sea quark polarization in the $\overline{\rm MS}$ scheme. Although the results in the AB scheme appeal to our intuition because of the apparent conservation of quark chirality and its compliance with the static quark model it is at the moment not practical to use this scheme for the extraction of parton distributions. The reason is that all coefficient functions, not only for DIS but also for other possible processes, and the splitting functions would have to be known at NLO in this scheme,

which is not the case. However, as stated in [Bod90], the choice of convention defining either a hard gluon contribution to Γ_1^p (AB) or absorbing it into a soft part of quark distributions ($\overline{\text{MS}}$) does not affect any physical observable such that from data there cannot be a conclusion of which scheme is the preferred one, and the size of the gluonic contribution to the first moment of g_1 will stay obscure. This does not apply to the quantity $\Delta G(x, Q^2)$ itself that can be measured directly in semi-inclusive processes, as will be discussed in the next section.

2.7 Direct Measurements of the Gluon Polarization

Direct measurements of the gluon polarization can be performed by enhancing experimentally the processes in which gluons are involved in the initial state. In leading order, for DIS this would be the photon-gluon fusion (PGF) process as it is depicted in figure 2.6 (b) for light quarks $\gamma^* g \to q\bar{q}$ producing high-p_T jets or hadrons. As shown in figure 2.18 for heavy (charm) quarks the PGF process $\gamma^* g \to Q\bar{Q}$ would lead to charmed mesons in the final state. In hadronic collisions, e.g., in polarized $\vec{p}\vec{p}$ scattering the leading order processes are

- High-p_T ('prompt') photon production $qg \to \gamma q$ (figure 2.19 (a)),
- Jet production from gluon-gluon scattering $gg \to gg$ and gluon-quark scattering $qg \to gq$ (figure 2.19 (b)) and
- Heavy flavor production in gluon-gluon fusion $gg \to Q\bar{Q}$ (figure 2.19 (c)).

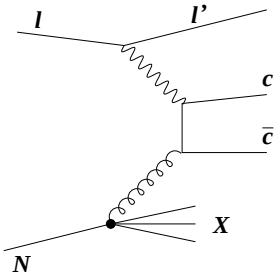

Figure 2.18: The Photon-Gluon Fusion diagram for charm leptoproduction.

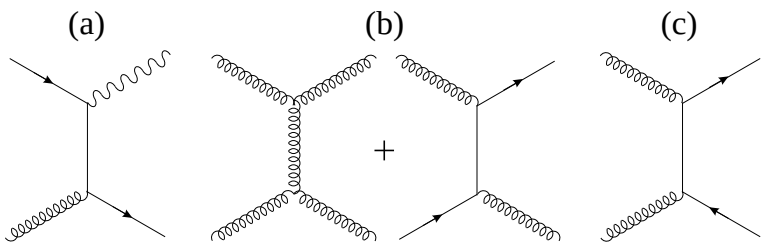

Figure 2.19: Some LO Feynman diagrams for processes in pp collisions with gluons in the initial state: (a) quark-gluon Compton process (prompt photon production), (b) gluon-gluon and gluon-quark scattering for jet production, and (c) gluon-gluon fusion for the production of a heavy quark pair.

Most of these processes have already been used as a powerful probe of the unpolarized gluon distribution in unpolarized DIS and hadron scattering. In the following, some of the options for using gluon initiated processes to probe the polarized gluon distribution will be discussed.

2.7.1 Heavy Flavor Production

At the center of mass energies available at present, the intrinsic charm (bottom) content of the nucleon is considered negligible [Ing97]. The dominating process is then 'extrinsic' production where the heavy quark pair is created by initial state gluons. Here, only charm production will be discussed [5]. If the other invariants involved in the process (the squared center of mass energy s or the transverse momentum p_T of the outgoing hadrons) are not significantly larger, the charm mass is naturally taken as the scale of the process $\mu_f = \mu_r = 2m_c \simeq 3.1$ GeV. The final state mesons can be either J/ψ mesons ('Hidden charm') or 'open charm' mesons like D^0, D^{*+}. Experimentally,

[5] The material for this section is mainly from Ref. [Lam98] and the references therein.

the J/ψ can be detected by its decay to lepton ($\mu^+\mu^-$ or e^+e^-) pairs giving a clean signature with very little background. Theoretically, the description of J/ψ production is problematic though, for two reasons. First, in DIS, a contribution of the photon splitting $\gamma^* \to c\bar{c}$ might lead to J/ψ production as described in the VMD model. In this case the process would be sensitive to the charm content of the photon rather than the gluon content of the proton. The 'resolved photon' component becomes particularly relevant, if one wants to measure the cross section in the quasireal photoproduction limit (i.e. at very small Q^2, cf. section 2.5) which is in principle possible because the scale is given by the charm mass. Second, the $c\bar{c}$ pair created in PGF is not in a color singlet state. Since the bound state J/ψ meson has to be colorless, additional gluons have to be emitted from at least one of the quarks. There are two distinct models describing the formation of the bound state. In the color-singlet model, a hard gluon is emitted (perturbatively) from one of the quarks at short distances $\Delta x \sim 1/m_{J/\psi}$. Predictions for unpolarized J/ψ and Υ cross sections from the color-singlet mechanism fail to describe experimental data taken at Tevatron (see, e.g. [Abe92]) underestimating the cross section by almost an order of magnitude. This is why more recently also the color-octet mechanism has been considered. In this model only the production of the $c\bar{c}$ is perturbative and its subsequent hadronization to a color-singlet state is described by multiple, nonperturbative soft gluon emission. However, the theoretical uncertainties are still quite large even for the unpolarized case, such that for measurements of the polarized quantity ΔG, J/ψ production might not yet be applicable.

The open charm channel is less uncertain from the theoretical side, but since it experimentally involves the detection of the decay products, mainly kaons and pions, it represents a challenge in terms of geometrical acceptance, particle identification and background reduction. As proposed for the COMPASS experiment [Nas98], ΔG can be extracted from double-spin asymmetries in DIS with muons of about 100 GeV on a fixed target. In terms of virtual photon cross sections, the asymmetry for open charm production can be written as:

$$A_1^{c\bar{c}}(x,Q^2) = \frac{\Delta\sigma^{\gamma^* p\to c\bar{c}}}{\sigma^{\gamma^* p\to c\bar{c}}} = \frac{\int_{-1}^{1} d\cos\theta^* \int_{\left(1+\frac{4m_c^2}{Q^2}\right)x}^{1} \frac{dx'}{x'} \Delta G(x',\mu_f^2)\Delta\hat{\sigma}\left(\frac{x}{x'},Q^2\right)}{\int_{-1}^{1} d\cos\theta^* \int_{\left(1+\frac{4m_c^2}{Q^2}\right)x}^{1} \frac{dx'}{x'} G(x',\mu_f^2)\hat{\sigma}\left(\frac{x}{x'},Q^2\right)}. \tag{2.130}$$

The angle θ^* is the angle of the c quark relative to the gluon direction in the photon-gluon center of mass system. In order to increase statistics the measurement will be taken at low Q^2, in quasireal photoproduction. The cross section in this limit can be obtained from the DIS cross section by letting $Q^2 \to 0$ and $z = \frac{x}{x'} \to 0$, such that the photon-gluon center of mass energy $\hat{s} = (p+q)^2 = Q^2\frac{1-z}{z} \simeq \frac{Q^2}{z}$ stays fixed. In this limit, the hard cross sections are given by

$$\Delta\hat{\sigma}(z,Q^2) = \frac{4}{9}\frac{2\pi\alpha\alpha_s}{\hat{s}}\left(3\beta - \ln\frac{1+\beta}{1-\beta}\right) \tag{2.131}$$

$$\hat{\sigma}(z,Q^2) = \frac{4}{9}\frac{2\pi\alpha\alpha_s}{\hat{s}}\left(-\beta(2-\beta)^2 + \frac{1}{2}(3-\beta^4)\ln\frac{1+\beta}{1-\beta}\right). \tag{2.132}$$

Here, $\beta = \sqrt{1-\frac{4m_c^2}{\hat{s}}}$, with $\hat{s} = x's_\gamma = x'W^2$. By varying the photon energy, the x dependence of ΔG can in principle be explored, with very high photon energies corresponding to small x. At small x, however, the asymmetry is expected to be small, once because the polarized hard cross section changes sign at around $x \simeq 10^{-3}$, but also because the unpolarized gluon distribution rises much stronger than the polarized one towards small x. The photon energies between 35 and 85 GeV of the COMPASS experiment are just about adequate for this type of measurement. The sensitivity to ΔG can be further enhanced by introducing cuts on the transverse momentum of the outgoing charmed meson. This is due to the fact that when integrating over k_T (or alternatively, the angle θ^*) the hard cross section from the low k_T region cancels that of the large k_T region. For a cut on the D transverse momentum $p_T^D < 1$ GeV and a beam energy of 100 GeV, an estimate of the possible precision for the virtual photon asymmetry and the corresponding muon-proton asymmetry ($A_{\mu p}^{c\bar{c}} = DA_1^{c\bar{c}}$) is shown in figure 2.20. In this estimate, the experimental errors from

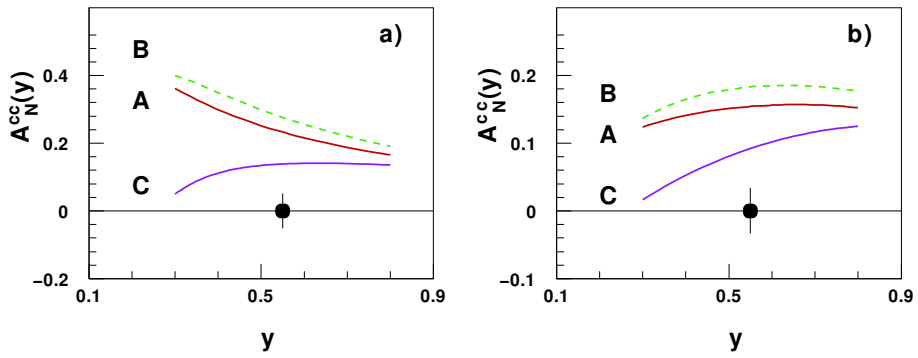

Figure 2.20: The estimated asymmetry (a) $A_{\gamma p}^{c\bar{c}}$ and (b) $A_{\mu p}^{c\bar{c}}$ at the average y of COMPASS with 100 GeV muons. The curves correspond to three (extremely) different parametrizations of ΔG from Ref. [Geh95].

combinatorial background, the beam and target polarizations etc. are included. The fragmentation of the charm quarks to $D^0, \bar{D}^0$ or D^{*+} (via the decay $D^{*+} \to D^0\pi^+$) was simulated with the LUND string fragmentation model and yielded an average of 1.2 D^0 or $\bar{D}^0$ mesons per $c\bar{c}$ event. Also for open charm production there could in principle be a resolved photon component. At the center of mass energy of COMPASS, however, it is not expected to contribute more than 4% to the cross section [Glü96]. More problematic is the scale dependence. As the choice of scale μ_f to be $2m_c$ is probably reasonable, but not certain, the scale dependence of the cross section reflects our ignorance about higher order corrections. An approximate NLO calculation exists for COMPASS energies [Boj99]. For the NLO polarized cross section at COMPASS the scale dependence of the asymmetry (its variation with respect to a change of the scale between $\frac{\mu}{2}$ and 2μ) is significantly reduced to ±10% compared to -15% to 35% at LO. At energies just above the charm threshold there is an additional large uncertainty of about 30% on the asymmetry introduced by the uncertainty of the charm mass itself making the situation even less conclusive.

Hadronic heavy quark production can be measured at RHIC, in polarized $\vec{p}\vec{p}$ scattering at $\sqrt{s} = 50 - 500$ GeV. At these energies, the gluon initiated subprocess $gg \to c\bar{c}(b\bar{b})$ is the dominant one, and the polarized cross section is [Lam98]

$$\Delta\sigma_{pp}^{Q}(s) = \int_{\frac{4m_Q}{s}}^{1} dx_1 \int_{\frac{4m_Q}{x_1 s}}^{1} dx_2\, \Delta G(x_1,\mu_f^2)\Delta G(x_2,\mu_f^2)\Delta\hat{\sigma}^{gg\to Q\bar{Q}}(x_1x_2s,\mu_f^2). \tag{2.133}$$

The unpolarized cross section is analogous to this, with $G(x_i,\mu_f^2)$ instead of $\Delta G(x_i,\mu_f^2)$, and the unpolarized partonic cross section $\hat{\sigma}^{gg\to Q\bar{Q}}$ instead of $\Delta\hat{\sigma}^{gg\to Q\bar{Q}}$. The partonic cross sections are known, but for the polarized cross section a NLO calculation is still missing. Again, the measurement proceeds via spin-spin asymmetries

$$A_{pp}^{Q}(s) = \frac{\Delta\sigma_{pp}^{Q}(s)}{\sigma_{pp}^{Q}(s)}. \tag{2.134}$$

Heavy flavor production can be selected at RHIC for example by looking at charmed meson production $pp \to \mu^+ D^0 X$, but also by the leptonic decays of heavy quarks, e.g., $pp \to \mu^\pm(e^\pm)X$, $pp \to \mu^+\mu^-(e^+e^-)X$ or $pp \to \mu^\pm e^\mp X$. Also for these hadronic processes, the asymmetry is expected to be sizeable only at smaller energies $\sqrt{s} < 100$ GeV, and may be enhanced by a p_T cut [Bun00].

2.7.2 Prompt Photon Production

Prompt photon production has been the classical tool for determining the unpolarized gluon density at intermediate and large x. The favored subprocess in the reaction $pp \to \gamma X$ is $qg \to \gamma q$ as opposed

to $q\bar{q} \to \gamma g$ in proton-antiproton collisions. An isolated photon from these processes would produce a distinct detector signal and the analyzing power $\hat{a}_{LL} = \frac{\Delta\hat{\sigma}}{\hat{\sigma}}$ is large (cf., for instance Ref. [Bun00]). The coupling of the quark to the photon on the upper vertex in figure 2.19 (a) is proportional to its squared charge, such that the spin-spin asymmetry for prompt photon production becomes:

$$A_{LL} \simeq \frac{\Delta G(x_1)}{G(x_1)} \left[\frac{\sum_q e_q^2(\Delta q(x_2) + \Delta\bar{q}(x_2))}{\sum_q e_q^2(q(x_2) + \bar{q}(x_2))} \right] \cdot \hat{a}_{LL}(gq \to \gamma q) + (1 \leftrightarrow 2). \tag{2.135}$$

Here $x_{1,2}$ are the momentum fractions of the partons in the two protons that can be partly reconstructed experimentally. Figure 2.21 shows the sensitivity to ΔG the STAR experiment at RHIC can achieve by reconstructing the parton kinematics in photon-plus-jet events at $\sqrt{s} = 200$ and 500 GeV. There are some background processes also in this channel. An additional contribution to

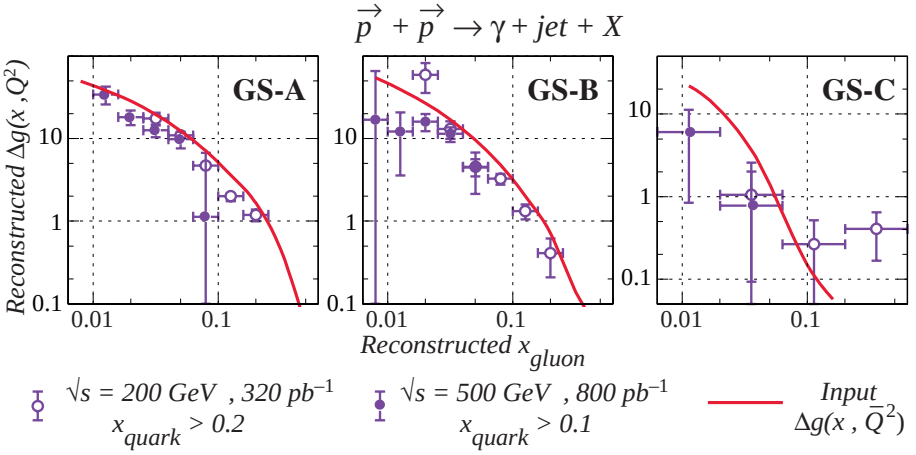

Figure 2.21: Sensitivity of STAR measurements of $\Delta G(x)$ in the channel $p\bar{p} \to \gamma + \text{jet} + X$. The solid curves in each plot are the input gluon densities, taken from [Geh95].

high-p_T photons can come from partons produced in a QCD reaction that fragment into a photon and a number of hadrons. The fragmentation function for quarks into photons has been measured at LEP, however, the data are sparse. Theoretical predictions made from photon fragmentation functions predict non-negligible fractions of the observed photons to come from fragmentation. Also, in hadronic reactions large numbers of π^0s are produced along with other hadrons in jets that decay into two photons. If both photons are unambiguously detected, their invariant mass can indicate their origin from π^0 decay. If one of the photons escapes from the detector, or the two photons are too close to each other to be separately detected, a π^0 can fake a single photon event. Both kinds of background sources can be suppressed by imposing an isolation cut ensuring that a given spatial neighborhood of the photon is free of energetic hadron tracks. Although next to leading order calculations are available for unpolarized prompt photon production, there are still discrepancies between p_T distributions of fixed target data and theory, see, for instance [Apa98]. There, reasonable agreement of the data with theory could only be achieved if the smearing of the intrinsic ('primordial') k_T of the initial state partons of a few hundred MeV due to the finite size of the proton was increased to much larger values of around 1.2 to 1.4 GeV. Recently, much theoretical progress has been made describing the smearing of primordial k_T by multiple soft gluon emission. Multiple soft gluon emission can be treated perturbatively using methods where the large leading logarithmic terms of the partonic cross section generated by soft gluons are resummed to all orders. These resummation methods have lead to improvements in the description of prompt photon production in the fixed target regime (see, for instance Refs. [Lae00] and [Lai98]). Clarification of the problem leading to a better understanding of the prompt photon process may offer valuable information about ΔG.

2.7.3 High-p_T Jet Production

In the late 80s it has been proposed by Carlitz, Collins and Müller (CCM) to measure the gluon contribution to g_1 from dijet events in polarized DIS at high energy [Car88]. The important quantity in this experiment is the jet transverse momentum that can be related to the parton transverse momentum k_T. In the discussion about inclusive DIS the parton k_T has always been integrated over. In the naive parton model, k_T is explicitly neglected. Also in the QCD improved parton model at leading order no significant transverse momentum can be created, since the DGLAP equations that govern the evolution of parton distributions only describe the small p_T radiation off partons. In semi-inclusive DIS on the other hand, nonperturbative effects can lead to non-zero hadron transverse momentum. These effects are described by the intrinsic ('primordial') k_T of the partons in the initial state hadron, a consequence of the uncertainty principle. The primordial k_T smearing of ≈ 0.4 GeV can be significantly enhanced by multiple soft gluon emission (cf. section 2.7.2), and may lead to a much larger, effective smearing of $k_T \approx 1$ GeV. Transverse momentum is also produced during the fragmentation process at the point where the string breaks, or if a gluon is radiated from the string. The nonperturbatively created k_T smearing of partons can phenomenologically be described by Gaussian distributions

$$\frac{d\sigma}{dk_T^2} \sim \exp\left(-\frac{k_T^2}{\sigma^2}\right), \tag{2.136}$$

where $\sigma^2 = \langle k_T^2 \rangle$ is the average of the squared partonic k_T. Note that, in leading twist inclusive DIS, (intrinsic) transverse momentum does not play a role. It may play a role for the power suppressed structure function g_2, though, that still lacks an interpretation within the parton model.

Only at NLO, the transverse momentum created in hard subprocesses such as $g \to q\bar{q}$ or $q \to qg$ becomes important. These processes lead to dijet events with large p_T compared to the nonperturbatively created transverse momentum. The contribution of dijet events to the first moment of g_1 can be written in terms of the variable $\lambda = \frac{4k_T}{Q^2}$:

$$\frac{d}{d\lambda}\int_0^1 dx g_1(x,Q^2,\lambda) = \frac{\alpha_s(\mu_r)}{4\pi}\sum_q e_q^2 \left[C_F M_q(\lambda)(\Delta q(\mu_f^2) + \Delta\bar{q}(\mu_f^2)) + T_R M_g(\lambda)\Delta G(\mu_f^2)\right], \tag{2.137}$$

where $C_F = 4/3$ and $T_R = 1/2$, and the functions $M_i(\lambda)$ give the contributions from the process $\gamma^* q \to qg$ (QCD-Compton scattering, QCDC) and $\gamma^* g \to q\bar{q}$ (PGF) for $i = q$, g respectively.

$$M_q(\lambda) = \frac{\frac{11}{8}\lambda + \frac{13}{4} + \frac{2}{\lambda}}{(1+\lambda)^{3/2}} \ln\frac{\sqrt{1+\lambda}+1}{\sqrt{1+\lambda}-1} - \frac{12+11\lambda}{4\lambda(1+\lambda)} \tag{2.138}$$

$$M_g(\lambda) = -\frac{\lambda(4+\lambda)}{4(1+\lambda)^{5/2}} \ln\frac{\sqrt{1+\lambda}+1}{\sqrt{1+\lambda}-1} + \frac{\lambda-2}{2(1+\lambda)^2} \tag{2.139}$$

The renormalization and factorization scales are taken to be $\mu_{f,r}^2 = Q^2$, but the choice $\mu_{f,r}^2 = p_T^2$ might work equally well. The hard partonic matrix element M_g in combination with a positive ΔG gives a negative contribution to the polarized jet cross section, Eq. 2.137. Naturally, one would measure double-spin asymmetries in jet production, as a function of the jet p_T or double differentially as a function of x and p_T. At small x the contribution from gluons dominates over that from quarks, such that the clearest signatures can be expected in the small x region. However, the negative signal can be 'spoiled' by a possibly much larger unpolarized gluon distribution than the polarized one, but also by the competing QCDC process leading to positive asymmetries over the whole x and p_T range. The contribution from quarks can be suppressed by imposing experimental cuts on the jet properties and thus exploiting the slightly different behavior of gluon jets compared to jets originating from quarks. NLO calculations of the polarized multi-jet cross section for a hypothetical polarized *ep* collider at HERA ($\sqrt{s} \simeq 300$ GeV, beam polarization 70%) lead to asymmetries of ≈ -0.015 [Mir97]. This result can be changed by a factor 2 if a different parametrization

for ΔG is used. For further references and more details see Ref. [Lam98]. To increase statistics, the quasireal photoproduction region may be also included also here. In this case, the jet transverse momentum would serve as the scale of the process. Calculations have been performed for possible future polarized colliders at LO [Str97]. For photoproduction again the contribution from resolved photons has to be taken into account that in view of the determination of the gluon helicity distribution in the *nucleon* is to be considered as background. From the LO calculation in [Str97] it can be inferred that at negative rapidities (positive rapidities are defined by the proton direction) and large transverse momentum, this contribution is at most subdominant. At NLO, one would in principle have to calculate the $\mathcal{O}(\alpha_s)$ corrections to the resolved photon component as well because due to the factorization procedure of collinear singularities only the sum of the direct and resolved components becomes factorization scheme independent.

In the near future, measurements of this type could only be performed at fixed target experiments, at energies much smaller than those of the proposed colliders. For HERMES ($\sqrt{s} = 7$ GeV) and COMPASS ($\sqrt{s} \sim 15$ to 20 GeV) the energies are too small for jets being produced. Instead, analogous measurements involving high-p_T hadrons could be performed, which will be discussed below.

Also at RHIC, double spin asymmetries of high-p_T jet events at $\sqrt{s} = 500$ GeV can be used to determine ΔG. At the kinematic region accessible for the STAR experiment, the gluon-initiated diagrams of figure 2.19 b) dominate. NLO calculations for the projected asymmetries also lead to small values that are rather different for different input gluon densities, though (see figure 2.22). As the expected statistical precision is good, a discrimination between the various parametrizations seems feasible. For more details, see Ref. [Bun00] and the references therein.

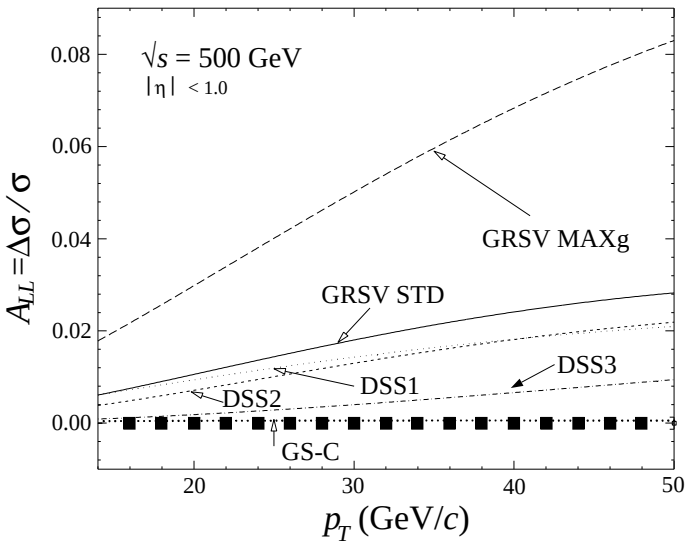

Figure 2.22: Asymmetry vs. jet transverse momentum for various polarized parton density sets. See the references in [Bun00] for the meaning of the labels. The point at $p_T = 48$ GeV shows the projected experimental accuracy for the standard luminosity assumed. At lower p_T the expected errors are even smaller than the points.

2.7.4 High-p_T Hadron Pair Production

Collimated hadronic jets to be associated with partons that emerged from a hard reaction only appear at high energies. The energies of the fixed target experiments in polarized DIS are not large enough for the final state hadrons to form jets. The hadron multiplicity is rather low, and the angular spread around the original parton direction is relatively large. Instead, there are several

suggestions for measurements analogous to those in jet production using high-p_T hadrons or high-p_T hadron pairs. Calculations exist for various energies ($\sqrt{s} = 27$ and 170 GeV [Per94], $\sqrt{s} = 300$ GeV [DeF98], $\sqrt{s} = 7$ and 10 GeV [Afa98, Afa99], $\sqrt{s} = 20$ GeV [Bra98], most of them in the quasireal photoproduction regime. A full, consistent NLO calculation including the resolved photon component in the $\overline{\text{MS}}$ scheme has been performed recently in Ref. [Jäg03a] for π^0 photoproduction at $\sqrt{s} = 100$ GeV.

In Ref. [Bra98] it was proposed to measure asymmetries of high-p_T hadron pairs. Assuming that only the hard partonic processes contribute to the cross section for high-p_T hadron pairs, a generic cross section in first order of QCD for $ep \to h_1 + h_2$ can be written as:

$$\begin{aligned}(\Delta)\sigma^{h_1+h_2} &= \sum_q \left\{(\Delta)q \otimes (\Delta)\hat{\sigma}^{\gamma^* q \to q} \otimes D_q^{h_1+h_2}\right\} + \sum_q \left\{(\Delta)q \otimes (\Delta)\hat{\sigma}^{\gamma^* q \to qg} \otimes D_{q,g}^{h_1+h_2}\right\} \\ &\quad + \sum_q \left\{(\Delta)G \otimes (\Delta)\hat{\sigma}^{\gamma^* g \to q\bar{q}} \otimes D_{q,\bar{q}}^{h_1+h_2}\right\}. \end{aligned} \tag{2.140}$$

Here, the fragmentation functions appear explicitly as the probabilities that a quark ($D_q^{h_1+h_2}$), a quark-gluon system ($D_{q,g}^{h_1+h_2}$) or a quark-antiquark pair ($D_{q,\bar{q}}^{h_1+h_2}$) fragment into a hadron pair. In the LUND string fragmentation model the transverse momentum acquired by hadrons during the fragmentation process is distributed as a Gaussian with $\sigma_{p_{T,F}} \simeq 0.36$ GeV. This value was obtained from fits to LEP e^+e^- data [Abr96]. Taking into account an intrinsic k_T of the initial state partons $\sqrt{\langle k_T^2 \rangle} \simeq 0.44$ GeV, the transverse momentum of hadrons originating from the LO DIS process ($\gamma^* q \to q$) should be distributed according to $\exp\left(-\frac{p_T^2}{\langle p_T^2 \rangle}\right)$ with

$$\langle p_T^2(z) \rangle \sim \langle p_{T,F}^2 \rangle + z^2 \langle k_T^2 \rangle. \tag{2.141}$$

In contrast to the exponential drop in the leading order process, the cross sections for the first order QCD subprocesses fall roughly like $1/\hat{p}_T^2$ and one may expect a power law dependence for the outgoing hadrons. Requiring $p_T > 1.5$ GeV for at least one of the hadrons would thus reduce the fraction of events originating from LO DIS processes to 10^{-3} [Bra98]. Figure 2.23 shows the subprocess asymmetries for PGF and QCDC as a function of the center of mass scattering angle $\hat{\theta}$. Although both asymmetries are Q^2 dependent, the outstanding difference between them is that

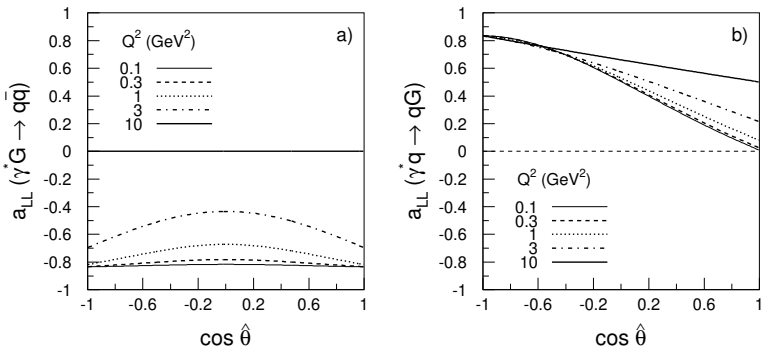

Figure 2.23: The subprocess asymmetries $\hat{a}_{LL} = \frac{\Delta\hat{\sigma}}{\hat{\sigma}}$ for PGF (a) and QCDC (b) as a function of the c.m. scattering angle $\hat{\theta}$, for a fixed value of squared partonic c.m. energy $\hat{s} = 10$ GeV^2 and $y = 0.7$ (corresponding to $D = 0.83$). The various curves are for different values of Q^2

the PGF asymmetry is negative, while the QCD Compton asymmetry is positive. It should be stressed that in contrast to the analogous measurement of high-p_T jets at collider energies, the subprocess asymmetries are large, indicating very good sensitivity to the subprocesses. If one succeeds in selecting a data sample such that the competing QCD Compton process is suppressed,

one would expect a clear negative signal from PGF in the measured asymmetry (for positive gluon polarization). To enhance the PGF signal a set of cuts is proposed as a consequence of some assumptions about the fragmentation process:

- The concept of favored and unfavored fragmentation – the fragmentation of a particular quark flavor into hadrons containing this quark flavor is preferred over fragmentation into hadrons not containing that flavor. As an example, the probability for a u quark to fragment into a π^+ should be larger than that for a d quark. On the other hand, a u quark preferably fragments into π^+ while a $\bar{u}$ quark favors fragmenting into π^-. Such, if the partonic configuration is $q\bar{q}$, the probability for a charge symmetric hadronic final state is large (this is also implied by charge conservation).
- Strangeness suppression – the production of strange hadrons from non-strange light quarks should be disfavored, with a suppression factor around 0.2 to 0.3 [6]. That way, the production of a kaon pair from non-strange quarks should be much less probable than that from an original $s\bar{s}$ pair created in the hard subprocess.

Cuts based on these assumptions are suggested in [Bra98]:

a) require $p_T > 1$ to 1.5 GeV for each of the outgoing hadrons,

b) possibly impose an invariant mass cut $m(h_1, h_2) > 2 - 3$ GeV – to serve as a lower limit on the partonic center of mass energy, $\sqrt{\hat{s}}$, especially in photoproduction, where most of the time the event kinematics are not known,

c) select oppositely charged hadron or kaon pairs

d) select hadrons that are almost opposite in azimuth (if both hadrons come from partons created in the hard process, their transverse momenta should cancel each other).

e) impose constraints on $x_F > 0$ or $z > 0.1$ (selecting the 'forward' hemisphere) to reduce possible correlations of the selected hadrons with the target fragments.

The projected asymmetries for the COMPASS experiment are shown in figure 2.24. They were obtained using the Monte Carlo program POLDIS [Bra97] and applying the above mentioned cuts to the generated hadron pairs. The asymmetries are plotted versus the parton momentum fraction η that can be reconstructed from the hadron pair kinematics taking into account a certain smearing due to the fragmentation process. Apparently, there is a strong sensitivity to the gluon polarization due to the large subprocess asymmetries and signal to background ratios. The validity of the assumptions on the fragmentation has to be proven, though. With the proposed method, the only way to do this is to compare the Monte Carlo model that has been used to calculate the asymmetries with the data in the relevant observables, e.g. p_T distributions, cross sections, etc. This becomes even more critical, if the suggested procedure is to be adapted for the HERMES kinematics at slightly lower center of mass energy.

The assumptions on the fragmentation rely on strong correlations between the outgoing partons and the hadron pairs in the final state. If there was a high probability that only two, oppositely charged hadrons emerged from a $q\bar{q}$ pair the above mentioned cuts would indeed strongly suppress contributions from the LO DIS process as well as from QCD Compton scattering (there, however, a large uncertainty arises from the gluon fragmentation function). In reality, the average hadron multiplicity at $\sqrt{s} = 7$ GeV is around 5 to 6, even for the LO DIS process (where only one hard parton is produced) as Monte Carlo studies for HERMES using the Lund fragmentation model show [Mex03]. The strong correlation between partons and hadrons might thus be spoiled. Furthermore, the cuts on x_F and/or z might not completely exclude additional correlations to

[6] The strangeness suppression factor is defined as the probability to create a $s\bar{s}$ pair during fragmentation relative to that of a $u\bar{u}$ or $d\bar{d}$ pair.

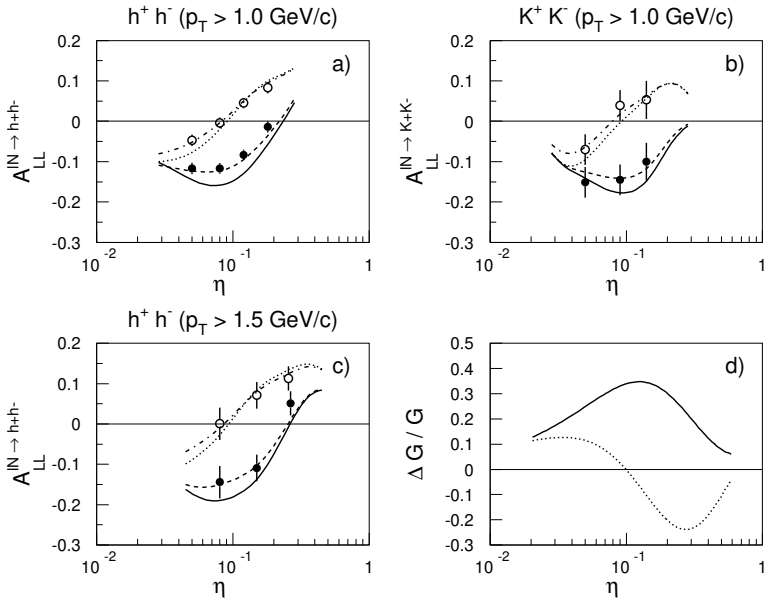

Figure 2.24: Projected cross section asymmetries $A_{LL}^{\mu N \to h^+h^-(K^+K^-)}$ for one year of COMPASS running as a function of the (true) parton momentum fraction η. The upper and lower curves correspond to different parton density inputs from [Geh96], as shown in the lower right panel (set A: solid line, set C: dotted line). The circles show the reconstructed asymmetries as a function of η_{rec}, and the dash-dotted and dashed curves indicate the smearing of the asymmetries due to the finite width of the reconstructed parton momentum. The plot is taken from Ref. [Bra98]

the fragments of the target remnant. The situation is even more difficult for kaon pairs, since no direct measurements exist for the fragmentation of strange quarks. For parametrizations of kaon fragmentation functions additional assumptions on symmetries etc. have to be used introducing large uncertainties [Kni01]. It has also been observed that the strangeness suppression factor measured in μN [Ada94] or ep [Aid96] collisions differs significantly from that measured in e^+e^- collisions [Abr96]. The reason here is believed to be again multiple soft gluon emission which is different in lepton-nucleon and hadronic collisions. On the other hand, there is a substantial contribution from the fragmentation of light quarks to vector mesons such as ρ, K^*, ... having been measured to occur with a probability of around 0.4 relative to the fragmentation to pseudoscalar mesons [Abr96]. The decay products of these vector mesons would, as part of the hadron pair sample, 'blur' the kinematic correlations with the original partons. Multiple soft gluon emission might smear the effective value for the intrinsic k_T, such contaminating the hadrons sample with $p_T > 1$ GeV more than expected.

In the quasireal photoproduction regime the contribution from resolved photon processes or VMD has to be taken into account as well. It is to be regarded as background, and will usually be subtracted using Monte Carlo calculations. Estimates of this contribution might differ considerably with the model used. At higher Q^2, this contribution could in principle be suppressed for the cost of loosing a large fraction of the available statistics.

HERMES published data on asymmetries of high-p_T hadron pairs in quasireal photoproduction, using the data taken with a longitudinally polarized proton target in the years 1996 and 1997 [Air00]. Quasireal photoproduction events are selected at HERMES by antitagging the scattered positron (i.e., requiring the positron *not* to be detected). The result is shown in figure 2.25 where the asymmetry for oppositely charged hadron pairs is shown as a function of the transverse momentum $p_T(h_2)$ of one of the hadrons, while the other hadron has $p_T(h_1) > 1.5$ GeV. For $p_T(h_2) > 1$ GeV, a negative signal was observed, with a significance of about two standard deviations. From this signal, using the PYTHIA 5.7/JETSET 7.4 Monte Carlo program [Sjö94], a

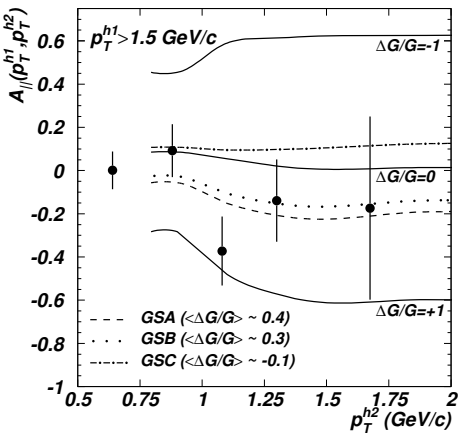

Figure 2.25: Asymmetry for oppositely charged hadron pairs h_1h_2 on hydrogen measured at HERMES [Air00]. The asymmetry is plotted versus the transverse momentum of h_2, while h_1 was required to have $p_T(h_1) > 1.5$ GeV. The curves show asymmetries calculated with PYTHIA 5.7 [Sjö94], using sets A to C from [Geh96]

value of $\Delta G/G = 0.41 \pm 0.18(stat.) \pm 0.03(syst.)$ was derived. The quoted systematic error accounts for experimental uncertainties only. This result has to be regarded as completely dependent on the model implemented in PYTHIA 5.7. Last but not least, for both experiments, the scale dependence of the LO cross sections might play a significant role. It is not obvious at all that the scale is defined by $\hat{p}_T$ (even if it can indeed be reconstructed from the hadron transverse momentum), it can be as well any other kinematic quantity like $\hat{s}$ or Q^2 or a combination of those. At the relatively small scales accessible for the two experiments, the NLO corrections to the cross sections are large, as can be seen in figure 2.26 where the ratio of *unpolarized* cross sections $\frac{\sigma(\mu)}{\sigma(\mu/2)}$ is shown for a selection of experiments and processes. The scale dependence for cross section asymmetries might be smaller, though. On the other hand, the information used for the extraction of $\Delta G/G$ with the method proposed by [Bra98] essentially relies on the knowledge of the *unpolarized* cross section, which might induce a large systematic error to the extracted values.

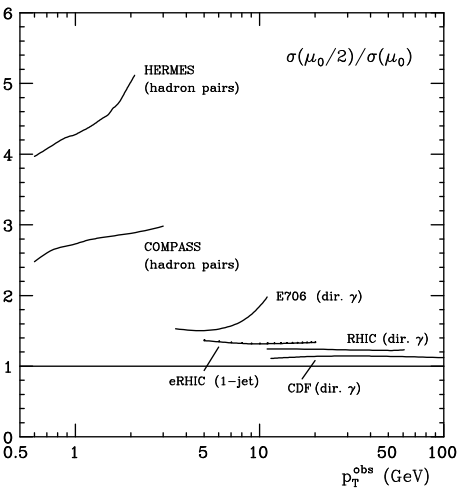

Figure 2.26: Scale dependence of unpolarized cross sections for processes sensitive to gluon distributions for HERMES and COMPASS (high-p_T hadron pairs, E706 (fixed target), RHIC and CDF (prompt photon production and the proposed (polarized) electron-proton collider eRHIC ($\sqrt{s} \simeq 100$ GeV at RHIC (inclusive jet photoproduction). The plot is taken from [Str02]

2.7.5 Inclusive High-p_T Hadron production

Because of the limited statistics available for hadron pairs measurements of asymmetries of *inclusive* high-p_T hadrons in photoproduction have also been considered [Afa98, Afa99]. The cross sections can be computed in the same manner as in Eq. 2.140, by exchanging $h_1 + h_2 \to h^{\pm}$ – effectively integrating Eq. 2.140 over the p_T of one of the hadrons. If one neglects contributions from the leading order DIS process at low Q^2, only the first order QCD processes contribute and Afanasev et al. showed that one would expect large and positive asymmetries of ≈ 0.2 to 0.3 for $ep(n) \to \pi^+ X$ and large and negative asymmetries of ≈ -0.2 to -0.1 for $ep(n) \to \pi^- X$ at $p_T(\pi^{\pm})$ between 1 and

2.5 GeV at HERMES kinematics [Afa98]. The negative asymmetries for negative pions persist also if $\Delta G = 0$, thus showing that there must be a significant contribution from the QCD Compton scattering on d quarks (remember that Δd is negative). In a later calculation by Afanasev et al. [Afa99] it was revealed that the contribution from soft, resolved photon processes (VMD) in the photoproduction data could be as large as 90% at small to medium p_T, practically reducing the asymmetries to zero for $p_T < 2$ GeV, as shown in figure 2.27. As explained in the previous

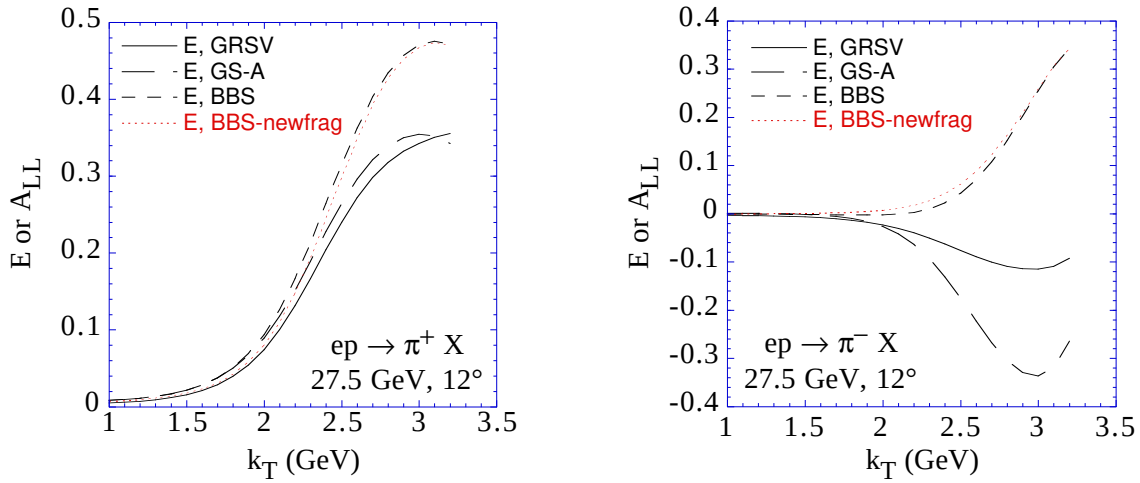

Figure 2.27: Theoretical calculations for $A_{\parallel}$ vs. hadron transverse momentum for positive (left) and negative pions (right) from Afanasev et al. with the method as in [Afa99]. The asymmetries are calculated for a hadron lab angle of 12° The various curves for the asymmetries are for different input parton distributions and fragmentation functions, the labels are defined in [Afa99]).

section, asymmetries in quasireal photoproduction are obtained by antitagging the scattered lepton. The data sample may therefore contain events where the positron scattering angle was *larger* than the maximum angle of 0.22 mrad allowed for the scattered lepton to be within the geometrical acceptance of the HERMES experiment. Such events can be associated with correspondingly large angles of the virtual photon with respect to the z axis of the experiment. The antitagging procedure brings about the ignorance about the true event kinematics that cannot be reconstructed. The hadron transverse momentum, measured against the z axis, is then large although the true transverse momentum with respect to the virtual photon direction is not. Measurements of inclusive hadron and pion asymmetries on a hydrogen target at HERMES [Lie01] showed results different in the sense that a deviation from zero is observed already at smaller p_T values around 1 GeV (see figure 2.28). Monte Carlo studies using a new generator, PYTHIA 6.1 [Sjö01] indicated that a substantial fraction of the inclusive hadron sample at large $p_T > 1$ might come from the LO DIS process at high Q^2 induced by the undetected leptons at large angles. For the predictions in figure 2.27 the LO DIS contribution has not been considered. The necessity for detailed Monte Carlo studies in order to interpret the data is obvious.

The main issue of this thesis is to perform a data – Monte Carlo comparison with the goal of estimating the feasibility to extract values for $\Delta G/G$ from inclusive high-p_T hadron asymmetries. In order to optimize the result, not only in the quasireal photoproduction regime but possibly also in the DIS ($Q^2 > 1$ GeV^2) and transition (small Q^2, small x) regimes accessible at HERMES kinematics will be investigated.

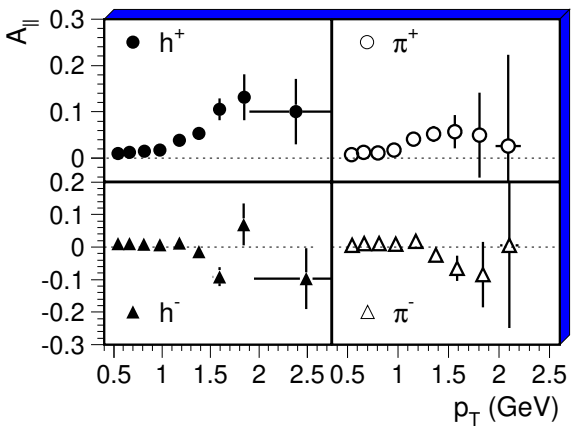

Figure 2.28: Inclusive asymmetries of charged hadrons and identified pions in quasireal photoproduction on hydrogen measured at HERMES [Lie01] as a function of hadron transverse momentum. The pions have momenta between 3.8 and 13 GeV.

Chapter 3

Data Analysis

As illustrated in section 2.7, one of the possibilities for the extraction of $\Delta G/G$ is the measurement of double-spin asymmetries of high-p_T hadrons in semi-inclusive DIS and quasireal photoproduction. In this chapter, the analysis of these asymmetries and systematic studies of the results will be presented.

3.1 HERMES Data Structure and Data Quality

Two types of data are measured and stored in parallel during HERMES data taking. On the one hand, there is information on the hits in the tracking and PID detectors that is read out by the data acquisition system every time a trigger is generated and accepted.] On the other hand, there are the slow control data that are read out regularly at a much smaller rate and record all information about the status of all detectors and the experimental conditions, for instance the beam and target polarizations, luminosity etc. The raw detector data are translated from the EPIO (Experimental Physics Input Output) format to an ADAMO data base format using the HERMES decoder program HDC. The decoded detector information is then passed to the track reconstruction code HRC, and the reconstructed track data are again stored in ADAMO format. For physics analysis so called μDSTs are produced where the track information is synchronized with the slow control data. This later enables analyzers to judge whether events from a given period may be included in the analysis, based on certain requirements on the detector performance, beam and target parameters and so on. The μDSTs contain only a reduced data set where loose cuts on events or tracks were applied already. The data are structured in three levels. The lowest level, an event, contains all the reconstructed tracks in the spectrometer for an accepted trigger. The events are grouped in bursts, corresponding to about ten seconds of data taking. At this level, the slow control data is synchronized with the 'event' data. These bursts are parts of runs which in turn are defined by the size of a raw EPIO data volume of about 450 MB. The length of a run is about ten minutes for polarized data taking at maximum beam current. For each run a μDST is produced that can be separately analyzed. Usually, the data productions are iterated one or more times in order to calibrate detectors, calculate the parent distributions for the PID, tracking efficiencies, and so on.

The polarized data taken up to now at HERMES can basically be separated into four groups. The first longitudinally polarized data were taken with a ^{3}He target during the commissioning year of the experiment in 1995. In 1996 and 1997 the longitudinally polarized target was hydrogen, from 1998 to 2000 it was deuterium with the bulk of the statistics from 2000. All polarized deuterium data thus have the information from the RICH detector available that was installed after the 1997 data taking period. Since 2001 a transversely polarized hydrogen target has been installed in HERMES. The relevant data for this analysis are the hydrogen data of 1996 and 1997 and the deuterium data of 2000, all longitudinally polarized.

3.1.1 Data Quality for Unpolarized Data

The quality of the data is monitored online during data taking, using slow control information as well as trigger and event rates. However, since the online data are uncalibrated it is difficult to judge whether a given data set is suitable for analysis. Also, the requirements on the performance of detectors and external conditions (background, beam and target parameters) may differ from one analysis to another, depending on the information to be used. A careful study of offline data (after iteration) by the responsible group results in a burst wise selection of data according to a defined set of criteria. Those criteria are usually the same for all years with some exceptions. In this thesis also data will be presented that were taken with an unpolarized target, or where the beam and target polarizations were averaged over. The data shown in sections 3.4 and 4 are mainly unpolarized (and averaged polarized) hydrogen data from 1997 and 2000. The cuts applied to ensure good data quality in this case are summarized in table 3.1. The second cut in table 3.1 refers to a flag set in

#	Data Quality	Cuts/Requirements
1	Gas type	Hydrogen (1996 and 1997, 2000), Deuterium (2000)
2	Run analyzable?	YES (g1Quality.iExpment=1)
3	High voltage trips of BC, FC	0
4	Cherenkov/RICH, TRD, Preshower, Calorimeter	OK
5	Calorimeter dead blocks	0 (1 for 1996)
6	Luminosity monitor dead blocks	0
7	Life time of Trigger 21 (τ_{Tr21})	$0.5 < \tau_{Tr21} <= 1$
8	Average life time of all Triggers (τ_{Tr})	$0.5 < \tau_{Tr} <= 1$
9	Artificial dead time correction	NONE
10	Burst length (t_{Burst})	$0 < t_{Burst} < 11$ s
11	Beam current (I_{Beam})	$5 < I_{Beam} <= 50$ mA
12	Bad μDST records	NONE
13	First burst in a run	rejected

Table 3.1: The cuts applied to the data for unpolarized analysis.

the log book during data taking, it excludes runs taken under such problematic conditions that it is highly improbable that they contain useful data. Cut #3 ensures that the drift chambers used for track reconstruction were working properly, cut #4 does the same for the PID detectors. In addition it is required that neither the calorimeter nor the luminosity monitor had malfunctioning blocks. The exception is for one particular dead block in 1996 that was sitting on the outer rim of the calorimeter and did not have an effect on most of the data. Cuts #7 to #9 ensure that the DAQ system was functioning and that the calculated trigger life time has physical values. Even with large background the life time never dropped below 0.5. The 'artificial dead time correction' factor was necessary for some of the data in 1997, data with a factor different from 1 are discarded. The ranges given for the burst length and the beam current cover all possible reasonable values for these quantities. Cut #12 rejects data with synchronization problems, no information on, e.g., the calorimeter threshold setting, table overflows, jumps in event or burst numbers etc. that may occur during μDST production. Also, the last burst of a fill with reconstructed events is cut out. Finally, the first burst in a run is discarded because information may be lost or mixed during the initialization of the DAQ system at the beginning of a run.

3.1.2 Data Quality for Double Spin Asymmetries

Table 3.2 summarizes all cuts necessary to ensure stability and quality of polarized data used for double spin asymmetries. These cuts are applied in addition to the cuts in table 3.1. The target mode is set run wise in the log book and defines which polarization states are injected into the

#	Data Quality	Cuts/Requirements
1	Gas type	Hydrogen (1996 and 1997), Deuterium (2000)
2	Target mode	2-states (1996 and 1997), 4-states (2000)
3	Target data quality	$0 < \alpha_0$, $0.7 < \alpha_R$ (1996/97)
		Target data quality flag OK (2000)
4	Target polarization	$0.6 < P_T < 1.5$ (1996/97), $0 < P_T < 1.5$ (2000)
5	Continuity	Require reasonable *previous* P_T measurements
6	Target polarization state	parallel or antiparallel w.r.t. beam
7	Beam polarization	$0.3 < P_B < 0.8$
8	Beam polarization fit	last fitted value less than 300 secs. ago
9	Fitted luminosity	$5 < \mathcal{L}_{fitBstGain} < 80$ Hz

Table 3.2: Special cuts applied to data for analysis of double spin asymmetries.

target cell. For the proton data, these should only be the two vector polarization states whereas for the deuteron data also tensor polarization states were injected. For the target data quality in general a flag is set by the target experts, but this was erroneous in 1996/97. Instead, for these data, cuts on the target polarization and α are applied to ensure that the target was operating normally. With cut #6 only those bursts or parts of burst are selected where the target was in a definite state parallel or antiparallel to the beam direction. For the hydrogen and deuterium data the target spin was flipped randomly at a frequency of about 90 seconds. Usually, the spin flip occurred during a burst such that the burst was divided into three parts (records): the initial spin state, the undefined flipping state which is about 2 seconds long and the final spin state. The lower cut on the beam polarization rejects data taken at small beam polarization values that do not contribute significantly to asymmetries. By cut #8 it is ensured that the last available fitted beam polarization value is from less than five minutes ago, in order to avoid discontinuities and therefore large uncertainties in the polarization values. In order to be applicable for asymmetry analysis, the luminosity rate measured by the luminosity monitor needs to be fitted. Due to the residual *electron* polarization in the target, the cross sections for Møller/Bhabha scattering and e^+e^- annihilation have small asymmetries that would bias the normalization of the data in each spin state if the raw values were used. Instead, the luminosity rate measured by the luminosity monitor is fitted on a fill-by-fill basis, such that the asymmetry is averaged out in the fit. Two methods are applied to smooth the luminosity rate. For the quantity $\mathcal{L}_{fit}$, the luminosity rate itself is fitted while for $\mathcal{L}_{fitBstGain}$, the standard value used in asymmetry analyses, the ratio of the (PMT-) gain corrected luminosity rate to the beam current is fitted. This ratio is proportional to the target density which is a stable quantity throughout a fill.

Of the runs taken with polarized beam and target, the data quality cuts shown in tables 3.1 and 3.2 exclude about 17% of the data in 2000 [DeN02], and about 32% in 1997 [Gär01]. Nevertheless the usefulness of data obtained with these cuts has to be tested for each individual analysis.

3.1.3 Time Dependence of Yields

For double spin asymmetries it is important that the quantities relevant for the measurement of the cross section or normalized yields (see below) do not depend on the spin states of the target and/or the beam. The important quantities in this case are the performance (and possibly the acceptance) of the individual tracking and PID detectors, the track reconstruction efficiency and resolution, the trigger efficiency and the luminosity rate. The time dependence of yields normalized to luminosity

$$Y = \frac{\int dt \frac{dN}{dt}}{\int dt \mathcal{L}'} \tag{3.1}$$

is a measure of the stability of the detector performance. $\mathcal{L}'$ is here the luminosity rate $\mathcal{L}$ corrected for the trigger life time τ, $\mathcal{L}' = \mathcal{L}\tau$. For the following plots, yields have been calculated on a run-by-run basis

$$Y_{run}^{(\rightrightarrows,\rightleftarrows)} = \frac{\sum_{bursts\,(\rightrightarrows,\rightleftarrows)} N^{(\rightrightarrows,\rightleftarrows)}}{\sum_{bursts\,(\rightrightarrows,\rightleftarrows)} \mathcal{L}^{(\rightrightarrows,\rightleftarrows)} \tau_{Tr}^{(\rightrightarrows,\rightleftarrows)} t_{burst}^{(\rightrightarrows,\rightleftarrows)}} \tag{3.2}$$

and then averaged over a fill. The sum is over all burst fulfilling the data quality cuts defined in section 3.1.2. The integrated count rate N has been measured for leptons and hadrons separately. The superscript $(\rightrightarrows,\rightleftarrows)$ stands for the beam and target polarizations parallel $(\rightrightarrows)$ and antiparallel $(\rightleftarrows)$, and t_{burst} is the length of the burst. Hadrons (positrons and electrons) have been selected with a PID cut (cf. Eq. 1.15) smaller than -1 (greater than 1). The standard cuts on kinematics, track parameters and PID applied to hadrons and leptons for all further analysis are shown in table 3.3. The fiducial volume cut is applied on the projection of the track onto the $x-y$ plane 18 cm from

Parameter	Cuts/Requirements
Fiducial volume cut (x and y position of tracks at the calorimeter)	$33 < y_{Calo} < 108$ cm, $\lvert x_{Calo}\rvert < 175$ cm
Transverse vertex (t_{Vtx})	$t_{Vtx} < 0.75$ cm
Longitudinal vertex (z_{Vtx})	$\lvert z_{Vtx}\rvert < 18$ cm
HRC-reconstruction	$\left(\frac{0.2998}{p_{xz}} \cdot 1.3\ \text{Tm} - 0.031\right) \leq \Delta\theta_x \leq \left(\frac{0.2998}{p_{xz}} \cdot 1.3\ \text{Tm} + 0.036\right)$
Particle Identification	$\text{pid3} + \text{pid5} - \Phi > 1$ ($e^{\pm}$) $-100 < \text{pid3}+\text{pid5}-\Phi < -1$ (hadrons)

Table 3.3: Standard track and PID cuts applied in this analysis.

the upstream end of the calorimeter lead glass blocks where the electromagnetic shower starts to develop. For charged tracks within the fiducial volume the shower energy leaking out of the edges of the calorimeter is negligible, such that the particle identification by the calorimeter is reliable. The lower cut in y corresponds to about 2/3 of the row closest to the beam pipe, the x and upper y cuts accordingly cut out 2/3 of the outer blocks. The deflection angle in the spectrometer magnet should be distributed according to the relation

$$\Delta\theta_x = \pm\frac{0.2998}{p_{xz}} \int Bdl \quad \text{with} \int Bdl \simeq 1.3\ \text{Tm}, \tag{3.3}$$

where p_{xz} is the track momentum projected onto the $x-z$ plane and the $+$ sign is for negative, the $-$ sign for positive particles. θ_x is the x-projection of the track slope. The cut on $\Delta\theta_x$ affects about 0.1 % of all tracks and rejects a large fraction of wrongly reconstructed tracks whose assigned charge and/or momentum is inconsistent with their deflection angle [Lie01]. Figure 3.1 shows the yields averaged over beam and target polarizations for positive and negative hadrons and positrons per fill for the polarized proton and deuterium data. In addition to the above cuts a cut on $p > 1.4$ GeV corresponding to the minimum energy necessary to fire the main physics trigger (see below) is applied on positrons. The yields as defined in Eq. 3.2 are proportional to the total efficiency and the geometrical acceptance of the detector. The detector acceptance, if ever, can only change if the detector, or parts of it change positions with respect to the beam or the target, or if detectors are replaced with others having different geometrical parameters. Normally, detector replacements or upgrades happened only in between years, such that changes in the yields due to changing acceptance can be excluded for the data of one year. An exception is the luminosity monitor whose coincidence rate depends on the beam position and slope. These can change during the course of a fill and also from fill to fill. Still, the largest effect on the time dependence of the yields seen in figure 3.1, especially that of the hadrons, comes from the time dependence of the trigger efficiencies. The data taken at HERMES are dominantly selected by two first level triggers

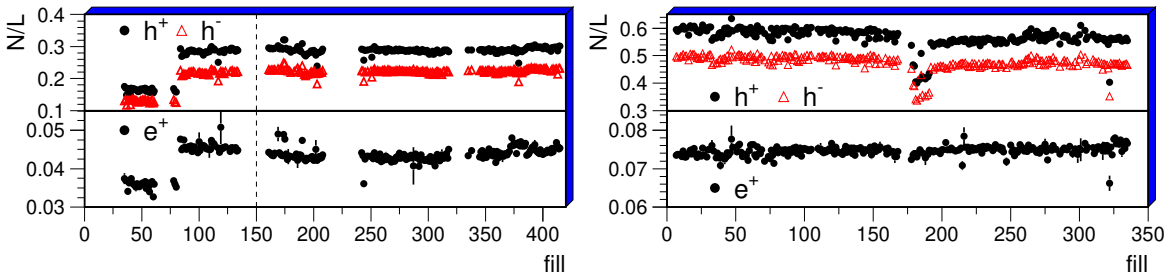

Figure 3.1: Yields per fill for the polarized proton data of 1996 and 1997 (left) and the deuterium data of 2000 (right), for positive and negative hadrons (top panel) and positrons (bottom panel). The vertical dashed line in the left plot indicates the end (start) of the 1996 (1997) data taking periods. The yields are averaged over beam and target polarizations.

with very distinct, momentum and event topology dependent efficiencies. In table A.1 the trigger logics of some HERMES triggers are displayed, here only a summary for the 'physics' triggers – the triggers mainly used for physics analyses – is given.

- Trigger 21: This trigger is intended to select potential deep inelastic scattering events using characteristic signals from the scattered positron. The requirements of coincident hits in all three hodoscopes (H0, H1 and H2) and an energy deposit of more than 1.4 GeV in two adjacent columns of calorimeter blocks have to be fulfilled in the top *or* the in bottom half of the detector. Additional information is available about from which detector half the coincidence signal originated. The coincidence signals in all three hodoscopes prevents triggers to be fired by photons showering in the preshower as well as from (backward flying) protons, the energy threshold of the calorimeter suppresses hadronic background from photoproduction events. For inclusive hadron photoproduction of hadrons with a normally rather small average momentum the efficiency of this trigger is quite low due to the calorimeter threshold. The obviously much smaller yields for both hadrons and positrons at the beginning of 1996 are explained by the fact that the calorimeter threshold for trigger 21 was set to 3.5 GeV at that time.

- Trigger 28/22: These are the so called 'photoproduction' triggers, mainly intended for low Q^2 events where the scattered positron does not leave the beam pipe, and hadrons or resonances are produced with a high track multiplicity. Events selected by these triggers should have at least one charged track in each detector half leaving coincidence signals in the three hodoscopes and the BCs (trigger 28) or the MCs (trigger 22). In addition there is an upper cut on the hit multiplicity in the front hodoscope, necessary for background reduction.

- In addition, a variety of 'calibration' triggers exists enabling analyzers to calculate the efficiencies of the various components involved in the 'physics' triggers. How this can be done is explained in appendix A.1.

The time dependence of the trigger 21 and trigger 28 efficiencies for hadrons in 2000 is shown in figure 3.2. The drop in the trigger 28 efficiency for the fills 175 to 190 is not a detector hardware effect but due to the fact that during this period the background rate caused by the HERA proton beam was extraordinary high, such that the rates for all triggers but trigger 21 had to be prescaled by factors up to ten[1] in order to reduce the dead time of the DAQ system. In the polarized data taken in 2000 about 70% of the hadrons came from events with trigger 21, and about 20% from events with trigger 28. The time dependence of hadron yields as seen in the top of the plots in figure 3.1 can thus be explained by the time dependence of these two trigger efficiencies. In contrast

[1]Prescaling a trigger by a factor m means that only every mth generated trigger is accepted by the DAQ system.

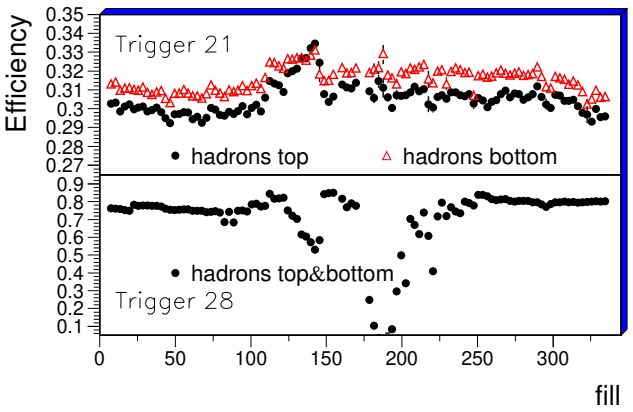

Figure 3.2: Trigger efficiencies for hadrons during polarized data taking in 2000 as a function of the fill number. In the top panel, the trigger 21 efficiencies are shown for top and bottom separately, in the bottom panel the trigger 28 efficiency is shown for events with at least one hadron in each detector half.

to that, 98% of all positrons came from events with trigger 21 such that its efficiency (which varied less than 3% during the year and was on the level of about 97% for the top and 98% for the bottom detector) is directly reflected in the relatively stable yields of positrons. Trigger efficiencies for positrons and for 1997 are evaluated in appendix A.2. Asymmetries will not be affected by time dependent inefficiencies if the time scale at which these were changing is much larger than the time scale of the target spin flips (assuming that asymmetries do not depend on the beam helicity, which will be shown in the next section). Figure 3.3 shows that the ratio of yields

$$R = \frac{Y^{\rightrightarrows}}{Y^{\rightleftarrows}} \tag{3.4}$$

for hadrons and positrons is constant over the whole year, even on a fill-by-fill basis.

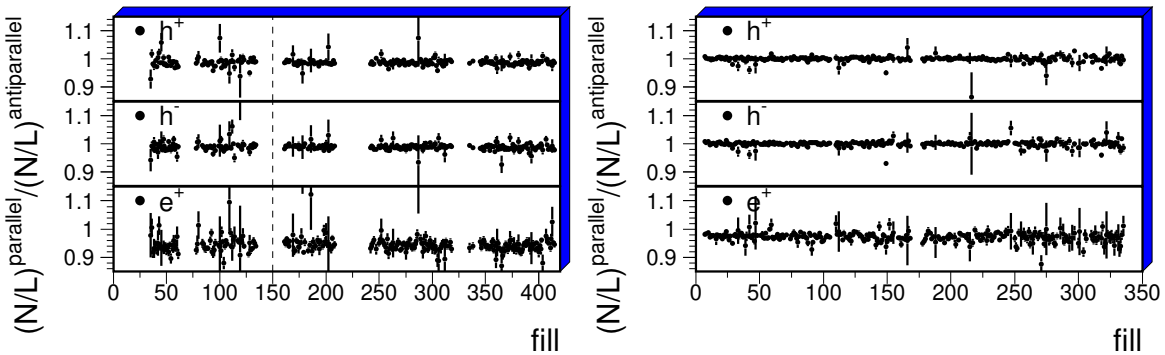

Figure 3.3: Ratio of hadron (top and middle) yields and positron yields with parallel and antiparallel target and beam spin configuration per fill in 1996/1997 (left plot) and 2000 (right plot).

3.2 Double Spin Asymmetries of High-p_T Hadrons

In this section studies and results on double spin asymmetries of high-p_T hadrons will be presented. First the kinematic cuts for different kinematic regions will be motivated and the method to calculate the asymmetries will be introduced. Systematic studies on the various asymmetries follow.

3.2.1 Kinematic Regions and Cuts

A priori it is not clear in which kinematic region accessible by HERMES the signal for PGF would be large enough to extract the gluon polarization. The statistics available within a certain kinematic region does not only depend on the cross section but also on the detector acceptance and efficiency.

The signal to background ratio has to be considered as well as the possible scale dependence of the various processes contributing to the measured asymmetry. For this reason, three regions are defined by appropriate cuts on the event kinematics as well as on the properties of positrons and hadrons. The first region, labeled '(quasireal) Photoproduction' region is defined by the antitagging of the scattered positron, which in reality means that every event where a positron *or* electron is detected will be rejected. The left plot on figure 3.4 gives an impression of the range in y and Q^2 that can possibly be covered by events selected with this 'positron veto'. The second region, called the 'Transition' region, is basically characterized by the process $ep \rightarrow ehX$ without additional constraints. In practice this means that $Q^2 > 0.1$ GeV^2. For a number of comparisons to MC simulations below, cuts on $W^2 > 4$ GeV^2 and $y < 0.95$ or $y < 0.91$ are applied. In any case these cuts do not reduce the available data sample by more than a few percent. The covered range in (y, Q^2) by the data is indicated by the dark shaded area in the right plot of figure 3.4. Note that, in contrast to the 'Photoproduction' region, in the 'Transition' region the information about the event kinematics can be retrieved from the scattered positron. The third region is named 'SIDIS' region because the cuts applied to the data are the same as used for instance in the standard HERMES analysis for the extraction of the $\Delta q(x)$ from semi-inclusive asymmetries [Air03]. The region is defined by a lower Q^2 cut of 1 GeV^2, $W^2 > 10$ GeV^2 and $y < 0.85$ and additional cuts on the hadron kinematics. The upper y cut is introduced to reduce the size of electromagnetic radiative corrections that tend to be largest at high y. The 'SIDIS' region is a subsample of the 'Transition' region, represented by the lighter shaded region on the right of figure 3.4. This subsample contains about one third of the statistics of the 'Transition' region. The 'SIDIS' region

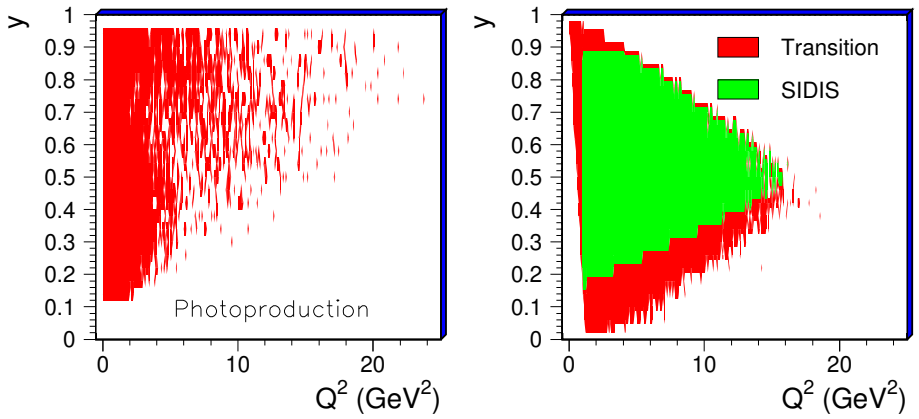

Figure 3.4: Left: Kinematic range in (y, Q^2) covered by the 'Photoproduction' data sample obtained by antitagging positrons and electrons. Right: The dark shaded area shows the kinematic coverage in (y, Q^2) for the 'Transition' region, the light shaded area shows the same for the 'SIDIS' region. The plots are obtained from a Monte Carlo simulation with PYTHIA (cf. section 4.1)

is considered separately because of the possibility to compare the data to QCD calculations and DIS Monte Carlo simulations, as both of these often use lower limits on Q^2 and W^2 corresponding to the cuts applied in this region. It may also be interesting to study the behavior of the data when changing from the theoretically relatively safe 'SIDIS' region to the 'Transition' region. If this behavior could be understood it may in principle be possible to use the 'Transition' region with its higher statistics to extract the PGF signal. The standard cuts applied to the data to extract the double spin asymmetries are summarized in table 3.4.

3.2.2 Extraction of Double Spin Asymmetries

Double spin asymmetries are defined as the cross section ratio of the polarized cross section to the unpolarized cross section. Since the polarizations of beam and target are not 100%, the unpolarized cross section in Eq. 2.16 has to be weighted with a factor $P = P_B P_T$. The number of hadrons in

General Cuts	
event kinematics	$0 < P_{sum} < 28$, with $P_{sum} = \sum_{tracks} p_{track}$
hadron kinematics	$0.5 < p_h < 28$
pion identification	1996/97: $4 < p_h < 13.8$ GeV and #photoelectrons (Cherenkov)< 0.25
	2000: $2 < p_h < 15$ GeV and RICH π ID with $rQp > 0$
kaon identification	2000: $2 < p_h < 15$ GeV and RICH K ID with $rQp > 0$
Photoproduction Region	
positron kinematics	veto events with identified $e^{\pm}$
Transition Region	
positron kinematics	$W^2 > 4$, $Q^2 > 0.1$ GeV^2, $y < 0.95$
SIDIS Region	
positron kinematics	$W^2 > 10$, $Q^2 > 1$ GeV^2, $y < 0.85$, $E_{e^+}(Calo) > 3.5$ GeV
hadron kinematics	$0.2 < z_{\pi,K} < 0.8$, $x_F > 0.1$

Table 3.4: Standard cuts applied for the asymmetries in the different kinematic regions.

each spin configuration is then ($\sigma^{\rightrightarrows(\rightleftarrows)} = \frac{1}{2}\sigma(1 \mp PA_\parallel)$):

$$N^{\rightrightarrows(\rightleftarrows)} = \frac{1}{2}\int dt\sigma\mathcal{E}(t)\mathcal{L}(t)\left(1 \mp P_B(t)P_T(t)A_\parallel\right) \tag{3.5}$$

Experimentally it is most of the time sufficient to measure the normalized yields in each spin configuration of beam and target. Quantities such as efficiencies and the geometrical acceptance, expressed by the factor $\mathcal{E}(t)$, that do not change at a short time scale cancel in the ratio of cross sections. Using

$$L^{\rightrightarrows(\rightleftarrows)} = \int dt\mathcal{L}^{\rightrightarrows(\rightleftarrows)}(t) \qquad \text{and } L_P^{\rightrightarrows(\rightleftarrows)} = \int dt\left(P_B(t)P_T(t)\mathcal{L}(t)\right)^{\rightrightarrows(\rightleftarrows)} \tag{3.6}$$

Eq. 3.5 can be solved for $A_\parallel$ in terms of the number of hadron counts for each spin state:

$$A_\parallel = \frac{1}{L_P^{\rightleftarrows}L_P^{\rightleftarrows}}\,\frac{N^{\rightleftarrows}/L^{\rightleftarrows} - N^{\rightrightarrows}/L^{\rightrightarrows}}{N^{\rightleftarrows}/L_P^{\rightleftarrows} + N^{\rightleftarrows}/L_P^{\rightrightarrows}} = \frac{N^{\rightleftarrows}L^{\rightrightarrows} - N^{\rightrightarrows}L^{\rightleftarrows}}{N^{\rightleftarrows}L_P^{\rightrightarrows} + N^{\rightrightarrows}L_P^{\rightleftarrows}}. \tag{3.7}$$

If nuclear targets with only a fraction f_D of polarizable nucleons were in use the measured asymmetry would be reduced by this so called 'target dilution factor' f_D. For the pure hydrogen and deuterium targets of HERMES, $f_D = 1$, for a pure ^{3}He target it is 1/3. The statistical error of the asymmetry can be calculated using Gaussian error propagation for not too small $N^{\rightleftarrows(\rightrightarrows)}$ and not too large $|A_\parallel|$ with $\delta N^{\rightleftarrows(\rightrightarrows)} = \sqrt{N^{\rightleftarrows(\rightrightarrows)}}$:

$$\delta A_\parallel = \frac{L^{\rightrightarrows}P^{\rightleftarrows} + L^{\rightleftarrows}P^{\rightrightarrows}}{\left(N^{\rightleftarrows}P^{\rightrightarrows} + N^{\rightrightarrows}P^{\rightleftarrows}\right)^2}\sqrt{\left(N^{\rightrightarrows}\right)^2 N^{\rightleftarrows} + \left(N^{\rightleftarrows}\right)^2 N^{\rightrightarrows}}. \tag{3.8}$$

Important factors (besides the count statistics) for the error on double spin asymmetries are thus the beam and target polarizations, as the error goes approximately as $1/\langle P_B P_T\rangle$.

3.2.3 Results for the Raw Asymmetries

For the following studies, the hadron counts are binned in transverse momentum. For the 'Photoproduction' asymmetries of hadrons and pions 15 (non-equidistant) bins between 0 and 3.5 GeV in the lab transverse momentum p_T^{lab} defined with respect to the beam (z) axis are used, for kaons

the same range is divided into 10 bins. The same ten bins are also used for the semi-inclusive asymmetries in the 'Transition' and 'SIDIS' regions, but here the transverse momentum is defined in the $\gamma^* - nucleon$ center of mass frame with respect to the direction of the virtual photon. Figure 3.5 shows the asymmetries obtained from the hydrogen target in the years 1996 and 1997. As the

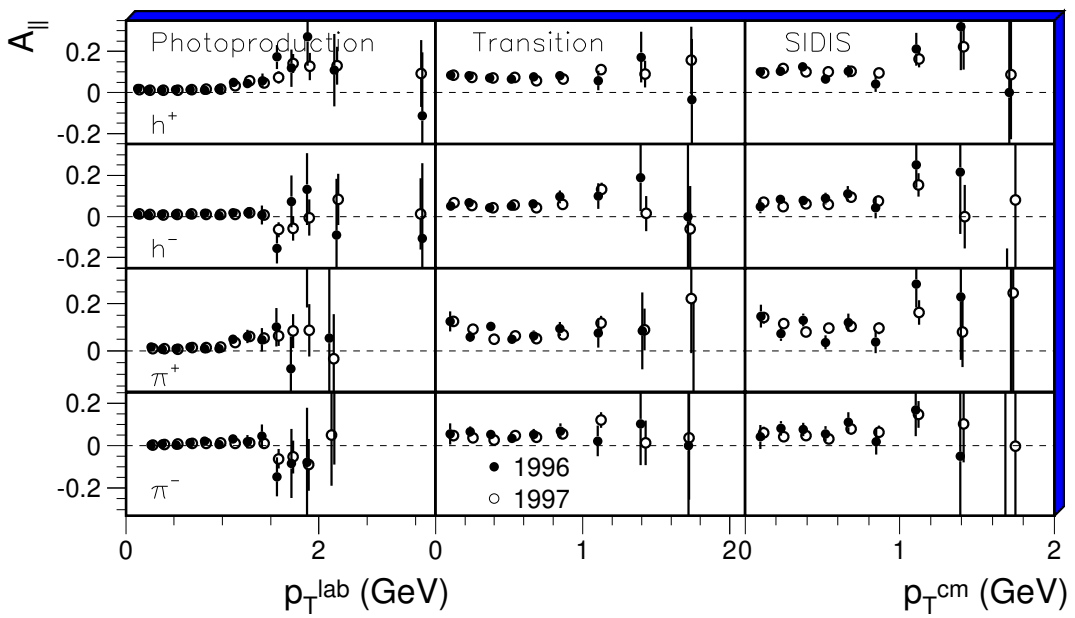

Figure 3.5: Raw (uncorrected for background) double spin asymmetries from the 1996 (solid circles) and 1997 hydrogen data (open circles). The columns of this plot are the asymmetries in the 'Photoproduction', 'Transition' and 'SIDIS' regimes from left to right, the rows are positive and negative unclassified hadrons and positive and negative identified pions (with $4 < p < 13.8$ GeV) from top to bottom.

data were taken in different years under different experimental conditions, the compatibility of the two data sets needs to be verified. A common way to do this is to compute the quantity

$$t_i = \frac{A_\parallel^{96} - A_\parallel^{97}}{\sqrt{\sigma_{96}^2 + \sigma_{97}^2}} \tag{3.9}$$

for each p_T-bin i. The t_i should follow Student's distribution with a mean around 0 and a standard deviation of approximately 1 for a large number of degrees of freedom [Blo98]. Figure 3.6 shows the t_i for all asymmetries, together with the χ^2 per degree of freedom (n is the number of bins with at least 5 entries):

$$\chi^2/ndf = \frac{1}{n}\sum_{i=1}^{n} \frac{(A_\parallel^{96} - A_\parallel^{97})^2}{\sigma_{96}^2 + \sigma_{97}^2} = \frac{1}{n}\sum_{i=1}^{n} t_i^2. \tag{3.10}$$

In 1996 the molecular recombination of the H atoms in the target cell was rather high, $1 - \alpha_R \approx 12\%$, leading to a very large systematic error of the target polarization due to the poor knowledge of the molecular polarization β (cf. Eq. 1.9). In order to reduce this systematic error the inclusive asymmetry A_1 of 1996 was fitted to that of 1997 by leaving the (average) target polarization as a free parameter [Bec03]. The resulting target polarization for 1996 is 0.759 ± 0.042. Since by this normalization method the asymmetries of both years are partially correlated, the χ^2 per degree of freedom are smaller than 1 in most cases. From the distribution of the t_i in figure 3.6 one can judge that the two data sets are statistically compatible, but due to their correlation it is not possible to make a quantitative statement about the confidence level. In the following, the two asymmetries will be merged to one proton asymmetry using the error weighted average. In general, the error weighted average of M independent measurements of the same quantity and its standard deviation

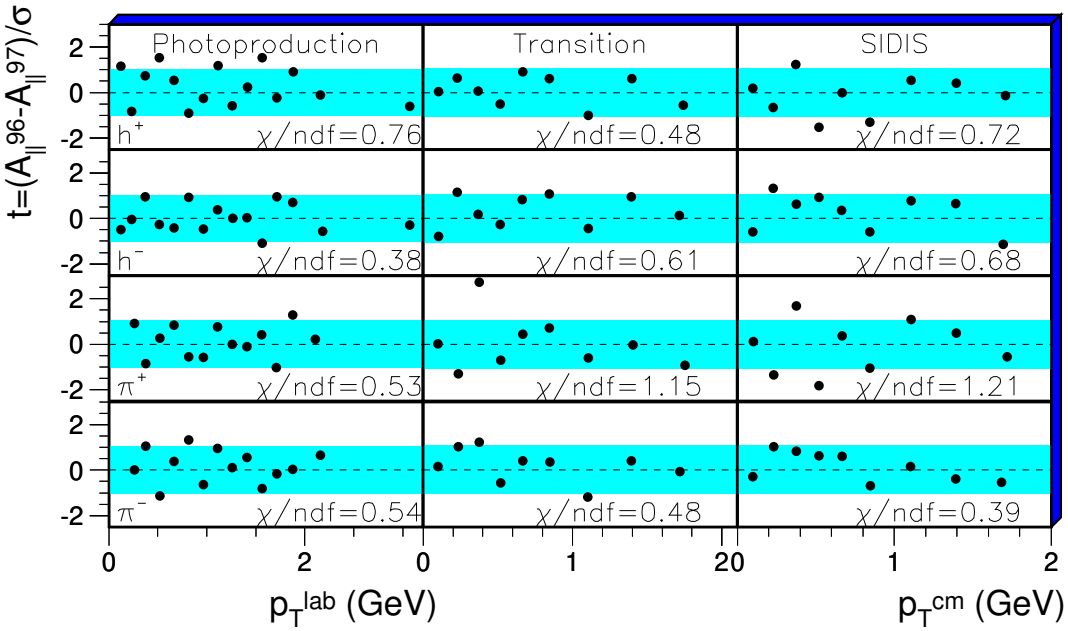

Figure 3.6: The error weighted difference t of the 1996 and 1997 asymmetries. The shaded bands indicate the standard deviation of the mean value of t at ≈ 1, the numbers in the lower right corners are the χ^2 per degree of freedom. The fields correspond to the asymmetries in figure 3.5.

can be calculated from the measurements E_i and their standard deviation σ_i using:

$$\langle A\rangle = \frac{\sum_{i=1}^{M} \frac{E_i}{\sigma_i^2}}{\sum_{i=1}^{M} \frac{1}{\sigma_i^2}}, \qquad \frac{1}{\sigma_E^2} = \sum_{i=1}^{M} \frac{1}{\sigma_i^2}. \tag{3.11}$$

The results for the deuteron asymmetries from the 2000 data are shown in figure 3.7 together with the merged proton asymmetries of 1996 and 1997. Because of the information available from the RICH detector it was possible to extract also kaon asymmetries from the 2000 data. The momentum range for pions and kaons is different from the proton data, namely $2 < p < 15$ GeV.

The raw measured asymmetries are subject to corrections for background, and need to be checked for their stability with respect to (possible) acceptance and efficiency effects.

3.2.4 Possible Sources of Background: Charge Symmetric Events

In the 'Transition' and 'SIDIS' regions the asymmetries depend on the kinematics of the scattered positron. Positrons can also be produced in charge symmetric processes, one of which is the conversion of a photon into an electron-positron pair in some detector material or the collimator right in front of the target cell, and another one is the decay $\pi^0 \to e^+e^-\gamma$. Although the branching ratio for this decay is only 1.2%, neutral pions are abundant from photoproduction events. Due to the inherent charge symmetry of lepton pair production, the rate and kinematic distributions of electrons should be the same as those of positrons stemming from charge symmetric processes. In order to correct the positron yields for this contribution, the electron count rate can thus be subtracted from the positron count rate. In practice this is done by first calculating all kinematic properties of an event regardless of the charge of the detected lepton and then applying a weight $w = +1(-1)$ if the lepton was a positron (electron). If there are two leptons in an event, the kinematics and charge of the leading (i.e., the lepton with the highest momentum) one are taken into account. The asymmetry and its error can be calculated with weighted events by replacing

$$N^{\rightleftarrows(\rightrightarrows)} \to \sum_{hadrons} w_i, \qquad \delta N \to \sqrt{\sum w_i^2} \tag{3.12}$$

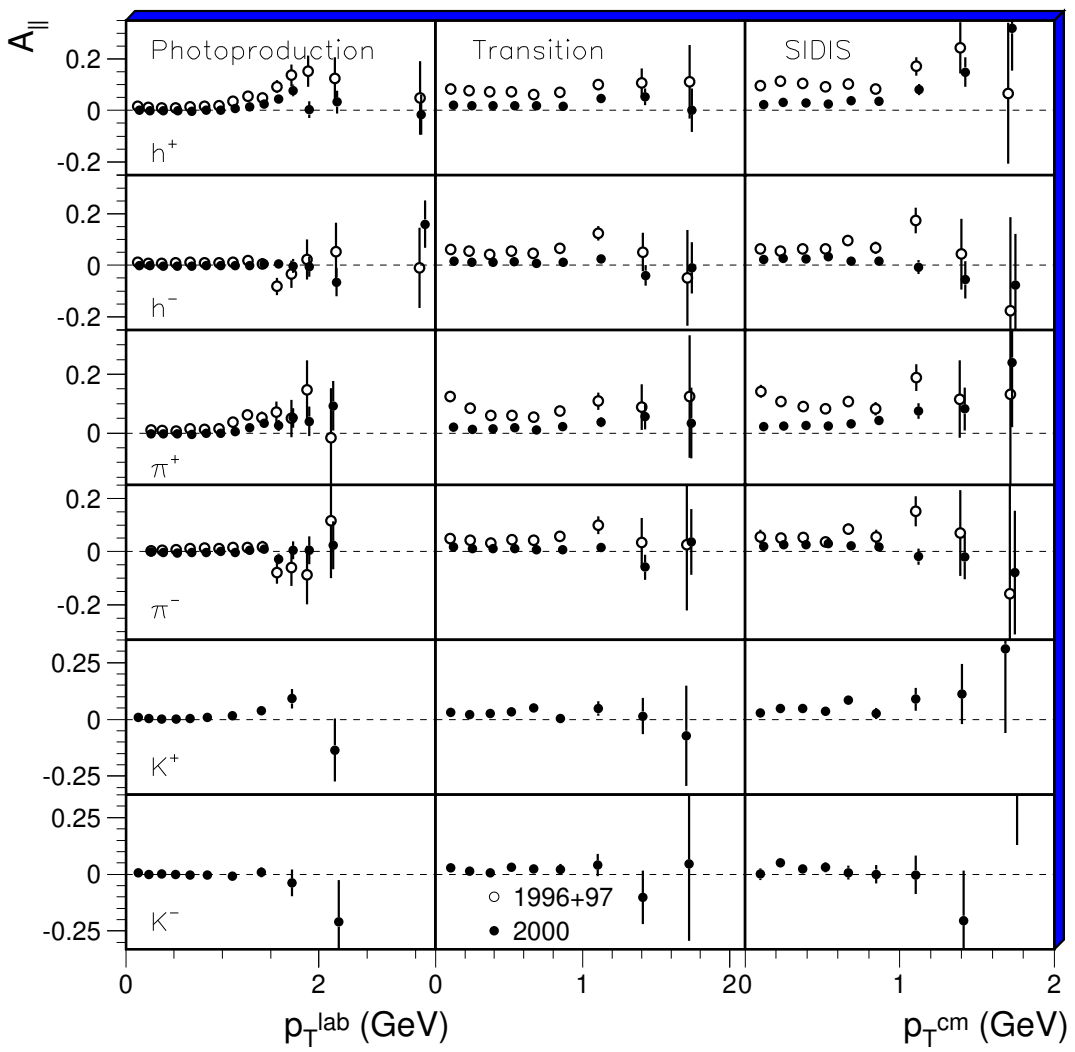

Figure 3.7: Raw (uncorrected for background) double spin asymmetries from 2000 deuterium data (solid circles) compared to those of the hydrogen data from 1996 and 1997 (open circles). The columns and rows of this plot have the same meaning as in figure 3.5. The momentum range for pions and kaons for the 2000 data is $2 < p < 15$ GeV.

in Eqs. 3.7 and 3.8. Leptons from these charge symmetric processes usually have small momenta, such that the highest contribution should be at high $\nu = E - E'$ corresponding to high W^2 and small x. The asymmetries shown in the previous section were calculated requiring the charge of the (leading) lepton to be positive. With respect to this data sample, the charge symmetric correction to the semi-inclusive yields for the proton data is 19% (6.7%) at $W^2 > 34$ GeV^2 for the 'Transition' ('SIDIS') regions while it decreases rapidly with smaller W^2. As a function of p_T, the maximum background ratio is about 8% (3%) in the 'Transition' ('SIDIS') region at medium p_T. The corrections are slightly smaller for the deuteron data. Figure 3.8 shows as an example the relative correction $\frac{A_\parallel^{cs} - A_\parallel^{raw}}{A_\parallel^{raw}}$ to the semi-inclusive asymmetries of positive hadrons. $A_\parallel^{raw}$ is in this case the raw, uncorrected asymmetry, $A_\parallel^{cs}$ the corrected one. Note that the correction for the 'SIDIS' region is scaled by a factor of 10. For the 'Transition' region the correction is sizeable, whereas the effect is negligible for the 'SIDIS' region. In the following, only the charge-symmetric corrected asymmetries will be considered.

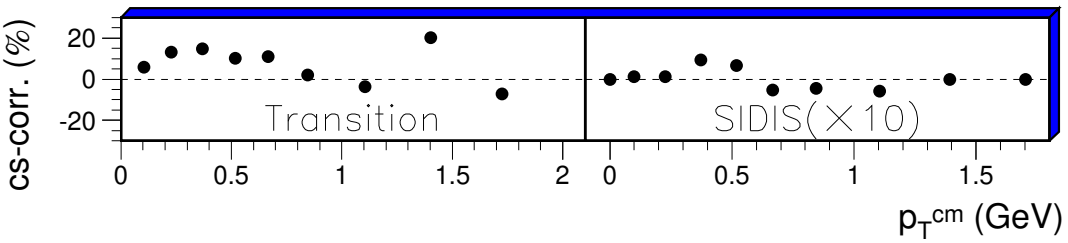

Figure 3.8: The relative charge-symmetric correction to semi-inclusive asymmetries of positive hadrons for the hydrogen data in percent. On the left the correction is shown for the 'Transition' region, the corrections on the right for the 'SIDIS' region are enlarged by a factor of 10.

3.2.5 Possible Sources of Background: Lepton/Hadron Separation

Another possible source of background that would affect all asymmetries is particle misidentification. 'Photoproduction' asymmetries can be affected in two ways: Directly, leptons (positrons or electrons) can be misidentified as hadrons and contaminate the signal. More indirectly, the misidentification of leptons reduces the number of events rejected by the 'positron-veto' and might thus contaminate the signal with DIS events. This is to be considered a subleading effect, though, since the rate of photoproduction events is ten times higher than the rate of DIS events, and the misidentification probability is small. In case of the semi-inclusive asymmetries, positrons can actually be misidentified hadrons. In principle the coincident hadrons might also be misidentified leptons, but due to the small rate of events with more than one lepton this is rather unlikely. The contamination C_h^e of the hadron sample with misidentified leptons (resp. the contamination C_e^h of leptons with misidentified hadrons) can be calculated within the regular PID scheme at HERMES (cf. section 1.3.3.1), depending on the PID cut in use.

$$C_h^e(\text{cut}) = \frac{\int_{-\infty}^{cut} d\text{PID}\, P^e(PID) N^h(PID)}{\int_{-\infty}^{cut} d\text{PID}\, N^h(PID)} \tag{3.13}$$

$$C_e^h(\text{cut}) = \frac{\int_{cut}^{\infty} d\text{PID}\, P^h(PID) N^e(PID)}{\int_{cut}^{\infty} d\text{PID}\, N^e(PID)} \tag{3.14}$$

$$\tag{3.15}$$

$N^{e(h)}$ is here the number of counts with a particular PID value usually identified as leptons (hadrons). The probabilities $P^{e(h)}$ for a particle to be a lepton (hadron) can be obtained from its PID value $PID = \lg \frac{P^e}{P^h}$ and the requirement that the sum of the hadron and lepton probabilities be $P^e + P^h = 1$:

$$P^e = \frac{10^{PID}}{1 + 10^{PID}}, \qquad P^h = \frac{1}{1 + 10^{PID}}. \tag{3.16}$$

The identification efficiency can be derived by considering the fraction of leptons (hadrons) lying above (below) the PID cut:

$$\epsilon^{h(e)}(\text{cut}) = \frac{\int_{-\infty}^{cut} \left(\int_{cut}^{\infty}\right) d\text{PID}\, P^{h(e)}(PID) N^{h(e)}(PID)}{\int_{-\infty}^{\infty} d\text{PID}\, P^{h(e)}(PID) N^{h(e)}(PID)}. \tag{3.17}$$

Loosening the PID cut means that the contamination of the sample rises, but also the identification efficiency. Usually one chooses cuts such that an acceptable compromise is achieved. The contaminations and efficiencies are presented in figure 3.9 as a function of transverse momentum for hadrons, and as a function of the lab momentum for leptons for the PID cuts 0, $\pm 1 \pm 5$, ± 8. The efficiencies and contaminations drop rapidly the tighter the PID cuts are and depend strongly on the particle momentum. The contaminations for $|PID| > 5$ are basically zero. For a PID cut $|PID| > 1$ the efficiencies are usually bigger than 95%, and the contaminations are some few per mill at maximum. The size of a possible correction to the measured asymmetry depends on

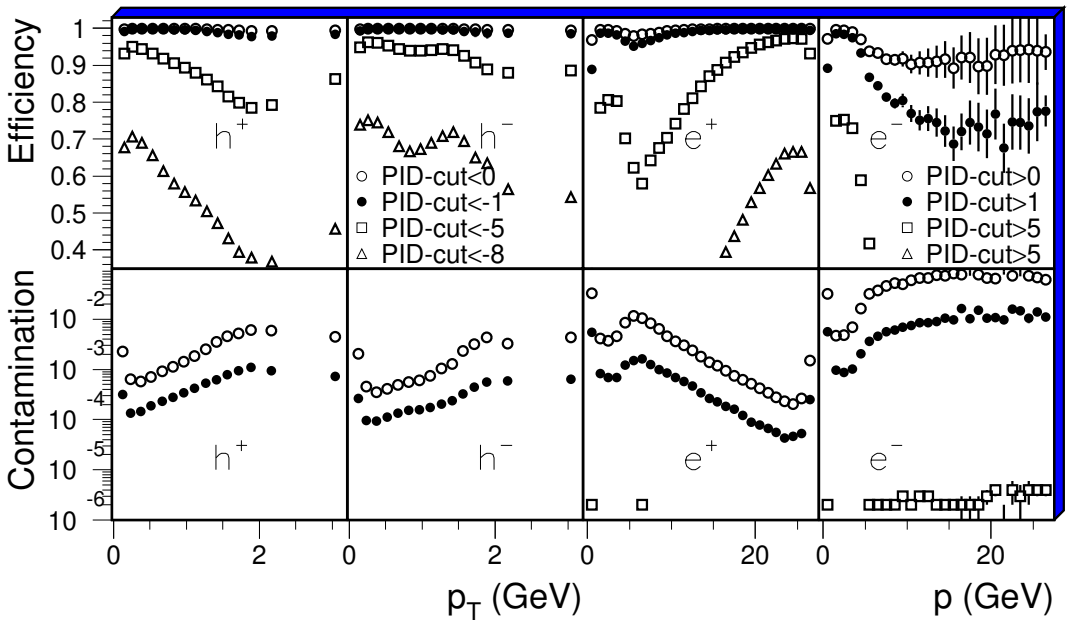

Figure 3.9: The PID-cut efficiencies (top row) and contaminations (bottom row) for four different PID cuts. The left two columns are for positive and negative hadrons vs. the lab transverse momentum, the right two columns are for positrons and electrons vs. the lab momentum.

the size of the background asymmetry. The measured 'Photoproduction' asymmetries with the contributions from hadrons and leptons can be written as:

$$A_{\parallel}^{h^{\pm},meas} = \frac{N^{e^{\pm}}}{N^{h^{\pm}}+N^{e^{\pm}}}A_{\parallel}^{e^{\pm}} + \frac{N^{h^{\pm}}}{N^{h^{\pm}}+N^{e^{\pm}}}A_{\parallel}^{h^{\pm}} \quad \longrightarrow \quad A_{\parallel}^{h^{\pm}} = \frac{A_{\parallel}^{h^{\pm},meas} - C_{h^{\pm}}^{e}A_{\parallel}^{e^{\pm}}}{1-C_{h^{\pm}}^{e}}. \qquad (3.18)$$

The second equation follows from the fact that the number of leptons $N^{e^{\pm}}$ in the hadron sample is $N^{h^{\pm}}(1-C_{h^{\pm}}^{e})/C_{h^{\pm}}^{e}$. The asymmetry of positrons (electrons) as a function of the lab transverse momentum is displayed in figure 3.10. The positron asymmetry is rising with p_T,[2] and is quite

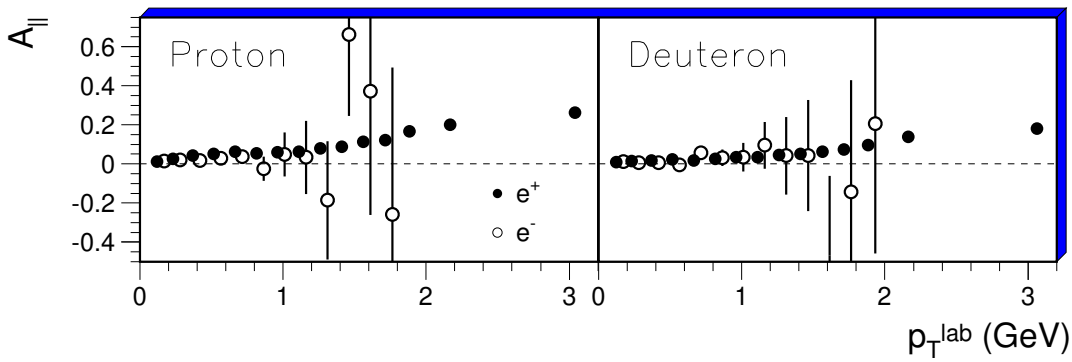

Figure 3.10: The asymmetry $A_{\parallel}^{e^{\pm}}$ for the proton data (left) and the deuteron data (right) as a function of the lab transverse momentum. The closed circles show the asymmetry for positrons, the open circles that of the electrons.

sizeable at $p_T > 1$ GeV. The electron asymmetry is small and compatible with 0 at high p_T. The corrected asymmetry has been calculated from Eq. 3.18 and the difference $A_{\parallel}^{h^{\pm}} - A_{\parallel}^{h^{\pm},meas}$ is assigned as a systematic error to the 'Photoproduction' asymmetries. The resulting error is

[2]This is a consequence of the correlation of the quantity $p_T = p\sin(\theta) = E'\sin(\theta)$ with $Q^2 \sim E'\sin(\theta/2)$ and the fact that the average x rises with Q^2, and therefore also the inclusive asymmetry [Gär01],[DeN02].

typically a fraction of a percent. For the kaon 'Photoproduction' data in 2000 no systematic error due to lepton contamination is assigned since the additional information from the RICH detector practically excludes the possibility that the kaon is a lepton.

Analogously it is possible to correct the semi-inclusive asymmetry, but in this case the underlying background asymmetry would be that of hadron pairs (in quasireal photoproduction). Their asymmetry can be estimated by selecting a positive hadron and assigning the role of the positron to it. All kinematic quantities are then calculated relative to this particular hadron. These asymmetries are shown in figure 3.11. To estimate the *maximum* systematic error arising

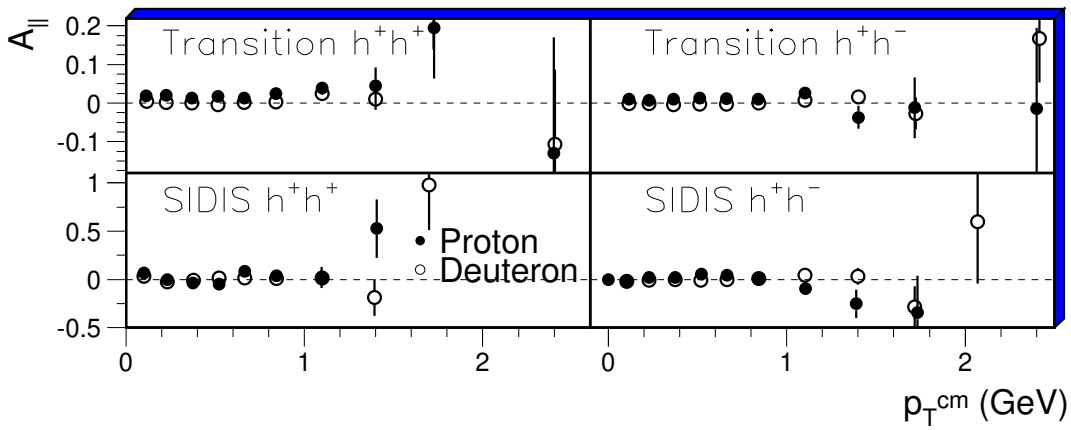

Figure 3.11: The asymmetries $A_{\parallel}^{h^+h^+}$ (left) and $A_{\parallel}^{h^+h^-}$ (right) for the proton data (close circles) and the deuteron data (open circles) as a function of the transverse momentum, calculated with the assumption that the first positive hadron was a positron. The top row shows the asymmetries for the 'Transition'-, the bottom row those for the 'SIDIS' region.

from a contamination of the positron sample, Eq. 3.18 is modified adequately with a maximum value for the positron contamination. This maximum value is 0.5% (0.2%) for the proton data and 0.2% (0.2%) for the deuteron data in the 'Transition' ('SIDIS') regions. The resulting error is 1% at maximum for high p_T, and much less for most of the kinematic region.

A common way to check the influence of the PID algorithm on asymmetries is to calculate the variation of the asymmetries with respect to changing PID cuts. For asymmetries as a function of x it turned out that these are independent of the PID cut [Wen03]. In this analysis, a similar study was performed, varying the upper cut on the hadron PID for the 'Photoproduction' asymmetries, and applying symmetric PID cuts on hadrons ($PID^h < -cut$) and leptons ($PID^e > cut$) for the semi-inclusive asymmetries. From the asymmetries obtained this way the average of the ratio

$$R_i = \frac{A_{\parallel}^{|PID|<cut} - A_{\parallel}^{|PID|<1}}{\sqrt{|\sigma_{A,1}^2 - \sigma_{A,1}^2|}}, \qquad \sigma_{R_i} = 1 \tag{3.19}$$

was calculated. The denominator of R_i is the error of the numerator in this expression, taking into account the correlation between the two asymmetries. The error of R_i is thus one, and the average can be calculated as

$$\langle R \rangle = \frac{1}{N}\sum_{i=1}^{N} R_i, \qquad \sigma_{\langle R \rangle}^2 = \frac{1}{N(N-1)}\sum_{i=1}^{N}(R_i - \langle R \rangle)^2. \tag{3.20}$$

Non-statistical deviations were observed for the semi-inclusive asymmetries for large values of the PID cut. The deviations for the 'Photoproduction' asymmetries are rather small and within the statistically allowed range. The reason for the non-statistical behavior is the momentum dependence of the PID-cut efficiencies (cf. figure 3.9). This results in shifted kinematics,

towards lower momentum in the case of the 'Photoproduction' data, and towards smaller x for the semi-inclusive data. To illustrate this, the ratio of yields of positive hadrons observed with $|PID| > cut$ ($cut = 2$, 5, 8) to the yields obtained using the the standard cuts $|PID| > 1$ is shown in figure 3.12 as a function of momentum for the 'Photoproduction' region and as a function of x for the semi-inclusive region. The effect of the kinematic shift may be twofold: On the one hand,

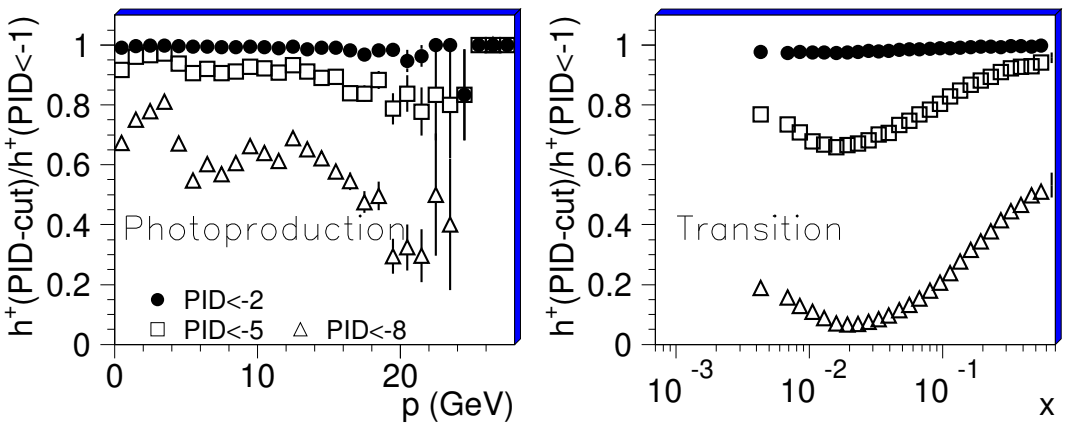

Figure 3.12: The ratios $N^{h^+}(PID < -cut)/N^{h^+}(PID < -1)$ for the 'Photoproduction' data vs. lab momentum (left) for varying PID cuts, and for the semi-inclusive data vs. x (right). Note that the leptons in the semi-inclusive region were selected with $PID^e > cut$.

at increasing x and fixed ν the asymmetries increase as well, as has been measured at HERMES [Wen03]. On the other hand the increasing momentum of positrons means decreasing the average ν, and therefore decreasing the depolarization factor $D(y)$ (cf. Eq. 2.28). In fact, the same reasoning applies to the (unknown) kinematics of the 'Photoproduction' data, since there the lower (average) hadron momentum means that also the lower limit on ν decreases ($\nu \geq p_h$). This effect is very small, though.

3.2.6 Possible Sources of Background: Pion/Kaon Separation

For the identified pion and kaon samples in the deuteron data another effect has to be considered. So far all pion and kaon asymmetries have been calculated using the information about the most probable particle type assigned to a hadron track by the RICH (cf. section 1.3.3.1). However, the calculation of the probabilities is not perfect, due to instrumental effects as well as problems inherent in the algorithm itself [Hom03]. The resulting inefficiencies can be expressed in a matrix

$$P = \begin{pmatrix} P_{\pi\pi} & P_{\pi K} & P_{\pi p} \\ P_{K\pi} & P_{KK} & P_{Kp} \\ P_{p\pi} & P_{pK} & P_{pp} \\ P_{X\pi} & P_{XK} & P_{Xp} \end{pmatrix}, \tag{3.21}$$

where the elements P_{ij} ($i, j = \pi$, K, p) are the *conditional* probabilities that a hadron of a true type j is identified as a hadron of type i. The fourth row of the so called 'P-Matrix' contains the probabilities P_{Xj} that a hadron of type j is not identified, i.e., $rQp = 0$ (cf. Eq. 1.17). The diagonal elements of the truncated square matrix P' (where the last row is taken off) then resemble identification efficiencies whereas the non-diagonal elements would be misidentification probabilities. The *measured* flux of hadrons can be represented by a vector $\vec{\Phi}^{meas} = (N_\pi^{meas}, N_K^{meas}, N_p^{meas}, N_X^{meas})$. This flux is related to the true flux $\vec{\Phi}^{true} = (N_\pi^{true}, N_K^{true}, N_p^{true})$ by $\vec{\Phi}^{meas} = P \cdot \vec{\Phi}^{true}$. Disregarding the unidentified hadrons (by cutting on $rQp > 0$) one can use the truncated P-matrix to obtain the true flux from the measured one [Hom03a]:

$$\vec{\Phi}^{true} = (P')^{-1}\vec{\Phi}'^{meas}. \tag{3.22}$$

Due to the momentum dependence of the Cherenkov angles the elements of the P-matrix depend on the track momentum. They have been extracted from data [Lip02] by measuring the change in the observed yields of decaying particles (for example from two-body decays of ρ^0, ϕ, K_S, Λ^0) and in the background under their invariant mass peaks requiring none, one, or all of the hadrons from the decay to be identified. However, the P-matrix also depends on the topology of the rings in the RICH photo multiplier matrix if more than one particle traverse one detector half. The probabilities P_{ij} might be different depending on type and momentum of the accompanying track(s) are. The reason is that if more Cherenkov rings appear on the matrix it becomes more difficult to decide to which track a photon hit belongs. Since the topology of, e.g, ρ or ϕ decays is very different from that of semi-inclusive DIS events, other P-matrices were extracted using a DIS Monte Carlo generator and a GEANT description of the RICH detector [Hom03, Miy03]. To take into account different topologies, these P-matrices were calculated for one, two and three tracks per detector half separately. For more detailed studies, P-matrices are available depending on the type of the accompanying track (e, π, k, p) for the two-track topology.

Asymmetries for the *true* hadron type j can be calculated as follows: For each hadron identified as type i a weight $w = \left\{(P')^{-1}\right\}_{ij}$ is applied for each j, and the weights are summed up for each spin state separately. Since some of the non-diagonal elements of the inverse P-matrix are negative (accounting for misidentification), the 'unfolded' true hadron yields may be smaller than the measured ones. This is especially the case for kaons. The biggest effect on the asymmetries is thus not due to identification inefficiencies, but to the contamination of the pion- or kaon sample with hadrons of another type and a different asymmetry. Figure 3.13 shows the size of the correction relative to the raw (not unfolded) positive pion and kaon asymmetries. The effect on the unfolding

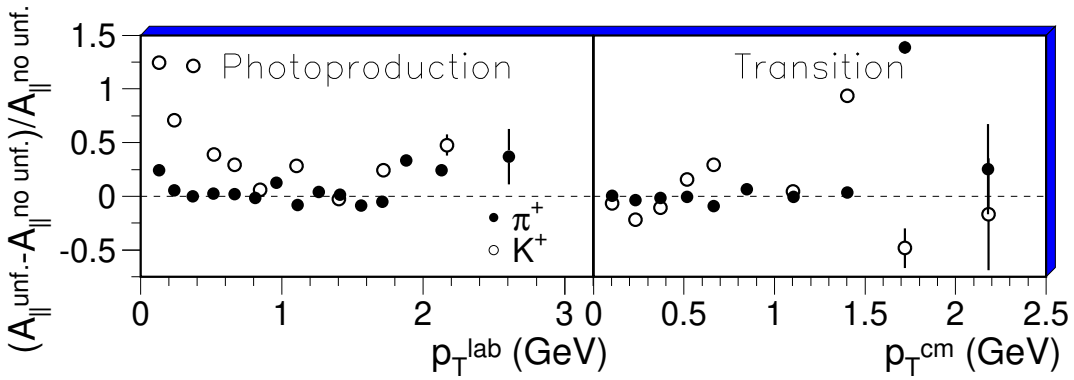

Figure 3.13: The ratio $\frac{A_\parallel^{\text{unfolded}} - A_\parallel^{\text{not unfolded}}}{A_\parallel^{\text{not unfolded}}}$ for positive pions and kaons in the 'Photoproduction' (left) and 'Transition' (right) regions.

is much larger for kaons than for pions. The reason is the large flux of pions (approximately 5 to 10 times that of kaons), such that even a small probability to misidentify a pion as a kaon leads to a large contamination of the kaon sample with pions. The unfolding was performed using P-matrices generated from Monte Carlo. In order to reduce the dependence on the event topology, partner particle dependent P-matrices were used for events with two (full) tracks in one detector half. In the 'Photoproduction' regime this applies to about 10%, in the semi-inclusive regime to 15% of the data. The Monte Carlo description of the RICH detector does not perfectly describe the behavior of the data. Extensive studies of the Monte Carlo parameters relevant for the RICH were performed leading to a variation of P-matrices according to the uncertainties in those parameters. The parameter uncertainties are believed to contribute the most to the systematic error [Miy03]. For an estimate of the systematic error due to the uncertainty in the unfolding, asymmetries were unfolded using a different set of P-matrices accounting for the Monte Carlo parameters to be changed within their uncertainties. The relative deviation of the asymmetries unfolded with this new set and the standard set is shown in figure 3.14. The figure shows the quantity $\Delta^{unfold} = \frac{A_\parallel^{\text{unf., MC}} - A_\parallel^{\text{unf, std}}}{A_\parallel^{\text{unf, std}}}$ whose errors are calculated as follows. The data sample going

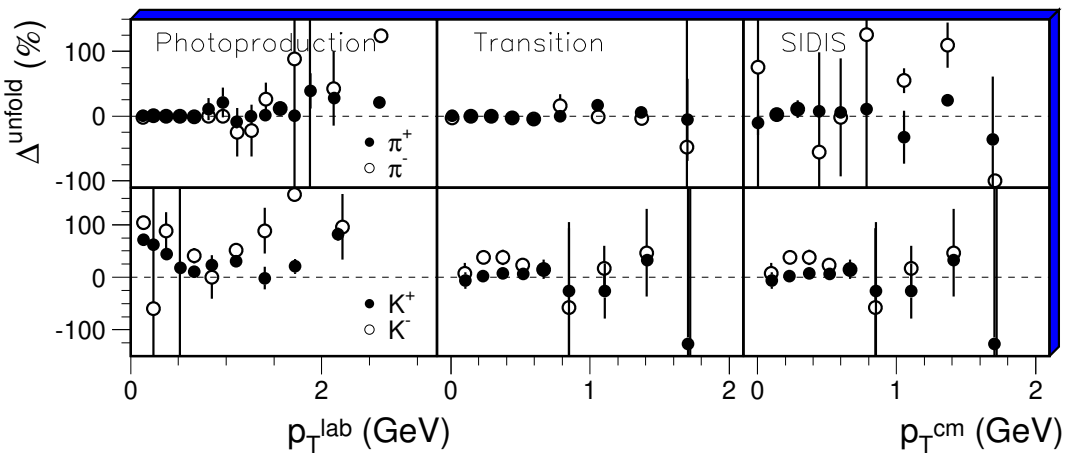

Figure 3.14: The ratio $\Delta^{unfold} = \frac{A_\parallel^{\text{unf., MC}} - A_\parallel^{\text{unf, std}}}{A_\parallel^{\text{unf, std}}}$ in percent for pions and kaons in the 'Photoproduction' (left), 'Transition' (middle) and 'SIDIS' (right) regions.

into the calculation of the asymmetries is exactly the same such that they are completely correlated with each other. Only the weights applied to the hadrons are different. In general, a Gaussian error of a function $f(x, y)$ propagates as follows:

$$\sigma_f^2 = \left(\frac{\partial f}{\partial x}\right)^2 \sigma_x^2 + \left(\frac{\partial f}{\partial y}\right)^2 \sigma_y^2 + 2\frac{\partial f}{\partial x}\frac{\partial f}{\partial y} cov(x, y), \tag{3.23}$$

where $cov(x, y)$ is the 'covariance' of the two measured quantities x and y. For the completely correlated asymmetries, $cov(A_\parallel^1, A_\parallel^2) = \sigma_1\sigma_2$. The error of the ratio $R = \frac{A_\parallel^2 - A_\parallel^1}{A_\parallel^1}$ is then

$$\sigma_R = \frac{A_\parallel^2}{A_\parallel^1}\sqrt{\frac{\sigma_1^2}{(A_\parallel^1)^2} + \frac{\sigma_2^2}{(A_\parallel^2)^2} - 2\frac{\sigma_1\sigma_2}{A_\parallel^1 A_\parallel^2}}. \tag{3.24}$$

For the pion asymmetries the deviations are small within the errors in most of the kinematic region, except at high p_T, where there is a small effect. The kaon asymmetries, however, show large differences of the order of the asymmetries themselves. This is not only due to the larger sensitivity of kaons to changes in the P-matrices, but also to the smallness of the kaon asymmetries. The *absolute* deviations are usually a few per mill. The difference in the asymmetries has to be added to the systematic error.

3.3 Systematic Studies on the Measured Asymmetries

In the following the effect of varying quantities the asymmetries should ideally *not depend on*, on the asymmetries will be studied.

3.3.1 Time dependence of Asymmetries

As explained in section 3.1.3, changes in the experimental efficiencies should not have large effects on the measured asymmetry if they happen at large time scales. Studying the time dependence of asymmetries is therefore a good check of the stability of the experimental environment. For this study, the data sample was divided into periods of typically 20 fills (corresponding to about 20 days of data taking), and the average asymmetry was computed for each period and each kinematic region. The results are shown in figure 3.15 together with a fit to a constant for each asymmetry. Except for the 'Photoproduction' asymmetries for the fills> 250 in 2000 no time dependence can be

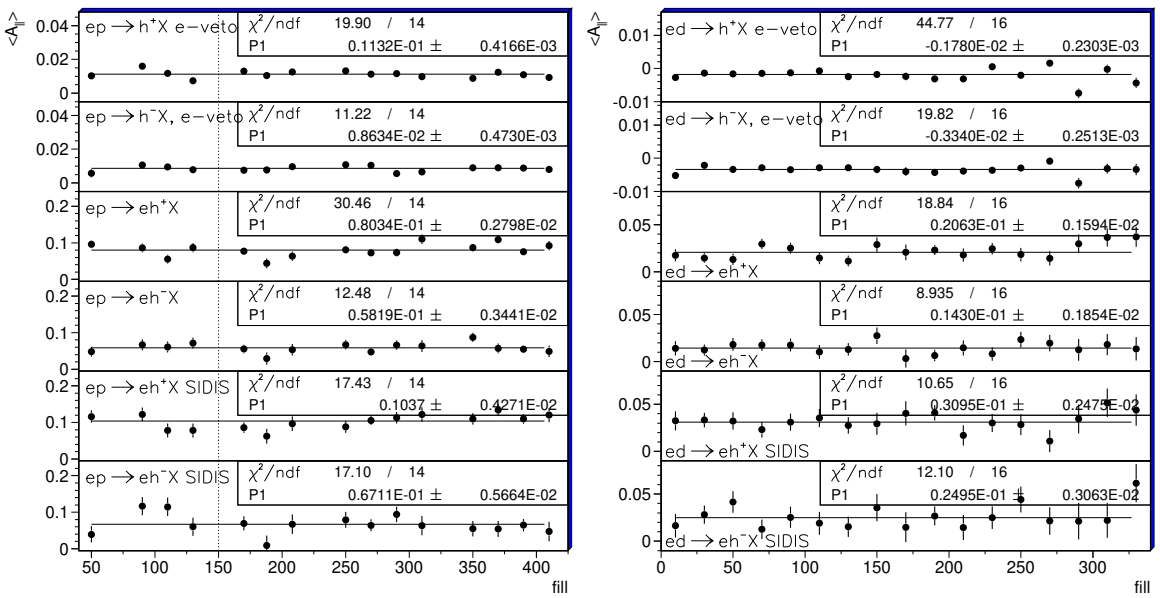

Figure 3.15: Average asymmetries for about 20 fills vs. fill number for proton (left) and deuteron data (right). The asymmetries are for h^+, h^- ('Photoproduction' region), h^+, h^- ('Transition' region) and h^+, h^- ('SIDIS' region) from top to bottom. The line is a result of a fit to a constant. The vertical line in the left plot indicates the boundary between the 1996 and 1997 data taking periods.

detected within the statistical errors (note that the 'SIDIS' asymmetries are completely correlated with the 'Transition' asymmetries). The points for the 'Photoproduction' asymmetries of 2000 show some unusually large fluctuations during the fills 260-280, leading to a large χ^2 of the fit. The fluctuations fall in a period of negative beam helicity and tensor polarized target operation (i.e., the target spin states were not only flipped between the two vector polarization states, but also between the four tensor polarization states of deuterium). The target polarization in this period is about 1-2% different from the average value used for the calculation of the asymmetries. This difference *cannot* account for the large jump in the asymmetries observed. The fluctuations stay also, if the asymmetries are calculated using the burst wise readout of the target polarization instead of the average value. The behavior of other quantities such as the beam polarization, beam slopes, proton background, trigger efficiencies etc. during that time was studied. Nothing unusual was observed. In order to check the influence of the fluctuations on the asymmetries averaged over the year, the 'Photoproduction' asymmetries were calculated using only the runs up to fill 250. These asymmetries were compared bin by bin with the standard asymmetry, and no deviation was observed outside the statistical errors. This is why for the time being, the analysis will be pursued with the standard asymmetry.

3.3.2 Beam Helicity

The asymmetries should only depend on the relative orientation of beam and target spins. A dependence of the asymmetries on the beam polarization could point to (spin dependent) normalization uncertainties in the beam or target polarization. During 2000, the beam helicity was flipped several times throughout the year, such that it is possible to divide the data sample into two independent samples of almost equal size according to the respective beam helicity. The asymmetries were compared by calculating t as in Eq. 3.9, and the average of the t values $\langle t \rangle = \frac{1}{n} \sum t_i$. The results for hadron and pion asymmetries are shown in figure 3.16. No trends are seen, the asymmetries are compatible within their errors.

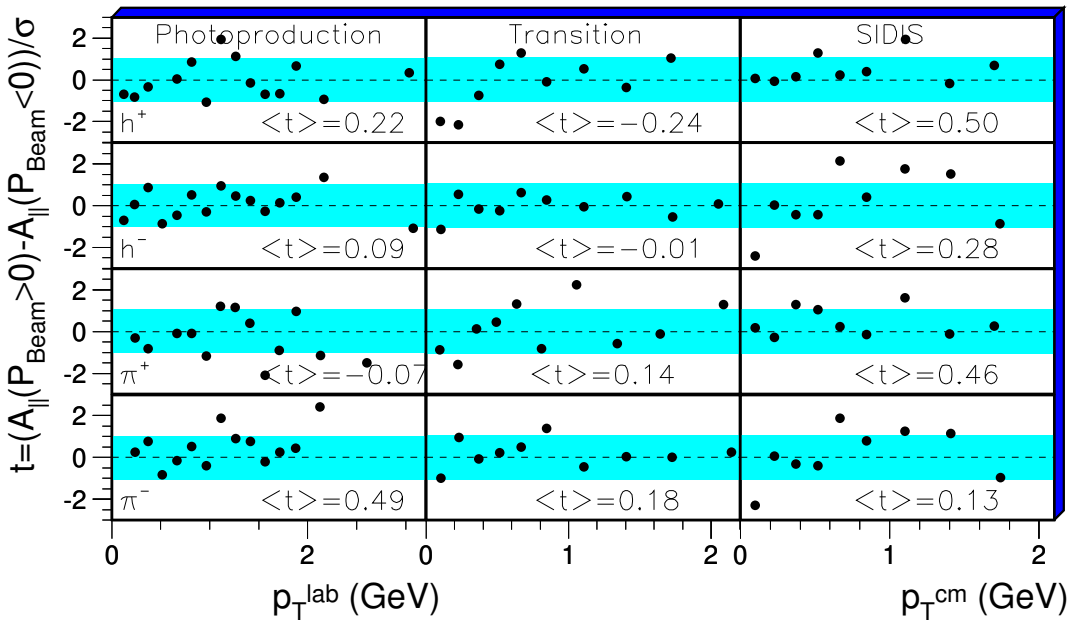

Figure 3.16: The error weighted difference t of the asymmetries from data with positive and negative beam helicity in 2000. The shaded bands indicate the standard deviation of the mean value of t at ≈ 1, the numbers in the lower right corners are the χ^2 per degree of freedom. The fields correspond to the asymmetries in figure 3.7 for hadrons and pions.

3.3.3 Normalization Uncertainties

The yields $N^{\rightleftarrows(\rightrightarrows)}$ entering the calculation of the asymmetries are usually normalized to the fitted luminosity. The difference between the asymmetries normalized to the fitted luminosity and those normalized to the raw luminosity rate can be attributed to a large extent to an asymmetry in Bhabha scattering if the residual electron polarization in the target is nonzero. This asymmetry is assumed to cancel between the target spin states such that the fitted luminosity (which averages over the target spin states) should not have a residual Bhabha asymmetry. The Bhabha asymmetry can be calculated from the total luminosities for each spin configuration and another normalization parameter that is known to be spin independent, for instance the beam current $\mathcal{I}$. In this case [DeN02]:

$$\frac{P_e}{P_T} A_{Bhabha} = \frac{L^{\rightleftarrows}_{rate} I^{\rightrightarrows} - L^{\rightrightarrows}_{rate} I^{\rightleftarrows}}{L^{\rightleftarrows}_{rate} I^{\rightrightarrows}_P + L^{\rightrightarrows}_{rate} I^{\rightleftarrows}_P}, \tag{3.25}$$

where I is the integrated and trigger life time corrected beam current, P_e is the *electron* polarization in the target, I_P is the integrated beam- and target polarization weighted beam current and L_{rate} is the integrated raw luminosity rate. In order to test the assumption that the fitted luminosity is spin independent one can replace the luminosity rate with the fitted luminosity. The difference of asymmetries $A^1_\parallel - A^2_\parallel$ normalized with two different 'luminosities' $L_{1,2}$ is [DeN03]:

$$\begin{aligned} \Delta A_L = A^{L_1}_\parallel - A^{L_2}_\parallel &\simeq \frac{P_e}{P_T} A_{Bhabha} \frac{N^{\rightrightarrows} N^{\rightleftarrows} (P^{\rightrightarrows} + P^{\rightleftarrows})}{(N^{\rightrightarrows} P^{\rightleftarrows} + N^{\rightleftarrows} P^{\rightrightarrows})^2} \\ &= \frac{P_e}{P_T} A_{Bhabha} C \simeq \frac{P_e}{P_T} A_{Bhabha}. \end{aligned} \tag{3.26}$$

$$\sigma_{\Delta A_L} = \sqrt{\sigma^2_{A_{\parallel,L_1}} + \sigma^2_{A_{\parallel,L_2}} - 2\sigma_{A_{\parallel,L_1}} \sigma_{A_{\parallel,L_2}}} \tag{3.27}$$

The factor C is close to 1 if the asymmetry is small, i.e., the yields are about the same in both spin states as well as the polarizations $P \equiv L_P/P$. In section 3.1.2 it was mentioned that there are two different methods to smooth the luminosity. With the the standard method a constant is fitted to

the quantity

$$K = \frac{\mathcal{L}_{rate}\sqrt{T_{cell}}}{I} \sim \frac{\mathcal{L}_{rate}}{I\rho} \quad \left(\rho \sim \frac{1}{\sqrt{T_{cell}}}\right) \quad \Longrightarrow \quad \mathcal{L}_{fitBstGai} = \frac{IK}{\sqrt{T_{cell}}} \rightarrow L^1_{fit}, \tag{3.28}$$

where ρ is the target density and T_{cell} is the target cell temperature. The other method is an exponential fit to the luminosity rate

$$\frac{d\mathcal{L}_{fit}}{dt} \sim \exp\left(\frac{t-t_0}{\tau_{Beam}}\right), \quad \tau_{Beam} = const. \quad \Longrightarrow \quad \mathcal{L}_{fit} \rightarrow L^2_{fit}. \tag{3.29}$$

It has been observed that this fit does not describe the data very well because the 'beam decay' constant τ_{Beam} is in fact a function of the beam current and therefore time dependent. The differences $A_\parallel^I - A_\parallel^{L^{1,2}_{fit}}$ and $A_\parallel^{L_{rate}} - A_\parallel^I$ between 'Photoproduction' asymmetries normalized with current I and fitted luminosity $L^{1,2}_{fit}$ or raw luminosity rate L_{rate} are displayed in table 3.5. The

Year	$A_\parallel^I - A_\parallel^{L^1_{fit}}$	$A_\parallel^I - A_\parallel^{L^2_{fit}}$	$A_\parallel^{L_{rate}} - A_\parallel^I$
1996	$(2.9517 \pm 0.0017) \cdot 10^{-4}$	$(9.8105 \pm 0.0062) \cdot 10^{-4}$	$(-7.1066 \pm 0.0042) \cdot 10^{-3}$
1997	$(-4.0405 \pm 0.0061) \cdot 10^{-4}$	$(3.7537 \pm 0.0018) \cdot 10^{-4}$	$(-8.3495 \pm 0.0026) \cdot 10^{-3}$
2000	$(-8.5338 \pm 0.0013) \cdot 10^{-4}$	$(-8.3675 \pm 0.0012) \cdot 10^{-4}$	$(-5.3460 \pm 0.0008) \cdot 10^{-4}$

Table 3.5: The difference of 'Photoproduction' asymmetries of positive hadrons with different normalizations. The values are for the years 1996, 1997 and 2000.

beam current should be truly spin independent such that the Bhabha asymmetry should be reflected in $\frac{P_e}{P_T}A_{Bhabha} \sim A_\parallel^{L_{rate}} - A_\parallel^I$ (cf. Eq. 3.25). If the Bhabha asymmetry would completely cancel in the fitted luminosity one would expect that $\Delta A_\parallel^{Norm} \equiv A_\parallel^I - A_\parallel^{L^{1,2}_{fit}} = 0$. This is not the case in any of the years. Note that A_{Bhabha} is a factor of 10 *smaller* in 2000 than in 1996/97, whereas $\Delta A_\parallel^{Norm}$ is always of the same order of magnitude. The nonzero 'fake' asymmetry $\Delta A_\parallel^{Norm}$ is not necessarily correlated to some 'residual' Bhabha asymmetry, and so far it is believed that it is due to a wrong synchronization of the fitted luminosity data with the other slow control data. Although the 'fake' asymmetries are very small, they would constitute a considerable systematic error for the rather small 'Photoproduction' asymmetries, especially in 2000. It should be safe to normalize the asymmetries to the beam current instead of the fitted luminosity, since the beam current measurement has small statistical fluctuations and is not correlated to the spin configurations. For the final results in this thesis thus the beam current will be used as normalization.

3.3.4 Detector Alignment

In many cases, effects of the detector geometry, i.e., the acceptance functions on which the observed cross sections depend, are spin independent such that they cancel in the ratio of cross sections in an asymmetry. This is not necessarily true for special applications, for instance, if the semi-inclusive asymmetry is measured as a function of p_T but depends also on other variables like x and y that are integrated over. In this case it is at least necessary to measure the average kinematics for each p_T bin in order to be able to compare the results with another experiment or with Monte Carlo. Another issue related to this kinematic dependence is a possible misalignment of the HERMES spectrometer, or of parts of it. It has been shown for instance that in 2000 there was an offset of 5 mm between the points where charged particles hit the calorimeter as measured by the tracking system and those of the actual energy clusters in the calorimeter in the top detector [Ell03]. No such offset was observed for the bottom detector. A survey of the calorimeter in 2003 revealed that the calorimeter position is correct, indicating that one or more of the wire chambers are shifted

with respect to their assumed positions used for track reconstruction. A shift of 5 mm corresponds to an error of $\simeq 1$ mrad in the measured angles.

The possible influence of a detector misalignment on asymmetries can be checked by changing the geometrical cuts on track positions. Especially in the case of the asymmetries vs. p_T one has to be aware of potential biases arising from changing the average kinematics by changing geometric cuts. An upper cut on the polar angle of 'Photoproduction' hadrons for instance would shift their average momentum towards higher values for fixed p_T. A lower angular cut on positrons would raise the average x for semi-inclusive asymmetries. Due to the non-isotropic azimuthal acceptance of the spectrometer, a binning of asymmetries in the azimuthal angle ϕ would result in ϕ dependent lower and upper polar angle cuts and thus also influence the momentum or x. The least bias is achieved if the data sample can be split in independent parts that should be kinematically equivalent. It is then possible to examine their compatibility. One option is to calculate asymmetries separately for the top and bottom detector halves. For semi-inclusive asymmetries, this can be done in two ways: either the positron or the hadron can be required to be in one of the detector halves. A semi-inclusive event with two equally charged hadrons in opposite halves, where both of them fall into the same p_T bin is highly unlikely – this is why semi-inclusive asymmetries for hadrons in the top and bottom detectors as a function of p_T are practically uncorrelated. This is not completely true for semi-inclusive asymmetries as a function of inclusive variables like x, but it turned out that the correlation is only a few percent. Note that an observed difference between 'top' and 'bottom' asymmetries may point to problems in the alignment or to position and momentum dependent inefficiencies, the absence of such differences, however, does not mean that such problems do not exist. In the latter case the only conclusion to be drawn is that the difference of 'top' and 'bottom' asymmetries is not sensitive to a possible misalignment or inefficiencies. An influence of the latter on the asymmetries themselves can thus not be excluded.

Using otherwise the standard geometrical cuts, no statistically significant deviation has been found for all semi-inclusive asymmetries, where the sample was subdivided according to the *positron* being in the top or in the bottom. Again, the quantity measured was the relative deviation t (Eq. 3.9) between the top and bottom asymmetries. Asymmetries divided into top and bottom hadron samples (also for the 'Photoproduction' region) were compatible with each other as well, with the exception of those of negative hadrons and pions in 1997 in the semi-inclusive regions. The corresponding plot showing the t-distribution for all asymmetries in 1997 is shown in figure 3.17. Although the average t value is still within the allowed range, almost all t_i for the negative hadrons and even more so for negative pions lie significantly above 0. That the 'top' pion asymmetries are definitely larger than the 'bottom' asymmetries can be seen in figure 3.18 for the 'SIDIS' region. Several studies were performed as a consequence of this finding. The fact that only negative hadrons are affected points to some position dependent effect. The spectrometer magnet deflects negatively charged particles to the left (looking into the direction of beam momentum) and positively charged particles to the right. A possible effect of an inefficiency of the Cherenkov detector (which could be position dependent due to different mirror or PMT performances) was excluded by excluding the Cherenkov information from the PID, i.e., using $PID2 + PID5$ instead of $PID3 + PID5$. Analogously, the particle identification efficiencies of the calorimeter and the TRD were ruled out as the cause of the discrepancy. The position dependence of trigger efficiencies has been studied by dividing each half of the detector into 'right' and 'left' (negative and positive x) parts. On this rather large scale, no position dependence of trigger efficiencies has been observed, except for the difference in top and bottom efficiencies seen in figures A.1 and A.2. A spatial dependence of identification or detection efficiencies is thus unlikely to be the reason for the discrepancy in the asymmetries.

It has been investigated if by varying cuts on the y position of tracks (in fact the y-projection of their trajectory at the calorimeter) can change the relative behavior of the asymmetries in top and bottom. This could be the case if there is a misalignment between the top and bottom detectors *relative* to the beam position and to each other. However, the observed difference between the top and bottom negative hadron asymmetries stays evident for all y-cuts.

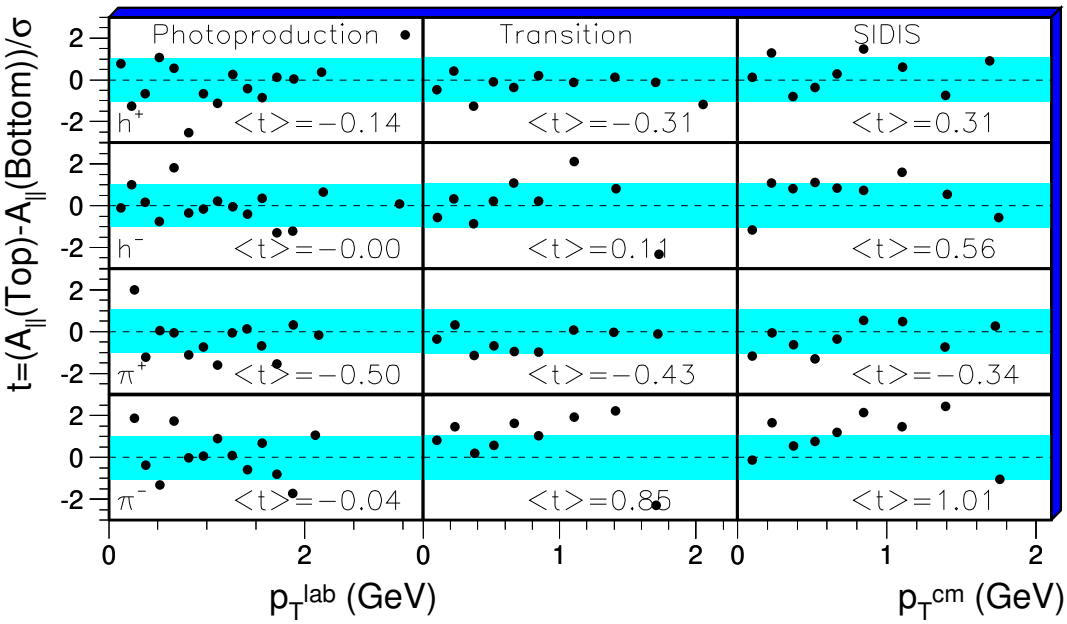

Figure 3.17: The error weighted difference $(A_{\parallel}^{Top} - A_{\parallel}^{Bottom})/\sqrt{\sigma_{top}^2 + \sigma_{Bottom}^2}$ of the 1997 asymmetries with the hadron in either of the top and bottom detector halves. The shaded bands indicate the standard deviation of the mean value of t at ≈ 1, the numbers in the lower right corners are the average t values. The fields correspond to the asymmetries in figure 3.5 for hadrons and pions.

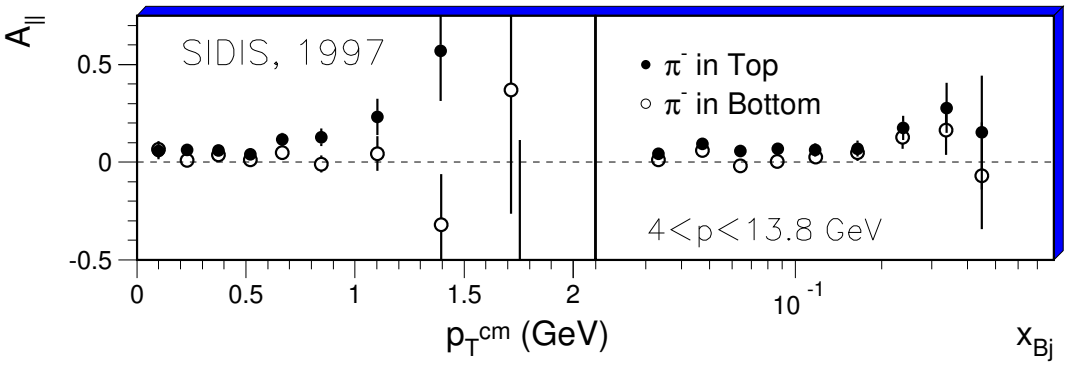

Figure 3.18: The 1997 'SIDIS' asymmetries $A_{\parallel}^{Top}$ (closed circles) and $A_{\parallel}^{Bottom}$ (open circles) for negative pions in the top resp. bottom detector halves as a function of transverse momentum (left) and x (right).

Misalignment effects can be studied in the top/bottom dependence of cross sections (yields) and the average kinematics in each bin. If the detector were completely symmetric with respect to the $x-z$ plane, the ratio of cross sections observed in the top to those observed in the bottom for instance should be constant. It should be one if the efficiencies were the same for the bottom and top detectors. Figure A.1 in appendix A.2 shows that the trigger 21 efficiency in 1997 was indeed smaller in the top detector, such that the ratio $\sigma_{top}^h/\sigma_{Bottom}^h$ should be smaller than one for the photoproduction data. In the semi-inclusive case the trigger efficiency is dominated by the positron efficiency that was almost equal in both halves.

The topology of semi-inclusive events is rather different from photoproduction events because at least two tracks, one of which is the scattered positron, are required. The asymmetries are composed of two classes of events. Most events come with a hadron in one and the positron in the other half. A smaller fraction of events has both the positron and the hadron in the same half. This leaves four possible top/bottom configurations:

1. The hadron is detected in the top, the positron in the bottom half.
2. The hadron and the positron are both detected in the top half.
3. The hadron is detected in the bottom, the positron in the top half.
4. The hadron and the positron are both detected in the bottom half.

This sheds some light on the fact that discrepancies between asymmetries in the top and bottom detector halves are observed for the case when the hadrons are required to be in a particular half, but not if the same requirement is placed on the positron. If the hadron is required to be in the top (bottom) half, combinations 1 and 2 (3 and 4) are possible. If the positron is required in the top (bottom), this leaves combinations 2 and 3 (1 and 4). For events with the tracks in opposite halves, hadron asymmetries in the top are equivalent to positron asymmetries in the bottom and vice versa. The difference then lies in the configurations where both tracks are detected in the same half. Asymmetries and yields with these configurations have therefore been studied separately. Figure 3.19 shows the cross section ratios between top and bottom for pions with $4 < p < 13.8$ GeV as a function of p_T, in all three kinematic regions. The cross section ratios are indeed not

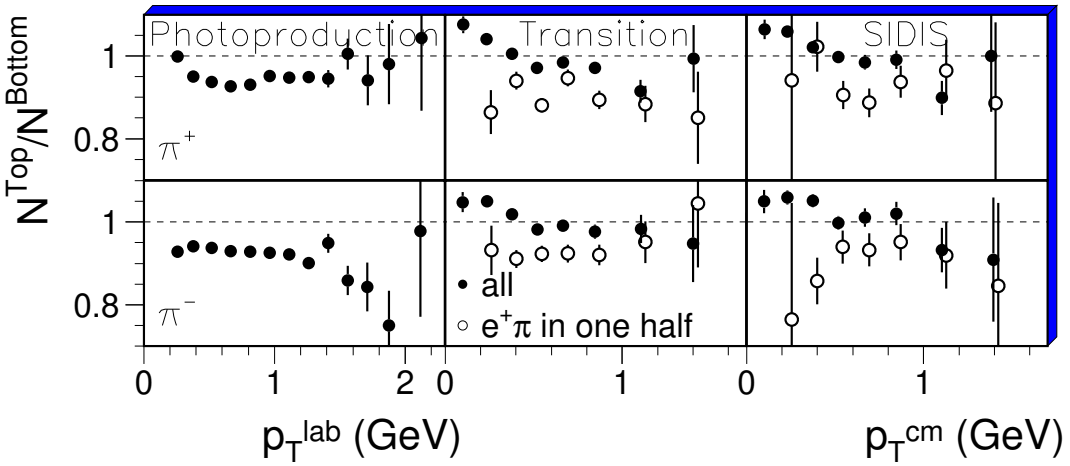

Figure 3.19: The ratio N^h_{Top}/N^h_{Bottom} as a function of p_T for positive (top row) and negative (bottom row) pions in the 'Photoproduction' (left column), 'Transition' (middle column), 'SIDIS' (right column) regions. Closed circles are for all events, open circles for events where positron and hadron are in the same detector half.

only p_T dependent, but in fact also slightly different for positive and negative pions, especially in the 'Photoproduction' region. The most striking feature is the difference between the top-bottom ratios of events with positron and hadron in the same half and the top-bottom ratios of all events. The behavior seems to be symmetric with respect to the hadron charge, but maybe slightly more distinct for negative pions. The contribution of the events where positron and hadron are in the same half to the complete sample is shown as a function of p_T in figure 3.20. The plot shows clearly a strong kinematic dependence, where the ratio is slightly higher in the bottom than in the top detector. As a function of x the ratio rises towards smaller x, reaching maxima of 0.4 at small $x \approx 0.004$ in the 'Transition' and 0.2 at $x \approx 0.03$ in the 'SIDIS' region.

The average value of a kinematic observable ψ in each p_T bin can be calculated as follows:

$$\langle\psi\rangle = \frac{\int d\psi \psi \frac{d\sigma(\psi,\omega)}{d\psi}}{\int d\psi \frac{d\sigma(\psi,\omega)}{d\psi}} \Rightarrow \frac{1}{N_h}\sum_{i=1}^{N_h}\psi_i, \tag{3.30}$$

where ω here denotes a set of other independent variables the cross section depends on. The average values have been calculated in the 'Photoproduction' region for p and θ, and in the semi-inclusive

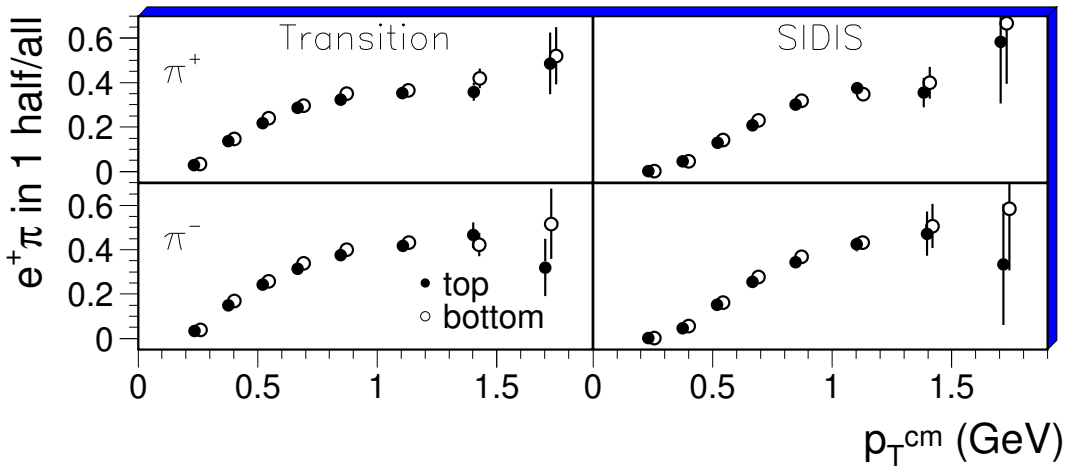

Figure 3.20: The ratio of events with positron and hadron in one half to all events as a function of p_T for positive (top row) and negative (bottom row) pions in the 'Transition' (left) and 'SIDIS' (right) regions. Closed circles show the ratio for the top, open circles for the bottom detector.

regions for x, y, and Q^2. As an example, figure 3.21 shows the average x and y of semi-inclusive (negative) pions in 1997, for all events and for events with the scattered positron and hadron in one half. At small p_T, the kinematics of the events with both tracks in one half is very different

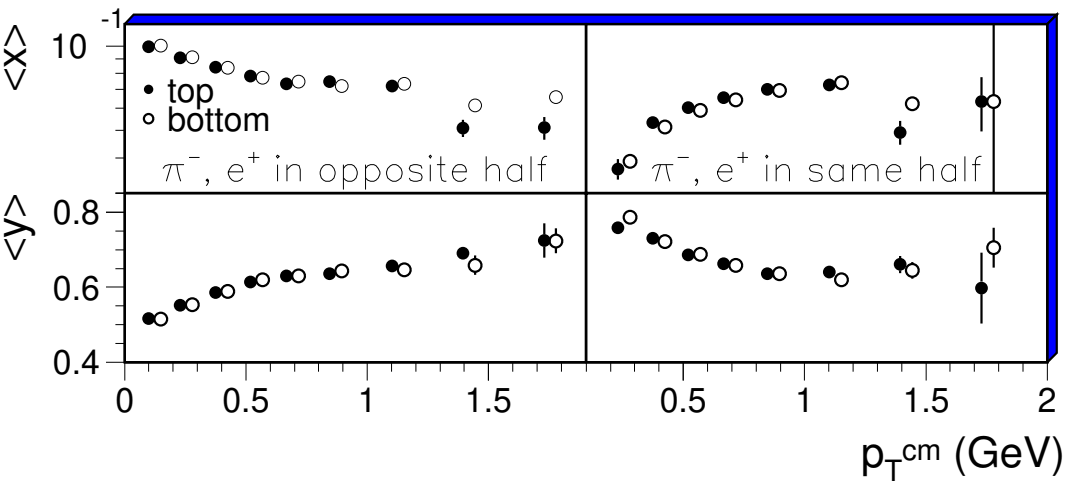

Figure 3.21: The average x (top) and y (bottom) of negative pions in the 'SIDIS' region, for 1997. The right plots are for all events, the left plots for those where both hadron and positron are in one half. The open circles are for hadrons in the bottom, the closed circles for hadron in the top detector.

from that of all events. There is no significant difference between top and bottom, though. With an unknown misalignment it is of course possible that the positron (and hadron) kinematics are reconstructed wrongly, such that the *true* kinematics can be shifted with respect to the measured values.

The asymmetries of the events with both tracks in one half only are shown in figure 3.22 vs. p_T and x. The difference of top and bottom asymmetries for the events with both tracks in one half is, even in view of the larger error bars, much larger than for the whole data sample. It is puzzling that despite the smaller measured x at small p_T for the events with positron and pion in one half, their asymmetry in the top is significantly larger than that of all events. If the data with both tracks in one half are subtracted from the event sample, the asymmetries of top and bottom pions move towards each other, but some non-statistical deviation stays. This indicates

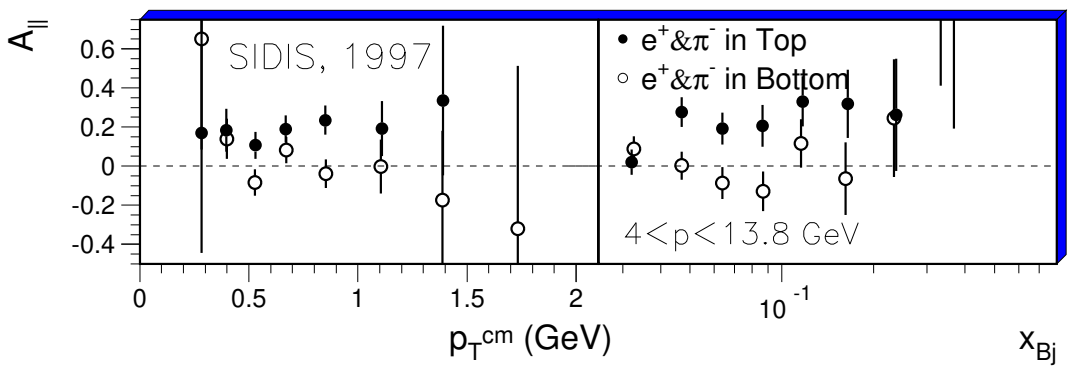

Figure 3.22: The 1997 'SIDIS' asymmetries $A_{\parallel}^{Top}$ (closed circles) and $A_{\parallel}^{Bottom}$ (open circles) for positrons and negative pions in the top resp. bottom detector halves as a function of transverse momentum (left) and x (right).

that, whatever the reason for the observed deviation is, its effect is amplified in the events with positron and pion in one half, but is also existent in the other events.

The presented studies show that the behavior of the top and bottom detectors is asymmetric, probably due to misalignment in one or both detector halves. Effects of this misalignment have also been reported by the HERMES collaboration in Ref. [Air03a]. There the ratio of the inclusive DIS cross section on Krypton to that on Deuterium σ^{Kr}/σ^{D} was found to be different in the top and bottom detectors, with a dependence of the difference on x. In this special case where only inclusive observables are used it was possible to tune the parameters relevant for the detector alignment using MC simulations. The information on the alignment parameters obtained from this study is not applicable for semi-inclusive data, though, due to the more complicated relation of the kinematics of hadron and positron. It would be necessary to include the correct alignment in the track reconstruction from the beginning. With the track reconstruction method used so far it is not completely possible to reconstruct the alignment parameters from data, because it is not capable of dealing with rotated detectors. The resulting alignment parameters are 'effective' in the sense that a detector that may be rotated around one or more of the axes will produce 'unreal' *offsets* in any of the axes. Those may work well for some data set, but may be wrong for a kinematically different data set. This is why at present neither the exact cause of the top-bottom discrepancy can be found nor the problem can be solved using correct alignment parameters. It is also not possible to estimate a systematic error due to the detector alignment, since it is not clear if the top, the bottom, the average of both or none of the asymmetries is the correct one. In the case of the above mentioned nuclear cross section ratios it turned out that the *average* of the top and bottom cross section ratio is in good agreement with data from a symmetrically aligned Monte Carlo production [Gar03]. This should also in this case lead to the assumption that the average of the top and bottom asymmetries is least subject to misalignment effects. Since this assumption cannot be proven, it should be kept in mind, though, for future comparisons with Monte Carlo.

3.3.5 Systematic Uncertainties

The main sources of systematic uncertainties arise from the uncertainties of the beam and target polarization measurements and particle misidentification. An additional normalization uncertainty due to the luminosity measurement is not taken into account, since the spin independent beam current is used for normalization (cf. section 3.3.3).

- **Beam Polarization**
  The TPOL was used for the beam polarization measurement in the years 1996 to 1998. Its relative systematic uncertainty is 3.4% for all years (see section 1.1). From 1999 on, the LPOL measurements were used, except for some periods when the TPOL performance was

considered to be better than that of the LPOL. The relative systematic uncertainty of the LPOL is 1.6%, the total systematic uncertainty for 2000 is 1.9%, taking into account the weight of time periods when the TPOL measurement with the larger systematic error was used [Wen03]. The systematic uncertainty of the measured asymmetries is related to that of the beam polarization ($A_\parallel \sim 1/P_B$):

$$\frac{\delta A_\parallel}{A_\parallel}(P_B) = \left|\frac{\delta P_B}{P_B}\right|. \tag{3.31}$$

- **Target Polarization**
  The systematic uncertainty of the target polarization arises mainly from the sampling correction in the measurement of the molecular recombination α_R and the molecular polarization β [Reg03]. The average target polarization and its error were determined for the years 1997 and 2000. The relative error is 3.9% for 1997, and 3.4% (3.0%) for 2000 for the target polarization parallel (antiparallel) to the beam momentum. The target polarizations for the years 1996 and 1998/99 were obtained from these measurements by normalizing the inclusive asymmetries of these years to those of 1997 and 2000, respectively. The target polarization error for these years is the squared sum of the systematic error determined from 1997 or 2000,respectively, and the statistical error from the normalization procedure [Bec03]. Similar to the beam polarization error the target polarization error propagates into that of the asymmetries ($A_\parallel \sim 1/P_T$) like:

$$\frac{\delta A_\parallel}{A_\parallel}(P_T) = \sqrt{\left(\frac{\langle \delta P_T\rangle}{\langle P_T\rangle}\right)^2 + \left(w^{96}\frac{\delta n}{n}\right)^2}, \tag{3.32}$$

  where the average of the systematic errors for positive and negative polarization is taken, and $w^{96} = L^{96}/L^{96+97}$ is the weight of the 1996 data for the combined proton asymmetries ($w^{96} = 0$ for the 2000 data). The relative normalization error is $\frac{\delta n}{n} = 0.027$.

- **Lepton/Hadron misidentification**
  As discussed in section 3.2.5, the systematic error arising from the (small) misidentification probability of hadrons as leptons and vice versa can be estimated from the difference of the measured to the background corrected asymmetry, Eq. 3.18. The error is calculated from the average values of the measured background asymmetries (see figures 3.10 and 3.11) and the respective contaminations as described in section 3.2.5. For the systematic error on the negative hadron and pion asymmetries in the 'Photoproduction' region, the electron asymmetry is averaged over the region $p_T^{lab} > 0.75$ GeV. The error is assumed to be 0 for 'Photoproduction' kaon asymmetries, since the information from the RICH basically excludes a contamination of the kaon sample with leptons. The relative systematic error is:

$$\frac{\delta A_\parallel}{A_\parallel}(PID) = \frac{A_\parallel^{corr} - A_\parallel^{meas}}{A_\parallel^{meas}}. \tag{3.33}$$

  The sign of the deviation is taken into account. The contribution of this uncertainty is basically negligible, and will not be given separately.

- **Pion/Kaon misidentification**
  The systematic error of the pion and kaon asymmetries of 2000 due to the uncertainties in the RICH unfolding is estimated from the difference of asymmetries obtained using different P-matrices (cf. section 3.2.6). The relative deviations are shown in figure 3.14:

$$\frac{\delta A_\parallel}{A_\parallel}(RICH) = \frac{A_\parallel^{\text{unf., MC}} - A_\parallel^{\text{unf, std}}}{A_\parallel^{\text{unf, std}}} \tag{3.34}$$

  where $A_\parallel^{\text{unf., MC}}$ stands for the asymmetry obtained using a P-matrix taking into account the uncertainties in MC parameters describing the RICH that are believed to be the largest

source of uncertainties for the RICH unfolding. Also here, the error is considered with a sign. Since in some regions the deviations are themselves subject to relatively large fluctuations, the errors were smoothed with a cubic spline.

The total systematic error is calculated as:

$$\delta A_{\parallel}^{syst} = A_{\parallel}\left[\pm\sqrt{\left(\frac{\delta A_{\parallel}}{A_{\parallel}}(P_T)\right)^2+\left(\frac{\delta A_{\parallel}}{A_{\parallel}}(P_B)\right)^2}+\frac{\delta A_{\parallel}}{A_{\parallel}}(PID)+\frac{\delta A_{\parallel}}{A_{\parallel}}(RICH)\right], \tag{3.35}$$

where $\frac{\delta A_{\parallel}}{A_{\parallel}}(RICH) = 0$ for $h^{\pm}$ from all years and $\pi^{\pm}$ from 1997. The final results on the asymmetries, the statistical and systematic errors are summarized in the tables of section D.2 in the appendix. Figure 3.23 is the corresponding plot showing the final, corrected asymmetries with their systematic error shown separately the statistical error bars. For the pion 'Photoproduction'

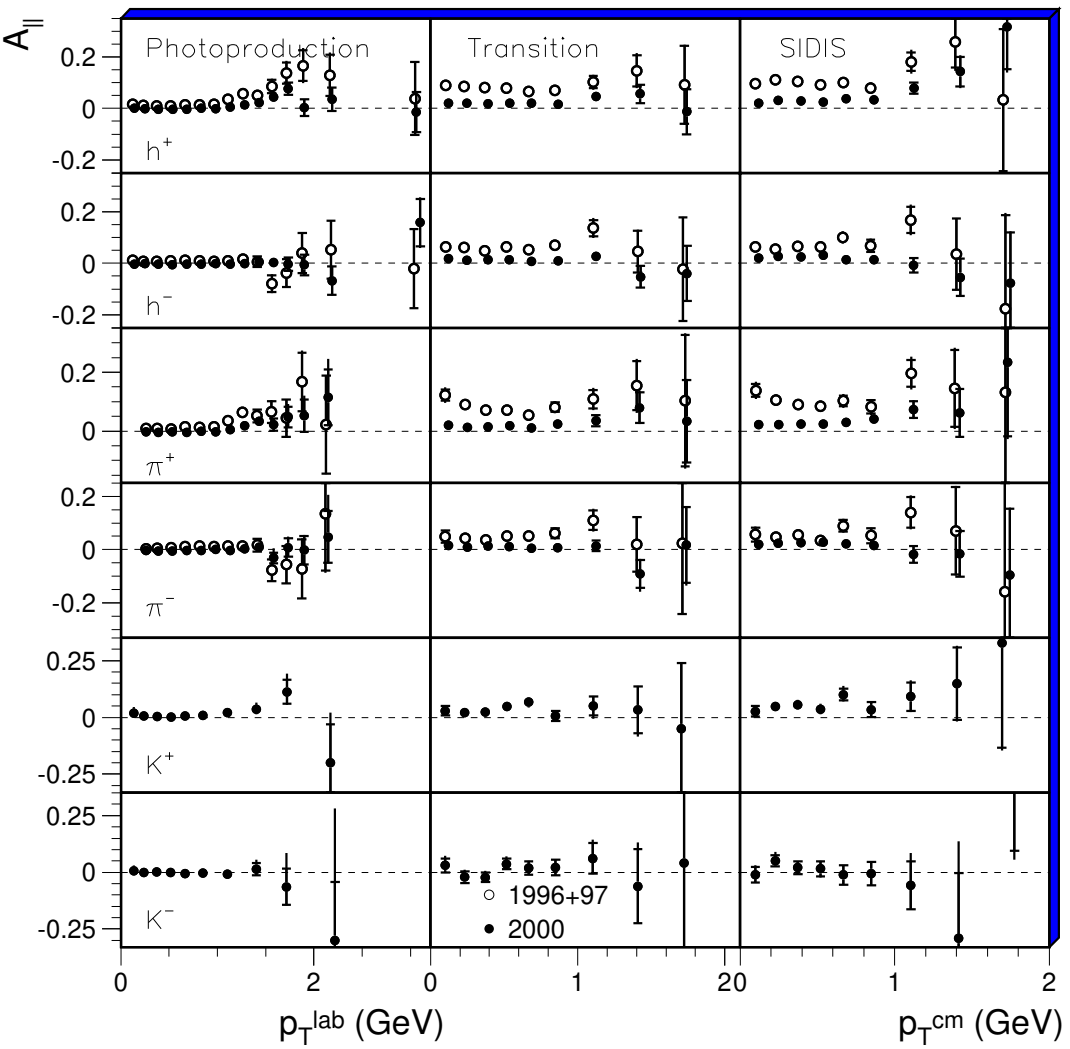

Figure 3.23: The final results on the proton (1996+1997) asymmetries (empty circles) and deuteron (2000 data) asymmetries (filled circles) for the 'Photoproduction-' (left column), 'Transition-' (middle column) and 'SIDIS' region (right column) for positive and negative hadrons, positive and negative pions and positive and negative kaons (from top to bottom). The (asymmetric) systematic error is added on top of the statistical error and separated from it by the horizontal tick marks.

and the kaon asymmetries, the relative error from the RICH unfolding is comparable to that from

the polarization uncertainties in some of the kinematic bins. However, practically everywhere, the absolute systematic uncertainty is substantially smaller than the statistical error of the asymmetry.

3.4 Observed Cross Sections

The data to Monte Carlo comparisons that will be discussed in section 4 are mainly based on the comparison of observed cross sections in the same three kinematic regions as are considered for the asymmetries. Although with the HERMES implementation of the Monte Carlo generators the geometrical and kinematic acceptance of the spectrometer can be simulated, the trigger- and PID efficiencies cannot. It is thus necessary to either correct the data for inefficiencies or to at least know the efficiencies in order to estimate the systematic error of the observed cross sections. Cross sections can be obtained from the measured number of events (or particles) and the integrated luminosities (cf. Eq. 3.1):

$$\sigma = \frac{\int dt \frac{dN}{dt}}{\int dt \mathcal{L} \tau C_L}. \tag{3.36}$$

The rate $\mathcal{L}$ of coincidences of highly energetic e^+e^- (or $\gamma\gamma$) pairs measured in the luminosity monitor has to be related to the (known) Bhabha or annihilation cross section and the acceptance of the luminosity monitor in order to be converted to a luminosity. This is the purpose of the factor C_L. Since the acceptance of the luminosity monitor depends strongly on the beam position and slope, the factor C_L needs to be determined for each year using a Monte Carlo simulation of the luminosity monitor and the beam. For 1997 and 2000, the constants are $C_L^{1997} = (0.426 \pm 0.36)\mu b^{-1}$ and $C_L^{2000} = (0.417 \pm 0.30)\mu b^{-1}$ respectively [Els02]. The relatively large systematic errors of 7-8% are mainly due to the uncertainty in the measurements of the beam position and slope at the HERMES IP. An alternative to the integrated luminosity rate is the number of DIS events measured $\int dt \frac{dN^{DIS}}{dt}$ that can be related to the luminosity using a similar constant C_{DIS}:

$$\int dt \mathcal{L}^{DIS} = C_{DIS} \int dt \frac{dN^{DIS}}{dt}. \tag{3.37}$$

C_{DIS} can again be determined from Monte Carlo, using

$$\sigma_{DIS} = \frac{\int N_{DIS}^{Obs} \epsilon \mathcal{A}}{\int dt \mathcal{L}}, \tag{3.38}$$

where $\epsilon\mathcal{A}$ accounts for efficiency and acceptance effects. However, the result of this method depends on the Monte Carlo model used to describe $F_2(x, Q^2)$ and also involves a large systematic error. It is also not advisable to compare data normalized with a constant obtained from a particular Monte Carlo model to the same model. This is why in this thesis the luminosity normalization will be applied.

3.4.1 Semi-inclusive Cross Sections

Semi-inclusive cross sections are calculated using essentially the same kinematic cuts for the 'Transition' and 'SIDIS' regions as in the asymmetry analysis. Since only unpolarized cross sections are considered, the data quality cuts of table 3.2 need not be applied. The comparison to Monte Carlo concerns mainly proton data, which is why the 1997 polarized and the 2000 unpolarized hydrogen data are analyzed. The advantage of using the 2000 data set is that the RICH provides information about kaons and protons, and hadron separation in general is possible over a wider momentum range ($2 < p < 15$) GeV than in 1997 where only pions between $4 < p < 13.8$ GeV could be identified. The drawback is that the high calorimeter threshold for trigger 21 and the suppression of other triggers during unpolarized data taking results in a very low efficiency for events with $E' < 4$ GeV. An additional cut on

$$\nu < 23.57 \text{ GeV}, \qquad \text{(2000 unpolarized data)} \tag{3.39}$$

is therefore necessary to ensure that the trigger efficiency is close to 1 for the whole kinematic region. This affects only the 'Transition' region, since in the 'SIDIS' region the cut on $y < 0.85$, meaning $E' > 4.1$ GeV, is sufficient. The data on identified pions, kaons and protons in 2000 were unfolded using the RICH P-matrices as for the asymmetries. The identified pion data in 1997 need to be corrected for the detection inefficiency of the Cherenkov detector, which is relatively large in the region of 4-6 GeV for pions. At $p \simeq 4$ GeV, the Cherenkov efficiency is for instance only about 70%. The efficiency can be calculated as [DeS00]:

$$\epsilon(CER) = 1 - \exp\left\{-N_0\left(1 - \frac{\gamma_{th}^2}{\gamma^2}\right)\right\}, \tag{3.40}$$

with $N_0 = 6.3$ the yield of photoelectrons for pions with $\beta \to 1$, the threshold for Cherenkov radiation of pions at $\gamma_{th} = 28.24$ and γ being the actual Lorentz boost factor of the pion identified with a photo electron yield $N_{pe} > 0.25$. The factor $\frac{1}{\epsilon(CER)}$ was multiplied as a weight to each identified pion. The contamination of pions with subthreshold kaons and protons should be negligibly small. Examples of the observed differential cross sections in 1997 can be seen in figure 3.24 as a function of W^2 for positive and negative hadrons in the 'Transition' and 'SIDIS' regions, and as a function of p_T for positive hadrons and identified pions with $4 < p < 13.8$ GeV. For comparison, vs. p_T also the cross section for pions from the 2000 data with $2 < p < 15$ GeV is shown.

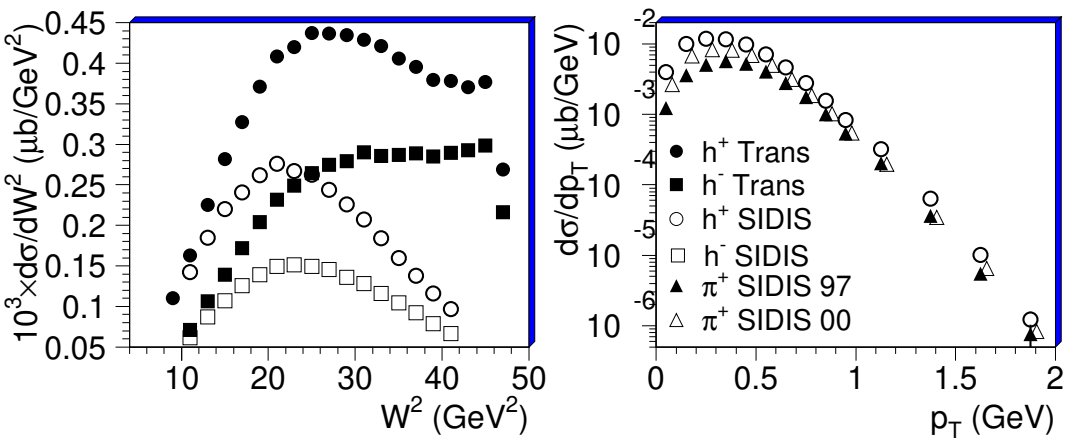

Figure 3.24: Observed differential cross sections $\frac{d\sigma}{dW^2}$ (left) and $\frac{d\sigma}{dp_T}$ (right) for hadrons and pions from 1997, obtained using the cuts of table 3.4. The momentum range for pions from 2000 is $2 < p < 15$ GeV, for 1997 it is $4 < p < 13.8$ GeV.

The systematic error on the semi-inclusive cross section due to inefficiencies can be roughly estimated using the trigger efficiencies for semi-inclusive events (cf. appendix A.3) and the PID-cut efficiencies for positrons and hadrons vs. momentum. The momentum distributions can be weighted with these efficiencies and then integrated over momentum:

$$\Delta\sigma^{eff} = \int_{p_e} dp_e \frac{d\sigma_e^{semi}}{dp_e}\left(\frac{1}{\epsilon(21)\epsilon(PID_e)} - 1\right) + \int_{p_h} dp_h \frac{d\sigma_h^{semi}}{dp_h}\left(\frac{1}{\epsilon(PID_h)} - 1\right). \tag{3.41}$$

For pions and kaons in 2000 the systematic error from the uncertainty of the P-matrices has to be added. This is done in a procedure similar to that used for the asymmetries, comparing the yields of pions (kaons) extracted using different P-matrices. The average systematic deviation $\Delta\sigma^{unf}$ can be estimated for the total observed cross section using the integral over the momentum as in Eq. 3.41. The total relative systematic error is then

$$\Delta\sigma^{tot} \simeq \pm\frac{\Delta C_L}{C_L} + \frac{\Delta\sigma^{eff}}{\int_{p_h} dp_h \frac{d\sigma_h^{semi}}{dp_h}} + \frac{\Delta\sigma^{unf}}{\int_{p_{\pi(k)}} dp_{\pi(k)} \frac{d\sigma_{\pi(k)}^{semi}}{dp_{\pi(k)}}}. \tag{3.42}$$

The pions in 1997 are corrected for the efficiency of the Cherenkov detector according to Eq. 3.40, with $N_0 = 6.324 \pm 0.138$. An error can be estimated using the maximum (minimum) of N_0 from its statistical error to obtain the efficiencies $\epsilon^{max,min}$ (Eq. 3.40) and weighting the ratio $\epsilon^{max,min}/\epsilon^{mean}$ with the cross section like in Eq. 3.41. The average systematic deviations are summarized in table 3.6.

	Lumi	Efficiency	$\pi(k)$-ID	+Total	-Total
1997					
h^+	±8.5	+3.2/2.4		11.7/10.9	8.5/8.5
h^-		+3.1/2.1		11.6/10.6	8.5/8.5
π^+		+3.3/2.3	±0.8	11.8/10.8	8.5/8.5
π^-		+3.1/2.0	±0.8	11.6/10.5	8.5/8.5
2000					
h^+	±7.2	+2.4/2.8		9.6/10.0	7.2/7.2
h^-		+2.0/1.8		9.2/9.0	7.2/7.2
π^+		+2.4/2.8	+1.7/1.3	11.3/11.3	7.2/7.2
π^-		+2.0/1.8	+2.0/1.5	11.2/10.5	7.2/7.2
K^+		+2.5/2.0	-7.5/-5.6	9.7/9.2	14.7/12.8
K^-		+2.2/1.8	-16.9/-13.1	9.4/10.0	24.1/20.3

Table 3.6: Average relative systematic deviations in percent of the semi-inclusive cross sections for the polarized 1997 and the unpolarized 2000 hydrogen data. The numbers left and right of the slash are for the 'Transition' and 'SIDIS' regions, respectively.

Aside from the normalization error, the error for the semi-inclusive hadron and pion cross sections is dominated by the PID-cut efficiencies of positrons, whereas the error for kaons is dominated by the unfolding uncertainty. Here also a strong kinematic dependence is to be expected. Figure 3.25 shows the cross section for kaons as a function of transverse momentum together with the contribution to the systematic error from the RICH unfolding calculated for each bin and the total systematic error. In this case it turned out that the bin-by-bin error is very similar to the average error.

Of course the inefficiencies depend on the kinematics of positrons and hadrons, and for a detailed analysis it would be necessary to correct for inefficiencies in each kinematic bin separately. The average values given here are only used to provide an impression of the uncertainty of the data when comparing with Monte Carlo cross sections.

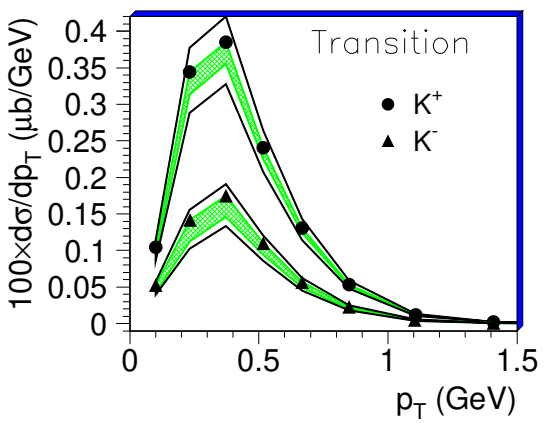

Figure 3.25: Observed differential kaon cross sections in p_T in the 'Transition' region from the 2000 unpolarized hydrogen data. The lines around the data points indicate the total systematic error, the shaded band the contribution from the RICH unfolding to the systematic error only.

3.4.2 Exclusive ρ^0 Production

An important part of Monte Carlo model to be used for the extraction of ΔG is the phenomenological description of minimum bias photon and hadron physics using the VMD model (cf. section 2.5.2). The analysis of exclusively produced vector mesons, ρ^0 in particular, is the essential tool to check how well this model is suited for the HERMES kinematic region. The elastic production of a vector meson is a kinematically distinct process that can be isolated relatively easy. In this process a virtual photon turns into an on-shell vector meson with essentially the same properties as the original photon. Only a small momentum is transferred to the nucleon such that it is left intact. The experimental signature of this process are the decay products of the vector meson ($\pi^+\pi^-$ from ρ^0) that can be reconstructed to give the mass and momentum of the vector meson. The momentum of the vector meson should be close to that of the virtual photon, meaning that only little energy and momentum has been taken by the proton. At HERMES it is not possible to detect the recoiling proton, and because of the restricted spectrometer acceptance the observation of exactly two pions does not exclude that other particles were produced in the event as well. If the kinematics of the process are reconstructed under the assumption of an exclusive event it is possible to impose a set of cuts reducing the background from non-exclusive events to a large extent. The important kinematic variables in this analysis of the process $ep \to e'p\rho^0$ are introduced in table 3.7. The quantity t_{min} is the minimum momentum transfer of the interaction. For $t = t_{min}$, the

p_ρ	reconstructed four momentum of the vector meson	$p_\rho = p_{\pi^+} + p_{\pi^-}$
M_ρ	reconstructed mass of the vector meson	$M_\rho^2 = (p_{\pi^+} + p_{\pi^-})^2$
t	momentum transfer squared $(P - P')^2$ to the proton	$t = (q - p_\rho)^2$
t'	transverse momentum squared transferred to the proton	$t' = t - t_{min}$
ΔE	missing energy of the detected $e'\pi^+\pi^-$ system	$\Delta E = \frac{M_X^2 - M^2}{2M} \overset{\text{lab}}{=} \nu - E_\rho + \frac{t}{2M}$

Table 3.7: Variables used to select elastic ρ^0 production processes.

vector meson would be exactly parallel to the incoming virtual photon. It can be calculated as $t_{min} = (\hat{E}_\gamma - \hat{E}_\rho)^2 - (|\hat{\vec{q}}| - |\hat{\vec{p}}_\rho|)^2$, where all variables are defined in the photon-nucleon center of mass system [Mei00]. Since the proton stays intact, $M_X = M$, and $\Delta E = 0$. The transverse momentum transfer t' follows a steep exponential distribution (see Eq. 2.92). The experimental resolution smears the reconstructed values of ΔE to a Gaussian distribution with a width of around 200 MeV. The standard set of cuts applied to select elastic ρ^0 production events is summarized in the left column of table 3.8, labeled by 'Clean Sample'. In the right column of this table, labeled 'Distributions', cuts are defined that are later used for the comparison of kinematic distributions with the MC. They are less strict in the sense that they allow more non-exclusive background. The third cut is applied on unclassified hadrons. It rejects kaons from the decay of exclusive ϕ that would be reconstructed to masses in the ρ^0 region and to small ΔE when applying the pion hypothesis. The cut on $M_{KK} > 1.06$ ensures that the invariant mass of the two hadrons with the kaon hypothesis is larger than that of the ϕ.

The mass distribution for events with exactly one positron and one negative and one positive hadron is shown in the top left plot of figure 3.26. For comparison, in the bottom left the mass distribution for events with all cuts (except for that on $M_{\pi\pi}$) is shown. The vertical lines indicate the range of the mass cut applied to select ρ^0 events. The shaded area in the top plot is the same histogram as in the one in the bottom. The ΔE distributions are displayed in the right plot of this figure, once for all three track events with $0.6 < M_{\pi\pi} < 0.94$ GeV and once with the additional cut on $-t' < 0.4$ GeV^2. The cut on t' reduces background mainly in the region of high ΔE, not so much in the exclusive region (to the left of the vertical line). The data in this plot were obtained

	'Clean' Sample	Distributions
Number of reconstructed tracks	3 ($e'h^+h^-$)	
z-vertex differences	$\lvert z^{e^+}_{vtx} - z^{h^\pm}_{vtx}\rvert < 20$ cm, $\lvert z^{h^+}_{vtx} - z^{h^-}_{vtx}\rvert < 20$ cm	
mass ($M_{K^+K^-}$)	$M_{KK} > 1.06$ GeV	
mass ($M_{\pi^+\pi^-}$)	$0.6 < M_\rho < 0.94$ GeV	$0.6 < M_\rho < 0.95$ GeV
t'	$-t' < 0.4$ GeV^2	$-t' < 1$ GeV^2
ΔE	$\Delta E < 0.6$ GeV	$\Delta E < 1$ GeV

Table 3.8:
The cuts applied to ρ^0 candidates for cross section analysis (left column) and for kinematic distributions (right column).

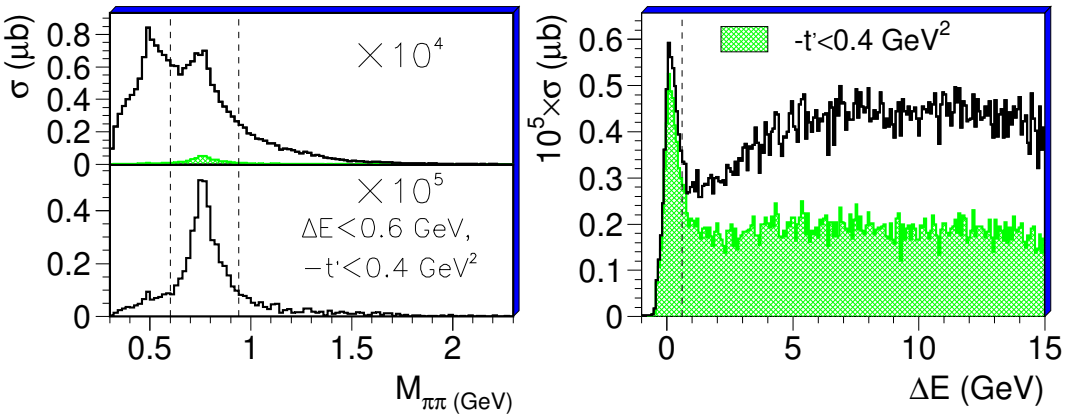

Figure 3.26: Observed cross sections for the process $ep \to e'h^+h^-$. Left: The invariant $\pi^+\pi^-$ mass distribution. The top plot is scaled by a factor 10^4, the bottom plot by 10^5. Right: ΔE distributions, scaled by a factor 10^5. See text for details.

imposing additional kinematic cuts on

$$Q^2 > 0.1 \text{ GeV}^2,\ W^2 > 10 \text{ GeV}^2,\ y < 0.91. \tag{3.43}$$

Some of the comparisons in section 4 were performed using the combined data set of the 1997 polarized and unpolarized hydrogen data. In those cases a cut on

$$y < 0.85 \tag{3.44}$$

is applied in order to take into account the higher calorimeter threshold for trigger 21 in use for the unpolarized data taking. The systematic error due to inefficiencies of the trigger and the PID system can be estimated using the same method as for the semi-inclusive cross section, Eq. 3.41. Since the trigger efficiency for three track semi-inclusive events is nearly one for polarized data, the only relevant errors come from the PID-cut efficiency for the positron and the two hadrons. The total systematic error (aside from the normalization) amounts to less than 1.3%. What is more crucial is the efficiency of the ΔE cut, i.e., the fraction of exclusive events contained within $\Delta E < 0.6(1)$ GeV. This efficiency is different between 1997 and 2000 due to the decreased resolution of the spectrometer after the implementation of the RICH. The efficiency is difficult to estimate since a Monte Carlo simulation would be necessary that can reproduce the width and shape of the reconstructed ΔE distribution of the data. As it is the purpose of this analysis to merely compare normalized distributions to Monte Carlo, it should be sufficient to compare the data to MC within the ΔE cuts with a good enough detector model employed for the smearing.

3.4.3 Photoproduction Cross Sections

In the quasireal photoproduction regime there are two important cross sections to be analyzed. One is the inclusive hadron production cross section, and the other one is the 'exclusive' pion pair production cross section. 'Exclusive' here means exclusive by detection, i.e., only a $\pi^+\pi^-$ pair is reconstructed. As in the semi-inclusive case it is possible that other particles were produced but were not accepted by the spectrometer. Unfortunately, there is no kinematic quantity in photoproduction that can be used to reduce non-exclusive background.

The number of detected photoproduction events is mainly influenced by the efficiency of the trigger system. The main trigger at HERMES (trigger 21) is most efficient for events with a positron, for hadrons this trigger has an efficiency of only $\sim 30\%$ on average. There is another hadron trigger, trigger 28, that is most efficient (about 70%) for events with at least one track in each half of the detector. For the specific mixture of inclusive or 'exclusive' photoproduction events it is necessary to know the efficiency of the combination of triggers 21 and 28 (in 2000 there is an additional trigger 22 that is similar to trigger 28 and often redundant) and to correct the cross section for the inefficiency. The exact procedure of calculating the efficiency and correcting the data event wise is described in section A.3. In fact, each event is weighted by a factor $\frac{1}{\epsilon}$ according to the momenta of the particles and the topology, i.e., its potential to generate a certain set of triggers. The resulting inclusive cross section is shown in figure 3.27 for positive and negative hadrons in 1997 as a function of momentum, and for pions with $4 < p < 13.8$ GeV as a function of the lab transverse momentum. The largest systematic error on the 'Photoproduction' cross section comes

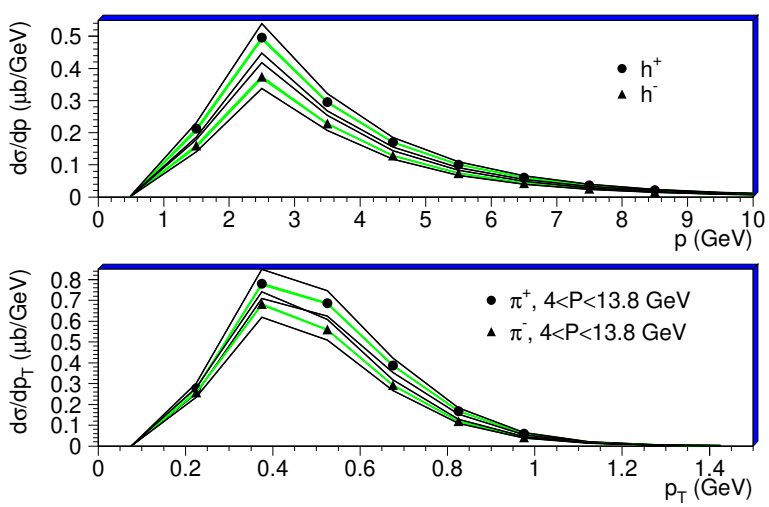

Figure 3.27: Observed differential 'Photoproduction' cross sections for hadrons vs. p (left) and for pions vs. p_T (right) from the 1997 polarized hydrogen data. The lines around the data points indicate the total systematic error, the shaded band the contributions from the uncertainty of the trigger efficiencies and the error due to the PID-cut efficiency to the systematic error only.

from the uncertainty in the luminosity normalization. Errors from the uncertainty in the applied trigger efficiencies and due to the PID-cut inefficiency are less than $\pm 1\%$. The lab momentum and transverse momentum are, aside from the azimuthal distribution, the only independent observables for inclusive photoproduction. The hadron momentum is correlated to the virtual photon energy ν and the its fraction z of the energy the hadron acquires during the fragmentation process. The lab transverse momentum is correlated to the angle of the virtual photon and to the transverse hadron momentum with respect to that of the virtual photon. It is not possible to retrieve further information on the underlying kinematics of the event from the data. If information about the event kinematics is necessary – as for the interpretation of the 'Photoproduction' asymmetries – it has to be obtained from Monte Carlo, thereby relying completely on the specific Monte Carlo model.

The cross section for 'exclusive' pion pair 'Photoproduction' is displayed in figure 3.28 as a function of the invariant mass of the $\pi^+\pi^-$ system. The contribution from events where the pion pair is completely contained in one detector half is shown separately in the shaded area. It is dominant in the mass region below the ρ mass. Within the ρ mass region between 0.6 and 0.94

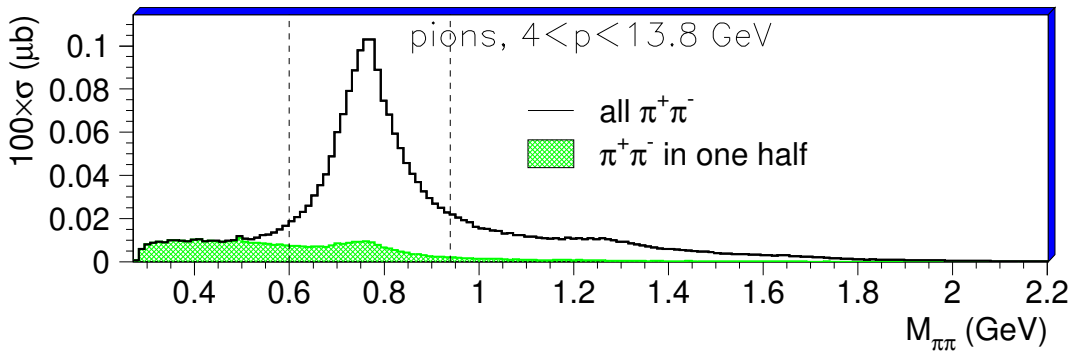

Figure 3.28: Observed cross sections for the process $ep \to \pi^+\pi^-$ as a function of the invariant mass. See text for details.

GeV (indicated by the vertical lines) the fraction of events with one pion in the top and one in the bottom half of the detector is larger than 90%. The mass distribution of these two types of events can be explained by the spectrometer acceptance. In the laboratory system a small invariant mass corresponds to a small opening angle between the two pions. This small angle is not enough to bridge the gap between the two detector halves, such that low mass pions can only be detected in either half of the spectrometer. The reason that at higher masses events with one track in each half dominate is not only that this is made possible by the larger opening angle, but mainly the fact that in the top-bottom configuration the total momentum of the $\pi\pi$ system lies close to the beam axis. It is therefore highly probable that the particles have been produced at small virtual photon angles, corresponding to small Q^2 and a larger cross section. The total systematic error from the uncertainty of the trigger efficiencies is 1.1%, the error arising from the PID-cut efficiency is 0.5%. Again, the dominating source of the systematic error on the cross section is the normalization uncertainty.

Chapter 4

Adaption of PYTHIA 6.2 to the HERMES Data

For the extraction of the polarized gluon distribution from the HERMES data on high-p_T hadron asymmetries the knowledge about the subprocesses contributing to the observed asymmetries is most crucial. This information can be obtained from Monte Carlo. Two Monte Carlo models are in principle available for this task. One of them is the LEPTO [Ing97a] generator which covers the semi-inclusive region of HERMES, but simulates only the leading order and next to leading order processes in DIS. It is not applicable for the simulation of quasireal photoproduction data. The other Monte Carlo generator is PYTHIA 6.2 [Sjö01], which in contrast to LEPTO contains a model of soft (non-perturbative) as well as perturbative DIS processes and spans the whole region from real and quasireal photoproduction to high Q^2 DIS. For this reason, PYTHIA was chosen to be the generator used to derive the final results of this analysis. In order to achieve some reliability of the Monte Carlo information it has to be shown that the model describes the data in the relevant observables. This chapter deals with a number of studies performed to compare Monte Carlo data mainly from PYTHIA, but also from LEPTO and other Monte Carlo models to the HERMES data.

4.1 The PYTHIA 6.2 Generator

In this section, some basics of Monte Carlo in general and of PYTHIA 6.2 in particular will be introduced.

4.1.1 Monte Carlo Methods

The application of Monte Carlo techniques in high energy physics event generators is twofold. On the one hand, there is the simulation of events in a physical process which is intrinsically random by virtue of quantum mechanics. On the other hand, Monte Carlo methods are used for the efficient integration of (often multidimensional) functions, for instance a differential cross section in one or more phase space variables. The general problem is to generate events according to a known distribution $f(x)$. In this probabilistic approach the function $f(x)$ has to be non-negative within the allowed range $x_{min} \leq x \leq x_{max}$. A phase space variable x has to be picked at random, such that the probability to find an event with a given x is proportional to $f(x)$. There are three basic methods to find such an x:

1. The integral of the distribution is the total area under $f(x)$. A fraction R of this area should then be to the left of x:

$$\int_{x_{min}}^{x} f(x)dx = R \int_{x_{min}}^{x_{max}} f(x)dx = R\left(F(x_{max}) - F(x_{min})\right), \qquad 0 \leq R \leq 1, \tag{4.1}$$

If $f(x)$ is simple so that it can be analytically integrated, and the integral is invertible, then

$$x = F^{-1}\left[F(x_{min}) + R\left(F(x_{max}) - F(x_{min})\right)\right]. \tag{4.2}$$

For a series of random numbers R_i the distribution of x_i then follows $f(x)$ by construction. The integral of the distribution function can then be computed by summing the values $f(x_i)$:

$$I = \frac{1}{N}\sum_{i=1}^{N} f(x_i)\left(F(x_{max}) - F(x_{min})\right), \tag{4.3}$$

where the 'Jacobian factor' $(F(x_{max}) - F(x_{min}))$ is necessary if $f(x)$ is not normalized (i.e., the area under $f(x)$ is not 1) or if the range of x is limited to a certain fraction of the allowed range. For large N, this estimate of the integral converges to its true value as $1/N$.

2. Often the function of interest is not as simple for method 1.) to work. If the maximum of the distribution is known $f(x) \leq f_{max}$ the accept–reject method can be applied:

   a) In the first step, x is chosen with uniform probability in the allowed range: $x = x_{min} + R_1(x_{max} - x_{min})$ by selecting first a random number R_1 with $0 \leq R_1 \leq 1$.

   b) In the next step, a new random number R_2 is compared with the ratio $f(x)/f_{max}$, if $R_2 < f(x)/f_{max}$, x is retained, otherwise it is rejected and the process is started again from point a).

   The probability that $f(x)/f_{max} > R_2$ is proportional to $f(x)$, so again the distribution of the x_i follows $f(x)$. This 'hit or miss' method has of course a smaller efficiency than method 1.), but has the advantage that no integration is needed. To find the Monte Carlo integral with this method, the $f(x_i)$ have to be summed over all tries:

$$I = \frac{1}{N_{tries}}\sum_{i=1}^{N_{tries}} f(x_i)\left(x_{max} - x_{min}\right). \tag{4.4}$$

3. If a simple function $g(x)$ exists, for which the integral and the inverse of the integral is known, and for which $f(x) \leq g(x)$ for all x of interest, a combination of method 1.) and 2.) can be applied:

   a) In the first step, x is selected from $g(x)$ using method 1.)

   b) In the next step, a new random number R_2 is compared with the ratio $f(x)/g(x)$, the value is retained if $R_2 < f(x)/g(x)$. If this is not true, the chosen x is rejected and a new value needs to be picked from point a).

   The probability to choose a point x in step a) is $P_1(x) = g(x)dx$, the probability to keep this value in step b) is $P_2(x) = f(x)/g(x)$, the total probability to choose a particular x is then $P(x) = P_1(x)P_2(x) = f(x)dx$ which is what is desired.

Several other, more complicated methods are available in order to improve the efficiency and to comply with more complicated situations. A description of the presented and other methods can be found, in more detail, for instance in Refs. [Sjö01], [Blo98] and [Wei00].

4.1.2 The Hermes Monte Carlo Implementation

For some issues discussed below it is important to understand how in general the Monte Carlo is implemented into the HERMES software. This will be explained in the following. A number of 'physics' Monte Carlo generators is available in the standard HERMES software for various physics analyses, among them LEPTO, PEPSI [Man92a] (a modified LEPTO version capable of

integrating polarized cross sections), PYTHIA and others with more specific applications. All generators are integrated into a general scheme based on the KUIP language and the FFREAD package contained in the CERN library [Cer03]. In this frame it is possible to define certain options of the generation range, model parameters and selectors [1]. The 'physics' generators are part of a complete Monte Carlo chain, in which their information is next fed into a GEANT [Cer03] adaption for the HERMES detector called HMC. With GEANT the interaction of the particles generated by the 'physics' generators with the detector material is simulated, and 'detector information' on the particles traversing the spectrometer is generated. Eventually, the output of HMC is proceeded further within the ordinary track reconstruction scheme. At this stage, Monte Carlo data are treated as if they were real data. The information from every stage is stored in an ADAMO based format and kept throughout the procedure. It is also possible to stop the chain before invoking HMC, if this is not desired.

The HMC stage is very time-consuming, and for some purposes it was shown to be sufficient if the effects of the detector geometry, material and resolution are 'simulated' with a much faster program. This program is called HSG (HERMES Smearing Generator) [Men01]. It works as follows:

1. A sample is generated with a 'physics' generator.

2. From this sample, the fraction of particles passing the cuts on the momentum dependent, geometrical acceptance of the spectrometer (The acceptance function is momentum dependent due to the bending of angles in the field of the spectrometer magnet) is analyzed. This can be done using a lookup table of the magnetic field and the information about the geometrical parameters of the spectrometer magnet and the calorimeter (as the point that has to be reached by a 'full' track).

3. The momentum of each of the particles passing these cuts is smeared according to a smearing function using Monte Carlo methods again. The smearing function can be obtained for every particle type by comparing a fully tracked MC sample with a sample with particles fulfilling only the acceptance cuts on the level of step 2.). In the smearing function also losses of tracks due to smearing out of the acceptance and decays of charged hadrons to muons are taken into account.

For most of the applications in this analysis the smearing generator is used.

The 'physics' generators are integrated into a common FORTRAN frame called 'GMC'. All available codes in this frame are consequently labeled by the prefix 'gmc' (that is, instead of the stand alone generators, normally 'gmc_PYTHIA', 'gmc_PEPSI' etc. are used). Some more elaborate frame exists for the combination of PEPSI or LEPTO with a generator of inclusive DIS events. This hybrid is called 'gmc_DISNG'. The installation if this code was motivated by the need to introduce (polarized) QED radiative corrections to LEPTO (PEPSI) using the RADGEN 1.0 code [Aku99]. A consequence of QED radiation at HERMES is that not for all DIS events a hadronic final state is produced because photon radiation off the lepton may reduce its energy by that large an amount that only elastic *ep* scattering is possible. LEPTO and PEPSI are not capable of simulating such a final state, but nevertheless these elastic events constitute a background in the inclusive DIS data. The hybrid gmc_DISNG cures this problem by including QED corrections as well as the capability of generating inclusive DIS events without the need for a final hadronic state. In this thesis gmc_DISNG will be used for comparisons to data and to PYTHIA such that it is worthwhile to describe how it works:

[1] With a selector it is possible to define certain event topologies to be accepted, for instance to require the scattered positron and a $\pi^+\pi^-$ pair to be within the geometrical acceptance of the spectrometer, with the mass of the $\pi^+\pi^-$ pair to be around 0.5 GeV. This reduces the generated Monte Carlo sample to a K_s sample and optimizes analysis and disk usage for some specific applications.

- The kinematics of the virtual photon, (y, Q^2), are picked by gmc_DISNG, where two independent inclusive variables are chosen according to a simple function (a flat distribution or $f(x) = 1/x$). The two inclusive variables have the meaning of observed quantities.

- gmc_DISNG calculates the derived kinematic quantities and the Born level cross section. This cross section can either be calculated from a parametrization of world data on $F_2(x, Q^2)$ or from the parton model $F_2 = \sum x e_q^2 q(x)$, where the $q(x)$ are taken from one of the PDF sets available.

- For a Born level Monte Carlo the kinematics would be handed over to LEPTO or PEPSI for the choice of the struck quark according to the parton distributions, and for the generation of the hadronic final state.

- The information on the cross section from LEPTO (PEPSI) is not used. Instead the event is weighted with the cross section calculated by gmc_DISNG:

$$w_i = \sigma_{Born}(y, Q^2) \cdot W_y(\Delta y, \Delta Q^2, f(y, Q^2)), \tag{4.5}$$

  where $W_y(\Delta y, f(y))$ stands for the integral of the user selected generation function within a specified range (the Jacobian factor), and $\sigma_{Born}(y)$ is the corresponding differential Born cross section.

- If radiative corrections are to be calculated, gmc_DISNG would hand the selected kinematics first to RADGEN which calculates the observed cross section and eventually generates a bremsstrahlung photon. How this is exactly done is described in appendix B.2.

The information about the actual distribution and cross section of events is stored in the event weights w_i that need to be applied in order to obtain meaningful Monte Carlo distributions. The important point is that with gmc_DISNG inclusive events can be generated without invoking LEPTO or PEPSI at all. The implementation of RADGEN in gmc_DISNG within the standard HERMES software will be used as a reference for the realization of QED radiative corrections in PYTHIA, as described in appendix B.2.

4.1.3 The Physics of PYTHIA 6.2

The important part of the PYTHIA model for this analysis is the description of the $ep(n)$ cross section through the properties of the emitted virtual photon and the nucleon. This model can be used by choosing the option γ^*/e to define the beam particles. The authors of PYTHIA 6.2 aim at a smooth interpolation between real photoproduction ($Q^2 = 0$) data and the truly deep inelastic region ($Q^2 \to \infty$), see for instance Ref. [Fri00] and [Schu93]. The main event classes considered to be part of the total photon-nucleon cross section are pictured in figure 4.1. Only the basic graphs are depicted, additional partonic activities are allowed in each class. See also section 2.5 for some more detailed description of the physics motivation.

The meaning of these three diagrams is about as follows:

a) is a picture of a VMD process where the photon is 'resolved', i.e., it turns into a vector meson with the same quantum numbers as the photon before the interaction with the nucleon. The description is that of hadron–hadron scattering where processes like elastic and diffractive scattering, but also soft and hard non-diffractive processes are included. Hard non-diffractive VMD processes proceed via the exchange of a hard gluon. The initial (beam) partons are generated according to parton distributions of the *vector meson*. In soft non-diffractive VMD processes, the (valence-like) parton distributions of the vector meson as well as that of the nucleon are modeled using SU(3). A soft gluon is exchanged between the two partons, and the final state hadrons are smeared in transverse momentum only by the hadronization process.

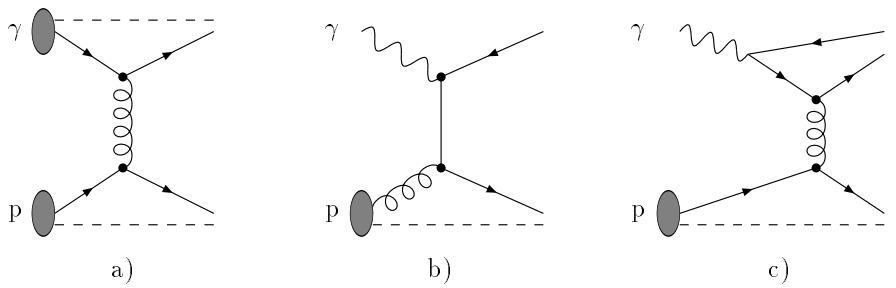

Figure 4.1: Possible event classes in γp interactions: a) VMD, b) direct photon and c) anomalous photon events. The dashed lines indicate the possible beam remnants from spectator partons. Partons giving rise to high-p_T jets (in hard interactions) are represented by the full lines.

b) depicts a 'direct' photon process, the interaction of a bare photon with the nucleon. For real photons, only Photon-Gluon Fusion and QCD Compton scattering are allowed, virtual photons can also be absorbed by partons of the nucleon in the leading order (LO) DIS process.

c) is an example of the anomalous photon processes. The photon is 'resolved' but it splits into partons perturbatively, and one of these partons interacts with a parton of the nucleon. Then all kinds of QCD $2 \to 2$ processes are allowed, such as $q_i q_j \to q_i q_j$, $q\bar{q} \to gg$ and so on. The difference to the hard non-diffractive processes in a) is that here the parton distributions of the *photon* are relevant.

The three event classes are distinguished by means of their beam remnants. Usually the nucleon will always leave a remnant with the 'spectator' partons. Resolved photons will also leave a beam remnant, except for the very distinct case of elastic and single diffractive VMD events. In soft, non-diffractive VMD processes the remnant will normally have small primordial k_T (transverse momentum) smearing, whereas for the anomalous class the 'beam remnant' coming from the $\gamma \to q\bar{q}$ splitting has a well defined k_T from some cutoff $k_0 \approx 0.5$ GeV onwards. The direct photon does not leave a remnant, all its energy goes into the hard subprocess.

The total γp cross section is the sum of the three contributions

$$\sigma_{tot}^{\gamma p} = \sigma_{VMD}^{\gamma p} + \sigma_{direct}^{\gamma p} + \sigma_{anomalous}^{\gamma p}. \tag{4.6}$$

The admixture of these event classes is done according to the scales involved. The 'hard' process of $\mathcal{O}(\alpha\alpha_s)$ is basically always the same. An exception exists if the photon is virtual. Then the LO DIS process which is of order α can contribute as well. The relevant scales for for γp and $\gamma^* p$ interactions are shown in figure 4.2. So the decision about which class an event belongs to is made in the real photon case by comparing the two scales set by k_T and p_T, the transverse momenta of partons emerging from the photon and the proton side. On the right side of figure 4.2 a third scale is introduced for interactions with virtual photons, the photon virtuality Q^2. The basic concept of combining these processes looks like this:

- If $k_T < k_0$, the transverse momentum at the $\gamma \to q\bar{q}$ vertex is small and the process is VMD.
- If $k_T > k_0$, there are two possibilities:
  a) $k_T > p_T$, then the hard process would be $\gamma g \to q\bar{q}$, with the gluon being part of the gluon distribution in the nucleon, and the photon is direct.
  b) $k_T < p_T$, then the hard process would be $q\bar{q}' \to q\bar{q}'$, a completely different process, where the $q\bar{q}$ at the photon vertex is the part of the quark distribution inside the photon. This is an anomalous process.

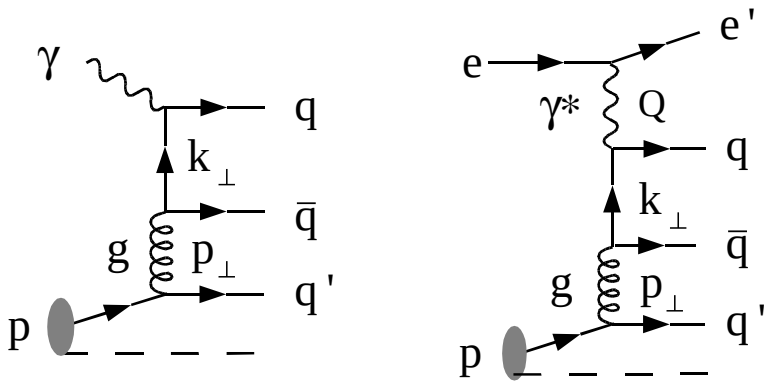

Figure 4.2: Left: Schematic diagram of the hard subprocess in γp interactions, with two different scales. Right: Schematic diagram of the hard subprocess in $\gamma^* p$ interactions, with three different scales.

The direct and anomalous event classes are thus subdivided along $k_T = p_T$.

An additional classification needs to be done for virtual photons, comparing Q^2 with k_T^2 and p_T^2:

- The LO DIS process is usually considered when $Q^2 > k_T^2 > p_T^2$.
- The situation when $k_T^2 > Q^2 \gg p_T^2$ corresponds to $\mathcal{O}(\alpha_s)$ corrections to LO DIS, the two processes $\gamma^* g \to q\bar{q}$ (PGF) and $\gamma^* q \to qg$ (QCDC). For large enough Q^2 this process is implicitly included in the *total* DIS cross section, and shows up in the (logarithmic) scaling violation of F_2. The dividing line $k_T^2 > Q^2$ is somewhat arbitrary and was introduced to extrapolate to the region of small $Q^2 \to 0$ where the LO DIS process should be vanishing, but not the $\mathcal{O}(\alpha_s)$ processes.

PYTHIA models the elastic and diffractive VM cross section with the description of the total γp and the hadronic cross sections σ^{Vp} from Donnachie and Landshoff ([Don92]) and the additive quark model [Lev65, Lip66]. The total VMD cross section is then (Eq. 2.93)

$$\sigma_{VMD}^{\gamma p}(s) = \sum_V \frac{4\pi\alpha_{em}}{f_V^2}\sigma_{tot}^{Vp}, \tag{4.7}$$

For a virtual photon, the splitting probability is suppressed with Q^2 by a factor $\left(\frac{m_V^2}{m_V^2+Q^2}\right)^2$ (see Eq. 2.98). Single and double diffractive events are modeled by a pomeron-type parametrization, whereas the elastic cross section also contains the Regge behavior for small energies. The non-diffractive part of VMD is the difference of the sum of elastic and diffractive cross sections to the total σ^{Vp} cross section.
For the purpose of unitarization at really high energies, VMD processes are not cut off at $k_T \leq k_0 \approx 0.5$ GeV, but at a much higher value k_1 depending logarithmically on W^2 (about 1.4 GeV at the HERMES energy). The region in between these two scales is the so called GVMD region where the photon does split into $q\bar{q}$ perturbatively, but it interacts just like a vector meson with the same quark content (i.e., $u\bar{u}$ and $d\bar{d}$ like ρ and ω, $s\bar{s}$ like ϕ). The spectrum of these 'diffractive states' gives rise to a non-resonant, or non-diagonal, contribution to the VMD cross section. Hard non-diffractive VMD processes are incorporated into the GVMD region together with the anomalous processes.
For the direct part of the cross section, σ_{dir}, the following ansatz is used:

$$\sigma_{dir}^{\gamma^* p} \simeq \sigma_{DIS}^{\gamma^* p} = \sigma_{LODIS}^{\gamma^* p} + \sigma_{PGF}^{\gamma^* p} + \sigma_{QCDC}^{\gamma^* p} = \left(\frac{Q^2}{Q^2+m_\rho^2}\right)^m \frac{4\pi\alpha_{em}^2}{Q^2} F_2(x,Q^2). \tag{4.8}$$

The first factor in front of F_2 is there to prevent $\sigma_{DIS}^{\gamma^* p}$ from going to infinity as $Q^2 \to 0$. $m = 0, 1, 2$ can be changed by a switch in PYTHIA. The PYTHIA default is $m = 2$, making σ_{DIS} vanish in the limit $Q^2 \to 0$. This again would lead to $\sigma_{LODIS} < 0$, because σ_{PGF} and σ_{QCDC} stay finite in the $Q^2 \to 0$ limit. In order to avoid this, the LO DIS cross section is exponentially suppressed by a Sudakov form factor:

$$\sigma_{LODIS}^{\gamma^* p} = \sigma_{DIS}^{\gamma^* p} - (\sigma_{PGF}^{\gamma^* p} + \sigma_{QCDC}^{\gamma^* p}) \quad \longrightarrow \quad \sigma_{DIS}^{\gamma^* p} \exp\left(-\frac{\sigma_{PGF}^{\gamma^* p} + \sigma_{QCDC}^{\gamma^* p}}{\sigma_{DIS}^{\gamma^* p}}\right). \tag{4.9}$$

In reality, and especially at HERMES energies, the scales p_T, k_T and Q^2 might be close to each other such that it is sometimes not possible to unambiguously choose an event type. There is a variety of possible treatments and suppression factors to avoid double counting in those cases. The factor

$$\left(\frac{W^2}{W^2 + Q^2}\right)^n = (1 - x)^n \tag{4.10}$$

with $n \simeq 3$ being a tunable parameter is used to suppress VMD with respect to the LO DIS process in the region where $Q^2 > k_T$, but $k_T < k_1$, i.e. a region where it cannot easily be decided whether the event still belongs to the resolved or already to the direct class. Altogether, the PYTHIA cross section model for $\gamma^* p$ interactions forms like this:

$$\begin{aligned} \sigma_{tot}^{\gamma^* p} &= \sigma_{DIS}^{\gamma^* p} \exp\left(-\frac{\sigma_{PGF} + \sigma_{QCDC}}{\sigma_{DIS}}\right) + \sigma_{PGF}^{\gamma^* p} + \sigma_{QCDC}^{\gamma^* p} \\ &+ \left(\frac{W^2}{W^2 + Q^2}\right)^n \left(\sigma_{VMD}^{\gamma^* p} + \sigma_{GVMD}^{\gamma^* p}\right). \end{aligned} \tag{4.11}$$

The conversion of $\sigma^{\gamma^* p}$ to σ^{ep} is done by weighting with a photon flux in the Weizsäcker-Williams approach (see below).

4.1.4 Strategy to Adjust PYTHIA Parameters to HERMES Data

In this section those PYTHIA parameters will be explained which seem to be relevant for the outcome of the PYTHIA model. Some of them might be considered in a tuning procedure to be adjusted to HERMES data.

- Parameters related to the general PYTHIA model

MSEL, MSTP(14)	The combination of these values defines the mixture of subprocesses switched on, for the full model in the γ^*/lepton mode, MSEL=1 or 2 and MSTP(14)=30 have to be used.
PARP(2)	Minimum cm. energy of the whole event accepted, has to be set to ≤ 7 GeV for HERMES.
MSTP(3), PARP(1)	Λ_{QCD} used in running α_s.
MSTP(15)	Treatment of the *anomalous* photon component with respect to scale choices and cut-offs of hard processes.
MSTP(18), (PARP(15))	Choice of $k_{T,min}$ for direct processes to be distinguished from GVMD/anomalous ones, either $k_{T,min}$ =PARP(15). or $k_{T,min} = 1.9\left(\frac{s}{1TeV^2}\right)^{0.08}$ GeV$\approx$ 1.4 GeV for HERMES.
MSTP(19)	Treatment of partonic F_2 in the LO DIS process (99), i.e., various options (0 to 5) for suppression factors at $Q^2 \to 0$.
MSTP(20)	Factor $(W^2/(W^2 + Q^2))^{MSTP(20)}$ to suppress resolved photon events in a region of intermediate Q^2 and

	small W^2.
MSTP(32)	The definition of the hard Q^2 scale for $2 \rightarrow 2$ processes.
MSTP(51),MSTP(55)	proton (51), photon (55) parton distribution set.
MSTP(57)	Options for the Q^2 dependence of PDFs.
PARP(91-100)	Parameters for beam remnant treatment.
PARP(111)	Minimum invariant mass of hadronic beam remnant.

- Parameters related to the PYTHIA VMD model

MSTP(17), PARP(165)	Choice of the factor $1 + \text{PARP}(165)\epsilon R$ to correct the cross sections of resolved photon processes for contributions of longitudinal photons. $R(Q^2, \mu^2(M_\rho^2))$ is chosen with options 0 to 5.
MSTP(31)	Model for the parametrization of hadronic (total, elastic and diffractive) cross sections, can be user-defined.
MSTP(102)	θ distribution of decay pions from elastically or diffractively produced ρ^0 (in the ρ^0 rest system).
MSTP(101), PARP(101)	Quark/gluon structure of a diffractive system.
PARP(15)	Minimum transverse momentum k_0 in $\gamma \rightarrow q\bar{q}$ events to separate VMD from GVMD.
PARP(18)	Scale k_ρ^2, the suppression factor of GVMD relative to VMD goes with k_ρ^2/k_T^2.
PARP(102)	Start of the mass spectrum in single- and double diffractive scattering is at M+PARP(102), where M is the mass of the excited particle. In VMD the γ has the mass of the vector meson.
PARP(103)	A diffractive state is forced to decay in a two-body chanel if its mass is less than M+PARP(103) (with M as above), otherwise string fragmentation is performed.
PARP(104)	The threshold for hadronic (resp. VMD) interactions is set to $\sqrt{s} > M_A + M_B$+PARP(104), with $M_{A(B)}$ the masses of the hadrons.
PARP(161-164)	photon-VM couplings $4\pi/f_V^2$ for $\rho,\ \omega,\ \phi,\ J/\psi$.

The third set of parameters are fragmentation parameters being part of the JETSET package [Sjö94]. At HERMES, analyses have been performed to tune the JETSET parameters by minimizing χ^2 between semi-inclusive pion, kaon and proton multiplicities from data and the LEPTO Monte Carlo, see, for instance Ref. [Hil03] for the more recent results. In the further analysis, a slight modification of the results presented there will be used (see table D.2).

The sheer number of PYTHIA parameters, the correlations among them and their complexity makes it impossible to perform a fit to data observables like in the case of the JETSET parameters for LEPTO. The strategy for 'tuning' the PYTHIA cross section parameters is rather to compare PYTHIA output to data observables sensitive to different aspects of the model, like

- The overall parametrization of the cross section
  - inclusive and semi-inclusive differential cross sections,
  - correlations between inclusive and semi-inclusive observables, i.e., two-dimensional distributions, average kinematics etc.

- The parametrization of the VMD cross section
  - exclusive $\rho(\phi)$ production cross section, missing energy distributions.
- The admixture of subprocesses, especially the ratio between the 'direct' and 'resolved' event classes
  - the ratio of pions (kaons) from exclusive $\rho(\phi)$ production to the semi-inclusive pions (kaons),
  - double spin asymmetries – since the subprocess asymmetries are different from each other,
  - to some degree hadron multiplicities and multiplicity ratios.

4.1.5 The Virtual Photon Flux Factor

As mentioned above, all cross sections in PYTHIA are calculated as virtual photon cross sections, and then converted to ep cross sections by weighting with the virtual photon flux. In the original PYTHIA code, a parametrization of the photon flux is used which is valid only for high W^2, where the target mass is negligible. This is certainly not true for all of the HERMES kinematic region. The cross section in PYTHIA is:

$$\frac{d\sigma^{ep}}{d\log y\, d\log Q^2} = \Gamma_T(1+\epsilon R)\frac{d\sigma^{\gamma^* p}}{d\log y\, d\log Q^2} \quad \text{with } \Gamma_T = \frac{\alpha_{em}}{2\pi}\left(\frac{1+(1-y)^2}{y}\frac{1}{Q^2} - \frac{2m_e^2 y}{Q^4}\right). \quad (4.12)$$

A more suitable expression for the photon flux was inserted instead of this approximation (cf. Eq. 2.19):

$$\Gamma_T \quad \rightarrow \quad \frac{\alpha_{em}}{2\pi}(1-x)\left(\frac{1+(1-y)^2-\frac{Q^2}{2E^2}-\gamma^2 y^2}{y}\frac{1}{Q^2} - \frac{2m_e^2 y}{Q^4}\right). \quad (4.13)$$

The implemented ratio $\Gamma_L/\Gamma_T = \epsilon$ was changed accordingly, using Eq. 2.20. A difference between the original PYTHIA flux factor and the modified one exists mainly at small W^2 where the proton mass is relevant. This can be seen in figure 4.3 where the two flux factors are compared for three Q^2 values. The ratio of fluxes ϵ does not change significantly. Note that not all of the y range is

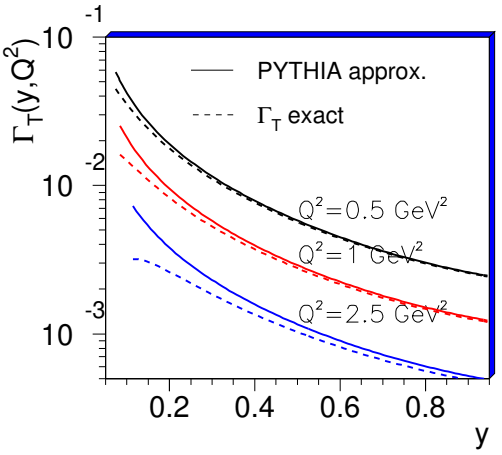

Figure 4.3: The approximation of the photon flux $\Gamma_T(y, Q^2)$ used by PYTHIA (solid lines) compared to the more accurate formula for HERMES kinematics (dashed lines). The values are calculated for $Q^2 = 0.5,\ 1,\ 2$ GeV^2 from top to bottom respectively.

kinematically accessible for all Q^2 in the figure, due to the lower limit on $W^2 > 4$ GeV for PYTHIA.

4.2 Implementation of QED Radiative Corrections to PYTHIA

Cross sections in PYTHIA are calculated on the Born level, i.e, neither the radiation of a photon by the incoming (or outgoing) lepton nor the radiation of a gluon by an incoming (or outgoing)

quark are taken into account for the generation of events. There are switches in PYTHIA to employ radiation off quarks (MSTP(61) and MSTP(71)) but hard cutoffs in the Q^2 scale of such radiative events prevent any noticeable effect within the Hermes kinematics. The radiation of real photons off the incoming or outgoing *lepton* is not foreseen for the γ^*/e option. QED radiative corrections can have large effects on the measured inclusive DIS cross section, but also asymmetries and the semi-inclusive cross sections are subject to corrections from QED radiation. In general it is possible to estimate the size of radiative corrections (RC) from the ratio $\sigma^{RC}(y,Q^2)/\sigma^{Born}(y,Q^2)$ that can be found by numerical integration. For many purposes this is not enough, though, for instance it might be necessary to know the true kinematics of events which migrated in phase space through the radiation of a bremsstrahlung photon. In this case, QED radiation needs to be simulated by Monte Carlo. There are two reasons to introduce RC to the PYTHIA Monte Carlo. One is that the kinematic range of the gmc_DISNG generator combined with LEPTO or PEPSI does not cover the full kinematic range of the data relevant for this analysis. The other one is more practical, in the sense that comparisons of data and Monte Carlo cross sections, kinematics etc. are much more simple if the Monte Carlo data are generated according to the *observed* cross section. Otherwise the data need to be unfolded (i.e., corrected for migration in each kinematic bin) for each kinematic distribution of interest separately. The following sections deal with the physics of QED radiative corrections and the comparisons of the results for the RC obtained with PYTHIA to those obtained from gmc_DISNG. The details of the implementation of the radiative corrections to PYTHIA are described in appendix B.2.

4.2.1 Physical Issues of QED radiative corrections

Figure 4.4 shows the contributing Feynman diagrams to the experimentally measurable inclusive or semi-inclusive cross section. The first diagram a) defines the Born cross section, diagrams b)

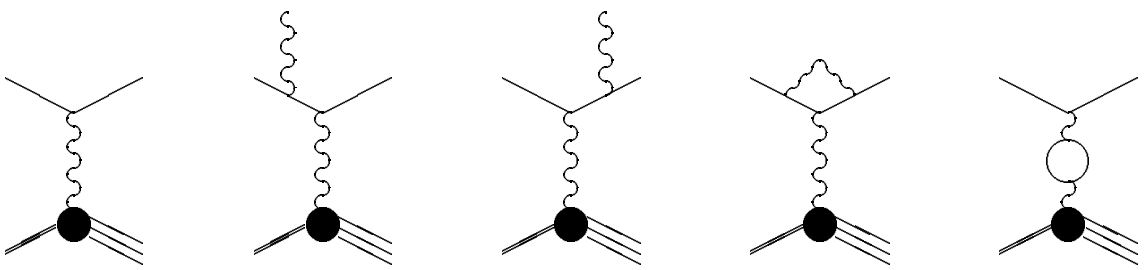

Figure 4.4: The Feynman diagrams contributing to the measured cross section at $O(\alpha^2)$ (b) to e)) and the Born diagram (a)).

and c) depict the radiation of a real photon off the incoming and the outgoing lepton, respectively (initial and final state radiation). The last two diagrams describe loop and vertex corrections at the same order in α as diagrams b) and c). In principle, the real photon of diagrams b) and c) can be detected, whereas in diagrams d) and e) no photon is actually radiated. According to the rules of quantum mechanics, the observed cross section is proportional to the square of the sum of Feynman diagrams with the same, in principle detectable final state - thus diagrams a), d) and e) may interfere with each other as well as diagrams b) and c).
Regarding the possible effects of these second order diagrams on the observed cross section in DIS, the correction to the Born level DIS cross section $\delta\sigma_{RC}$ can be written as:

$$\delta\sigma_{RC} = \sigma_{in} + \sigma_{(q)el} + \sigma_v, \tag{4.14}$$

where σ_v contains the loop corrections. σ_{in} and $\sigma_{(q)el}$ are both caused by the radiation of a real photon. Practically, an additional variable Δ for the lower cutoff on the real photon energy ω is

introduced that is necessary for the handling of infrared divergent terms of the diagrams b) and c). This cutoff Δ divides the *total* observed cross section into a radiative and a non-radiative part, where the non-radiative part is defined such that it contains the soft photon spectrum of energies from 0 to Δ as well. The radiative part of the cross section is conveniently subdivided into the 'inelastic tail' (σ_{in}), i.e., the cross section for inelastic events and the '(quasi-)elastic tail' ($\sigma_{(q)el}$), i.e. the cross section for (quasi-)elastic scattering on the proton (nucleus):

$$\sigma_{in} = \int_{\Delta}^{\omega(W_T^2=(M+m_\pi)^2)} d\omega \int_{\theta_\gamma} d\theta_\gamma \frac{d\sigma(x,y,\theta_\gamma,\omega)}{dxdyd\theta_\gamma d\omega}, \tag{4.15}$$

$$\sigma_{(q)el} = \int_{\omega(W_T^2=(M+m_\pi)^2)}^{\omega(W_T^2=M^2)} d\omega \int_{\theta_\gamma} d\theta_\gamma \frac{d\sigma(x,y,\theta_\gamma,\omega)}{dxdyd\theta_\gamma d\omega}. \tag{4.16}$$

The 'true' invariant mass (indicated by the subscript 'T') of the γ^*-nucleon system after radiation of the real photon is

$$W_T^2 = W^2 - 2\omega\left(\nu + M - \sqrt{\nu^2+Q^2}\cos\theta_\gamma\right). \tag{4.17}$$

The polar angle θ_γ of the real photon with respect to the lepton direction is the second independent variable to describe the real photon, the third variable, the azimuthal angle ϕ_γ, is omitted here. The subdivision into inelastic and (quasi-)elastic events is necessary because an inelastic event can contribute to the measured semi-inclusive cross section at shifted kinematics, whereas an elastic event cannot. In that sense the elastic scattering is an additional subprocess which is normally not handled by MC generators such as LEPTO or PYTHIA. 'Inelastic' here means that the remaining energy after the photon radiation is enough to produce at least a pion ($W_T^2 > (M_p + m_\pi)^2$).

The size of the different parts of the measured cross section can be calculated as in [Mo69], and these calculations have been implemented in the RADGEN code [Aku99] for numerical integration. The fourfold differential cross section $\frac{d\sigma(x,y,\theta_\gamma,\omega)}{dxdyd\theta_\gamma d\omega}$ does not only depend on the amplitude for the emission of a real photon with energy ω and angle θ_γ, but also on the amplitude for the absorption of a virtual photon with energy $\nu_T = \nu - \omega$ and virtuality $Q_T^2 = Q^2 + 2\omega(\nu - \sqrt{\nu^2+Q^2}\cos\theta_\gamma)$ by the nucleon. Therefore the size of the radiative correction depends directly on the model in use to describe the *ep* interactions.

The non-radiative part of the cross section, $\sigma_{Born}(x,y)$, becomes dependent on Δ due to the integration over the soft photon spectrum:

$$\sigma_{Born} = \int_0^{\Delta} d\omega \int_{\theta_\gamma} d\theta_\gamma \frac{d\sigma(x,y,\theta_\gamma,\omega)}{dxdyd\theta_\gamma d\omega}. \tag{4.18}$$

Altogether the measured cross section for a certain value of the (observed) kinematic point (x,y) becomes:

$$\sigma_{obs} = \delta(\Delta)\sigma_{Born}(1 + \delta_{Vac} + \delta_{Vert} + \delta_{sm}) + \sigma_{in}(\Delta) + \sigma_{(q)el}. \tag{4.19}$$

The factors δ_{Vac}, δ_{Vert}, δ_{sm} are corrections from vacuum polarization by lepton pairs, vertex corrections and the residuum of infrared divergent terms, respectively. The Born cross section has to be multiplied by $\delta(\Delta)$, an approximate factor accounting for infrared divergences and soft multiple photon emission. If Δ is chosen properly, that is, large enough to avoid numerical instabilities and small enough to avoid large errors inherent in the approximation of $\delta(\Delta)$, the total observed cross section should be independent of Δ. Typically (for HERMES), $\Delta \simeq 100$ MeV, also considering the experimental acceptance for photons below that energy and the resolution of the calorimeter.

One important point to remember is that in this method to calculate the radiative corrections the *Born cross section has to be known.*

4.2.2 A Structure Function for PYTHIA

Radiative corrections can only be calculated consistently for Monte Carlo data, if the cross section model used for the Monte Carlo is the same as the one used to calculate the QED corrections. For

LEPTO the solution was to introduce a new MC generator, gmc_DISNG, to calculate cross sections *and* radiative corrections at the same time (cf. sections 4.1.2 and B.1). In this case, the cross section information from LEPTO itself is not used anymore. In gmc_DISNG, RADGEN is used to obtain the RC. RADGEN accepts different parametrizations of the inelastic (DIS) cross section, in the format of a linear combination of $F_1(x,Q^2)$ and $F_2(x,Q^2)$, or $F_2(x,Q^2)$ and $R(x,Q^2)$ (see Eqs. 2.13 and 2.25). The cross section in gmc_DISNG is obtained using either a parametrization of the world data on F_2 and R, for instance from [Abr97] and [Whi90], or the parton model F_2 with a PDF set and a parametrization of R.

The situation is more complicated in the case of PYTHIA, since in the Monte Carlo approach the cross section is calculated for each generated event according to the selected subprocess, and the summed cross section over all subprocesses can only be evaluated *after* a MC run. The 'closest approach' to a parametrization of the PYTHIA cross section can probably be achieved using an approximation of Eq. 4.11, omitting the small contribution from QCD radiative processes (PGF and QCD Compton) and from GVMD. This should not disregard more than 10% of the cross section. Using

$$\sigma_T^{\gamma^* p,DIS} = \frac{4\pi^2\alpha}{Q^2(1-x)} 2xF_1^{DIS}, \quad F_2^{DIS} = \frac{2xF_1^{DIS}}{1+\gamma^2} \tag{4.20}$$

$$\sigma_T^{\gamma^* p,VMD} = \sum_V \frac{4\pi^2\alpha}{f_V^2}\left(\frac{m_V^2}{m_V^2+Q^2}\right)^n \sigma_{tot}^{Vp} \tag{4.21}$$

$$\equiv \frac{4\pi^2\alpha}{Q^2(1-x)} 2xF_1^{VMD}, \quad F_2^{VMD} = \frac{2xF_1^{VMD}(1+R^{VMD})}{1+\gamma^2}. \tag{4.22}$$

R^{VMD} is the longitudinal to transverse cross section ratio for resolved photon processes, it can be taken either from the default expression in PYTHIA (MSTP(17)=4 with PARP(165)=0.5) or from the HERMES modification of the code MSTP(17)=6 (see section 4.3). The suppression factors defined by setting the PYTHIA parameters MSTP(19)$\rightarrow m$ and (20)$\rightarrow k$ are taken into account:

$$F_1^{DIS} \rightarrow \left(\frac{Q^2}{Q^2+m_\rho^2}\right)^m F_1^{DIS} = \left(\frac{Q^2}{Q^2+m_\rho^2}\right)^m \frac{1}{2}\sum_q e_q^2 q(x,Q^2) \tag{4.23}$$

$$F_1^{VMD} \rightarrow \left(\frac{W^2}{Q^2+W^2}\right)^k F_1^{VMD}. \tag{4.24}$$

$$\tag{4.25}$$

Figure 4.5 shows a two-dimensional cross section comparison between the PYTHIA generated cross section and the parametrization (solid line). At small x the generated cross section is smaller than the parametrization, despite the fact that parts of the cross section are neglected. In this region, phase space edge effects have to be considered because the area of a bin in (x,Q^2) is not completely covered by the available phase space. The generated cross section has not been corrected for these effects, such that it comes out smaller than the parametrization. The points on the outer edge of the bins can also be explained by this effect. If the binning is made smaller, also the deviations become smaller. At high Q^2, the generated cross section is slightly larger than the parametrized one, but altogether it can be stated that the PYTHIA parametrization of F_2 relates to the generated Born cross section much better than the ALLM parametrization (shown by the dotted line in figure 4.5).

4.2.3 PYTHIA Results with Radiative Corrections

In appendix B.3 it is shown that the radiative corrections obtained from the integration of RADGEN into PYTHIA are in good agreement with those obtained from the standard HERMES Monte Carlo (gmc_DISNG) for an inclusive data sample with $W_T^2 > 4$ GeV^2 generated in the full 4π solid angle. For the semi-inclusive data including detector acceptance and smearing effects, the correction factors $\sigma_{RC}(x,Q^2)/\sigma_{Born}(x,Q^2)$ look as depicted in figure 4.6. In general there is good

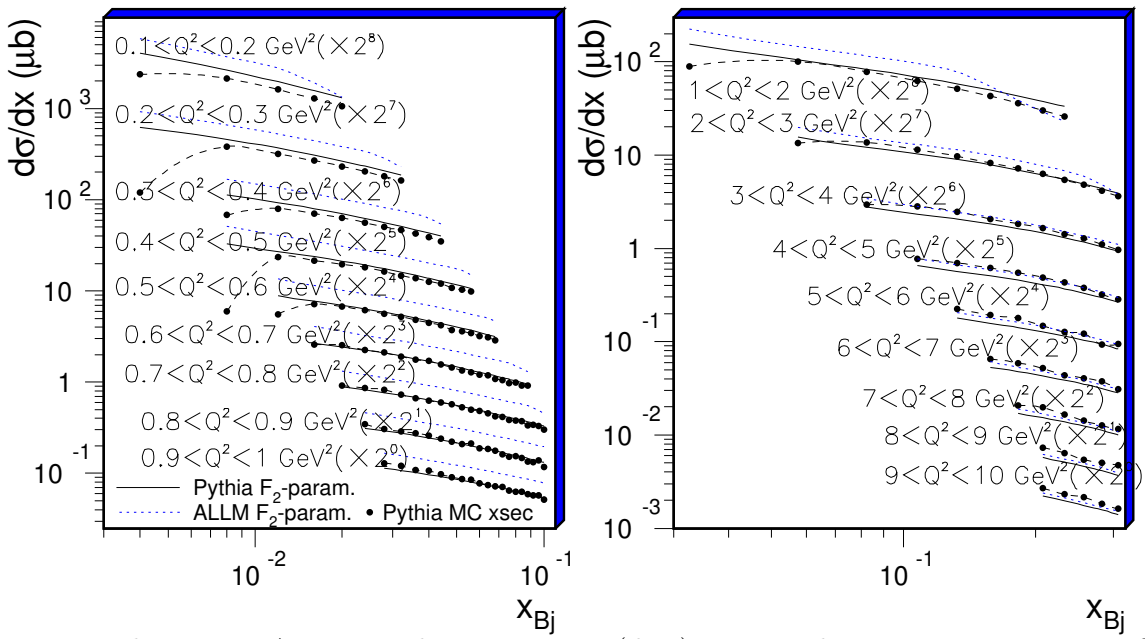

Figure 4.5: The PYTHIA generated cross section (dots) compared to a parametrization of the PYTHIA cross section (solid line) and to the cross section from the ALLM parametrization of F_2 [Abr97] (dotted line). The cross section is shown in Q^2 bins as a function of x.

agreement between the gmc_DISNG and PYTHIA radiative corrections. The large deviations at $Q^2 < 1$ GeV^2 can be explained by the limited capability of LEPTO to handle semi-inclusive events with $Q^2 < 0.5$ GeV^2, as opposed to PYTHIA where Q_T^2 can extend down to 0. A comparison of semi-inclusive cross sections from PYTHIA for pions ($2 < p < 15$ GeV) with and without RC is presented in figure 4.7, together with the observed cross sections obtained from the 2000 unpolarized hydrogen data ($\nu < 23.6$ GeV). The general effect is that the RC cross section is somewhat smaller than the Born cross section at small W^2, and higher at high W^2. A discussion on the performance of the PYTHIA model in describing the semi-inclusive cross section follows below in section 4.5. Another cross check of the results for radiative corrections would be to compare the cross section for bremsstrahlung photons from gmc_DISNG and PYTHIA with the data. For this analysis, photons were not considered, but instead of analyzing photons directly, it is also possible to check the spectra of radiated energies, i.e., the $\omega = \nu - \nu_T$ distributions of events, and compare the two Monte Carlo results with each other. As can be seen from figure 4.8 where the cross section for photons in inclusive events within full 4π geometry is shown in nine bins of Q^2 and x as a function of energy, the agreement is acceptable when considering the shapes of the distributions. The difference in the normalization is due to the difference of the *Born* Monte Carlo cross sections (see figure 4.5). For further data – Monte Carlo comparisons and the tuning of model parameters, PYTHIA will be used with radiative corrections applied.

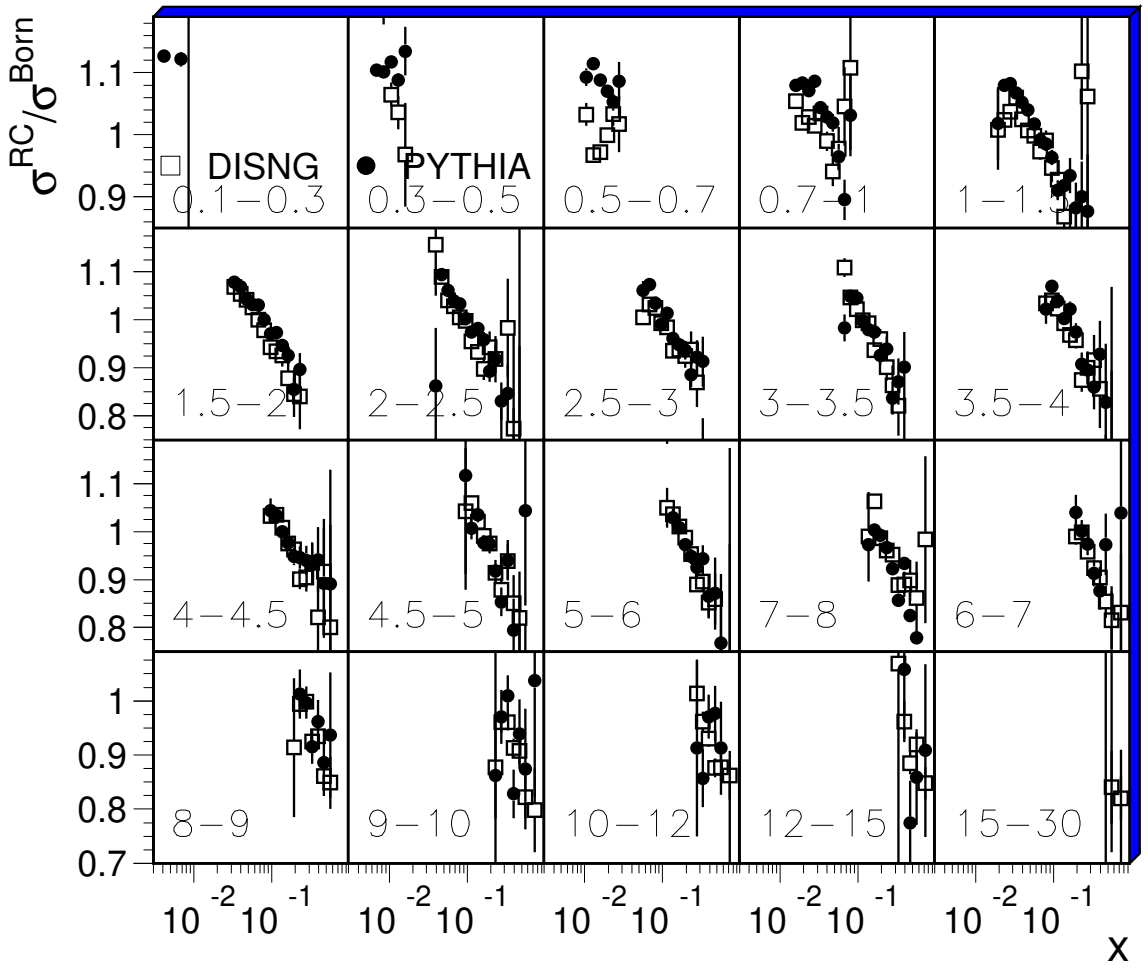

Figure 4.6: The radiative correction factors $\sigma_{RC}(x,Q^2)/\sigma_{Born}(x,Q^2)$ as a function of x for PYTHIA and gmc_DISNG for the observed semi-inclusive data. Each field corresponds to a bin in Q^2 whose range is indicated by the numbers in the field.

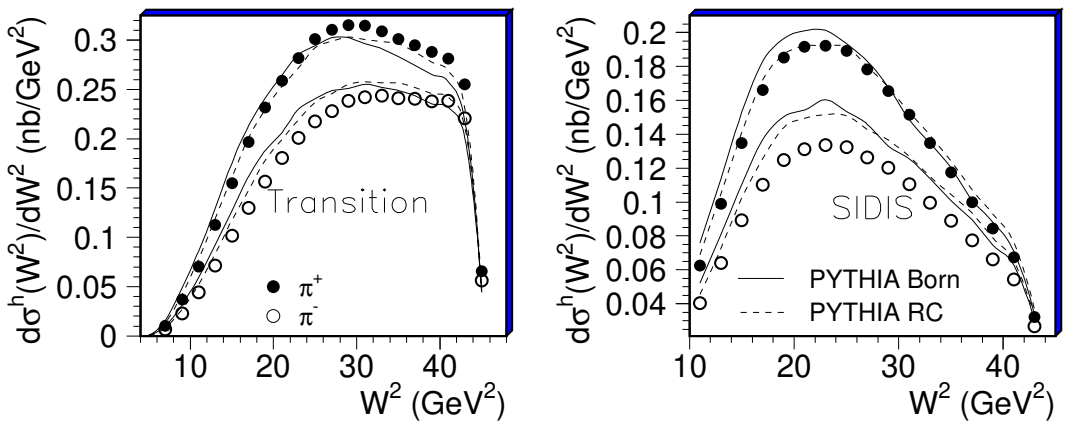

Figure 4.7: Semi-inclusive pion cross sections with and without radiative corrections from PYTHIA, compared to the 2000 H data.

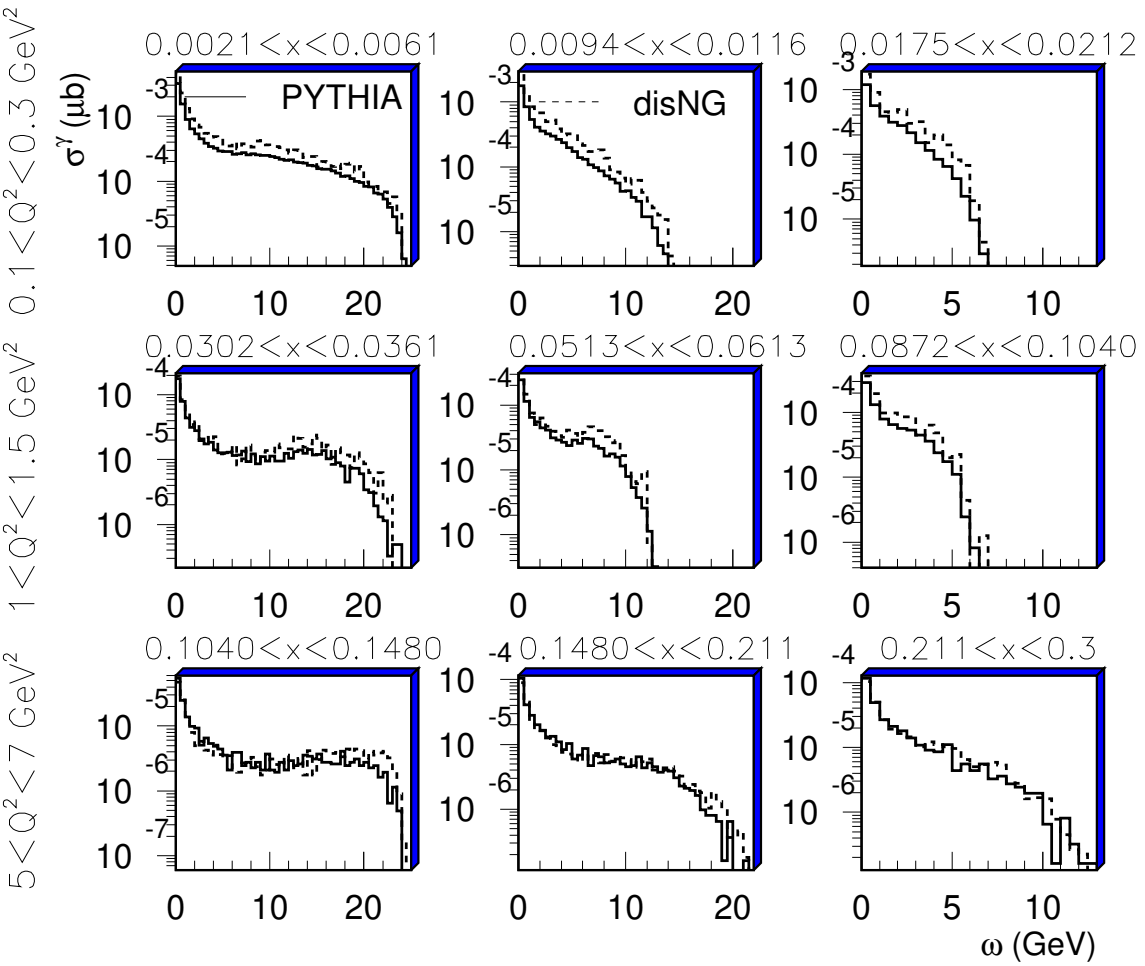

Figure 4.8: The photon energy spectra for inclusive events with $W_T^2 > 4$ GeV^2 in the full 4π phase space of events. The spectra are normalized to give absolute cross sections. The x range is given as a headline for each field, the Q^2 range is given on the left edge of each row of panels.

4.3 The Vector Meson Dominance Model in PYTHIA

This section deals with studies on the description of soft (resolved) photoproduction processes in PYTHIA. The cross sections are compared with the data and other Monte Carlo models of VMD. The rather misleading term 'resolved photoproduction' obscures the fact that the contribution of resolved photon process is also relevant for the semi-inclusive region at the rather small Q^2 accessible at HERMES. A method to estimate this contribution on the basis of data on exclusive ρ^0 (ϕ) production and a Monte Carlo acceptance correction will be introduced in section 4.4.

4.3.1 Exclusive Vector Meson Cross Sections

The exclusive ρ^0 cross section and distributions of a number of variables has been analyzed from the 1997 data (polarized and unpolarized) and Monte Carlo. The default version of PYTHIA 6.2[2] was found to give an observed cross section higher than that of the data by a factor of 6. Several reasons for this were found, and consequently the code or VMD parameters were changed in the model:

- The probably smallest, but nevertheless non-negligible effect came from the approximation of the photon flux in PYTHIA (cf. section 4.1.5) which was modified to account for effects of the nucleon mass.
- For most variables, the distributions of exclusive ρ^0 candidates or their decay pions are completely determined by the geometrical acceptance of the spectrometer and thus insensitive to the model describing the cross section in these variables. There are exceptions, though. In general, three independent angles describe production and decay of the vector meson. One is the azimuthal angle Φ between the scattering plane spanned by the incoming and outgoing positron and the 'production plane' spanned by the vectors of virtual photon and vector meson momentum. The other two are the azimuthal angle ϕ and the polar angle θ of one of the decay pions (conventionally the π^+) in the rest system of the vector meson, where the $\hat{z}$ axis is defined along the vector meson momentum in the center of mass system of the vector meson and the recoiling nucleon. The distribution of these angles depends on the spin projection $m = S_z$ of the vector meson and is described in the corresponding spin density matrix (for details, see, for instance Ref. [Schi73]). The most distinctive distribution is that of the polar decay angle, and due to the correlation of this angle to the momenta of the pions in the lab system it should also be most sensitive to the model for the spin density matrix of the vector meson. The distributions of $\cos(\theta)$ and pion momentum of experimental and PYTHIA data obtained with the cuts defined in the left column of table 3.8 is shown in figure 4.9. There is an obvious discrepancy between the data and the PYTHIA distributions. Note that the pion momentum distribution is only a consequence of the angular distribution. In most models of VMD 's-Channel Helicity Conservation' (SCHC) is presumed. SCHC has been shown to describe the HERMES data rather well [Tyt01]. The assumption of SCHC implies that the helicity of the virtual photon is retained by the vector meson. The decay angular distribution then depends only on the polarization of the virtual photon and the ratio of the hadronic cross sections of longitudinally to transversely polarized vector mesons, R_{VMD}. Integrating over the two other angles, the polar angle distribution becomes [Tyt01]:

$$\frac{d\sigma}{d\theta} = \frac{3}{4}\left(1 - r_{00}^{04} + (3r_{00}^{04} - 1)\cos^2\theta\right), \quad \text{with} \quad r_{00}^{04} = \frac{\epsilon R_{VMD}}{1 - \epsilon R_{VMD}}. \tag{4.26}$$

  where r_{00}^{04} is one of the spin density matrix elements and ϵ is the ratio of longitudinal to transverse photon flux. For $Q^2 = 0$ also $R_{VMD} \to 0$, so that $r_{00}^{04} = 0$. In this case $\frac{d\sigma}{d\theta} \sim$

[2] More specific, default means here that some of the fragmentation parameters (which are not so much relevant for the VMD model) have been adjusted to the HERMES semi-inclusive data, the code and the parameters of the VMD model were left unchanged, however.

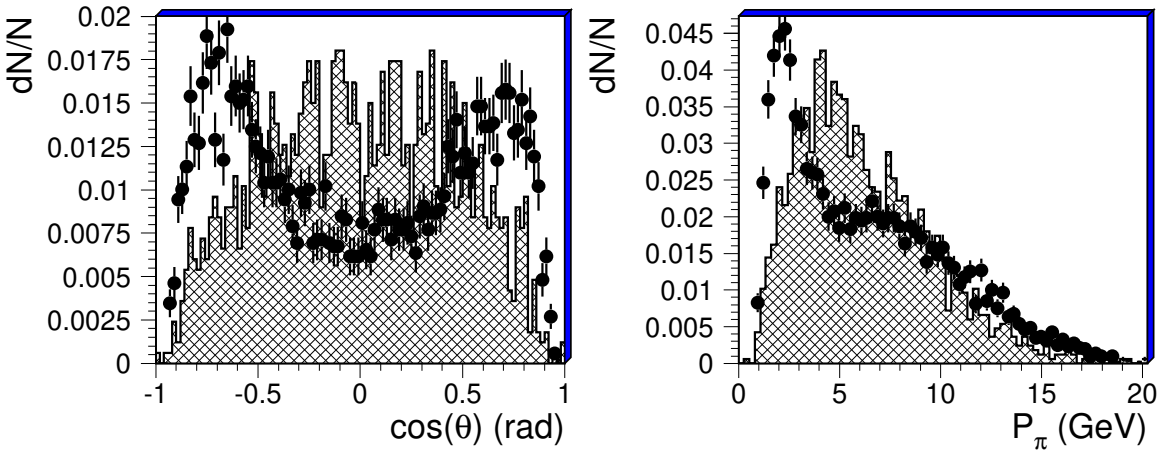

Figure 4.9: The decay angle and pion momentum distributions of exclusive ρ for the 97 data (polarized and unpolarized hydrogen - dots) compared to those of PYTHIA (proton target, acceptance simulated with momentum lookup table (no smearing) - shaded histograms). The histograms are normalized to unity.

$\sin^2\theta$. This distribution is what is modeled in PYTHIA with the option MSTP(102)=1 (the other option is MSTP(102)=0 with which a flat distribution is simulated). If $Q^2 > 0$ also $R_{VMD} = R_{VMD}(Q^2) > 0$, so that the distribution changes gradually from $\sin^2\theta$ to $\cos^2\theta$ for large Q^2. This results in a distribution as in figure 4.9 for an average $\langle Q^2 \rangle \approx 1.7$ GeV. The solution of this problem was to replace the $\sin^2\theta$ distribution in the original PYTHIA code with equation 4.26 for MSTP(102)=1 [Har02].

- The PYTHIA model of R_{VMD} going into Eq. 4.26 and also into the total resolved photon cross section $\sigma^{\gamma^{ep}_{VMD}} \sim \Gamma_T(1 + \epsilon R_{VMD})$, does not correspond to the parametrization of HERMES and world data that can be found for instance in Ref. [Ack00]. This parametrization is

$$R_{VMD} = C\left(\frac{Q^2}{M_\rho^2}\right)^{0.61} \quad \text{with} \quad C = \begin{cases} 0.33 \text{ for } 4 < W < 7 \text{ GeV}^2 \\ 0.48 \text{ for } W > 7 \text{ GeV}^2 \end{cases}. \tag{4.27}$$

In contrast, the PYTHIA parametrization is by default (C=PARP(165), MSTP(17)=4)

$$R = C\frac{4M_\rho^2 Q^2}{(M_\rho^2 + Q^2)^2} \quad \text{with} \quad C = 0.5. \tag{4.28}$$

Figure 4.10 shows the difference of the R_{VMD} parametrization as a function of Q^2. At small Q^2, R_{VMD} from the default PYTHIA is about twice as high as the parametrization of the HERMES data, at $Q^2 > 1$ GeV^2 it is much too small. Therefore, a new option was introduced, MSTP(17)=6, selecting Eq. 4.27 with PARP(165) for C.

- The relation between the real and virtual resolved photon cross sections is given by the 'dipole form factor' (cf. Eq. 2.98)

$$D = \left(\frac{m_V^2}{m_V^2 + Q^2}\right)^m \quad \text{with} \quad m = 2 \tag{4.29}$$

in the conventional VMD model. Data of various experiments, for instance of E665 [Ada97] and also of HERMES [Air00a] indicate that the slope of the Q^2 distribution is much steeper, $m \approx 2.5$. Since m is not a tunable parameter, m was changed in the code to be $m = 2.575$, the average value of m found in [Tyt01] by a fit to HERMES data.

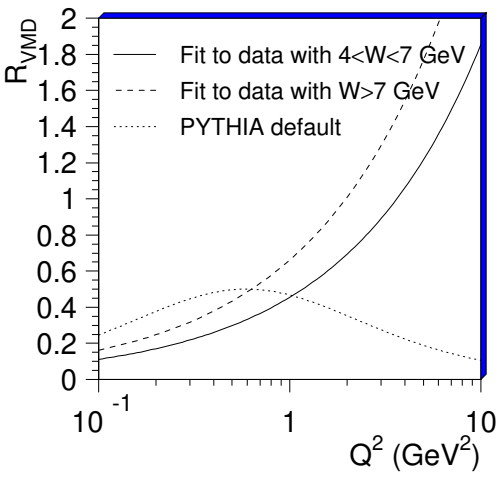

Figure 4.10: The parametrization for the ratio $R = \frac{\sigma_L}{\sigma_T}$ used by (default) PYTHIA compared to fits to Hermes ($4 < W < 7$ GeV) and world data ($W > 7$ GeV).

- The photon–vector meson coupling constants $\frac{f_V^2}{4\pi}$ set by PARP(161–164) are the geometric averages of the two different values obtained from measurements of the decay $\rho \to e^+e^-$ and vector meson photoproduction (see Eqs. 2.96 and 2.97, respectively). The cross section is about 15% smaller, if the values are taken *only* from the photoproduction measurements [Gro97].

The effect to be expected on the total (i.e. 4π) elastic ρ^0 production cross section by changing the photon flux factor, the parametrization of R_{VMD} and the Q^2 slope m can be seen in figure 4.11 where the function

$$\sigma^{ep\to e'\rho^0 p}(y, E_B) = \Gamma_T(1 + \epsilon R_{VMD}) \left(\frac{m_V^2}{m_V^2 + Q^2}\right)^m \sigma^{\gamma p\to\rho^0 p} \tag{4.30}$$

is plotted for $E_B = 27.57$ GeV, $\sigma^{\gamma p\to\rho^0 p} = 11$ μb and $Q^2 = 1.7$ GeV^2. Already these changes

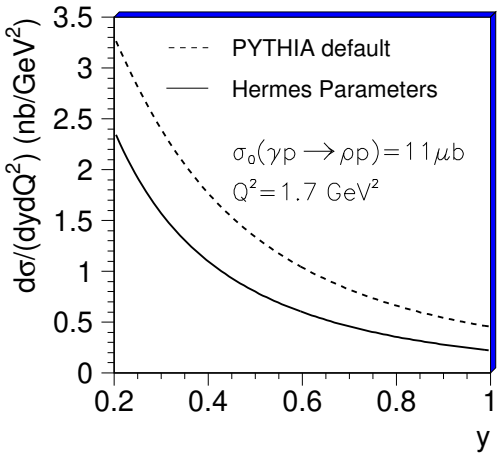

Figure 4.11: The 4π cross section for $ep \to e'\rho p$ calculated according to Eq. (4.30) using the parameters and photon flux from (default) PYTHIA (dashed line) compared to the cross section using the corresponding fitted Hermes parameters and flux. The real photon cross section was taken to be 11 μb.

account for a reduction of the cross section by 30–50%. The largest difference can be attributed to the modified angular distribution, Eq. 4.26. This does only affect the observed cross section, due to the very different acceptance functions resulting from the different pion momenta correlated to the decay angle. This can be explained the following way: Other than for angles distributed as $\cos^2\theta$, in the case of a $\sin^2\theta$ distribution the pions tend to decay at 90° from the ρ^0 direction. In the lab system this means that both pions have almost the same momenta, each roughly half of the ρ^0 momentum. If the angles are distributed like $\cos^2\theta$, one of the pions goes almost in the direction of the ρ^0, the other one goes in the opposite direction, flying backward in the ρ^0 rest system. Boosting back to the lab system, one of the pions has taken almost all of the ρ^0 momentum, the other one very little. The bending in the spectrometer magnet reduces the chance for the low momentum pion

to make it to the back part of the spectrometer, and the probability to reconstruct *both* decay pions decreases. The issue of the chance being rather high that only one of the two pions is reconstructed in the spectrometer will be considered in the next section.

4.3.2 Comparisons of Exclusive ρ^0 Cross Sections

The output of the modified and tuned PYTHIA VMD model was found to be in good agreement with the data, as can be seen from figure 4.12 where the cross sections for both PYTHIA and the data are displayed for various variables. Another cross check was performed by comparing

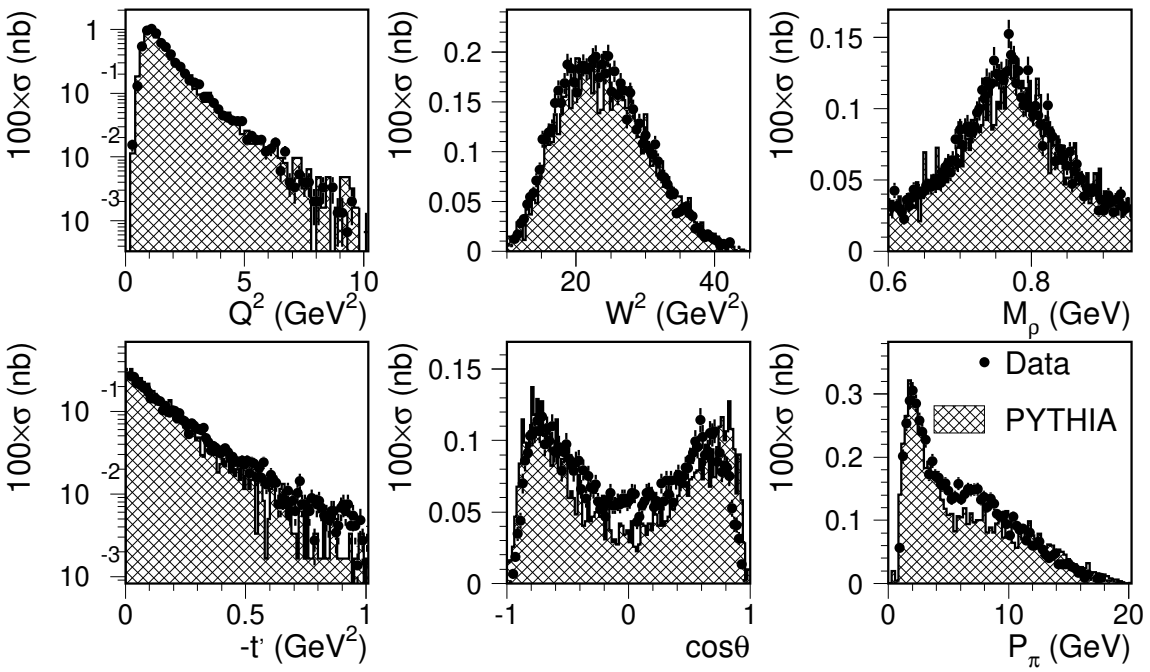

Figure 4.12: The observed cross section of exclusive ρ^0 for the 97 data (polarized and unpolarized hydrogen - dots) compared to that of the modified PYTHIA (proton target, smeared using 99 HSG setup, with QED radiative corrections - shaded histograms).

PYTHIA with other Monte Carlo models designated for the simulation of elastic vector meson production. Two of these MC generators are available at HERMES. One of them is DIPSI which uses the model by Ryskin based on Pomeron exchange [Rys92, Arn96] to describe elastic diffraction of various vector mesons (cf. section 2.5.2). It cannot be expected that DIPSI will reproduce our measured data on the cross section level because DIPSI mainly relies on pQCD. The mass and decay distributions of the model are, on the other hand, quite sophisticated and allow for a comparison of normalized shapes. The other event generator is rhoMC, a 'home made' HERMES MC generator including a number of purely phenomenological descriptions of the elastic cross section and a set of tunable parameters to match, e.g., the Q^2 slope, angular and t' distributions. The parameters used for this comparison can be found in Ref. [Tyt01]. The model used for the cross section comparison here is based on that of Donnachie and Landshoff [Don92] combined with the additive quark model [Lip66]. This is similar, but not exactly the same as the model used in PYTHIA (see also section 2.5.2). Due to inconsistencies in the code, it is not possible to normalize rhoMC data to get a meaningful absolute cross section. For that reason, also for this MC the data – Monte Carlo comparisons are given for normalized shapes only. The output of both the dedicated exclusive vector meson generators is shown together with the data in figure 4.13.

The difference between cross sections of the modified PYTHIA and that of the data is less than 10% which is excellent in view of the almost 10% normalization error of the experimental

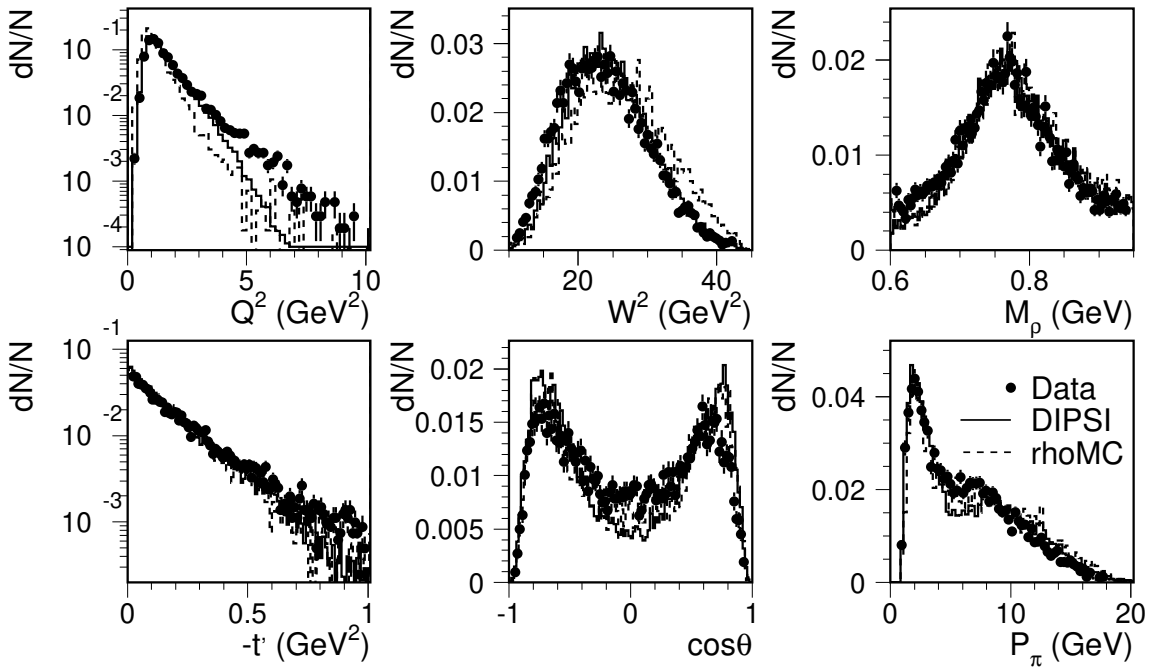

Figure 4.13: The kinematic distributions of exclusive ρ^0 for the 97 data (polarized and unpolarized on hydrogen - dots) compared to those of rhoMC 2.04 (dashed line) and DIPSI (solid line). All histograms are normalized to unity.

data. The kinematic distributions as well as the mass and $\cos\theta$ distributions are well matched with the data, although the $\cos\theta$ distribution is a bit too sharp at the edges ± 1. Also, the slope of the t' distribution is slightly too steep. The t'-slope is governed by the parameter b in Eq. 2.92 that has been measured at HERMES to be $b = 7.08 \pm 0.14(\text{stat.})^{+0.58}_{-0.08}(\text{syst.})$ [Tyt01]. In PYTHIA, the slope parameter has a non-tunable, energy dependent value which for HERMES energies is around $b \approx 8.4$. For DIPSI b was set to 6.7, so that in this case a too large slope parameter cannot be responsible for the slightly too steep t' distribution. The Q^2 distributions of DIPSI and rhoMC do not describe the data very well, with the rhoMC distribution being worse than that of DIPSI. For rhoMC, also the W^2 distribution is not correct. It should be noted that in contrast to these two pure elastic VMD generators, PYTHIA also simulates non-exclusive background, and that the signal to background ratio is smaller at large Q^2 than at small Q^2. This could explain part of the discrepancies of the exclusive VM generators with the data. The decay angular distributions, not only of $\cos\theta$, but also of ϕ and Φ (not shown) from rhoMC are in excellent agreement with the data. Altogether it can be stated that all three MC generators describe the data well enough to be applicable for acceptance studies. However, the PYTHIA model is the only one able to reproduce the absolute cross section.

4.3.3 Exclusive ω and ϕ Cross Sections

Apart from the ρ^0, also the ω and ϕ mesons can be produced elastically through VMD. Both processes have been analyzed at HERMES. The exclusive ω cross section was estimated to be about 15% of the exclusive ρ^0 cross section [Tyt01]. For the data – Monte Carlo comparison in this thesis, ω production has not been analyzed. The ω to ρ^0 cross section ratio in PYTHIA is about 0.1, consistent with SU(3) symmetry. This leads to the expectation that the observed cross section may be underestimated in PYTHIA.

Exclusive ϕ production has been analyzed using the decay $\phi \to K^+K^-$. For the reconstruction of exclusive ϕ the following the cuts presented in table 4.1 were applied. The resulting

ϕ, (K^+K^--pairs)	Cuts/Requirements
Invariant mass of K^+K^--system	$1.01 < M_{KK} < 1.03$ GeV
Identification of K^+K^--system	at least one hadron identified by the RICH with smRich.rQp> 0
Exclusive event	
Transverse momentum transfer ($t' = t - t_0$)	$-t' < 0.6$ GeV^2
Missing energy	$\Delta E < 1$ GeV

Table 4.1: The cuts applied to the 2000 data for the ϕ cross section analysis. All other cuts are the same as for the ρ analysis (table 3.8).

distributions were compared with PYTHIA, DIPSI and rhoMC predictions. The degree of agreement considering only shapes was found to be of a similar quality as in case of the ρ^0. A comparison of normalized shapes of ϕ candidates is shown in figure 4.14 for the 2000 unpolarized hydrogen data and PYTHIA.

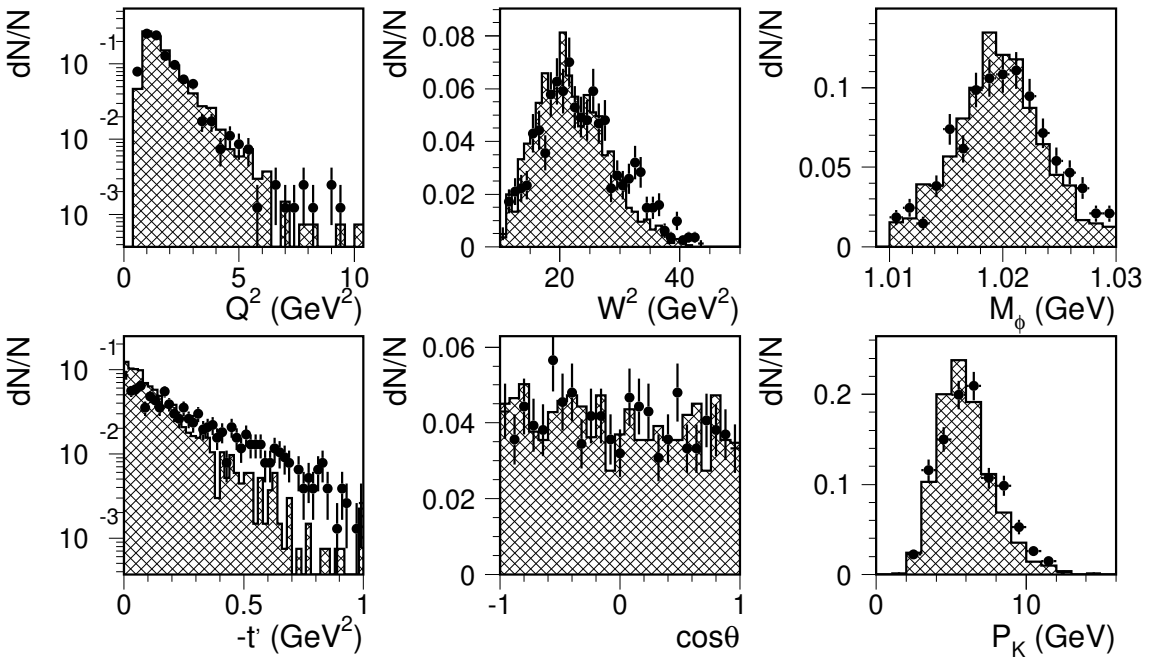

Figure 4.14: The kinematic distributions of exclusive ϕ mesons for the 2000 unpolarized hydrogen data (dots) compared to those of PYTHIA (proton target, tracked using 99 geometry setup for HMC, with QED radiative corrections - shaded histograms). All histograms are normalized to unity.

The t' distribution of PYTHIA does not agree with that of the data, because in the PYTHIA model the b parameter is the same for all light vector mesons. The data at $W \simeq 5$ GeV suggest $b \approx 4$ GeV^{-2}, though [Rak00]. Since the cross section at $t = 0$ behaves as $1/b^2$, the total elastic ϕ cross section comes too small, by out about a factor of 2.

4.3.4 Non-resonant Exclusive π Production

In addition to decay pions from exclusive ρ^0 production, also non-resonant $\pi^+\pi^-$ pairs can be produced exclusively. These pion pairs would lead to a missing energy of $\Delta E \simeq 0$, but need not necessarily to have the mass of the ρ^0. Since the non-resonant $\pi^+\pi^-$ pairs are indistinguishable

from the decay products of the ρ^0, both final states are produced coherently and interfere. Usually, this is accounted for by the skewing of the relativistic Breit-Wigner $\pi^+\pi^-$ mass shape or the parametrization of the invariant mass distribution with a Söding shape [Tyt01, Lip02]. Any of these can be optionally chosen in rhoMC as well as DIPSI. In PYTHIA, on the other hand, non-resonant pion production is incorporated into the framework of the 'GVMD' model where contributions from a continuum of vector meson ($q\bar{q}$) states are added *incoherently*. A $q\bar{q}$ equivalent (defined by the same quantum numbers) exist for ρ, ω and ϕ mesons. The mass of these 'diffractive states' is roughly $M_{q\bar{q}} = 2k_T$, with k_T being the transverse momentum at the $\gamma^* \to q\bar{q}$ vertex. A factor k_V^2/k_T^2 regulates the relative contribution of these $q\bar{q}$ ('diffractive') states with k_V tunable by PARP(18) and $k_V^2 = 0.4$ as PYTHIA default. To estimate and tune the fraction of exclusive, non-resonant pion pairs from data, the abundance of events with $\Delta E \simeq 0$ has to be measured for different mass regions. For this study, the mass cuts were changed accordingly to divide the complete mass spectrum into three parts with $M_{\pi\pi} < 0.6$, $0.6 < M_{\pi\pi} < 0.95$ and $M_{\pi\pi} > 1$ GeV. Fits to the ΔE spectra of the form Gaussian+polynomial were performed, see figure 4.15. There exists no physics reason for the assumption of the particular shape of the background. The systematic uncertainties on the size of the signal may be large. For the purpose of this study the estimates are good enough, though. The signal to background ratios in the range $\Delta E < 0.6$ GeV are 0.5, 3 and 1 respectively. The ratios of low- and high mass cross sections to the ρ mass cross sections are

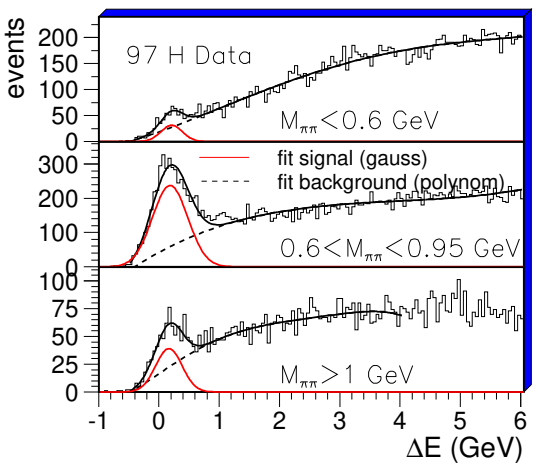

Figure 4.15: The ΔE spectra for $ep \to e'\pi^+\pi^-$ in the low mass ($M_{\pi\pi} < 0.6$) GeV (top), ρ mass ($0.6 < M_{\pi\pi} < 0.95$) GeV (middle) and high mass ($M_{\pi\pi} > 1$) GeV (bottom) regions. The corresponding fits are also shown ((red) solid line: signal, (black) dashed line: background).

$$C_{low} = \frac{\sigma^{M<0.6}}{\sigma^{0.6<M<0.95}} \simeq 0.07 \pm 0.01 \quad \text{and } C_{high} = \frac{\sigma^{M>1}}{\sigma^{0.6<M<0.95}} \simeq 0.13 \pm 0.01,$$

respectively. Decreasing the PYTHIA scale factor PARP(18)= k_V^2 from its default value 0.4 to 0.17 results in $C_{high}^{PYTHIA} \simeq 0.18$ which is still too high, but much less than with the default setting. In principle, PARP(18) could have been reduced even more in order to match the high end of the mass spectrum to the data (note that PARP(18) does not affect the low mass ΔE distributions). Alternatively, it was suggested [Sjö02] to rather change the fragmentation threshold of diffractive states, PARP(103)+M_V (PARP(103)=1 GeV by default),[3] and/or the parameter related to the production threshold of single diffractive states in the process $\rho^0 p \to Xp$, PARP(102)+M_V (PARP(102)=0.28 GeV by default). Also these processes contribute significantly to the exclusive peak for $M_{\pi\pi} > 1$ GeV. Regarding only the contribution from elastic processes the relative cross section would be $C_{high} \simeq 0.1$, about 25% smaller than in the data. PARP(102) was raised to 0.5 GeV while PARP(103) was lowered to 0.5 GeV. The effect to be expected is not only a smaller production rate of exclusive diffractive states, but almost all of them should also fragment into a number of hadrons instead of decaying into an exclusive $\pi^+\pi^-$ pair. The missing energy obtained under the assumption of an exclusive $\pi^+\pi^-$ state would then be reconstructed at larger values, and

[3] Above $M_{q\bar{q}} = M_\rho + PARP(103)$ the diffractive state is treated as a jet and hadronizing through the regular JETSET fragmentation.

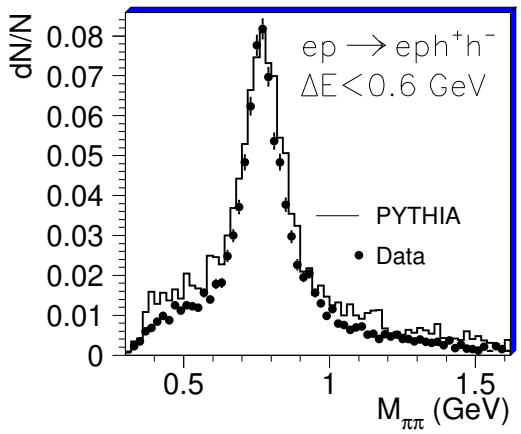

Figure 4.16: The mass distribution of $\pi^+\pi^-$ events from PYTHIA (histogram) compared to 97 Hydrogen data (dots) for $\Delta E < 0.6$ GeV. The data histogram is normalized to unity, the MC histogram is normalized such that the maxima at $M = M_\rho$ coincide.

the contribution of diffractive states would not be visible in the exclusive peak at $\Delta E < 0.6$ GeV. The mass distributions resulting from changing the mentioned parameters for 'exclusive' $\pi^+\pi^-$ events with $\Delta E < 0.6$ GeV from PYTHIA compared to data is displayed in figure 4.16. The exclusive non-resonant cross section indeed turns out to be a little smaller. Almost all diffractive states also fragmented, but the final states still happened to be exclusive $\pi^+\pi^-$ pairs, reconstructed in the exclusive peak. Besides reducing PARP(18) even further, another option would be to increase the threshold scale of the GVMD model which by default is $k_0 = 0.5$ GeV and can be changed by increasing PARP(15). The minimum mass of GVMD states would then be $M_{q\bar{q}}^{min} = 2k_0 > 1$ GeV. A study of the influence of PARP(15) has been performed only with regard to the semi-inclusive cross section (cf. section 4.5.2) because PARP(15) is also closely connected to other aspects of the model.

The low mass $M < 0.6$ GeV region of PYTHIA contains the exclusive ρ from the tail of the Breit-Wigner distribution. This tail leads to $C_{low} \simeq 0.19$, almost a factor three higher than in the data. The reason here is most likely the shape of the Breit-Wigner distribution itself. In PYTHIA, a non-relativistic Breit-Wigner shape is generated whereas the data were found to match well with a relativistic p-wave Breit-Wigner including a skewing parameter [Tyt01].

4.4 Contribution of Diffractive Events to the Semi-inclusive Data

As already mentioned in the previous section, it is necessary to estimate the contribution of VMD processes to the semi-inclusive data. More precisely, here the fraction of hadrons originating from an exclusively produced vector meson in the semi-inclusive hadron sample is investigated. For a variety of analyses of semi-inclusive data at HERMES, a possible VMD contribution to the data has to be considered as background. This concerns for instance the analysis of semi-inclusive asymmetries to extract the helicity distributions $\Delta q(x)$, which is performed using purities obtained from LEPTO. It may also effect the extraction of fragmentation functions because hadrons from exclusive vector meson decay did not take part in the fragmentation process and follow different kinematic distributions. The fraction of hadrons from elastic VMD is also interesting for the analysis of single hadrons in this thesis in the sense that an alternative, less model dependent method for its determination is applied that can provide a sanity check for the completely model dependent fraction of the corresponding subprocess to be extracted from PYTHIA alone.

4.4.1 Extraction Method

The determination of the fraction of pions (kaons) from exclusive ρ^0 (ϕ) decay in the semi-inclusive data proceeds in two steps:

1. Determine the ratio (multiplicity) $m(x,(z,p_T))$ of pions (kaons) from *reconstructed* exclusive ρ^0 (ϕ) to all semi-inclusive pions (kaons)

$$m^{h,\pi}_{data}(x) = \frac{\sigma^{h^\pm(\pi^\pm)}(\rho)}{\sigma^{h^\pm(\pi^\pm)}}, \quad m^{K}_{data}(x) = \frac{\sigma^{K^\pm}(\phi)}{\sigma^{K^\pm}} \tag{4.31}$$

from the experimental data. Exclusive ρ^0 and ϕ candidates can be identified using the cuts of the left column in table 3.8 and in table 4.1, respectively. Pions (unclassified hadrons and identified pions with $4 < p < 13.8$ GeV) or kaons originating from these candidates have to fulfill the cuts defining a semi-inclusive data sample. In this study, the cuts used to define the 'SIDIS' region are applied for the multiplicities vs. x and z_π, and the cuts for the 'Transition' region for the multiplicities vs. p_T. The semi-inclusive samples of unclassified hadrons ($h^\pm$), pions ($\pi^\pm$) and kaons ($K^\pm$) are defined consistently, and are obtained from the same data set as the hadrons (pions) from ρ^0 decay ($h(\pi)^\pm(\rho)$) and kaons from ϕ decay ($K^\pm(\phi)$). Non-exclusive or non-resonant background in the sample of the decay particles can be estimated from MC. In this study, the background under the exclusive peak with $\Delta E < 0.6(1)$ GeV and $-t' < 0.4(0.6)$ GeV^2 has been extracted from PYTHIA for ρ^0 (ϕ) candidates, using the information about the parent particle and subprocess. A factor F^{MC} is used to normalize cross sections of data and Monte Carlo in the semi-inclusive region ($\Delta E > 2$ GeV) to each other.

$$N_{Bg} = F^{MC}\sigma^{MC}_{Bg} L^{Data} \quad \text{with } F^{MC} = \frac{\sigma^{Data}_{Bg}(2 < \Delta E < 5 \text{ GeV})}{\sigma^{MC}_{Bg}(2 < \Delta E < 5 \text{ GeV})}, \tag{4.32}$$

This is only one way out of many to determine the background, and in a more detailed analysis it would be necessary to use more than one method to estimate the systematic uncertainty on the background determination. The values obtained in this study should be viewed as a coarse estimate serving the purpose. The background ratio is between 10 and 15% for most of the kinematic region, except at $x > 0.1$ or $z < 0.3$ where it is slightly larger. This is in agreement with the values obtained in other studies [Tyt01, Lip02].

2. The next step involves the determination of an acceptance function from Monte Carlo, where here only the information about the exclusive cross section is needed. The acceptance function is defined as:

$$A^{MC} = \frac{\sigma^h_{elastic,\,\rho^0}(\text{semi-incl.})}{\sigma^h_{elastic,\,\rho^0}(\text{recons.})}. \tag{4.33}$$

In words, the acceptance factor is the ratio of the number of all semi-inclusive, detected hadrons passing the cuts for the semi-inclusive data sample and originating from elastically produced ρ^0 to the number of semi-inclusive, detected hadrons passing the same semi-inclusive cuts and originating from elastically produced ρ^0 that could be reconstructed to ρ^0 candidates meeting the requirements of the exclusive data sample. An acceptance factor for identified pions from ρ^0 decay and kaons from ϕ decay can be defined analogously. The yield of semi-inclusive hadrons from ρ^0 (ϕ) in the numerator of A is integrated over the whole kinematic region where exclusive vector mesons are produced, thereby taking into account the cut efficiency:

$$\frac{1}{\epsilon_{cut}} = \frac{\int_{2m_\pi}^{\infty} dM_{\pi\pi} \int_{-\infty}^{P_B} d\Delta E \int_{-\infty}^{0} dt' \sigma^h_{elastic,\,\rho^0}(\text{semi-incl.})}{\int_{0.6}^{0.94} dM_{\pi\pi} \int_{-\infty}^{0.6} d\Delta E \int_{t'=-0.4}^{0} dt' \sigma^h_{elastic,\,\rho^0}(\text{semi-incl.})}. \tag{4.34}$$

The full contribution of hadrons from exclusive vector meson production to the semi-inclusive hadrons can be obtained by multiplying the data ratios m with the acceptance correction

$$C^{MC}_{excl} = A^{MC} \cdot m. \tag{4.35}$$

If necessary, the additional effect of non-resonant, exclusive VMD processes and of hadrons originating from exclusive ω or ϕ production can be taken into account by calculating the

factor (for example for pions):

$$C^{MC}_{non-res} = \frac{\sigma^h_{elastic,\,\rho^0} + \sigma^h_{elastic,\,non-res} + \sigma^h_{elastic,\,\omega} + \sigma^h_{elastic,\,\phi}}{\sigma^h_{elastic,\,\rho^0}}. \tag{4.36}$$

This factor can be obtained from PYTHIA and is about 1.1 to 1.2, with the uncertainties as discussed in section 4.3.4 above. The statistical errors of m and $A^{MC}$are propagated independently into C^{MC}_{excl}, although the total statistical error is finally dominated by the error of m.

There are two disadvantages to this method. One is its model dependence that can only be avoided if the acceptance correction is calculated and applied in multi-dimensional bins of as many variables as the cross section depends on. This would be two inclusive variables, t', the invariant mass and the azimuthal production and decay angles and the polar decay angle, i.e., seven independent variables. They could eventually be reduced to five or six, but the available data statistics do not allow more than two dimensions. The other disadvantage is that in order to find a nonzero C_{excl} there *have to be fully reconstructed* events in the data. In reality, the true contribution of exclusive events to the semi-inclusive data this does not depend on if full events could be reconstructed. It is possible to imagine situations where *only one* of the vector meson decay products can be detected in the event. For the determination of the exclusive VM contribution vs. x in the 'SIDIS' region this is not problematic, as for $x < 0.4$ the spectrometer allows to reconstruct ρ^0 events and at larger x the VMD cross section becomes negligible. The situation is different if the VMD fraction is to be evaluated as a function of p_T instead because the requirement of high transverse momentum of one of the pions makes it at some point impossible to detect the other pion as well.

4.4.2 Fractions of Exclusive ρ^0/ϕ Events in the Semi-inclusive Data

Figures 4.17 and 4.18 show the ratios m vs. x and z in the 'SIDIS' region for hadrons (pions) from exclusive ρ^0 and for kaons from exclusive ϕ decay in the 2000 hydrogen data.
The ratio for pions is higher than that for unidentified hadrons mostly because the semi-inclusive hadron sample contains all hadron types, while the hadrons from ρ^0 decay are all pions of course. The smaller semi-inclusive cross section for negative hadrons makes the negative hadron ratios higher than the ones for positive hadrons. The apparent accumulation of pions from exclusive ρ at high z_π is striking. This is a direct result of the non-flat decay angle distribution of the pions. As explained in section 4.3.1, the bath tub like shape of the polar angle distribution implies that most of the ρ^0 mesons decay in their rest system such that one of the pions goes more or less into the direction where the ρ^0 was flying ($\cos(\theta) \to +1$), while the other one goes backward ($\cos(\theta) \to -1$). Because of the correlation of photon and ρ^0 energies ($E_{\rho^0} \simeq \nu$), $z \to 1$ for $\cos(\theta) \to +1$. The forward pion thus has $z_f \simeq 1$, the backward pion has $z_b = 1 - z_f \simeq 0$. Pions from ρ then accumulate at $z \simeq 0(1)$. On the other hand, semi-inclusive pions follow a steep fall off in z, leaving very little statistics at $z > 0.8$.

Owing to the different behavior of the semi-inclusive kaon cross section and the exclusive ϕ cross section and its decay, the ratios of kaons from ϕ look very distinguished from those of the hadrons from ρ^0. Quite outstanding is the difference between the ratios for positive and negative kaons coming from the much lower cross section for negative kaons. Because the decay angle θ for kaons from exclusive ϕ is distributed much more flatly than that of pions from ρ^0, the kaon z distribution is shallower. The semi-inclusive kaons in turn fall of much more steeply in z than the pions, such that the ratios come out largest at medium z. The hadron (pion, kaon) ratios have also been determined for the polarized deuterium target (not shown). They are larger than the hydrogen ones for positive hadrons and slightly smaller for negative ones. The differences can be attributed solely to the differences of the *semi-inclusive* cross sections, the exclusive cross sections are compatible with each other.

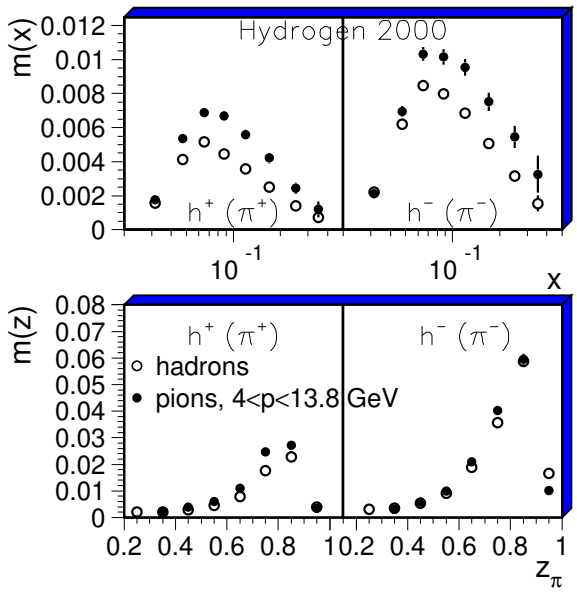

Figure 4.17: The ratio m of hadrons (pions) originating from reconstructed ρ^0 to semi-inclusive hadrons (pions) as a function of x (top) and z_π (bottom) in the 'SIDIS' region. The ratios are extracted from the 2000 unpolarized hydrogen data. No background correction has been applied.

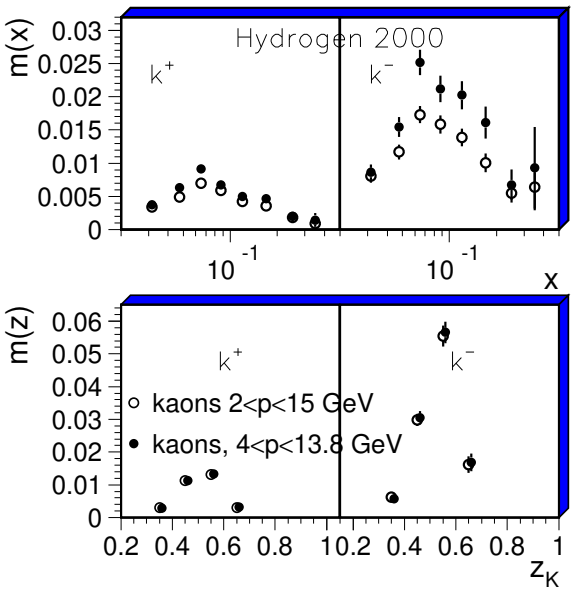

Figure 4.18: The ratio m of kaons originating from reconstructed ϕ to semi-inclusive kaons as a function of x (top) and z_K (bottom)in the 'SIDIS' region. The ratios are extracted from the 2000 unpolarized hydrogen data. No background correction has been applied.

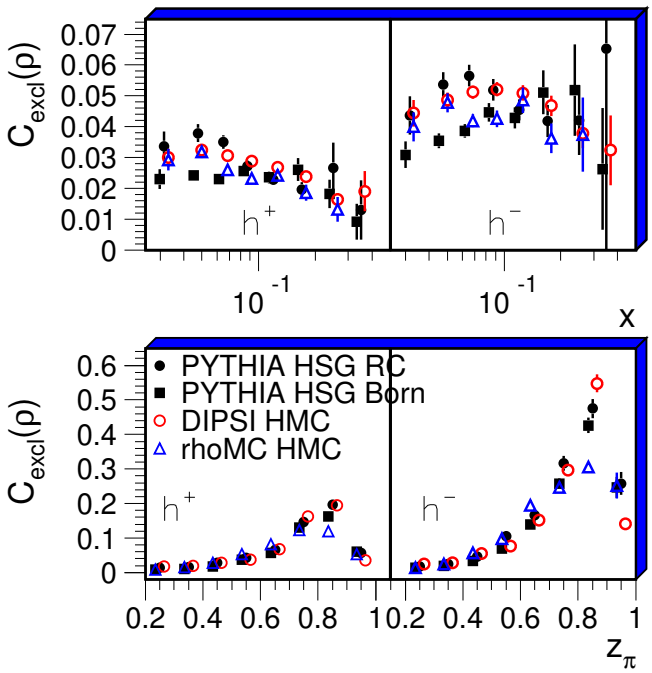

Figure 4.19: The ratios C_{excl}^{DIPSI} (empty circles), C_{excl}^{rhoMC} (empty triangles), $C_{excl}^{PYTHIA-Born}$ (full squares) and $C_{excl}^{PYTHIA-RC}$ (full circles) for 1997 hydrogen data of pions originating from exclusive ρ to semi-inclusive hadrons as a function of x (top) and z_π (bottom).

For the three Monte Carlo models rhoMC, DIPSI and PYTHIA the results on the ratios C_{excl}^{MC} are shown in figure 4.19. From the four sets of points shown there, only the three without radiative corrections can be directly compared (none of rhoMC and DIPSI have RC implemented so far). From these three, DIPSI gives the highest contribution for all x values, whereas PYTHIA gives the lowest at small $x < 0.1$. Vs. z, the relative deviations between the MC models are small for $z < 0.5$, whereas rhoMC displays a completely different shape than DIPSI and PYTHIA at

higher z, leading to almost 100% difference at $z \simeq 0.85$. In general, the reason must be that the correlations between two or more variables are different for each MC model. To illustrate this, the correlations between z and Q^2 and between y and Q^2 for the three MC models are presented in figure 4.20. The right plots show the correlations for fully reconstructed ρ^0, compared to the data. The left plots show the same correlations for the single hadrons from ρ^0. Whereas the average y

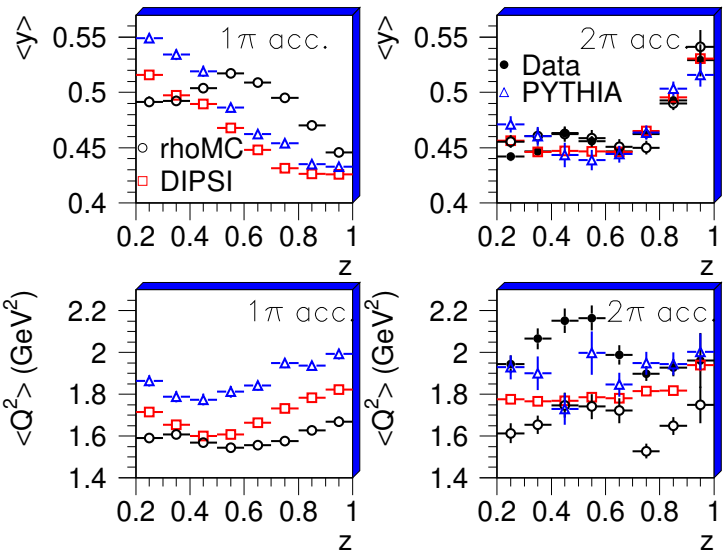

Figure 4.20: The average y (top) and Q^2 (bottom) vs. z for the three MC models (PYTHIA with RC), in the acceptance of the reconstructed ρ^0 (right) and of single pions from ρ^0 (left). The 2000 hydrogen data were used for comparison

agrees well with the data for all three models if both decay pions are in the acceptance, the models deviate clearly from each other if only one pion needs to be in the acceptance. The difference between the acceptance factors for one and two pions is not so large for the average Q^2 vs. y, but here it can be clearly seen that PYTHIA is much closer to the data than DIPSI and rhoMC which both produce a too small Q^2 compared to the data. Q^2 to a large extent determines the angle of the ρ which in turn, together with the pion decay angles, of course directly determines whether one or two pions enter the spectrometer. Comparing PYTHIA with and without RC it is apparent that the MC with radiative correction gives the larger fractions. The reason for this is that if a bremsstrahlung photon was radiated, the values for ΔE calculated from observed kinematics are larger than 0, whereas the true $\Delta E_T = 0$ if calculated from the true lepton kinematics. The cut efficiency is thus smaller, i.e., $1/\epsilon_{cut}$ is larger if it is calculated from an MC with radiative corrections.

There is hardly any model dependence of the exclusive ϕ ratios for kaons (not shown). In this case the acceptance factor is completely dominated by the spectrometer acceptance.

The final results for the exclusive ρ^0 fractions of hadrons and identified pions from in the 'SIDIS' region is shown in figures 4.21 and 4.22 for the hydrogen data vs. x and z respectively. The total systematic error, indicated by the hatched error band, consists of the error of the background correction to the data, the model uncertainty and an error assigned to the differences between fully tracked and smeared (using HSG) Monte Carlo data. The error of the background correction and the model uncertainty are derived from comparing the results of PYTHIA data with the standard settings to those of data generated with other PYTHIA settings that were slightly varied in the way the VMD cross section or the LO DIS cross section is modeled. The relative error of HSG is the relative difference of the results for C_{excl}^{MC} obtained with DIPSI or rhoMC and the full HMC chain to that with the same MC data generated using only HSG. As can be seen from the plots, this error (indicated by the darker shaded area) constitutes a large fraction of the total systematic error. It can of course be avoided when running PYTHIA with the full HMC chain, which is very time consuming, though.

The results for the exclusive ϕ fractions in the kaon sample with $2 < p < 15$ GeV are presented in figure 4.23 for the 2000 hydrogen data. Here, the systematic error is formed from the contribution of the background correction, the model uncertainty and the contribution from the

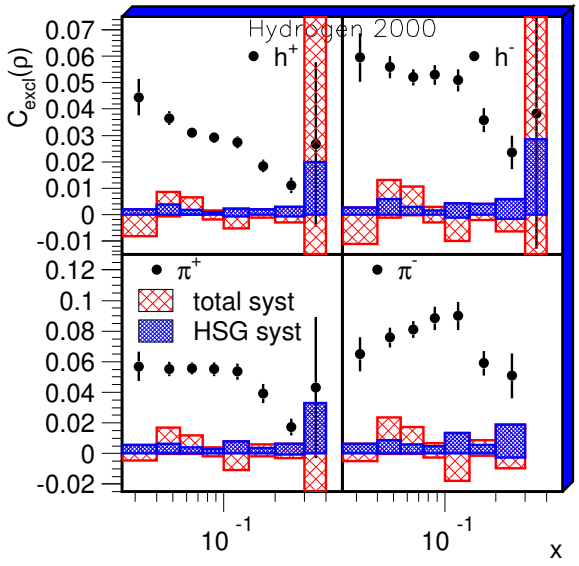

Figure 4.21: The fraction of pions originating from elastic ρ production in the semi-inclusive hadron/pion sample of the 2000 hydrogen data as a function of x_{Bj}. Identified pions have $4 < p < 13.8$ GeV. The systematic uncertainty is indicated by the error band. See text for details.

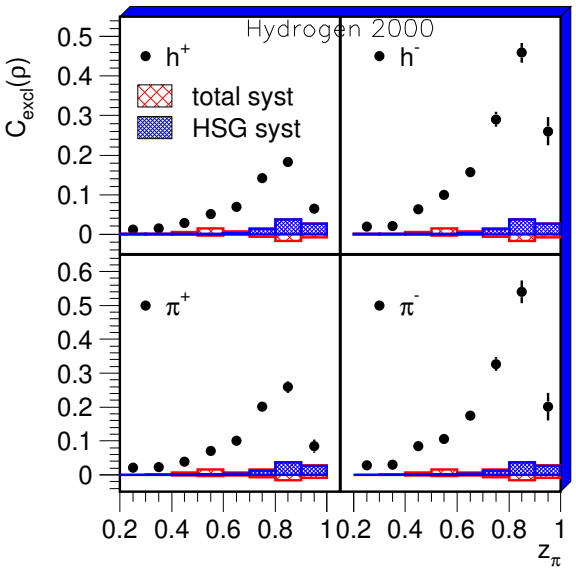

Figure 4.22: The fraction of pions originating from elastic ρ production in the semi-inclusive hadron/pion sample of the 2000 hydrogen data as a function of z. Identified pions have $4 < p < 13.8$ GeV. The systematic uncertainty is indicated by the error band. See text for details.

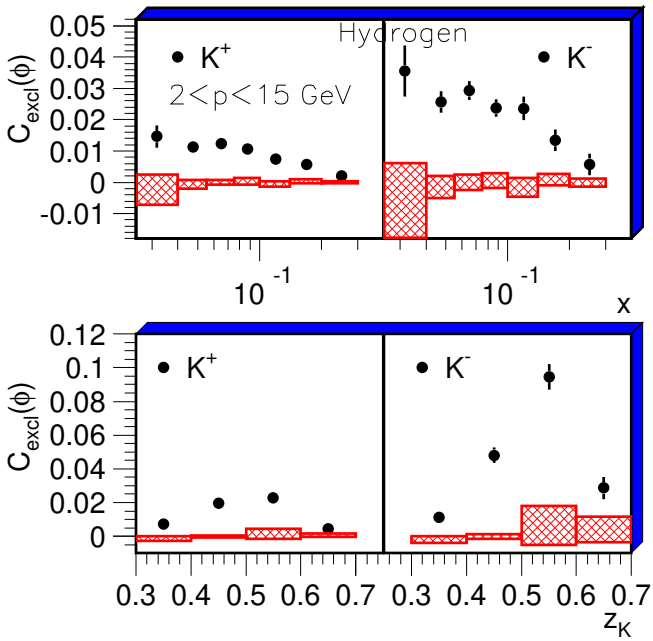

Figure 4.23: The fraction of kaons originating from elastic ϕ production in the semi-inclusive kaon sample of the 2000 hydrogen data as a function of x (top) and z (bottom). The systematic uncertainty is indicated by the error band. See text for details.

uncertainty of the RICH unfolding for kaons. Since all MC data were generated using the full MC chain with HMC and tracking, no error needs to be assigned for the smearing. The background correction was calculated for two different PYTHIA settings and their difference assigned as uncertainty. The model uncertainty is here the relative deviation of all of rhoMC, DIPSI and PYTHIA, and very small. The largest contribution comes from the error of the RICH unfolding.

4.4.3 Exclusive and Diffractive VMD Fractions from PYTHIA

The measured exclusive ρ^0 cross section seems to be reproduced by PYTHIA rather well. The *fraction* of hadrons from exclusive vector mesons in the semi-inclusive data generated in PYTHIA can then only be compatible with the data if the total semi-inclusive cross section is reproduced on the same level. The agreement for hadrons and pions is at around 10% to 20% (see section 4.5), such that a comparison of the fractions obtained from the acceptance correction method and from the semi-inclusive PYTHIA data makes sense. The fractions can be inferred directly from PYTHIA by selecting hadrons from the elastic subprocess (PYTHIA process 91). This process 91 includes contributions from non-resonant exclusive $\pi^+\pi^-$ production as well, such that in order to compare with the data from the acceptance correction method an additional cut on the parent of the pion to be a ρ^0 has to be placed. In figure 4.24 this comparison is shown for pions vs. x and z. Apparently, the acceptance method and PYTHIA fraction are in excellent agreement over the full

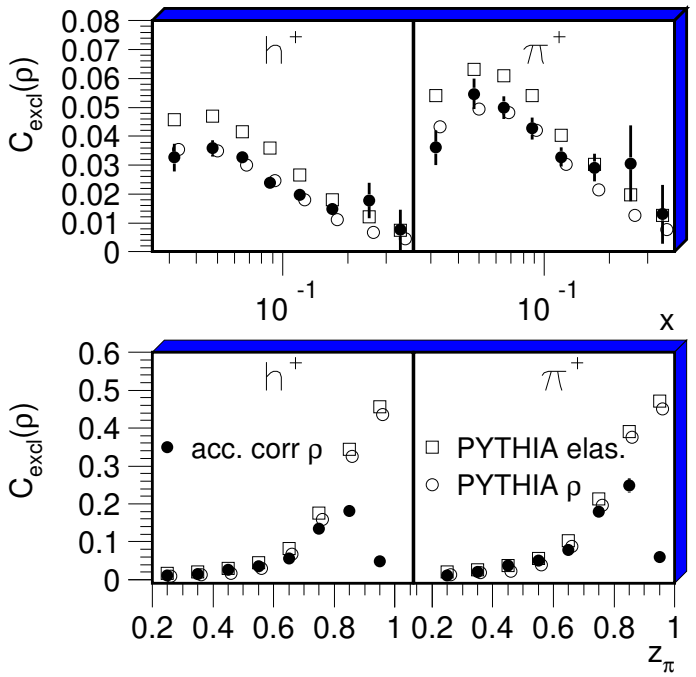

Figure 4.24: Comparison of exclusive ρ^0 fractions for pions ($4 < p < 13.8$ GeV) in the 'SIDIS' region extracted with the acceptance correction method (filled circles), the fraction of pions from process 91 with the ρ^0 as a parent (open circles) and the total process 91 fraction (open squares).

x range, and in reasonable agreement for $z < 0.8$. At very high z there are deviations, though. The reason is that the shape of the cross section of reconstructed ρ^0 is slightly different in PYTHIA than in the data, underestimating the cross section at small, and overestimating it at high z. This in turn can be related to the imperfect simulation of the $\cos\theta$ distribution of the decay pions as shown in figure 4.12, with the slightly too steep 'peaks' at $z \to \pm 1$. However, it is not possible in this case to decide if the acceptance correction method or the pure PYTHIA fraction are more correct, as it can well be that the PYTHIA acceptance factor comes out too small in the high z region. The open squares in figure 4.24 show the full contribution from elastic processes, i.e., the pions from exclusive ω, ϕ and the non-resonant diffractive states in addition to the exclusive ρ^0. As discussed in sections 4.3.3 and 4.3.4, the ω and ϕ contribution may be underestimated, whereas the non-resonant contribution at higher invariant masses may be slightly overestimated. Altogether the inferred value of an additional contribution of 20% might be a bit on the high side, but not completely impossible. Figure 4.25 shows the same quantities as in figure 4.24, but for positive hadrons and identified pions in the 'Transition' region as a function of p_T. At small p_T, deviations from the PYTHIA fraction and the acceptance method for hadrons are due to deviations between semi-inclusive cross sections in the data and MC (cf. figure 4.7). At high $p_T > 0.7$ GeV the effect of the aforementioned method bias can be seen, where the acceptance function is zero for the full reconstruction of a ρ^0, but nonzero for single hadrons from ρ^0. The open triangles in figure 4.26 represent the total *diffractive* VMD contribution. The additional contribution mainly from single

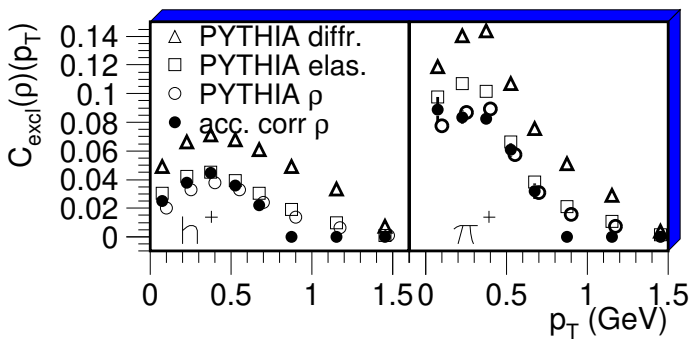

Figure 4.25: Comparison of exclusive ρ^0 fractions for pions ($4 < p < 13.8$ GeV) in the 'Transition' region extracted with the acceptance correction method (filled circles), the fraction of pions from process 91 with the ρ^0 as a parent (open circles) and the total process 91 fraction (open squares).

diffractive processes cannot be measured directly with the HERMES data, however, and is model dependent.

4.5 The Semi-inclusive Cross Section in PYTHIA

In this section, the PYTHIA model for the semi-inclusive cross section is investigated and compared to the data in the 'Transition' and 'SIDIS' regions. In addition to the modeling of the various subprocesses and their relative contribution, the semi-inclusive cross section also depends on the fragmentation model and parameters in use. For reference, in table D.2 in the appendix the parameters used as the standard setting for the HERMES adaption of PYTHIA which are different from the PYTHIA default are shown.

4.5.1 Tuning of Fragmentation Parameters

For the hadron fragmentation, PYTHIA uses the LUND String fragmentation model implemented in JETSET. Some of the parameters going into this model have to be viewed as 'effective' in the sense that for several reasons (cf. section 2.4) the PYTHIA default settings, mostly determined from e^+e^- data, do not describe the data sufficiently well. This concerns for instance the parameters a and b going into the fragmentation function, Eq. 2.72, or the average transverse momentum acquired during fragmentation. Other parameters of importance are the strangeness suppression factor, the production ratio of vector to pseudo scalar mesons and the baryon suppression. This leaves quite a large number of parameters to be tuned to the data. The recent results obtained from tuning pion, kaon and proton multiplicities from LEPTO to the HERMES data [Hil03] have been used for the results given in this section. Multiplicities for semi-inclusive events are defined as

$$\frac{dn_h}{dp_T} = \frac{\frac{d\sigma_h}{dp_T}}{\int dx \frac{d\sigma_{incl}}{dx}} = \frac{\frac{N_h(p_T)}{\Delta p_T}}{N_{DIS}} \tag{4.37}$$

as a function of p_T for example. The multiplicities for pions extracted from PYTHIA, LEPTO (within gmc_DISNG) and the data are shown in figures 4.26 and 4.27 vs. p_T and z. Both MC data sets were generated with QED radiative corrections. In order to be able to compare the multiplicities of the data and gmc_DISNG with those of PYTHIA where all events have $W_T^2 > 4$ GeV, the number of inclusive DIS events has to be corrected for the contribution of events with smaller W_T^2. In gmc_DISNG this is easily done by simply placing an additional cut $W_T^2 > 4$ GeV on all events. The data can be corrected by multiplying with the ratio of the number of inclusive events with $W_T^2 > 4$ GeV to that with all W_T^2 from gmc_DISNG:

$$N_{DIS} \rightarrow N_{DIS} \left(\frac{N_{DIS}(W_T^2 > 4)}{N_{DIS}(W_T^2 \geq M^2)} \right)^{DISNG} . \tag{4.38}$$

The semi-inclusive MC data always have $W_T^2 > 4$ GeV due to the internal cuts in JETSET, and with good reason this can also be assumed to be true for the experimental data. Although the settings

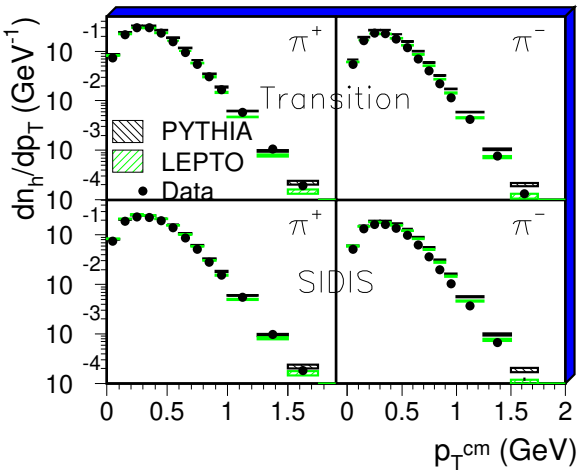

Figure 4.26: The pion multiplicities vs. p_T for the 2000 hydrogen data (dots), LEPTO (light (green) band) and PYTHIA (black band). The top panels are for the 'Transition'-, the bottom plots for the 'SIDIS' region. The pions have $2 < p < 15$ GeV.

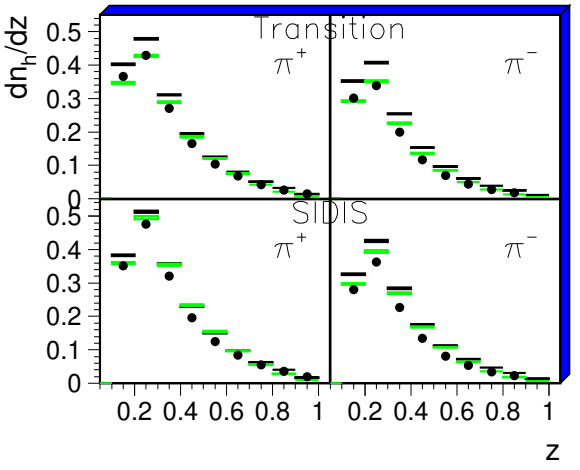

Figure 4.27: The pion multiplicities vs. z for the 2000 hydrogen data (dots), LEPTO (light (green) band) and PYTHIA (black band). The top panels are for the 'Transition'-, the bottom plots for the 'SIDIS' region. The pions have $2 < p < 15$ GeV.

of the JETSET parameters are the same in both cases, the multiplicities turn out to be different. In general, the multiplicities from LEPTO are slightly lower than the PYTHIA ones. Both MC are not able to describe positive and negative pions equally well, with a tendency to generate a more symmetric charge distribution in the MC than it is observed in the data. While in LEPTO only the fragmentation parameters directly influence the hadron multiplicities, in PYTHIA a number of other parameters has to be considered. This may seem natural since for instance a good part of the VMD processes in PYTHIA do either not involve JETSET fragmentation at all or start from a different distribution of final state partons (in the case of non-diffractive VMD). LEPTO does not simulate either of these (G)VMD processes, instead about 90% of the LEPTO data come from the LO DIS process with one quark in the hard process. The suppression of the LO DIS process and addition of (G)VMD processes in PYTHIA may then lead to different multiplicities for the same set of JETSET parameters. To illustrate this, in figure 4.28 the PYTHIA multiplicities are plotted separately for the resolved and the direct (including LO DIS) photon processes, as a function of x and of p_T. The multiplicity as a function a inclusive variable like x is defined as follows:

$$n_h(x) = \frac{\frac{d\sigma_h}{dx}}{\frac{d\sigma_{incl}}{dx}}, \tag{4.39}$$

i.e., in this case the inclusive cross section is taken as differential. The relative weight σ_i/σ_{tot} with which each event class contributes to the total cross section is plotted in the bottom panels of figure 4.28. The multiplicities of pions from the direct photon processes lie over those of the data at high x, but are on top of the data at small x. For the resolved photon processes, the multiplicities are significantly below the data at small x, and on top of the data at high x for positive pions, and above the data for negative pions. This very distinct behavior of the multiplicities, weighted with their contribution to the total cross section leads to an overestimate of the data at large x and an underestimate at small x. As a function of p_T, the fractions of resolved and direct processes are are much more flat. While the slope of the p_T distribution of the (dominating) direct processes approximately follows that of the data, the resolved processes show a much softer slope. It should be noted here that already the direct processes alone overestimate the multiplicities of the negative pions. While the fractions σ_i/σ_{tot} vs. x of the two event classes hardly depend on the charge of the

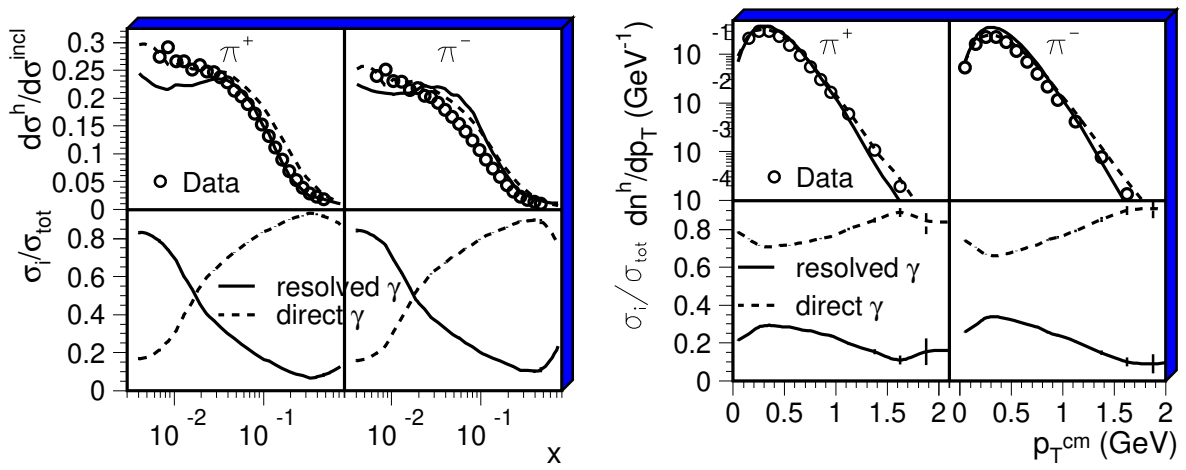

Figure 4.28: The pion multiplicities (top panels) vs. x (left) and p_T (right) from PYTHIA for the resolved photon processes (full line) and the direct photon processes (dashed line) in the 'Transition' region. The open circles represent the data multiplicities from the 2000 unpolarized H data. The bottom plots show the relative contribution of the resolved and direct processes to the total π^+ (π^-) cross section.

pions, they do as a function of p_T. This shows the increased sensitivity of multiplicities in p_T to the fragmentation parameters compared to multiplicities in inclusive variables like x, however, from the above discussion it follows that the influence of the PYTHIA cross section model is non-negligible for semi-inclusive multiplicities. Attempts to tune PYTHIA fragmentation parameters to the data multiplicities are made at the moment for a fixed set of cross section parameters. The results shown so far were generated with the current best set of parameters shown in table D.2. The next section will mainly deal with a study on the influence of PYTHIA model parameters on the absolute cross section and admixture of the various subprocesses. For completeness, in figure 4.29 the cross sections for kaons, protons and antiprotons are shown. While the description of the negative kaons is very good with the current fragmentation tune and that of the antiprotons is still reasonably good, PYTHIA does not seem to be able to describe protons and positive kaons. In the HERMES

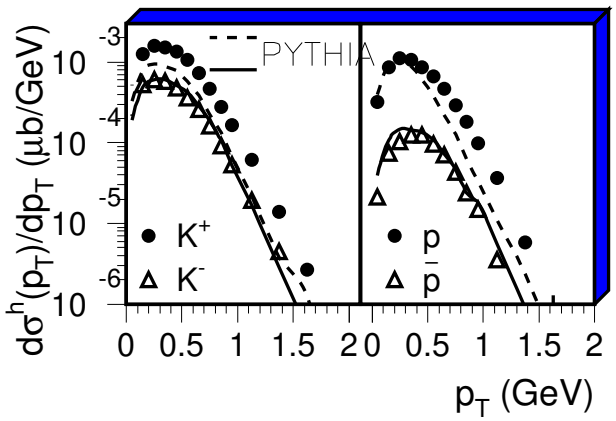

Figure 4.29: Comparison of semi-inclusive cross sections of kaons (left) and (anti)protons (right) obtained from PYTHIA (dashed lines for positive, full lines for negative particles) with the 2000 unpolarized hydrogen data (symbols) in the 'SIDIS' region.

kinematic region, a large fraction of the detected protons originates from the target remnant [Hil03]. Baryon production by fragmentation in general, and the fragmentation of the target remnant in particular are subject to large theoretical uncertainties such that an insufficient description of the proton yield by the LUND fragmentation model used in JETSET can be expected. In the case of the positive kaons it has been suggested that a significant contribution from fluctuations $p \to \Lambda_0 K^+$ may lead to the observed large yield of positive compared to that of negative kaons [Hil03].

4.5.2 Cross Section Parameters

In the following, studies on the influence of PYTHIA cross section parameters on the generated semi-inclusive cross section will be presented. This study is meant to be in a more qualitative sense, i.e., instead of scanning a multi-dimensional parameter space in order to find the set minimizing χ^2 in a comparison to the data, a selected number of parameters will be changed systematically, and for each parameter set the resulting PYTHIA cross sections, correlations between the transverse momentum and inclusive variables and double spin asymmetries are compared to the data. The latter two observables are chosen because they do not only depend on the total cross section, but also on the admixture of the different event classes involved. The final goal is to define one or more sets of parameters within the γ/e^+ option of PYTHIA resulting in acceptable agreement with the semi-inclusive HERMES data. These parameter sets will be later used to extract the PGF subprocess fractions. The fact that the average x in each bin in p_T is sensitive to the mixture of the contributing subprocesses is illustrated in the left panel of figure 4.30 where this quantity is plotted for diffractive and non-diffractive VMD, the leading order DIS and the direct QCD processes separately in the 'Transition' region for positive pions. A similar behavior was observed for the average Q^2 vs. p_T. The relative weight of these contributions then determines the average x for the whole sample. For comparison, the average from the combination of all processes is shown together

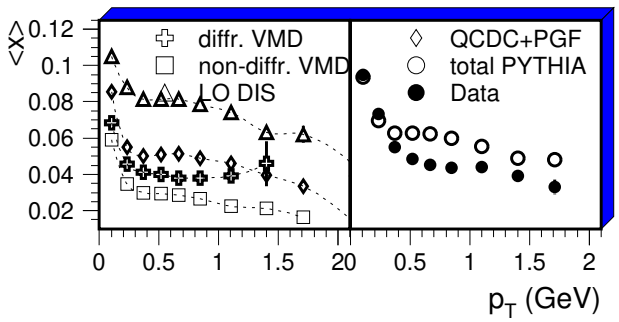

Figure 4.30: The average x of positive pions ($4 < p < 13.8$ GeV) in the 'Transition' region for several subprocesses from PYTHIA (left plot) and for the total cross section in PYTHIA and the polarized hydrogen data of 1997.

with that of the data in the right panel of figure 4.30.

Double spin asymmetries do not depend so much on the absolute cross section, but rather on the event kinematics and the subprocesses involved. PYTHIA itself has no information about the polarized cross section, however, double spin asymmetries can be constructed from the generated kinematics, the type of subprocess and the information about the struck parton from PYTHIA. How this is exactly done, is explained in appendix C.1. In general, a weight

$$a_i = \hat{a}(x, Q^2, \hat{s}, \hat{u}, \hat{t}) \frac{\Delta f(x, Q^2)}{f(x, Q^2)} \qquad f = q, \bar{q}, G \tag{4.40}$$

is applied to each event, where $\hat{s}, \hat{u}, \hat{t}$ are the Mandelstam variables for the partonic $2 \rightarrow 2$ subprocesses like PGF and QCD Compton. Besides the type of the struck parton, the corresponding parton polarizations are needed as the only additional information. This information is available from the *PDFLIB* [Plo00]. The hard subprocess asymmetries are known for the direct photon processes, i.e., DIS, PGF and QCD Compton and for hard VMD processes. There is an uncertainty in the treatment of the resolved photon processes that has to be regarded as a systematic error. As the gluon polarization should be extracted as the final result, for the tuning stage of the analysis of course no quantities should be used that are sensitive to it to a certain extent. For that reason, the asymmetries as a function of p_T are not regarded in the tuning. The contribution from PGF to the cross section as a function of x is at most 3%, so that it can be safely neglected in double spin asymmetries vs. x.

For the results presented so far, PYTHIA was run with one of the crucial parameters of the model, MSTP(18), different from the default. This parameter sets the dividing lower cutoff in

$\hat{p}_T$ for the generation of direct events. In the default, MSTP(18)=3, this cutoff is logarithmically dependent on W^2 and would for the HERMES kinematics be around 1.4 GeV. This does not leave too much phase space for the direct events, in particular PGF. To enhance the contribution of direct events below this cutoff, MSTP(18) can be set to 2, defining the cutoff to be PARP(15)=0.5 GeV (by default). This option has been used so far. However, the cut $\hat{p}_T > 0.5$ GeV is somewhat arbitrary, and the sensitivity of the cross section to the value of PARP(15) is to be investigated. On the other hand, the default treatment with MSTP(18)=3 is physically motivated by the model described in [Sjö01], so the effect of changing MSTP(18) back to the default value should be checked as well.

Another important model assumption is the suppression of the leading order DIS process at small Q^2:

$$\sigma^{LO\,DIS} \sim \left(\frac{Q^2}{Q^2 + M_\rho^2}\right)^{-n} \left[\frac{1}{Q^2} F_2(x, Q^2)\right], \tag{4.41}$$

where $n = 2$ in the default (MSTP(19)=4), leading to $\sigma^{LO\,DIS} \to 0$ for $Q^2 \to 0$. The minimal suppression factor necessary to prevent the DIS cross section from diverging at $Q^2 \to 0$ in this model is given for $n = 1$, corresponding to MSTP(19)=1. A suppression of the partonic part of F_2 with a factor of the form $Q^2/(Q^2 + Q_0^2)$ is also assumed in other models, for instance in [Szc00b] where, similar to the PYTHIA model, the cross section is divided into a (soft) resolved and a direct partonic part. With that respect it does not seem too arbitrary to set MSTP(19)=1 in order to compare the cross section with the default.

An important issue is the description of the p_T distributions by PYTHIA. Besides the mixture of subprocesses with soft and hard p_T spectra, the p_T distributions are influenced by the intrinsic p_T of the partons inside the nucleon and the (resolved) photon and by the spread of the transverse momenta k_T acquired by the fragmenting partons during hadronization. The former is governed by the Gaussian width σ_{p_T}=PARP(91)=0.44 GeV (PARP(99)=0.44 GeV for the intrinsic k_T of the partons in the photon) which has been set different from the default PARP(91)=PARP(99)=1 GeV. The latter is described by the parameter σ_{k_T}=PARJ(21)=0.36 GeV which again is the Gaussian width of the p_x and p_y distributions of primary hadrons. The large value of PARP(91) and PARP(99) in the default was motivated by the compensation for effects of multiple soft gluon radiation in some pp or $p\bar{p}$ reactions. (cf. section 2.7.2). Fits to the p_T spectra of pions and kaons showed that for the HERMES data it is not necessary to introduce such a large effective value for the primordial transverse momentum [Jgo00], and therefore a value of around 0.4 GeV is used corresponding to what is expected from the size of the nucleon. In the photoproduction region PYTHIA has a much softer p_T spectrum than the data, though. Increasing σ_{k_T} would therefore help to achieve better agreement with the data in this region (see section 3.27 below for details). The effect of a change of PARJ(21) will therefore also be studied in the semi-inclusive region.

4.5.3 Results of the Parameter Study

For each set of parameters the cross sections $\frac{d\sigma(x)}{dx}$, $\frac{d\sigma(Q^2)}{dQ^2}$ and $\frac{d\sigma(p_T)}{dp_T}$, the double spin asymmetries $A_\parallel(x)$ and the average kinematics $\langle x\rangle(p_T)$ and $\langle Q^2\rangle(p_T)$ will be calculated for positive and negative hadrons and pions and for the sum of the charged hadrons and pions. The χ^2 per degree of freedom with respect to the data for each quantity E is calculated as

$$\chi^2/ndf = \frac{1}{N}\sum_{i=1}^{N} \frac{(E_{MC} - E_{Data})^2}{\sigma_{E,MC}^2 + \sigma_{E,Data}^2}. \tag{4.42}$$

As can be expected from, e.g., figures 4.7 and 4.30, the MC is not statistically compatible with the data, so that in general $\chi^2 \gg 1$. Also, in this comparison the systematic errors of the observed cross sections are not taken into account. If the cross sections were shifted up or down according to the systematic uncertainty, χ^2 would be dramatically larger or smaller with respect to that for the central values depending on if the the MC over- or underestimates the cross section. What matters

here is rather the *relative change* of χ^2 with the parameters. The different sets used for this study are defined as follows:

Parameter/Switch	Set #1	Set #2	Set #3	Set #4	Set #5	Set #6
MSTP(19)	4	4	4	4	4	1
MSTP(18)	2	2	2	3	3	3
PARP(15)	0.5	0.75	1.0	0.5	0.5	0.5
PARJ(21)	0.36	0.36	0.36	0.36	0.45	0.36

The settings of the other parameters and switches are the same for all sets and shown in table D.2, if they deviate from the default values of PYTHIA 6.1. Set #1 is the set that was used for all results shown so far. Table 4.2 shows the χ^2/ndf for all the above defined sets for the cross sections and average kinematics. For the interpretation of this table it is necessary to know that there are

	χ^2/ndf											
	Transition region						SIDIS region					
Quantity/Set#	1	2	3	4	5	6	1	2	3	4	5	6
$\sigma(p_T)(h^+)$	297	330	333	397	*199	1479	*45	58	60	163	171	332
$\sigma(p_T)(\pi^+)$	*38	57	63	39	420	1043	57	35	40	*24	194	430
$\sigma(p_T)(h^-)$	164	121	*117	163	608	1803	304	249	233	*192	406	821
$\sigma(p_T)(\pi^-)$	225	178	*167	225	657	1809	346	296	275	*229	448	829
$\sigma(p_T)(h^+ + h^-)$	113	*94	107	160	496	2974	82	*34	37	55	347	924
$\sigma(p_T)(\pi^+ + \pi^-)$	149	*122	128	133	999	2829	325	252	246	*168	586	1225
$\sigma(x)(h^+)$	207	251	245	*79	120	765	*91	120	123	98	119	188
$\sigma(x)(\pi^+)$	186	218	215	73	*72	599	87	82	84	47	*28	318
$\sigma(x)(h^-)$	218	191	188	104	*37	985	222	173	160	151	*76	594
$\sigma(x)(\pi^-)$	238	211	206	135	*66	911	234	191	176	164	*98	555
$\sigma(x)(h^+ + h^-)$	354	371	370	109	*87	1707	160	143	142	89	*49	673
$\sigma(x)(\pi^+ + \pi^-)$	363	368	367	146	*83	1471	266	222	214	157	*78	837
$\sigma(Q^2)(h^+)$	325	399	394	*88	154	984	115	157	162	*75	124	206
$\sigma(Q^2)(\pi^+)$	291	347	344	*92	100	762	135	141	144	55	*46	350
$\sigma(Q^2)(h^-)$	331	312	313	142	*63	1258	290	251	236	181	*105	658
$\sigma(Q^2)(\pi^-)$	318	300	295	163	*85	1112	290	254	237	189	*124	614
$\sigma(Q^2)(h^+ + h^-)$	571	626	632	140	*133	2183	244	250	251	87	*75	744
$\sigma(Q^2)(\pi^+ + \pi^-)$	526	559	559	179	*116	1792	367	338	332	186	*117	924
$\langle x\rangle(h^+)$	237	248	254	*59	87	386	120	130	140	78	100	*8.4
$\langle x\rangle(\pi^+)$	354	372	385	170	356	*14	125	131	142	92	334	*26
$\langle x\rangle(h^-)$	393	389	387	135	136	*130	65	72	70	46	46	*5.0
$\langle x\rangle(\pi^-)$	431	439	424	230	420	*14	100	110	105	87	274	*22
$\langle Q^2\rangle(h^+)$	405	443	459	*65	83	321	129	147	159	60	69	*4.7
$\langle Q^2\rangle(\pi^+)$	333	351	372	128	164	*20	100	107	120	55	32	*6.7
$\langle Q^2\rangle(h^-)$	517	547	548	149	138	*91	88	106	106	51	45	*2.3
$\langle Q^2\rangle(\pi^-)$	372	393	385	166	201	*5.1	72	87	84	52	27	*6.7

Table 4.2: χ^2/ndf for PYTHIA generated with the parameter sets 1 to 6 in the 'Transition' region (first six columns) and in the 'SIDIS' region (last six columns). The leftmost column contains the observable studied. The set with the minimal χ^2 in each region is marked with a '*'.

a factor of 2 more semi-inclusive events in the 'Transition' region than in the 'SIDIS' region. The ratio of positive hadrons to negative hadrons is about 1.5, that of positive to negative pions is about 1.2. The ratio of hadrons to pions is 1.4 (1.2) for positively and negatively charged particles. As can be seen from Eq. 4.42, the χ^2/ndf changes proportionally to $\frac{1}{\sigma^2} \sim \frac{1}{N}$. For instance, if the Monte Carlo would describe the data in the 'Transition' region as well as in the 'SIDIS' region, i.e., with the same relative deviation, χ^2/ndf would reduce by a factor 1/2 in the 'SIDIS' compared to the 'Transition' region. Qualitatively, the following results were obtained:

- The description of cross sections positive hadrons and pions vs. the inclusive variables x and Q^2 is in general slightly better in the 'SIDIS' than in the 'Transition' region. That of negative hadrons and pions is *worse* in the 'SIDIS' region (since χ^2/ndf does not change significantly there). The situation is different for the cross sections vs. p_T, where only the positive hadrons are described better in the 'SIDIS' region.

- In the inclusive variables, the best fitting cross sections are achieved with sets #4 and #5 having in common that MSTP(18)=3. The p_T distributions of set #4 are not much better than that of the standard and the other sets (except for set #6), and that of set #5 is worse than the other sets because of the too hard p_T spectrum of pions and negative hadrons due to the increased width of k_T in the fragmentation.

- As was already mentioned in section 4.5.1, negative hadrons and pions do not fit the data as well as positive hadrons and pions. In a few cases it can be observed that the sum of the charged hadron (pion) cross sections is better described than the individual ones. The reason is most likely the smaller sensitivity to the fragmentation functions.

- In terms of cross sections, set #6 does not match the data at all. At low Q^2, the cross section is overestimated by more than 50% because for MSTP(19)=1 the extra contribution from the LO DIS process is added on top of the cross section for set #4. For the kinematic distributions in p_T, set #6 gives an extraordinarily good description compared to the other sets, except for unidentified positive hadrons in the 'Transition' region. Also set #4 seems to agree acceptably well with the data concerning the kinematic distributions.

More generally, it can be stated that apparently none of the variations is able to describe the data better than any other with respect to all variables and all hadron charges and types. This implies that from the considered different parameter sets, none is truly preferred or excluded by the data. This means also that for the final extraction of the gluon polarization a reasonable selection of the presented settings must be chosen for an estimate of the systematic uncertainty. The criteria for this selection should also regard a relative weighting of the results of this comparison. For asymmetries for instance the absolute normalization of the cross sections is not so important, but rather the kinematics and the p_T slopes of each subprocess.

The asymmetries vs. x themselves turn out to be remarkably stable against a variation of the parameters. The variation of the MC asymmetries from the different sets is usually less than the variation from the different possibilities to describe the spin dependence of the resolved photon processes as shown in the appendix C.1. The χ^2/ndf ranges are mostly between 1 and 2. This also illustrates that despite the large deviations of the MC with respect to the cross section, the asymmetries can be reproduced rather well.

Another variation can be achieved if other unpolarized parton distributions are used. The proton PDFs used for the settings studied above were the CTEQ5LO sets [Lai00]. These were exchanged for the parameters of set #1 with the PDFs from GRV98 [Glü98] and the central gluon set of MRST98 [Mar98]. A variation of the photon PDFs (in the default SaS-G 1D [Schu96] is used) was also studied by using GRV-G [Glü92] instead. The χ^2/ndf for the cross sections and kinematic correlations were usually in the same range as for set 1 to 3, i.e., qualitatively the agreement with the data does not change considerably. The resulting changes can also be regarded in terms of a systematic error on the final result.

4.6 The Quasireal Photoproduction Cross Section in PYTHIA

After having shown that the PYTHIA cross sections of hadrons and pions in the semi-inclusive region agree with those of the data on a 10 to 20% level it remains to investigate how the PYTHIA model is able to describe the 'Photoproduction' region. At HERMES this region is defined by the antitagging of the scattered lepton in the acceptance for the bulk of the data meaning that the

lepton angle is too small for it to be detected and therefore Q^2 is very small. On the other hand there is a small contribution of events where the lepton angle is too *large* for detection and Q^2 is rather large (cf. figure 3.4). Since the event kinematics in the 'Photoproduction' region are unknown it is hardly possible to compare the data directly with possible parametrizations in PYTHIA. The only observables that can be used for a comparison are the distributions of momentum and transverse momentum of hadrons. Ideally it should be possible to use those PYTHIA parameters known to describe the semi-inclusive data well also for quasireal photoproduction. In the following, a comparison of PYTHIA with the data is performed that is mainly based on the parameter set given in table D.2. In the 'Photoproduction' region QED radiative effects are negligible which is why the PYTHIA data shown were generated at Born level.

4.6.1 The Pion Pair Production Cross Section

At low Q^2 and transverse momentum the cross section should according to the PYTHIA model be completely dominated by soft VMD processes. In diffractive VMD, dominantly ρ^0 are produced leading to a more or less exclusive $\pi^+\pi^-$ final state. For pions PYTHIA predicts a large fraction of elastic VMD events of around 30 to 40% at $p_T \approx 0.5$ GeV. Since no other MC generator is available at HERMES for quasireal photoproduction data it is not possible to perform a sanity check as in section 4.4 where the fraction of elastic ρ^0 events in the semi-inclusive pion sample was derived from data with an acceptance correction from various MC models. It is possible however to compare both the exclusive ρ^0 cross section and the inclusive hadron cross section from PYTHIA to the data. Because of the unknown event kinematics of course it is not possible to unambiguously select exclusively produced pion pairs. However, the fraction of pion pairs from elastically produced ρ^0 in PYTHIA is about 70–80% in the ρ^0 mass region from 0.6 to 0.95 GeV for events with only the two pion tracks in the acceptance. So the mass distributions of 'exclusive' hadron or pion pairs and other distributions of ρ^0 candidates in the ρ^0 mass region can give some hint on the compatibility of the PYTHIA VMD model with the data. Figure 4.31 shows the mass distribution of h^+h^- and $\pi^+\pi^-$ pairs of the 1997 polarized hydrogen data compared to those of PYTHIA with the standard parameter setting, table D.2. The plot clearly shows that the mass distributions of the data and

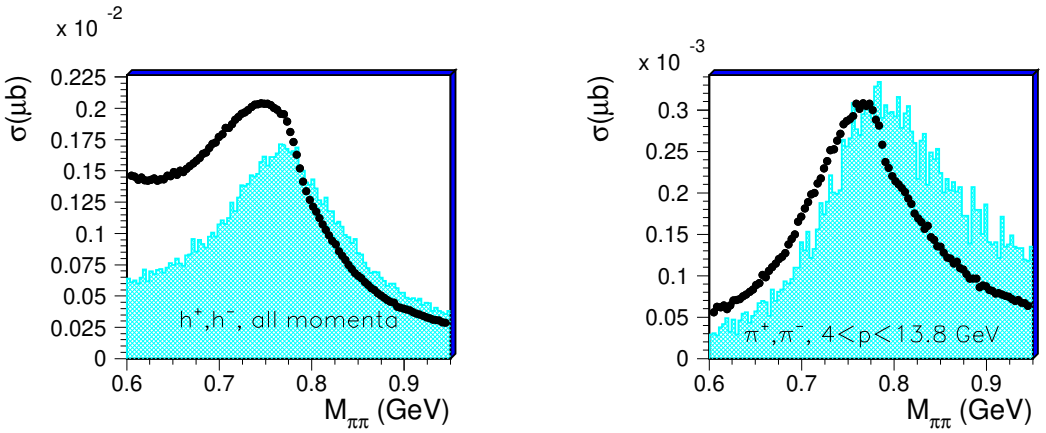

Figure 4.31: Cross section of h^+h^- (left) and $\pi^+\pi^-$ pairs as a function of the two pion invariant mass in the 'Photoproduction' region. The points show the 1997 polarized hydrogen data, the histograms the result from PYTHIA. The data have been corrected for trigger efficiencies.

the MC do not agree. The behavior depends on the momentum cut ($p > 0$ GeV for hadrons, $p > 4$ GeV for both pions), since for hadrons the MC underestimates the cross section in the low mass region and overestimates it for pions in the high mass region. Similarly, the extrapolation to masses smaller than 0.6 GeV or higher than 1 GeV results in the corresponding cross sections to be lower resp. higher than the data. The reason for this can be made out to lie in the way PYTHIA simulates the mass distribution of the elastically produced ρ^0. PYTHIA by default (MSTJ(24)=2)

generates the mass distribution of decaying particles with a non-relativistic Breit-Wigner function:

$$\frac{dN}{M_{\pi\pi}} \sim \frac{\Gamma_\rho/2}{4(M_\rho - M_{\pi\pi})^2 + \Gamma_\rho^2}, \tag{4.43}$$

where M_ρ and Γ_ρ are the nominal mass and width of the ρ^0 resonance. It is possible to change this to a form of a relativistic Breit-Wigner (MSTJ(24)=3):

$$\frac{dN}{M_{\pi\pi}} \sim \frac{M_\rho^2\Gamma_\rho}{(M_\rho^2 - M_{\pi\pi}^2)^2 + M_\rho^2\Gamma_\rho^2}, \tag{4.44}$$

For broad resonances there exist more complicated forms of the relativistic Breit-Wigner function taking into account that the width of a resonance can depend on its actual mass. For the ρ^0 a commonly used form is [Tyt01]:

$$\frac{dN}{M_{\pi\pi}} = BW(M_{\pi\pi}) \sim \frac{M_{\pi\pi}M_\rho\Gamma_{\pi\pi}}{(M_\rho^2 - M_{\pi\pi}^2)^2 + M_\rho^2\Gamma_{\pi\pi}^2}, \tag{4.45}$$

where the nominal width has been replaced with a mass dependent width

$$\Gamma_{\pi\pi} = \Gamma_\rho \left(\frac{q}{q_0}\right)^{2l+1} \frac{M_\rho}{M_{\pi\pi}} \tag{4.46}$$

with $l = 1$ for a spin 1 resonance and

$$q = \frac{1}{2}\sqrt{M_{\pi\pi}^2 - 4M_\pi^2}, \qquad q_0 = \frac{1}{2}\sqrt{M_\rho^2 - 4M_\pi^2}. \tag{4.47}$$

The left plot of figure 4.32 shows the distribution from the non-relativistic Breit-Wigner of Eq. 4.43 compared to the relativistic p-wave Breit-Wigner of Eq. 4.45. The relativistic p-wave Breit-

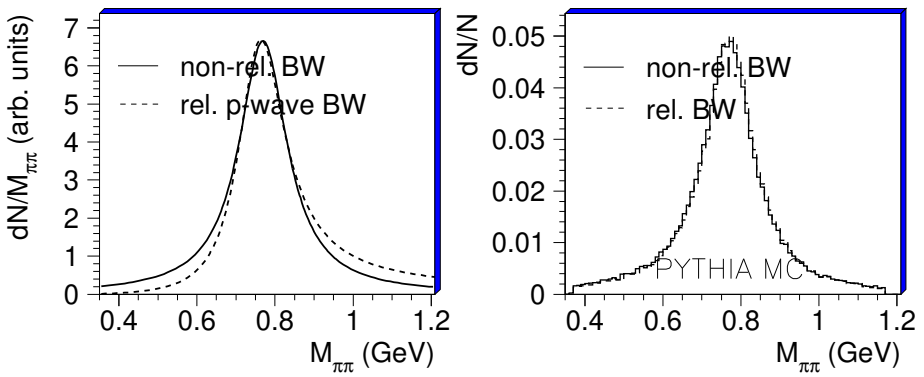

Figure 4.32: Left: A non-relativistic Breit-Wigner shape (solid line) compared to the shape of a relativistic p-wave Breit-Wigner (dashed line). Right: Mass distributions generated with PYTHIA and option MSTJ(24)=2 (non-relativistic Breit-Wigner – solid histogram) and option MSTJ(24)=3 (relativistic Breit-Wigner (Eq. 4.44) – dashed histogram.

Wigner is clearly asymmetric with respect to the nominal ρ^0 mass, with a suppression of lower and an enhancement of higher masses. On the right side of figure 4.32 a comparison of the PYTHIA generated mass distributions for the two options MSTJ(24)=2,3 is displayed. There is hardly any difference between the relativistic and non-relativistic Breit-Wigner distributions in the Monte Carlo, and both are rather symmetric. The choice of the Breit-Wigner function in the MC alone does not yet explain the discrepancies of the mass distributions. If a Breit-Wigner of the form 4.45 would be used instead of the PYTHIA options, the disagreement would get even worse, since the low mass region would be even less populated, and the high mass region even more. However, neither of

the above Breit-Wigner functions is able to describe the mass distributions of elastically produced ρ^0 in the VMD model. It was proposed by Ross and Stodolsky that for elastic ρ^0 production from real photons, the mass distribution should be modified by a factor $M_\rho^4/M_{\pi\pi}^4$ [Ros66] leading to a *skewing* of the Breit-Wigner by a noticeable amount, and to a shift of the mass peak. Experimentally, elastic ρ^0 data are fitted to a mass distribution of the form

$$\frac{dN}{dM_{\pi\pi}} = BW(M_{\pi\pi}) \left(\frac{M_\rho}{M_{\pi\pi}}\right)^{n_{skew}}. \tag{4.48}$$

The skewing parameter n_{skew} is Q^2 and t dependent and has been measured by various experiments. The HERMES results range between $n_{skew} = 3.6 \pm 0.3$ for $Q^2 \simeq 0.8$ GeV^2 and $n_{skew} = 1.5 \pm 0.5$ for $Q^2 \simeq 3.7$ GeV^2 [Tyt01]. For quasireal photoproduction data from ZEUS n_{skew} was measured to be 5.13 ± 0.13 [Bre98], H1 measured $n_{skew} = 5.84 \pm 1.05$ [Aid96a]. Indeed the measured values of n_{skew} rise as Q^2 gets smaller but are rather W^2 independent. This suggests that also for the HERMES kinematics in elastic (quasireal) photoproduction of ρ^0 Eq. 4.48 should be applied, with a skewing parameter of around 5 to 6. This statement can be tested by applying an additional weight to the PYTHIA data for ρ^0 from the elastic process $\gamma^* p \to \rho^0 p$ (process 91) and comparing the resulting cross sections again with the data. In principle the skewing factor would have to be applied to data generated according to Eq. 4.45, but since this is not possible the ratio of the relativistic p-wave Breit-Wigner $BW(M_{\pi\pi})$ (Eq. 4.45) to the non-relativistic Breit-Wigner (Eq. 4.43) has to be multiplied with the skewing factor of Eq. 4.48 to 'correct' the generated PYTHIA mass distribution:

$$C(M_{\pi\pi}) = \frac{M_{\pi\pi} M_\rho \Gamma_{\pi\pi}}{(M_\rho^2 - M_{\pi\pi}^2)^2 + M_\rho^2 \Gamma_{\pi\pi}^2} \frac{4(M_\rho - M_{\pi\pi})^2 + \Gamma_\rho^2}{\Gamma_\rho} \left(\frac{M_\rho}{M_{\pi\pi}}\right)^6. \tag{4.49}$$

The mass dependence of the cross section of hadron and pion pairs from PYTHIA reweighted with the factor $C(M_{\pi\pi})$ is depicted in figure 4.33 and compared to that of the data. In all mass

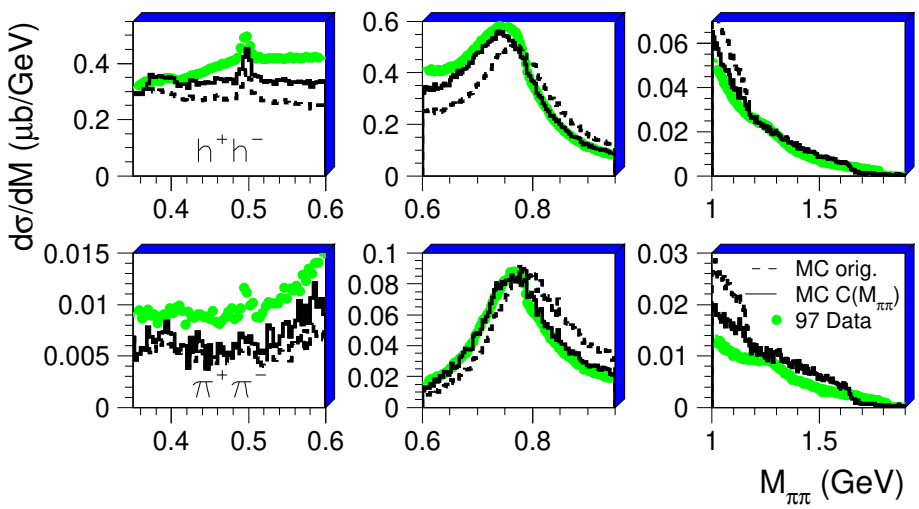

Figure 4.33: The differential cross section of hadron pairs (top plots) and pion pairs with $4 < p_\pi < 13.8$ GeV (bottom) plots as a function of the invariant two-pion mass from the 97 polarized data (dots) and PYTHIA (lines). The dashed line is the PYTHIA cross section generated with option MSTJ(24)=2, the full line depicts the same cross section weighted with the factor $C(M_{\pi\pi})$ (Eq. 4.49).

regions the reweighted PYTHIA cross sections agrees better with the data. This is also true for the momentum and angular distributions of the h^+h^- ($\pi^+\pi^-$) system and of and the individual hadrons (pions). The agreement of the reweighted cross section in the ρ^0 mass region with the

data is excellent. The conclusion from figure 4.33 is that the lack of skewing in the generated mass distribution of elastically produced ρ^0 is likely to be the reason for the bad description of the h^+h^- data in the 'Photoproduction' region. The effect of this skewing on the *inclusive* hadron and pion cross section remains to be investigated in the next section.

4.6.2 Inclusive Hadron Cross Sections

Inclusive cross sections of charged unidentified hadrons and identified pions, kaons, protons and antiprotons have been measured in the 'Photoproduction' region as a function of their momentum and transverse momentum, and compared to the cross section generated by PYTHIA. Figure 4.34 shows the experimental cross sections from the 2000 polarized deuteron data vs. p_T. For uniden-

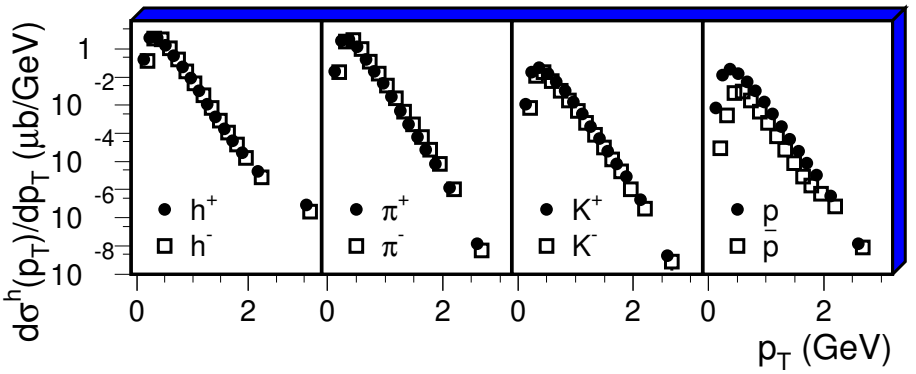

Figure 4.34: The differential cross section of charged hadrons, pions, kaon and protons/antiprotons (from left to right) vs. p_T from the 2000 polarized deuteron data. The identified hadrons have $2 < p < 15$ GeV. The data have been corrected for trigger efficiencies. The filled circles are for positive hadrons, the open squares for negative hadrons. The points for the negative hadrons have been shifted by 0.075 GeV for more visibility.

tified hadrons there is no upper momentum cut that, in combination with the acceptance of the spectrometer, leads to a significantly larger cross section of hadrons at large p_T than for the sum of all identified hadrons with $p < 15$ GeV. At small p_T, the kaon to pion cross section ratio is around 9% for positive and 6% for negative particles. The proton to (positive) pion cross section ratio is about 7%, the antiproton to (negative) pion cross section ratio is only about 2%. The p_T spectrum of both kaons and protons/antiprotons is much harder than that of the pions, as the cross section ratios rise to about 0.3 for kaons, to 0.25 for antiprotons and to 0.5 for protons.

The cross section ratio $\frac{\sigma(Data)}{\sigma(MC)}$ of hadrons and pions is shown in figure 4.35 as a function of p_T and p. Two different parameter sets are compared to the data, the standard set #1 and set #5 of section 4.5.3. For set #5 the width of the p_T acquired during fragmentation (PARJ(21)) was increased to 0.45 GeV from the default of 0.36 GeV. In table 4.2 it was shown that the agreement of semi-inclusive cross sections vs. p_T gets worse if the p_T spectrum is made harder. In the 'Photoproduction' region a harder spectrum than the one obtained by the standard setting seems to be necessary to better describe the measured cross section at $p_T > 0.5$ GeV. Especially in the p_T range of 0.5 to 1.5 GeV the data to Monte Carlo ratio improves considerably. The larger σ of the p_T distribution should be viewed as an effective value to account for unknown effects not included in the Monte Carlo (for instance soft gluon radiation) which is justified only by the better agreement with the data. Therefore, for the extraction of the final result, the difference between sets #1 and #5 has to be taken into account as a systematic uncertainty. The effect of increasing the width of the *intrinsic* k_T of partons in the nucleon and in the photon was investigated by setting the values PARP(91) and/or PARP(99) to the default of 1 GeV. This should actually have a similar effect as the increase of the fragmentation width, but it was found that the agreement of the cross sections gets even worse than with sets #1 and #5. The reason for this was not further investigated, it is

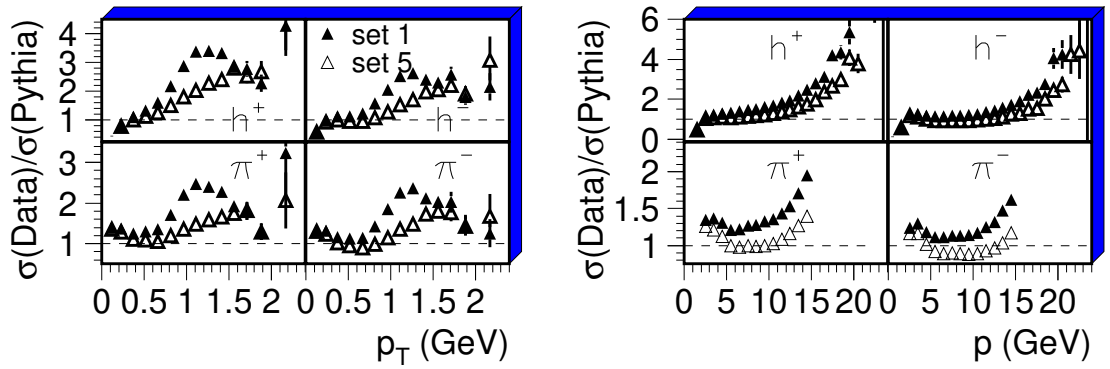

Figure 4.35: Cross section ratios Data/MC for hadrons (top panels) and pions (bottom panel) vs. p_T (left) and p (right). The data are the 2000 polarized deuterium data, the MC is obtained using parameter sets #1 (filled symbols) and #5 (open symbols).

believed that it has to do with the correlations of transverse and total momentum in the acceptance of the spectrometer. It was also investigated whether the enhancement of the LO DIS process with MSTP(19)=1 (i.e. set #6 of section 4.5.3) could improve the description of the data. The cross section changed only marginally, though.

The largest difference between MC and data is seen for positive unidentified hadrons. There are two reasons for this. First, the Monte Carlo apparently does not reproduce the momentum spectra very well, independent of the hadron type as is shown in the right plot of figure 4.35 for hadrons and pions as an example. The deviations between data and MC get larger the larger the momentum is. Since there is no upper momentum cut for unidentified hadrons, the difference in the momentum spectra clearly shows up there at higher p_T. The second reason is that the cross section for protons and positive kaons is off by factors from the data. They agree even less than in the semi-inclusive region (figure 4.29). The cross section ratio for kaons and (anti-) protons is shown in figure 4.36 vs. p_T. In general, the disagreement of the Monte Carlo cross sections

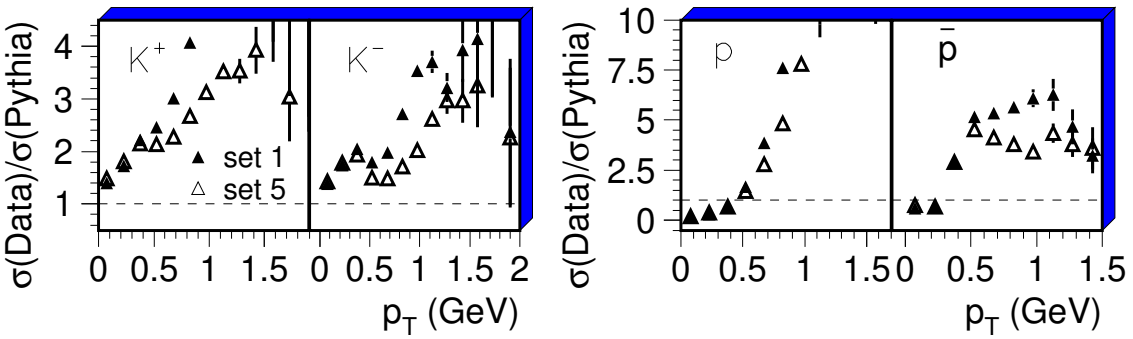

Figure 4.36: Cross section ratios Data/MC for kaons (right plot) and protons and antiprotons (left plot) vs. p_T. The data are the 2000 polarized deuterium data, the MC is obtained using parameter sets #1 (filled symbols) and #5 (open symbols).

with the data is more or less due to the fact that at the rather low HERMES energy processes might contribute which lead to distinct hadron spectra and which are not included in PYTHIA. In PYTHIA instead the so called 'low-p_T' process is the minimum bias process accounting for that part of the cross section that cannot be parametrized by diffractive VMD and pQCD processes. The hadron spectrum in this process is created generically by fragmenting partons and smearing them in p_T. It is obvious that this generic process will not be able to describe the spectra arising from, for example, exclusive processes like $\gamma^* p \to \pi^+ n$ and $\gamma^* p \to K^+ \Lambda$. Due to the unknown kinematics it is also impossible to exclude contributions from such processes from the data sample. It may

also be possible that at small p_T the data receive contributions from $W^2 < 4$ GeV^2. This region is below the lower cutoff of PYTHIA. Without any further knowledge on the event kinematics and the variety of the contributing processes it may thus not be possible to improve further on the Monte Carlo description of the data.

In section 4.6 it was shown that the MC cross section of 'exclusive' $\pi^+\pi^-$ pairs in the 'Photoproduction' region would agree fairly well with the data, if the skewing of the mass distribution of elastically produced ρ^0 were taken into account. The possible effect of this skewing can also be investigated for the case of the inclusive pion cross sections by weighting each pion track in the Monte Carlo with the factor $C(M_{\pi\pi})$ from Eq. 4.49 if it originated from an elastic VMD process with a ρ^0. The ratio of the weighted to the unweighted Monte Carlo cross section for pions is plotted in figure 4.37. From this figure follows that if the mass skewing were included correctly in

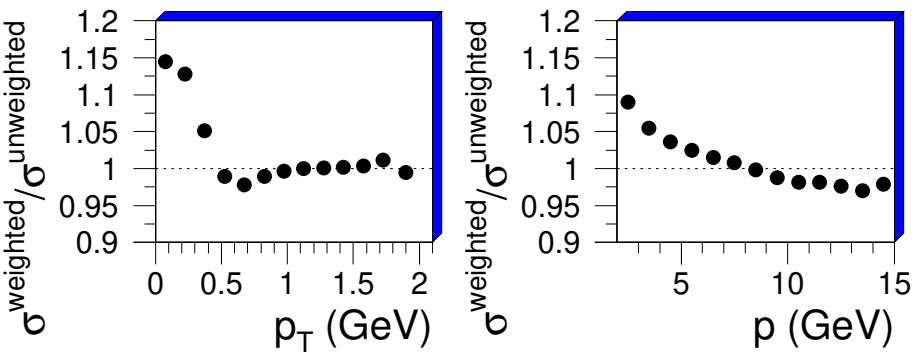

Figure 4.37: The ratio of PYTHIA cross sections (set #5) with and without the correction factor $C(M_{\pi\pi})$ for the mass skewing of the ρ^0.

the MC, the pion cross section would be maximum 15% percent larger at small p_T, thus improving the agreement with the data only at small p_T and momentum. It can also be seen that at larger p_T there is no effect from the skewing so that the contribution of elastic VMD to the cross section there can be considered to be correct also without the reweighting.

Chapter 5

Extraction of the Gluon Polarization

This chapter deals with the extraction of the gluon polarization in the nucleon, based on the HERMES data on double spin asymmetries of high-p_T hadrons. The first part addresses some general considerations about the extraction method, systematic and statistical uncertainties and cut optimization. In the second part results will be given for the different kinematic regions and interpreted in the context of the PYTHIA model described earlier.

5.1 General Considerations

5.1.1 Formalism

For the extraction of the gluon polarization from the measured asymmetries of single high-p_T hadrons Monte Carlo information is required about the event kinematics, the fractions of the contributing subprocesses f_i and their asymmetries $A_\parallel^i$. All this information can be retrieved using the Monte Carlo asymmetries constructed as described in appendix C.1. The measured asymmetry $A_\parallel^{meas}$ can be pictured as the incoherent sum of the contributions of all possible subprocesses i:

$$A_\parallel^{meas} = \sum_i f_i A_\parallel^i. \tag{5.1}$$

The contributing subprocesses in the PYTHIA model are diffractive and non-diffractive VMD, anomalous photon processes, leading order DIS, QCD Compton scattering and Photon-Gluon Fusion. The hard resolved photon processes $qg \to qg$, $gg \to q\bar{q}$ and $gg \to gg$ and the Photon-Gluon Fusion process (may) involve a target gluon and are therefore sensitive to the gluon polarization in the nucleon. Defining the fraction of the sum of these processes as the 'signal' contribution f_{sig} and, consequently, the fraction of the sum of all other processes as 'background' f_{BG}, the measured asymmetry is

$$A_\parallel^{meas} = f_{BG} A_\parallel^{BG} + f_{sig} A_\parallel^{sig} = \frac{1}{N_{tot}} \left[\sum_{i=1}^{N_{BG}} a_i^{BG} + \sum_{i=1}^{N_{sig}} a_i^{sig} \right] \tag{5.2}$$

with $N_{tot} = N_{BG} + N_{sig}$ the total number of events and a_i the event asymmetry weight calculated as in appendix C.1. For the signal processes

$$a_i^{sig} = \hat{a}_i(Q^2, \hat{s}, \hat{t}, \hat{u}) \frac{\Delta G(\hat{Q}^2, x_G)}{G(\hat{Q}^2, x_G)} \tag{5.3}$$

where $\hat{a}_i(Q^2, \hat{s}, \hat{t}, \hat{u})$ is the hard subprocess asymmetry depending on the type of the $2 \to 2$ process, the parton kinematics described by the Mandelstam variables and the photon virtuality. The gluon polarization is probed at the hard scale of the process, $\hat{Q}^2$, and the nucleon momentum fraction

carried by the struck gluon $x_G = x(1 + \hat{s}/Q^2)$. For a given bin or range in the measured p_T the 'signal' asymmetry can be written as

$$\sum_{i=1}^{N_{sig}(p_T)} a_i^{sig} \equiv N_{sig}(p_T)\langle \hat{a}^{sig}(p_T)\rangle \left\langle \frac{\Delta G}{G} \right\rangle (p_T) \tag{5.4}$$

The average gluon polarization $\left\langle \frac{\Delta G}{G} \right\rangle$ is then in that given range:

$$\left\langle \frac{\Delta G}{G} \right\rangle (p_T) = \frac{1}{N_{sig}(p_T)\langle \hat{a}^{sig}\rangle (p_T)} \left[N_{tot}(p_T) A_\parallel^{meas}(p_T) - N_{BG}(p_T) A_\parallel^{BG}(p_T) \right]. \tag{5.5}$$

The statistical error of the gluon polarization is (cf. section C.2 in the appendix):

$$\begin{aligned} \delta^2 \left\langle \frac{\Delta G}{G} \right\rangle &= \frac{1}{N_{sig}^2 \langle \hat{a}^{sig}\rangle^2} \Bigg[N_{tot}^2 \delta^2 A_\parallel^{meas} + N_{BG}^2 \delta^2 A_\parallel^{BG} + \frac{N_{BG}}{N_{sig}} N_{tot} \left(A_\parallel^{meas} \right)^2 \\ &\quad + \left(N_{tot} A_\parallel^{meas} - N_{BG} A_\parallel^{BG} \right)^2 \frac{\delta^2 \langle \hat{a}^{sig}\rangle}{\langle \hat{a}^{sig}\rangle^2} \Bigg], \end{aligned} \tag{5.6}$$

where the p_T dependence was omitted. In principle the Monte Carlo statistics can be made large enough for $\delta^2 A_\parallel^{BG}$ and $\delta^2 \langle \hat{a}^{sig}\rangle$ to vanish. As the measured asymmetry is usually small and the term in front of $(A_\parallel^{meas})^2$ only proportional to N_{tot} the dominant contribution comes from the first term in Eq. 5.6. Depending on particular lower ($p_{T,cut}$) and upper cuts ($p_{T,max}$) on p_T the error can then be approximated by:

$$\delta \left\langle \frac{\Delta G}{G} \right\rangle_{cut} = \frac{\int_{p_{T,cut}}^{p_{T,max}} dp_T \left[\frac{1}{\langle \hat{a}^{sig}\rangle} \frac{N_{tot}}{N_{sig}} \delta A_\parallel^{meas} \right] (p_T)}{\int_{p_{T,cut}}^{p_{T,max}} dp_T}. \tag{5.7}$$

To reach a minimum of the quantity $\delta \left\langle \frac{\Delta G}{G} \right\rangle_{cut}$ it is thus necessary to choose $p_{T,cut}$ and $p_{T,max}$ such that the statistical error of the data asymmetry, the signal to background ratio (i.e., the fraction of the PDF subprocess) and the subprocess kinematics are optimized against each other. The influence of cuts on p_T and possibly W^2 (or the total energy sum of the particles in 'Photoproduction' events) has to be studied. The fraction of PGF events as a function of p_T is shown in figure 5.1 for positive and negative hadrons in the 'Photoproduction', 'Transition' and 'SIDIS' regions. While the PGF

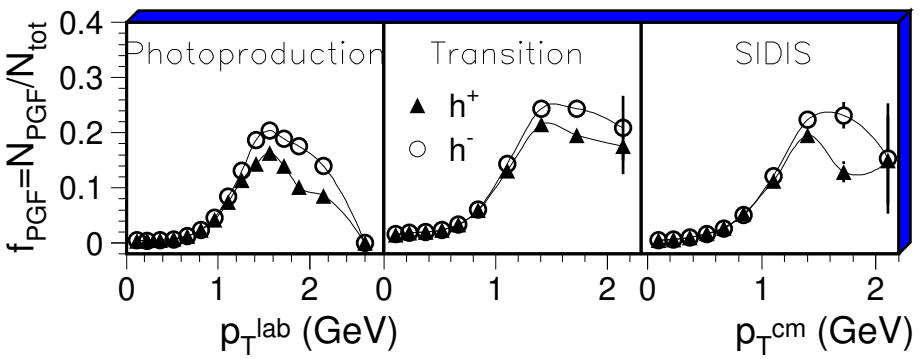

Figure 5.1: The fractions of events from the PGF subprocess in the 'Photoproduction-' (left), 'Transition-' and 'SIDIS' regions (right) as a function of p_T for positive (filled triangles) and negative (open circles) hadrons. The fractions are obtained from PYTHIA generated with parameter set #1.

fractions are negligible below $p_T = 1$ GeV, they rise above that to some maximum value of about 20 to 25% for negative hadrons, and slightly less for positive hadrons. The reason for the drop in

the 'Photoproduction' region at $p_T > 1.5$ GeV is that there the LO DIS process starts to dominate due to the 'tagging' of large Q^2 DIS events with the requirement of large hadron angles at large p_T (corresponding to large angles of the virtual photon and scattered lepton, see section 2.7.4). The PGF subprocess asymmetry in the three kinematic regions is displayed in figure 5.2 vs. the lab transverse momentum for the 'Photoproduction' data and vs. the transverse momentum in the $\gamma^* p$ system for the semi-inclusive data. The subprocess asymmetry clearly depends on the kinematics,

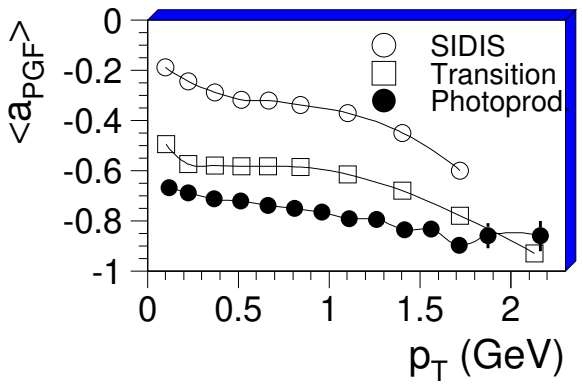

Figure 5.2: The average PGF subprocess asymmetry vs p_T for the 'SIDIS'- (open circles), the 'Transition'- (squares) and the 'Photoproduction' region (filled circles) for positive and negative hadrons.

its magnitude is largest in the 'Photoproduction' region and smallest in the 'SIDIS' region. The reason for the different size of $\langle a_{PGF} \rangle$ in the three kinematic regions lies in Eqs. C.11 to C.13 expressing the Q^2 dependence of the PGF subprocess asymmetry. At $Q^2 \approx 0$ as (for PGF) in the 'Photoproduction' region, the asymmetry is close to -1, while its absolute value decreases the larger Q^2 becomes.

5.1.2 Cut Studies

There are two aspects to the cut optimization. First and mainly it is necessary to define the region in p_T from which the gluon polarization should be extracted. The need for lower (and possibly upper) cuts on p_T can be seen in figure 5.1 from which it becomes clear that the sensitivity to the gluon polarization through the PGF process depends strongly on p_T. This sensitivity is very small at small p_T and becomes more significant at p_T above 1 GeV. As explained in section 2.7.4, this is what is to be expected if the width of the transverse momentum distribution of hadrons from processes not involving hard gluons, i.e., the nonperturbatively generated p_T is, (cf. Eq. 2.141)

$$\langle p_T^2(z) \rangle \sim \langle p_{T,F}^2 \rangle + z^2 \langle k_T^2 \rangle. \tag{5.8}$$

With an average $z \approx 0.5$ of hadrons, and the average intrinsic k_T and the transverse momentum from the fragmentation $p_{T,F}$ both being about 0.4 GeV, the average nonperturbative p_T ranges between 0.4 to 0.5 GeV. Therefore, at $p_T \approx 1$ GeV, about two times the width of the nonperturbative transverse momentum, the contribution of the LO DIS and nonperturbative processes should be reduced considerably and the PGF contribution consequently enhanced. From figure 4.25 it can be seen that also the fraction of diffractive processes is very small for $p_T > 1$ GeV. The fraction of PGF events in the data not only determines the statistical error (through Eq. 5.7), but also the systematic uncertainties, due to the fact that the uncertainties on the size and the asymmetry of the background propagate into that of $\frac{\Delta G}{G}$ with a factor $1/f_{PGF} = \sigma_{tot}/\sigma_{PGF}$. One more consideration is that the measured p_T should be correlated to the $\hat{p}_T$ of the hard subprocess controlling the scale at which the gluon distribution is probed. To reduce the scale dependence of the result, this scale should be as large as possible.

As a second aspect, it might be worthwhile to check if further constraints on the phase space and inclusive kinematics improve the significance of the result. Several combinations of of

cuts on p_T and an additional variable, for instance W^2 or z in the semi-inclusive regions or the sum of hadron momenta in a 'Photoproduction' event were studied. Although the fraction of PGF events was found to depend on all of these variables, no cut or range could be determined that would decrease the statistical error of $\frac{\Delta G}{G}$ (Eq. 5.7) by more than about 5%.

p_T-Range in the 'Photoproduction' Region

For the 'Photoproduction' region figure 5.3 depicts the quantity $\delta \left\langle \frac{\Delta G}{G} \right\rangle_{cut}$, defined by Eq. 5.7, as a function of the lower limit on p_T from which the integration over the data starts. There is clearly

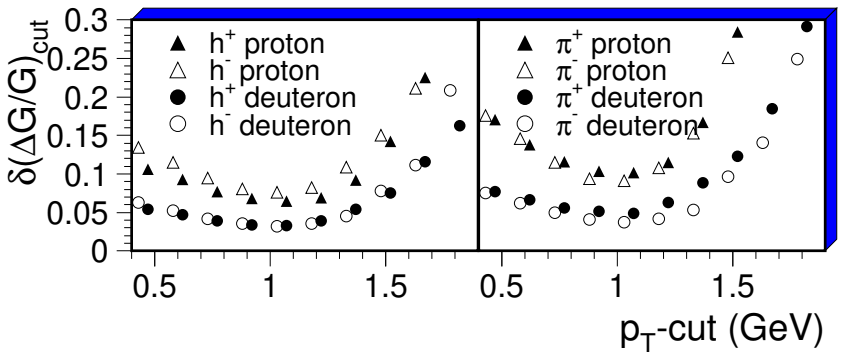

Figure 5.3: The dependence of the statistical error of $\Delta G/G$ on the lower cut on p_T imposed on the asymmetries of high-p_T hadrons in the 'Photoproduction' region. The left plot is for hadrons, the right plot for identified pions with $4 < p < 13.8$ GeV (proton) and $2 < p < 15$ GeV (deuteron).

a minimum at about $p_T \simeq 1$ GeV for all hadrons and all targets, coinciding with the 'theoretical' minimum p_T discussed above. The projected statistical error is quite small in the 'Photoproduction region' such that, if it is possible to combine the results on proton and deuteron, several bins in p_T can be defined for which a result on $\frac{\Delta G}{G}$ can be extracted. Due to the MC underestimating the cross section at large p_T, it is practically impossible to populate the last p_T bin of 2.5 to 5 GeV for the MC data, although the experimental data of unclassified hadron data have a sufficient amount of events. Because of that, and also because the fraction of PGF events is close to 0 at very high p_T, also an *upper* cut of $p_T < 2.5$ GeV will be imposed on the data.

The correlation between the measured hadron transverse momentum and the partonic transverse momentum generated in the PGF process predicted by PYTHIA can be seen in figure 5.4. Only above $p_T(h) \approx 1$ GeV a correlation can be observed while at smaller $p_T(h)$ the average $\hat{p}_T$ is

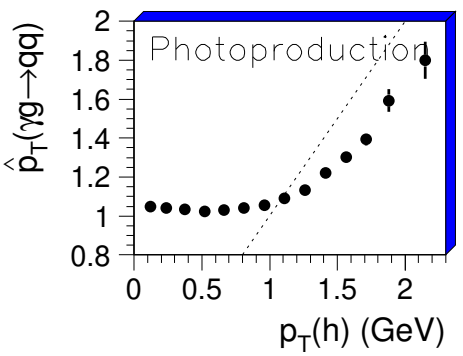

Figure 5.4: The average $\hat{p}_T$ of the PGF process from PYTHIA as a function of the measured p_T of the hadrons. The line goes along $\hat{p}_T = p_T(h)$.

constant, indicating that it is in this region dominated by the internal cutoffs and scales in PYTHIA or in parton distributions. Using PYTHIA, results on $\frac{\Delta G}{G}$ should therefore be only extracted for p_T above 1 GeV.

p_T-Range in the Semi-inclusive Regions

In the semi-inclusive region the situation is quite different. First, the statistical error of $\frac{\Delta G}{G}$ is much larger than in the 'Photoproduction' region. Second, there can be no clear minimum found for any lower cut on p_T in the 'Transition' region. The error is not depending on the cut below $p_T \approx 1$ GeV, and is then rising, as it is shown in the left panel of figure 5.5 for hadrons and pions from deuteron. Although a minimum for the projected error on $\frac{\Delta G}{G}$ exists in the 'SIDIS' region, again

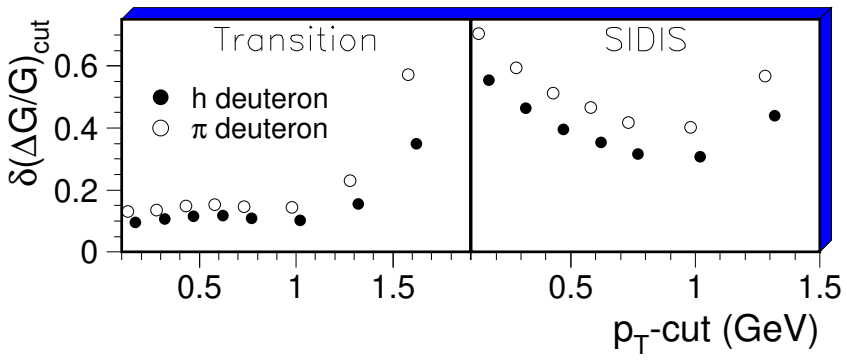

Figure 5.5: The dependence of the statistical error of $\Delta G/G$ on the lower cut on p_T imposed on the asymmetries of charged high-p_T hadrons ($h^+ + h^-$) and pions with $2 < p < 15$ GeV in the 'Transition' region (left) and the 'SIDIS' region (right) for deuterium.

at $p_T \approx 1$ GeV, the error is even at this point too large to obtain a statistically meaningful result from the 'SIDIS' region only. Note that a combination with the proton data would yield about 25% more statistics and therefore not lead to a real improvement. Responsible for the large statistical uncertainty is not only the twice as large statistical error of the measured asymmetries (cf. figure 3.23), but also the twice as small magnitude of the PGF subprocess asymmetry compared to the 'Transition' region. In the following, the 'SIDIS' region will not be considered separately anymore. The term 'semi-inclusive data' will refer to data from the 'Transition' region.

Obviously, also in the 'Transition' region the statistical errors are too large to consider more than one bin in p_T for extracting results on $\frac{\Delta G}{G}$. For the decision on a possible lower p_T cut definitely other criteria than a statistical optimum are required. Figure 5.6 shows the combined asymmetry for charged hadrons on proton together with hypothetical Monte Carlo asymmetries for $\frac{\Delta G}{G} = -1$ (upper 3 lines), $\frac{\Delta G}{G} = 0$ (middle 3 lines) and $\frac{\Delta G}{G} = +1$ (lower 3 lines). The different curves correspond to three different methods of treating the background asymmetry (cf. section C.1) (solid line: $A_1^{low-p_T} \sim A_1^{exp}$, dashed line: $A_1^{low-p_T} = 0$, dotted line: $A_1^{low-p_T} \sim A_1^{exp}$, $A_1^{diffr} \approx 2A_1^{exp}$). Below $p_T = 0.75$ GeV the data are not sensitive to even an extreme variation of $\frac{\Delta G}{G}$. However, only above $p_T > 1$ GeV the theoretical uncertainties arising from the variation of the background asymmetry are small enough to allow a clear statement about the value of $\frac{\Delta G}{G}$. A correlation between the measured p_T and that of the hard subprocess exists, like in the 'Photoproduction' region, only for $p_T > 1$ GeV, as it is shown in figure 5.7 where the average of the Monte Carlo generated $\hat{p}_T$ for PGF is plotted against the measured hadron transverse momentum $p_T(h)$. Together with the above considerations this leads to the conclusion that also in the semi-inclusive region a cut on $p_T > 1$ GeV should be imposed.

5.2 Results for the 'Photoproduction' Region

In this section, the results on the gluon polarization determined from the 'Photoproduction' data with the above described formalism will be presented together with systematic studies. Here, the data are integrated over p_T from a lower cut on, and eventually this lower cut will be varied to

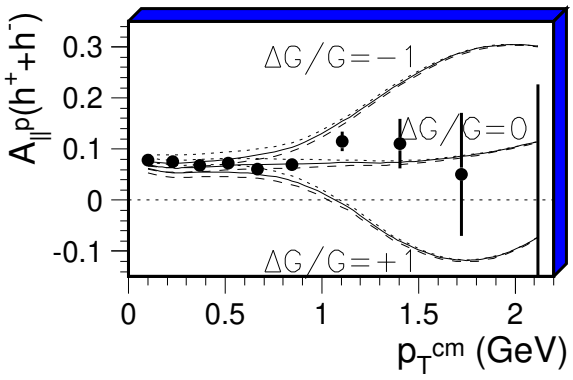

Figure 5.6: The MC projections for asymmetries of charged hadrons on proton with $\frac{\Delta G}{G} = \pm 1, 0$ superimposed with the measured asymmetry. See text for details.

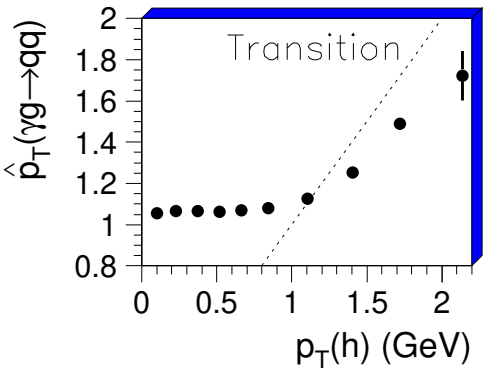

Figure 5.7: The average $\hat{p}_T$ of the PGF process from PYTHIA as a function of the measured p_T of the hadrons. The line goes along $\hat{p}_T = p_T(h)$.

investigate the dependence of the result on it. Later, in section 5.5.1, the results will be presented as a function of p_T for several bins in the range $0.9 < p_T < 2.5$ GeV.

5.2.1 Results From the Standard Monte Carlo

In a first step, $\frac{\Delta G}{G}$ will be extracted from positive and negative hadrons, positive and negative pions and the proton and the deuteron data separately for $1.05 < p_T < 2.5$ GeV. All results will be checked for their mutual consistency. For this purpose, the standard set (set #1 defined in table D.2) of PYTHIA parameters will be used. The Monte Carlo data were generated on proton for the proton data, and with an equal number of events on proton and neutron targets to simulate the deuteron data. The slightly different smearing of the proton data taken in 1996 and 1997 as compared to the deuteron data taken in 2000 was found to have no effect on the signal to background ratios and asymmetries in the Monte Carlo. This is why the smearing for all MC data was taken to be that of the detector geometry from 2000. Also, since the effect of QED radiative smearing was found to be negligible in the 'Photoproduction' region (see figure B.3), the Monte Carlo was generated at the Born level.

For the 'standard' extraction of $\frac{\Delta G}{G}$ explained below a definition of how the background asymmetry is calculated from Monte Carlo and how the events from anomalous photon processes are treated (cf. appendix C.1) is required:

- The low-p_T process in PYTHIA is weighted with the experimental parametrization A_1^{exp} (Eqs. C.17 and C.18). The longitudinal part of the unpolarized cross section is parametrized with R_{VMD}, Eq. 4.27.

- These parametrizations are also applied if $x < x_{min} = 10^{-5}$ or $Q^2 < Q^2_{min} = 0.22$ GeV^2 (i.e., for the bulk of the events from the low-p_T process). In this case, $A_1^{exp,p} \to 0.019$ and $A_1^{exp,d} \to 0$. The minimum values x_{min} and Q^2_{min} are given by the lower limit at which the polarized PDFs can be retrieved by a call to PDFLIB [Plo00].

- Diffractive VMD events are treated as a dilution, i.e., $A_1^{diffr} = 0$.

- Hard resolved photon events are split into events where the target parton (i.e., the struck parton in the nucleon) is a gluon and events where it is not. The former are counted together with the PGF events as signal, the latter as background.

- The polarization of partons in the photon is set to zero in the asymmetry of hard resolved photon events. The events involving a target gluon then act as a dilution to the average subprocess asymmetry of the signal.

Figure 5.8 shows the resulting $\frac{\Delta G}{G}$ for positive and negative hadrons, pions and kaons and the corresponding charged sums ($h^{\pm}$, $\pi^{\pm}$, $K^{\pm}$) from the proton (indicated with 'p', without kaons) and deuteron data (indicated with 'd'). The kaons are binned differently in p_T (10 bins instead of 15, cf. tables D.11 and D.12) which is why the result for kaons is given for $1 < p_T < 2$ GeV. From this

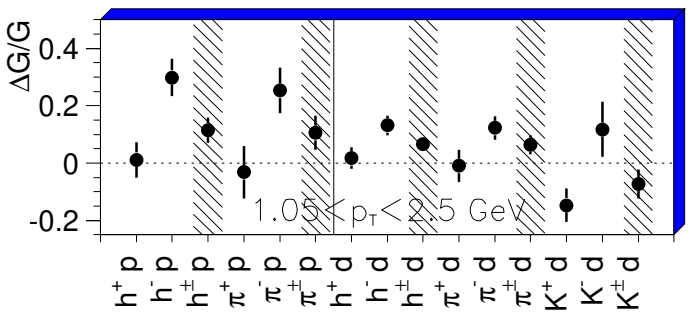

Figure 5.8: The result for $\frac{\Delta G}{G}$ for different data sets with $p_T > 1.05$ GeV ($p_T > 1$ GeV for kaons) in the 'Photoproduction' region. The vertical line divides the proton and deuteron data sets, the shaded areas highlight the points for the sum of charged hadrons.

figure it can be concluded that the various independent data sets appear to be not consistent. The results from positive hadrons (pions) do not comply with those obtained from the negative hadrons (pions). Also, the results from negative hadrons (pions) is higher for proton than for deuteron. In general the hadron results are compatible with the corresponding pion results, indicating that the restriction of the upper momentum of identified pions has hardly any influence on the result as well as the inclusion of other hadrons in the unclassified hadron sample. The kaon results will be discussed below.

The charge average of the hadrons (pions) seems to be compatible for both targets. This is only true for this particular lower cut on p_T imposed on the data, though. If this cut is varied, the data for negative hadrons from proton and deuteron seem to deviate even more from each other, as can be seen in figure 5.9 where $\frac{\Delta G}{G}$ is plotted for positive and negative hadrons as a function of the lower p_T cut. The result for negative hadrons is qualitatively the same for both targets, rising

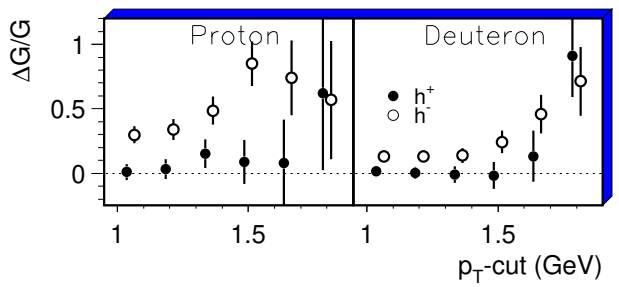

Figure 5.9: The result for $\frac{\Delta G}{G}$ for positive and negative hadrons from proton (left) and deuteron (right) in the 'Photoproduction' region as a function of the lower p_T cut.

with the p_T cut. Quantitatively the rise is much stronger for proton, starting from a much higher value than for deuteron. The result for positive hadrons stays stable and close to zero for both proton and deuteron, except for the largest p_T cut, $p_T > 1.8$ GeV. Only for this high cut, where the statistical error is almost 100% for the proton data and 30% for the deuteron data, both data sets and all charges seem to give consistent results.

The cause of this behavior becomes clear from figure 5.10 where the asymmetries for hadrons from proton and deuteron are plotted together with the MC asymmetries with different assumptions for $\frac{\Delta G}{G} = -1$ (upper lines), $\frac{\Delta G}{G} = 0$ (middle lines) and $\frac{\Delta G}{G} = +1$ (lower lines). The solid and dashed

lines are for the standard asymmetry and for an asymmetry with $A_1^{low-p_T} = 0$, respectively. For

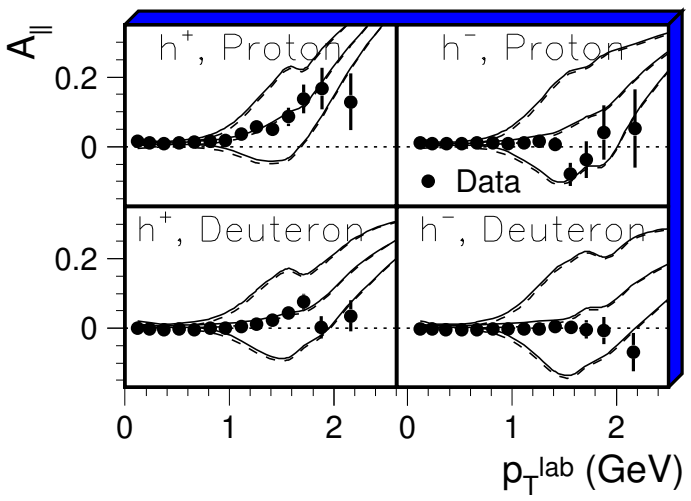

Figure 5.10: The MC projections for asymmetries of positive and negative hadrons on proton and deuteron with $\frac{\Delta G}{G} = \pm 1, 0$ superimposed with the measured asymmetry. See text for details.

the proton, the PYTHIA asymmetry for $\frac{\Delta G}{G} = 0$ is right on top of the data for positive hadrons. The negative hadron asymmetries on proton are slightly negative, thus lying below the curves for $\frac{\Delta G}{G} = 0$. On deuterium both measured asymmetries are much smaller, and again the PYTHIA curves for $\frac{\Delta G}{G} = 0$ are on top of the data for positive hadrons, but they are only slightly above the data for negative hadrons. From all asymmetries in figure 5.10 it can be inferred that the value for $\frac{\Delta G}{G}$ is p_T dependent. This is related to a correlation of the measured p_T with the gluon momentum fraction x_G and the scale $\hat{Q}^2$ at which the gluon distribution is probed. The p_T dependence of the results will be investigated in section 5.5.1.

All this points to an incorrect description of either or both the proton or the deuteron data by PYTHIA in terms of the subprocess fractions or the contribution of the different quark flavors in DIS or QCD Compton processes. The contributions from PGF to the data are, according to PYTHIA, the same for both targets. The deuteron DIS and QCD Compton subprocess fraction is smaller by maximum 5% (relative) at large p_T than the proton ones. The positive contribution to the asymmetries at high p_T from PYTHIA comes mostly from DIS or QCD Compton processes at relatively large $x \approx 0.2$ where the large positive polarization of the u quark dominates. There are two possibilities to explain the inconsistencies. First, it could be that the fractions of PGF compared to those for scattering on quarks (DIS and QCDC) are much more different for the different charges as indicated by figure 5.1. Second, the correlation of the detected hadrons with the flavor of the struck quark in DIS and QCD Compton processes might not be correct. This has not only to do with the unpolarized parton distributions – which are evaluated at the rather 'safe' scales $Q^2 \geq 4$ GeV^2 for DIS and $\hat{Q}^2 \approx 2$ GeV^2 for QCDC – but also with the fragmentation of the quarks into hadrons. In this respect it is also possible to imagine that effects from the various quark flavors cancel at least partially in the deuteron due to the isospin rotation of the quark densities in the nucleon.

Figure 4.30 indicates that the kinematic correlations between the measured p_T and the inclusive variables in the 'Transition' region are not reproduced correctly in PYTHIA. Of course, the average x and Q^2 at which partons are probed in DIS or QCD Compton determines the size of the background asymmetries, and can therefore also influence $\frac{\Delta G}{G}$. In the 'Photoproduction' region it is not possible to check whether the kinematic correlations are described correctly. An effect of wrong kinematics cannot be excluded, though. The issues of fragmentation and event kinematics will be pursued further in section 5.4.

5.2.2 Kaon Results

The kaon results in figure 5.8 are consistent with the corresponding pion results from deuteron within one standard deviation. The fraction of PGF events in the kaon sample is larger than for hadrons and pions, 30 to 35% compared to 20 to 25%. The larger sensitivity of kaons to PGF reduces the statistical error of $\frac{\Delta G}{G}$, although for negative kaons it is still too large for a significant result. The question if kaons should be considered separately can be answered by considering the following issues:

- Besides in soft reactions, kaons are produced in QCD Compton or DIS processes, mostly by the fragmentation of u and $\bar{u}$ quarks and much more rarely by the fragmentation of (anti)strange quarks. In PGF, kaons are produced either directly from the process $\gamma^* g \to s\bar{s}$, or from the fragmentation of $u\bar{u}$ or $d\bar{d}$ pairs produced in the reaction.

- The rate of kaons from each of the contributing processes is therefore extremely sensitive to the fragmentation process, in particular to the strangeness suppression factor determining the probability of $s\bar{s}$ production during the fragmentation process and to the fragmentation function for strange quarks to kaons.

- The fragmentation function for strange quarks to kaons can hardly be constrained by data [Kre01]. The strangeness suppression factor has been tuned to kaon multiplicities, however, the multiplicities for positive kaons are not reproduced using this tuned parameter (cf. figure 4.29). It was mentioned in section 4.5.1 that it is believed that nonperturbative processes not included in the MC contribute significantly to the production of positive kaons. As long as the size of this contribution is not known, the tuned strangeness suppression factor has to be considered as having a large systematic error. A slight change in its value would lead to considerably different predictions for the rate of kaons, the subprocess fractions and the background asymmetries going into the calculation of $\frac{\Delta G}{G}$.

- Although the sensitivity of kaons to strange quarks in the nucleon is small (about 10%), another source of uncertainty is the ignorance about the unpolarized and polarized strange quark distributions. The strange quark distributions are normally derived by *assuming* some ratio of strange to $\bar{u}$ and $\bar{d}$ quarks at the input scale, but there are hardly any constraints from data.

In view of the above discussed theoretical uncertainties, the relatively large systematic error on the asymmetries from the RICH unfolding, and the fact that the results for kaons are not different from those for pions it is concluded that kaons need not to be treated separately. For the following studies therefore kaons will be omitted from the discussion.

5.2.3 Systematic Studies

In the following, a study is presented on the effect of using different parton distributions for PYTHIA, different parton polarizations for the MC asymmetries and different PYTHIA parameters that may change the subprocess fractions and/or the kinematic correlations of the measured p_T with the subprocess kinematics.

Treatment of Low-p_T Processes

There is a considerable uncertainty in the way how the asymmetry of the low-p_T process is to be evaluated. The uncertainty in the treatment of the low-p_T process is certainly an issue because the fraction of events originating from soft non-diffractive VMD stays large even at high p_T. For $p_T > 1$ GeV it is still approximately 40% for all charges and targets. The different possibilities of interpreting this process in terms of an asymmetry are explained in section C.1 in the appendix.

In quasireal photoproduction the low-p_T process happens mostly at very small Q^2 and x, leading to small or zero asymmetries depending on the method in use. The possible effect of different treatments can be already estimated from figure 5.10 where the MC results for letting $A_1^{low-p_T} = 0$ (dashed line) and $A_1^{low-p_T} = A_1^{exp}$ are shown. The difference seems to be very small, but since the differences are to be multiplied with a factor $1/f_{PGF}$, the effect on $\frac{\Delta G}{G}$ needs to be investigated. The following methods are considered (cf. section C.1):

1. The standard method described above, i.e., setting $A_1^{low-p_T} = A_1^{exp}$ for all x and Q^2.
2. $A_1^{low-p_T} = A_1^{exp}$ as in method 1.), but only if x and Q^2 are above the minimum $x_{min} = 10^{-5}$ and $Q^2_{min} = 0.22$ GeV^2, i.e., only a few percent of the events . Otherwise the asymmetry is set to zero.
3. $A_1^{low-p_T} = 0$, i.e., the low-p_T process is spin independent as expected if it was interpreted as soft, minimum bias VMD interactions.
4. $A_1^{low-p_T} = g_1(W^2)/F_1$, where F_1 is taken from [Abr97] and [Whi90], and $g_1(W^2)$ is a modification of the model of Ref. [Koc03] that is claimed to be valid for small x and Q^2. The suggested modification [Koc04] of the model has two free parameters that should be fitted to the data, such that the model describes proton as well as deuteron data. This task would have been very elaborate, which is why only one parameter was adjusted to the data. This common factor was then different for proton and deuteron, leading to the approximately 1% positive asymmetry in the proton case (tables D.3 and D.6) and to the smaller, but negative asymmetry in the deuteron case (tables D.7 to D.10) at small p_T.
5. The fit parameters in the model of method 4.) should in fact be the same for proton and deuteron, but if only one parameter is adjusted, they are not. For this reason, also the results are considered where for each target the asymmetry weight is calculated with the respective other fit parameter, i.e., g_1^p for proton will be calculated with the factor matching the deuteron data and vice versa (see also figure C.3).

Figure 5.11 shows, for different p_T cuts, the results obtained for the sum of the charged hadrons with the five different methods. The charge dependence of the result will be discussed below. In

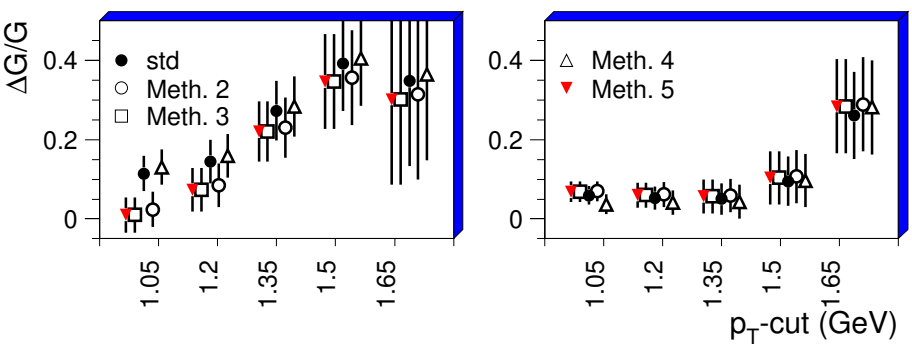

Figure 5.11: The results on $\frac{\Delta G}{G}$ in the 'Photoproduction' region for $h^+ + h^-$ obtained for the five different methods of treating the low-p_T process in the calculation of the background MC asymmetry as a function of the p_T cut. the left plot is for the proton data, the right plot for the deuteron data.

the case of the proton target, the standard method and method 4., the two methods describing the data at small p_T give a larger result than the three other methods which at small p_T give zero or slightly negative asymmetries. For the deuteron target the result is smaller for the only method

describing the deuteron asymmetries, namely method 4 with the fit parameter adjusted to the deuteron data. All other methods give zero or slightly positive asymmetries. Generally, the results for $\frac{\Delta G}{G}$ differ depending on if the low-p_T asymmetry is chosen such that the MC asymmetry agrees with the measured asymmetry at small p_T or such that it is zero or small with a wrong sign.

As discussed in section C.1 of the appendix, the low-p_T process can be interpreted in the way as it is described in the PYTHIA model. Then it would not have an asymmetry. Since the PYTHIA model itself has limitations in its ability to describe the wide variety of possible nonperturbative processes, the low-p_T process can also be reinterpreted in the sense of *replacing* the PYTHIA model with some other 'model' that describes the data. If this is correct, then the observed deviations between the different methods have to be regarded as a systematic uncertainty on the final result. This systematic uncertainty on the other hand should cover already some part of the 'model' uncertainty, the uncertainty arising from using one particular model, that of PYTHIA, for the extraction of $\frac{\Delta G}{G}$. From figure 5.11 it can be seen that the systematic uncertainty might be as large as 100% if the lower p_T cut has a small value. A small systematic error can only be achieved if $p_T > 1.35$ GeV where the deviations are smaller due to the smaller influence of the low-p_T processes ($\approx 50\%$ at $1.05 < p_T < 1.35$ GeV vs. $\approx 30\%$ at $p_T > 1.35$ GeV). Note that, due to the inherent charge symmetry of both setting $A_1^{low-p_T} = 0$ and $A_1^{low-p_T} \sim A_1^{exp}$ or g_1/F_1, the shifts are the same for positive and negative hadrons and can therefore not account for the inconsistencies between the results for the different charges. Of course it could be that in reality, whatever processes contribute to the measured cross sections and asymmetries, they are charge dependent, but with the available information it is impossible to account for this with the PYTHIA model. In any case a charge dependence of the asymmetries must be small because at the very small x of the low-p_T events sea quarks dominate with small polarizations that are approximately symmetric between quarks and antiquarks.

Choice of Parton Distributions

The choice of parton distributions is relevant at two stages in the extraction of $\frac{\Delta G}{G}$. There is first the choice of the cross section and of the struck quark in the PYTHIA event generation. Here, the unpolarized parton distribution determines the subprocess fractions and, to some degree, the relative behavior of different hadron types and charges. Next, when the MC asymmetries are calculated, the choice of the polarized parton distributions determines the size of the background asymmetry. The models for PDFs usually differ in the input scale, the functional form of the parametrizations at the input scale, the use of constraints from data and theory and on the data used in the fit. In the region of interest, $p_T > 1$ GeV, Q^2 and x are relatively large so that different models for parton distributions give reasonable and similar results for the measured F_2. Still, a considerable uncertainty in the unpolarized gluon distribution remains (cf. figure 2.9). A variation of unpolarized and polarized parton distributions therefore gives an estimate on the possible range of subprocess fractions and the background asymmetries. Due to time, disk space and technical constraints, only one parton distribution different from the standard (CTEQ5 [Lai00] as unpolarized PDF in PYTHIA, GRSV2000 [Glü01] as polarized PDF for asymmetries) was used for each the polarized and unpolarized sets. For the unpolarized PDF GRV98 [Glü98] was chosen, for the polarized one GS (set B) [Geh95]. Figure 5.12 shows the result for $\frac{\Delta G}{G}$ obtained for each possible combination of polarized and unpolarized PDFs, for all data sets from proton and deuteron.

What can be inferred from this figure is that the choice of the unpolarized parton distribution has usually a small effect, whereas the choice of the polarized parton distribution changes $\frac{\Delta G}{G}$ more significantly to smaller values. The absolute shifts in the result are smaller for deuteron, but relatively of a similar size as for proton. The overall picture does not change dramatically, although the systematic error arising from the choice of PDFs is not negligible. There is no indication that the differences in $\frac{\Delta G}{G}$ obtained for the different charges and targets are due to the choice of the parton distributions.

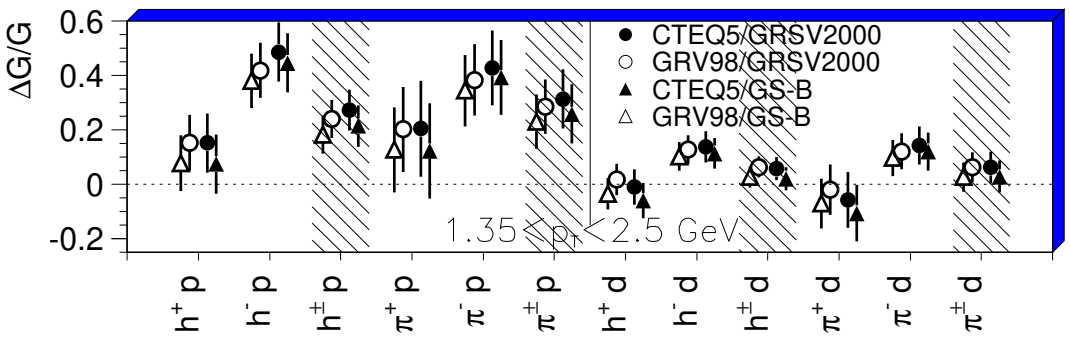

Figure 5.12: The result for $\frac{\Delta G}{G}$ for different data sets with $p_T > 1.35$ GeV in the 'Photoproduction' region. The vertical line divides the proton and deuteron data sets, the shaded areas highlight the points for the sum of charged hadrons. The various symbols are for different combinations of polarized and unpolarized parton distribution.

The relative size of the differences is remarkably constant as a function of the lower p_T cut, as is shown in figure 5.13 for charged hadrons as an example.

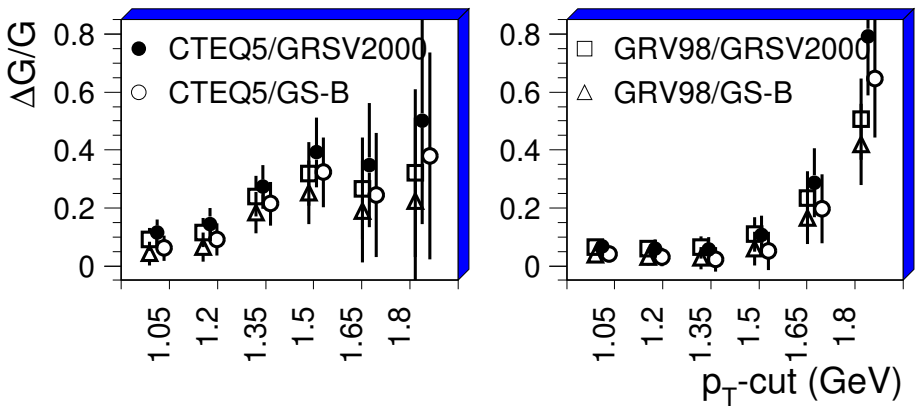

Figure 5.13: The results on $\frac{\Delta G}{G}$ in the 'Photoproduction' region for $h^+ + h^-$ obtained for the four different combinations of PDFs as a function of the p_T cut. The left plot is for proton, the right plot for deuteron.

PYTHIA Model Parameters

In section 4.5.2 results were presented on the agreement between data and MC for different PYTHIA parameter settings in the semi-inclusive region. The general conclusion there was that no distinctive set could be found with which all data are described well in all quantities. All sets should therefore be treated on an equal footing. Based on the results in the semi-inclusive region (see table 4.2), different sets were also studied in the 'Photoproduction' region. The most remarkable result was that an increase of the average p_T acquired during fragmentation resulted in a better description of the data at high p_T. In the semi-inclusive region the variation of this effective parameter led to a too hard p_T slope, but also to better agreement in the inclusive variables and the kinematic correlations. On the other hand, changing MSTP(19) to 1 to reduce the suppression of the LO DIS cross section hardly improved the MC cross sections in the 'Photoproduction' region.

A systematic study on the effects of PYTHIA parameters should involve two aspects. One is that in principle one would like to have one set for both regions describing them equally well.

Such a parameter set has not yet been found, but still the MC model should be used in a consistent way. This is why for the standard results, set #1 is used in both regions. Another set to be studied is set #4, with MSTP(18) set to the default. With this set, in both kinematic regions a harder p_T distribution is achieved. This leads to a small improvement of the 'Photoproduction' cross sections in p_T. In the semi-inclusive region the p_T distributions did not improve very much compared to the data, but the distributions in inclusive variables did. So there is good reason to take set #4 into account for the 'Photoproduction' as well as the 'Transition' region. The other aspect of the parameter study is of course that the MC cross sections should be as close to the data as possible. This can be achieved in the 'Photoproduction' region with set #5, where compared to set #4 in addition the average p_T from the fragmentation is increased, and therefore the p_T distributions match the data better. Both sets #4 and #5 particularly influence the weights of different subprocesses due to different modeling of the cross section in p_T, such that the possible variation of the results using different options of the model can be studied with these two sets. For set #4, MSTP(18) was set such that a larger, W^2 dependent cutoff scale between resolved and direct processes is used ($p_{T,min} \approx 1.4$ GeV instead of $p_{T,min} = 0.5$ GeV in the standard). The effect is that the subprocess fractions of DIS and anomalous photon processes increase slightly, while they decrease for QCDC and PGF. The low-p_T process is hardly affected. Contrary to that, for set #5 with the increased p_T from fragmentation – PARJ(21)=0.45 GeV *in addition to letting MSTP(18)=3* – it is mainly the direct and the anomalous photon processes being reduced, especially at high p_T, whereas the low-p_T process is enhanced significantly. How this change of the parameters influences the extracted value for $\frac{\Delta G}{G}$ is depicted in figure 5.14 for the individual data samples. The cut on $p_T > 1.35$ GeV was chosen because with this cut the influence of the low-p_T

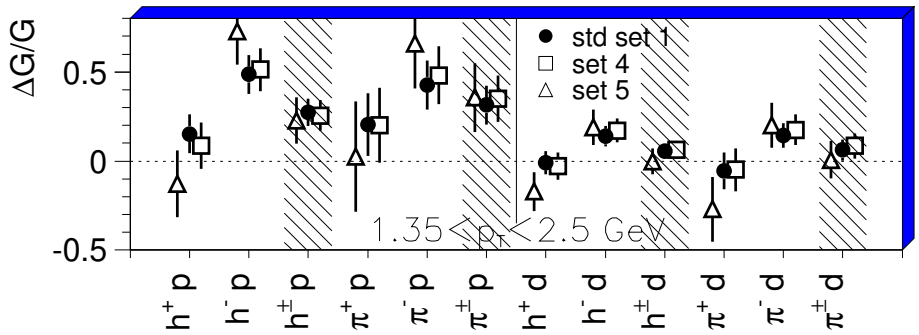

Figure 5.14: The result for $\frac{\Delta G}{G}$ for different data sets with $p_T > 1.35$ GeV in the 'Photoproduction' region. The vertical line divides the proton and deuteron data sets, the shaded areas highlight the points for the sum of charged hadrons (pions). The various symbols are for the standard and two variations of PYTHIA parameter sets. See text for details

process is reduced (cf. figure 5.11). The striking features of figure 5.14 are first that only set #5 with PARJ(21)=0.45 GeV leads to visibly different results and second that the error bars for set #5 are almost a factor 2 larger than for the other sets. Both features are correlated, as will be explained in the following.

The reason for the differences obtained with set #5 is not so much the different subprocess fractions but rather the different subprocess asymmetries, especially that of PGF which is, depending on p_T, only $\frac{1}{2}$ to $\frac{2}{3}$ of that predicted by sets #1 and #4. This can be seen in the rightmost plot of figure 5.15. Already in section 4.5.2 it was shown that with MSTP(18)=3 the description of the cross sections in x and Q^2 got significantly better as well as the average x and Q^2 vs. p_T. This is, on the one hand, caused by the different mixing of subprocesses for the two options MSTP(18)=2 or 3 [1], on the other hand it points to a nontrivial correlation between p_T and inclusive variables, introduced by the spectrometer acceptance. Apparently, a similar effect occurs

[1]For MSTP(18)=3 not only the p_T cutoff between GVMD and direct processes is higher than for MSTP(18)=2, but also the DIS process is enhanced compared to GVMD, if $Q^2 > p_T^2$. See Ref. [Sjö01] for details.

in the 'Photoproduction' region. In the DIS process, the average x is about two thirds smaller for sets #4 and #5 with MSTP(18)=3 than for the standard set with MSTP(18)=2, leading to smaller DIS asymmetries. For QCD Compton, the average x_P and $\hat{p}_T$ is larger than in the standard set by almost a factor $\frac{3}{2}$, leading to larger QCDC asymmetries. The average x_G and $\hat{p}_T$ for PGF are shown in figure 5.15 for the three sets. For MSTP(18)=3 alone, i.e., set #4, $\hat{p}_T$ and x_G are

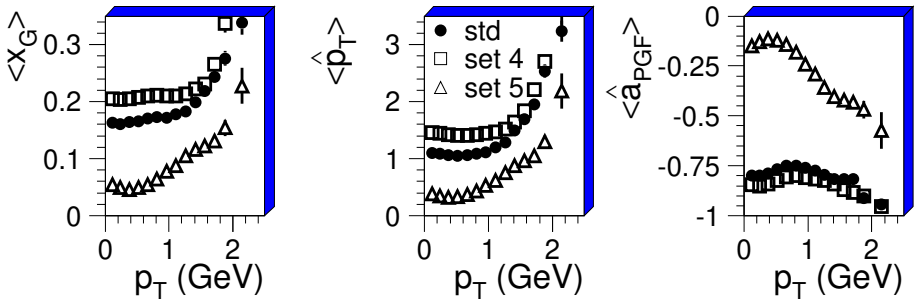

Figure 5.15: The average x_P (left) and $\hat{p}_T$ (middle) for PGF in PYTHIA generated with sets #1 (filled circles), #4 (squares) and #5 (triangles). The right plot shows the resulting subprocess asymmetries.

larger than in the standard set #1. If in addition the nonperturbative p_T is spread more by setting PARJ(21)=0.45 instead of 0.36 GeV, as for set #5, x_G and $\hat{p}_T$ become much smaller than in the other sets. The consequence of this is that the subprocess asymmetry for PGF is dramatically reduced. The small PGF subprocess asymmetry is the main reason for the larger error bars, and also for the larger values of $\frac{\Delta G}{G}$ for negative hadrons. The increased differences between positive and negative hadrons provide an impression on how the generation of the underlying kinematics, and therefore also the correlations of the partons in the hard subprocess with the outgoing hadrons may change the result. It could well be that *decreasing* PARJ(21) brings the positive and negative hadron results closer together. However, the reason for *increasing* PARJ(21) was that the cross sections in the high-p_T region were described better. The description would be even worse if the smearing in p_T were decreased. As there is no motivation to choose an effective parameter such that the agreement between MC and data gets worse, the result would be very doubtful.

Photon Parton Densities

To estimate the effect of the parton densities of the photon, again the unpolarized densities going into PYTHIA can be varied as well as the polarized ones going into the calculation of the asymmetries. For the latter no measured distributions exist, and they can only be constrained from boundary conditions and sum rules. The range of possible parton polarizations of the photon can be covered by setting them to constant values as proposed in section C.1 of the appendix. That means, quark polarizations are varied between -0.5 and +1, gluon polarizations between -0.1 and +1. In the standard treatment, all polarizations are set to 0. All processes where a gluon from the nucleon is involved (about half of the anomalous processes) are counted together with the PGF processes into the signal, while processes involving quarks are counted as background. The effect of the gluon processes can be regarded as a variation of the subprocess asymmetry $\langle \hat{a}_{sig} \rangle$ going into the extraction of $\frac{\Delta G}{G}$, while the quark processes vary the background asymmetry. The unpolarized parton distribution was changed from the default one implemented in PYTHIA, SaS-G 1D [Schu96], to GRV-G [Glü92].

The variation of the results with the possible combinations of polarized and unpolarized photon PDFs is shown for positive and negative hadrons from proton and deuterium in figure 5.16. The set with the default unpolarized photon PDF was chosen to be set #4 (MSTP(18)=3), because it gives larger fractions of anomalous processes than set #1. The circles in this figure stand for the

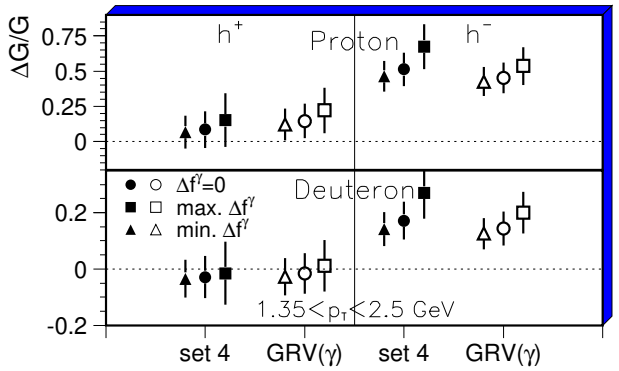

Figure 5.16: The result for $\frac{\Delta G}{G}$ positive and negative hadrons (left and right panels) with $p_T > 0.75$ GeV for two unpolarized photon PDFs (filled and open symbols) and three different assumptions for polarized photon PDFs. See text for details.

standard method of extraction, i.e., $\Delta f^\gamma = 0$. The triangles are obtained with the 'minimal' photon polarization with $\Delta q^\gamma = -0.5$ and $\Delta G^\gamma = -0.1$, the squares with the 'maximal' polarization with $\Delta q^\gamma = \Delta G^\gamma = +1$. The filled symbols are extracted from set #4, the open symbols from PYTHIA with the parameters of set #1, but with GRV-G instead of SaS-G 1D. The minimal photon parton polarizations always give the smallest, the maximal polarizations the largest value for $\frac{\Delta G}{G}$. The deviations are large compared to the standard value, especially for negative hadrons. The value for positive hadrons remains consistent with zero for all options. Also with an even larger p_T cut of 1.8 GeV the differences between different scenarios remain sizeable. It should be noted that also the choice of the photon PDFs does not change the discrepancies between the results for the different charges and targets.

5.3 Results in the 'Transition' Region

In this section, studies analogous to those in the 'Photoproduction' region are presented for the 'Transition' region. The results are obtained for one point given by a lower and upper cut on p_T.

5.3.1 Results From the Standard Monte Carlo

The formalism of the extraction of $\frac{\Delta G}{G}$ is the same as for the 'Photoproduction' region, and the background asymmetries are treated as in section 5.2.1. Similar to there, the asymmetries are calculated first for all data sets separately in order to check their consistency. Again, the Monte Carlo with the parameters of set #1 is used. In order to save time, and because there is not yet a functioning routine calculating radiative corrections for the *neutron*, also here the Monte Carlo was generated on the Born level. The size of the error made by omitting QED radiative corrections will be investigated below. In figure 5.17 the values for $\frac{\Delta G}{G}$ calculated for $p_T > 0.75$ and $p_T > 1$ GeV are shown. In the 'Transition' region, the p_T slope from the Monte Carlo is slightly too hard compared to the data, leading to an overestimate of the cross section in the last p_T-bin. There are no or only a few events in the data in this bin with $p_T > 2$ GeV, leading to meaningless values of $\frac{\Delta G}{G}$ there. Therefore an upper cut on $p_T < 2$ GeV is imposed on both MC and data. The large error bars prevent a conclusion on the consistency of the data like in the 'Photoproduction' region. However, especially for deuteron, qualitatively a similar picture emerges. Here again, using positive hadrons leads to a different value than using negative hadrons. The proton data for negative hadrons tend to give negative or zero values of $\frac{\Delta G}{G}$ consistent with the results for the positive hadrons. This is different from the 'Photoproduction' region, where for negative hadrons a positive result was obtained. The size of the error bars does not allow a decision on the compatibility with the corresponding deuteron data. From kaons a negative or zero result is derived. Despite the increased sensitivity to PGF, especially of positive kaons – the fraction of PGF events is almost 40%, compared to about 20% for positive pions – the statistical error bars are still very large. In view of the large statistical uncertainties, and by applying the same considerations about kaon

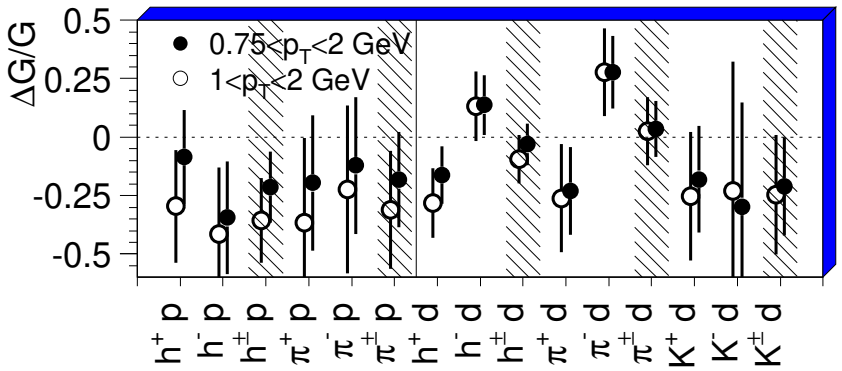

Figure 5.17: The result for $\frac{\Delta G}{G}$ for different data sets with $p_T > 0.75$ GeV (filled circles) and $p_T > 1$ GeV (open circles)in the 'Transition' region. The vertical line divides the proton and deuteron data sets, the shaded areas highlight the points for the sum of charged hadrons (pions).

fragmentation as in section 5.2.1 it can again be concluded that there is not too much gain in information from kaons. Therefore also here the kaons will not be regarded separately anymore. The harder p_T cut of 1 GeV shifts the proton results to larger absolute values of $\frac{\Delta G}{G}$. There is only a small effect on the deuteron data.

Comparing the above figure to the corresponding one in the 'Photoproduction' region (figure 5.8) raises the suspicion that the better consistency among the different data sets here is to a large extent only a consequence of the larger error bars. In contrast to the 'Photoproduction' region where x and Q^2 of the DIS process are quite large at high p_T, they are relatively small in the 'Transition' region, $x \leq 0.05$ and $Q^2 \approx 1.5$ GeV^2 for $p_T > 1$ GeV (see also figure 4.30). However, for the QCD Compton and PGF processes, $\hat{p}_T$ and x_P are completely compatible for both kinematic regions, if $p_T > 1.2$ GeV in the 'Photoproduction' region, and $p_T > 1$ GeV in the 'Transition' region. The only quantity that is different is the hard scale of the process, which in PYTHIA by default is calculated as:

$$\hat{Q}^2 = \hat{p}_\perp^2 + \frac{Q^2}{2}, \tag{5.9}$$

where $\hat{p}_\perp$ is the transverse momentum at the $g \to q\bar{q}$ (or $q \to qg$) vertex. Since $Q^2 \approx 1.5$ in the 'Transition' region, the scale is larger there ($\hat{Q}^2 \approx 2$ GeV^2) than in the 'Photoproduction' region ($\hat{Q}^2 \approx 1.3$ GeV^2). The expression for the scale at which the parton distributions and α_s are probed in QCD $2 \to 2$ processes can be changed by setting the switch MSTP(32) to a value different from the default (MSTP(32)=8 corresponding to Eq. 5.9). In the 'Photoproduction' region $Q^2 \approx 0$, such that $\hat{Q}^2 = \hat{p}_\perp^2$ in the default. In the 'Transition' region, the equivalent expression can be used if MSTP(32)=2, corresponding to $\hat{Q}^2 = \hat{p}_\perp^2 + m_3^2 + m_4^2$, where $m_{3,4} = 0$ are the masses of the outgoing quarks. With this different scale, the result on $\frac{\Delta G}{G}$ in the 'Transition' region comes out as depicted in figure 5.18. No change in the result can be observed. That means that the

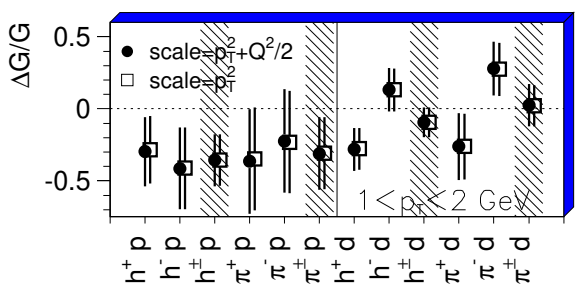

Figure 5.18: The result for $\frac{\Delta G}{G}$ for different data sets with $p_T > 1$ GeV for MSTP(32)=8 (filled circles) and MSTP(32)=2 (open squares) in the 'Transition' region. The vertical line divides the proton and deuteron data sets, the shaded areas highlight the points for the sum of charged hadrons (pions).

difference in the results for negative hadrons from proton in the 'Photoproduction' and 'Transition' regions cannot be explained with a scale dependence in the PYTHIA model. This also implies that the 'Photoproduction' and 'Transition' region results are not compatible for negative hadrons. Other results, like those for positive hadrons from both targets, agree only on a 2 σ level. The stability of the results with respect to the scale choice is indeed surprising, as it could have been expected that at the small scales involved the subprocess fractions of PGF and QCD Compton change considerably.

The result for negative hadrons from the proton data deserves some special attention. In section 3.3.4 it was described how the measured semi-inclusive asymmetries differ if the coincident hadrons are required to be either in the top or in the bottom detector half. A nonstatistical deviation was found between the two cases the reason of which could not be detected. In order to estimate a possible effect of this top-bottom difference, $\frac{\Delta G}{G}$ was derived using one time the asymmetries measured with hadrons in the top and another time in the bottom detector. The result for these two cases is shown in figure 5.19 for the proton data. The difference between the result from the

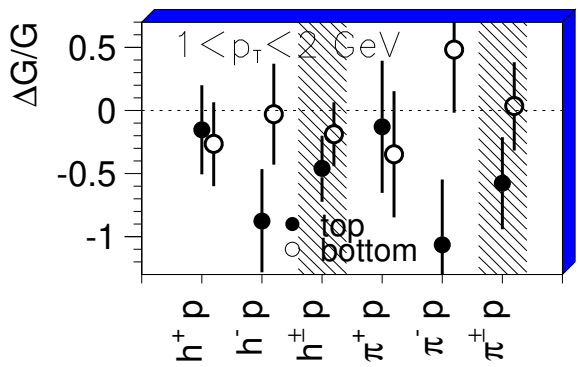

Figure 5.19: The result for $\frac{\Delta G}{G}$ extracted with the asymmetries for hadrons either in the top (filled circles) or in the bottom detector half (open circles) for positive and negative hadrons from proton data with $p_T > 1$ in the 'Transition' region.

top and bottom asymmetries for negative hadrons and pions is clearly evident, especially for the negative pions, where also larger deviations were observed in the data. Interestingly enough, if only the results from the 'bottom' asymmetries were regarded, the results for $\frac{\Delta G}{G}$ would be consistent with the 'Photoproduction' results as well as with the one from deuteron in the 'Transition' region. The conclusion to be drawn from this is that the results from the proton data on negative hadrons or pions cannot be considered as meaningful. For completeness, the results for the negative hadrons in the following analysis of section 5.3.2 will also be shown, but they will not be regarded for the interpretation.

In the following it will be investigated, if and how different treatments of the background MC asymmetries, different PYTHIA parameters and different parton distributions can influence the results.

The difference between $\frac{\Delta G}{G}$ extracted with and without QED radiative corrections is -3% for $p_T > 1$ GeV. This is most likely due to the statistical uncertainty of the MC data, and can be neglected compared to the overall statistical error of about 50%.

5.3.2 Systematic Studies

Diffractive and Non-diffractive VMD

As in the 'Photoproduction' region, the modeling of the MC asymmetries concerning the low-p_T process will be studied. Fortunately the contribution of the low-p_T process to the cross section is very small, about 10 to 15% at high p_T. Also, the problem of the extrapolation of any parametrization of A_1 to the unmeasured region in (x, Q^2) does not occur in the 'Transition' region. The model

of Ref. [Koc03] gives, for $Q^2 > 0.1$ GeV, nearly the same result as the experimental parametrization for A_1, therefore it does not need to be studied separately. What will be compared is the difference of results obtained with $A_1^{low-p_T} = 0$ and with $A_1^{low-p_T} = A_1^{exp}$. In the semi-inclusive region, an additional uncertainty arises from the treatment of *diffractive* VMD processes, in particular elastic ρ^0 production (cf. appendix C.1). As a third method the result will be extracted using $A_1^{low-p_T} = A_1^{exp}$ as in the standard treatment as well as $A_1^{diff} \approx 2A_1^{exp}$. In figure 5.20 the results obtained for the three different methods are shown for $p_T > 0.75$ as well as $p_T > 1$ GeV. The deuteron data are obviously insensitive to the different methods, while, at least for $p_T > 0.75$

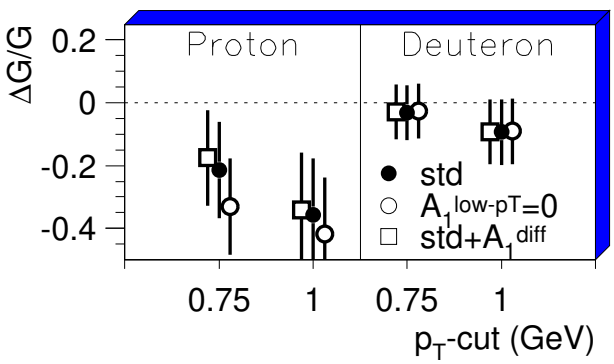

Figure 5.20: The results on $\frac{\Delta G}{G}$ for $h^+ + h^-$ in the 'Transition' region obtained for the three different methods of treating the low-p_T process in the calculation of the background MC asymmetry as a function of the p_T cut. The left side plot is for proton, the right side for deuteron.

GeV, the proton data show a considerable difference between treating the low-p_T process as a dilution and giving it a small, but positive asymmetry. Diffractive events do not contribute very much at high p_T (cf. figure 4.25 in section 4.4), which is why the difference between $A_1^{diff} = 0$ and $A_1^{diff} \approx 2A_1^{exp}$ is negligible. In the deuteron case, the absolute value of A_1^{exp} is very small, only a few per mill. Weighted with the small contribution of low-p_T and diffractive events, this has practically no effect on the background asymmetry.

Choice of Parton Distributions

As in the previous section, for the study on the sensitivity to the unpolarized and polarized parton distributions, the unpolarized distributions were changed to GRV98 in PYTHIA, and the polarized distributions were taken from GS-B. The result for $\frac{\Delta G}{G}$ was extracted for each combination of polarized and unpolarized distributions. The variations for all hadron types and charges of both targets can be seen in figure 5.21. In all cases the choice of the unpolarized distributions does not

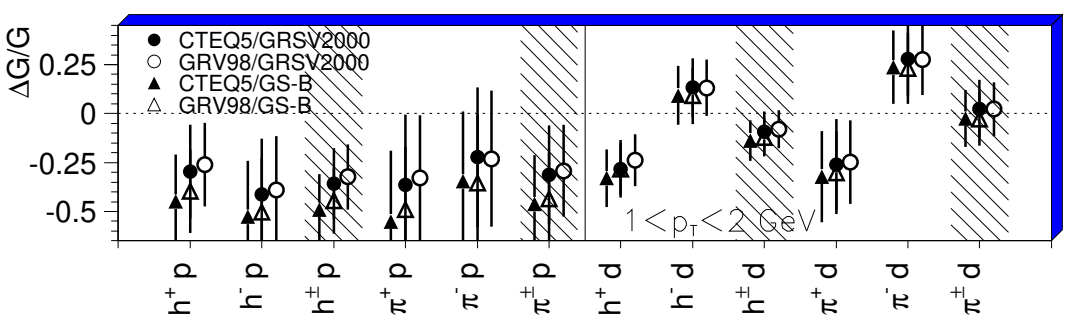

Figure 5.21: The result for $\frac{\Delta G}{G}$ for different data sets with $p_T > 1$ GeV in the 'Transition' region. The vertical line divides the proton and deuteron data sets, the shaded areas highlight the points for the sum of charged hadrons (pions). The various symbols are for different combinations of polarized and unpolarized parton distributions.

affect the result as much as that of the polarized PDFs. Also, the deviations are more sizeable than in the 'Photoproduction' region (cf. figure 5.12). It might be surprising that the unpolarized distributions have such a little effect, especially if the (competing) fractions of quark and gluon scattering processes are considered. The fractions of events coming from DIS and QCD Compton on the one hand and from PGF on the other hand for the two different unpolarized sets can be seen in figure 5.22 for charged hadrons from proton. At high p_T apparently with the CTEQ5 PDFs a

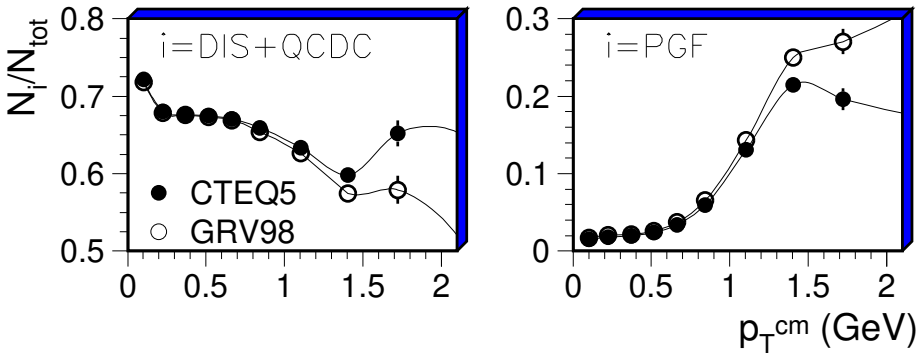

Figure 5.22: The subprocess fractions for DIS and QCD Compton (left plot) and PGF (right plot) from PYTHIA with CTEQ5 (filled circles) and with GRV98 (open circles). The plots are for charged hadrons from proton.

larger fraction of DIS and QCDC is predicted than with GRV98, and consequently a smaller PGF fraction. The mixture of different quark flavors is the same for both PDF sets, as the background asymmetries for DIS and QCDC are nearly the same. In the special case considered here, the smaller weight of the background asymmetry due to the smaller background fraction is almost canceled by the larger fraction of signal events (cf. Eq. 5.5). This is of course not like this in general, because the effect of different subprocess fractions depends on the combination of background and data asymmetries. Consider for instance a case where the background asymmetry is zero. In this case the values for $\frac{\Delta G}{G}$ would be inversely proportional to the fraction of signal events, and not directly depend on the background fraction.

Systematic deviations for the deuteron are usually smaller than for proton, the reason of which could again be partial cancellations between effects of the proton and the neutron parton distributions, especially the polarized ones.

PYTHIA Model Parameters

As in the 'Photoproduction' region, the results obtained using different sets of PYTHIA model parameters will be compared. For this study, again set #4 with MSTP(18)=3 will be used. Different from the 'Photoproduction' region, set #5 will not be regarded because in the 'Transition' region apparently the effective increase of the width of the p_T from fragmentation is here not necessary or even counterproductive. Instead, set #6 is chosen for the comparison, which in addition to MSTP(18)=3 has MSTP(19)=1, i.e., the LO DIS process is less suppressed at small Q^2. It was stated in section 4.1.4 that with this set cross sections are overestimated by a large amount. However, it was also seen that kinematic correlations between the measured p_T and inclusive variables become significantly better. The most important quantities going into the extraction of $\frac{\Delta G}{G}$ are not cross sections, but the subprocess fractions and the event kinematics that can be expected to change by a considerable amount if MSTP(19)=1.

The comparison of the results obtained for set #1, #4 and #6 is presented in figure 5.23. The changes for set #4 are moderate, albeit not negligible. In general, the results have larger absolute values than with the standard Monte Carlo. Very similar to the 'Photoproduction' region, also

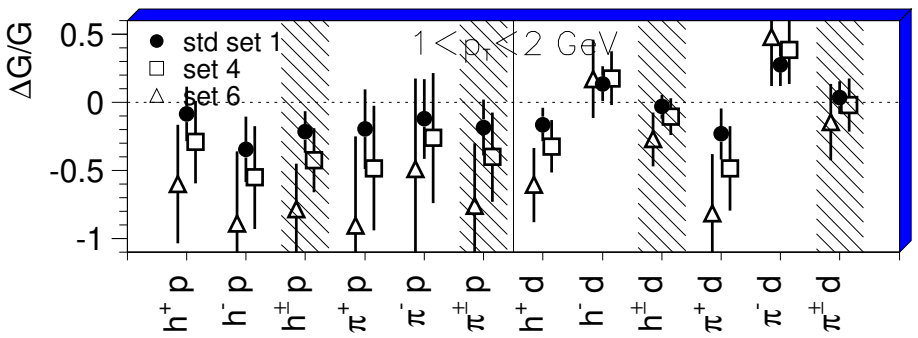

Figure 5.23: The result for $\frac{\Delta G}{G}$ for the different data sets with $p_T > 1$ GeV in the 'Transition' region. The vertical line divides the proton and deuteron data sets, the shaded areas highlight the points for the sum of charged hadrons (pions). The various symbols are for the standard and two variations of PYTHIA parameter sets. See text for details

here deuteron data and the charged sum of the hadrons are less affected. The largest changes occur for set #6. How these changes come about for the different targets and charges can be demonstrated with figure 5.24. This plot is laid out in analogy to figure 5.10 for the 'Photoproduction'

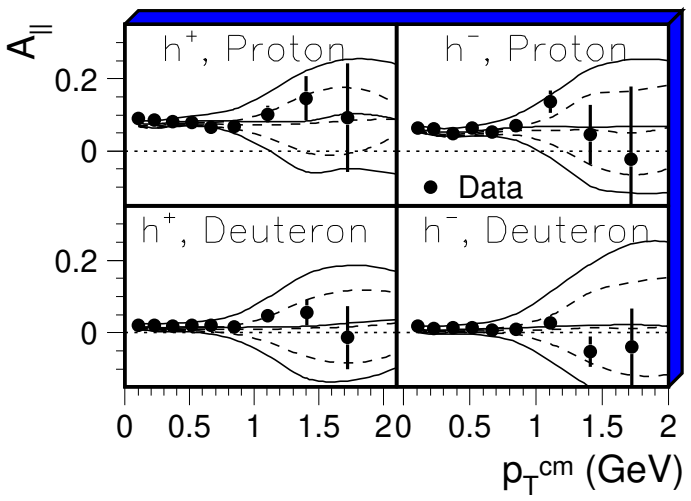

Figure 5.24: The MC projections for asymmetries in the 'Transition' region of positive and negative hadrons on proton and deuteron with $\frac{\Delta G}{G} = \pm 1, 0$ superimposed with the measured asymmetry. See text for details.

data. Shown are the four measured asymmetries for positive and negative hadrons, proton and deuteron. Plotted on top are the MC asymmetries for $\frac{\Delta G}{G} = -1$ (upper lines), $\frac{\Delta G}{G} = 0$ (middle lines) and $\frac{\Delta G}{G} = +1$ (lower lines). The solid lines show the result for the standard parameter set, the dashed lines that for MSTP(19)=1 (set #6). Forcing more DIS events to be generated at small Q^2 leads to a smaller weight of the PGF events. The smaller separation between the extremes for $\frac{\Delta G}{G}$ is the direct consequence of this and results not only in a change of the extracted values, but also in an increase of the statistical error by almost 100 % (cf figure 5.23). The background asymmetry weighted with the background fraction, $f_{BG} A_{\parallel}^{BG}$ (in the plot corresponding to the middle lines for $\frac{\Delta G}{G} = 0$) does not change for the two MC sets, because the smaller DIS asymmetry for set #6 at smaller Q^2 and x is compensated by a larger background fraction.

The observed changes here are, for both MC sets, not due to a change in kinematics but mainly due to a change of the subprocess fractions. Since this change is quite small for set #4, the deviations stay moderate there. The data seem to favor a larger DIS fraction as in set #6 with respect to the relation between inclusive and semi-inclusive variables (p_T), but not with respect to

the measured cross sections (cf. table 4.2). The enhanced DIS contribution also does not lead to a better agreement between proton and deuteron data, or between positive and negative hadrons. It could be argued that the agreement of the other sets with the observed cross sections may be only accidental. In the kinematic region of HERMES, NLO corrections to the pQCD processes might be very large, and therefore it is not necessarily to be expected that the LO parametrizations implemented in PYTHIA lead to correct cross sections. However, their comparison using LO and NLO quark distributions, respectively, together with an estimate of their statistical errors as they can be retrieved from the CTEQ6 PDFs [Lai02], does not yield deviations of more than ±25% in the relevant kinematic region $x = \mathcal{O}(0.01)$ and $Q^2 \approx 1$ GeV^2. The increase in the LO DIS cross section by factors 1.5 to 2 with MSTP(19)=1 does therefore not compensate for missing NLO corrections. In this respect, the systematic deviations observed with set #6 may be viewed as somewhat doubtful, as it is clear, that the fraction of events from LO DIS is overestimated by PYTHIA. Considering this, the deviations for set #6 in figure 5.23 should not be regarded as a systematic error on the result on $\frac{\Delta G}{G}$.

Photon Parton Densities

Also in the semi-inclusive region the contribution of hard resolved photon events at high p_T is not negligible, for set #4 it is 6 to 9% in the p_T region of interest. The same study as in section 5.2.3 for the 'Photoproduction' region will be carried out in order to estimate the influence of a variation of unpolarized photon parton densities as well as the uncertainty due to the ignorance about the polarized densities. Again, the GRV-G distributions are chosen for the unpolarized photon PDF and compared to the default photon PDF set in PYTHIA. According to Ref. [Glü01a] the theoretical constraints on the polarized photon parton densities do not dramatically change with the photon virtuality. Thus in the 'Transition' region the same range of maximum and minimum polarizations can be explored as in the 'Photoproduction' region. The results are shown in figure 5.25. Also in

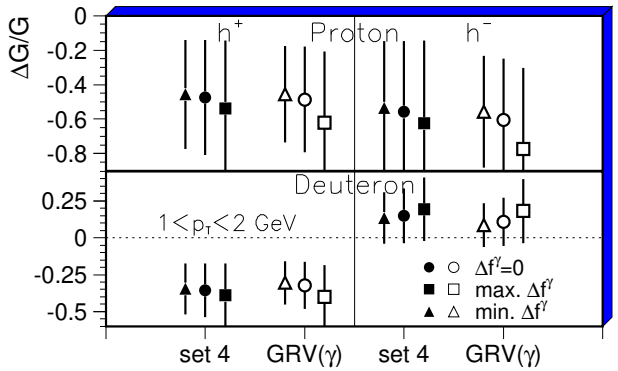

Figure 5.25: The result on $\frac{\Delta G}{G}$ for positive and negative hadrons (left and right panels) with $p_T >$ 1 GeV using two unpolarized photon PDFs (filled and open symbols) and three different assumptions for polarized photon PDFs. The plot is analogous to figure 5.16.

the 'Transition' region, the lack of knowledge about the photon parton polarization constitutes a non-negligible uncertainty. The effect is larger for the 'maximal' scenario, shifting the result for $\frac{\Delta G}{G}$ to larger absolute values. This is mostly due to the reduction of the subprocess asymmetry of the signal processes when $\hat{a}(\Delta G/G)^\gamma = \hat{a}_{anom} > 0$ is added to the negative PGF asymmetry. Using the GRV-G distributions, the relative contribution of anomalous events is doubled compared to those of set #4 with MSTP(18)=3 and the default SaS-G 1D distributions, and almost tripled compared to the standard MC set. Consequently the deviations are also larger here for the GRV-G distributions. This is different from the 'Photoproduction' region, where the anomalous fraction was largest for MSTP(18)=3 with the default SaS-G 1D distributions.

5.4 Interpretation of the Results

Using the results from the systematic studies on the different hadrons types and kinematic regions, an interpretation will be given here in view of a final result on the gluon polarization.

5.4.1 The Internal Consistency of the Data

In section 5.2.1 it was argued that the observed discrepancies, in particular, but not only, in the 'Photoproduction' region between the results for different charges and targets can be related to a wrong correlation of the outgoing hadrons to the struck quarks in background processes that have a large asymmetry, i.e., DIS and QCD Compton. The reason for this argument is that, as it was shown in the previous section, even if it is possible to change the subprocess fractions and kinematics considerably using different MC parameters and PDFs, this always affects all charges and targets in a similar way. The inconsistencies therefore remain within the PYTHIA/JETSET model. Also, as a similar behavior of 'Photoproduction' and semi-inclusive data was seen, it can be excluded that the somewhat dubious simulation of the low-p_T process is solely responsible for the inconsistent results obtained from positive and negative hadrons since it is suppressed by a large amount in the semi-inclusive data. A possible influence of this low-p_T process on the difference between the results for the proton and deuteron data in the 'Photoproduction' region will be discussed below.

What is possibly, at least partially, at fault is a process with a large, charge and target dependent asymmetry. This could be DIS as well as QCD Compton, probably both of them. Considering these processes, the correlation between the detected hadrons and the struck quarks can be expressed in terms of purities $P^h(q)$, i.e., the probabilities that a detected hadron of a given type and charge originated from a scattering on a quark of flavor q. The purities quantify the sensitivity to the flavor (and in polarized DIS also to the spin) of the struck quark. For hadrons the purities vs. p_T, extracted from PYTHIA for the DIS and QCD Compton processes, are shown in figure 5.26. According to PYTHIA, the positive *and* negative hadrons from proton

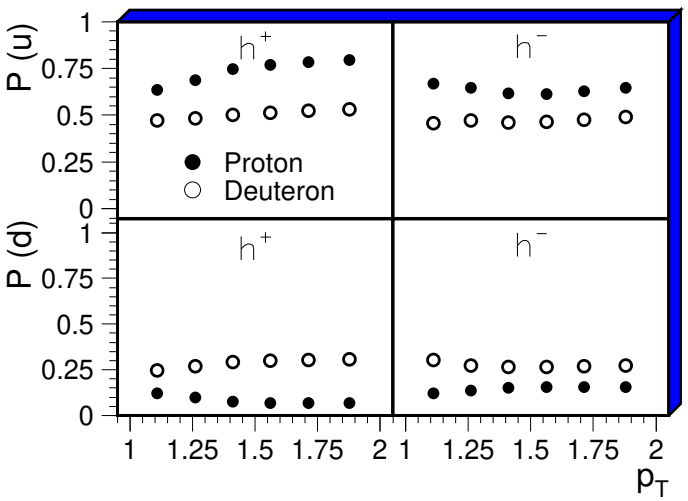

Figure 5.26: The purities for u and d quarks (top, resp. bottom panels) and positive and negative hadrons (left, resp. right panels) from PYTHIA for the LO DIS and QCD Compton processes. Filled symbols are for proton, open symbols for deuteron target. The quark flavors have been isospin rotated for the neutron (i.e., $u \leftrightarrow d$).

are completely dominated by scattering on u quarks, while for deuteron the d quark contribution is a bit enhanced. In the deuteron case about half of the contribution comes from u quarks. [2] Apparently, the purities are also more symmetric between charges for deuteron than for proton. Even if it is assumed that the quark content of the nucleon is completely correct in the MC, a wrong simulation of the hadronization might explain at least part of the observed inconsistencies,

[2]Note that for the neutron target the quark flavors have been isospin rotated, such that $u_n = d_p$ etc. The name u or d quark refers to the distributions in the proton then.

as will be shown in the following. For the fragmentation functions (FFs) $D_{q/h}$ (cf. section 2.4), charge conjugation and isospin symmetry imply that

$$D_{u/h^+} = D_{d/h^-} = D_{\bar{d}/h^+} = D_{\bar{u}/h^-} \equiv D_1 \tag{5.10}$$
$$D_{d/h^+} = D_{u/h^-} = D_{\bar{u}/h^+} = D_{\bar{d}/h^-} \equiv D_2, \tag{5.11}$$

where D_1 and D_2 are called favored and unfavored fragmentation functions. Isospin symmetry should be a good assumption for u and d quarks and the respective antiquarks fragmenting to pions at high energies. For instance, the relation between $P^{h^+}(u)$ and $P^{h^-}(u)$ is given by the ratio of the favored to unfavored FFs $D_{u/h^+}/D_{u/h^-}$. If this ratio were too small in the MC it could be that the correlation of u quarks with π^+ is too small just like that of d quarks with π^-. This can be seen from a simple description of (polarized) DIS cross sections for proton and neutron. Considering only u and d valence quarks, the cross sections for charged hadrons can be written as (omitting kinematic dependencies):

$$\begin{array}{ll} \sigma(h_p^+) \sim e_u^2 D_1 u_p + e_d^2 D_2 d_p & \sigma(h_n^+) \sim e_u^2 D_1 u_n + e_d^2 D_2 d_n \\ \sigma(h_p^-) \sim e_d^2 D_1 d_p + e_u^2 D_2 u_p & \sigma(h_n^-) \sim e_d^2 D_1 d_n + e_u^2 D_2 u_n \end{array} \tag{5.12}$$

where the subscripts p and n stand for proton and neutron target, respectively, and $q = u, d$ stand for the quark densities. The ratio of charges is $e_u^2 : e_d^2 = 4 : 1$, such that for proton one obtains:

$$\sigma(h_p^+) \sim 4D_1 \left(u_p + \frac{D_2}{4D_1} d_p \right) \tag{5.13}$$
$$\sigma(h_p^-) \sim D_1 \left(d_p + 4\frac{D_2}{D_1} u_p \right) \tag{5.14}$$

The polarized cross sections are analogous to that, with a Δ in front of the spin dependent quantities σ and $q_{p,n}$. If the MC would model the ratio D_2/D_1 too large compared to the data the effect would be the following. Since the d quark is negatively polarized, the MC DIS asymmetries for proton would come out too small for positive and too large for negative hadrons. Consequently, the extracted value for $\frac{\Delta G}{G}$ would be too small resp. too large. Note that the effect of a wrong D_2/D_1 is enhanced by a factor 4 in the case of negative hadrons. The cross sections for the neutron can be obtained by isospin rotating the u and d quark distributions, i.e., $u_n = d_p$ and $d_n = u_p$. The deuteron is a mixture of proton and neutron, giving the cross sections

$$\sigma(h_d^+) \sim 4D_1 \left(u_p + d_p \right) \left[1 + \frac{D_2}{4D_1} \right] \tag{5.15}$$
$$\sigma(h_d^-) \sim D_1 \left(u_p + d_p \right) \left[1 + 4\frac{D_2}{D_1} \right] \tag{5.16}$$

and analogous for the polarized cross sections. Again, a wrong ratio of favored to unfavored fragmentation functions would be more significant for negative hadrons. As opposed to the proton, in the deuteron case u and d contribute on an equal footing to both charges. This is what can also be seen in the deuteron purities of figure 5.26. To demonstrate the sensitivity of asymmetries to the fragmentation, figure 5.27 shows the asymmetries of proton and deuteron vs. x. for positive and negative hadrons. It can be clearly seen that the proton asymmetries are larger than the deuteron asymmetries as a consequence of the u quark dominance in the proton. It can also be observed that at large x, on proton the negative hadron asymmetry is smaller than the positive hadron asymmetry, while they are almost the same on deuteron. The former is due to a larger sensitivity of negative hadrons to the d quark, as can be inferred from comparing Eqs. 5.13 and 5.14. The latter comes from the equal sensitivities of both charges to each quark flavor in Eqs. 5.15 and 5.16. From Eqs. 5.13 and 5.14, on the other hand, it can be seen that a larger D_2/D_1 would decrease the sensitivity to the 'favored' quark flavor and make at least the proton asymmetries more symmetric with respect to the charge.

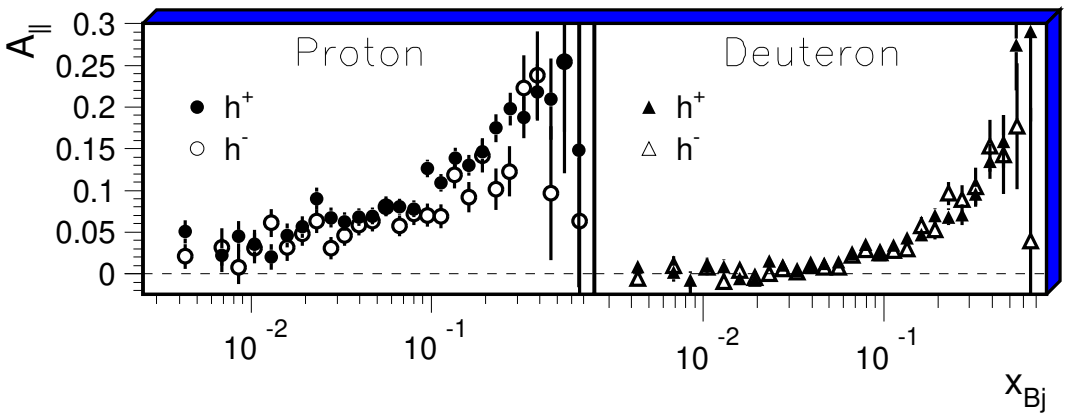

Figure 5.27: The measured asymmetries of positive (filled symbols) and negative hadrons (open symbols) in the 'Transition' region as a function of x. The left plot is for proton, the right plot for deuteron data.

It could be argued that in the *asymmetries* relevant for the extraction of $\frac{\Delta G}{G}$ the effect of a wrong ratio of fragmentation functions cancels with a deuteron target, as can be seen when writing out the corresponding asymmetry for positive hadrons as an example

$$\frac{\Delta\sigma}{\sigma}(h_d^+) \sim \frac{(\Delta u_p + \Delta d_p)\left[1 + \frac{D_2}{4D_1}\right]}{(u_p + d_p)\left[1 + \frac{D_2}{4D_1}\right]}, \tag{5.17}$$

which does not depend on the fragmentation functions anymore. However, in this special formalism it is not the asymmetry itself being used, but the asymmetry weighted with the unpolarized cross section (cf. Eq. 5.2) $\sigma^{DIS}A_\parallel^{DIS}$. Since other processes like PGF involve different combinations of fragmentation functions, the influence of the fragmentation might not completely cancel in the expression for $\frac{\Delta G}{G}$, and therefore also for deuteron the result can depend on the ratio of favored to unfavored fragmentation functions. This might explain that a difference between results for positive and negative hadrons remains also in the deuteron, albeit reduced in size. Of course in reality the DIS cross section cannot be expressed as simple. Already from figure 5.26 it can be seen that, since the sum of the purities of u and d quarks is only approximately 0.8, about 20% percent of the hadrons at $p_T > 1$ GeV should come from events involving antiquarks or strange sea quarks. Incorporating these into the above expressions would lead to charge and fragmentation dependent dilutions in asymmetries, as the polarization of sea quarks is very small or even zero. The situation is even more complicated in the 'Transition' region where the DIS process probes the parton distributions at smaller $x \approx 0.05$ and is therefore more sensitive to sea quarks.

Semi-inclusive charged hadron cross section ratios should to some degree be sensitive to the fragmentation function ratio D_2/D_1. For instance, the ratios

$$R_p = \frac{\sigma(h_p^+) + \sigma(h_p^-)}{\sigma(h_p^+) - \sigma(h_p^-)} \approx \frac{1 + \frac{D_2}{D_1}}{1 - \frac{D_2}{D_1}} \frac{1 + \frac{d+4\bar{u}}{d+4u}}{1 - \frac{d+4\bar{u}}{d+4u}} \equiv \frac{1 + \frac{D_2}{D_1}}{1 - \frac{D_2}{D_1}} f_p(x) \tag{5.18}$$

$$R_d = \frac{\sigma(h_d^+) + \sigma(h_d^-)}{\sigma(h_d^+) - \sigma(h_d^-)} \approx \frac{5}{3} \frac{1 + \frac{D_2}{D_1}}{1 - \frac{D_2}{D_1}} \frac{1 + \frac{\bar{u}+\bar{d}}{u+d}}{1 - \frac{\bar{u}+\bar{d}}{u+d}} \equiv \frac{1 + \frac{D_2}{D_1}}{1 - \frac{D_2}{D_1}} f_d(x) \tag{5.19}$$

can be used to retrieve information about D_2/D_1, if the functions of the quark distributions, $f_{p,d}(x)$ are known. The results for $R_{p,d}$ then of course depend on the model for the parton distributions. For the MC, this dependence can be reduced if the CTEQ5 LO distributions [Lai00] are taken that the MC was generated with. As the resulting D_2/D_1 should not depend on the target, a comparison between the results from R_p and R_d should indicate the size of the residual model dependence to

be expected in the experimental data. The values for D_2/D_1 obtained from R_p and R_d are shown in figure 5.28. The difference of the ratios for proton and deuteron is relatively small for both the

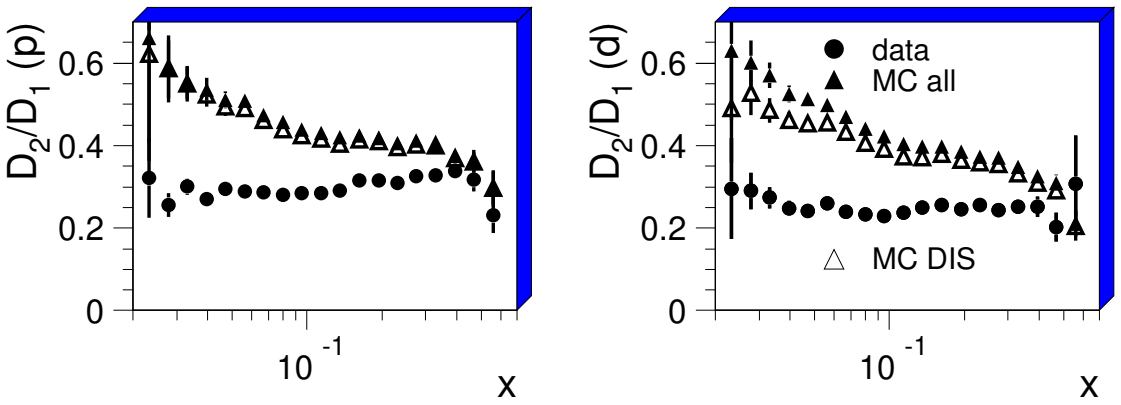

Figure 5.28: The ratios D_2/D_1 (in the HERMES acceptance) obtained from Eqs. 5.18 and 5.19 from proton (left plot) and deuteron data (right plot), using the CTEQ5 PDFs. See text for details.

MC and the data, indicating only little dependence on the very different quark combinations going into the expressions for D_2/D_1. As Eqs. 5.18 and 5.19 are only valid for the LO DIS process, for comparison the MC ratios are shown for all processes (filled triangles) and for the DIS process only (open triangles). It can be seen that at small x, the ratio for the DIS process alone is smaller for deuteron than for proton. This is most likely due to the neglect of *strange* quarks in the expressions for the cross section which affects the deuteron ratio more than the proton ratio. Also, in the small x region other processes than DIS contribute more to the cross section. The ratio D_2/D_1 for all processes on proton behaves exactly like that of only the DIS process whereas it is different on deuteron. Reversely, this means that processes other than DIS, mostly low-p_T processes, behave similar to DIS on proton, but not on deuteron. This issue will be proceeded further below.

At medium $x \approx 0.1$ the data are about 2/3 smaller than those from the MC. It can be clearly seen that the ratio extracted from the data is not only much smaller in size than that of the MC, but also different in the shape vs. x. A dependence of the fragmentation function ratio on x by itself is not yet problematic because, although the fragmentation functions by definition depend only on z, the acceptance function of the spectrometer depends on x and z. At different x therefore different ranges in z can be accessed, leading to a variation of the 'measured' D_2/D_1. While the data show a very small variation in x, the Monte Carlo clearly follows a trend. At high x, where in the MC the DIS process dominates, therefore the different shape indicates a different average z than in the data. The average z from Monte Carlo and data is shown in figure 5.29 as a function of x and p_T for pions with $4 < p < 13.8$ GeV in the 'SIDIS' region. From the plots of figure 5.29 it can be concluded that neither at the large $x > 0.1$ of the DIS process that is important in the 'Photoproduction' region, nor at the large p_T relevant for the QCD Compton and PGF processes in both the 'Photoproduction' and the 'Transition' region, the Monte Carlo correctly reproduces the z distributions for both charges. At large x, the MC tends to have a more symmetric z distribution between positive and negative pions than the data where the positive pions are clearly above the negative ones. At large p_T, the average z of the positive pion data is higher than in the MC, whereas the MC is in agreement with the negative pions. The observed disagreements may again be correlated to a wrong favored to unfavored fragmentation ratio. On the other hand it should be considered that, in addition to the detector acceptance also the simulated nonperturbative intrinsic k_T and the smearing of the hard partonic p_T during fragmentation influences the z distributions, especially as a function of the hadron p_T.

Assuming a constant factor of 0.6 between the measured unfavored to favored fragmentation ratios in the data and the MC, the MC data can be 'corrected' in order to estimate the effect of the too large fragmentation ratios. Each hadron originating from a DIS or QCD Compton scattering

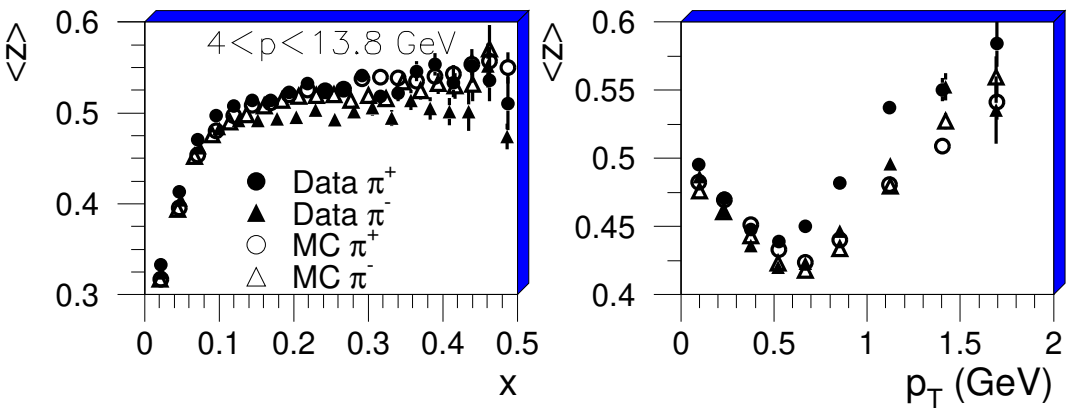

Figure 5.29: Left: The average z of positive (circles) and negative pions (triangles) from the 1997 data (filled symbols) and PYTHIA (open symbols) as a function of x in the 'SIDIS' region. The pions have $4 < p < 13.8$ GeV, no cuts on z were applied. Right: Same data showing the average z as a function of p_T.

on an 'unfavored' quark (i.e., $\bar{u}$ and d for h^+, $\bar{d}$ and u for h^-) is weighted with 0.6 in the calculation of cross sections and asymmetries. This procedure does not change the shape of the ratio D_2/D_1, but moves its magnitude towards that of the data. In order to change the shape, a more realistic, z dependent factor would have to be applied. This would in particular influence the shape at small x, where the average z varies strongly with x.

Using this simple reweighting method to derive cross sections, the cross section of negative pions in the 'SIDIS' region improves considerably compared to the uncorrected cross section, as it is shown in the right plot of figure 5.30 as a function of W^2. The MC cross sections in this figure are without QED radiative corrections. The full lines are the uncorrected Born cross sections predicted by PYTHIA, the dashed lines the cross sections obtained by reweighting the DIS and QCDC processes as described above. The positive pion cross section reduces also, but much less, therefore increasing the ratio $\sigma(h^+)/\sigma(h^-)$. In the 'Transition' region a better agreement of the

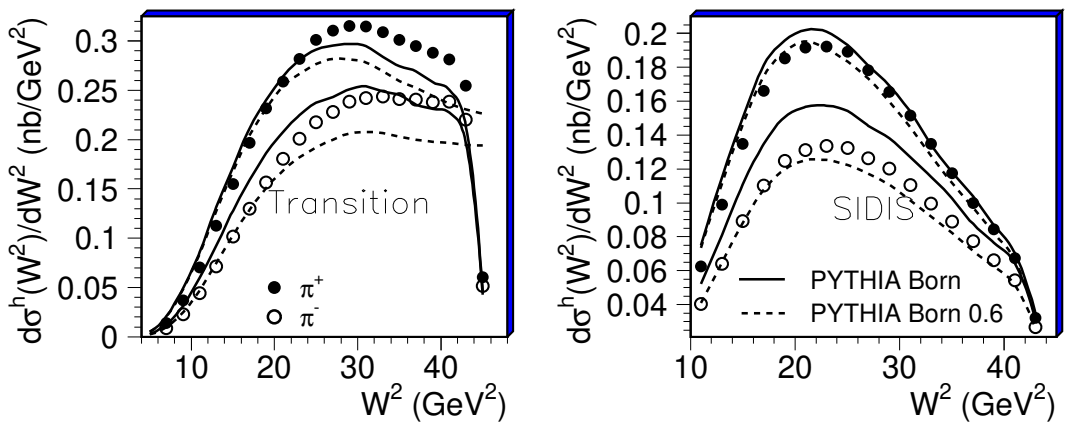

Figure 5.30: Semi-inclusive pion cross sections with and without the correction for D_2/D_1 from PYTHIA, compared to the 2000 H data. See text for details.

negative pion cross sections can only be detected at small W^2 when using the weight factor, at high W^2 the agreement to the data actually gets worse. The corresponding results for deuteron (not shown) are similar. Of course, applying a constant factor to only a fraction of the cross section is a rather crude approach, such that only a qualitative statement about the possible effect of a

different unfavored to favored fragmentation ratio can be made. Also, at large W^2 (corresponding to small x) in the 'Transition' region other processes like VMD dominate.

By reweighting Monte Carlo events for the calculation of asymmetries the results for $\frac{\Delta G}{G}$ change as shown in figure 5.31, for a cut on $p_T > 1.35$ GeV. The proton results for positive

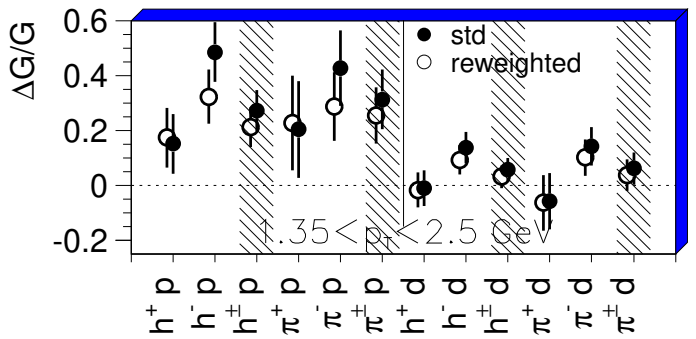

Figure 5.31: The results for $\frac{\Delta G}{G}$ in the 'Photoproduction' region obtained using a weight of 0.6 for the unfavored fragmentation function in DIS and QCDC (open circles) compared to the unweighted MC results (full circles) for positive and negative hadrons and pions from proton and deuteron.

and negative hadrons indeed move closer together. As expected, for deuteron the effect is much smaller. Also, the result from the proton data stays much larger than that from the deuteron data. The behavior of the data as a function of the p_T cut is shown in figure 5.32. The modified

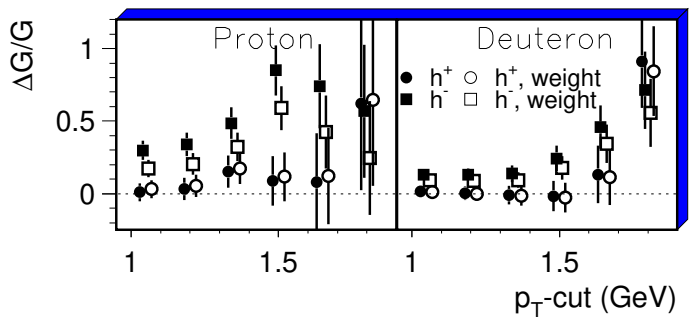

Figure 5.32: The results for $\frac{\Delta G}{G}$ obtained using a weight of 0.6 for the unfavored fragmentation function in DIS and QCDC (open circles) compared to the unweighted MC results (full circles) for positive and negative hadrons and from proton and deuteron as a function of the p_T cut in the 'Photoproduction' region.

fragmentation function ratios can indeed reduce the inconsistencies between positive and negative hadrons observed in the 'Photoproduction' region. Some discrepancies stay, though, because the applied constant factor cannot make up for a probably necessary complicated function of z and p_T.

As shown in figure 5.33, in the semi-inclusive region the effects are much smaller for both proton and deuteron. This can be expected from figure 5.28 from which an even smaller fragmentation ratio at the smaller $x \approx 0.05$ probed in the 'Transition' region can be inferred. In this region mainly sea quarks are probed, whose polarization is small and $\Delta u_s \approx \Delta d_s$, such that the resulting asymmetries are smaller and almost equal for positive and negative pions.

The question remains why the fragmentation should be not correctly simulated within the PYTHIA/JETSET Monte Carlo. Most of the knowledge about fragmentation functions comes from e^+e^- collider data (cf. section 2.4). What is measured in the process $e^+e^- \to hX$ is the combination $D_1 + D_2$, because the final state partons in the hard subprocess are $q\bar{q}$ pairs. The e^+e^- data are therefore not particularly sensitive to the individual functions D_1 and D_2. Fragmentation functions for individual charges from e^+e^- data can therefore be only obtained by imposing additional assumptions on the relative behavior of the various hadron flavors. This has been pursued for instance in Ref. [Kre00] where input parametrizations of the form

$$D_q^h(z, \mu_0^2) = N_q^h z^{\alpha_q^h} (1-z)^{\beta_q^h} \tag{5.20}$$

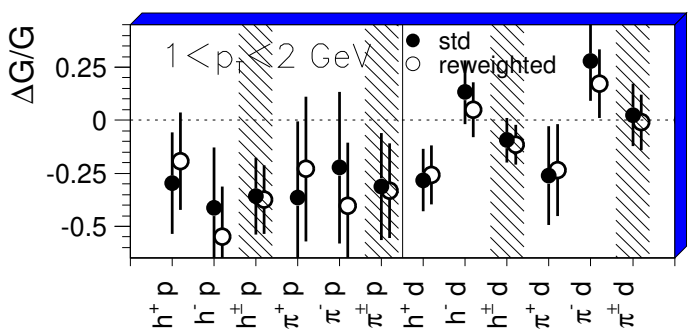

Figure 5.33: The results for $\frac{\Delta G}{G}$ in the 'Transition' region obtained using a weight of 0.6 for the unfavored fragmentation function in DIS and QCDC (open circles) compared to the unweighted MC results (full circles) for positive and negative hadrons and pions from proton and deuteron.

were used to fit LEP data on flavor inclusive as well as flavor tagged e^+e^- annihilation cross sections. It was further assumed that $D_2/D_1 = (1-z)$. This behavior is compatible with measurements, for instance from EMC [Arn89]. In fact, fits to the semi-inclusive pion multiplicities measured by HERMES [Air01] exist where additional input from the singlet fragmentation function measured at LEP was used [Kre01]. These fits are remarkably well compatible with the results from the fits to LEP data only. In other models for FFs only the sum of charged hadrons is fitted. The universality of the resulting FFs has only been tested using charge averaged data, see, for instance Ref. [Kni01]. None of the available fits have so far been compared to charge separated SIDIS data.

An important premise going into basically all FF parametrizations is that of isospin symmetry. The main difference of the fragmentation process in e^+e^- annihilation and DIS is the existence of a target remnant in the latter. Strict isospin symmetry only holds for the light u and d (anti-)quarks, but not in the fragmentation of the target remnant which most of the time is a diquark. The reason for the breaking of isospin symmetry in the fragmentation of diquarks is that the possible final state baryons differ depending on the combination of the diquark with a quark from the vacuum. The kinematic range of HERMES is too small to separate hadrons in a very forward region in rapidity, the so called 'current' region, where the correlation of the hadrons to the target remnant should be negligible and the universality of FFs should hold. Instead the HERMES data might indeed be sensitive to the flavor structure of the target remnant and the way it hadronizes.

The Monte Carlo simulation, on the other hand, employs the LUND string fragmentation model, Eq. 2.73 that in principle should properly take care about the target remnant. However, also the treatment of the remnant in the MC relies heavily on assumptions. In order to learn more about the target fragmentation, fragmentation functions need to be measured on different targets and for identified hadrons of both charges. Up to now only the measurements of EMC have been published. These data have not explicitly been used in fits for FFs so far. In the MC, the large z behavior of hadron spectra goes like $(1-z)^a$ with a common parameter a for all quarks and hadrons. The different hadron multiplicities then emerge as a consequence of the average number of string breaks necessary to produce a certain hadron h, starting from an outgoing parton q and diquark q_iq_j [3]. The values for the default JETSET parameters a and b, as well as those for the additional suppression of strange quark, baryon and vector meson production have been estimated using e^+e^- data. These values have been seen to not reproduce HERMES data [Gei98] as well as data taken by ZEUS in the target fragmentation region [Lev03]. It can therefore be concluded that the MC model of the fragmentation process might not be flexible enough to account completely for the complicated target fragmentation process in lepton-nucleon scattering and that the HERMES charge separated data might be particularly sensitive to this process. In general, the generation of hadrons according to the LUND symmetric fragmentation function, Eq. 2.73, is based on phase

[3] If an antiquark was struck, the remnant is a four-quark system whose treatment introduces additional uncertainties. This is even more so because in PYTHIA a struck quark, as opposed to an antiquark, is never allowed to be a sea quark which in turn would leave behind an antiquark and three valence quarks.

space arguments, and is assumed to be accurate for infinitely large energies. At the small HERMES energies where only a few string breaks occur in the fragmentation, phase space constraints might invalidate the assumption of a common parameter a in the LUND FF.

Less sensitive to modeling favored and unfavored fragmentation functions should be the production of π^0 whose flavor content is symmetric in u, d and the corresponding antiquarks. It may therefore be worthwhile to extract a value for $\frac{\Delta G}{G}$ from high-p_T asymmetries of π^0. Due to the limited acceptance of the two photons from the decay $\pi^0 \rightarrow \gamma\gamma$ the statistics may be significantly reduced compared to the charged pion data, however. Last it should be mentioned that inconsistencies similar to those detected here for $\frac{\Delta G}{G}$ were observed for polarized *quark* distributions fitted to polarized semi-inclusive data. In Ref. [Nav03], different polarized PDFs were obtained depending on if the weight of positive or negative hadron data was enhanced in the fit. This result turned out to be independent from the data used (SMC [Ade96, Ade98], or HERMES [Ack99]). The fit also used parametrized FFs, thereby indicating that the problem is not only inherent in the Monte Carlo, but in general in the (known) models for fragmentation functions.

5.4.2 Kinematic Correlations and the Low-p_T Processes

In the 'Transition' region it was observed that the kinematics of the events are not reproduced very well by the MC (cf. figure 4.30). This could potentially lead to an additional problem affecting the background asymmetries, but possibly also the gluon momentum fraction x_G. The use of the MC prediction for the average kinematics in each p_T bin is inherent to the extraction method of $\frac{\Delta G}{G}$. It is therefore not possible to use the information on the experimentally measured average x consistently with the MC and extract $\frac{\Delta G}{G}$ from the measured kinematics. The reason is the model dependence of the average x, as is illustrated for LO DIS, PGF and the sum of all processes in the 'Transition' region in figure 5.34. Here, the average x are compared for set #1, #4 and #6 (cf.

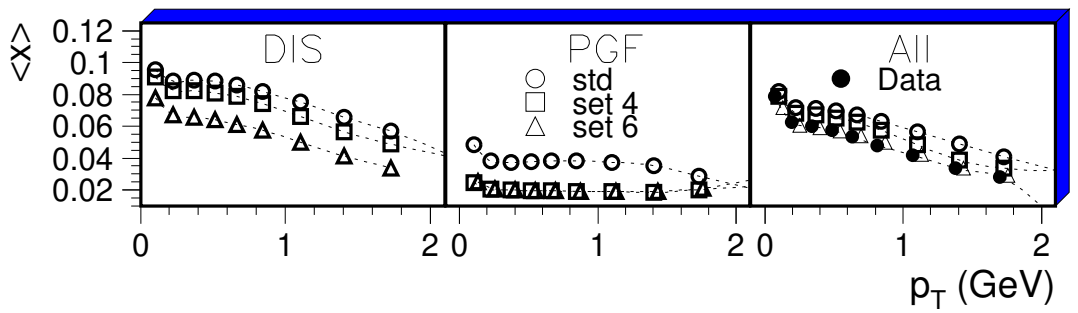

Figure 5.34: The average x in the LO process (left), the PGF process (middle) and all processes (right) on proton for hadrons in the 'Transition' region, for the standard set, set #4 and set #6. For comparison, the proton data are plotted for comparison in the right panel.

section 5.3.2). For the LO DIS process in set #4, x is significantly smaller than in the standard set, and using set #6 reduces x even more. The average x of the data fits best to set #6, as can be seen from the right panel of figure 5.34. The average x for the PGF process shown in the middle panel is much smaller for the two sets with MSTP(18)=3. This illustrates that by changing parameters in PYTHIA, the average kinematics of one process (DIS) cannot be changed independently from those of other processes. As described in section 5.3.2, also the subprocess fractions change accordingly.

In the 'Photoproduction' region the MC kinematics cannot be compared with the data, but of course wrong kinematics would also here influence the results – even more so since the background DIS process contributes at large x, where the asymmetries are varying strongly with x and are charge and target dependent. Also here, the average x vs. p_T is model dependent, as can be seen from figure 5.35, where sets #1, #4 and #5 are compared.

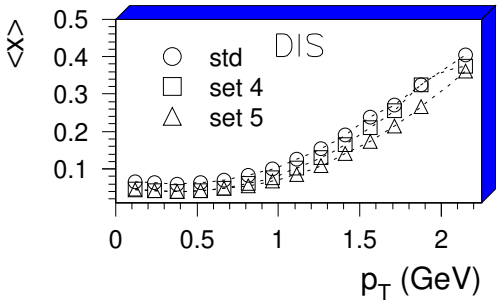

Figure 5.35: The average x in the LO process on proton for hadrons in the 'Photoproduction' region, for the standard set, set #4 and set #5.

In both kinematic regions the variation of PYTHIA model parameters led to a reduction of the average x vs. p_T compared to the standard set. A smaller x for the DIS process is favored by the data, as can be seen from the right panel of figure 5.34 where the values from set #6 with the enhanced DIS contribution are on top of the data, while they are too high for the other two sets. The DIS asymmetries are monotonically rising functions of x for all charges and targets. If the DIS asymmetry is to be evaluated at a smaller x, the MC background asymmetry becomes smaller, and the value for $\frac{\Delta G}{G}$ larger. The expected shifts in $\frac{\Delta G}{G}$ are shown in figure 5.36, where the standard extracted values are compared to those with the background asymmetry from set #5 (#6) in the 'Photoproduction' ('Transition') region, *but using the subprocess fractions and PGF subprocess asymmetries of the standard set.* Significant shifts can only be observed for the proton

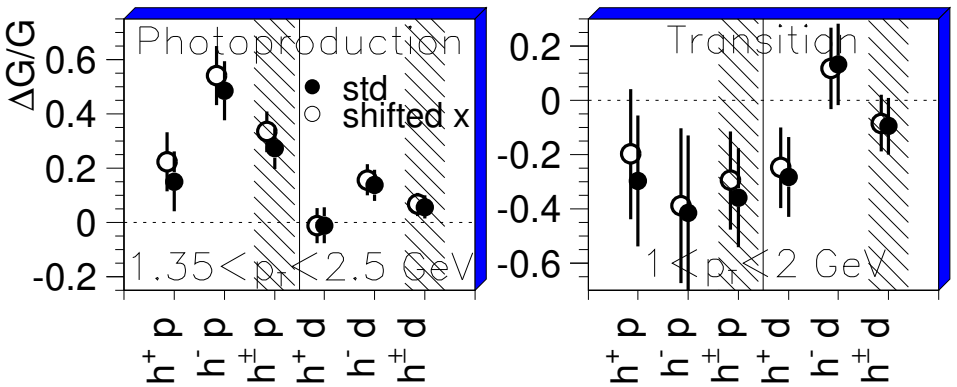

Figure 5.36: Comparison of $\frac{\Delta G}{G}$ extracted with the standard set (full dots) and with the fractions and PGF asymmetries from set #1 together with the background asymmetry of sets #4 and #6 for the 'Photoproduction' (left) and 'Transition' region, respectively (empty dots).

data. As almost all values shift into the same direction, the inconsistencies between charges and targets cannot be explained by wrongly simulated kinematics. As stated before, the treatment used to obtain the 'kinematics corrected' $\frac{\Delta G}{G}$ is inconsistent and therefore the deviations in figure 5.36 should not be considered as a systematic error. Eventually it may be necessary to find the reason for the wrong kinematic correlations in PYTHIA, be it the model for the subprocess mixture, the subprocess kinematics or the fragmentation or a combination of all. Because the ratio D_2/D_1 is z dependent, and due to the coupling of z with the acceptance even the detected wrong fragmentation function ratio may influence the kinematic distributions of events.

One more problem remains from the low-p_T process. It is assumed here that this minimum bias process has a zero or small asymmetry corresponding to a phenomenological g_1/F_1 at small x and Q^2. By definition, the treatment of the low-p_T process in the calculation of asymmetries is charge independent. The way that it is simulated in the MC it is not, though. Since there are

no hard kinematics, the partons involved in this process are chosen according to 'counting rules': The $\gamma \to q\bar{q}$ splitting is chosen such that a $u\bar{u}$ pair occurs 4 times more often than a $d\bar{d}$ pair. An additional suppression is introduced for strange quark pairs compared to the $d\bar{d}$ pairs. In the nucleon, the involved quark flavors have a valence structure, i.e., $u : d = 2 : 1$ for proton, and $u : d = 1 : 1$ in the deuteron. Hadrons emerging from the $q\bar{q}$ pairs of the photon should therefore be charge symmetric while from the proton an excess of positive particles can be expected. From the deuteron again a charge symmetric distribution would be expected. For both the LO DIS and the low-p_T processes the proton is therefore dominated by the u quark. For the deuteron different quark mixtures in the low-p_T and DIS processes (for DIS the scattering ratio on u compared to d is 9:5 in the deuteron) lead to a different behavior of DIS and low-p_T processes. The results for deuteron are therefore much more sensitive to how the low-p_T process is actually simulated. Conversely, especially the proton results might change considerably, if the initial quark distributions were generated less valence like. In the 'Photoproduction' region, the fraction of low-p_T events in positive and negative hadrons, proton and deuteron data is determined by this specific treatment, and may therefore also enhance or decrease the relative contribution of the perturbative processes charge and target dependent. For a cut on $p_T > 1.8$ GeV, the contribution of low-p_T events to the cross section is reduced to 20% compared to the about 35% at $p_T > 1.35$ GeV. This in turn might explain why at these large p_T the results of proton and deuteron become more consistent (cf. figure 5.9).

5.5 Final Results and Systematic Errors

The results of the previous section can be summarized as follows. From cross sections for charged hadrons and their ratios it can be concluded that the Monte Carlo overestimates the ratio of unfavored to favored fragmentation functions. The possible effect of such an overestimate was investigated, showing that it can at least partially explain the discrepancies observed for $\frac{\Delta G}{G}$ from positive and negative hadrons. Using only a simple constant correction factor applied to the Monte Carlo data it is not possible to reduce all discrepancies, especially not the ones observed between the results from proton and deuteron targets. As the largest discrepancies are observed in the 'Photoproduction' region, the low-p_T process, more accurately the way it is simulated by PYTHIA, is identified as a possible candidate to explain the different results from the two targets.

Leaving the detected problems aside, in the following the p_T dependence of the 'Photoproduction' results will be studied. A systematic error based on the analysis described in section 5.2.3 will be evaluated considering also the results of the previous section. A final result will also be given for the 'Transition' region and compared to that obtained from the 'Photoproduction' region.

The statistical error on the unpolarized gluon distribution has not been taken into account. Estimates for the statistical errors on PDF exist only for NLO distributions. From the error analysis of (NLO) CTEQ6 PDFs [Lai02] an error of $\pm 20\%$ can be estimated for the gluon distribution at $Q^2 = 1.5$ GeV^2 and $x < 0.4$. At larger x the error increases to up to 100%. This statistical error propagates, together with the correlated errors on the quark densities, into those of the fractions of processes. Also, the scale dependence of the results has not been evaluated. The scale for $2 \to 2$ processes was varied for the 'Transition' region to be $\hat{p}_T^2$ instead of $\hat{p}_T^2 + Q^2/2$ in the default (cf. figure 5.18) with no apparent changes in the result. For the 'Photoproduction' region the scale $\hat{Q}^2 \approx \hat{p}_T^2$ was multiplied by factors 0.5 and 2, respectively, again with only insignificant changes in the PGF cross sections, subprocess fractions and the final result. This does not necessarily imply that the scale dependence of the results is small in reality. It can be that the insensitivity to the scale variations arises from technical reasons in PYTHIA. Also, in PYTHIA the scale cannot be changed consistently for all contributing processes – the scale for LO DIS is always Q^2.

5.5.1 p_T and x_G Dependence of $\frac{\Delta G}{G}$ in the 'Photoproduction' Region

The large statistics of the 'Photoproduction' data offer a unique possibility to study the dependence of $\frac{\Delta G}{G}$ on p_T and therefore the gluon momentum fraction. This can be seen from figure 5.15 where the strong correlation of the measured p_T to the average x_G in PGF is shown for several PYTHIA parameter sets. For the combination of PGF and hard resolved processes used in the extraction of $\frac{\Delta G}{G}$ the average x_G is smaller than for PGF alone while the dependence on p_T remains, leaving the range between $0.1 < \langle x_G \rangle < 0.2$ for investigation.

The data are subdivided into five bins in p_T from 0.9 to 2.5 GeV. For these points also the theoretical uncertainties (i.e., uncertainties arising from different assumptions on, e.g., the subprocess asymmetries or the PDFs) and those inherent to the PYTHIA model discussed in section 5.2.3 will be estimated. The central value for $\frac{\Delta G}{G}$ is obtained using PYTHIA parameter set #1, and by setting $A_1^{low-p_T} = g_1/F_1(W^2)$ for all x and Q^2. This way for both deuteron and proton data $A_1^{low-p_T}$ is chosen consistently such that the MC asymmetries fit the data at small p_T (cf. sections C.1 and 5.2.3). The individual deviations arising from comparing $A_1^{low-p_T} = 0$ to $A_1^{low-p_T} = g_1/F_1(W^2)$, the choice of combinations of unpolarized and polarized proton PDFs, the choice of the unpolarized photon PDFs and varying PYTHIA parameters are obtained from the differences to the results of the standard set

$$\Delta\left(\frac{\Delta G}{G}\right)_i = \left(\frac{\Delta G}{G}\right)_i - \left(\frac{\Delta G}{G}\right)_0 . \tag{5.21}$$

To take the effect of PYTHIA set #5 into account, the difference is taken to be

$$\Delta\left(\frac{\Delta G}{G}\right)_{set\,\#5} = \left(\frac{\Delta G}{G}\right)_{set\,\#5} - \left(\frac{\Delta G}{G}\right)_{set\,\#4} . \tag{5.22}$$

in order to avoid double counting of the effect of MSTP(18)=3 common to both set #5 and #4. The uncertainty from the maximal and minimal scenarios for the polarized photon PDFs combined with each unpolarized photon PDF is taken to be

$$\Delta\left(\frac{\Delta G}{G}\right)_{\Delta f^\gamma} = \frac{\left(\frac{\Delta G}{G}\right)(\Delta f^\gamma = max, min) - \left(\frac{\Delta G}{G}\right)(\Delta f^\gamma = 0)}{\left(\frac{\Delta G}{G}\right)(\Delta f^\gamma = 0)} \left(\frac{\Delta G}{G}\right)_{set\#1} . \tag{5.23}$$

This procedure takes into account that the effects of the polarized photon PDFs have been studied using different PYTHIA sets than the standard one, and that the deviations apparently scale with the central value of $\frac{\Delta G}{G}$ (cf. section 5.2.3 and figure 5.16).

For the total theoretical and PYTHIA inherent systematic uncertainty the sum of the maximum positive and negative deviations from each independent group is calculated. This total uncertainty will be quoted as 'model' uncertainty, although it should be kept in mind that an uncertainty accounting for the use of PYTHIA itself as the Monte Carlo model to extract the results (instead of any other hypothetically possible MC model) cannot be evaluated and is therefore not included. The experimental systematic error on $A_\parallel$ is propagated into $\frac{\Delta G}{G}$ according to

$$\Delta\left(\frac{\Delta G}{G}\right)^{exp} = \frac{N_{tot}}{N_{sig}} \Delta A_\parallel^{\pm}, \tag{5.24}$$

where the maximum and minimum systematic uncertainties displayed in the tables of section D.2 are used.

The data consist of four independent samples, the measured asymmetries on h^+ and h^- on proton and deuteron. Identified pions need not to be considered separately, as the results of section 5.2 were always similar to the hadrons results, but with smaller statistics. The extracted gluon polarization is shown as a function of p_T for the individual sets in figure 5.37 together with the (model dependent) average x_G in each bin obtained from sets #1, #4 and #5. The total systematic

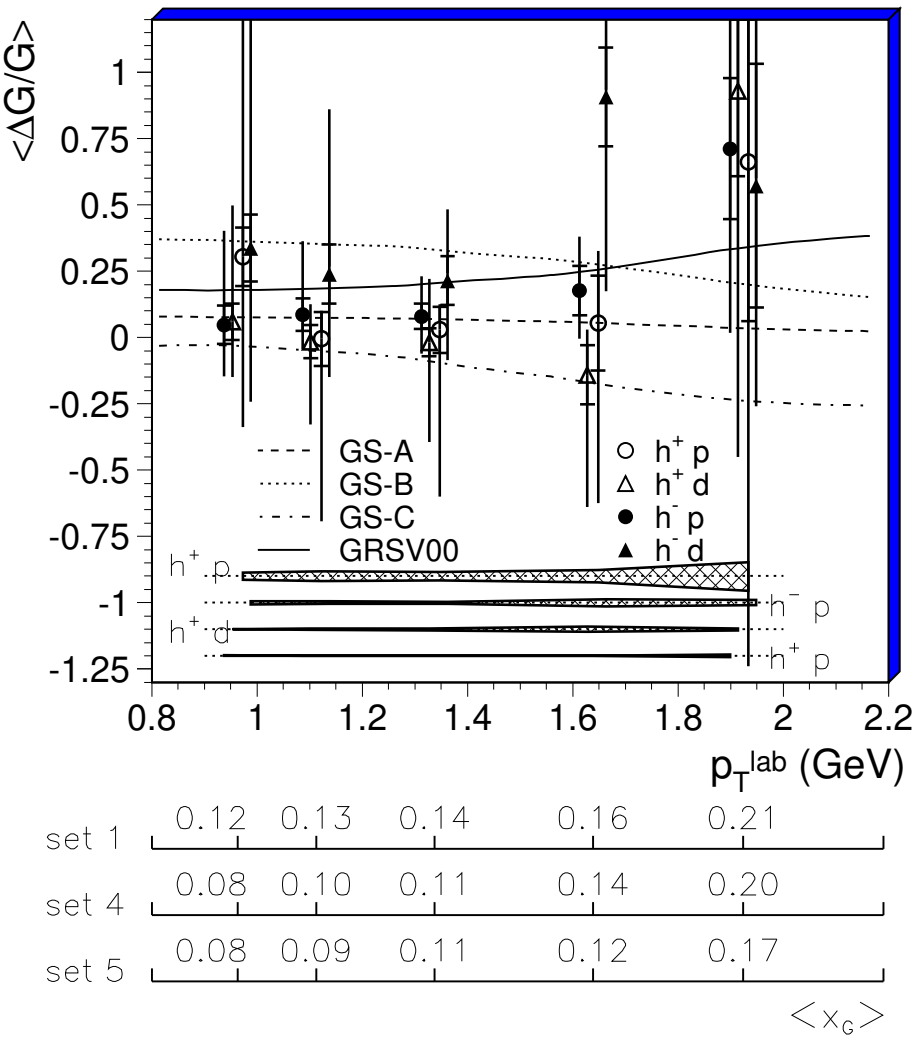

Figure 5.37: Extracted values for $\frac{\Delta G}{G}$ as a function of p_T for positive hadrons (open symbols) and negative hadrons (filled symbols) from proton (circles) and deuteron (triangles). The model uncertainty is added linearly on top of the statistical error bars, separated with a horizontal tick mark. The shaded bands show the (asymmetric) experimental systematic uncertainties for each data set.

model uncertainty is added there linearly on top of the statistical error and separated from it by the horizontal tick marks. The values and errors for each bin are given in tables D.34 to D.37. The curves for $\frac{\Delta G}{G}$ obtained from four different models for polarized PDFs are plotted on top of the data. These models are in particular GS [Geh96] with three scenarios for the gluon distribution at the input scale (Gluon A, B and C) and GRSV2000 [Glü01]. The theoretical values are obtained from the Monte Carlo data and integrated over the same (model dependent) kinematic range.

The correlation between the measured p_T and x_G can be estimated from figure 5.38. This figure shows that there is clearly a correlation between p_T and the gluon momentum fraction. The width of the x_G distribution does not allow to *directly* determine $\frac{\Delta G}{G}(x)$ by using the information on the average $\langle x_G \rangle$ for each p_T bin. Still, the result on $\frac{\Delta G}{G}$ extracted as a function of p_T depends on the shape of the x_G distribution and on the function $\frac{\Delta G}{G}(x)$. Reversely, the p_T dependence of the result is sensitive to the shape of $\frac{\Delta G}{G}(x)$. So eventually it should be possible to use the p_T dependence of $\frac{\Delta G}{G}$ to retrieve information on its shape as a function of x_G.

The inconsistencies between the four individual results are also obvious from figure 5.37. The t and χ^2/ndf values (cf. Eq. 3.9, where only the statistical errors are considered) between four

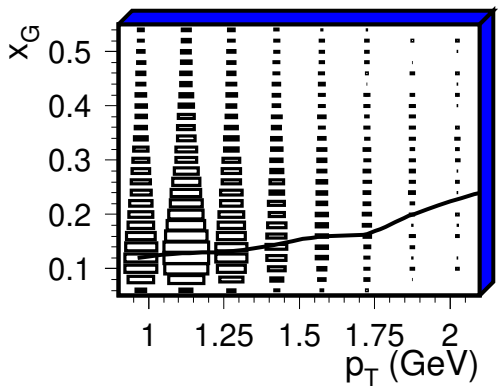

Figure 5.38: x_G vs. p_T from PYTHIA set #1. The curves goes along the average values given in figure 5.37 for set #1.

combinations of two sets, $h^{\pm}$ (proton) vs. $h^{\pm}$ (deuteron), and h^+ vs. h^- for proton and deuteron, are shown in figure 5.39. Here, the same picture emerges as already seen in figure 5.8 where the data

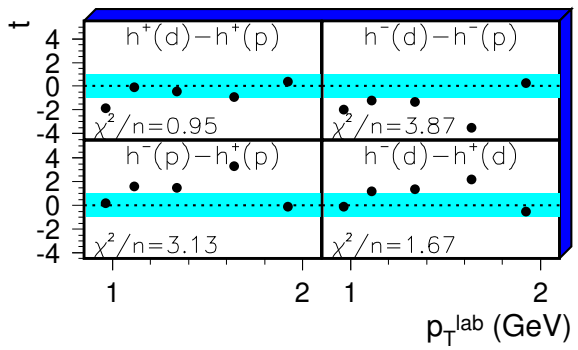

Figure 5.39: t values for $\frac{\Delta G}{G}$ for h^+ on deuteron vs. proton, h^- h^- on deuteron vs. proton, h^+ vs. h^- on proton, h^+ vs. h^- on deuteron.

were integrated over p_T. The positive hadrons give consistent results for proton and deuteron, the deuteron data from negative hadrons are significantly below the proton data, and for both targets the negative hadron results are above the positive hadrons results in the region $1 < p_T < 1.8$ GeV. The deviations are mostly on a 1 to 2 σ level. Even when regarding the large systematic errors, the inconsistencies remain, as most of them are correlated between bins, charges and targets (cf. tables D.34 to D.37). The results obtained from combining either the charges or the targets are plotted in figures 5.40 and 5.41, respectively, as a function of p_T. For the combined data on proton and deuteron the error weighted mean has been evaluated. The largest weight (75%) lies on the deuteron data. For the combined statistical error the errors due to the data (i.e., the part proportional to $\delta^2 A_{\parallel}$) have been treated as independent errors, while the errors arising from the MC statistics (about 5 to 10% of the total statistical error of $\frac{\Delta G}{G}$) have been calculated using a correlation $\rho = 0.4$ taking into account that 40% of the MC statistics are common to the proton and deuteron MC data. An interesting feature in figure 5.40 is that apparently parts of the model uncertainties cancel in the charge average.

In section 5.4.1 it was argued that a part of the inconsistencies may come from a wrongly modeled fragmentation. It was also shown that, if this is true, most likely it is the result from the negative hadrons, in particular from proton, that is overestimated (cf. figure 5.31). One can therefore imagine that the 'truth' to be found out once a more adequate model for the fragmentation would be implemented into the MC, lies somewhere *in between* the positive and negative hadron results from proton. The deuteron results on negative hadrons are also in between these two extremes, owing to the partial cancellations of residual effects of quarks in the combination of proton and neutron. Therefore the spread of the individual results seen in figure 5.37 can be considered

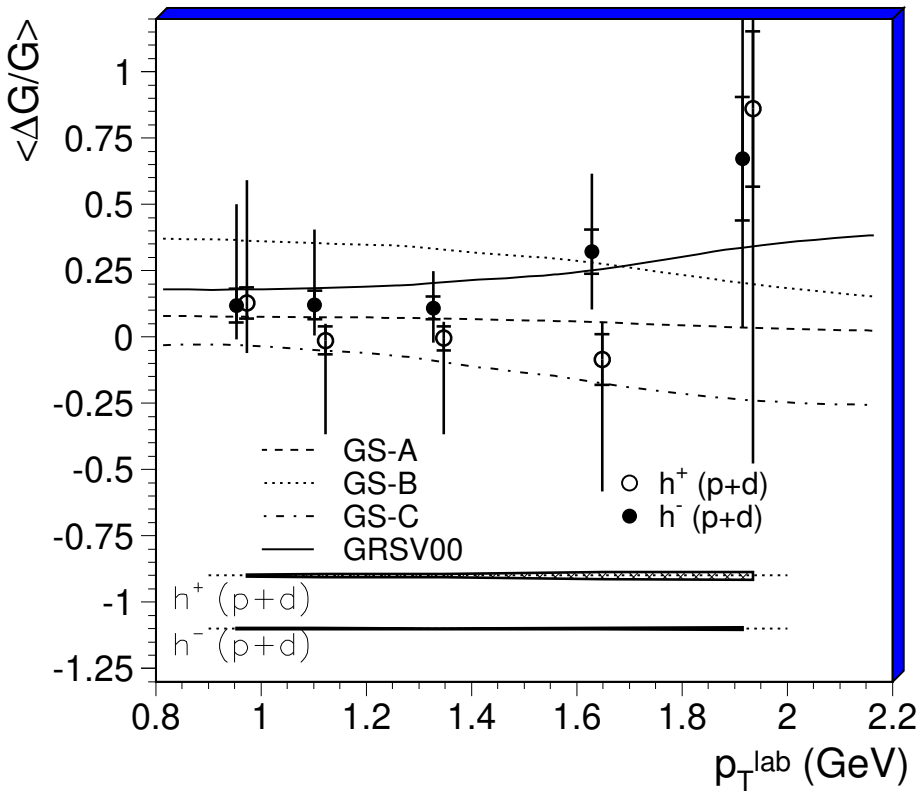

Figure 5.40: Extracted values for $\frac{\Delta G}{G}$ as a function of p_T for positive hadrons (open circles) and negative hadrons (filled circles) from proton and deuteron combined. The model uncertainty is added linearly on top of the statistical error bars, separated from it with a horizontal tick mark. The shaded bands show the (asymmetric) experimental systematic uncertainties for each combined data set.

as an otherwise not quantifiable systematic uncertainty, modulo the influence of the statistical fluctuations. In the combinations of charges and/or targets, some of the residual effects might cancel. For the combinations of figures 5.40 and 5.41 the corresponding t values are shown in figure 5.42. As can be seen from there, the incompatibility of the charges remains for the combination of proton and deuteron data, whereas for the combination of all charges the agreement gets better.

In a last step, all data can be combined. Again, the final values are determined by the deuteron data due to their overwhelming statistical weight. The result is shown in figure 5.43, with a similar layout than that of figure 5.37. The average gluon momentum fraction is shown separately on the three x axes for each of the three considered PYTHIA sets. The $\hat{Q}^2$ scale ranges (model dependent) between 0.6 GeV^2 for the lowest and 2 GeV^2 for the highest p_T bin. The final results on the values and errors are given in table D.38. In general, the extracted values are small. Taking the combined result at face value, a preference towards the Gluon-A scenario of Ref. [Geh96] can be observed. When comparing to any of the theoretical models it should be remembered, though, that the curves have to be associated with potentially large statistical errors. An estimate of the statistical error on the helicity density $\Delta G(x)$ at NLO is given by the shaded area in figure 2.10, the corresponding error on the unpolarized distribution $G(x)$ can be seen from figure 2.9. It is of course not possible to determine from these two figures how both statistical errors would propagate into the ratio $\frac{\Delta G}{G}$, because they can be partially correlated.

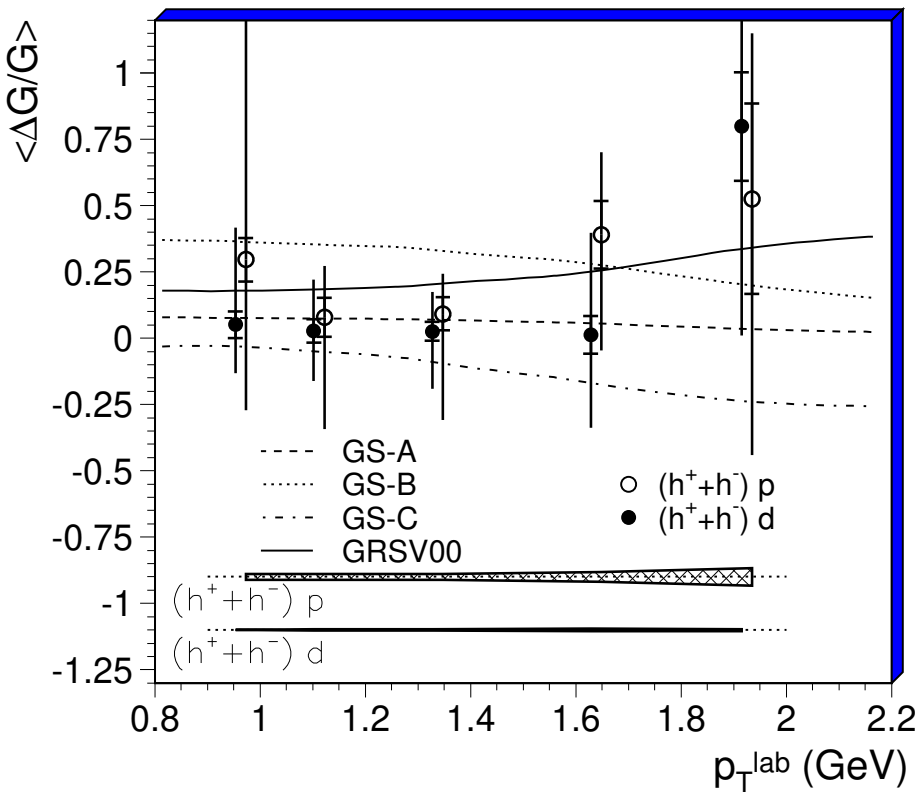

Figure 5.41: Extracted values for $\frac{\Delta G}{G}$ as a function of p_T for charged hadrons from proton (open circles) and deuteron (filled circles). The model uncertainty is added linearly on top of the statistical error bars, separated from it with a horizontal tick mark. The shaded bands show the (asymmetric) experimental systematic uncertainties for each combined data set.

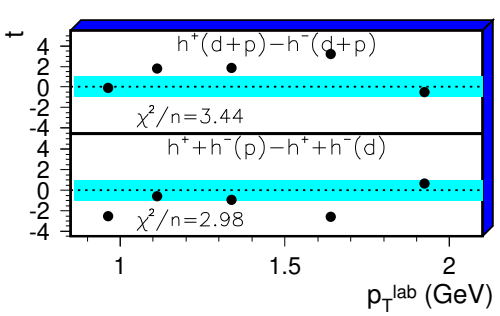

Figure 5.42: t values for $\frac{\Delta G}{G}$ for the combined proton and deuteron data on h^+ vs. h^- and for the charge average of hadrons from proton vs. deuteron.

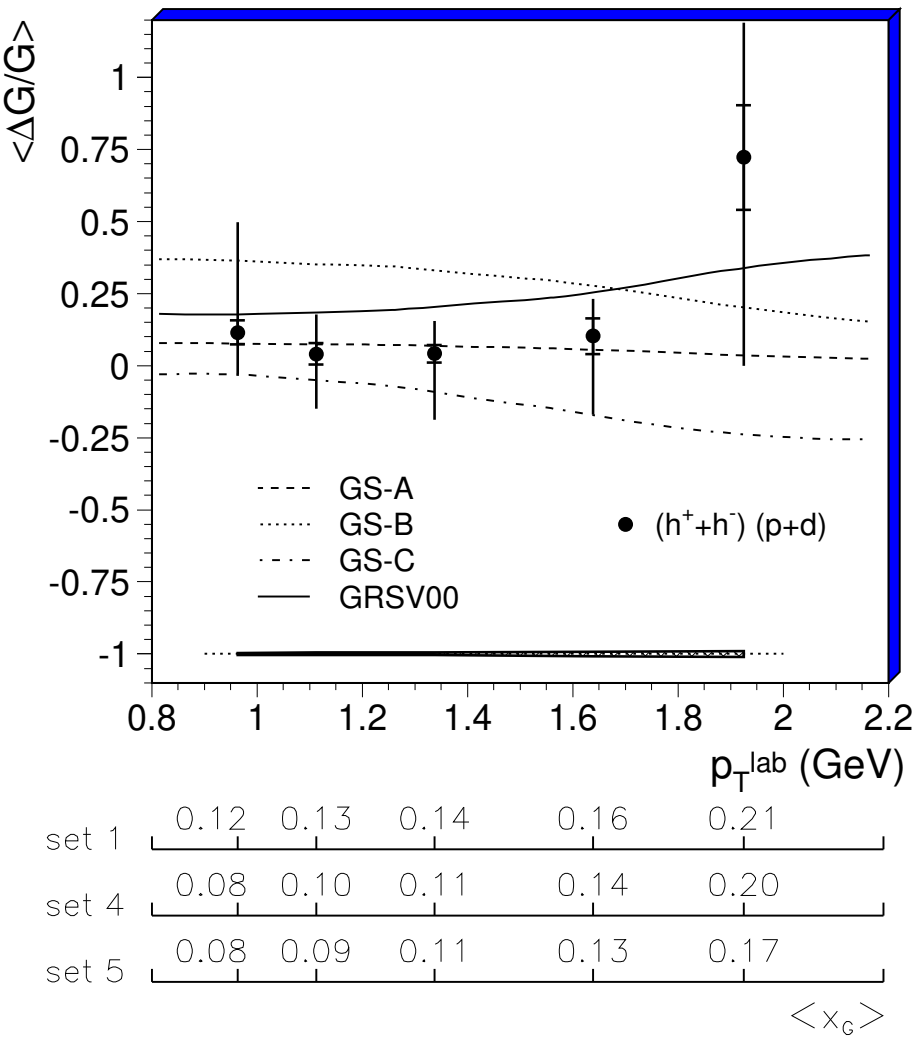

Figure 5.43: Extracted values for $\frac{\Delta G}{G}$ for the combined data on charged hadrons from proton and deuteron as a function of p_T. The model uncertainty is added linearly on top of the statistical error bars, separated with a horizontal tick mark. The shaded bands show the (asymmetric) experimental systematic uncertainties for each data set.

5.5.2 Integrated Values for $\frac{\Delta G}{G}$

Although the sensitivity to the Photon-Gluon Fusion process is just as large as in the 'Photoproduction' region, in the 'Transition' region it is not possible to study the p_T dependence of $\frac{\Delta G}{G}$. This is due to the large statistical error bars arising from a factor of two smaller yield in the data, and from the smaller magnitude of the PGF subprocess asymmetry (cf. section 5.1.2). Integrated values for the range $1 < p_T < 2$ GeV have been studied in section 5.3. Those studies are summarized here, giving a final value obtained from standard PYTHIA set #1 and the model uncertainties calculated in a similar manner as in the previous section for the 'Photoproduction' data. Different from the 'Photoproduction' region, the (small) error arising from setting $A_1^{diffr} \approx 2A_1^{exp}$ is taken into account, and for the uncertainty in the PYTHIA model parameters only the difference between set #4 and set #1 is regarded as an error (cf. section 5.3.2). Only the combined charged hadron data from deuteron are considered because of the uncertainty arising from the nonstatistical discrepancies between top and bottom asymmetries of negative pions in 1997 (see section 3.3.4 and figure 5.19). For comparison, the integrated result from the 'Photoproduction' region from proton and deuteron data will also be shown. The range will be $1.35 < p_T < 2.5$ GeV, corresponding to approximately the same average x_G as in the 'Transition' region for $1 < p_T < 2$ GeV. Figure 5.44 shows the two integrated points at their average x_G together with four theoretical curves as a function of x_G. The curves are from the same PDF sets as used in the previous section. The

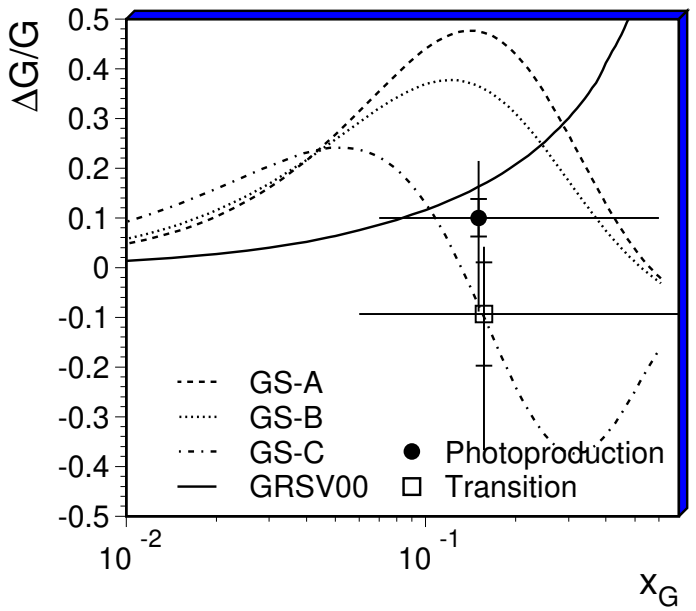

Figure 5.44: Extracted values for $\frac{\Delta G}{G}$ integrated over p_T for the 'Transition' and 'Photoproduction' regions vs. x_G. The points are plotted on their average x_G, the (LO) curves are plotted as a function of x_G at a scale $\hat{Q}^2 = 1.5$ GeV^2. The theoretical and model uncertainty is added together with the experimental systematic error linearly on top of the statistical error bars, separated with a horizontal tick mark.

horizontal error bars in this figure mark the range in x_G covered by the data. Regarding only the statistical errors, the deviation between the two points is approximately 1.8 σ. Within their experimental and model systematic errors, however, they are compatible, although it should be noted that also for the integrated results they are partially correlated. The deviations due to the choice of PDFs for instance often point into the same direction for both kinematic regions. As the experimental systematic error is mostly a normalization error, this error is almost 100% correlated between the two data sets. Compared to the model uncertainty, the experimental systematics are negligible, though. The correlations can be taken from table D.33 where the integrated values on

$\frac{\Delta G}{G}$ are given together with the total statistical and systematic errors and the individual sources of the model uncertainty. The result from the 'Photoproduction' region is

$$\frac{\Delta G}{G}\Big|^{Photo}_{\langle x_G\rangle=0.15} = 0.10 \pm 0.04(\text{stat.}) \pm 0.01(\text{exp. syst.})^{+0.07}_{-0.14}(\text{model syst.}) \tag{5.25}$$

at an average gluon momentum fraction $\langle x_G\rangle \approx 0.15$ (measured in the range $0.07 < x_G < 0.6$) and scale $\hat{Q}^2 \approx 1.3$ GeV^2. The result from the 'Transition' region is

$$\frac{\Delta G}{G}\Big|^{semi}_{\langle x_G\rangle=0.16} = -0.09 \pm 0.10(\text{stat.}) \pm 0.01(\text{exp. syst.})^{+0.02}_{-0.16}(\text{model syst.}) \tag{5.26}$$

at an average gluon momentum fraction $\langle x_G\rangle \approx 0.16$ (measured in the range $0.06 < x_G < 0.65$) and scale $\hat{Q}^2 \approx 1.8$ GeV^2.

Summarizing the results of the last two sections it can be stated that the HERMES data, especially in the 'Photoproduction' region have a remarkable statistical power, leading to statistically significant results for the gluon polarization within a range of $0.06 < x_G < 0.6$, at an average of x_G between 0.1 and 0.2. However, large systematic uncertainties remain from the model and the assumptions used for the extraction, with the largest ones coming from the PYTHIA Monte Carlo. The PYTHIA model is at the moment the only available MC that can reproduce aspects of the data in the 'Photoproduction' region. Therefore the presented results should be viewed as the best possible ones that could be retrieved from the HERMES data. Eventually it remains to be checked how the results would change if a different Monte Carlo model were used, however, so far there exists none for the 'Photoproduction' data. For the statistically less important 'Transition' region, LEPTO could be used as an alternative. This analysis is performed at the moment in the context of another thesis.

Effort is also being put from the theory side into understanding the fragmentation mechanism at relatively small energies, and it can be hoped that in the future some of the theoretical issues discussed above may get solved, such that a reanalysis of the data could lead to more consistent results with smaller systematic errors. In the near future also data on $\frac{\Delta G}{G}$ are awaited from COMPASS and RHIC-Spin experiments (cf. section 2.7) which can provide more insight regarding the size and shape of $\frac{\Delta G}{G}$ in the nucleon.

Conclusions

The HERMES experiment has contributed a lot to the present knowledge of the quark helicity densities in the nucleon through precision measurements of spin dependent cross section asymmetries in inclusive and semi-inclusive deep inelastic scattering. The contribution of the spin of quarks to the nucleon spin has been measured so far by the former and present spin experiments. The result is that the largest fraction of the nucleon spin is not carried by quarks but shared among the spin of the gluons and the orbital angular momenta of quarks and gluons. The knowledge about the polarized gluon density is therefore an important piece of information towards the understanding of the dynamics of bound state quarks and gluons within the framework of Quantum Chromodynamics. The size of the quark helicity densities is by now relatively well established, such that this information can in turn be used to retrieve information about the gluon polarization from the data. This thesis was dedicated to a measurement of the helicity density of gluons inside the nucleon using data on spin dependent cross section asymmetries of single high-p_T hadrons taken with the HERMES experiment.

Asymmetries of charged high-p_T hadrons, identified pions and kaons were measured on proton and deuteron targets in two distinct kinematic regions, the 'Photoproduction' region and the semi-inclusive 'Transition' region. Both regions suffer from a large background to the process sensitive to the gluon helicity, the Photon-Gluon Fusion (PGF) process. As the energy range covered by HERMES is relatively low it is not possible to describe all contributing processes by perturbation theory. This introduces a large theoretical uncertainty on the determination of the size of the Photon-Gluon Fusion signal and its asymmetry. In the 'Photoproduction' region, a large contribution to the systematic uncertainty comes from the lack of knowledge about the polarization of partons in a resolved photon. In addition, the energy available at HERMES is not large enough that jets can be formed from the outgoing partons. It is also not possible to clearly separate the fragments of the target remnant from those of the interacting partons. A realistic model is therefore necessary to describe how the partons from the interaction and the spectator partons in the target remnant hadronize.

In this analysis, the extraction formalism applied is based on using one particular Monte Carlo model (PYTHIA 6.2) to obtain the information necessary about the signal to background ratio, the hard subprocess kinematics and the background asymmetry. In view of the relatively small sensitivity of the HERMES data to the PGF process of about 20% and the large influence of hadronization processes the application of Monte Carlo independent methods (e.g., fits to the data) appear not to be feasible. For the 'Photoproduction' region, no other MC is available so far that could cover as wide a range of possible subprocesses, especially nonperturbative ones, as PYTHIA. As an alternative to replacing the PYTHIA MC with a different one, the crucial parameters of the PYTHIA model were varied as much as it was feasible and seemed to make sense. The variation of the results on the gluon polarization $\frac{\Delta G}{G}$ with the PYTHIA parameters has been presented and discussed. In addition to the uncertainty about the model parameters, the ignorance about the spin dependence of soft and hard VMD, which especially in the 'Photoproduction' region constitute a non-negligible amount of the background, introduces inevitable uncertainties. An estimate about the possible size of these uncertainties could be obtained from comparing different 'extremes' for the parametrization of asymmetries arising from resolved photon processes. The kinematic constraints at HERMES energies also circumvent reaching out to a transverse momentum region that does not

only guarantee a small (factorization and renormalization) scale dependence of the result, but also a small sensitivity to the specific cutoffs used in the MC to retain numeric stability and prevent double counting of processes.

The main focus of this thesis was to optimize PYTHIA 6.2 for the description of the HERMES data. The optimization included a modification and tuning of the model to data on exclusive vector meson production and semi-inclusive cross sections and asymmetries. QED radiative effects that modify the observed cross section and kinematics were incorporated into the Monte Carlo. An excellent description of exclusive ρ^0 production cross sections was achieved, and good agreement between the data on semi-inclusive pion cross sections and Monte Carlo. The data in the 'Photoproduction' region are well described in terms of exclusive ρ^0 production cross sections, while the inclusive hadron and pion cross sections at medium and large p_T are underestimated by a factor two. Considerable progress was made during the course of this work towards the understanding of the HERMES data in terms of the contribution of different subprocesses. For instance, the fraction of events in the HERMES data from diffractive processes could be constrained to a large extent.

With the optimized Monte Carlo the fractions of the contributing subprocesses and the background asymmetry were determined. Both were used together with the measured asymmetries to extract a value for the average gluon polarization $\left\langle \frac{\Delta G}{G} \right\rangle$. It turned out that the extracted values depend on the data sample – positively or negatively charged hadrons, proton or deuteron target – they are extracted from. This means that the Monte Carlo, although tuned to match the HERMES data over a wide region, is not able to correctly simulate the mechanisms of high-p_T hadron production at HERMES energies. In the 'Photoproduction' region, where the cross sections themselves are severely underestimated by the Monte Carlo, it can be argued that some nonperturbative processes are missing in the model or that the scales involved are too small to make safe predictions on the cross sections of perturbative QCD processes. However, it has been shown that the values extracted for $\left\langle \frac{\Delta G}{G} \right\rangle$ are sensitive to the hadronization mechanism, and that a wrong or incomplete model for the fragmentation process results in a bad description of the correlations between the detected hadrons and the struck quarks they originated from and whose polarization the measured asymmetries are sensitive to. As long as the knowledge about the fragmentation mechanism is poor, as it may be especially in the case of small energies as for HERMES, it might not be feasible to assign those correlations to hadrons with the necessary amount of confidence to extract a 'firm' result on the gluon polarization. HERMES data on pion, kaon and proton multiplicities can potentially help in constraining the fragmentation mechanism further and improve the model.

Besides the problems associated with PYTHIA and the fragmentation model themselves, the systematic errors arising from uncertainties in the model parameters, the parton distributions and the modeling of the subprocess asymmetries are large. However, some of the systematic uncertainties cancel in the combination of charges and targets, and it was argued that the differences between the results from independent data samples can be viewed as an additional systematic uncertainty. The statistics of the data in the 'Photoproduction' region are so large, though, that it may eventually be possible to study the x dependence of the gluon polarization via its p_T dependence, using the kinematic correlations between p_T and x_G. The experimental systematic uncertainty is very small in both kinematic regions.

The gluon polarization has been determined as a function of p_T for $0.9 < p_T < 2.5$ GeV in the 'Photoproduction' region. It was found to be compatible with predictions from models for polarized PDFs using fits to inclusive data. For the first time, in this thesis a (partial) estimate of the model uncertainty could be achieved. The integrated results from both the 'Photoproduction' and the semi-inclusive regions are compatible within the combined statistical model uncertainties.

Acknowledgments

First I would like to thank my family, especially my parents, for their love and support throughout ... years.

I am indebted to my group leader Dr. Wolf-Dieter Nowak who gave me the opportunity to work with the HERMES Zeuthen group in Hamburg and to accomplish this thesis. He has always been helpful in organizational matters and was a careful proofreader in the final stage of writing. I also owe thanks to Prof. Dr. Rolf-Dieter Heuer who has taken over the role of my official 'Doktorvater' at the Hamburg University. I appreciate him taking care of all the formalities, for his support and his impatience towards me to finish my thesis.

I am most grateful to Elke-Caroline Aschenauer who has always been there when things got stuck, and who always had a minute to spare even though she was loaded with work for the experiment. We spent nights together fighting with the Monte Carlo (and sometimes with each other). Thanks for all the discussions and advice, thanks for all the help in debugging codes and cross checking results, and thanks for being a friend.

Knowing that it is not possible to name everyone I would like to thank all recent and former members of the HERMES collaboration for their tremendous efforts in running the experiment and providing the data for this analysis. For the risk of incompleteness, I would especially like to thank Antje Brüll, Naomi Makins, Marc Beckmann, Matthias Hartig, Larry Felawka, Maurice Bouwhuis, Michael Tytgat, Jim Stewart, Uta Stösslein, Katarina Lipka, Anton Jgoun and Vanessa Mexner for fruitful discussions, advice and assistance – my apologies to everyone I might have forgotten. Special thanks to Frank Ellinghaus for having to share the office with me, and for helping out so many times with PAW, Latex and other tools for solving problems that without them would not exist.

The quality of this thesis was considerably improved through the input from theorists, first of all from Torbjorn Sjöstrand who spent days with us to listen to our problems with the Monte Carlo and who gave invaluable hints for the tuning. There was not one question about PYTHIA we asked left unanswered. Other people who contributed with discussions and professional advice were Andreas Schäfer, Hannes Jung, Barbara Badelek, Stefan Kretzer, Werner Vogelsang, Andrey Vinnikov, Andrei Afanasev and Nikolai Kochelev.

Last but not least I thank the offsite crew in Hamburg for a fun time together.

Appendix A

Trigger Efficiencies

A.1 Trigger Logic

A variety of triggers is used at HERMES to extract information for physics analyses and calibration and monitoring purposes. The trigger logic is summarized in table A.1 where the subscript $T(B)$ refers to the top (bottom) detector half. The symbol 'CA' means the requirement of an energy deposit of 1.4 (3.5) GeV (cf. section 1.3.4) in two adjacent columns of blocks in the calorimeter. All triggers have to be generated within some time window corresponding to the passage of a HERA positron bunch through the interaction point (HERA clock). The exact requirements on the hit

Trigger (Year)	Logic
17 (1996/97)	$(H0 \cdot H1 \cdot H2)_T + (H0 \cdot H1 \cdot H2)_B$
18 (1996/97)	$(H1 \cdot H2 \cdot CA)_T + (H1 \cdot H2 \cdot CA)_B$
18 (2000)	$(H1 \cdot H2 \cdot CA \cdot MC)_T + (H1 \cdot H2 \cdot CA \cdot MC)_B$
19 (1996/97)	$(H0 \cdot H1 \cdot CA)_T + (H0 \cdot H1 \cdot CA)_B$
19 (2000)	$(H0 \cdot H2 \cdot CA \cdot MC)_T + (H0 \cdot H2 \cdot CA \cdot MC)_B$
20 (1996/97)	$(H0 \cdot H2 \cdot CA)_T + (H0 \cdot H2 \cdot CA)_B$
20 (2000)	$(H0 \cdot H1 \cdot CA \cdot MC)_T + (H0 \cdot H1 \cdot CA \cdot MC)_B$
21	$(H0 \cdot H1 \cdot H2 \cdot CA)_T + (H0 \cdot H1 \cdot H2 \cdot CA)_B$
24 (1997)	$Tr21 \& Tr5 \rightarrow (H0 \cdot H1 \cdot H2 \cdot CA)_T$
24 (2000)	$(H0 \cdot H1 \cdot H2 \cdot CA)_T$
25 (1997)	$Tr21 \& Tr4 \rightarrow (H0 \cdot H1 \cdot H2 \cdot CA)_B$
25 (2000)	$(H0 \cdot H1 \cdot H2 \cdot CA)_B$
22 (2000)	$(H0 \cdot H1 \cdot H2 \cdot MC)_T * (H0 \cdot H1 \cdot H2 \cdot MC)_B * (H0 \leq 8)$
28 (1996)	$(H0 \cdot H1 \cdot H2)_T * (H0 \cdot H1 \cdot H2)_B * ((2 \leq H0 \leq 8) \cdot (2 \leq H1) \cdot (2 \leq H2) \cdot (2 \leq BC))$
28 (1997/2000)	$(H0 \cdot H1 \cdot H2 \cdot BC)_T * (H0 \cdot H1 \cdot H2 \cdot BC)_B * (H0 \leq 8)$

Table A.1: Trigger logic for the main physics and calibration triggers for the years 1996/1997 and 2000. The '$*(\cdot)$' and '$+$' signs stand for logical 'AND' and 'OR'.

multiplicities of the BCs and H0 changed since the implementation of trigger 28 in 1996, resulting in different efficiencies for each setup. The efficiencies of triggers 21 and 22/28 for a particular class of events (photoproduction or DIS events) can be calculated from the efficiencies of the detector components taking part in the trigger. These can be retrieved from the count rates of the calibration triggers 18, 19 and 20 in combination with those of trigger 21. For instance, for 2000 one gets the efficiencies:

$$\epsilon(H0) = \frac{N_{18\&21}}{N_{18}}, \quad \epsilon(H1) = \frac{N_{19\&21}}{N_{19}}, \quad \epsilon(H2) = \frac{N_{20\&21}}{N_{20}}. \tag{A.1}$$

For the calorimeter efficiency no separate calibration trigger exists. In principle this would have been trigger 17 as it was defined in 1997, however, the rates were extraordinary high such that events that fired *only* trigger 17 were disregarded already by the track reconstruction program. The calorimeter efficiency can instead be extracted from events with trigger 28 (or 22):

$$\epsilon(CA) = \frac{N_{28\&21}}{N_{28}}, \tag{A.2}$$

but here care has to be taken since the event topologies for trigger 28 and trigger 21 are very different such that the efficiency may be biased. The signature for a trigger 28 event would be at least one track in the top *and* bottom half of the detector. For a trigger 21 *in coincidence* with trigger 28 only either of the tracks had to produce a trigger signal for trigger 21. Given the calorimeter efficiency, the total efficiency of trigger 21 can be calculated as:

$$\epsilon(T21) = \epsilon(H0) \cdot \epsilon(H1) \cdot \epsilon(H2) \cdot \epsilon(CA). \tag{A.3}$$

The efficiency for trigger 28 (22) becomes:

$$\epsilon(T28) = (\epsilon(H0)_T \epsilon(H0)_B) \cdot (\epsilon(H1)_T \epsilon(H1)_B) \cdot (\epsilon(H2)_T \epsilon(H2)_B) \cdot \epsilon(H0mult \cdot BC(MC))_{TB}. \tag{A.4}$$

The efficiency for the specific hit multiplicity in the H0 and topology of hits in the BCs or MCs $\epsilon(H0mult \cdot BC(MC))_{TB}$ can only be calculated for the top-bottom combination using coincidences with trigger 21:

$$\epsilon(H0mult \cdot BC(MC))_{TB} = \frac{N_{21\&28}}{N_{21}}. \tag{A.5}$$

In about 50% of the events coming from a trigger 21 a track reconstructed in one half is accompanied by a trigger 21 coincidence signal in the other half, and often this coincidence signal does not correspond to a reconstructed track. In such a case the trigger 21 signal is associated *accidentally* with the reconstructed track, and the fraction of events where this happens depends on the track momentum, event topology and background conditions. If the purpose of the calculation is to check the performance of the detector/trigger system it might be necessary to select a less biased data sample. This can be achieved by requiring event properties close to the trigger requirements in use. The triggers 24 and 25 carry the information about in which detector half the trigger 21 signal was generated. The trigger 21 efficiency for the top (bottom) detector can then be calculated by replacing trigger 21 with triggers 24 (25) in Eqs. A.1 and A.2. For the calorimeter efficiency only events should be counted with reconstructed tracks in the top and bottom of the detector. The results would come out even cleaner if for the hodoscope efficiencies only events with *exactly* one track in the required detector half and no track in the other half were regarded. This does not exclude the possibility that hits from unreconstructed particles in the other half could fire a trigger as well, though.

A.2 Time Dependence of Trigger Efficiencies

The time dependent trigger efficiencies shown below were calculated for each run (and then averaged over a fill). The loss of statistics would be too large if the selection of events would be restricted to the exact event topology suitable for this trigger. For the calorimeter efficiency it was required that there is at least one track in the top and bottom half. In addition, for the positron efficiency the energy deposit of the positrons in the calorimeter should be above the trigger 21 threshold. This cut is not necessarily to be applied for hadron efficiencies, since for hadrons the energy deposit is not as clearly correlated to the momentum. Hadron efficiencies calculated with this method are shown in figure 3.2 in section 3.1.3. For completeness, the hadron efficiencies for the 1997 data (about 75% of all polarized proton data) are shown here in figure A.1. In comparison to the 2000 data, the trigger 21 efficiency for hadrons is about 10% smaller in 1997. Positron efficiencies of trigger 21 for both 1997 and 2000 are shown in the top panels of figure A.2. The middle and bottom panels show the

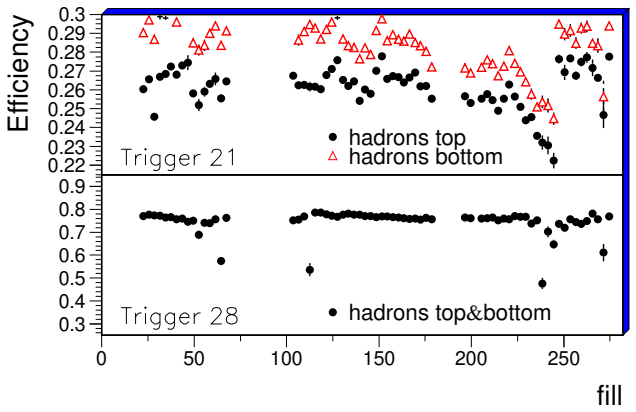

Figure A.1: Trigger efficiencies for hadrons during polarized data taking in 1997 as a function of the fill number. In the top panel, the trigger 21 efficiencies are shown for top and bottom separately, in the bottom panel the trigger 28 efficiency is shown for events with at least one hadron in each of the top and bottom halves.

calorimeter and H0 efficiencies for positrons, respectively. These two efficiencies are the ones which are contributing most to the total trigger 21 efficiencies, the other two hodoscope show a stable efficiency very close to one. The positron efficiencies seem to be less dependent on the calorimeter

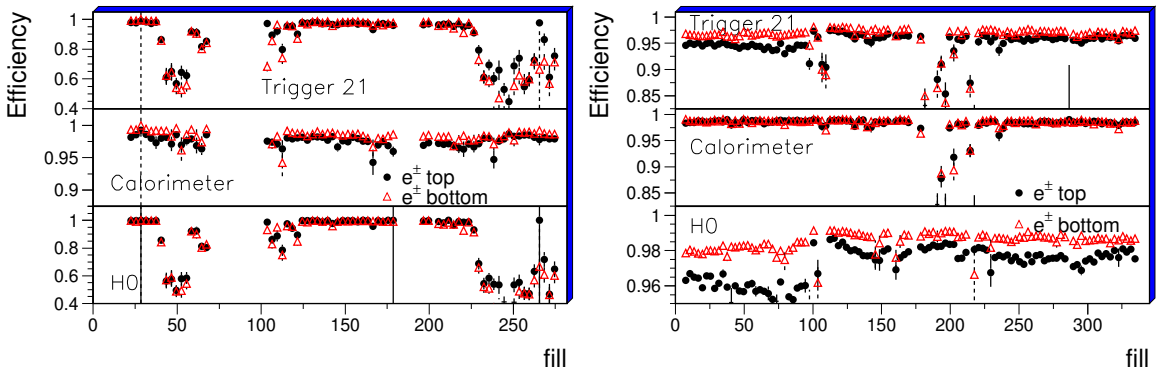

Figure A.2: 1997 (left) and 2000 (right) positron efficiencies for trigger 21 during polarized data taking. The top panels show the total efficiency of trigger 21, the middle panels show the contribution of the calorimeter and the bottom panels show the H0 efficiency.

performance than the hadron efficiencies. In fact the trigger 21 efficiency is here is dominated by the H0. The large drops of the H0 efficiency in 1997 were caused by double pulsing problems. The yields at the same time (cf. figure 3.1) are not affected to this extent by this problem. In 2000, the calorimeter efficiency drops by approximately 20-25% in the region of fills 175 to 190 where the trigger 28 was prescaled (cf. section 3.1.3). That this is just an artifact of the trigger 21/trigger 28 combination used to calculate the efficiency can be seen from the positron yields in figure 3.1 which do not show such a large decrease during that time.

A.3 Trigger Efficiencies for Cross Sections

For the analysis of cross sections it might be necessary to know the trigger efficiencies for a certain type of events, and eventually to correct the observed cross section for inefficiencies. As there is no clear-cut way to exclude accidental hits which could fire a trigger, it is necessary to define event topologies for which the trigger efficiencies are going to be calculated. If those trigger efficiencies are then used to, e.g., correct a measured cross section, care has to be taken that the topologies of the to-be-corrected events are exactly the same as the ones used to derive the efficiencies. For this thesis, mainly three classes of events are of interest:

1. Inclusive and semi-inclusive DIS events. The trigger efficiency of this type of events is dominated by the probability of the scattered positron to generate a trigger 21 signal, if the

positron energy is above the calorimeter threshold for trigger 21. In 80% of the DIS events the produced hadrons escape the acceptance of the detector, and the event consists of only one positron track. In about 85% of the semi-inclusive events the hadron(s) are detected in the detector half opposite to that where the positron was scattered. For such events it is possible that a trigger 28 was generated as well. In general, the probability to fire any of the triggers 21, 22 or 28 is higher if more tracks are in the event.

2. Inclusive photoproduction events. These events are usually characterized by one or more hadron tracks. 50% of the events have only one track, in 60% of events with two or more tracks there is at least one track in each half. The generated triggers are a mixture of trigger 21 and 28 (22).

3. 'Exclusive' photoproduction of $\pi^+\pi^-$. For these events *exclusively* one positive and one negative hadron are required. 82% out of these are top-bottom events, such that the sample should be dominated by triggers 28 (and 22).

For simplicity, only the efficiencies of triggers 21, 22 and 28 were considered, thereby disregarding about 3% of the photoproduction events selected mostly by triggers 19 and 20. The following topologies were found to accommodate a large fraction of the events under consideration:

- DIS-events:

  1. Events with exactly one positron or electron track in one detector half and exactly one other track in the opposite half,
  2. Events with one positron or electron track in one detector half and (at least) one other track in the opposite half.
  3. Events with (at least) one positron or electron track,
  4. Events with exactly one track positron or electron track,

  The first two topologies describe most of the semi-inclusive events, the last two are considered for systematic studies. The difference between the first and the second event type is that in the second case there can be additional hadron tracks in the same detector half and more than one track in the other half of the detector.

- Photoproduction events (antitagging of leptons):

  1. Events with exactly one hadron track
  2. Events with exactly one hadron track in one detector half and exactly one hadron track in the opposite half,
  3. Events with exactly two hadron tracks in one detector half
  4. Events with one hadron track
  5. Events with one hadron track in one detector half and one hadron track in the opposite half,
  6. Events with two hadron tracks in one detector half

  The difference between the first and the last three topologies is that for the latter it is allowed that short tracks (particles deflected in the magnet at too large angles to make it to the beck part of the spectrometer) or tracks that do not meet the fiducial volume cuts are allowed to be in the event. These tracks are not counted for the trigger efficiencies, though. The first set of (three) topologies is used for the $\pi^+\pi^-$ pair analysis, the others for the inclusive analysis.

Trigger efficiencies are calculated for each year, separately for the running with polarized gas (calorimeter threshold 1.4 GeV) and for the running with unpolarized gas, where in addition to the higher calorimeter threshold (3.5 GeV) usually the triggers 22 and 28 were prescaled by large factors. The efficiencies are obtained as a function of track momentum, for the one track topology in 1 GeV bins from 0 to 28 GeV, for the two track topology in a 28×28 matrix for the momenta of each track. Except for the top/bottom separation (by requiring either trigger 24 or 25 for the track in the corresponding detector half) no spatial dependence was regarded. The calorimeter efficiency was calculated from two track top-bottom events. It can be directly applied to get the trigger 21 efficiency for the top-bottom topology by multiplying each element of the matrix of hodoscope efficiencies with the corresponding element of the calorimeter efficiency:

$$\epsilon(21)_{T_iB_j} = \{\epsilon(H0) \cdot \epsilon(H1) \cdot \epsilon(H2)\}_{T_iB_j} \{\epsilon(CA)\}_{T_iB_j} . \tag{A.6}$$

For one track events the vector of the hodoscope efficiencies is multiplied with the sum of the rows (columns) of the calorimeter efficiency matrix for bottom (top) tracks.

$$\epsilon(21)_{T_i(B_j)} = \{\epsilon(H0) \cdot \epsilon(H1) \cdot \epsilon(H2)\}_{T_i(B_j)} \frac{\sum_{j(i)} \{N_{28\&21}\}_{T_iB_j}}{\sum_{j(i)} \{N_{28}\}_{T_iB_j}}. \tag{A.7}$$

The hodoscope efficiencies for events with two tracks in one half can be calculated straightforward in a two dimensional matrix of the two momenta. For the calorimeter efficiency it would be necessary to count events with two tracks in one and one track in the other half. The available statistics are small, though. Alternatively the one track calorimeter efficiencies as in Eq. A.7 can be used:

$$\begin{aligned} \epsilon(21)_{T_iT_j} \;=\; & \{\epsilon(H0) \cdot \epsilon(H1) \cdot \epsilon(H2)\}_{T_iT_j} \cdot \\ & \left\{\epsilon(CA)_{T_i}\epsilon(CA)_{T_j} + \epsilon(CA)_{T_i}\left(1-\epsilon(CA)_{T_j}\right) + \left(1-\epsilon(CA)_{T_i}\right)\epsilon(CA)_{T_j}\right\}, \end{aligned} \tag{A.8}$$

where the probabilities are taken into account that either or both of the two tracks generate the calorimeter signal. In figure A.3 examples of the trigger 21 efficiency of the top detector half in 2000 are presented for positrons. The open triangles show the efficiency for 'exclusive' DIS events

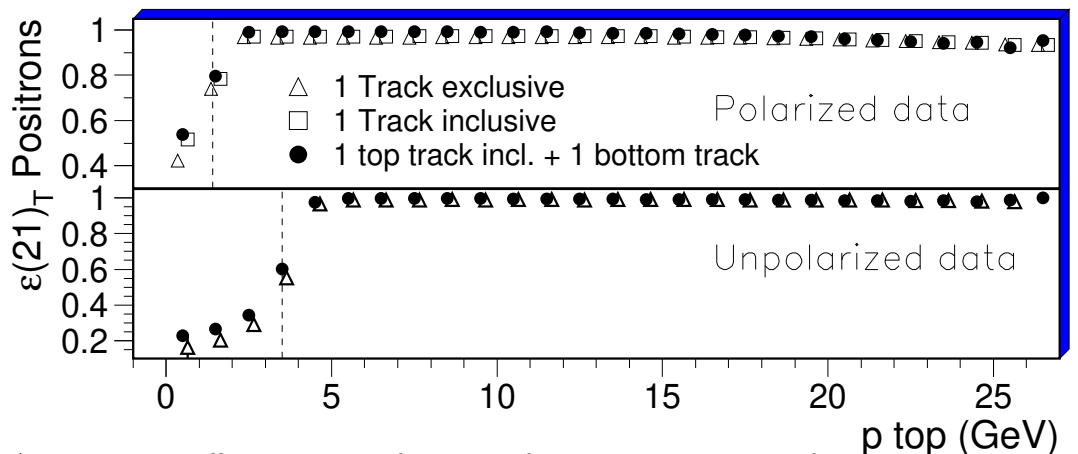

Figure A.3: Positron efficiencies as a function of positron momentum for the top detector in 2000. The symbols are explained in the text. The top plot is for data taken with polarized deuterium, the bottom plot is for data taken with unpolarized hydrogen. The vertical lines indicate the calorimeter thresholds at 1.4 and 3.5 GeV.

(configuration 4.)), i.e., for events with exactly one positron in the top detector and no additional (reconstructed) track. The open squares are for 'inclusive' events with one positron track in the top, but this time without any requirement on the absence of other tracks (configuration 3.)). The closed circles finally represent the efficiency for 'inclusive' top-bottom events, i.e., one positron is

detected in the top and at least one other track in the bottom (configuration 2.)). The top plot is for polarized deuterium data, the bottom plot for unpolarized hydrogen data, most of which were taken during the high density end-of-fill running. The effect of the higher calorimeter threshold during unpolarized data taking can be clearly seen in the comparison of the top and bottom plots. The difference between the various configurations is apparent mainly below the threshold. The top-bottom configuration 2.) is slightly above the other two for momenta up to $\simeq 17$ GeV.

Examples of trigger 21 efficiencies for photoproduction events are shown in figure A.4. There the open triangles show the efficiency for events with one hadron in the top and bottom

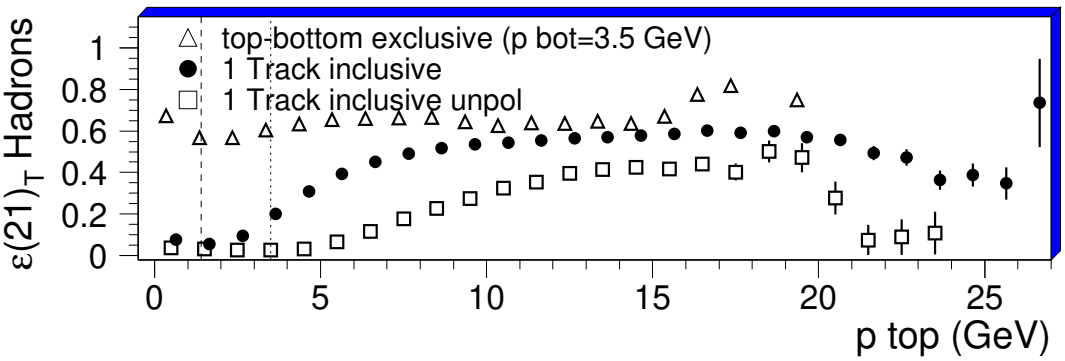

Figure A.4: Hadron efficiencies as a function of hadron momentum for the polarized data in 1997, and the unpolarized hydrogen data in 2000. The symbols are explained in the text. The vertical lines indicate the calorimeter thresholds at 1.4 and 3.5 GeV.

each (the 'exclusive' configuration 2.)), where the momentum of the bottom track was restricted to $3 < p_{Bot} < 4$ GeV and the absence of any other reconstructed track is required. The filled circles are for 'inclusive' one track events with one hadron in the top (configuration 4.)). Both efficiencies are calculated for polarized data. For comparison the open circles show the efficiency of configuration 4.) for unpolarized data. The one track efficiencies are calculated with trigger 24 events, while the top-bottom efficiency is for trigger 21, i.e., at least one of triggers 24 and 25 had to be generated.

The trigger 28 efficiency is even more subtle to calculate. Eq. A.5 is in fact not accurate, as can be seen if the equation is written out using the trigger logic for events having generated a trigger 21 *as well as* a trigger 28 (the indices T_iB_j are omitted):

$$\epsilon(H0mult \cdot BC)^{21}_{TB} \rightarrow \frac{\epsilon(H0 \cdot H1 \cdot H2 \cdot CA)_T * \epsilon(H0 \cdot H1 \cdot H2 \cdot CA)_B * \epsilon(H0mult \cdot BC)_{TB}}{\epsilon(H0 \cdot H1 \cdot H2 \cdot CA)_T + \epsilon(H0 \cdot H1 \cdot H2 \cdot CA)_B}. \tag{A.9}$$

It is clear that the combined hodoscope and calorimeter efficiencies in the numerator and in the denominator are not the same, such that they do not cancel. Instead the coincidences with trigger 24 and 25 can be used, and there are three possibilities to combine these with trigger 28 to retrieve the BC/H0 hit multiplicity efficiency (the indices T_iB_j are omitted):

$$\frac{T28\&T24}{T24} \rightarrow \frac{\epsilon(H0 \cdot H1 \cdot H2 \cdot CA)_T * \epsilon(H0 \cdot H1 \cdot H2)_B * \epsilon(H0mult \cdot BC)_{TB}}{\epsilon(H0 \cdot H1 \cdot H2 \cdot CA)_T}, \tag{A.10}$$

$$\frac{T28\&T25}{T25} \rightarrow \frac{\epsilon(H0 \cdot H1 \cdot H2)_T * \epsilon(H0 \cdot H1 \cdot H2 \cdot CA)_B * \epsilon(H0mult \cdot BC)_{TB}}{\epsilon(H0 \cdot H1 \cdot H2 \cdot CA)_B}, \tag{A.11}$$

$$\frac{T28\&T24\&T25}{T24\&T25} \rightarrow \frac{\epsilon(H0 \cdot H1 \cdot H2 \cdot CA)_T * \epsilon(H0 \cdot H1 \cdot H2 \cdot CA)_B * \epsilon(H0mult \cdot BC)_{TB}}{\epsilon(H0 \cdot H1 \cdot H2 \cdot CA)_B * \epsilon(H0 \cdot H1 \cdot H2 \cdot CA)_B}. \tag{A.12}$$

The full trigger 28 efficiency can then be calculated from either of the three efficiencies:

$$\epsilon(28)_{T_iB_j} = \left\{\frac{T28\&T24}{T24}\right\}_{T_iB_j} \epsilon(H0\cdot H1\cdot H2)_{T_i} \quad \text{(A.13)}$$

$$= \left\{\frac{T28\&T25}{T25}\right\}_{T_iB_j} \epsilon(H0\cdot H1\cdot H2)_{B_j} \quad \text{(A.14)}$$

$$= \left\{\frac{T28\&T24\&T25}{T24\&T25}\right\}_{T_iB_j} \epsilon(H0\cdot H1\cdot H2)_{T_i}\,\epsilon(H0\cdot H1\cdot H2)_{B_j}. \quad \text{(A.15)}$$

Figure A.5 shows the two-dimensional efficiency of the combined top-bottom BC and H0 multiplicity signals for the 2000 polarized data obtained from Eq. A.12 as a function of the momenta of the top and bottom tracks. The efficiency of trigger 28 for 'inclusive' top-bottom events (configuration 5.)) is shown on the right as obtained from Eqs. A.13 (dashed line), A.14 (dotted line) and A.15 (solid line) as a function of the top track momentum with the bottom track momentum fixed to $3 < p < 4$ GeV. For the bulk of the data the efficiency of the BCs combined with the H0

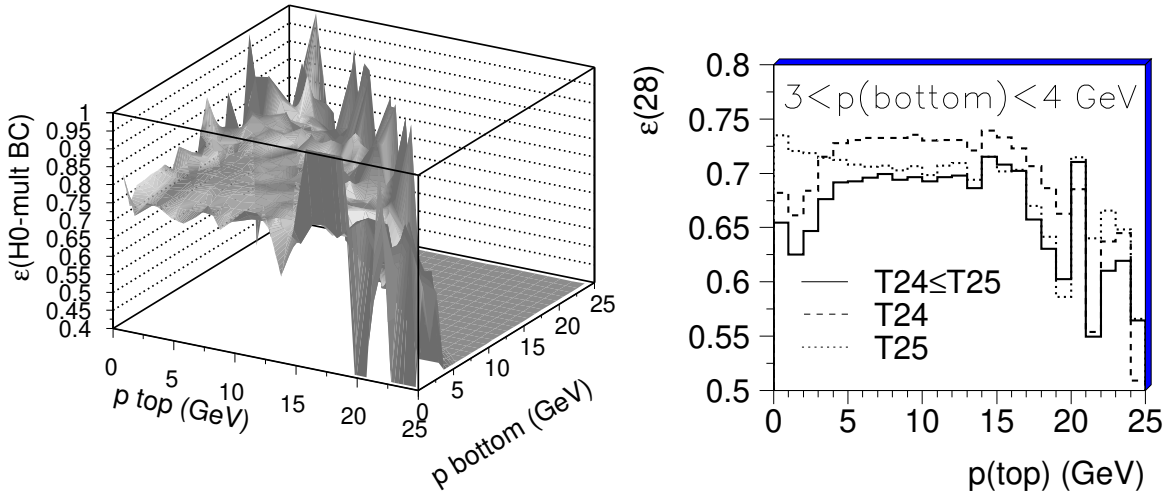

Figure A.5: Left: 2-dimensional efficiency $\epsilon(H0mult\cdot BC)$ as a function of the hadron momenta in the top and bottom half. Right: Total trigger 28 efficiency obtained with three different methods for events where the momentum of the hadron in the bottom half is fixed to $3 < p < 4$ GeV. See text for details.

multiplicity requirement is around 75%. Although mathematically Eqs. A.13, A.14 and A.15 are equivalent, there is an apparent discrepancy between all of them, with the largest difference between the efficiencies obtained with either one of triggers 24 or 25 and that obtained with both triggers. Furthermore, the shape of the latter efficiency looks as if it is the product of the two others. It was checked that the rates of the trigger combinations $T28\&T24$, $T28\&T25$ and $T28\&T24\&T25$ do not differ by much more than 2% which is what can be expected from the different hodoscope efficiencies going into these quantities (cf. Eqs. A.10, A.11 and A.12). The disagreement must then be due to the different hodoscope efficiencies applied to get the total efficiency as in Eqs. A.13, A.14 and A.15. It is not obvious why this is so. The hodoscope efficiencies to be multiplied are obtained from events where no track has been reconstructed in the respective other detector half, and no trigger 21 has been generated in that half (that means for instance that for the top efficiencies no trigger 25 was allowed). The hodoscope H0 in the front of the spectrometer magnet has the largest inefficiency of all hodoscopes. The efficiency of H0 can of course be artificially increased, if background particles produce hits in H0 in coincidence with a passing 'real' track. The background rate in the front region is known to be large, and different in top and bottom. In principle one can picture a situation where this artificial efficiency is different for one track events and events with

top *and* bottom tracks. This would mean that

$$\epsilon(H0_T \cdot H0_B) \neq \epsilon(H0_T) \cdot \epsilon(H0_B). \tag{A.16}$$

Correlated hits in the top and bottom hodoscopes could in principle lead to a behavior as seen in figure A.5. Also, top-bottom events are slightly less peaked at small θ_y (the slope of the particle momentum in the y direction) than one track events such that a *strong* spatial dependence of the hodoscope efficiencies could give different results for the different event classes. A spatial variation of the H0 efficiency has been observed in 2000 [DeN02], however it is unlikely that the variations are large enough to account for the observed effect. Also, the situation is similar for 1997 for which no such spatial dependence was reported. The problem cannot be solved for the moment, which is why the difference between $\frac{1}{2}(\epsilon(T28)_{T24} + \epsilon(T28)_{T25}) - \epsilon(T28)_{T24\&T25}$ has to be regarded as a systematic uncertainty.

The application of trigger efficiencies to correct cross sections is not unambiguous. In general it should be optimal to use trigger efficiencies derived using constraints as close to those of the data under consideration as possible. In this analysis this concerns mainly the cross section of inclusive photoproduction events and of exclusive $\pi^+\pi^-$ pair photoproduction. The data are weighted event by event with a factor $\frac{1}{\epsilon}$ according to their topology and their trigger configuration. Included are the topologies 1.) to 3.) for the $\pi^+\pi^-$ pair photoproduction, and 4.) to 6.) for inclusive events. In the latter case, three more topologies are allowed: Two hadrons in the top and one in the bottom half and vice versa, and two or more hadrons in each half. The probability of any of the four tracks to generate a trigger signal should be close to one, so that in the last case the efficiency is set to one. Events with one or two hadron tracks in the top (bottom) are required to have fired trigger 24 (25) but not trigger 25 (24). The correction factor is then directly $\frac{1}{\epsilon(24)}\left(\frac{1}{\epsilon(25)}\right)$. About 10% of these track events are rejected because, although only tracks in the top (bottom) have been reconstructed, instead of trigger 24 (25) trigger 25 (24) was generated. On the other hand, the efficiencies obtained for instance for one top track with trigger 24 are about 10% lower than the efficiencies obtained for the same events, but using trigger 21 (trigger 24 *or* trigger 25) instead. The reason are the accidental coincidences from unreconstructed tracks or background hits in the bottom mentioned above. In this case the factor $\frac{1}{\epsilon(24)} \approx 1.1\frac{1}{\epsilon(21)}$, thus 'retrieving' the rejected events. This example shows how important the compatibility of the trigger efficiencies with the event configurations is. For an accurate analysis of cross sections it may be necessary to apply different trigger efficiencies under different, but consistent requirements and compare the results.

There are two possibilities to handle events with configurations 2.) or 5.) (one hadron in the top and bottom halves each). One is to ask for a trigger 28 in the event and to weight this event with $\frac{1}{\epsilon(28)}$. In this case the uncertainty of the event weights is directly proportional to the uncertainty in the determination of the trigger 28 efficiency. To reduce this uncertainty the other possibility is to regard every event with at least one of triggers 24, 25, 28 (and/or 22) and weight it with the combined efficiency of all these triggers:

$$\begin{aligned}\epsilon(TB)_{ij}^{1996/97} = {} & \epsilon(24)_{T_i}\left(1-\epsilon(25)_{B_j}\right) + \epsilon(25)_{B_j}\left(1-\epsilon(24)_{T_i}\right) \\ & + \left(1-\epsilon(24)_{T_i}\right)\left(1-\epsilon(25)_{B_j}\right)\epsilon(28)_{T_iB_j}\end{aligned} \tag{A.17}$$

$$\begin{aligned}\epsilon(TB)_{ij}^{2000} = {} & \epsilon(24)_{T_i}\left(1-\epsilon(25)_{B_j}\right) + \epsilon(25)_{B_j}\left(1-\epsilon(24)_{T_i}\right) \\ & + \left(1-\epsilon(24)_{T_i}\right)\left(1-\epsilon(25)_{B_j}\right)\left[\epsilon(28)_{T_iB_j} + \epsilon(22)_{T_iB_j} - \epsilon(28)_{T_iB_j}\epsilon(22)_{T_iB_j}\right]\end{aligned} \tag{A.18}$$

These relations follow from the fact that the observed number of events can be expressed as a function of the probabilities to trigger an event and the 'true' number of photoproduction events, for instance for 1997 with only trigger 21 and trigger 28:

$$N_{TB}^{Obs} = \left[\epsilon(24,\overline{25},\overline{28}) + 24 \leftrightarrow 25 + \epsilon(24,25,\overline{28}) + \epsilon(24,\overline{25},28) + \cdots + \epsilon(\overline{24},\overline{25},28)\right] N_{TB}^{True} \tag{A.19}$$

For 2000 this equation has to be modified to take into account the additional probability that a trigger 22 was generated.

For events with two tracks in one half and one in the other half the probabilities are calculated for each possible 'basic' event topology. For instance, if the two tracks are in the top and one in the bottom half the possible configurations are: a two track top event, a one track bottom event and two top-bottom events combining either top hadron with the bottom hadron. The total efficiency of this event to fire a trigger is then obtained by permuting all possibilities that any of these configurations fired any of the triggers:

$$\begin{aligned}\epsilon^{1-Bot,2-Top} &= \epsilon_B^{1-track}(25)\epsilon_T^{2-track}(24)\epsilon_{TB}^{Top,1}\epsilon_{TB}^{Top,2} + \epsilon_B^{1-track}(25)\epsilon_T^{2-track}(24)\epsilon_{TB}^{Top,1}\left(1-\epsilon_{TB}^{Top,2}\right) \\ &\cdots + \epsilon_B^{1-track}(25)\epsilon_T^{2-track}(24)\left(1-\epsilon_{TB}^{Top,1}\right)\left(1-\epsilon_{TB}^{Top,2}\right) + \ldots \\ &\cdots + \left(1-\epsilon_B^{1-track}(25)\right)\left(1-\epsilon_T^{2-track}(24)\right)\left(1-\epsilon_{TB}^{Top,1}\right)\epsilon_{TB}^{Top,2}. \qquad \text{(A.20)}\end{aligned}$$

For inclusive photoproduction of (positive) hadrons, the resulting number of true events using all allowed configurations is displayed in figure A.6 compared to the number of observed events . The left plot shows the hadron counts, the right plot shows the ratio of true (corrected) to observed (uncorrected) hadron counts. At low momentum the correction factors are relatively large due to

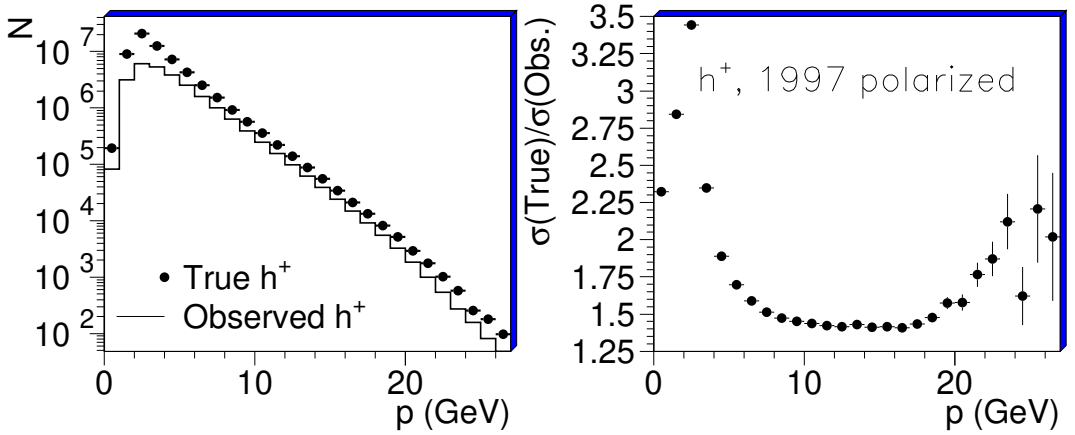

Figure A.6: Left: True (corrected for trigger efficiencies) and observed number of positive hadrons as a function of momentum for the 1997 polarized data. Right: Ratio of true to observed hadrons for the same case.

the small efficiency for one track events. There is also an increase of the correction factor at high momentum that is related to the fact that most high momentum hadrons are detected in one-track events where only triggers 24/25 can be generated. The impact of the efficiency correction on the mass distribution of 'exclusive' h^+h^- pairs can be seen in figure A.7. The mass distribution was plotted there for unclassified hadrons (no momentum cut) with the assumption of the hadron to be a pion. Again, the left plot shows the corrected and uncorrected yields, the right plot shows the ratios. The events obtained with the method of combining all possible triggers are represented by the closed circles, trigger 28 events only obtained using Eq. A.15 by the open triangles. At low masses, the weight factors are large because, due to the small opening angle between the two hadrons correlated to small masses, a large fraction of the events are events with the two hadrons in one half and can therefore only be selected by triggers 24 or 25. From $M_{\pi\pi} > 0.5$ GeV on most events are top-bottom events such that trigger 28 can be generated in addition. Since trigger 28 dominates in this region, also the discrepancy in the number of true events for the two different methods is largest there.

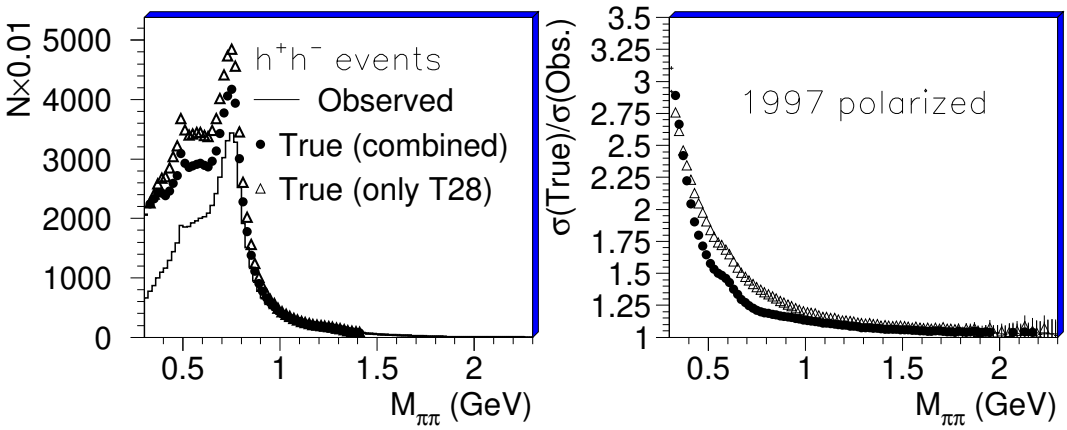

Figure A.7: Left: True (corrected for trigger efficiencies) and observed number of hadron pairs as a function of the invariant pion-pion mass for the 1997 polarized data. Right: Ratio of true to observed hadrons for the same case. see text for details.

Appendix B

Practical Implementation of QED Radiative Corrections into PYTHIA 6.2 using RADGEN 1.0

In this chapter the technical details of the RC implementation into the PYTHIA code within the HERMES Monte Carlo frame (GMC) are explained.

B.1 Radiative Corrections in gmc_DISNG

RADGEN was implemented into and tested extensively within the GMC framework for GMC_DISNG, a hybrid of LEPTO and an inclusive Monte Carlo generator. The general features of this code are described in section 4.1.2, here only the aspects relevant for the running with RADGEN will be considered. Its basic method of operation will be adopted for PYTHIA.

For a given set of kinematic observables (y, Q^2) resembling the measured kinematics of the outgoing positron, gmc_DISNG calls the RADGEN code. RADGEN then proceeds in the following way (in the following, the term $\sigma(y, Q^2)$ refers to a twofold differential inclusive cross section):

1.) It calculates the corrections to the Born cross section at the chosen (observed) kinematics, returning a factor

$$sig_{RadCor} = \frac{\sigma_{obs}(y, Q^2)}{\sigma_{Born}(y, Q^2)} \tag{B.1}$$

that will be applied to *each* event:

$$w_i^{RC} = \sigma_{Born}(y, Q^2) sig_{RadCor} \cdot W_y(\Delta y \Delta Q^2, f(y, Q^2)). \tag{B.2}$$

$\sigma_{obs}(y, Q^2)$ is computed by numerical integration using Eq. 4.19 and a parametrization of the structure functions used to obtain the Monte Carlo Born cross section. Here, also the *elastic ep* cross section has to be known.

2.) According to the contribution of the different parts to the total measured cross section (Eqs. 4.15, 4.16 and 4.18) RADGEN generates a real photon with energy $\omega > \Delta$ and angle θ_γ (or does not generate a photon at all) using Monte Carlo methods.

3.) If a real photon was accepted, RADGEN calculates the correct (true) virtual photon kinematics (y_T, Q_T^2).

4.) Finally the event is classified as non-radiative, inelastic or (quasi-) elastic.

Elastic events and inelastic events with $W_T^2 < 4$ GeV^2 (low–E events) are not proceeded further, however, the events are accepted and marked accordingly, the lepton kinematics and weights are stored for analysis of inclusive DIS data. Inelastic events with $W_T^2 > 4$ GeV^2 are handed over to LEPTO (PEPSI) with the information about the *true* kinematics to generate the flavor of the struck quark, QCD effects and the hadronic final state. For an inclusive sample on generator level within 4π geometry, the resulting cross sections and correction factors $\sigma_{RC}/\sigma_{Born}$ are shown in figure B.1 for $0.15 < y < 0.95$, $W^2 > 4$ GeV^2 and $Q^2 > 0.1$ GeV^2 as a function of the observed $y = \nu/E_B$. In the left panel, the absolute observed cross sections are compared to the Born cross section (dotted line). The solid line represents the full cross section, including the contribution from elastic *ep* scattering and low–E events. The dashed line contains the contribution from events with $W_T^2 > 4$ GeV^2 only. This is the part of the cross section with a potentially detectable semi-inclusive final state. As can be seen from this plot, the major part of the RC comes from the elastic and low W_T^2 events which are absent in samples with a generated hadronic final state ($W_T^2 > 4$ GeV^2). In this case, the corrections are about 10% only.

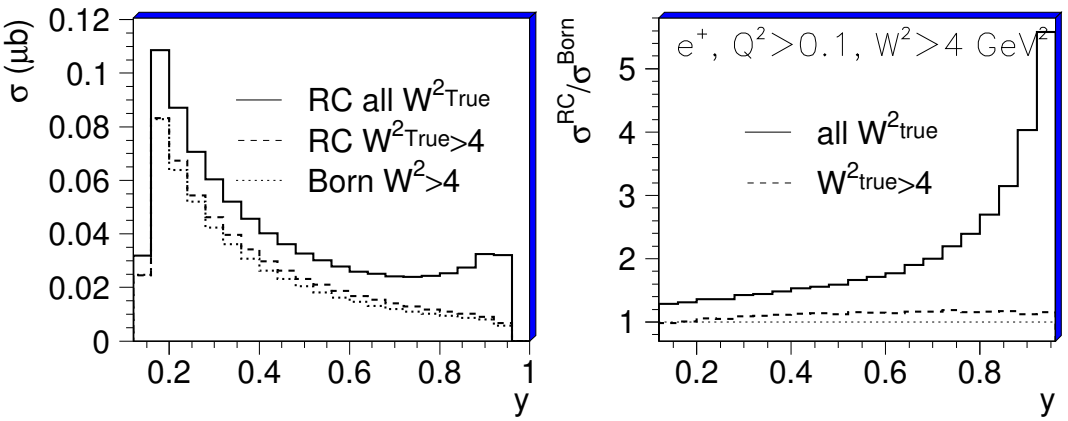

Figure B.1: Radiative cross sections and factors $\sigma_{RC}/\sigma_{Born}$ from DISNG. See explanations in the text.

The main difference between gmc_DISNG and PYTHIA is that for the latter the cross section will be calculated in the course of the generation process for the particular *true* kinematic point and the selected subprocess. In order to understand how the method of gmc_DISNG can be modified to be used with PYTHIA it might be necessary to reflect on how the event weights and RC correction factors come about in gmc_DISNG. Roughly, the observed cross section consists of two parts, the non-radiative ($\sigma^{0\gamma}$) and the radiative part ($\sigma^{1\gamma}$). The individual contributions come from σ_{in} and $\sigma_{(q)el}$ for the radiative part (cf. Eqs. 4.15 and 4.16) and from Eq. 4.18 for the non-radiative part. In the RADGEN language, these individual contributions are called 'tails', referring to some background under a true distribution. These tails are labeled T_{inel}, T_{elas} and T_{Born} in the following for the inelastic, elastic and non-radiative contributions, respectively. The total cross section is

$$\sigma_{tot}^{obs}(DISNG) = \sigma^{0\gamma} + \sigma^{1\gamma} = T_{Born} + T_{inel} + T_{elas}. \tag{B.3}$$

The radiative contribution is $\sigma^{1\gamma} \geq 0$ because it comes from the squaring two diagrams (see figure 4.4, b,c). The non-radiative cross section can receive negative contributions from the virtual corrections, but usually these are of the order of only a few per cent, such that also $T_{Born} \geq 0$. The total observed cross section may be smaller than the Born level cross section, however.

In gmc_DISNG a given number of events is generated, each weighted with $w = \sigma_{Born}(y, Q^2)$. From RADGEN, a fraction of these events will be returned without having radiated a real photon.

The probability that no photon is radiated, is:

$$P(0\gamma) = \frac{\sigma^{0\gamma}}{\sigma^{0\gamma} + \sigma^{1\gamma}} = \frac{T_{Born}}{T_{Born} + T_{inel} + T_{elas}}. \tag{B.4}$$

The probability for events with a radiated photon is

$$P(1\gamma) = 1 - P(0\gamma) = \frac{\sigma^{1\gamma}}{\sigma^{0\gamma} + \sigma^{1\gamma}} = \frac{T_{inel} + T_{elas}}{T_{Born} + T_{inel} + T_{elas}}. \tag{B.5}$$

The *effective* weight for a given event is then:

$$w^{0(1)} = P\left(0(1)\gamma\right) w, \quad \text{with } w^0 + w^1 = w = \sigma_{Born}. \tag{B.6}$$

The radiation of a photon corresponds to the inclusion of an additional subprocess in the cross section to be calculated. Therefore, to obtain the correct cross section from a fixed number of generated events, each event has to be corrected with a factor $P^{-1}\left(0(1)\gamma\right)$. In addition, a factor $T_{Born}/\sigma_{Born}(y, Q^2)$ has to be taken into account for the reduction of the Born cross section to the 'Born' tail of non-radiative events, and the factor $(T_{inel} + T_{elas})/\sigma_{Born}(y, Q^2)$ is necessary to compensate for the difference of cross sections at the true and observed kinematic points of radiative events. The total cross section obtained in gmc_DISNG should then be:

$$\begin{aligned}
\sigma^{RC} &= P^{-1}(0\gamma)\left[\frac{T_{Born}}{\sigma_{Born}(y,Q^2)}\right] P(0\gamma)\sigma_{Born}(y,Q^2) + P^{-1}(1\gamma)\left[\frac{T_{inel}+T_{elas}}{\sigma_{Born}(y,Q^2)}\right] P(1\gamma)\sigma_{Born}(y,Q^2) \\
&= P^{-1}(0\gamma)\left[\frac{T_{Born}}{\sigma_{Born}(y,Q^2)}\right] w^0 + P^{-1}(1\gamma)\left[\frac{T_{inel}+T_{elas}}{\sigma_{Born}(y,Q^2)}\right] w^1 \\
&= \frac{T_{Born}+T_{inel}+T_{elas}}{T_{Born}}\left[\frac{T_{Born}}{\sigma_{Born}(y,Q^2)}\right] w^0 + \frac{T_{Born}+T_{inel}+T_{elas}}{T_{inel}+T_{elas}}\left[\frac{T_{inel}+T_{elas}}{\sigma_{Born}(y,Q^2)}\right] w^1 \\
&= \frac{T_{Born}+T_{inel}+T_{elas}}{\sigma_{Born}(y,Q^2)} w^0 + \frac{T_{Born}+T_{inel}+T_{elas}}{\sigma_{Born}(y,Q^2)} w^1 \\
&= sig_{RadCor}(y,Q^2) w = T_{Born} + T_{inel} + T_{elas} = \sigma_{tot}^{obs}(DISNG).
\end{aligned} \tag{B.7}$$

The factor sig_{RadCor} applied to the Born weights can thus be viewed as a correction factor to account for the addition of new processes.

B.2 Merging PYTHIA with RADGEN

Since PYTHIA works very differently from gmc_DISNG, at the beginning the code structure of PYTHIA is explained in order to motivate the way RADGEN is introduced in PYTHIA. The final goal is to calculate correction factors and generate bremsstrahlung photons analogously to gmc_DISNG without interfering with any other function in PYTHIA but at the same time preserving the cross section information from PYTHIA. The methods PYTHIA uses for event generation are mostly methods 2.) or 3.) of section 4.1.1, that is, 'hit-or-miss' methods. Consequently, events are generated according to the cross section and have a weight $w = 1$. An event is generated by calling the routine PYEVENT as follows:

1. From PYEVENT, the routine PYRAND is called. The first step in this routine is to pick randomly one among N possible subprocesses, according to the ratio of their cross section maxima (to be evaluated at initialization) $\sigma^1_{max} : \sigma^2_{max} \cdots : \sigma^N_{max}$.

2. Next, the routine PYGAGA is called to select a kinematic point (y, Q^2), and the photon flux factor Γ_T is calculated according to Eq. 4.13. This factor is used for weighting the event during the cross section calculation.

3. In the following, the participating partons and their kinematics are chosen from random distributions, and the differential cross section for the $\gamma^* p$ subprocess is calculated. The actual event cross section is then $\sigma_i = \Gamma_T \sigma^{\gamma^* p}$. The ratio $\sigma_i / \sigma^j_{max}$ for the chosen subprocess j is to be compared with a new random number, and the event is accordingly accepted or rejected. This step is repeated until an accepted event is found.

The cross section for a given kinematic bin (for instance (y, Q^2)) can be obtained from the number of accepted events in that bin:

$$\sigma^{PYTHIA}_{Born}(y, Q^2) = \frac{N_{acc}(y, Q^2)}{N_{generated}} \frac{1}{N_{tried}} \sum_{i=1}^{N_{tried}} \sigma_i \equiv \frac{N_{acc}(y, Q^2)}{L^{MC}}, \tag{B.8}$$

where N_{tried} is the total number of tries needed to generate $N_{generated}$ successful events and the 'Monte Carlo luminosity' is defined by

$$N_{generated} = \sigma^{tot} \int \mathcal{L}^{MC} dt = \sigma^{tot} L^{MC} \quad \rightarrow \quad L^{MC} = \frac{N_{generated}}{\sigma^{tot}} = \frac{N_{generated}}{\frac{1}{N_{tried}} \sum_{i=1}^{N_{tried}} \sigma_i}. \tag{B.9}$$

The natural point to call RADGEN in PYTHIA would be the routine PYGAGA, where the virtual photon kinematics are selected. The original routine is called with flags 1 to 4 invoking different functions. In order to leave the original PYTHIA code untouched, a fifth flag was introduced. This flag is set by GMC, if the PYTHIA option MSTP(199)=1 is given[1]. If that is the case, a modified PYGAGA function is called. The new code structure can be summarized like this:

1. In PYGAGA, the measured (y, Q^2) are chosen according to logarithmic distributions, within ranges defined by GMC. Note that these ranges are in general not the same as the ones defined by the PYTHIA parameters CKIN(73), CKIN(74) = y_{min}, y_{max} and CKIN(65), CKIN(66) = Q^2_{min}, Q^2_{max}. These parameters define restrictions on the true kinematics, not the observed ones. With RC on, it is recommended to leave the full true kinematic range open, and to only restrict the observed range. Next, the derived lepton kinematics are calculated. It is checked if the kinematic point is physically allowed and if $W^2 > 4$ GeV^2. If either is not the case, new observed kinematics are tried. This is repeated, until an allowed point is found.

2. In this step, RADGEN is called with (x, y) as input. The RADGEN method is the same as described above. If RADGEN did not generate a bremsstrahlung photon, $y_T = y$ and $Q^2_T = Q^2$. If it did, y_T, Q^2_T will be taken from the true values returned by RADGEN.

3. Elastic events are ignored, that is, if RADGEN returns with an event marked as elastic, the routine will return to the point where RADGEN is called. This is repeated until an inelastic event is found. Ignoring these event means here that the number of RADGEN tries to find an inelastic event is not counted for the normalization. This corresponds to an ineffective way of putting $T_{elas} \equiv 0$.

4. Also in the case of an inelastic event with $(M_p + m_\pi)^2 < W^2_T < 4$ GeV^2, RADGEN is called anew. This time, however, the number of tries until RADGEN finds an inelastic or non-radiative event with $W^2_T > 4$ GeV^2 is counted and stored in the variable MINT(199). This variable is initialized to 0 for each new event.

5. Once an inelastic or non-radiative event with $W^2_T > 4$ GeV^2 is found it is checked whether it meets the restrictions on the true kinematics that are set by the CKIN parameters. If it does not, the procedure is repeated from the point where the observed kinematics are chosen. For a successful point, the photon flux $\Gamma(y_T, Q^2_T)$ is calculated from the *true* kinematics.

[1] MSTP(199) and MINT(199) are common PYTHIA parameters which so far are left blank. Should a new version of PYTHIA be developed using this parameter, the RC correction flag has to be moved of course.

6. A weight analogous to sig_{RadCor} is calculated to correct the cross section of the to-be-generated PYTHIA event. This weight is obtained combining several pieces of information from RADGEN. How this is exactly done, is described in the next section.

7. After this point, event handling is proceeded as in the original PYTHIA code.

PYTHIA is a solely semi-inclusive generator, meaning that for each event a hadronic final state is produced. To include elastic *ep* scattering into PYTHIA would be like including an additional subprocess. There is no model for the elastic cross section implemented in PYTHIA, though. On the other hand it may be difficult to include a user defined subprocess into the working concept of how PYTHIA models the total cross section. Moreover, the only drawback of setting $T_{elas} \equiv 0$ is that *inclusive* data cannot be directly compared to the PYTHIA output. Semi-inclusive data are inelastic by definition and such not affected by the exclusion of elastic events. A similar reasoning applies to the treatment of low–E events. If semi-inclusive events with $W^2 \geq 4$ GeV^2, but $W_T^2 < 4$ GeV^2 would exist within the acceptance of the spectrometer, it should be possible to observe events that have $W_T^2 \leq W^2 < 4$ GeV^2 as well. In the data practically no semi-inclusive events are observed with $W^2 < 4$ GeV^2. This might be different for the full phase space in the 4π geometry, but in any case it is possible to restrict a semi-inclusive cross section measurement to $W_T^2 > 4$ GeV^2. Technically it is more difficult to set $T_{inel}(W_T^2 < 4) \equiv 0$, because the program crashes if the input F_2 parametrization is explicitly set to 0. One solution would be to accept a low–E event and have PYTHIA reject it at a later stage (the latest stage where it has to be rejected is when calling JETSET, the event would then be marked as 'event that fails fragmentation cuts'). The correct normalization of the cross section for $W^2 \geq (M + m_\pi)^2$ would then have to be taken care of by PYTHIA and would be somewhat doubtful. Another, more effective option is the handling of low–E events as described above, with a normalization of the cross section for $W_T^2 > 4$ GeV^2, using the number of RADGEN tries necessary to obtain an event with $W_T^2 > 4$ GeV^2, as explained in the next section.

B.3 Normalization of PYTHIA Events

It should be clear from section B.1 that it is not sufficient to hand the true kinematics over to PYTHIA and have PYTHIA calculate the cross section. Also here, it is necessary to correct the events for the *effective* weight $w^{0(1)} = P(0(1)\gamma)\sigma(y_T, Q_T^2)$ (see Eq. B.6, with the difference that here the cross section is evaluated at the true kinematic point) they acquire due to the addition of another subprocess by RADGEN. The application of the correction factor is straightforward for non-radiative events, where $y = y_T, Q^2 = Q_T^2$ (note that $T_{elas} \equiv 0$):

$$\begin{aligned}
\sigma^{0\gamma} &= P^{-1}(0\gamma)\left[\frac{T_{Born}}{\sigma_{Born}(y,Q^2)}\right] P(0\gamma)\sigma_{Born}^{PYTHIA}(y,Q^2) \\
&= \frac{T_{Born}+T_{inel}}{T_{Born}}\left[\frac{T_{Born}}{\sigma_{Born}(y,Q^2)}\right] w^0 \\
&= sig'_{RadCor} w^0 \equiv w_{0\gamma}^{RC} w^0. \qquad \text{(B.10)}
\end{aligned}$$

The quantity $\sigma_{Born}^{PYTHIA}(y,Q^2)$ is here the Born cross section as it would be generated by PYTHIA without radiative corrections, Eq. B.8. The factor $sig'_{RadCor} = (T_{Born} + T_{inel})/\sigma_{Born}(y,Q^2)$ is the weight necessary to correct the *effective* PYTHIA cross section to the desired $\sigma^{0\gamma} = T_{Born}$. In contrast to the PYTHIA generated cross section, $\sigma_{Born}(y,Q^2)$ is the cross section calculated by RADGEN from the input for $F_2(x,Q^2)$, and $\sigma_{Born}(y,Q^2) \approx \sigma_{Born}^{PYTHIA}(y,Q^2)$ for a sufficiently large number of events. The compliance of the cross section parametrization and the MC generated value eventually approaches the agreement seen in figure 4.5.

Radiative events are weighted differently. If $\sigma_{RC}^{PYTHIA}(y,Q^2)$ is defined as follows:

$$\sigma_{RC}^{PYTHIA}(y,Q^2) = \frac{N_{acc}^{1\gamma}(y,Q^2)}{N_{generated}} \frac{1}{N_{tried}} \sum_{i=1}^{N_{tried}} \sigma_i(y_T \neq y, Q_T^2 \neq Q^2) \tag{B.11}$$

the radiative cross section can be constructed (using $w^1 = P(1\gamma)\sigma_{RC}^{PYTHIA}(y,Q^2)$):

$$\begin{aligned}
\sigma^{1\gamma} &= P(1\gamma)^{-1} \left[\frac{T_{inel}}{\sigma_{Born}(y_T,Q_T^2)}\right] P(1\gamma)\sigma_{RC}^{PYTHIA} \\
&= \frac{T_{Born}+T_{inel}}{T_{inel}} \left[\frac{T_{inel}}{\sigma_{Born}(y,Q^2)}\right] \left(\frac{\sigma_{Born}(y,Q^2)}{\sigma_{Born}(y_T,Q_T^2)}\right) w^1 \\
&= sig'_{RadCor} \left(\frac{\sigma_{Born}(y,Q^2)}{\sigma_{Born}(y_T,Q_T^2)}\right) w^1 \equiv w_{1\gamma}^{RC} w^1.
\end{aligned} \tag{B.12}$$

Here, $\sigma_{Born}(y_T,Q_T^2)$ is the Born cross section at the *true* kinematic point, calculated from the F_2 parametrization that is also used in RADGEN. The factor $T_{inel}/\sigma_{Born}(y_T,Q_T^2)$ takes into account that the point y_T, Q_T^2 at which the cross section is to be evaluated by PYTHIA was picked in RADGEN with a probability $P(y_T,Q_T^2) = \sigma_{Born}(y_T,Q_T^2)/T_{inel}$ out of the whole possible phase space for inelastic events. As the inelastic tail T_{inel} is what is relevant for the observed cross section, the event weight has to compensate also for this probability. Reversely, the sum of radiative and non-radiative cross sections with the applied weights is:

$$\begin{aligned}
&\sigma_{tot}^{obs}(PYTHIA) = \sigma^{0\gamma} + \sigma^{1\gamma} \\
&= sig'_{RadCor} w^0 + sig'_{RadCor} \left\langle \frac{\sigma_{Born}(y,Q^2)}{\sigma_{Born}(y_T,Q_T^2)} \right\rangle w^1 \\
&\simeq sig'_{RadCor} P(0\gamma)\sigma_{Born}^{PYTHIA}(y,Q^2) + sig'_{RadCor} P(1\gamma)\sigma_{Born}^{PYTHIA}(y_T,Q_T^2) \\
&= \frac{T_{Born}+T_{inel}}{\sigma_{Born}(y,Q^2)} (P(0\gamma)+P(1\gamma))\sigma_{Born}^{PYTHIA}(y,Q^2) \\
&\simeq T_{Born} + T_{inel}.
\end{aligned} \tag{B.13}$$

This is the desired result, relying on the assertion that for a large enough number of events

$$\left\langle \frac{\sigma_{Born}(y,Q^2)}{\sigma_{Born}(y_T,Q_T^2)} \right\rangle \approx \frac{\sigma_{Born}^{PYTHIA}(y,Q^2)}{\sigma_{RC}^{PYTHIA}(y,Q^2)}. \tag{B.14}$$

To conclude, in order to obtain the observed cross section from PYTHIA, the event weights $w_{0\gamma}^{RC}$ ($w_{1\gamma}^{RC}$) have to be applied for non-radiative (radiative) events. This is already necessary to obtain the correct kinematic distributions, because the weights depend on (y,Q^2). The technical solution is here to multiply the flux factor in the routine PYGAGA with the proper weight, so that PYTHIA generates events according to the reweighted cross section, and takes the weight into account for the integrated cross section. For the absolute normalization it is then possible to use the MC luminosity L_{RC}^{MC} obtained by PYTHIA. To obtain ratios $\sigma^{RC}/\sigma^{Born}$ it is possible to generate reference Born level samples by using the option MSTP(199)=1, but setting the variable GENRAD to 'NO'. In this case the same modified PYTHIA functions are called as with radiative corrections (if GENRAD='POL'), but without invoking RADGEN. This is different from just letting MSTP(199)=0, because then the original PYTHIA functions in PYGAGA would be called that use different kinematic variables to generate the virtual photon kinematics.

There is one more subtlety in the calculation of the PYTHIA weights that has been neglected so far. In the previous section it was established that the cross section should be calculated for

$W_T^2 > 4$ GeV^2. The inelastic tail as calculated by RADGEN can be written as:

$$\begin{aligned} T_{inel} &= \int_{\Delta}^{\omega(W_T^2=4)} d\omega \int_{\theta_\gamma} d\theta_\gamma \frac{d\sigma(x,y,\theta_\gamma,\omega)}{dxdyd\theta_\gamma d\omega} + \int_{\omega(W_T^2=4)}^{\omega(W_T^2=(M+m_\pi)^2)} d\omega \int_{\theta_\gamma} d\theta_\gamma \frac{d\sigma(x,y,\theta_\gamma,\omega)}{dxdyd\theta_\gamma d\omega} \\ &= T_{inel}|_{W_T^2>4} + T_{inel}|_{W_T^2<4}. \end{aligned} \tag{B.15}$$

The total cross section for $W_T^2 > 4$ GeV^2 is $T_{inel}|_{W_T^2>4} + T_{Born}$:

$$T_{inel}|_{W_T^2>4} + T_{Born} = \frac{T_{inel} + T_{Born}}{1 + \dfrac{T_{inel}|_{W_T^2<4}}{T_{inel}|_{W_T^2>4} + T_{Born}}}. \tag{B.16}$$

The number of tries where RADGEN returns with a low–E event relative to the number of tries where $W_T^2 > 4$ GeV^2 is

$$\frac{T_{inel}|_{W_T^2<4}}{T_{inel}|_{W_T^2>4} + T_{Born}} = \frac{N^{RADGEN}(\text{low–E})}{N(W_T^2 > 4)}. \tag{B.17}$$

The ratio depends on (y, Q^2), which is why it has to be taken into account on an event-by-event basis. For a single, accepted event, definitely is $W_T^2 > 4$ GeV^2, so $N(W_T^2 > 4) = 1$. The number of low–E events occurring during the generation of this successful event is stored in MINT(199). Thus, the event weights $w_{0\gamma}^{RC}$ and $w_{1\gamma}^{RC}$ have to be replaced by

$$w_{0,1\gamma}^{RC} \quad \rightarrow \quad \frac{1}{1 + MINT(199)} w_{0,1\gamma}^{RC}. \tag{B.18}$$

In practice, this method does not work well, probably because if RADGEN returns with a *non-radiative* event after the first try, as in about 70% of the cases, the weight is not reduced (MINT(199)=0). For these events then the full weight is applied also containing the contribution from $W_T^2 < 4$ GeV^2. If the cross section for $W_T^2 < 4$ GeV^2 would be large, this would result in an overestimate of the total radiatively corrected cross section. Therefore, and for efficiency reasons, the cross section for $W^2 < 4$ GeV^2 is calculated from the PYTHIA structure function at $W^2 = 4$ GeV^2 by multiplying it with a suppression factor

$$F_2^{PYTHIA}(W^2 < 4, Q^2) \equiv \left[\frac{W^2 - M^2}{4 - M^2}\right]^{10} F_2^{PYTHIA}(W_0^2 = 4, Q^2) \tag{B.19}$$

that reduces the probability that a low–E event would be picked by RADGEN. This may seem a bit arbitrary, but the large suppression guarantees that the uncertainty due to the (unknown) cross section at $W^2 < 4$ GeV^2 is negligible.

Figure B.2 shows the final results on the observed PYTHIA cross section and the ratio $\sigma_{RC}/\sigma_{Born}$ obtained with this method. The cuts on the inclusive PYTHIA data are the same as for figure B.1, with the implicit cut on $W_T^2 > 4$ GeV^2. For comparison, also the RC cross section and the ratio $\sigma_{RC}/\sigma_{Born}$ from gmc_DISNG are shown for $W_T^2 > 4$ GeV^2. The correction factor from PYTHIA is compatible with that of gmc_DISNG. The remaining differences, showing up in some regions of y and Q^2 if the ratios are calculated as a two-dimensional function, can be explained with the different shape of the Born cross sections from the F_2 (ALLM) and R (1990) parametrization used for gmc_DISNG and the PYTHIA cross section model. This is clearly evident from figure 4.5, where both Born cross sections are displayed as a function of x and Q^2. In section 4.2.3 it is shown that the inclusion of RC to PYTHIA leads to a considerable improvement of the description of the data, mainly in the 'Transition' region, where the correction factors are relatively large.

The possibility to include radiative corrections was extended to the 'Photoproduction' region. This extension involved major changes to the RADGEN code, mainly in the way it generates a lookup table in an appropriate x-y binning for efficient integration [Abr04]. The range of x in

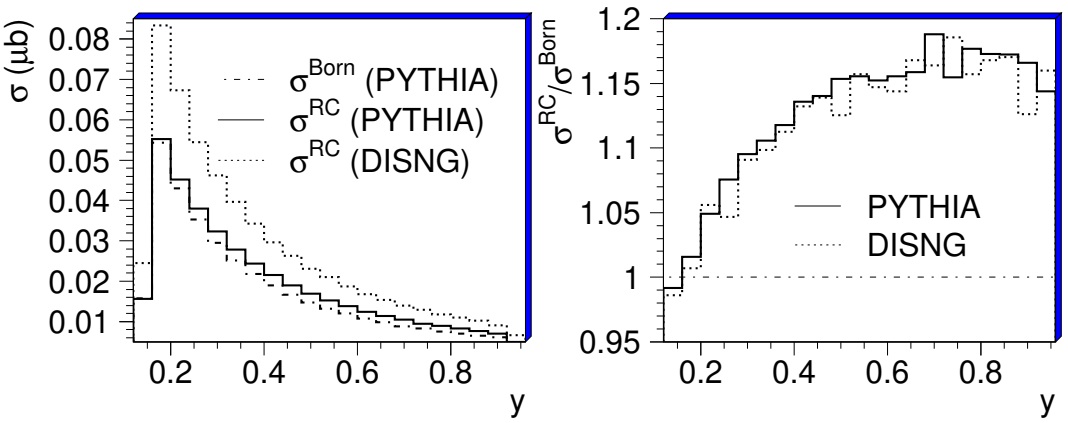

Figure B.2: Radiatively corrected cross sections and factors $\sigma_{RC}/\sigma_{Born}$ from PYTHIA. The dotted line corresponds to the results obtained from gmc_DISNG for $W_T^2 > 4$ GeV^2.

the 'Photoproduction' region extends down to 10^{-9} for $0.05 < y < 0.95$, which required a rather coarse binning. As the radiative corrections in the small x region are relatively flat, a wider binning does not result in a large loss of information. (Note that the elastic contribution of the radiative corrections is switched off, i.e., $T_{ine} \equiv 0$ for the quasireal photoproduction region.) In order to avoid numerical instabilities the lookup table is generated only for a minimum $x_{min} = 10^{-7}$. If PYTHIA is run with RADGEN using this lookup table, an extrapolation routine is used to calculate the correction for smaller values of x. The resulting cross sections and correction factors $\sigma_{RC}/\sigma_{Born}$ are shown in figure B.3. The correction factors are very small compared to the 'Transition' region

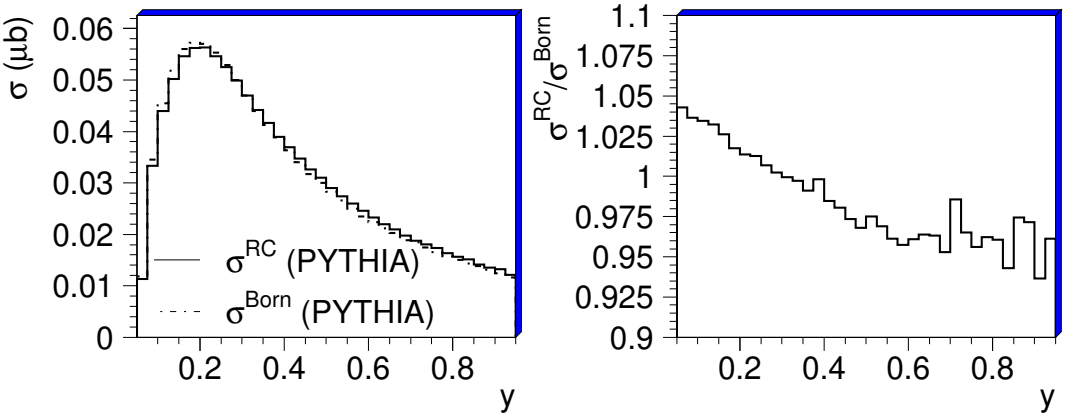

Figure B.3: Radiatively corrected cross sections and factors $\sigma_{RC}/\sigma_{Born}$ from PYTHIA for the 'Photoproduction' region (defined by the positron veto).

due to the fact that the radiative corrections become smaller with smaller x.

Last it should be noted that it is not at all necessary to run PYTHIA together with RADGEN in the GMC framework. A stand alone code exists that includes independent versions of PYTHIA and RADGEN within a wraparound code and has been tested to give the same results as the GMC version [Asch04].

Appendix C

Monte Carlo Asymmetries

C.1 Event Wise Asymmetry Calculation for PYTHIA

Asymmetries extracted from Monte Carlo (PYTHIA) are needed for two reasons: First, for the extraction of the gluon polarization from the measured asymmetries vs. p_T it is necessary to subtract the asymmetry of the background (i.e., all processes not involving a target gluon) from the data. Second, asymmetries as a function of x are sensitive to the mixture of different subprocesses modeled by PYTHIA and can therefore be used to check the consistency of the PYTHIA model with the data. Since PYTHIA has no information about spin dependent cross sections, asymmetries from the PYTHIA model have to be constructed externally. A relatively uncomplicated way of doing this is to calculate asymmetries on an event-by-event basis and to apply them as a weight to each event. This method was used for the POLDIS generator [Bra97]. For this analysis, this method was adapted to the different kinematic range and subprocess structure of PYTHIA, and is applied in an external code analyzing the PYTHIA data. The event wise information available from PYTHIA is the kinematics (x, Q^2) at which the nucleon is probed, the type of the subprocess, the flavor of the struck parton and, for the direct $2 \to 2$ processes (PGF and QCDC), the hard subprocess kinematics $\hat{s} = (p_a + p_b)^2$, $\hat{t} = (p_a - p_c)^2$ and $\hat{u} = (p_a - p_d)^2$ (Mandelstam variables) for the generic (partonic) subprocess $ab \to cd$. Additionally, the information about the asymmetries of the hard subprocesses $\hat{a}$ given in [Bra97] and the polarizations of the struck parton are needed. Some selected sets of polarized parton distributions are available from the PDFLIB [Plo00]. The asymmetry weight for a given event can be constructed as

$$a_i = \hat{a}(x, Q^2, \hat{s}, \hat{t}, \hat{u}) \frac{\Delta f(x, Q^2)}{f(x, Q^2)}, \qquad f = q, \bar{q}, G. \tag{C.1}$$

The weights include the depolarization factor $D(y, Q^2)$ for the transformation from the virtual photon asymmetry to the lepton–nucleon asymmetry. Generically, the lepton–nucleon asymmetry can be written as (cf. section 2.1.2):

$$A_\parallel = \frac{\Delta\sigma^{ep}}{\sigma^{ep}} = \frac{\Delta\Gamma_T \Delta\sigma_T^{\gamma^* p}}{\Gamma_T \sigma_T^{\gamma^* p} + \Gamma_L \sigma_L^{\gamma^* p}} \tag{C.2}$$

with

$$\Delta\Gamma_T = \frac{1}{2}\left[1 - (1-y)^2 - y y^2 \frac{2m_e^2}{Q^2} + \frac{1}{2}\gamma^2 y^2 (2-y)\right] \tag{C.3}$$

$$\Gamma_T = \frac{1}{2}\left[1 + (1-y)^2 - y^2 \frac{2m_e^2}{Q^2}(1+\gamma^2) + \frac{1}{2} y^2 \gamma^2\right] \tag{C.4}$$

$$\Gamma_L = \epsilon\Gamma_T = 1 - y - \frac{1}{4} y^2 \gamma^2. \tag{C.5}$$

In all three equations above the terms proportional to $\gamma^2 = \frac{Q^2}{\nu^2}$ and to m_e^2 have been added to the terms given in [Bra97]. In particular, the term $2y^2 m_e^2/Q^2$ in the expression for $\Delta\Gamma_T$ is necessary to constrain $D(y, Q^2)$ to values below 1 in the region $Q^2 \to 0$ [Ade99]. The lepton–nucleon asymmetry measured in a given bin in p_T or x is then the average of all event weights in this bin:

$$A_\parallel = \frac{\sum_{i=1}^N a_i}{N}, \qquad \Delta A_\parallel = \sqrt{\frac{\sum_{i=1}^N (a_i - A_\parallel)^2}{N(N-1)}}. \tag{C.6}$$

The different asymmetry weights in particular are calculated as follows (a common factor $4\pi\alpha^2 e_q^2/(xQ^2)$ is omitted from the hard subprocess cross sections):

LO DIS: The $\gamma^* p$ asymmetry in this case is +1, independent of the kinematics. The ep asymmetry is then just $\Delta\Gamma_T/\Gamma_T$. Note that $R = \sigma_L/\sigma_T = 0$ for this process. The parton distributions are evaluated at the x and Q^2 of the event.

QCDC: In this case

$$\sigma_T = \frac{2\alpha_s}{3\pi}\frac{1}{(\hat{s}+Q^2)^2}\left[2 - \frac{2\hat{u}Q^2}{(\hat{s}+Q^2)^2} - \frac{Q^4+\hat{u}^2}{\hat{s}\hat{t}}\right] \tag{C.7}$$

$$\Delta\sigma_T = \frac{2\alpha_s}{3\pi}\frac{1}{(\hat{s}+Q^2)^2}\frac{2(Q^2-\hat{u})}{\hat{s}+Q^2} - \frac{Q^4+\hat{u}^2}{\hat{s}\hat{t}} \tag{C.8}$$

$$\sigma_L = -\frac{2\alpha_s}{3\pi}\frac{1}{(\hat{s}+Q^2)^2}\frac{4Q^2\hat{u}}{(\hat{s}+Q^2)^2}. \tag{C.9}$$

$R = \sigma_L/\sigma_T$ is here implicitly taken into account. Since PYTHIA generates the longitudinal and transverse photon cross sections separately (i.e., in different subprocesses) it is basically possible to calculate the asymmetry only for the transverse photons, disregarding σ_L. The events of *both* longitudinal and transverse photon processes would then have to be counted independently, which involves more technical effort and a larger statistical error. It is much simpler to count both processes as one and apply Eqs. C.7 to C.9. The parton distributions are evaluated at the the parton momentum fraction

$$x_P = x\left(\frac{\hat{s}}{Q^2}+1\right) \tag{C.10}$$

and at the scale evaluated by PYTHIA according to the option MSTP(32), usually involving a combination of the hard transverse momentum $\hat{p}_T^2$ and Q^2.

PGF: For this process

$$\sigma_T = \frac{\alpha_s}{4\pi}\frac{1}{(\hat{s}+Q^2)^2}\frac{Q^4+\hat{s}^2}{(\hat{s}+Q^2)^2}\frac{\hat{u}^2+\hat{t}^2}{\hat{u}\hat{t}} \tag{C.11}$$

$$\Delta\sigma_T = \frac{\alpha_s}{4\pi}\frac{1}{(\hat{s}+Q^2)^2}\frac{Q^2-\hat{s}}{\hat{s}+Q^2}\frac{\hat{u}^2+\hat{t}^2}{\hat{u}\hat{t}} \tag{C.12}$$

$$\sigma_L = \frac{\alpha_s}{4\pi}\frac{1}{(\hat{s}+Q^2)^2}\frac{8Q^2\hat{s}}{(\hat{s}+Q^2)^2} \tag{C.13}$$

and with the same considerations as for QCDC the longitudinal and transverse photon processes are added. Also here, the gluon distribution is evaluated at x_P and the scale given by MSTP(32).

Anomalous photon and hard non-diffractive VMD: These processes involving the perturbative structure of the resolved photon (cf. section 2.5.1) were not considered in [Bra97].

To leading order, the possible partonic processes are: $qq' \to qq'$, $q\bar{q} \to q'\bar{q}'$, $q\bar{q} \to gg$, $qg \to qg$,$gg \to q\bar{q}$ and $gg \to gg$. The subprocess asymmetries of the hard resolved photon processes are known to leading [Bab79] and next to leading order [Jäg03]. The event weight can be constructed as

$$a_{i,res} = \hat{a}^{ab\to cd}(x, Q^2, \hat{s}, \hat{t}, \hat{u}) \frac{\Delta f_{a/\gamma}(x, Q^2)}{f_{a/\gamma}} \frac{\Delta f_{b/N(x,Q^2)}}{f_{b/N(x,Q^2)}}, \qquad f = q, \bar{q}, G, \tag{C.14}$$

where in contrast to the direct photon contribution also the polarization of the partons in the *virtual photon* has to be known. Polarized photon parton distributions have not been measured so far, such that $a_{i,res}$ is completely unknown. An evaluation of the possible range for the polarized photon PDFs has been performed recently in Refs. [Glü01a, Glü01b]. The 'positivity' constraint for the polarized parton distributions in the photon means that

$$0 \leq \left| \frac{g_1^\gamma}{F_1^\gamma} \right| \leq 1. \tag{C.15}$$

At leading order this applies also to the individual parton distributions, i.e., $|\Delta f^\gamma| \leq f^\gamma$ for $f = q, \bar{q}, G$. These constraints lead to a minimal and a maximal scenario at the input scale, which at leading order are [Glü92a]:

$$\begin{aligned} \Delta f^\gamma_{min}(x, \mu^2) &= 0, \\ \Delta f^\gamma_{max}(x, \mu^2) &= f^\gamma_{max}(x, P^2), \qquad f = q, \bar{q}, G. \end{aligned} \tag{C.16}$$

Using the polarized evolution equations for the photon parton densities, the input distributions from the maximal and minimal scenarios can be evolved to any given $Q^2 > \mu^2$. The result for the parton polarizations $\Delta u^\gamma / u^\gamma$ and $\Delta G^\gamma / G^\gamma$ at $Q^2 = 10$ GeV^2 is shown in figure C.1. For the maximal scenario both $\Delta u^\gamma / u^\gamma$ and $\Delta G^\gamma / G^\gamma$ are positive, whereas for the

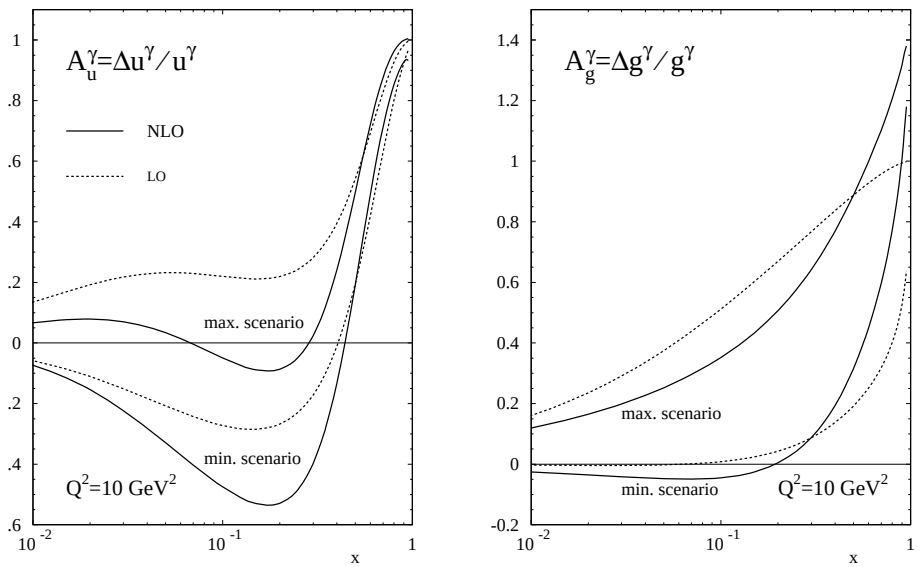

Figure C.1: The parton polarizations $\Delta u^\gamma / u^\gamma$ and $\Delta G^\gamma / G^\gamma$ at $Q^2 = 10$ GeV^2 for the maximal and minimal scenarios. The plot is taken from Ref. [Glü01b].

minimal scenario their sign changes from negative to positive at some point in $x > 0.1$. The maximum positive polarization is 1 for $x \to 1$, the minimum negative polarization is about -0.5 for quarks, and larger than -0.1 for gluons. The behavior does not change dramatically with the Q^2 scale, see for instance Ref. [Glü01a]. The fraction of the hard resolved photon

processes is around 10% in the 'Photoproduction', and usually less than 10% percent in the 'Transition' region at $p_T > 1$ GeV, however, in view of the relatively small fraction of PGF events of 10–20% it might not be negligible. Therefore, a careful treatment of these processes has to be considered. The subprocess asymmetries can be calculated from the formulas given in Ref. [Bab79] using the additional information about the flavor of the *final* state quarks from PYTHIA. The polarization of the partons in the photons can be varied between the extremes for the maximal and minimal scenarios, i.e., $\Delta u^\gamma/u^\gamma = 1$, $\Delta G^\gamma/G^\gamma = 1$ for the maximal, $\Delta u^\gamma/u^\gamma = -0.5$, $\Delta G^\gamma/G^\gamma = -0.1$ for the minimal scenario. A constant value is used over the whole kinematic range. With this procedure it should be possible to estimate the maximum 'theoretical' uncertainty of the anomalous photon contribution. The longitudinal cross sections are parametrized as $\sigma_L = R_{VMD}\sigma_T$ using the parametrization 4.27 for R_{VMD}.

Soft non-diffractive VMD: These 'low-p_T processes' are modeled in PYTHIA by the exchange of a soft gluon between partons of the resolved photon (vector meson) and partons of the nucleon. The soft gluon provides the color flux necessary to form a string for the subsequent hadronization. No hard process, and therefore no hard subprocess kinematics are associated with these processes. In principle, such soft processes should not exhibit any spin dependence, i.e. $\Delta\sigma^{low-p_T} = 0$ [Schä04]. It should be kept in mind, though, that this 'minimum bias' description of the cross section is to a certain degree physically motivated, but arbitrary in the sense that it involves a decision between the different scales occurring in the process, the transverse momenta at the photon and 'nucleon' vertices as well as the photon virtuality (cf. figure 4.2). Basically, a low-p_T process is generated if neither scale is large enough for a perturbative QCD calculation to work. The cutoffs are in general determined by Λ_{QCD} and usually set to be around 500 MeV. The fact that perturbative calculations fail at scales below this cutoffs provides a view on the PYTHIA low-p_T process as a tool to fill the unknown cross section in this region and not so much as a well determined model. As this process constitutes a large fraction of the cross section in the 'Transition' as well as the 'Photoproduction' region it cannot be neglected and it may be necessary to consider different possible interpretations in terms of its asymmetry.

a) The non-diffractive VMD ('low-p_T') events can be treated as a dilution to the asymmetry i.e., $\Delta\sigma^{low-p_T} \equiv 0$.

b) Due to the above mentioned ambiguities in the scale choices, the (phenomenological) description of a large part of the cross section by the low-p_T process to some degree parametrizes our ignorance about soft higher order (and higher twist) processes. The asymmetry of these processes must be then contained in the measured $A_1 = g_1/F_1$. As a crude estimate, $\Delta\sigma^{low-p_T}$ can then be put equal to g_1/F_1. The contribution of longitudinal photons to the unpolarized cross section is again $\Gamma_L R_{VMD}\sigma_T$. In the 'Transition' and 'SIDIS' regions a parametrization of the measured $A_1(x)$ can be used. Alternatively, the model for $g_1(x, Q^2)$ described in Ref. [Koc03], together with their model for $F_2(x, Q^2)$ can be applied. In order to obtain F_1 from $F_2(x, Q^2) = 2x(1 + R)F_1(x, Q^2)$, a parametrization for R from [Whi90] is used. Instead of the $F_2(x, Q^2)$ from [Koc03] it is also possible to combine g_1 with a different F_2 parametrization, for instance the ALLM parametrization [Abr97]. None of these alternatives has a true physical motivation except for an attempt to describe the measured asymmetries using the PYTHIA model. As can be seen in figure C.2 the data in the 'Transition' region, where the contribution of the low-p_T process is almost 70% at low x are not well described by $\Delta\sigma^{low-p_T} \equiv 0$, but also a very large asymmetry is excluded by the data. Indeed putting $0 < \Delta\sigma^{low-p_T} \approx g_1/F_1 \ll 1$ results in acceptable agreement with the data. Nevertheless, as with this option the PYTHIA model is somehow forced to agree with the data, the difference between $\Delta\sigma^{low-p_T} \equiv 0$ and $\Delta\sigma^{low-p_T} = g_1/F_1$ should be regarded as part of the theoretical (or model-) uncertainty.

c) Another problem arises in the 'Photoproduction' region where x and/or Q^2 are often much smaller than the values covered so far by measurements, i.e., $Q^2 > 0.1$ and $x \geq 10^{-4}$. Then the above method cannot be applied without additional assumptions on the behavior of g_1/F_1 at very small x and Q^2. One option is to put $g_1 \equiv 0 \rightarrow \Delta\sigma^{low-p_T} \equiv 0$ for all values of x and Q^2 smaller than a given minimum. Another option is to extend the model of [Koc03] to $Q^2 \rightarrow 0$. This model involves a Regge approach to parametrize g_1 and F_1, with Q^2 dependent Reggeon intercepts for g_1. The third possibility is to apply the parametrization of the measured A_1 data using functions of the form

$$A_1^p(x) = c_{0,p} + x^{c_{1,p}}\left(1 - e^{-c_{2,p}x}\right) \quad \Longrightarrow \quad A_1^p \overset{x\rightarrow 0}{\rightarrow} c_{0,p} \tag{C.17}$$

$$A_1^d(x) = \left({c_{0,d}}^{c_{1,d}} - x^{c_{1,d}}\right)\left(1 - e^{-c_{2,d}x}\right) \quad \Longrightarrow \quad A_1^d \overset{x\rightarrow 0}{\rightarrow} 0. \tag{C.18}$$

in the unmeasured region as well. This would correspond to setting $g_1/F_1 \equiv const.$ below $x_{min} \approx 10^{-3}$. Also in this case the difference of the various approaches has to be considered as part of the uncertainty.

d) Ignoring the low-p_T contribution, i.e., setting $\Delta\sigma^{low-p_T} = \sigma^{low-p_T} = 0$ and rescaling the fractions of the other subprocesses would be another possibility, however, besides the fact that the cross sections come out way too small for all kinematic regions, also the asymmetries would be significantly larger than the measured ones.

- **diffractive VMD**: As opposed to non-diffractive VMD, the contribution of the diffractive VMD (elastic and single/double dissociative processes) to the cross section can in principle be measured (see. for instance figure 2.17 for HERA data), and for the elastic part the PYTHIA model has been proven to be consistent with the HERMES data (cf. section 4.3). Several models exist predicting a double spin asymmetry in exclusive vector meson production. In some of them the asymmetry depends on the parity of the particle(s) exchanged in the t channel of the reaction. An asymmetry arises if an interference of exchange particles with 'natural' $P = +(-1)^J$ and 'unnatural' parity $P = -(-1)^J$ contributes to the cross section, where J is the total angular momentum of the exchanged particle. At high energies, the exchanged particle is either pictured as a Pomeron or a di-gluon system which both have natural parity, so no asymmetry is expected. At energies like that of HERMES, Reggeons or a di-quark system with unnatural parity is believed to contribute to the cross section as well, leading to a possible interference between natural and unnatural parity exchange and therefore to double spin asymmetries. The model of Ref. [Fra79] relates the double-spin asymmetry in exclusive ρ^0 production to that in inclusive DIS:

$$A_1^\rho = \frac{2A^N}{1 + (A_1^N)^2} \approx 2A^N. \tag{C.19}$$

This prediction has been found to be consistent with the double spin asymmetries of exclusive ρ^0 measured by HERMES on proton and deuteron targets [Air03b]. Another model uses the description of DIS structure functions (F_2 and g_1) within a Regge approach to extract the relevant parameters (intercepts and slopes of exchange trajectories) for the predictions of the cross section and double spin asymmetries of vector meson electroproduction on the proton, neutron and the deuteron [Koc02, Koc03]. At least for the proton also this model seems to be consistent with the measured HERMES data [Air03b], but not so much for the deuteron. The HERMES data themselves have only a rather weak statistical precision. For the asymmetry integrated over x and Q^2 (for $9 < \nu < 22$ GeV) HERMES found $A_1^\rho = 0.23 \pm 0.14(stat.) \pm 0.02(syst.)$ for the proton and $A_1^\rho = -0.04 \pm 0.076(stat.) \pm 0.013(syst.)$ for the deuteron. The asymmetries for exclusive ϕ production were found to be consistent with zero. In the quasi-real photoproduction region all asymmetries were measured to be zero within the (small) statistical uncertainties. For the standard calculation of PYTHIA asymmetries the diffractive VMD processes will be thus considered to be a dilution to the

asymmetry, i.e., $\Delta\sigma^{diffr} \equiv 0$, however, the variation of the result from using the model of [Fra79] (Eq. C.19) for the light vector meson states will tested as well for hadron and pion asymmetries in the 'Transition' and 'SIDIS' regions.

If polarized parton distributions are to be calculated from the PDFLIB they have to be isospin rotated for the neutron target. In PYTHIA, the deuteron is simulated by mixing an equal number of events on proton and neutron. The deuteron asymmetry is then obtained from the proton and neutron asymmetries using

$$A_{\parallel}^{d} = \frac{\sigma_p A_{\parallel}^{p} + \sigma_n A_{\parallel}^{n}}{\sigma_p + \sigma_n} \left[1 - \frac{3}{2}\omega_D\right], \tag{C.20}$$

where $\sigma_{p(n)}$ are the total proton (neutron) cross sections computed by the MC. The factor in angular brackets accounts for the (small) probability $\omega_D = 0.05 \pm 0.01$ for the deuteron to be in a D state, reducing its polarization [Mac87]. Technically, the correct deuteron asymmetries and subprocess fractions can be retrieved if each event generated on a neutron target is weighted with the factor σ_n/σ_p, and if for each run on proton and neutron the factor $1 - \frac{3}{2}\omega_D$ is applied to all asymmetry weights calculated from parton distributions. The factor $\sigma_n/\sigma_p \approx 0.9$ in the 'Transition' region, in the 'Photoproduction' region it is around 0.98 and can be safely neglected.

For charged unidentified hadrons in the 'Transition' region the resulting PYTHIA asymmetries are shown in figure C.2 as a function of x for four different options of treating the VMD processes. The contribution from hard processes involving a target gluon of 5% maximum at small x has been excluded from both the polarized and unpolarized cross sections. The photon parton polarizations have been put to zero. The full curve was obtained by setting $\Delta\sigma^{diffr} \equiv 0$ and

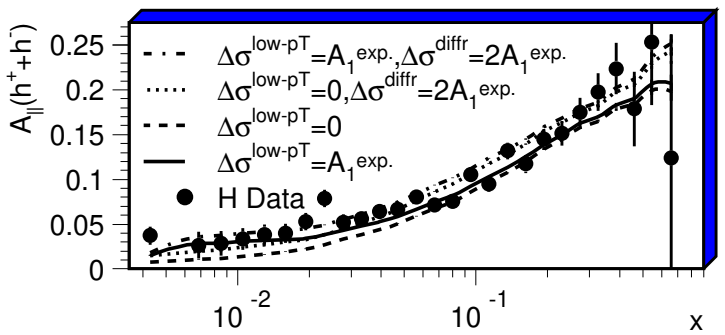

Figure C.2: The asymmetry for charged hadrons as a function of x from the hydrogen data (dots) and from PYTHIA. The different curves correspond to various methods to describe the asymmetry of VMD processes (see text for details).

$\Delta\sigma^{low-p_T}/\sigma^{low-p_T} = A_1(x)$, with A_1^{exp} from the parametrization of experimental data, Eq. C.17. The dashed curve is the result of regarding all VMD processes as a dilution, $A^{VMD} \equiv 0$ which is obviously too low at small x, where the contribution from low-p_T processes is large. For the dotted curve the low-p_T asymmetry was put to zero, but the asymmetry of diffractive VMD to the value of Eq. C.19 with A_1^{exp} from Eq. C.17. The dash-dotted curve finally is obtained using Eq. C.19 for diffractive *and* $\Delta\sigma^{low-p_T}/\sigma^{low-p_T} = A_1(x)$ for non-diffractive VMD. Apparently, the three asymmetries where any of the VMD asymmetries is different from zero describe the data equally well. [1] In the 'SIDIS' region a diffractive asymmetry $A_1^{diffr} \approx 2A_1^{exp}$ overestimates the data significantly, however. Table C.1 gives the χ^2/ndf obtained for the asymmetries of charged hadrons vs. x in the 'Transition' and 'SIDIS' regions for 27 resp. 9 degrees of freedom.

The photoproduction asymmetries of positive and negative pions with $4 < p < 13.8$ GeV on the hydrogen target are shown in figure C.3 as a function of transverse momentum. Also here, the contribution from PGF and anomalous processes involving a target gluon was disregarded. It is between 10 and 20% at $p_T > 1$ GeV, at smaller p_T it is negligible. The different curves in the figure represent four different methods of treating the low-p_T process which constitutes the dominant contribution to the cross section ($> 50\%$) at small p_T. For the solid line, the experimental $A_1(x)$

[1] Remember that the contribution from PGF has been neglected, this contribution would shift all curves down ($\Delta G > 0$) or up ($\Delta G < 0$) by a few per mill at small x.

Region	$A^{low-pT} \neq 0$				$A^{low-pT} = 0$	
	$A^{diffr} = 0$			$A^{diffr} \approx 2A_1(x)$	$A^{diffr} = 0$	
'Transition'	1.820	1.769	1.883	2.200	2.080	3.956
'SIDIS'	1.947	1.939	1.861	5.947	3.819	2.364

Table C.1: χ^2/ndf from PYTHIA asymmetries compared to data asymmetries of charged hadrons as a function of x for different methods of handling VMD processes. 1st column: $A^{diffr} = 0$, $A^{low-p_T} = A_1(x)$ with A_1^{exp} from Eq. C.17, 2nd column: $A^{diffr} = 0$, $A^{low-p_T} = g_1(x,Q^2)/F_1(x,Q^2)$ with g_1 and F_2 from [Koc03], R from [Whi90], 3rd column: like second, but with F_2 from [Abr97], 4th column: $A^{low-p_T} = A_1(x)$ as in column 1, $A^{diffr} \approx 2A_1(x)$ (Eq. C.19, with A_1 from Eq. C.17, 5th column: $A^{low-p_T} = 0$, $A^{diffr} \approx 2A_1(x)$ as in column 4, 6th column: $A^{low-p_T} = 0$, $A^{diffr} = 0$.

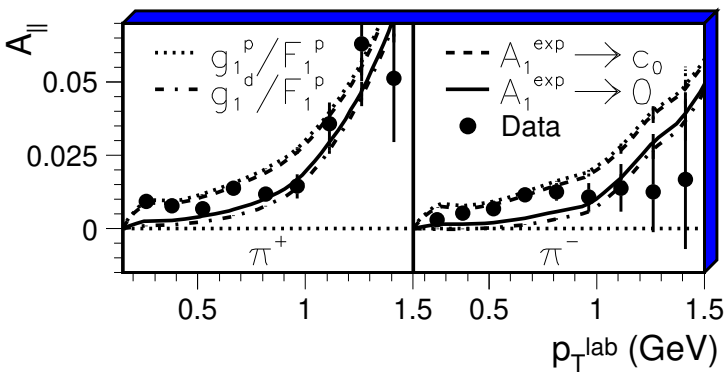

Figure C.3: The asymmetry for positive (left) and negative (right) pions with $4 < p < 13.8$ GeV as a function of p_T from the hydrogen data (dots) and from PYTHIA. The different curves correspond to various methods to describe the asymmetry of the low-p_T process (see text for details).

parametrization Eq. C.17 was applied to the low-p_T process if $Q^2 > 0.1$ GeV^2 and $x > 10^{-5}$. This is only true for less than 10% of the events. For the other 90% of the low-p_T events $A^{low-p_T} = 0$. The solid curve will thus not differ much from a curve where the low-p_T process is treated as a dilution to the asymmetry (not shown). The dotted curve corresponds to the model of Ref. [Koc03], where a different intercept of the normal f_1 and a_1 Reggeons is used than in the paper (-0.14 instead of 0.62) [Koc04]. For F_2 the parametrization of [Abr97] was used which is known to reproduce the world data down to $Q^2 = 0$. For the adaption of this model to the quasireal photoproduction limit it was necessary to rewrite the equation for g_1 [Koc04]

$$g_1 \sim \sum A_i \frac{1}{x^{\alpha_{R,i}(0)}} \quad \rightarrow \quad g_1 \sim \sum A_i \left(\frac{W^2}{M^2}\right)^{\alpha_{R,i}(0)} \tag{C.21}$$

as a function of W^2 rather than x. Here, the $\alpha_{R,i}(0)$ are the intercepts of the (three) different Reggeons and the A_i are the corresponding couplings. An additional factor in front of this Q^2 independent form of g_1 is left as a free parameter and can be fitted to the data. The dotted curve is the result of the matching of the proton data with such a factor. In the model, the same factor should also describe the deuteron data, which is not the case. As the deuteron asymmetries are slightly negative at small p_T it will not be possible to find a common factor describing both data sets at the same time. It was suggested to fit two independent factors for each the 'anomalous' and the 'regular' Reggeons of the model simultaneously to the proton and deuteron data [Koc04] instead. However, this would have been a rather elaborate task. Still the model can be used by taking the difference between the curve describing the proton data (at $p_T < 0.8$ GeV) to one obtained with a common factor that describes the deuteron data (the dash-dotted curve in figure C.3) for an estimate of the model uncertainty associated with the low-p_T process. Interestingly enough, the proton data can as well be described if for the low-p_T asymmetry the experimental parametrization is used without setting $A^{low-p_T} = 0$ at small x and $Q^2 < 0.1$ GeV^2. As Eq. C.17 approaches a constant for $x < 10^{-3}$, the asymmetry survives also at small x with the result as depicted by the dashed curve. This might be accidental, though, as the same good agreement cannot be achieved for the deuteron data.

C.2 The Statistical Error of $\Delta G/G$

The derivation of the statistical error of $\Delta G/G$ extracted with the Monet Carlo method (cf. section 5.1.1) will be outlined here. The gluon polarization can be obtained from Eq. 5.5:

$$\left\langle \frac{\Delta G}{G} \right\rangle (p_T) = \frac{1}{N_{sig}(p_T)\langle \hat{a}^{sig} \rangle (p_T)} \left[N_{tot}(p_T) A_{\parallel}^{meas}(p_T) - N_{BG}(p_T) A_{\parallel}^{BG}(p_T) \right]. \tag{C.22}$$

with

$$A_{\parallel}^{BG} = \frac{1}{N_{BG}} \sum_{i=1}^{N_{BG}} a_i^{BG}. \tag{C.23}$$

The statistical error of the gluon polarization, taking into account the MC statistical errors on the background events N_{BG}, the signal events N_{sig}, the background asymmetry $A_{\parallel}^{BG}$, the hard subprocess asymmetry of PGF $\langle \hat{a}^{sig} \rangle$ and the error of the measured asymmetry $A_{\parallel}^{meas}$ is then

$$\delta^2 \left\langle \frac{\Delta G}{G} \right\rangle = \sum_i \left[\frac{\partial}{\partial x_i} \left\langle \frac{\Delta G}{G} \right\rangle \right]^2 \delta^2 x_i \tag{C.24}$$

assuming a Gaussian error distribution of all independent variables x_i. The partial derivatives are in detail:

$$\frac{\partial}{\partial N_{sig}} \left\langle \frac{\Delta G}{G} \right\rangle = \frac{1}{N_{sig}\langle \hat{a}^{sig} \rangle} \left(1 - \frac{N_{tot}}{N_{sig}} \right) A_{\parallel}^{meas}, \tag{C.25}$$

$$\begin{aligned} \frac{\partial}{\partial N_{BG}} \left\langle \frac{\Delta G}{G} \right\rangle &= \frac{1}{N_{sig}\langle \hat{a}^{sig} \rangle} \left(A_{\parallel}^{meas} - A_{\parallel}^{BG} + N_{BG} \frac{\sum_{i=1}^{N_{BG}} a_i^{BG}}{N_{BG}^2} \right) \\ &= \frac{1}{N_{sig}\langle \hat{a}^{sig} \rangle} A_{\parallel}^{meas}, \end{aligned} \tag{C.26}$$

$$\frac{\partial}{\partial A_{\parallel}^{meas}} \left\langle \frac{\Delta G}{G} \right\rangle = \frac{N_{tot}}{N_{sig}\langle \hat{a}^{sig} \rangle}, \tag{C.27}$$

$$\frac{\partial}{\partial A_{\parallel}^{BG}} \left\langle \frac{\Delta G}{G} \right\rangle = \frac{N_{BG}}{N_{sig}\langle \hat{a}^{sig} \rangle}, \tag{C.28}$$

$$\frac{\partial}{\partial \langle \hat{a}^{sig} \rangle} \left\langle \frac{\Delta G}{G} \right\rangle = -\frac{N_{tot}}{N_{sig}\langle \hat{a}^{sig} \rangle} \frac{1}{\langle \hat{a}^{sig} \rangle} \left(N_{tot} A_{\parallel}^{meas} - N_{BG} A_{\parallel}^{BG} \right). \tag{C.29}$$

Using this together with Eq. C.24 and $\delta^2 N_{BG} = N_{BG}$, $\delta^2 N_{tot} = N_{tot}$ the total statistical error becomes

$$\begin{aligned} \delta^2 \left\langle \frac{\Delta G}{G} \right\rangle &= \frac{1}{N_{sig}^2 \langle \hat{a}^{sig} \rangle^2} \Bigg[N_{tot}^2 \delta^2 A_{\parallel}^{meas} + N_{BG}^2 \delta^2 A_{\parallel}^{BG} + \frac{N_{BG}}{N_{sig}} N_{tot} \left(A_{\parallel}^{meas} \right)^2 \\ &\quad + \left(N_{tot} A_{\parallel}^{meas} - N_{BG} A_{\parallel}^{BG} \right)^2 \frac{\delta^2 \langle \hat{a}^{sig} \rangle}{\langle \hat{a}^{sig} \rangle^2} \Bigg]. \end{aligned} \tag{C.30}$$

Appendix D

Tables

D.1 Standard PYTHIA Parameter Settings

MSTP(1)=2	maximum number of particle generations
MSTP(17)=6	Parametrization of $R = \sigma_L/\sigma_T$, cf. section 4.3.1
MSTP(18)=3	cf. section 4.1.4
MSTP(19)=4	cf. section 4.1.4
MSTP(20)=0	cf. sections 4.1.4, 4.3.1
MSTP(51)=4046	Proton PDF CTEQ5LO [Lai00]
MSTP(52)=1	Proton PDF from PDFlib
MSTP(58)=3	maximum number of quark flavors used for parton distributions
MSTP(61)=0	Initial state QED and QCD radiation switched off
MSTP(71)=0	Final state QED and QCD radiation switched off
MSTP(81)=0	Multiple interactions switched off
MSTP(92)=4	energy partitioning of jets in hadron or resolved photon remnant
MSTP(101)=1	structure of diffractive system (forward quark and diquark)
PARP(2)=7	minimum center of mass energy
PARP(18)=0.17	suppression factor of GVMD compared to VMD processes
PARP(91)=0.44 GeV	primordial k_T of the nucleon (Gaussian width)
PARP(93)=2 GeV	upper cutoff of primordial k_T distribution inside nucleon
PARP(99)=0.44 GeV	primordial k_T of the photon (Gaussian width)
PARP(100)=2 GeV	upper cutoff of primordial k_T distribution inside photon
PARP(102)=0.5 GeV	start of the mass spectrum of diffractive states is at PARP(102) above the mass of the diffractively excited particle
PARP(103)=0.5 GeV	A diffractive state decays isotropically if its mass is less than PARP(103) above the mass of the diffractively excited particle, otherwise string fragmentation is applied
PARP(104)=0.3 GeV	minimum energy above threshold for which total hadronic cross sections are defined
PARP(111)=0 GeV	minimum invariant mass of the remnant hadronic system, after the interacting partons have been taken away
PARP(161)=2.69	coupling $f_V^2/4\pi$ of photon to ρ^0 [Gro97]
PARP(162)=24.6	coupling $f_V^2/4\pi$ of photon to ω [Gro97]
PARP(163)=18.8	coupling $f_V^2/4\pi$ of photon to ϕ [Gro97]
PARP(165)=0.33	multiplicative factor for the expression of σ_L^{VMD} given by MSTP(17)

Table D.1: Standard PYTHIA parameter settings tuned to HERMES data which are different from the default. The default settings can be found in [Sjö01]. Continued on the next page.

PARJ(1)=0.25	suppression of diquark compared to quark production in the filed of a string
PARJ(2)=0.12	suppression of strange compared to up/down quark production in the filed of a string
PARJ(3)=0.25	suppression of strange diquark to compared to strange quark production in the filed of a string
PARJ(11)=0.25	probability that a light meson in fragmentation has spin 1
PARJ(12)=0.3	probability that a strange meson in fragmentation has spin 1
PARJ(21)=0.38 GeV	width of the p_T-distribution of the primary hadron in string fragmentation
PARJ(23)=0.03	fraction of the Gaussian p_T distribution with a σ larger than that given by PARJ(21) by a factor PARJ(24)
PARJ(24)=2.5	factor for the use of PARJ(23)
PARJ(33)=0.2 GeV	minimum energy for which the fragmentation of a jet system is stopped
PARJ(41)=1.1	parameter a for the LUND symmetric fragmentation function
PARJ(42)=0.37	parameter b for the LUND symmetric fragmentation function
PARJ(45)=0.8	factor to multiplied with PARJ(41) to obtain the a parameter for diquark production
MSTJ(12)=1	baryon production model, diquark treated as a unit
MSTU(112)=4	nominal number of flavors used for Λ in the expression for α_s
MSTU(113)=4	minimal number of flavors used in the expression for α_s
MSTU(114)=4	maximal number of flavors used in the expression for α_s

Table D.2: Standard PYTHIA parameter settings tuned to HERMES data which are different from the default (continued from the previous page). The default settings can be found in [Sjö01].

D.2 Measured Asymmetries

D.2.1 Photoproduction Region

p_T-bin (GeV)	$\langle p_T \rangle$ (GeV)	$A_\parallel$	$\Delta A_\parallel$ (stat.)	$\Delta A_\parallel$ (syst.,total)	$\Delta A_\parallel$ (syst., pol.)
0–0.15	0.12	0.0156	0.0018	+0.0008/-0.0008	±0.0008
0.15–0.3	0.23	0.0109	0.0007	+0.0006/-0.0006	±0.0006
0.3–0.45	0.37	0.0097	0.0007	+0.0005/-0.0005	±0.0005
0.45–0.6	0.52	0.0101	0.0009	+0.0005/-0.0005	±0.0005
0.6–0.75	0.67	0.0130	0.0014	+0.0007/-0.0007	±0.0007
0.75–0.9	0.81	0.0148	0.0021	+0.0008/-0.0008	±0.0008
0.9–1.05	0.96	0.0168	0.0033	+0.0009/-0.0009	±0.0009
1.05–1.2	1.11	0.0353	0.0055	+0.0018/-0.0019	±0.0018
1.2–1.35	1.26	0.0565	0.0095	+0.0029/-0.0030	±0.0029
1.35–1.5	1.41	0.0496	0.0157	+0.0026/-0.0026	±0.0026
1.5–1.65	1.56	0.0859	0.0257	+0.0045/-0.0045	±0.0045
1.65–1.8	1.71	0.1372	0.0412	+0.0072/-0.0072	±0.0072
1.8–2.	1.88	0.1665	0.0598	+0.0087/-0.0087	±0.0087
2–2.5	2.17	0.1287	0.0811	+0.0067/-0.0068	±0.0067
2.5–5	3.04	0.0379	0.1418	+0.0020/-0.0022	±0.0020

Table D.3: Photoproduction asymmetry and its error for positive hadrons on hydrogen target (combined 1996 and 1997 data). The first column gives the range of each bin in the lab transverse momentum, the second the average p_T in that bin, the third the measured asymmetry, the fourth its statistical error, the fifth its total (in general asymmetric) systematic error, the sixth the contribution of the beam and target polarization uncertainties only.

p_T-bin (GeV)	$\langle p_T \rangle$ (GeV)	$A_\parallel$	$\Delta A_\parallel$ (stat.)	$\Delta A_\parallel$ (syst.,total)	$\Delta A_\parallel$ (syst., pol.)
0–0.15	0.12	0.0109	0.0019	+0.0006/-0.0006	±0.0006
0.15–0.3	0.23	0.0082	0.0007	+0.0004/-0.0004	±0.0004
0.3–0.45	0.37	0.0079	0.0008	+0.0004/-0.0004	±0.0004
0.45–0.6	0.52	0.0096	0.0011	+0.0005/-0.0005	±0.0005
0.6–0.75	0.66	0.0119	0.0016	+0.0006/-0.0006	±0.0006
0.75–0.9	0.81	0.0105	0.0026	+0.0005/-0.0006	±0.0005
0.9–1.05	0.96	0.0083	0.0042	+0.0004/-0.0004	±0.0004
1.05–1.2	1.11	0.0098	0.0070	+0.0005/-0.0005	±0.0005
1.2–1.35	1.26	0.0161	0.0118	+0.0008/-0.0008	±0.0008
1.35–1.5	1.41	0.0062	0.0197	+0.0003/-0.0003	±0.0003
1.5–1.65	1.56	-0.0795	0.0328	+0.0042/-0.0041	±0.0041
1.65–1.8	1.71	-0.0381	0.0531	+0.0020/-0.0020	±0.0020
1.8–2.	1.88	0.0405	0.0777	+0.0021/-0.0021	±0.0021
2–2.5	2.18	0.0521	0.1129	+0.0027/-0.0027	±0.0027
2.5–5	3.04	-0.0206	0.1542	+0.0011/-0.0011	±0.0011

Table D.4: Photoproduction asymmetry and its error for negative hadrons on hydrogen target (combined 1996 and 1997 data). The first column gives the range of each bin in the lab transverse momentum, the second the average p_T in that bin, the third the measured asymmetry, the fourth its statistical error, the fifth its total (in general asymmetric) systematic error, the sixth the contribution of the beam and target polarization uncertainties only.

p_T-bin (GeV)	$\langle p_T \rangle$ (GeV)	$A_\parallel$	$\Delta A_\parallel$ (stat.)	$\Delta A_\parallel$ (syst.,total)	$\Delta A_\parallel$ (syst., pol.)
0–0.15	0.15	-0.1728	0.4338	+0.0090/-0.0090	±0.0090
0.15–0.3	0.26	0.0095	0.0024	+0.0005/-0.0005	±0.0005
0.3–0.45	0.38	0.0077	0.0013	+0.0004/-0.0004	±0.0004
0.45–0.6	0.52	0.0068	0.0014	+0.0004/-0.0004	±0.0004
0.6–0.75	0.67	0.0137	0.0018	+0.0007/-0.0007	±0.0007
0.75–0.9	0.81	0.0117	0.0026	+0.0006/-0.0006	±0.0006
0.9–1.05	0.96	0.0145	0.0041	+0.0008/-0.0008	±0.0008
1.05–1.2	1.11	0.0359	0.0071	+0.0019/-0.0019	±0.0019
1.2–1.35	1.26	0.0630	0.0126	+0.0033/-0.0033	±0.0033
1.35–1.5	1.41	0.0514	0.0217	+0.0027/-0.0027	±0.0027
1.5–1.65	1.56	0.0650	0.0367	+0.0034/-0.0034	±0.0034
1.65–1.8	1.71	0.0437	0.0629	+0.0023/-0.0024	±0.0023
1.8–2.	1.88	0.1670	0.0991	+0.0087/-0.0087	±0.0087
2–2.5	2.13	0.0217	0.1667	+0.0011/-0.0013	±0.0011
2.5–5	2.53				

Table D.5: Photoproduction asymmetry and its error for positive pions with $4 < p < 13.8$ GeV on hydrogen target (combined 1996 and 1997 data). The first column gives the range of each bin in the lab transverse momentum, the second the average p_T in that bin, the third the measured asymmetry, the fourth its statistical error, the fifth its total (in general asymmetric) systematic error, the sixth the contribution of the beam and target polarization uncertainties only.

p_T-bin (GeV)	$\langle p_T \rangle$ (GeV)	$A_\parallel$	$\Delta A_\parallel$ (stat.)	$\Delta A_\parallel$ (syst.,total)	$\Delta A_\parallel$ (syst., pol.)
0–0.15	0.15	-0.5613	0.4101	+0.0294/-0.0293	±0.0293
0.15–0.3	0.26	0.0030	0.0025	+0.0002/-0.0002	±0.0002
0.3–0.45	0.38	0.0054	0.0014	+0.0003/-0.0003	±0.0003
0.45–0.6	0.52	0.0068	0.0015	+0.0004/-0.0004	±0.0004
0.6–0.75	0.67	0.0115	0.0020	+0.0006/-0.0006	±0.0006
0.75–0.9	0.81	0.0126	0.0030	+0.0007/-0.0007	±0.0007
0.9–1.05	0.96	0.0109	0.0048	+0.0006/-0.0006	±0.0006
1.05–1.2	1.11	0.0139	0.0081	+0.0007/-0.0007	±0.0007
1.2–1.35	1.26	0.0126	0.0138	+0.0007/-0.0007	±0.0007
1.35–1.5	1.41	0.0169	0.0237	+0.0009/-0.0009	±0.0009
1.5–1.65	1.56	-0.0770	0.0407	+0.0041/-0.0040	±0.0040
1.65–1.8	1.71	-0.0568	0.0698	+0.0030/-0.0030	±0.0030
1.8–2.	1.87	-0.0721	0.1105	+0.0038/-0.0038	±0.0038
2–2.5	2.12	0.1339	0.2135	+0.0071/-0.0070	±0.0070
2.5–5					

Table D.6: Photoproduction asymmetry and its error for negative pions with $4 < p < 13.8$ GeV on hydrogen target (combined 1996 and 1997 data). The first column gives the range of each bin in the lab transverse momentum, the second the average p_T in that bin, the third the measured asymmetry, the fourth its statistical error, the fifth its total (in general asymmetric) systematic error, the sixth the contribution of the beam and target polarization uncertainties only.

p_T-bin (GeV)	$\langle p_T \rangle$ (GeV)	$A_\parallel$	$\Delta A_\parallel$ (stat.)	$\Delta A_\parallel$ (syst.,total)	$\Delta A_\parallel$ (syst., pol.)
0–0.15	0.12	0.0001	0.0010	+0.0000/-0.0000	±0.0000
0.15–0.3	0.23	-0.0014	0.0004	+0.0001/-0.0001	±0.0001
0.3–0.45	0.37	-0.0033	0.0004	+0.0001/-0.0001	±0.0001
0.45–0.6	0.52	-0.0028	0.0005	+0.0001/-0.0001	±0.0001
0.6–0.75	0.67	-0.0034	0.0008	+0.0001/-0.0001	±0.0001
0.75–0.9	0.81	-0.0003	0.0012	+0.0000/-0.0000	±0.0000
0.9–1.05	0.96	-0.0005	0.0019	+0.0000/-0.0000	±0.0000
1.05–1.2	1.11	0.0055	0.0031	+0.0002/-0.0002	±0.0002
1.2–1.35	1.26	0.0128	0.0053	+0.0005/-0.0005	±0.0005
1.35–1.5	1.41	0.0233	0.0087	+0.0009/-0.0009	±0.0009
1.5–1.65	1.56	0.0436	0.0143	+0.0017/-0.0017	±0.0017
1.65–1.8	1.71	0.0766	0.0230	+0.0030/-0.0030	±0.0030
1.8–2.	1.88	0.0026	0.0328	+0.0001/-0.0003	±0.0001
2–2.5	2.16	0.0354	0.0445	+0.0014/-0.0015	±0.0014
2.5–5	3.04	-0.0147	0.0775	+0.0007/-0.0006	±0.0006

Table D.7: Photoproduction asymmetry and its error for positive hadrons on deuterium target (2000 data). The first column gives the range of each bin in the lab transverse momentum, the second the average p_T in that bin, the third the measured asymmetry, the fourth its statistical error, the fifth its total (in general asymmetric) systematic error, the sixth the contribution of the beam and target polarization uncertainties only.

p_T-bin (GeV)	$\langle p_T \rangle$ (GeV)	$A_\parallel$	$\Delta A_\parallel$ (stat.)	$\Delta A_\parallel$ (syst.,total)	$\Delta A_\parallel$ (syst., pol.)
0–0.15	0.12	-0.0027	0.0011	+0.0001/-0.0001	±0.0001
0.15–0.3	0.23	-0.0023	0.0004	+0.0001/-0.0001	±0.0001
0.3–0.45	0.37	-0.0044	0.0004	+0.0002/-0.0002	±0.0002
0.45–0.6	0.52	-0.0053	0.0006	+0.0002/-0.0002	±0.0002
0.6–0.75	0.66	-0.0037	0.0009	+0.0002/-0.0001	±0.0001
0.75–0.9	0.81	-0.0030	0.0014	+0.0001/-0.0001	±0.0001
0.9–1.05	0.96	-0.0016	0.0022	+0.0001/-0.0001	±0.0001
1.05–1.2	1.11	-0.0026	0.0037	+0.0001/-0.0001	±0.0001
1.2–1.35	1.26	-0.0015	0.0061	+0.0001/-0.0001	±0.0001
1.35–1.5	1.41	0.0055	0.0100	+0.0002/-0.0002	±0.0002
1.5–1.65	1.56	0.0032	0.0166	+0.0001/-0.0001	±0.0001
1.65–1.8	1.71	-0.0037	0.0266	+0.0002/-0.0001	±0.0001
1.8–2.	1.88	-0.0066	0.0393	+0.0003/-0.0003	±0.0003
2–2.5	2.16	-0.0680	0.0550	+0.0027/-0.0027	±0.0027
2.5–5	3.08	0.1588	0.0921	+0.0063/-0.0062	±0.0062

Table D.8: Photoproduction asymmetry and its error for negative hadrons on deuterium target (2000 data). The first column gives the range of each bin in the lab transverse momentum, the second the average p_T in that bin, the third the measured asymmetry, the fourth its statistical error, the fifth its total (in general asymmetric) systematic error, the sixth the contribution of the beam and target polarization uncertainties only.

p_T-bin (GeV)	$\langle p_T \rangle$ (GeV)	$A_\parallel$	$\Delta A_\parallel$ (stat.)	$\Delta A_\parallel$ (syst.,total)	$\Delta A_\parallel$ (syst., pol.)	$\Delta A_\parallel$ (syst., RICH)
0–0.15	0.13	-0.0024	0.0020	+0.0001/-0.0001	±0.0001	±0.0000
0.15–0.3	0.24	-0.0033	0.0005	+0.0001/-0.0001	±0.0001	±0.0000
0.3–0.45	0.37	-0.0043	0.0005	+0.0002/-0.0002	±0.0002	±0.0000
0.45–0.6	0.52	-0.0036	0.0006	+0.0001/-0.0002	±0.0001	±0.0000
0.6–0.75	0.66	-0.0047	0.0009	+0.0002/-0.0002	±0.0002	±0.0000
0.75–0.9	0.81	-0.0017	0.0015	+0.0001/-0.0001	±0.0001	±0.0000
0.9–1.05	0.96	-0.0028	0.0024	+0.0001/-0.0001	±0.0001	±0.0000
1.05–1.2	1.11	0.0042	0.0041	+0.0002/-0.0002	±0.0002	±0.0000
1.2–1.35	1.26	0.0181	0.0071	+0.0009/-0.0007	±0.0007	+0.0002
1.35–1.5	1.41	0.0328	0.0122	+0.0016/-0.0013	±0.0013	+0.0004
1.5–1.65	1.56	0.0219	0.0208	+0.0017/-0.0009	±0.0009	+0.0009
1.65–1.8	1.71	0.0482	0.0351	+0.0085/-0.0019	±0.0019	+0.0066
1.8–2.	1.88	0.0519	0.0548	+0.0146/-0.0021	±0.0020	+0.0126
2–2.5	2.13	0.1144	0.0945	+0.0366/-0.0045	±0.0045	+0.0321
2.5–5	2.60	0.3716	0.4672	+0.1190/-0.0145	±0.0145	+0.1043

Table D.9: Photoproduction asymmetry and its error for positive pions with $2 < p < 15$ GeV on deuterium target (2000 data). The first column gives the range of each bin in the lab transverse momentum, the second the average p_T in that bin, the third the measured asymmetry, the fourth its statistical error, the fifth its total (in general asymmetric) systematic error, the sixth the contribution of the beam and target polarization uncertainties only, the seventh the contribution from the RICH unfolding uncertainty.

p_T-bin (GeV)	$\langle p_T \rangle$ (GeV)	$A_\parallel$	$\Delta A_\parallel$ (stat.)	$\Delta A_\parallel$ (syst.,total)	$\Delta A_\parallel$ (syst., pol.)	$\Delta A_\parallel$ (syst., RICH)
0–0.15	0.13	-0.0035	0.0020	+0.0001/-0.0002	±0.0001	-0.0001
0.15–0.3	0.24	-0.0032	0.0005	+0.0001/-0.0001	±0.0001	±0.0000
0.3–0.45	0.37	-0.0051	0.0005	+0.0003/-0.0002	±0.0002	+0.0001
0.45–0.6	0.51	-0.0056	0.0006	+0.0003/-0.0002	±0.0002	+0.0001
0.6–0.75	0.66	-0.0040	0.0010	+0.0002/-0.0002	±0.0002	±0.0000
0.75–0.9	0.81	-0.0037	0.0016	+0.0001/-0.0003	±0.0001	-0.0002
0.9–1.05	0.96	-0.0002	0.0025	+0.0000/-0.0000	±0.0000	±0.0000
1.05–1.2	1.11	-0.0039	0.0042	+0.0002/-0.0009	±0.0002	-0.0007
1.2–1.35	1.26	0.0036	0.0071	+0.0001/-0.0006	±0.0001	-0.0004
1.35–1.5	1.41	0.0101	0.0120	+0.0017/-0.0004	±0.0004	+0.0009
1.5–1.65	1.56	-0.0311	0.0203	+0.0160/-0.0012	±0.0012	+0.0147
1.65–1.8	1.71	0.0074	0.0342	+0.0068/-0.0003	±0.0003	+0.0066
1.8–2.	1.88	-0.0023	0.0538	+0.0027/-0.0001	±0.0001	+0.0026
2–2.5	2.13	0.0474	0.0974	+0.0605/-0.0018	±0.0018	+0.0586
2.5–5	2.62	-0.8843	0.7071	+1.1324/-0.0344	±0.0344	+1.0974

Table D.10: Photoproduction asymmetry and its error for negative pions with $2 < p < 15$ GeV on deuterium target (2000 data). The first column gives the range of each bin in the lab transverse momentum, the second the average p_T in that bin, the third the measured asymmetry, the fourth its statistical error, the fifth its total (in general asymmetric) systematic error, the sixth the contribution of the beam and target polarization uncertainties only, the seventh the contribution from the RICH unfolding uncertainty.

p_T-bin (GeV)	$\langle p_T \rangle$ (GeV)	$A_\parallel$	$\Delta A_\parallel$ (stat.)	$\Delta A_\parallel$ (syst.,total)	$\Delta A_\parallel$ (syst., pol.)	$\Delta A_\parallel$ (syst., RICH)
0–0.15	0.13	0.0185	0.0121	+0.0150/	-0.0007±0.0007	+0.0142
0.15–0.3	0.24	0.0066	0.0029	+0.0049/	-0.0003±0.0003	+0.0046
0.3–0.45	0.37	0.0034	0.0021	+0.0020/	-0.0001±0.0001	+0.0018
0.45–0.6	0.52	0.0021	0.0022	+0.0008/	-0.0001±0.0001	+0.0007
0.6–0.75	0.67	0.0054	0.0027	+0.0015/	-0.0002±0.0002	+0.0013
0.75–1	0.85	0.0094	0.0033	+0.0027/	-0.0004±0.0004	+0.0023
1–1.3	1.10	0.0210	0.0070	+0.0058/	-0.0008±0.0008	+0.0050
1.3–1.6	1.40	0.0359	0.0195	+0.0093/	-0.0014±0.0014	+0.0079
1.6–2	1.72	0.1129	0.0521	+0.0282/	-0.0044±0.0044	+0.0238
2–3.5	2.17	-0.2007	0.1705	+0.0501/	-0.0078±0.0078	+0.0422

Table D.11: Photoproduction asymmetry and its error for positive kaons with $2 < p < 15$ GeV on deuterium target (2000 data). The first column gives the range of each bin in the lab transverse momentum, the second the average p_T in that bin, the third the measured asymmetry, the fourth its statistical error, the fifth its total (in general asymmetric) systematic error, the sixth the contribution of the beam and target polarization uncertainties only, the seventh the contribution from the RICH unfolding uncertainty.

p_T-bin (GeV)	$\langle p_T \rangle$ (GeV)	$A_\parallel$	$\Delta A_\parallel$ (stat.)	$\Delta A_\parallel$ (syst.,total)	$\Delta A_\parallel$ (syst., pol.)	$\Delta A_\parallel$ (syst., RICH)
0–0.15	0.13	0.0077	0.0142	+0.0092/-0.0003	±0.0003	+0.0089
0.15–0.3	0.24	-0.0020	0.0033	+0.0020/-0.0001	±0.0001	+0.0019
0.3–0.45	0.37	0.0025	0.0025	+0.0014/-0.0001	±0.0001	+0.0013
0.45–0.6	0.52	-0.0009	0.0029	+0.0003/-0.0000	±0.0000	+0.0002
0.6–0.75	0.67	-0.0050	0.0038	+0.0015/-0.0002	±0.0002	+0.0013
0.75–1	0.85	-0.0041	0.0046	+0.0013/-0.0002	±0.0002	+0.0012
1–1.3	1.10	-0.0089	0.0098	+0.0049/-0.0003	±0.0003	+0.0046
1.3–1.6	1.40	0.0145	0.0275	+0.0133/-0.0006	±0.0006	+0.0127
1.6–2	1.72	-0.0639	0.0792	+0.0694/-0.0025	±0.0025	+0.0669
2–3.5	2.22	-0.2993	0.2560	+0.3250/-0.0117	±0.0117	+0.3134

Table D.12: Photoproduction asymmetry and its error for negative kaons with $2 < p < 15$ GeV on deuterium target (2000 data). The first column gives the range of each bin in the lab transverse momentum, the second the average p_T in that bin, the third the measured asymmetry, the fourth its statistical error, the fifth its total (in general asymmetric) systematic error, the sixth the contribution of the beam and target polarization uncertainties only, the seventh the contribution from the RICH unfolding uncertainty.

D.2.2 'Transition' Region

p_T-bin (GeV)	$\langle p_T \rangle$ (GeV)	$A_\parallel$	$\Delta A_\parallel$ (stat.)	$\Delta A_\parallel$ (syst.,total)	$\Delta A_\parallel$ (syst., pol.)
0–0.15	0.10	0.0897	0.0073	+0.0051/-0.0047	±0.0047
0.15–0.3	0.23	0.0860	0.0049	+0.0049/-0.0045	±0.0045
0.3–0.45	0.37	0.0813	0.0053	+0.0046/-0.0042	±0.0042
0.45–0.6	0.52	0.0787	0.0068	+0.0044/-0.0041	±0.0041
0.6–0.75	0.67	0.0654	0.0096	+0.0037/-0.0034	±0.0034
0.75–1	0.85	0.0692	0.0122	+0.0039/-0.0036	±0.0036
1–1.3	1.11	0.1020	0.0238	+0.0057/-0.0053	±0.0053
1.3–1.6	1.40	0.1464	0.0605	+0.0082/-0.0076	±0.0076
1.6–2	1.72	0.0922	0.1510	+0.0048/-0.0054	±0.0048
2–3.5	2.10	-1.1111	0.7652	+0.0632/-0.0577	±0.0577

Table D.13: 'Transition' region asymmetry and its error for positive hadrons on hydrogen target (combined 1996 and 1997 data). The first column gives the range of each bin in the lab transverse momentum, the second the average p_T in that bin, the third the measured asymmetry, the fourth its statistical error, the fifth its total (in general asymmetric) systematic error, the sixth the contribution of the beam and target polarization uncertainties only.

p_T-bin (GeV)	$\langle p_T \rangle$ (GeV)	$A_\parallel$	$\Delta A_\parallel$ (stat.)	$\Delta A_\parallel$ (syst.,total)	$\Delta A_\parallel$ (syst., pol.)
0–0.15	0.10	0.0636	0.0089	+0.0036/-0.0033	±0.0033
0.15–0.3	0.23	0.0605	0.0059	+0.0035/-0.0031	±0.0032
0.3–0.45	0.37	0.0479	0.0065	+0.0027/-0.0025	±0.0025
0.45–0.6	0.52	0.0635	0.0085	+0.0036/-0.0033	±0.0033
0.6–0.75	0.67	0.0527	0.0122	+0.0030/-0.0028	±0.0028
0.75–1	0.85	0.0707	0.0160	+0.0040/-0.0039	±0.0037
1–1.3	1.11	0.1367	0.0315	+0.0078/-0.0071	±0.0071
1.3–1.6	1.40	0.0459	0.0816	+0.0029/-0.0024	±0.0024
1.6–2	1.71	-0.0226	0.2018	+0.0012/-0.0012	±0.0012
2–3.5	2.15	1.4782	1.4182	+0.0851/-0.0767	±0.0767

Table D.14: 'Transition' region asymmetry and its error for negative hadrons on hydrogen target (combined 1996 and 1997 data). The first column gives the range of each bin in the lab transverse momentum, the second the average p_T in that bin, the third the measured asymmetry, the fourth its statistical error, the fifth its total (in general asymmetric) systematic error, the sixth the contribution of the beam and target polarization uncertainties only.

p_T-bin (GeV)	$\langle p_T \rangle$ (GeV)	$A_\parallel$	$\Delta A_\parallel$ (stat.)	$\Delta A_\parallel$ (syst.,total)	$\Delta A_\parallel$ (syst., pol.)
0–0.15	0.10	0.1222	0.0193	+0.0070/-0.0064	±0.0064
0.15–0.3	0.23	0.0910	0.0113	+0.0051/-0.0047	±0.0047
0.3–0.45	0.38	0.0716	0.0095	+0.0041/-0.0037	±0.0037
0.45–0.6	0.52	0.0712	0.0102	+0.0040/-0.0037	±0.0037
0.6–0.75	0.67	0.0538	0.0130	+0.0031/-0.0028	±0.0028
0.75–1	0.85	0.0811	0.0161	+0.0046/-0.0042	±0.0042
1–1.3	1.11	0.1087	0.0315	+0.0059/-0.0057	±0.0057
1.3–1.6	1.40	0.1538	0.0836	+0.0085/-0.0080	±0.0080
1.6–2	1.72	0.1030	0.2235	+0.0054/-0.0066	±0.0054
2–3.5					

Table D.15: 'Transition' region asymmetry and its error for positive pions with $4 < p < 13.8$ GeV on hydrogen target (combined 1996 and 1997 data). The first column gives the range of each bin in the lab transverse momentum, the second the average p_T in that bin, the third the measured asymmetry, the fourth its statistical error, the fifth its total (in general asymmetric) systematic error, the sixth the contribution of the beam and target polarization uncertainties only, the seventh the contribution from the RICH unfolding uncertainty.

p_T-bin (GeV)	$\langle p_T \rangle$ (GeV)	$A_\parallel$	$\Delta A_\parallel$ (stat.)	$\Delta A_\parallel$ (syst.,total)	$\Delta A_\parallel$ (syst., pol.)
0–0.15	0.10	0.0481	0.0228	+0.0027/-0.0025	±0.0025
0.15–0.3	0.24	0.0429	0.0132	+0.0025/-0.0022	±0.0022
0.3–0.45	0.38	0.0361	0.0108	+0.0021/-0.0019	±0.0019
0.45–0.6	0.52	0.0504	0.0117	+0.0028/-0.0026	±0.0026
0.6–0.75	0.67	0.0507	0.0149	+0.0029/-0.0026	±0.0026
0.75–1	0.85	0.0610	0.0187	+0.0035/-0.0032	±0.0032
1–1.3	1.11	0.1100	0.0369	+0.0063/-0.0057	±0.0057
1.3–1.6	1.40	0.0204	0.1026	+0.0014/-0.0011	±0.0011
1.6–2	1.71	0.0241	0.2656	+0.0015/-0.0013	±0.0013
2–3.5					

Table D.16: 'Transition' region asymmetry and its error for negative pions with $4 < p < 13.8$ GeV on hydrogen target (combined 1996 and 1997 data). The first column gives the range of each bin in the lab transverse momentum, the second the average p_T in that bin, the third the measured asymmetry, the fourth its statistical error, the fifth its total (in general asymmetric) systematic error, the sixth the contribution of the beam and target polarization uncertainties only, the seventh the contribution from the RICH unfolding uncertainty.

p_T-bin (GeV)	$\langle p_T \rangle$ (GeV)	$A_\parallel$	$\Delta A_\parallel$ (stat.)	$\Delta A_\parallel$ (syst.,total)	$\Delta A_\parallel$ (syst., pol.)
0–0.15	0.10	0.0210	0.0043	+0.0009/-0.0008	±0.0008
0.15–0.3	0.23	0.0199	0.0028	+0.0008/-0.0008	±0.0008
0.3–0.45	0.37	0.0185	0.0030	+0.0008/-0.0007	±0.0007
0.45–0.6	0.52	0.0209	0.0039	+0.0009/-0.0008	±0.0008
0.6–0.75	0.67	0.0201	0.0055	+0.0008/-0.0008	±0.0008
0.75–1	0.85	0.0150	0.0070	+0.0006/-0.0006	±0.0006
1–1.3	1.11	0.0461	0.0138	+0.0018/-0.0018	±0.0018
1.3–1.6	1.40	0.0561	0.0352	+0.0023/-0.0022	±0.0022
1.6–2	1.72	-0.0132	0.0874	+0.0010/-0.0005	±0.0005
2–3.5	2.18	0.2082	0.2896	+0.0088/-0.0081	±0.0081

Table D.17: 'Transition' region asymmetry and its error for positive hadrons on deuterium target (2000 data). The first column gives the range of each bin in the lab transverse momentum, the second the average p_T in that bin, the third the measured asymmetry, the fourth its statistical error, the fifth its total (in general asymmetric) systematic error, the sixth the contribution of the beam and target polarization uncertainties only.

p_T-bin (GeV)	$\langle p_T \rangle$ (GeV)	$A_\parallel$	$\Delta A_\parallel$ (stat.)	$\Delta A_\parallel$ (syst.,total)	$\Delta A_\parallel$ (syst., pol.)
0–0.15	0.10	0.0174	0.0050	+0.0007/-0.0007	±0.0007
0.15–0.3	0.23	0.0123	0.0032	+0.0005/-0.0005	±0.0005
0.3–0.45	0.37	0.0139	0.0035	+0.0006/-0.0005	±0.0005
0.45–0.6	0.52	0.0147	0.0046	+0.0006/-0.0006	±0.0006
0.6–0.75	0.67	0.0064	0.0066	+0.0003/-0.0002	±0.0002
0.75–1	0.85	0.0103	0.0085	+0.0004/-0.0004	±0.0004
1–1.3	1.11	0.0267	0.0170	+0.0011/-0.0010	±0.0010
1.3–1.6	1.40	-0.0523	0.0416	+0.0022/-0.0020	±0.0020
1.6–2	1.72	-0.0393	0.1064	+0.0016/-0.0015	±0.0015
2–3.5	2.18	0.3969	0.3596	+0.0160/-0.0155	±0.0155

Table D.18: 'Transition' region asymmetry and its error for negative hadrons on deuterium target (2000 data). The first column gives the range of each bin in the lab transverse momentum, the second the average p_T in that bin, the third the measured asymmetry, the fourth its statistical error, the fifth its total (in general asymmetric) systematic error, the sixth the contribution of the beam and target polarization uncertainties only.

p_T-bin (GeV)	$\langle p_T \rangle$ (GeV)	$A_\parallel$	$\Delta A_\parallel$ (stat.)	$\Delta A_\parallel$ (syst.,total)	$\Delta A_\parallel$ (syst., pol.)	$\Delta A_\parallel$ (syst., RICH)
0–0.15	0.10	0.0200	0.0065	+0.0010/-0.0008	±0.0008	+0.0002
0.15–0.3	0.23	0.0127	0.0040	+0.0006/-0.0005	±0.0005	+0.0001
0.3–0.45	0.37	0.0144	0.0039	+0.0006/-0.0006	±0.0006	±0.0000
0.45–0.6	0.52	0.0181	0.0049	+0.0008/-0.0009	±0.0007	-0.0002
0.6–0.75	0.66	0.0097	0.0070	+0.0004/-0.0005	±0.0004	-0.0001
0.75–1	0.85	0.0236	0.0092	+0.0010/-0.0009	±0.0009	±0.0000
1–1.3	1.11	0.0345	0.0190	+0.0024/-0.0013	±0.0013	+0.0010
1.3–1.6	1.40	0.0789	0.0521	+0.0064/-0.0031	±0.0031	+0.0033
1.6–2	1.72	0.0340	0.1402	+0.0028/-0.0016	±0.0013	+0.0014
2–3.5	2.18	1.0164	0.6417	+0.0856/-0.0396	±0.0396	+0.0429

Table D.19: 'Transition' region asymmetry and its error for positive pions with $2 < p < 15$ GeV on deuterium target (2000 data). The first column gives the range of each bin in the lab transverse momentum, the second the average p_T in that bin, the third the measured asymmetry, the fourth its statistical error, the fifth its total (in general asymmetric) systematic error, the sixth the contribution of the beam and target polarization uncertainties only.

p_T-bin (GeV)	$\langle p_T \rangle$ (GeV)	$A_\parallel$	$\Delta A_\parallel$ (stat.)	$\Delta A_\parallel$ (syst.,total)	$\Delta A_\parallel$ (syst., pol.)	$\Delta A_\parallel$ (syst., RICH)
0–0.15	0.10	0.0155	0.0070	+0.0006/-0.0006	±0.0006	±0.0000
0.15–0.3	0.23	0.0092	0.0042	+0.0004/-0.0004	±0.0004	±0.0000
0.3–0.45	0.37	0.0135	0.0041	+0.0006/-0.0006	±0.0005	±0.0000
0.45–0.6	0.52	0.0121	0.0053	+0.0005/-0.0005	±0.0005	-0.0001
0.6–0.75	0.66	0.0045	0.0075	+0.0002/-0.0002	±0.0002	±0.0000
0.75–1	0.84	0.0074	0.0098	+0.0003/-0.0003	±0.0003	±0.0000
1–1.3	1.10	0.0139	0.0201	+0.0006/-0.0006	±0.0005	±0.0000
1.3–1.6	1.40	-0.0912	0.0522	+0.0038/-0.0154	±0.0036	-0.0119
1.6–2	1.72	0.0176	0.1433	+0.0008/-0.0092	±0.0007	-0.0085
2–3.5	2.13	0.2603	0.7495	+0.0105/-0.2492	±0.0101	-0.2390

Table D.20: 'Transition' region asymmetry and its error for negative pions with $2 < p < 15$ GeV on deuterium target (2000 data). The first column gives the range of each bin in the lab transverse momentum, the second the average p_T in that bin, the third the measured asymmetry, the fourth its statistical error, the fifth its total (in general asymmetric) systematic error, the sixth the contribution of the beam and target polarization uncertainties only.

p_T-bin (GeV)	$\langle p_T \rangle$ (GeV)	$A_\parallel$	$\Delta A_\parallel$ (stat.)	$\Delta A_\parallel$ (syst.,total)	$\Delta A_\parallel$ (syst., pol.)	$\Delta A_\parallel$ (syst., RICH)
0–0.15	0.10	0.0290	0.0207	+0.0011/-0.0029	±0.0011	-0.0018
0.15–0.3	0.23	0.0199	0.0131	+0.0010/-0.0008	±0.0008	+0.0002
0.3–0.45	0.37	0.0240	0.0125	+0.0027/-0.0009	±0.0009	+0.0018
0.45–0.6	0.52	0.0475	0.0147	+0.0050/-0.0019	±0.0019	+0.0032
0.6–0.75	0.67	0.0670	0.0189	+0.0026/-0.0060	±0.0026	-0.0034
0.75–1	0.85	0.0070	0.0222	+0.0003/-0.0016	±0.0003	-0.0014
1–1.3	1.11	0.0504	0.0425	+0.0020/-0.0146	±0.0020	-0.0126
1.3–1.6	1.41	0.0339	0.1026	+0.0013/-0.0156	±0.0013	-0.0143
1.6–2	1.71	-0.0496	0.2902	+0.0019/-0.0398	±0.0019	-0.0379
2–3.5	2.12	0.1998	0.9012	+0.0078/-0.1945	±0.0078	-0.1868

Table D.21: 'Transition' region asymmetry and its error for positive kaons with $2 < p < 15$ GeV on deuterium target (2000 data). The first column gives the range of each bin in the lab transverse momentum, the second the average p_T in that bin, the third the measured asymmetry, the fourth its statistical error, the fifth its total (in general asymmetric) systematic error, the sixth the contribution of the beam and target polarization uncertainties only, the seventh the contribution from the RICH unfolding uncertainty.

p_T-bin (GeV)	$\langle p_T \rangle$ (GeV)	$A_\parallel$	$\Delta A_\parallel$ (stat.)	$\Delta A_\parallel$ (syst.,total)	$\Delta A_\parallel$ (syst., pol.)	$\Delta A_\parallel$ (syst., RICH)
0–0.15	0.10	0.0303	0.0315	+0.0113/-0.0012	±0.0012	+0.0101
0.15–0.3	0.23	-0.0215	0.0248	+0.0086/-0.0008	±0.0008	+0.0077
0.3–0.45	0.37	-0.0221	0.0212	+0.0085/-0.0009	±0.0009	+0.0076
0.45–0.6	0.52	0.0363	0.0232	+0.0101/-0.0014	±0.0014	+0.0087
0.6–0.75	0.67	0.0188	0.0292	+0.0028/-0.0007	±0.0007	+0.0021
0.75–1	0.85	0.0207	0.0339	+0.0026/-0.0008	±0.0008	+0.0018
1–1.3	1.10	0.0609	0.0673	+0.0168/-0.0024	±0.0024	+0.0144
1.3–1.6	1.41	-0.0616	0.1635	+0.0297/-0.0024	±0.0024	+0.0273
1.6–2	1.72	0.0415	0.5083	+0.0236/-0.0016	±0.0016	+0.0220
2–3.5	2.12	1.2533	0.7733	+0.7135/-0.0488	±0.0488	+0.6647

Table D.22: 'Transition' region asymmetry and its error for negative kaons with $2 < p < 15$ GeV on deuterium target (2000 data). The first column gives the range of each bin in the lab transverse momentum, the second the average p_T in that bin, the third the measured asymmetry, the fourth its statistical error, the fifth its total (in general asymmetric) systematic error, the sixth the contribution of the beam and target polarization uncertainties only, the seventh the contribution from the RICH unfolding uncertainty.

D.2.3 'SIDIS' Region

p_T-bin (GeV)	$\langle p_T \rangle$ (GeV)	$A_\parallel$	$\Delta A_\parallel$ (stat.)	$\Delta A_\parallel$ (syst.,total)	$\Delta A_\parallel$ (syst., pol.)
0–0.15	0.10	0.0964	0.0114	+0.0051/-0.0050	±0.0050
0.15–0.3	0.23	0.1121	0.0080	+0.0060/-0.0059	±0.0059
0.3–0.45	0.37	0.1054	0.0081	+0.0057/-0.0055	±0.0055
0.45–0.6	0.52	0.0925	0.0097	+0.0051/-0.0048	±0.0048
0.6–0.75	0.67	0.1001	0.0135	+0.0053/-0.0052	±0.0052
0.75–1	0.84	0.0787	0.0176	+0.0042/-0.0041	±0.0041
1–1.3	1.11	0.1815	0.0361	+0.0097/-0.0095	±0.0095
1.3–1.6	1.39	0.2581	0.0984	+0.0135/-0.0139	±0.0135
1.6–2	1.70	0.0327	0.2766	+0.0018/-0.0017	±0.0017
2–3.5					

Table D.23: 'SIDIS' asymmetry and its error for positive hadrons on hydrogen target (combined 1996 and 1997 data). The first column gives the range of each bin in the lab transverse momentum, the second the average p_T in that bin, the third the measured asymmetry, the fourth its statistical error, the fifth its total (in general asymmetric) systematic error, the sixth the contribution of the beam and target polarization uncertainties only.

p_T-bin (GeV)	$\langle p_T \rangle$ (GeV)	$A_\parallel$	$\Delta A_\parallel$ (stat.)	$\Delta A_\parallel$ (syst.,total)	$\Delta A_\parallel$ (syst., pol.)
0–0.15	0.10	0.0635	0.0150	+0.0035/-0.0033	±0.0033
0.15–0.3	0.23	0.0543	0.0105	+0.0030/-0.0028	±0.0028
0.3–0.45	0.37	0.0648	0.0107	+0.0035/-0.0034	±0.0034
0.45–0.6	0.52	0.0632	0.0129	+0.0033/-0.0033	±0.0033
0.6–0.75	0.67	0.1003	0.0180	+0.0053/-0.0052	±0.0052
0.75–1	0.84	0.0682	0.0242	+0.0037/-0.0036	±0.0036
1–1.3	1.10	0.1682	0.0509	+0.0092/-0.0088	±0.0088
1.3–1.6	1.40	0.0357	0.1389	+0.0023/-0.0019	±0.0019
1.6–2	1.72	-0.1763	0.3629	+0.0092/-0.0095	±0.0092
2–3.5					

Table D.24: 'SIDIS' asymmetry and its error for negative hadrons on hydrogen target (combined 1996 and 1997 data). The first column gives the range of each bin in the lab transverse momentum, the second the average p_T in that bin, the third the measured asymmetry, the fourth its statistical error, the fifth its total (in general asymmetric) systematic error, the sixth the contribution of the beam and target polarization uncertainties only.

p_T-bin (GeV)	$\langle p_T \rangle$ (GeV)	$A_\parallel$	$\Delta A_\parallel$ (stat.)	$\Delta A_\parallel$ (syst.,total)	$\Delta A_\parallel$ (syst., pol.)
0–0.15	0.10	0.1378	0.0219	+0.0074/-0.0072	±0.0072
0.15–0.3	0.23	0.1054	0.0135	+0.0057/-0.0055	±0.0055
0.3–0.45	0.37	0.0901	0.0124	+0.0049/-0.0047	±0.0047
0.45–0.6	0.52	0.0840	0.0139	+0.0046/-0.0044	±0.0044
0.6–0.75	0.67	0.1027	0.0181	+0.0054/-0.0054	±0.0054
0.75–1	0.84	0.0818	0.0227	+0.0043/-0.0043	±0.0043
1–1.3	1.11	0.1967	0.0460	+0.0104/-0.0103	±0.0103
1.3–1.6	1.38	0.1451	0.1306	+0.0076/-0.0081	±0.0076
1.6–2	1.72	0.1315	0.3707	+0.0071/-0.0069	±0.0069
2–3.5					

Table D.25: 'SIDIS' asymmetry and its error for positive pions with $4 < p < 13.8$ GeV on hydrogen target (combined 1996 and 1997 data). The first column gives the range of each bin in the lab transverse momentum, the second the average p_T in that bin, the third the measured asymmetry, the fourth its statistical error, the fifth its total (in general asymmetric) systematic error, the sixth the contribution of the beam and target polarization uncertainties only.

p_T-bin (GeV)	$\langle p_T \rangle$ (GeV)	$A_\parallel$	$\Delta A_\parallel$ (stat.)	$\Delta A_\parallel$ (syst.,total)	$\Delta A_\parallel$ (syst., pol.)
0–0.15	0.10	0.0566	0.0263	+0.0031/-0.0030	±0.0030
0.15–0.3	0.23	0.0468	0.0162	+0.0025/-0.0024	±0.0024
0.3–0.45	0.37	0.0548	0.0148	+0.0029/-0.0029	±0.0029
0.45–0.6	0.52	0.0335	0.0168	+0.0017/-0.0018	±0.0017
0.6–0.75	0.67	0.0894	0.0220	+0.0047/-0.0047	±0.0047
0.75–1	0.84	0.0525	0.0278	+0.0028/-0.0027	±0.0027
1–1.3	1.10	0.1400	0.0571	+0.0077/-0.0073	±0.0073
1.3–1.6	1.39	0.0706	0.1642	+0.0041/-0.0037	±0.0037
1.6–2	1.71	-0.1575	0.4352	+0.0094/-0.0083	±0.0083
2–3.5					

Table D.26: 'SIDIS' asymmetry and its error for negative pions with $4 < p < 13.8$ GeV on hydrogen target (combined 1996 and 1997 data). The first column gives the range of each bin in the lab transverse momentum, the second the average p_T in that bin, the third the measured asymmetry, the fourth its statistical error, the fifth its total (in general asymmetric) systematic error, the sixth the contribution of the beam and target polarization uncertainties only.

p_T-bin (GeV)	$\langle p_T \rangle$ (GeV)	$A_\parallel$	$\Delta A_\parallel$ (stat.)	$\Delta A_\parallel$ (syst.,total)	$\Delta A_\parallel$ (syst., pol.)
0–0.15	0.10	0.0213	0.0067	+0.0008/-0.0008	±0.0008
0.15–0.3	0.23	0.0307	0.0047	+0.0013/-0.0012	±0.0012
0.3–0.45	0.37	0.0287	0.0047	+0.0012/-0.0011	±0.0011
0.45–0.6	0.52	0.0247	0.0057	+0.0010/-0.0010	±0.0010
0.6–0.75	0.67	0.0372	0.0078	+0.0015/-0.0015	±0.0015
0.75–1	0.85	0.0327	0.0102	+0.0013/-0.0013	±0.0013
1–1.3	1.10	0.0789	0.0214	+0.0032/-0.0031	±0.0031
1.3–1.6	1.40	0.1427	0.0579	+0.0063/-0.0056	±0.0056
1.6–2	1.71	0.3176	0.1646	+0.0124/-0.0138	±0.0124
2–3.5	2.15	0.3104	0.8303	+0.0128/-0.0121	±0.0121

Table D.27: 'SIDIS' asymmetry and its error for positive hadrons on deuterium target (2000 data). The first column gives the range of each bin in the lab transverse momentum, the second the average p_T in that bin, the third the measured asymmetry, the fourth its statistical error, the fifth its total (in general asymmetric) systematic error, the sixth the contribution of the beam and target polarization uncertainties only.

p_T-bin (GeV)	$\langle p_T \rangle$ (GeV)	$A_\parallel$	$\Delta A_\parallel$ (stat.)	$\Delta A_\parallel$ (syst.,total)	$\Delta A_\parallel$ (syst., pol.)
0–0.15	0.10	0.0209	0.0083	+0.0009/-0.0008	±0.0008
0.15–0.3	0.23	0.0259	0.0058	+0.0011/-0.0010	±0.0010
0.3–0.45	0.37	0.0237	0.0058	+0.0010/-0.0009	±0.0009
0.45–0.6	0.52	0.0309	0.0070	+0.0013/-0.0012	±0.0012
0.6–0.75	0.67	0.0148	0.0097	+0.0006/-0.0006	±0.0006
0.75–1	0.84	0.0142	0.0130	+0.0006/-0.0006	±0.0006
1–1.3	1.10	-0.0079	0.0275	+0.0004/-0.0003	±0.0003
1.3–1.6	1.40	-0.0544	0.0730	+0.0023/-0.0021	±0.0021
1.6–2	1.73	-0.0782	0.1991	+0.0030/-0.0035	±0.0030
2–3.5	2.15	0.3104	0.8303	+0.0121/-0.0127	±0.0121

Table D.28: 'SIDIS' asymmetry and its error for negative hadrons on deuterium target (2000 data). The first column gives the range of each bin in the lab transverse momentum, the second the average p_T in that bin, the third the measured asymmetry, the fourth its statistical error, the fifth its total (in general asymmetric) systematic error, the sixth the contribution of the beam and target polarization uncertainties only.

p_T-bin (GeV)	$\langle p_T \rangle$ (GeV)	$A_\parallel$	$\Delta A_\parallel$ (stat.)	$\Delta A_\parallel$ (syst.,total)	$\Delta A_\parallel$ (syst., pol.)	$\Delta A_\parallel$ (syst., RICH)
0–0.15	0.10	0.022354	0.0084	+0.0011/-0.0009	±0.0009	+0.0002
0.15–0.3	0.23	0.022290	0.0058	+0.0010/-0.0009	±0.0009	±0.0000
0.3–0.45	0.37	0.024510	0.0059	+0.0010/-0.0011	±0.0010	-0.0002
0.45–0.6	0.52	0.024038	0.0071	+0.0009/-0.0012	±0.0009	-0.0003
0.6–0.75	0.66	0.030204	0.0100	+0.0012/-0.0015	±0.0012	-0.0003
0.75–1	0.84	0.040515	0.0133	+0.0016/-0.0021	±0.0016	-0.0005
1–1.3	1.10	0.073257	0.0286	+0.0029/-0.0035	±0.0029	-0.0006
1.3–1.6	1.40	0.061755	0.0814	+0.0032/-0.0026	±0.0024	-0.0002
1.6–2	1.71	0.233789	0.2509	+0.0091/-0.0106	±0.0091	±0.0000
2–3.5						

Table D.29: 'SIDIS' asymmetry and its error for positive pions with $2 < p < 15$ GeV on deuterium target (2000 data). The first column gives the range of each bin in the lab transverse momentum, the second the average p_T in that bin, the third the measured asymmetry, the fourth its statistical error, the fifth its total (in general asymmetric) systematic error, the sixth the contribution of the beam and target polarization uncertainties only, the seventh the contribution from the RICH unfolding uncertainty.

p_T-bin (GeV)	$\langle p_T \rangle$ (GeV)	$A_\parallel$	$\Delta A_\parallel$ (stat.)	$\Delta A_\parallel$ (syst.,total)	$\Delta A_\parallel$ (syst., pol.)	$\Delta A_\parallel$ (syst., RICH)
0–0.15	0.10	0.0196	0.0094	+0.0008/-0.0009	±0.0008	-0.0001
0.15–0.3	0.23	0.0243	0.0064	+0.0010/-0.0011	±0.0009	-0.0002
0.3–0.45	0.37	0.0265	0.0065	+0.0011/-0.0011	±0.0010	-0.0001
0.45–0.6	0.52	0.0282	0.0078	+0.0012/-0.0011	±0.0011	±0.0000
0.6–0.75	0.66	0.0218	0.0109	+0.0010/-0.0009	±0.0009	+0.0001
0.75–1	0.84	0.0158	0.0147	+0.0007/-0.0006	±0.0006	+0.0001
1–1.3	1.10	-0.0182	0.0311	+0.0009/-0.0007	±0.0007	±0.0000
1.3–1.6	1.40	-0.0156	0.0863	+0.0006/-0.0008	±0.0006	-0.0002
1.6–2	1.72	-0.0954	0.2487	+0.0037/-0.0063	±0.0037	-0.0016
2–3.5						

Table D.30: 'SIDIS' asymmetry and its error for negative pions with $2 < p < 15$ GeV on deuterium target (2000 data). The first column gives the range of each bin in the lab transverse momentum, the second the average p_T in that bin, the third the measured asymmetry, the fourth its statistical error, the fifth its total (in general asymmetric) systematic error, the sixth the contribution of the beam and target polarization uncertainties only, the seventh the contribution from the RICH unfolding uncertainty.

p_T-bin (GeV)	$\langle p_T \rangle$ (GeV)	$A_\parallel$	$\Delta A_\parallel$ (stat.)	$\Delta A_\parallel$ (syst.,total)	$\Delta A_\parallel$ (syst., pol.)	$\Delta A_\parallel$ (syst., RICH)
0–0.15	0.10	0.0264	0.0231	+0.0010/-0.0030	±0.0010	-0.0020
0.15–0.3	0.23	0.0486	0.0160	+0.0029/-0.0019	±0.0019	+0.0010
0.3–0.45	0.37	0.0553	0.0168	+0.0062/-0.0022	±0.0022	+0.0040
0.45–0.6	0.52	0.0357	0.0200	+0.0042/-0.0014	±0.0014	+0.0028
0.6–0.75	0.67	0.1004	0.0258	+0.0115/-0.0039	±0.0039	+0.0076
0.75–1	0.85	0.0345	0.0320	+0.0039/-0.0013	±0.0013	+0.0025
1–1.3	1.10	0.0913	0.0631	+0.0082/-0.0036	±0.0036	+0.0046
1.3–1.6	1.40	0.1485	0.1598	+0.0081/-0.0058	±0.0058	+0.0023
1.6–2	1.69	0.3270	0.4607	+0.0127/-0.0127	±0.0127	±0.0000
2–3.5						

Table D.31: 'SIDIS' asymmetry and its error for positive kaons with $2 < p < 15$ GeV on deuterium target (2000 data). The first column gives the range of each bin in the lab transverse momentum, the second the average p_T in that bin, the third the measured asymmetry, the fourth its statistical error, the fifth its total (in general asymmetric) systematic error, the sixth the contribution of the beam and target polarization uncertainties only, the seventh the contribution from the RICH unfolding uncertainty.

p_T-bin (GeV)	$\langle p_T \rangle$ (GeV)	$A_\parallel$	$\Delta A_\parallel$ (stat.)	$\Delta A_\parallel$ (syst.,total)	$\Delta A_\parallel$ (syst., pol.)	$\Delta A_\parallel$ (syst., RICH)
0–0.15	0.10	-0.0108	0.0339	+0.0080/-0.0004	±0.0004	+0.0075
0.15–0.3	0.23	0.0501	0.0247	+0.0163/-0.0020	±0.0020	+0.0143
0.3–0.45	0.37	0.0205	0.0276	+0.0008/-0.0031	±0.0008	-0.0023
0.45–0.6	0.52	0.0156	0.0335	+0.0006/-0.0043	±0.0006	-0.0037
0.6–0.75	0.67	-0.0115	0.0430	+0.0005/-0.0004	±0.0004	±0.0000
0.75–1	0.85	-0.0053	0.0517	+0.0022/-0.0002	±0.0002	+0.0020
1–1.3	1.10	-0.0573	0.1066	+0.0350/-0.0022	±0.0022	+0.0328
1.3–1.6	1.41	-0.2915	0.2893	+0.1378/-0.0114	±0.0114	+0.1264
1.6–2	1.77	1.0337	0.9378	+0.1820/-0.0403	±0.0403	+0.1417
2–3.5						

Table D.32: 'SIDIS' asymmetry and its error for negative kaons with $2 < p < 15$ GeV on deuterium target (2000 data). The first column gives the range of each bin in the lab transverse momentum, the second the average p_T in that bin, the third the measured asymmetry, the fourth its statistical error, the fifth its total (in general asymmetric) systematic error, the sixth the contribution of the beam and target polarization uncertainties only, the seventh the contribution from the RICH unfolding uncertainty.

D.3 Final Results on $\frac{\Delta G}{G}(p_T)$ in the 'Photoproduction' Region.

D.3.1 Integrated Results

	'Photoproduction'	'Transition'
	Proton+Deuteron	Deuteron
Value and kinematics		
$\Delta G/G$	0.100	-0.094
$\delta(\Delta G/G)$	0.037	0.104
$\langle x_G \rangle$	0.15	0.16
$\langle \hat{Q}^2 \rangle$ (GeV^2)	1.25	1.77
N_{sig}/N_{tot}	0.23	0.18
Systematic deviations due to:		
a) Treatment of soft VMD		
A^{low-p_T}	*-0.005	*0.003
A^{diffr}		*0.001
Choice of PDFs		
CTEQ5+GS-B	-0.041	*-0.043
GRV+GRSV2000	-0.004	* 0.015
GRV+GS-B	*-0.045	-0.028
GRV-G	*-0.003	*-0.058
b) Choice of PYTHIA parameters		
MSTP18=3	* 0.003	*-0.055
PARJ21=0.45 GeV^2	*-0.071	
c) Hard resolved γ processes:		
Δf^γ (max.) SaS 1D	* 0.068	* 0.003
Δf^γ (min), SaS 1D	*-0.020	-0.001
Δf^γ (max), GRV-G	0.046	*-0.005
Δf^γ (min), GRV-G	-0.016	-0.0001
total theor. syst. +	0.071	0.023
total theor. syst. -	0.145	0.161
exp. syst +	0.006	0.009
exp. syst -	0.006	0.008

Table D.33: Final integrated results for $\frac{\Delta G}{G}$ from the 'Photoproduction' region with $1.35 < p_T < 2.5$ GeV for the combined proton and deuteron data (2nd column) and the deuteron data in the 'Transition' region with $1 < p_T < 2$ GeV (3rd column). The data for all charged hadrons were used. The rows are from top to bottom: 1.) value of $\frac{\Delta G}{G}$, 2.) its statistical error, 3.) the average x_G (from set #1), 4.) the average scale $\hat{Q}^2$ (from set #1), 5.) the average signal process fraction (from set #1). The following rows give the individual sources of model uncertainties: 6.) Treatment of low-p_T process in the MC background asymmetry, 7.) Treatment of diffractive VMD process in the MC background asymmetry (only for the 'Transition' region), 8.) to 10.) combination of unpolarized and polarized proton PDFs, 11.) choice of unpolarized photon PDF, 12.) use of MSTP(18)=3 instead of MSTP(18)=3, 13.) use of PARJ(21)=0.45 GeV^2 instead of 0.36 GeV^2, 14.) and 15.) maximal and minimal scenarios for polarized photon PDFs using SaS-1d in set #4, 16.) and 17.) maximal and minimal scenarios for polarized photon PDFs using GRV-G. Rows 18.) and 19.) give the maximum positive (+) and negative (-) values of the total PYTHIA inherent and theoretical uncertainties, the values marked with a '*' in rows 6.) to 17.) are taken into account for the sum. The (asymmetric) experimental systematic error (+/-) is given in rows 20.) and 21.).

D.3.2 Positive Hadrons from Proton in the 'Photoproduction' Region

p_T-bin (GeV)	0.9–1.05	1.05–1.2	1.2–1.5	1.5–1.8	1.8–2.5
$\langle p_T \rangle$ (GeV)	0.96	1.11	1.34	1.64	1.93
Value and kinematics					
$\Delta G/G$	0.303	-0.005	0.029	0.055	0.663
$\delta(\Delta G/G)$	0.110	0.102	0.087	0.179	0.601
$\langle x_G \rangle$ (set #1)	0.12	0.13	0.13	0.16	0.20
$\langle \hat{Q}^2 \rangle$ (GeV^2) (set #1)	0.82	0.90	1.03	1.45	1.94
N_{sig}/N_{tot} (set #1)	0.062	0.105	0.171	0.225	0.14
Systematic deviations due to:					
a) Treatment of soft VMD					
A^{low-p_T}	-0.368	-0.196	-0.096	-0.062	-0.096
Choice of PDFs					
CTEQ5+GS-B	-0.080	-0.068	-0.067	-0.078	-0.159
GRV+GRSV2000	-0.015	0.002	-0.006	0.006	-0.257
GRV+GS-B	-0.092	-0.059	-0.067	-0.072	-0.380
GRV-G	0.016	-0.011	-0.041	0.024	0.004
b) Choice of PYTHIA parameters					
MSTP18=3	0.170	-0.051	-0.065	-0.070	-0.115
PARJ21=0.45 GeV^2	0.110	-0.260	-0.235	-0.267	-0.617
c) Hard resolved γ processes:					
Δf^γ (max), SaS 1D	0.666	0.0005	-0.040	-0.022	0.156
Δf^γ (min), SaS 1D	-0.070	-0.0004	0.010	0.006	-0.053
Δf^γ (max), GRV-G	0.134	0.002	-0.017	0.062	0.278
Δf^γ (min), GRV-G	-0.035	-0.0008	0.007	-0.018	-0.093
total theor. syst. +	0.963	0.003	0.010	0.093	0.281
total theor. syst. -	0.530	0.586	0.543	0.500	1.301
exp. syst (max)	0.014	0.017	0.016	0.023	0.054
exp. syst (min)	0.014	0.018	0.016	0.023	0.054

Table D.34: Final results for $\frac{\Delta G}{G}$ from positive hadrons on proton in the 'Photoproduction' region. The columns are for each bin in p_T, the first two rows give the range in p_T and the average p_T, respectively. The following rows are set up as in table D.33, except that row 7.) there (treatment of diffractive VMD process in the MC background asymmetry) is missing here. The total model uncertainty is calculated similar to that given in table D.33, by taking the maximum absolute values in each group separated by a horizontal line.

D.3.3 Negative Hadrons from Proton in the 'Photoproduction' Region

p_T-bin (GeV)	0.9–1.05	1.05–1.2	1.2–1.5	1.5–1.8	1.8–2.5
$\langle p_T \rangle$ (GeV)	0.96	1.11	1.34	1.64	1.92
Value and kinematics					
$\Delta G/G$	0.337	0.239	0.214	0.907	0.572
$\delta(\Delta G/G)$	0.127	0.112	0.091	0.187	0.459
$\langle x_G \rangle$ (set #1)	0.12	0.13	0.13	0.16	0.21
$\langle \hat{Q}^2 \rangle$ (GeV^2) (set #1)	0.83	0.92	1.02	1.34	2.05
N_{sig}/N_{tot} (set #1)	0.065	0.115	0.193	0.272	0.210
Systematic deviations due to:					
a) Treatment of soft VMD					
A^{low-p_T}	-0.335	-0.173	-0.089	-0.053	-0.037
Choice of PDFs					
CTEQ5+GS-B	-0.040	-0.035	-0.035	-0.046	-0.096
GRV+GRSV2000	-0.011	-0.025	-0.032	-0.141	-0.158
GRV+GS-B	-0.050	-0.058	-0.064	-0.181	-0.232
GRV-G	0.004	0.005	-0.030	-0.113	0.225
b) Choice of PYTHIA parameters					
MSTP18=3	0.297	0.131	0.019	-0.118	-0.057
PARJ21=0.45 GeV^2	0.192	0.141	0.064	0.466	0.355
c) Hard resolved γ processes:					
Δf^γ (max), SaS 1D	0.573	0.234	0.094	0.241	0.126
Δf^γ (min), SaS 1D	-0.067	-0.043	-0.024	-0.081	-0.047
Δf^γ (max), GRV-G	0.096	0.056	0.052	0.199	0.081
Δf^γ (min), GRV-G	-0.026	-0.017	-0.016	-0.056	-0.038
total theor. syst. +	1.067	0.511	0.177	0.707	0.706
total theor. syst.-	0.452	0.275	0.208	0.547	0.373
exp. syst (max)	0.007	0.004	0.003	0.013	0.010
exp. syst (min)	0.007	0.005	0.003	0.013	0.010

Table D.35: Final results for $\frac{\Delta G}{G}$ from negative hadrons on proton in the 'Photoproduction' region. The columns are for each bin in p_T, the first two rows give the range in p_T and the average p_T, respectively. The following rows are set up as in table D.33, except that row 7.) there (treatment of diffractive VMD process in the MC background asymmetry) is missing here. The total model uncertainty is calculated similar to that given in table D.33, by taking the maximum absolute values in each group separated by a horizontal line.

D.3.4 Positive Hadrons from Deuteron in the 'Photoproduction' Region

p_T-bin (GeV)	0.9–1.05	1.05–1.2	1.2–1.5	1.5–1.8	1.8–2.5
$\langle p_T \rangle$ (GeV)	0.96	1.11	1.34	1.64	1.92
Value and kinematics					
$\Delta G/G$	0.060	-0.016	-0.018	-0.140	0.930
$\delta(\Delta G/G)$	0.068	0.062	0.052	0.111	0.323
$\langle x_G \rangle$ (set #1)	0.12	0.13	0.14	0.16	0.21
$\langle \hat{Q}^2 \rangle$ (GeV^2) (set #1)	0.82	0.91	1.06	1.43	2.05
N_{sig}/N_{tot} (set #1)	0.060	0.104	0.166	0.222	0.172
Systematic deviations due to:					
a) Treatment of soft VMD					
A^{low-p_T}	0.121	0.062	0.027	0.010	-0.024
Choice of PDFs					
CTEQ5+GS-B	-0.026	-0.026	-0.031	-0.059	-0.207
GRV+GRSV2000	-0.005	0.003	0.008	0.035	-0.280
GRV+GS-B	-0.034	-0.021	-0.024	-0.024	-0.407
GRV-G	0.014	0.006	-0.011	0.002	-0.027
b) Choice of PYTHIA parameters					
MSTP18=3	0.024	-0.026	-0.044	-0.005	0.125
PARJ21=0.45 GeV^2	-0.080	-0.185	-0.182	-0.281	-0.512
c) Hard resolved γ processes:					
Δf^γ (max), SaS 1D	0.211	0.009	0.004	-0.043	0.282
Δf^γ (min), SaS 1D	-0.025	-0.003	-0.002	0.010	-0.087
Δf^γ (max), GRV-G	0.031	-0.013	0.151	0.013	0.328
Δf^γ (min), GRV-G	-0.009	0.004	-0.055	-0.006	-0.085
total theor. syst. +	0.370	0.081	0.186	0.060	0.453
total theor. syst. -	0.141	0.249	0.324	0.388	1.057
exp. syst (max)	0.0005	0.002	0.004	0.009	0.003
exp. syst (min)	0.0003	0.002	0.004	0.009	0.004

Table D.36: Final results for $\frac{\Delta G}{G}$ from positive hadrons on deuteron in the 'Photoproduction' region. The columns are for each bin in p_T, the first two rows give the range in p_T and the average p_T, respectively. The following rows are set up as in table D.33, except that row 7.) there (treatment of diffractive VMD process in the MC background asymmetry) is missing here. The total model uncertainty is calculated similar to that given in table D.33, by taking the maximum absolute values in each group separated by a horizontal line.

D.3.5 Negative Hadrons from Deuteron in the 'Photoproduction' Region

p_T-bin (GeV)	0.9–1.05	1.05–1.2	1.2–1.5	1.5–1.8	1.8–2.5
$\langle p_T \rangle$ (GeV)	0.96	1.11	1.34	1.64	1.92
Value and kinematics					
$\Delta G/G$	0.047	0.086	0.080	0.177	0.712
$\delta(\Delta G/G)$	0.072	0.062	0.048	0.093	0.266
$\langle x_G \rangle$ (set #1)	0.12	0.13	0.14	0.16	0.21
$\langle \hat{Q}^2 \rangle$ (GeV^2) (set #1)	0.83	0.92	1.03	1.38	2.06
N_{sig}/N_{tot} (set #1)	0.066	0.117	0.204	0.288	0.239
Systematic deviations due to:					
a) Treatment of soft VMD					
A^{low-p_T}	0.109	0.053	0.018	0.007	0.001
Choice of PDFs					
CTEQ5+GS-B	-0.017	-0.015	-0.016	-0.032	-0.095
GRV+GRSV2000	-0.005	-0.013	-0.012	-0.023	-0.292
GRV+GS-B	-0.022	-0.027	-0.028	-0.048	-0.342
GRV-G	0.0002	0.008	-0.009	-0.002	0.075
b) Choice of PYTHIA parameters					
MSTP18=3	0.027	0.040	0.020	-0.011	-0.005
PARJ21=0.45 GeV^2	-0.080	-0.016	-0.037	0.013	0.246
c) Hard resolved γ processes:					
Δf^γ (max), SaS 1D	0.147	0.116	0.066	0.092	0.023
Δf^γ (min), SaS 1D	-0.020	-0.024	-0.018	-0.028	-0.082
Δf^γ (max), GRV-G	0.022	0.035	0.042	0.066	0.096
Δf^γ (min), GRV-G	-0.007	-0.011	-0.014	-0.021	-0.045
total theor. syst. +	0.283	0.217	0.103	0.111	0.555
total theor. syst. -	0.123	0.067	0.092	0.089	0.429
exp. syst (max)	0.001	0.001	0.0005	0.0005	0.004
exp. syst (min)	0.001	0.001	0.0005	0.0005	0.004

Table D.37: Final results for $\frac{\Delta G}{G}$ from negative hadrons on deuteron in the 'Photoproduction' region. The columns are for each bin in p_T, the first two rows give the range in p_T and the average p_T, respectively. The following rows are set up as in table D.33, except that row 7.) there (treatment of diffractive VMD process in the MC background asymmetry) is missing here. The total model uncertainty is calculated similar to that given in table D.33, by taking the maximum absolute values in each group separated by a horizontal line.

D.3.6 Charged Hadrons from Proton and Deuteron in the 'Photoproduction' Region

p_T-bin (GeV)	0.9–1.05	1.05–1.2	1.2–1.5	1.5–1.8	1.8–2.5
$\langle p_T \rangle$ (GeV)	0.96	1.11	1.34	1.64	1.92
Value and kinematics					
$\Delta G/G$	0.115	0.041	0.421	0.103	0.72
$\delta(\Delta G/G)$	0.042	0.038	0.031	0.062	0.18
$\langle x_G \rangle$ (set #1)	0.12	0.13	0.14	0.16	0.21
$\langle \hat{Q}^2 \rangle$ (GeV^2) (set #1)	0.83	0.91	1.03	1.40	2.03
N_{sig}/N_{tot} (set #1)	0.063	0.110	0.183	0.248	0.184
Systematic deviations due to:					
a) Treatment of soft VMD					
A^{low-p_T}	-0.008	-0.004	-0.006	-0.008	-0.019
Choice of PDFs					
CTEQ5+GS-B	-0.031	-0.028	-0.030	-0.048	-0.140
GRV+GRSV2000	-0.007	-0.006	-0.006	-0.017	-0.248
GRV+GS-B	-0.039	-0.032	-0.035	-0.062	-0.336
GRV-G	0.006	0.005	-0.015	-0.0005	0.075
b) Choice of PYTHIA parameters					
MSTP18=3	0.068	0.003	-0.015	-0.024	0.0024
PARJ21=0.45 GeV^2	-0.023	-0.098	-0.107	-0.094	-0.114
c) Hard resolved γ processes:					
Δf^γ (max), SaS 1D	0.265	0.091	0.082	0.068	0.207
Δf^γ (min), SaS 1D	-0.032	-0.019	-0.023	-0.020	-0.072
Δf^γ (max), GRV-G	0.051	0.021	0.033	0.056	0.189
Δf^γ (min), GRV-G	-0.015	-0.007	-0.011	-0.018	-0.066
total theor. syst. +	0.339	0.099	0.082	0.068	0.285
total theor. syst. -	0.102	0.153	0.200	0.209	0.541
exp. syst (max)	0.003	0.004	0.004	0.008	0.011
exp. syst (min)	0.003	0.004	0.004	0.008	0.011

Table D.38: Final results for $\frac{\Delta G}{G}$ from the combined data on charged hadrons on proton and deuteron in the 'Photoproduction' region. The columns are for each bin in p_T, the first two rows give the range in p_T and the average p_T, respectively. The following rows are set up as in table D.33, except that row 7.) there (treatment of diffractive VMD process in the MC background asymmetry) is missing here. The total model uncertainty is calculated similar to that given in table D.33, by taking the maximum absolute values in each group separated by a horizontal line.

Bibliography

[Abe92] F. Abe et al., *Inclusive J/ psi , psi (2S), and b-quark production in p-barp collisions at sqrt s =1.8 TeV*, Phys. Rev. Lett. **69** (1992) 3704-3708.

[Abr96] P. Abreu et al., The DELPHI Collaboration, *Tuning and test of fragmentation models based on identified particles and precision event shape data*, Z. Phys. **C73** (1996) 11-60.

[Abr97] H. Abramowicz, A. Levy, *The ALLM parameterization of $\sigma_{tot}(\gamma * p)$ an update*, hep-ph/9712415 (1997).

[Abr04] A. Brüll, *private communication* (2004).

[Ack98] K.Ackerstaff et al., The HERMES Collaboration, *The HERMES Spectrometer*, DESY 98-057, Nucl. Instr. Meth. **A 417** (1998) 230.

[Ack99] K.Ackerstaff et al., The HERMES Collaboration, *Flavor decomposition of the polarized quark distributions in the nucleon from inclusive and semiinclusive deep inelastic scattering* Phys. Lett. **B464** (1999) 123-134.

[Ack00] K.Ackerstaff et al., The HERMES Collaboration, *Measurement of Angular Distributions and R=sigmaL/sigmaT in Diffractive Electroproduction of rho0 Mesons*, Eur. Phys. Jour. C 18 (2000) 303-316.

[Ada94] Adams et al., The E665 Collaboration, *Production of neutral strange particles in muon - nucleon scattering at 490-GeV*, Z. Phys. **C61** (1994) 539-550.

[Ada97] Adams et al., The E665 Collaboration, *Diffractive production of ρ^0 mesons in muon–proton interactions 470 GeV*, Z. Phys. **C74** (1997) 237-261.

[Ade96] B. Adeva et al., The Spin Muon Collaboration, *Polarization of valence and nonstrange sea quarks in the nucleon from semiinclusive spin asymmetries*, Phys. Lett. **B369** (1996) 93-100.

[Ade98] B. Adeva et al., The Spin Muon Collaboration, *Polarized quark distributions in the nucleon from semiinclusive spin asymmetries* Phys. Lett. **B420** (1998) 180-190.

[Ade99] B. Adeva et al., The Spin Muon Collaboration, *Spin asymmetries A(1) of the proton and the deuteron in the low x and low Q**2 region from polarized high-energy muon scattering*, Phys. Rev. **D60** (1999) 072004, Erratum-ibid. **D62** (2000) 079902.

[Adl69] L. Adler, W. A. Bardeen, *Absence of Higher-Order Corrections in the Anomalous Axial-Vector Divergence Equation*, Phys. Rev. **182** (1969) 1517-1536.

[Adl00] C. Adloff, et al, The H1 Collaboration, *Measurement of Di-jet Cross-Sections in Photoproduction and Photon Structure* Phys. Lett. **B483** (2000) 36-48.

[Adl01] C. Adloff, et al, The H1 Collaboration, *Measurement and QCD Analysis of Jet Cross Sections in Deep-Inelastic Positron-Proton Collisions at sqrt(s) of 300 GeV*, Eur. Phys. J. **C19** (2001) 289-311.

[Adl03] C. Adloff et al., The H1 Collaboration, *Measurement and QCD Analysis of Neutral and Charged Current Cross Sections at HERA*, Eur. Phys. **J C30** (2003) 1-32.

[Afa98] A. Afanasev et al., *Measuring polarized Gluon and Quark Distributions with Meson Photoproduction*, Phys. Rev. **D58** (1998) 054007.

[Afa99] A. Afanasev et al., *Soft Contributions to Hard Pion Photoproduction*, Phys. Rev. **D61** (2000) 034014.

[Aid96] S. Aid et al., The H1 Collaboration, *Strangeness production in deep inelastic positron - proton scattering at HERA*, Nucl. Phys. **B480** (1996) 3-34.

[Aid96a] S. Aid et al., The H1 Collaboration, *Elastic photoproduction of rho0 mesons at HERA*, Nucl. Phys. **B463** (1996) 3-32.

[Air00] A. Airapetian et al., The HERMES Collaboration, *Measurement of the Spin Asymmetry in the Photoproduction of Pairs of High-pT Hadrons at HERMES*, Phys. Rev. Lett. **84** (2000) 2584-2588.

[Air00a] A. Airapetian et al, The HERMES Collaboration, *Exclusive Leptoproduction of rho0 Mesons on Hydrogen at Intermediate W Values*, Eur. Phys. Jour. C 17 (2000) 389-398.

[Air01] A. Airapetian et al,The HERMES Collaboration, *Multiplicity of Charged and Neutral Pions in Deep-inelastic Scattering of 27.5 GeV Positrons*, Eur. Phys. J. **C21** (2001) 599-606.

[Air03] A. V. Airapetian et al., The HERMES Collaboration, *Quark helicity distributions in the nuclean for up-, down-, and strange-quarks from semi-inclusive deep-inelastic scattering*, in preparation (2003).

[Air03a] A. Airapetian et al, *Erratum to K. Ackerstaff et al, Phys. Lett. B 475 (2000) 386*, Phys. Lett. **B567** (2003) 339.

[Air03b] A. Airapetian et al, *Double-spin Asymmetries in the Cross Section of Diffractive rho0 and phi Production at Intermediate Energies*, Eur. Phys. J. **C29** (2003) 171 - 179.

[Aku99] I. Akushevich, H. Böttcher, D. Ryckbosch, *RADGEN 1.0 Monte Carlo Generator for Radiative Events in DIS on Polarized and Unpolarized Targets*, hep-ph 9906408 (1999).

[Alt77] G. Altarelli, G. Parisi, *Asymptotic freedom in parton language*, Nucl. Phys. **B126**, (1977) 298.

[Alt98] G. Altarelli et al., *Theoretical analysis of polarized structure functions*, Talks given at Cracow Epiphany Conference on Spin Effects in Particle Physics and Tempus Workshop, Cracow, Poland, 9-11 Jan 1998, Acta Phys. Polon. **B29** (1998) 1145-1173.

[And83] B. Anderson et al., *Parton fragmentation and string dynamics*, Phys. Rep. **97** (1983) 31.

[And01] A. Andreev et al, *Multiwire Proportional Chambers in the HERMES Experiment*, Nucl. Instrum. and Meth. **A 465** (2001) 482-497.

[Ako02] N. Akopov et al., *The HERMES Dual-Radiator Ring Imaging Cerenkov Detector*, Nucl.Instrum.Meth. **A479** (2002) 511-530.

[Ant03] P. L. Anthony et al., The E155 Collaboration, *Precision measurement of the proton and deuteron spin structure functions g(2) and asymmetries a(2)*, Phys. Lett. **B553** (2003) 18-24.

[Apa98] L. Apanasevich et al., Fermilab E706 Collaboration, *Evidence for parton k(T) effects in high p(T) particle production*, Phys. Rev. Lett. **81** (1998) 2642-2645.

[Arn89] M. Arneodo et al., The European Muon Collaboration, *Measurements of the u Valence Quark Distribution Function in the Proton and u Quark Fragmentation Functions*, Nucl. Phys. **321** (1989) 541.

[Arn96] M. Arneodo, L. Lamberti, M. Ryskin, *DIPSI: a Monte Carlo Generator for Elastic Vector Meson Production in Charged Lepton-Proton Scattering*, hep-ph/9610286, DESY 96-149 (1996).

[Asch03] E.C. Aschenauer, A. Hillenbrand, B. Maiheu, *Extraction of Hadron Multiplicities from 2000 Unpolarized Proton Data and Monte Carlo*, HERMES release report, April (2003).

[Asch04] E.C. Aschenauer, *private communication* (2004).

[Bab79] J. Babcock et al., *Quantum Chromodynamic Predictions for Inclusive Spin-Spin Asymmetries at Large Transverse Momentum*, Phys. Rev. **D19** (1979) 1483.

[Bad96] B. Badelek, J. Kwiecinski *Low Q**2, low x region in electroproduction: An overview*, Rev. Mod. Phys. **68** (1996) 445-471.

[Bad99] B. Badelek, J. Kwiecinski *Spin dependent structure function g(1) at small x and small Q**2*, Contributed to 3rd UK Phenomenology Workshop on HERA Physics, Durham, England, 20-25 Sep 1998, J. Phys. **G25** (1999) 1533-1535.

[Bal96] R. D. Ball et al., *Next-to-leading order determination of the singlet axial charge and the polarized gluon content of the nucleon*, Phys. Lett. **B378**, (1996) 255-266.

[Bar78] W. A. Bardeen et al., *Deep inelastic scattering beyond the leading order in asymptotically free gauge theories*, Phys. Rev. **D18**, (1978) 3998.

[Bar93] D.P. Barber et al., *The HERA Polarimeter and the first observation of electron spin polarization at HERA*, Nucl. Instr. Meth. **A329** (1993) 79.

[Bar94] D.P. Barber et al., *High spin polarization at the HERA electron storage ring*, Nucl. Instr. Meth. **A 338** (1994) 166.

[Bas98] S. V. Bashinsky, R. L. Jaffe, *Quark and gluon orbital angular momentum and spin in hard processes*, Nucl. Phys. **B536** (1998), 303-317.

[Bau78] T. H. Bauer et al., *The hadronic properties of the photon in high-energy interactions*, Rev. Mod. Phys. **50** (1978) 261-436.

[Bau02] Ch. Baumgarten et al., *An Atomic Beam Polarimeter to Measure the Nuclear Polarization in the HERMES Gaseous Polarized Hydrogen and Deuterium Target* Nucl. Instrum. and Meth. **A 482** (2002), 606.

[Bau03a] Ch. Baumgarten et al., *The storage cell of the polarized internal H/D gas target of the HERMES experiment at HERA*, Nucl. Instrum. and Meth. **A496** (2003) 277.

[Bau03b] Ch. Baumgarten et al., *Measurements of atomic recombination in the HERMES polarized hydrogen and deuterium storage cell target*, Nucl. Instrum. and Meth. **A496** (2003) 263.

[Bec00] M. Beckmann, *Extraction of Polarised Quark Distributions of the Nucleon from Deep Inelastic Scattering at the HERMES Experiment*, Dissertation, Albert-Ludwigs-Universität Freiburg (2000).

[Bec02] M. Beckmann et al, *The Longitudinal Polarimeter at HERA*, Nucl. Instr. Meth. **A 479/2-3** (2002) 334-348.

[Bec03] M. Beckmann, *Target polarisation values and their uncertainties used by the Deltaq analysis group for the 1996 to 2000 running periods*, HERMES Internal Note 03-005, (2003).

[Ben01] Th. Benisch et al., *The luminosity monitor of the HERMES experiment at DESY*, Nucl. Instr.and Meth. **A471** (2001) 314

[Ber98] S. Bernreuther, *The HERMES Back Drift Chambers*, Nucl. Instrum. Meth. **A416** (1998) 45-58.

[Beu01] M. G. van Beuzekom et al., *First experience with the HERMES silicon detector*, Nucl. Instrum. Meth. **A 461** (2001) 247-250. **A416** (1998) 45-58.

[Bjo66] J. D. Bjorken, *Applications of the chiral U(6) x (6) algebra of current densities*, Phys. Rev. **148** (1966) 1467-1478.

[Bjo69] J. D. Bjorken, E. A. Paschos, *Inelastic Electron-Proton and Gamma-Proton Scattering, and the Structure of the Nucleon*, Phys. Rev. **185** (1969) 1975-1982.

[Blo70] By E.D. Bloom, *Recent Results in Inelastic Electron Scattering*, Presented at the XV International Conference on High Energy Physics, Kiev, USSR, Aug 26-Sep4, 1970, SLAC-PUB-0796 (1970).

[Blo98] V. Blobel, E. Lohrmann, *Statistische und numerisch Methoden der Datenanalyse*, Textbook, B.G. Teubner Stuttgart-Leipzig (1998).

[Blü02] J. Bluemlein,H. Boettcher *QCD Analysis of polarized deep inelastic data and parton distributions*, Nucl. Phys. **B636** (2002) 225-263.

[Bod90] G. T. Bodwin, J. Qui, *Gluonic contribution to g_1 and its relationship to the spin-dependent parton distributions*, Phys. Rev. **D41**, (1990) 2755.

[Boj99] I. Bojak, M. Stratmann *Photoproduction of heavy quarks in next-to-leading order QCD with longitudinally polarized initial states*, Nucl. Phys. **B540** (1999) 345-381.

[Bra80] R. Brandelik et al., TASSO Collaboration, *EVIDENCE FOR A SPIN ONE GLUON IN THREE JET EVENTS*, Phys. Lett. **B97** (1980) 453.

[Bra97] A. Bravar et al., *POLDIS: A Monte Carlo for polarized (semiinclusive) deep inelastic scattering*, Comput. Phys. Commun. **105** (1997) 42-61.

[Bra98] A. Bravar et al., *Large gluon polarization from correlated high-p_T hadron pairs in polarized electroproduction*

[Bra01] J. T. Brack et al., *The HERMES forward tracking chambers: construction, operation and aging effects*, Nucl. Instr. Meth. **A 469** (2001) 47-54.

[Bre98] J. Breitweg et al.,ZEUS Collaboration , *Elastic and proton dissociative rho0 photoproduction at HERA*, Eur. Phys. J. **C2** (1998) 247-267.

[Bud75] V. M. Budnev et al., *The two-photon particle production mechanism. Physical problems. Applications. Equivalent photon approximation*, Phys. Rept. **15** (1974) 181-281.

[Bun00] G. Bunce et al. *Prospects for spin physics at RHIC*, Ann. Rev. Nucl. Part. Sci. **50**, (2000) 525-575.

[Cal69] C. G. Callan, D. J. Gross, *High-Energy Electroproduction and the Costitution of the Electric Current* Phys. Rev. Lett. **22** (1969) 156.

[Car88] R. D. Carlitz et al., *The role of the axial anomaly in measuring spin dependent parton distributions*, Phys. Lett. **B214** (1988) 229.

[Cas81] D.G. Cassel et al, *Exclusive rho0, omega and phi electroproduction*, Phys. Rev. **D24** (1981) 2787.

[Cas98] C. Caso et al. (Particle Data Group), *The Review of Particle Physics*, Eur. Phys. J. **C3** (1998) 1.

[Cer03] `http://wwwasd.web.cern.ch/wwwasd/geant/\newline`
`http://wwwasd.web.cern.ch/wwwasd/cernlib/`

.

[Cri97] J. A. Crittenden, *Exclusive production of neutral vector mesons at the electron - proton collider hera*, hep-ph/9704009, Springer , Berlin, Germany (1997).

[DeF98] D. de Florian, W. Vogelsang, *Next-to-leading order QCD corrections to inclusive-hadron photoproduction in polarized lepton-proton collisions*, Phys. Rev. **D57** (1998) 4376.

[DeN02] L. de Nardo, *Measurement of the Strucure Function g_1^d at Hermes and Extraction of Polarized Parton Distributions*, Ph.D. Thesis, University of Alberta (2002).

[DeN03] L. de Nardo, *How to interpret asymmetry differences due to different luminosity measurements*, Internal Note, (2003).

[DeN04] L. de Nardo, *private communication* (2004).

[DeS00] D. De Schepper, J. O. Hansen, H. E. Jackson, T. G. O'Neill, D. Potterveld, J. L. Orrell, *The HERMES Cerenkov Detector*, HERMES internal note 00-021 (2000).

[Dok77] Y. L. Dokshitzer *Calculation of the structure functions for deep inelastic scattering and e+ e- annihilation by perturbation theory in quantum chromodynamics* (in russian), Sov. Phys. JETP **46** (1977) 641-653.

[Don92] A. Donnachie, P. V. Landshoff, *Total cross sections*, Phys. Lett. **B296** (1992) 227.

[Don98] A. Donnachie, P. V. Landshoff, *Small x: Two Pomerons!*, Phys. Lett. **B437** (1998) 408-416.

[Ell74] J. R. Ellis, Robert L. Jaffe, *A sum rule for deep inelastic electroproduction from polarized protons*, Phys. Rev. **D9** (1974) 1444, Erratum-ibid. **D10** (1974) 1669.

[Ell03] F. Ellinghaus, *Beam-Charge and Beam-Spin Azimuthal Asymmetries in Deeply-Virtual Compton Scattering*, Dissertation, Humboldt-Universität zu Berlin, (2003).

[Els02] U. Elschenbroich, *Analysis of Luminosity Monitor Data for Different Years*, HERMES Internal Note 02-013 (2002).

[Eng96] R. Engel, *Hadronic photon-photon interactions at high-energies*, Phys. Rev. **D54** (1996) 4244-4262.

[Fey69] R. P. Feynman, *Very High-Energy Collisions of Hadrons*, Phys. Rev. Lett. **23** (1969) 1415-1417.

[Fie78] R. D. Field, R. P. Feynman, *A parametrization of the properties of quark jets*, Nucl. Phys. **B136** (1978) 1.

[Fra79] H. Fraas, *Cross-section asymmetries in vector meson electroproduction and in inelastic e p scattering with polarized beam and target*, Nucl. Phys. **B113** (1976) 532.

[Fri00] C.Friberg, T.Sjöstrand, *Total Cross Sections and Event Properties from Real to Virtual Photons*, J. High Energy Phys. (2000) 0009:010.

[Gar03] E. Garutti, *Nuclear Effects in Semi-Inclusive Deep Inelastic Scattering off ^{84}Kr and other nuclei*, Dissertation, Universiteit van Amsterdam (2003).

[Gär01] Y. Gärber, *Messung der Proton-Spinstrukturfunktion g_1 bis zu kleinstmöglichen Bjorken-x mit dem HERMES-Experiment*, Dissertation, Humboldt-Universität, Berlin (2001).

[Gei98] P. Geiger, *Measurement of Fragmentation Functions at HERMES*, Dissteration, Ruprecht-Karls-Universität, Heidelberg (1998).

[Geh95] T. Gehrmann, W. J. Stirling, *Spin dependent parton distributions from polarized structure function data.*, Z. Phys. **C65** (1995) 461-470.

[Geh96] T. Gehrmann, W. J. Stirling, *Polarized parton distributions in the nucleon*, Phys. Rev. **D53**, (1996) 6100-6109.

[Ger21] W. Gerlach, O. Stern, Z. Physik, **8** (1921), 110.

[Glü92] M. Glück et al., *Parton structure of the photon beyond the leading order*, Phys. Rev. **D45** (1992) 3986-3994.

[Glü92a] M. Glück, W. Vogelsang, *Polarized parton distributions of the photon*, Z. Phys. **C55** (1992) 353-356.

[Glü96] M. Glück et al., *Probing the parton densities of virtual photons at e p colliders*, Phys. Rev. **D54** (1996) 5515-5522.

[Glü98] M. Glück et al., *Dynamical parton distributions revisited*, Eur. Phys. J **C5** (1998) 461.

[Glü01] M. Glück et al., *Models for the polarized parton distributions of the nucleon*, Phys. Rev. D63 (2001) 094005.

[Glü01a] M. Glück et al., *Spin dependent structure functions of real and virtual photons*, Eur. Phys. J. **C20** (2001) 271-281.

[Glü01b] M. Glück et al., *Spin dependent structure functions of the photon*, Phys. Lett. **B503** (2001) 285-291.

[Got00] Y. Goto et al, Asymmetry Analysis Collaboration, *Polarized parton distribution functions in the nucleon*, Phys. Rev. **D62** (2000) 034017.

[Gri87] D. J. Griffiths, *Introduction to Elementary Particle Physics*, Textbook, John Wiley, New York (1987).

[Gri72] V.N. Gribov, L.N. Lipatov, *Deep inelastic e p scattering in perturbation theory*, Sov. J. Nucl. Phys. **15**, (1972) 438-450.

[Gro97] J. Große-Knetter, *Measurement of Elastic ω Photoproduction at HERA*, Dissertation, Universtät Hamburg, (1997).

[Hag02] L. K. Hagiwara et al., *The Review of Particle Physics*, Phys. Rev. **D66**, 010001 (2002).

[Hal84] F. Halzen, A.D. Martin, *Quarks and Leptons: An Introductory Course in Modern Particle Physics*, Textbook, John Wiley and Sons, New York, (1984).

[Han63] L. N. Hand, Phys. Rev. *Experimental investigation of pion electroproduction*, **129** (1963), 1834.

[Har02] M. Hartig *private communication*, (2002).

[Hil03] A. Hillenbrand, *Tuning of the LUND Model for Fragmentation Functions and Purities*, 11th International Workshop on Deep Inelastic Scattering (DIS 2003), St. Petersburg, Russia, Apr 23 - 27, (2003).

[Hom03] B. Hommez, *Study of Fragmentation Processes in the HERMES experiment using a Ring Imaging Cerenkov Detector*, Ph.D. thesis, University of Gent, (2003).

[Hom03a] B. Hommez, H. Jackson, R. Kaiser, Y. Miyachi, *Using the RICH Detector for Physics Analysis*, HERMES internal note, (2003).

[Ing97] G. Ingelman, M. Thunman, *Signals for Intrinsic Charm in High Energy Interactions*, Z. Phys. **C73** (1997) 505-515.

[Ing97a] G. Ingelman et al., *LEPTO 6.5: A Monte Carlo generator for deep inelastic lepton - nucleon scattering*, Comput. Phys. Commun. **101** (1997) 108-134.

[Jaf96] R. L. Jaffe, *Spin, Twist and Hadron Structure in Deep Inelastic processes*, hep-ph/9602236 (1996).

[Jäg03] B. Jäger et al., *Next-to-leading order qcd corrections to high p(t) pion production in longitudinally polarized pp collisions*, Phys. Rev. **D67** (2003) 054005.

[Jäg03a] B. Jäger et al., *Longitudinally Polarized Photoproduction of Inclusive Hadrons Beyond the Leading Order*, Phys. Rev. **D68** (2003) 114018.

[Ji97a] X. Ji, *Gauge-Invariant Decomposition of Nucleon Spin*, Phys. Rev. Lett. **78** (1997) 610-613.

[Ji97b] X. Ji, *Deeply virtual compton scattering*, Phys. Rev. **D55** (1997) 7114-7125.

[Jgo00] A.A. Jgoun, S.I. Manaenkov, *Measurement of z- and x-dependence of the mean value of pT for h, pi, and K0s*, HERMES Internal note 00-025 (2000).

[Kla02] M. Klasen, *Theory of Hard Photoproduction*, Rev. Mod. Phys. **74** (2002) 1221.

[Kni01] B. A. Kniehl et al., *Testing the universality of fragmentation functions*, Nucl. Phys. **B597** (2001) 337-369.

[Koc02] N.I. Kochelev et al. *A mechanism for the double spin asymmetry in electromagnetic rho production at hermes*, Phys. Rev. **D65** (2002) 097504.

[Koc03] N.I. Kochelev et al., *DIS structure functions and the double spin asymmetry in rho0 electroproduction within a regge approach*, Phys. Rev. **D67** (2003) 074014.

[Koc04] N.I. Kochelev, A. V. Vinnikov, *private communication* (2004).

[Kre00] S. Kretzer, *Fragmentation Function from flavor-inclusive and flavor-tagged e^+e^- annihilations*, Phys. Rev. **D62** (2000), 054001.

[Kre01] S. Kretzer et al., *Fragmentation functions from semiinclusive DIS pion production and implications for the polarized parton densities*, Eur. Phys. J. **C22** (2001) 269-276.

[Lae00] E. Laenen et al., *Higher order QCD corrections in prompt photon production*, Phys. Rev. Lett. **84** (2000) 4296-4299.

[Lai98] H. Lai, H. Li, *Origin of the k(t) smearing in direct photon production*, Phys. Rev. **D58** (1998) 114020.

[Lai00] H. L. Lai et al., The CTEQ Collaboration, *Global qcd analysis of parton structure of the nucleon: CTEQ5 parton distributions*, Eur. Phys. J. **C12** (2000) 375-392.

[Lai02] H. L. Lai et al., The CTEQ Collaboration, *New Generation of Parton Distributions with Uncertainties from Global QCD Analysis*, JHEP **0207** (2002) 012.

[Lam98] B. Lampe, E. Reya, *Spin Physics and Polarized Structure Functions*, Phys. Rept. **332** (2000) 1-163.

[Lev65] E. M. Levin, L. L. Frankfurt *The quark hypothesis and relations between cross-sections at high-energies*, JETP Lett. **2** (1965) 65-70.

[Lev03] B. Levchenko, The ZEUS Colaboration, *Strangeness in DIS*, Proceedings of High Energy Physics (HEP) conference EPS03, Aachen, Germany, Eur. Phys. J. **C** (2003).

[Lie01] P. Liebing, *Double Spin Asymmetries in Single Hadron Quasi-real Photoproduction at HERMES*, Diplomarbeit, Humboldt-Universität zu Berlin, DESY-THESIS-2001-003 (2001).

[Lim03] H. Lim, *ZEUS Results on Inclusive Diffraction*, Talk given at the XI International Workshop on Deep Inelastic Scattering (DIS2003), St. Petersburg, 23-27 April 2003.

[Lip66] H.J. Lipkin, F. Scheck, *Quark Model for Forward Scattering Amplitudes*, Phys. Rev. Lett. **16** (1966) 71-75.

[Lip02] K. Lipka, *Double-Spin Asymmetries in Diffractive Vector-Meson Production at HERMES*, Dissertation, Humboldt University of Berlin (2002).

[Mac87] R. Machleidt et al. *The Bonn meson exchange model for the nucleon nucleon interaction*, Phys. Rept. **149** (1987) 1-89.

[Man92] A. V. Manohar, *An introduction to spin dependent deep inelastic scattering*, Lectures presented at Lake Louise Winter School Feb. 1992, hep-ph/9204208, (1992).

[Man92a] L. Mankiewicz et al. *PEPSI: A Monte Carlo generator for polarized leptoproduction*, Comput. Phys. Commun. **71**, (1992) 305-318.

[Mar98] A. D. Martin et al., Parton distributions: a new global analysis, Eur. Phys. J. **C4** (1998) 463.

[Mar02] A. D. Martin et al., *MRST2001: partons and alpha(s) from precise deep inelastic scattering and tevatron jet data*, Eur. Phys. J. **C23**, (2002) 73-87.

[Mei00] F. Meissner,*Measurement of the J/ψ Cross Section and Double-Spin Asymmetries in Vector Meson Production in Polarised Lepton-Nucleon Scattering at HERMES*, Dissertation, Humbolt-Universität zu Berlin (2000).

[Mer96] R. Mertig, W.L. van Neerven, *The calculation of the two loop spin splitting functions p(ij)(1)(x)*, Z. Phys. **C70** (1996) 637-654.

[Men01] F. Menden *Determination of the Gluon Polarization in the Nucleon*, Dissertation, Albert-Ludwigs-Universitaet Freiburg im Breisgau, DESY-Thesis 2001-60 (2001).

[Mex03] V. Mexner, *private communication* (2003).

[Mex03a] V. Mexner, *MC Studies of single high-pt hadrons*, Talk given at HERMES Collaboration Meeting, March 2003 (2003).

[Mir97] E. Mirkes, S. Willfahrt, *QCD corrections to jet production in polarized ep scattering*, hep-ph/9711434 (1997).

[Miy03] Y.Miyachi, H.Nihongi, J. Shirono, *Systematic uncertainties on RICH P-matrix*, HERMES Internal note, (2003).

[Mo69] L.W. Mo, Y.S. Tsai, *Radiative corrections to Elastic and Inelasti ep and μp Scattering*, Rev. Mod. Phys. 41, 205 (1969).

[Mon94] L. Montanet et al., *Review of particle properties. Particle Data Group.*, Phys. Rev. **D50**, (1994) 1173-1823.

[Nas98] J. P. Nassalski, *Determination of delta(g)/g in COMPASS experiment at CERN*, Prepared for Cracow Epiphany Conference on Spin Effects in Particle Physics and Tempus Workshop, Cracow, Poland, 9-11 Jan 1998, Acta Phys. Polon. **B29** (1998), 1315-1341.

[Nas03] A. Nass et al., *The HERMES Polarized Atomic Beam Source* Nucl. Instrum. and Meth. **A 505/3** (2003) 633.

[Nav03] G. A. Navarro, R. Sassot, *Consistency in NLO analyses of inclusive and semi-inclusive polarized DIS data*, Eur. Phys. J. **C28** (2003) 321-328.

[Per94] J. Peralta et al., *Photoproduction of large-p_T hadrons by polarized beam and target*, Phys. Rev. **D49** (1994) 3148.

[Plo00] H. Plothow-Besch, *PDFLIB User's Manual*, CERN Computer Program Library, entry W5051, (2000).

[Pum02] J. Pumplin et al., *New generation of parton distributions with uncertainties from global qcd analysis*, JHEP **0207** (2002) 012.

[Rak00] G. L. Rakness, *Spin Polarization Transfer in Exclusive Phi Electroproduction*, Ph.D. thesis, University of Colorado at Boulder, (2000).

[Reg59] T. Regge., *Introduction to complex orbital momenta*, Nuovo Cim. **14** (1959) 951.

[Reg03] D. Reggiani, *Precision Polarization Measurement of ther HERMES H/D Gas Target*, Dissertation, Universita degli Studi di Ferrara, (2003).

[Rio74] E. M. Riordan et al., *Tests of Scaling of the Proton Electromagnetic Structure Functions*, Phys. Lett. **B52** (1974) 249.

[Rob90] R. G. Roberts, *The Structure of the Proton*, Textbook, Cambridge University Press, (1990).

[Ros66] M. Ross, L. Stodolsky, *Photon Dissociation Model for Vector-Meson Photoproduction*, Phys. Rev. **149** (1966) 1172.

[Rys92] M. G. Ryskin, *Cross-sections for high-energy hadron interactions in the leading log approximation of QCD*, Z. Phys. C56 (1992) 253-259.

[Sak60] J. J. Sakurai, *Theory of strong interactions*, Annals Phys. **11** (1960) 1-48.

[Sak72] J. J. Sakurai, D. Schildknecht, *Generalized vector dominance and inelastic electron - proton scattering*, Phys. Lett. **B40** (1972) 121-126.

[Schi73] K. Schilling, G. Wolf, *How to analyse Vecor-Meson Production in inelastic Lepton Scattering*, Nucl. Phys. B 61 (1973), 381.

[Schu93] G.A Schuler, T. Sjöstrand, *Toward a complete description of high-energy photoproduction*, Phys. Lett. B 300 (1993) 169.

[Schu96] G. A. Schuler , T. Sjöstrand, *Parton distributions of the virtual photon*, Phys. Lett. **B376** (1996) 193-200.

[Schä04] A. Schäfer, *private communication* (2004).

[Seh74] L. M. Sehgal, *Angular momentum composition of the proton in the quark parton model*, Phys. Rev. **D10** (1974) 1663, Erratum-ibid. **D11** (1975) 2016.

[Sjö94] T.Sjöstrand et al., *High-Energy-Physics Event Generation with PYTHIA 5.7 and JETSET 7.4*, Computer Physics Commun. **82** (1994) 74.

[Sjö01] T. Sjöstrand, P. Eden, C. Friberg, L. Lönnblad, G. Miu, S. Mrenna, E. Norrbin, PYTHIA 6.2 Physics and Manual, Computer Physics Commun. **135** (2001) 238.

[Sjö02] T. Sjöstrand, *private communication* (2002).

[Sok64] A. A. Sokolow, I. M. Ternov, *On Polarization and Spin Effects in the Theory of Synchrotron Radiation*, Sov. Phys. Dokl. **8** (1964) 1203.

[Ste95] G. Sterman et al., *Handbook of Perturbative QCD*, Reviews of Modern Physics, **67**, Number 1, (1995), 157-248.

[Str97] M. Stratmann, W. Vogelsang, *Photoproduction of jets and heavy flavors at future polarized e p colliders*, Z. Phys. **C74** (1997) 641.

[Str02] M. Stratmann, *Exploring nucleon spin structure in longitudinally polarized collisions*, Invited talk at 15th International Spin Physics Symposium (SPIN 2002), Long Island, New York, hep-ph/0211223, published in AIP Conf. Proc. **675** (2003) 112-121.

[Szc00a] A. Szczurek, V. Uleshchenko *On the range of validity of the QCD improved parton model*, Phys. Lett. **B475** (2000) 120-126.

[Szc00b] A. Szczurek, V. Uleshchenko *Nonpartonic components in the nucleon structure functions at small Q**2 in the broad range of x*, Eur. Phys. J. **C12** (2000) 663-671.

[Tho01] A. W. Thomas, W. Weise *The Structure of the Nucleon*, Textbook, Wiley-VCH Verlag Berlin GmbH, Berlin (2001).

[Tip99] B. Tipton, *Measurement of Polarized Parton Distributions With Spin-dependent Deep - inelastic Scattering*, Ph.D. Thesis, Massachusetts Institite of Technology, Boston (1999).

[Tyt01] M Tytgat, *Diffractive production of ρ^0 and ω vector mesons at HERMES*, DESY-Thesis 2001-018 (2001).

[Vog96] W. Vogelsang, *The spin dependent two loop splitting functions*, Nucl. Phys. **B475** (1996), 47-72. W. Vogelsang, *A rederivation of the spin dependent next-to-leading order splitting functions*, Phys. Rev. **D54** (1996) 2023-2029.

[Wan96] W. Wander, *Rekonstruktion hochergetischer Streuereignisse im HERMES Experiment*, Dissertation, Friedrich-Alexander Universität Erlangen-Núrnberg (1996).

[Wei00] S. Weinzierl, *Introduction to Monte Carlo Methods*, hep-ph/0006269 (2000).

[Wen03] J. Wendland, *Polarized Parton Distributions Measured At The Hermes Experiment*, Ph.D. Thesis, Simon Fraser University, (2003). (1996)

[Wen99] J.Wendland, *Improved Particle Identification at HERMES and Polarised Valence Quark Distributions in the Proton*, Thesis, Simon Fraser University (1999).

[Whi90] L. W. Whitlow et al., *A Precise Extraction of R=sigmaL/sigmaT From a Global Analysis of the SLAC Deep Inelastic ep and ed Scattering Cross-Sections*, Phys. Lett. **B250** (1990) 193-198.

[Zij94] E. B. Zijlstra, W. L. van Neerven, *Order alpha-s**2 corrections to the polarized structure function g1 (x,q**2)*, Nucl. Phys. **B417**, (1994) 61-100, Erratum-ibid. **B426** (1994) 245.